BIODEVICES 2008

International Conference on
Biomedical Electronics and Devices

Proceedings

Volume 2

Funchal, Madeira - Portugal · 28 - 31 January, 2008

TECHNICAL CO-SPONSORSHIP BY

IEEE EMB

CO-ORGANIZED BY

INSTICC

UNIVERSIDADE da MADEIRA

IN COOPERATION WITH

aaai

INSTICC PRESS

BIODEVICES 2008

Proceedings of the
First International Conference on
Biomedical Electronics and Devices

Volume 2

Funchal, Madeira - Portugal

January 28 – 31, 2008

Co-organized by
INSTICC – Institute for Systems and Technologies of Information, Control and Communication
and
UMA – University of Madeira

Technical Co-sponsorship by
IEEE EMB – Engineering in Medicine and Biology Society

In Cooperation with
AAAI – Association for the Advancement of Artificial Intelligence

Edited by Teodiano Bastos e Filho and Hugo Gamboa

Printed in Portugal

ISBN: 978-989-8111- 17-3

Depósito Legal: 268553/07

http://www.biodevices.org

secretariat@biodevices.org

BIODEVICES is part of BIOSTEC – International Joint Conference on Biomedical Engineering Systems and Technologies

BRIEF CONTENTS

INVITED SPEAKERS

Sérgio Cerutti

Polytechnic University of Milan

Italy

Kevin Warwick

University of Reading

U.K.

Fernando Henrique Lopes da Silva

University of Amsterdam

The Netherlands

Vipul Kashyap

Partners HealthCare System, Clinical Informatics R&D

U.S.A.

David Hall

Research Triangle Institute in North Carolina

U.S.A.

Albert Cook

University of Alberta, Faculty of Rehabilitation Medicine

Canada

ORGANIZING AND STEERING COMMITTEES

CONFERENCE CO-CHAIRS

Ana Fred, IST- Technical University of Lisbon, Portugal

Joaquim Filipe, INSTICC / Polytechnic Institute of Setúbal, Portugal

Hugo Gamboa, Telecommunications Institute / Portugal

Jorge Cardoso, University of Madeira - UMA / Madeira, Portugal

PROGRAM CO-CHAIRS

Teodiano Freire Bastos Filho, Federal University of Espírito Santo, Brazil

Hugo Gamboa, Telecommunications Institute, Portugal

LOCAL CHAIR

Paulo Sampaio, University of Madeira - UMA, Portugal

PROCEEDINGS PRODUCTION

Paulo Brito, INSTICC, Portugal

Marina Carvalho, INSTICC, Portugal

Helder Coelhas, INSTICC, Portugal

Vera Coelho, INSTICC, Portugal

Andreia Costa, INSTICC, Portugal

Bruno Encarnação, INSTICC, Portugal

Bárbara Lima, INSTICC, Portugal

Vitor Pedrosa, INSTICC, Portugal

Vera Rosário, INSTICC, Portugal

Mónica Saramago, INSTICC, Portugal

CD-ROM PRODUCTION

Paulo Brito, INSTICC, Portugal

GRAPHICS PRODUCTION AND WEB DESIGNER

Marina Carvalho, INSTICC, Portugal

SECRETARIAT AND WEBMASTER

Marina Carvalho, INSTICC, Portugal

PROGRAM COMMITTEE

Julio Abascal, University of the Basque Country-Euskal Herriko Unibertsitatea, Spain

Amiza Mat Amin, Universiti Malaysia Terengganu, Malaysia

Rodrigo Varejão Andreão, UFES, Brazil

Ramon Pallàs Areny, Technical University of Catalonia (UPC), Spain

Luis Azevedo, Instituto Superior Técnico - Technical University of Lisbon, Portugal

Rafael Barea, University of Alcalá, Spain

Antonio Barrientos, Universidad Politécnica de Madrid, Spain

Roberto Boeri, Universidad Nacional de Mar del Plata, Argentina

Luciano Boquete, Alcala University, Spain

Susana Borromeo, Universidad Rey Juan Carlos Spain, Spain

Eduardo Caicedo Bravo, Universidad del Valle, Colombia

Enrique A. Vargas Cabral, Facultad de Ciencias y Tecnología - Universidad. Católica de Asunción, Paraguay

Sira Palazuelos Cagigas, University of Alcalá, Spain

Leopoldo Calderón, Consejo Superior de Investigaciones Científicas - IAI, Spain

Alicia Casals, Technical university of Catalonia, Spain

Gert Cauwenberghs, University of California San Diego, U.S.A.

Ramón Ceres, Instituto de Automatica Industrial- CSIC, Spain

Luca Cernuzzi, Universidad Católica "Nuestra Señora de la Asunción", Paraguay

Alberto Cliquet Jr., USP, UNICAMP, Brazil

Fernando Cruz, School of Technology of Setúbal/Polytechnic Institute of Setúbal, Portugal

Pedro Pablo Escobar, Ingeniería Electromedica, Facultad de Ingeniería, Universidad Nacional del Centro, Argentina

Marcos Formica, Bioengineering Faculty, Entre Ríos National University, Argentina

Juan Carlos Garcia Garcia, University of Alcala, Spain

Gerd Hirzinger, German Aerospace Center (DLR), Germany

Jongin Hong, Imperial College London, U.K.

Giacomo Indiveri, UNI - ETH Zurich, Switzerland

Dinesh Kumar, RMIT University, Australia

Eric Laciar Leber, Universidad Nacional de San Juan, Argentina

José Luis Martinez, Universidad Politécnica de Madrid, Spain

Manuel Mazo, University of Alcala, Spain

Paulo Mendes, University of Minho, Portugal

José del R. Millán, IDIAP Research Institute, Switzerland

Joseph Mizrahi, Technion, Israel Institute of Technology, Israel

Raimes Moraes, Federal University of Santa Catarina, Brazil

Pedro Noritomi, Renato Archer's Research Center - CenPRA, Brazil

Maciej J. Ogorzalek, Jagiellonian University, Poland

Kazuhiro Oiwa, National Institute of Information and Communications Technology, Japan

José Raimundo de Oliveira, Universidade Estadual de Campinas, Brazil

Evangelos Papadopoulos, National Technical University of Athens, Greece

Laura Papaleo, University of Genova, Italy

Francisco Novillo Parales, Escuela Superior Politécnica del Litoral, ESPOL, Ecuador

Qibing Pei, University of California, Los Angeles, U.S.A.

José M. Quero, Universidad de Sevilla, Spain

Antonio Quevedo, University of Campinas, Brazil

Alejandro Ramirez-Serrano, University of Calgary, Canada

Adriana María Rios Rincón, Universidad del Rosario, Colombia

Joaquin Roca-Dorda, Universidad Politécnica de Cartagena (UPCT), Spain

Adson da Rocha, University of Brasilia, Brazil

Joel Rodrigues, Institue of Telecommunications / University of Beira Interior, Portugal

PROGRAM COMMITTEE (CONT.)

Carlos F. Rodriguez, Universidad de Los Andes, Colombia

Mario Sarcinelli-Filho, Federal University of Espirito Santo, Brazil

Fernando di Sciascio, Universidad Nacional de San Juan, Argentina

Jorge Vicente Lopes da Silva, "Renato Archer" Research Center, Brazil

Amir M. Sodagar, University of Michigan, U.S.A.

Juan Hernández Tamames, Rey Juan Carlos University, Spain

Mário Vaz, Faculty of Engineering University of Porto, Portugal

António Veloso, Faculty of Human Kinetics, Portugal

Peter Walker, University of Leeds, U.K.

Jonathan Wolpaw, Wadsworth Center, NY State Department of Health, U.S.A.

Miguel Yapur, Escuela Superior Politécnica del Litoral (ESPOL), Ecuador

AUXILIARY REVIEWERS

José M. R. Ascariz, Alcala University, Spain

Leandro Bueno, Politechnique University of Madrid, Spain

Natalia López Celan, Gabinete de Tecnología Médica, Instituto de Automática, Facultad Ingeniería, Universidad Nacional de San Juan, Argentina

Andre Ferreira, Federal University of Espirito Santo, Brazil

Vicente González, DEI - Univerisdad Católica "Nuestra Señora de la Asunción", Paraguay

Muhammad Suzuri Hitam, Universiti Malaysia Terengganu, Malaysia

Joaquin Roca-Gonzalez, Polytechnic University of Cartagena, Spain

Rober Marcone Rosi, Federal University of Espirito Santo, Brazil

Evandro Ottoni Teatini Salles, Federal University of Espirito Santo, Brazil

Hugo Humberto Plácido Silva, Instituto de Telecomunicações, Portugal

Andrés Valdéz, Gabinete de Tecnología Médica, Facultad Ingeniería, Universidad Nacional de San Juan, Argentina

SELECTED PAPERS BOOK

A number of selected papers presented at BIODEVICES 2008 will be published by Springer, in a book entitled Biomedical Engineering Systems and Technologies. This selection will be done by the conference co-chairs and program co-chairs, among the papers actually presented at the conference, based on a rigorous review by the BIOSTEC 2008 program committee members.

OFFICIAL CARRIER

FOREWORD

This volume contains the proceedings of the *First International Conference on Biomedical Electronics and Devices* (BIODEVICES 2008), organized by the Institute for Systems and Technologies of Information Control and Communication (INSTICC) and the University of Madeira, technically co-sponsored by the IEEE Engineering in Medicine and Biology Society (EMB) and in cooperation with AAAI.

The purpose of the *International Conference on Biomedical Electronics and Devices* is to bring together researchers and practitioners from electronics and mechanical engineering, interested in studying and using models, equipments and materials inspired from biological systems and/or addressing biological requirements. Monitoring devices, instrumentation sensors and systems, biorobotics, micro-nanotechnologies and biomaterials are some of the technologies addressed at this conference.

BIODEVICES is one of three integrated conferences that are co-located and constitute the International Joint Conference on Biomedical Engineering Systems and Technologies (BIOSTEC). The other two component conferences are HEALTHINF (International Conference on Health Informatics) and BIOSIGNALS (International Conference on Bio-inspired Systems and Signal Processing).

The joint conference, BIOSTEC, has received 494 paper submissions from more than 40 countries in all continents. 65 papers were published and presented as full papers, i.e. completed work (8 pages/30' oral presentation), 189 papers reflecting work-in-progress or position papers were accepted for short presentation, and another 86 contributions were accepted for poster presentation. These numbers, leading to a "full-paper" acceptance ratio below 14% and a total oral paper presentations acceptance ratio below 52%, show the intention of preserving a high quality forum for the next editions of this conference.

The conference included a panel and six invited talks delivered by internationally distinguished speakers, namely: Sergio Cerutti, Kevin Warwick, F. H. Lopes da Silva, Vipul Kashyap, David Hall and Albert Cook. Their participation has positively contributed to reinforce the overall quality of the Conference and to provide a deeper understanding of the field of Biomedical Engineering Systems and Technologies.

The proceedings of the conference will be indexed by several major indices including DBLP, INSPEC and ISI-Proceedings and it will also be submitted for indexing to EI. A book with the revised versions of a short list of selected papers from the conference will be published by Springer-Verlag in the new CS book series: Communications in Computer and Information Science (CCIS). Additionally, a special issue of the IEEE Transactions on Biomedical Circuits and Systems will be edited based on the very best papers of the conference.

The program for this conference required the dedicated effort of many people. Firstly, we must thank the authors, whose research and development efforts are recorded here. Secondly, we thank

FOREWORD (CONT.)

the members of the program committee and the additional reviewers for their diligence and expert reviewing. Thirdly, we thank the keynote speakers for their invaluable contribution and for taking the time to synthesise and prepare their talks. Fourthly, we thank the program chairs, Teodiano Freire Bastos Filho and Hugo Gamboa, whose collaboration was much appreciated. Finally, special thanks to all the members of the INSTICC team, especially Marina Carvalho at the conference secretariat, and the local organising committee from the University of Madeira, especially Jorge Cardoso and Paulo Sampaio, whose collaboration was fundamental for the success of this conference.

This year, the organization will distribute two paper awards at the conference closing session: the best paper award and the best student paper award. The decision was mainly based on the paper classifications provided by the Program Committee.

We wish you all an exciting conference and an unforgettable stay in the lovely island of Madeira. We hope to meet you again next year for the 2nd BIODEVICES, details of which are available at http://www.biodevices.org.

Joaquim Filipe

INSTICC/Polytechnic Institute of Setúbal

CONTENTS

INVITED SPEAKERS

KEYNOTE LECTURES

MULTIVARIATE, MULTIORGAN AND MULTISCALE INTEGRATION OF INFORMATION IN BIOMEDICAL SIGNAL PROCESSING

Sergio Cerutti
Department of Bioengineering, Polytechnic University, Milano, Italy
sergio.cerutti@polimi.it

Abstract: Biomedical signals carry important information about the behavior of the living systems under studying. A proper processing of these signals allows in many instances to obtain useful physiological and clinical information. Many advanced algorithms of signal and image processing have recently been introduced in such an advanced area of research and therefore important selective information is obtainable even in presence of strong sources of noise or low signal/noise ratio. Traditional stationary signal analysis together with innovative methods of investigation of dynamical properties of biological systems and signals in second-order or in higher-order approaches (i.e., in time-frequency, time-variant and time-scale analysis, as well as in non linear dynamics analysis) provide a wide variety of even complex processing tools for information enhancement procedures. Another important innovative aspect is also remarked: the integration between signal processing and modeling of the relevant biological systems is capable to directly attribute patho-physiological meaning to the parameters obtained from the processing and viceversa the modeling fitting could certainly be improved by taking into account the results from signal processing procedure. Such an integration process could comprehend parameters and observations detected at different scales, at different organs and with different modalities. This approach is reputed promising for obtaining an olistic view of the patient rather than an atomistic one which considers the whole as a simple sum of the single component parts.

BRIEF BIOGRAPHY

Sergio Cerutti is Professor in Biomedical Signal and Data Processing at the Department of Bioengineering of the Polytechnic University in Milano, Italy. In the period 2000-2006 he has been the Chairman of the same Department. His research interests are mainly in the following topics: biomedical signal processing (ECG, blood pressure signal and respiration, cardiovascular variability signals, EEG and evoked potentials), neurosciences and cardiovascular modelling. In his research activity he has put emphasis on the integration of information at different modalities, at different sources and at different scales in various physiological systems. Since 1983 he has taught a course at a graduate and a doc level on Biomedical Signal Processing and Modelling at Engineering Faculties (Milano and Roma) as well as at Specialisation Schools of Medical Faculties (Milano and Roma). He has been Elected Member of IEEE-EMBS AdCom (Region 8) in the period 1993-1996. He is actually Fellow Member of IEEE and of EAMBES and Associate Editor of IEEE Trans BME. He is a member of the Steering Committee of the IEEE-EMBS Summer School on Biomedical Signal Processing: he was the local organiser of four Summer Schools held in Siena. He has been Visiting Professor at Harvard-MIT Division Health Science and Technology, Boston, USA for an overall period of 1 year. He is the Author of more than 400 international scientific contributions (more than 180 on indexed scientific journals).

1 INTRODUCTION

Biomedical signals and imaging carry important information about the behavior of the living systems under studying. A proper processing of these signals and images allow in many instances to obtain useful physiological and clinical information. Actually, many advanced algorithms of digital signal and image processing are at disposal and therefore

important selective information is now obtainable even in presence of strong sources of noise or low signal/noise ratio. In most of the cases it is not sure whether such sources might derive even by complex and unknown interactions with other biological systems whose implications could be important from the physiological or clinical standpoints. Traditional stationary signal analysis together with innovative methods of investigation of dynamical properties of biological systems and signals in second-order or in higher-order approaches (i.e., in time-frequency, time-variant and time-scale analysis, as well as in non linear dynamics analysis) provide a wide variety of even complex processing tools for information enhancement procedures in the challenging studying of a better explanation of many physiological and clinical phenomena.

2 INTEGRATION BETWEEN SIGNAL PROCESSING AND PHYSIOLOGICAL MODELING

Another important innovative aspect to improve the information content from biomedical data is constituted by the integration between signal processing and modeling of the relevant biological systems, thus directly attributing patho-physiological meaning to the model parameters obtained from the processing; and, viceversa, the modeling fitting could certainly be improved by taking into account the results from signal/image processing procedures.

3 MONOVARIATE AND MULTIVARIATE SIGNAL PROCESSING

Other kinds of integration may be fulfilled, taking into account more signals from the same system in a multivariate way (i.e. from a single-lead vs multichannel EEG or ECG analysis) and combining also the action of different systems such as autonomic nervous system, cardiovascular and respiratory systems, etc. Sleep is a formidable example of multiorgan involvement in both physiological (sleep staging and correlation with cardiorespiratory system) and pathological conditions (sleep apnea, sleep deprivation, restless leg syndrome and so on).

4 MULTISCALE APPROACH

Further, modern rehabilition techniques (motor and /or cognitive) make use actually of objective indices obtained from the patient's biosignals and images to better "personalize" rehabilitation protocols (from EEG, EP's, ERP's, MRI, fMRI, NIRS, etc). In neurosciences such an integration process could comprehend parameters and observations detected also at different scales, from genome and proteome up to the single organ and to the entire body compartment. Examples will be described where an animal model (murine model) is developed by alterating a gene putative to a determined pathology (i.e.epilepsy) and changes in EEG signals are studied (spike/wave occurrences and modifications in signal power bands). In clinical applications, it is worth mentioning the important data fusion which could be fulfilled by the integration of simultaneous EEG recordings and fMRI in some epileptic patients during inter-critical or critical events.

Finally, another important integration can be obtained along different observation scales. Traditionally, biological signal analysis is carried out at the level of organ or system to be investigated (i.e., ECG or EEG signal, arterial blood pressure, respiration and so on). It is very clear the advantage of correlating this information with that one obtained about the same system, but at different scale level, i.e. at cellular level or even at subcellular level (for example, analyzing possible genetic correlates or typical patterns of proteins or even DNA/RNA sequences). Biomedical engineering as a dedicated discipline may strongly contribute to this multiscale information processing

Along this approach line, even the long-QT syndrome, can be efficiently studied at different scale level: a mutation in a portion of gene SCN5A which presents a phenotype compatible to long-QT3 type, is known to produce an altered function of Na+ channels. Through a proper model which describes the functioning of ventricular cells is possible to evidence that this alteration may induce a prolongation of QT duration, as detected on ECG tracing. This event is further correlated with an increased risk of ventricular tachyarrhythmias. Hence, the path is completed: from the genetic expression up to the disease manifestation (Clancy and Rudy, 1999), (Priori ey al., 2003). Many different signal processing and modeling are involved in this paradigmatic example: an integration along the various scales of observation may undoubtedly contribute to a better

understanding of the complex pathophysiological correlates.

A great effort is on course nowadays for creating very large databases and networking of models and technologies for integrating such information (Physiome project (Hunter et al., 2002), (Rudy, 2000) to be connected with Genome and Proteome projects and Virtual Physiological Human project – VPH – which is inserted into the activities of the 7th Framework Programme of EU).

Other examples are constituted by the studying of the profile of expressed proteins in 2D-gel supports, or after mass-spectrometry analysis, relative to a variety of pathologies (i.e. epilepsy, peripheral neuropathies or Amyotrophic Lateral Sclerosis (ALS), or in oncological studies) thus singling out the set of proteins which present a correlate with the pathology in respect to the control group.

This overall approach is reputed promising for obtaining an olistic view of the patient rather than an atomistic one which considers the whole as a simple sum of the single component parts.

REFERENCES

G. Baselli, S. Cerutti, S. Civardi, A. Malliani and M. Pagani, Cardiovascular variability signals: towards the identification of a closed-loop model of the neural control mechanisms, *IEEE Trans Biomed Eng*., vol.35(12):1033-46(1988).

E. N. Bruce, *Biomedical Signal Processing and Signal Modelling*, J. Wiley (2001).

C. E. Clancy and Y. Rudy, Linking a genetic defect to its cellular phenotype in a cardiac arrhythmia, *Nature*, vol. 400(6744):566-569 (1999).

A. Cohen, *Biomedical Signal Analysis*, Vol. I, II, CRC Press (1986).

P. Hunter, P. Robbins and D. Noble, The IUPS human physiome project, *Pflugers Arch-Eur. J. Physiol*., vol. 445:1-9 (2002).

R. I. Kitney, A nonlinear model for studing oscillations in the blood pressure control system*, J. Biomed. Eng*., vol I,n. 2: 88-89 (1979).

H. P. Koepchen, History of studies and concepts of blood pressure wave, in: *Mechanisms of blood pressure waves (*Miyakawa K., Koepchen, H.P., Polosa C. eds): 3-23, Springer-Verlag (1984).

M. C. Mackey and J.C. Milton, Dynamical diseases, *Ann N Y Acad.Sc.,* vol.504:16-32 (1987).

C.-K. Peng, S. Havlin, J.M. Hausdorff, J.E. Mietus, H.E. Stanley and A.L. Goldberger, Fractal mechanisms and heart rate dynamics long-range correlation and their breakdown with diseases, *Journal of Electrocardiology*, vol.28: 59-65 (1995).

S. G. Priori, P.J. Schwartz, C. Napolitano, R. Bloise, E. Ronchetti, M. Grillo, A. Vicentini, C. Spazzolini, J. Nastoli, G. Bottelli, R. Folli and D. Cappelletti, Risk stratification in the long-QT sindrome, *N Engl J Med*., May 8, vol.348(19):1866-74 (2003).

Y. Rudy, From Genome to Physiome: integrative models of cardiac excitation, *Ann. Biom. Engineer*, vol 28: 945-950 (2000).

Cerutti S, Esposti F, Ferrario M, Sassi R, Signorini MG, Long-term invariant parameters obtained from 24-h Holter recordings: a comparison between different analysis techniques, Chaos, vol.17(1):015108, (2007).

Foffani G, Ardolino G, Rampini P, Tamma F, Caputo E, Egidi M, Cerutti S, Barbieri S, Priori A., Physiological recordings from electrodes implanted in the basal ganglia for deep brain stimulation in Parkinson's disease: the relevance of fast subthalamic rhythms, Acta Neurochir Suppl, vol. 93:97-9, (2005).

OUTTHINKING AND ENHANCING BIOLOGICAL BRAINS

Kevin Warwick
University of Reading, UK

Keywords: Brain-Computer Interface, Biological systems, Implant technology, Feedback control.

Abstract: In this paper an attempt has been made to take a look at how the use of implant and electrode technology can now be employed to create biological brains for robots, to enable human enhancement and to diminish the effects of certain neural illnesses. In all cases the end result is to increase the range of abilities of the recipients. An indication is given of a number of areas in which such technology has already had a profound effect, a key element being the need for a clear interface linking the human brain directly with a computer. An overview of some of the latest developments in the field of Brain to Computer Interfacing is also given in order to assess advantages and disadvantages. The emphasis is clearly placed on practical studies that have been and are being undertaken and reported on, as opposed to those speculated, simulated or proposed as future projects. Related areas are discussed briefly only in the context of their contribution to the studies being undertaken. The area of focus is notably the use of invasive implant technology, where a connection is made directly with the cerebral cortex and/or nervous system.

Tests and experimentation which do not involve human subjects are invariably carried out *a priori* to indicate the eventual possibilities before human subjects are themselves involved. Some of the more pertinent animal studies from this area are discussed including our own involving neural growth. The paper goes on to describe human experimentation, in which neural implants have linked the human nervous system bi-directionally with technology and the internet. A view is taken as to the prospects for the future for this implantable computing in terms of both therapy and enhancement.

BRIEF BIOGRAPHY

Kevin Warwick is Professor of Cybernetics at the University of Reading, England, where he carries out research in artificial intelligence, control, robotics and cyborgs. He is also Director of the University KTP Centre, which links the University with Small to Medium Enterprises and raises £2.5 million each year in research income. As well as publishing 500 research papers, Kevin is perhaps best known for his experiments into implant technology. He has been awarded higher doctorates (DScs) both by Imperial College and the Czech Academy of Sciences, Prague. He was presented with The Future of Health Technology Award in MIT, was made an Honorary Member of the Academy of Sciences, St. Petersburg and in 2004 received The IEE Achievement Medal.

1 INTRODUCTION

Research is being carried out in which biological signals of some form are measured, are acted upon by some appropriate signal processing technique and are then employed either to control a device or as an input to some feedback mechanism (Penny et al., 2000), (Roitberg, 2005). In many cases neural signals are employed, for example Electroencephalogram (EEG) signals can be measured externally to the body, using externally adhered electrodes on the scalp (Wolpaw et al., 1990) and can then employed as a control input. Most likely this is because the procedure is relatively simple from a research point of view and is not particularly taxing on the researchers involved. However, reliable interpretation of EEG data is extremely complex – partly due to both the compound nature of the multi-neuronal signals being measured and the difficulties in recording such highly attenuated

In the last few years interest has also grown in the use of real-time functional Magnetic Resonance

Imaging (fMRI) for applications such as computer cursor control. This typically involves an individual activating their brain in different areas by reproducible thoughts (Warwick, 2007) or by recreating events (Pan et al., 2007). Alternatively fMRI and EEG technologies can be combined so that individuals can learn how to regulate Slow Cortical Potentials (SCPs) in order to activate external devices (Hinterberger et al., 2005). Once again the technology is external to the body. It is though relatively expensive and cumbersome.

It is worth noting that external monitoring of neural signals, by means of either EEG analysis or indeed fMRI, leaves much to be desired. Almost surely the measuring technique considerably restricts the user's mobility and, as is especially the case with fMRI, the situation far from presents a natural or comfortable setting. Such systems also tend to be relatively slow, partly because of the nature of recordings via the indirect connection, but also because it takes time for the individual themselves to actually initiate changes in the signal. As a result of this, distractions, both conscious and sub-conscious, can result in false indicators thus preventing the use of such techniques for safety critical, highly dynamic and, to be honest, most realistic practical applications. Despite this, the method can enable some individuals who otherwise have extremely limited communication abilities to operate some local technology in their environment, and, in any case, it can serve as a test bed for a more direct and useful connection.

The definition of what constitutes a Brain-Computer Interface (BCI) is extremely broad. A standard keyboard could be so regarded. It is clear however that various wearable computer techniques and virtual reality systems, e.g. glasses containing a miniature computer screen for a remote visual experience (Mann, 1997), are felt by some researchers to fit this category. Although it is acknowledged that certain body conditions, such as stress or alertness, can be monitored in this way, the focus of this paper is on bidirectional BCIs and is more concerned with a direct connection between a biological brain and technology, and ultimately a human and technology.

2 *IN VIVO* STUDIES

Non-human animal studies can be considered to be a pointer for what is potentially achievable with humans in the future. As an example, in one particular animal study the extracted brain of a lamprey, retained in a solution, was used to control the movement of a small wheeled robot to which it was attached (Reger et al., 2000). The lamprey innately exhibits a response to light reflections on the surface of water by trying to align its body with respect to the light source. When connected into the robot body, this response was utilised by surrounding the robot with a ring of lights. As different lights were switched on and off, so the robot moved around its corral, trying to position itself appropriately.

Meanwhile in studies involving rats, a group of rats were taught to pull a lever in order to receive a suitable reward. Electrodes were then chronically implanted into the rats' brains such that the reward was proffered when each rat thought (one supposes) about pulling the lever, but before any actual physical movement occurred. Over a period of days, four of the six rats involved in the experiment learned that they did not in fact need to initiate any action in order to obtain a reward; merely thinking about it was sufficient (Chapin, 2004).

In another series of experiments, implants consisting of microelectrode arrays have been positioned into the frontal and parietal lobes of the brains of two female rhesus macaque monkeys. Each monkey learned firstly how to control a remote robot arm through arm movements coupled with visual feedback, and it is reported that ultimately one of the monkeys was able to control the arm using only brain derived neural signals with no associated physical movement. Notably, control signals for the reaching and grasping movements of the robotic arm were derived from the same set of implanted electrodes (Carmena et al., 2003), (Nicolelis et al., 2000).

Such promising results from animal studies have given the drive towards human applications a new impetus.

3 ROBOT WITH A BIOLOGICAL BRAIN

Human concepts of a robot may involve a little wheeled device, perhaps a metallic head that looks roughly human-like or possibly a biped walking robot. Whatever the physical appearance our idea tends to be that the robot might be operated remotely by a human, or is being controlled by a simple programme, or even may be able to learn with a

microprocessor/computer as its brain. We regard a robot as a machine.
In a present project neurons are being cultured in a laboratory in Reading University to grow on and interact with a flat multi-electrode array. The neural culture, a biological brain, can be electronically stimulated via the electrodes and its trained response can be witnessed.

The project now involves networking the biological brain to be part of a robot device. In the first instance this will be a small wheeled robot. The input (sensory) signals in this case will be only the signals obtained from the wheeled robot's ultrasonic sensors. The output from the biological brain will be used to drive the robot around. The goal of the project initially will be to train the brain to drive the robot forwards without bumping into any object. Secondly, a separate biological brain will be grown to be the thinking process within a robot head (called Morgui) which houses 5 separate sensory inputs.

What this means is that the brain of these robots will shortly be a biological brain, not a computer. All the brain will know is what it perceives from the robot body and all it will do will be to drive the robot body around or control the robot head respectively. The biological brain will, to all intents and purposes, be the brain of the robot. It will have no life, no existence outside its robotic embodiment.

Clearly this research alters our concept of what a robot is, particularly in terms of ethical and responsibility issues. If a role of animal research is to open up possibilities for future human trials, then in this case the research could well be opening a window on the ultimate possibility of human neurons being employed in a robot body. All the 'human' brain would know would be its life as a robot.

4 HUMAN APPLICATION

At the present time the general class of Brain-Computer Interfaces (BCIs) for humans, of one form or another, have been specifically developed for a range of applications including military weapon and drive systems, personnel monitoring and for games consoles. However, by far the largest driving force for BCI research to date has been the requirement for new therapeutic devices such as neural prostheses.

The most ubiquitous sensory neural prosthesis in humans is by far the cochlea implant (Fin and LoPresti, 2003). Here the destruction of inner ear hair cells and the related degeneration of auditory nerve fibres results in sensorineural hearing loss. As such, the prosthesis is designed to elicit patterns of neural activity via an array of electrodes implanted into the patient's cochlea, the result being to mimic the workings of a normal ear over a range of frequencies. It is claimed that some current devices restore up to approximately 80% of normal hearing, although for most recipients it is sufficient that they can communicate to a respectable degree without the need for any form of lip reading. The typically modest success of cochlea implantation is related to the ratio of stimulation channels to active sensor channels in a fully functioning ear. Recent devices consist of up to 32 channels, whilst the human ear utilises upwards of 30,000 fibres on the auditory nerve. There are now reportedly well over 10,000 of these prostheses in regular operation.

Studies investigating the integration of technology with the human central nervous system have varied from merely diagnostic to the amelioration of symptoms (Warwick and Gasson, 2004). In the last few years some of the most widely reported research involving human subjects is that based on the development of an artificial retina (Rizzo, 2001). Here, small electrode arrays have been successfully implanted into a functioning optic nerve. With direct stimulation of the nerve it has been possible for the otherwise blind recipient to perceive simple shapes and letters. The difficulties with restoring sight are though several orders of magnitude greater than those of the cochlea implant simply because the retina contains millions of photodetectors that need to be artificially replicated. An alternative is to bypass the optic nerve altogether and use cortical surface or intracortical stimulation to generate phosphenes (Dobelle, 2000).

Most invasive BCIs monitor multi-neuronal intracortical action potentials, requiring an interface which includes sufficient processing in order to relate recorded neural signals with movement intent. Problems incurred are the need to position electrodes as close as possible to the source of signals, the need for long term reliability and stability of interface in both a mechanical and a chemical sense, and adaptivity in signal processing to deal with technological and neuronal time dependence. However, in recent years a number of different collective assemblies of microelectrodes have been successfully employed both for recording and stimulating neural activity. Although themselves of small scale, nevertheless high density

connectors/transmitters are required to shift the signals to/from significant signal processing and conditioning devices and also for onward/receptive signal transmission.

Some research has focussed on patients who have suffered a stroke resulting in paralysis. The most relevant to this paper is the use of a '3rd generation' brain implant which enables a physically incapable brainstem stroke victim to control the movement of a cursor on a computer screen (Kennedy, 2000), (Kennedy, 2004). Functional Magnetic Resonance Imaging (fMRI) of the subject's brain was initially carried out to localise where activity was most pronounced whilst the subject was thinking about various movements. A hollow glass electrode cone containing two gold wires and a neurotrophic compound (giving it the title 'Neurotrophic Electrode') was then implanted into the motor cortex, in the area of maximum activity. The neurotrophic compound encouraged nerve tissue to grow into the glass cone such that when the patient thought about moving his hand, the subsequent activity was detected by the electrode, then amplified and transmitted by a radio link to a computer where the signals were translated into control signals to bring about movement of the cursor. With two electrodes in place, the subject successfully learnt to move the cursor around by thinking about different movements. Eventually the patient reached a level of control where no abstraction was needed – to move the cursor he simply thought about moving the cursor. Notably, during the period that the implant was in place, no rejection of the implant was observed; indeed the neurons growing into the electrode allowed for stable long-term recordings.

Electronic neural stimulation has proved to be extremely successful in other areas, including applications such as the treatment of Parkinson's disease symptoms. With Parkinson's Disease diminished levels of the neurotransmitter dopamine cause over-activation in the ventral posterior nucleus and the subthalamic nucleus, resulting in slowness, stiffness, gait difficulties and hand tremors. By implanting electrodes into the subthalamic nucleus to provide a constant stimulation pulse, the over activity can be inhibited allowing the patient, to all external intents and purposes, to function normally (Pinter et al., 1999).

5 BRAIN WITHIN A BRAIN

Ongoing research, funded by the UK Medical Research Council, is investigating how the onset of tremors can be accurately predicted such that merely a stimulation current burst is required rather than a constant pulsing (Gasson et al., 2005: pp.16/1-16/4). This has implications for battery inter-recharge periods as well as limiting the extent of in-body intrusive signalling. The deep brain stimulator can be used to collect local field potential (LFP) signals generated by the neurons around the deep brain electrodes (Gasson et al., 2005: pp.16/1-16/4). Determining the onset of events can be investigated by using fourier transforms to transfer the time based signal to a frequency based spectrogram to determine the change in frequency at the critical time period. However, in addition to that, the frequency changes in the period of time immediately prior to the tremor occurrence can give important information.

Fig.1 shows the results of an initial attempt to train an artificial neural network to indicate not only that a Parkinsonian tremor is present but also that one is very likely to occur in the near future. The aim of this research is that, once a reliable predictor has been obtained, the stimulating pulsing will only be enacted when a tremor is predicted, in order to stop the actual physical tremor occurring before it even starts in the first place.

The bottom trace in Fig.1 shows emg (muscular) signals, measured externally, associated with movement due to the tremors. It can be seen that the tremors in this incident actually start at around the 45 to 50 second point. The trace just above this indicates the corresponding electrical data measured as deep brain Local Field Potentials in the Sub-Thalamic Nucleus of the patient involved. It can be witnessed how, in this case, the electrical data takes on a different form (in terms of variance at least) at around the 45 to 50 second point. The four top plots meanwhile indicate the outputs from 4 differently structured artificial neural networks, based on multi-layer perceptrons with different numbers of neurons in the hidden (middle) layer.

It can be seen how, for each network, the output of the network goes high (logic 1) at the 45 to 50 second point, to indicate the presence of a Parkinsonian tremor. This is all well and good, what is important however is that the output of the networks also briefly goes high around the 30

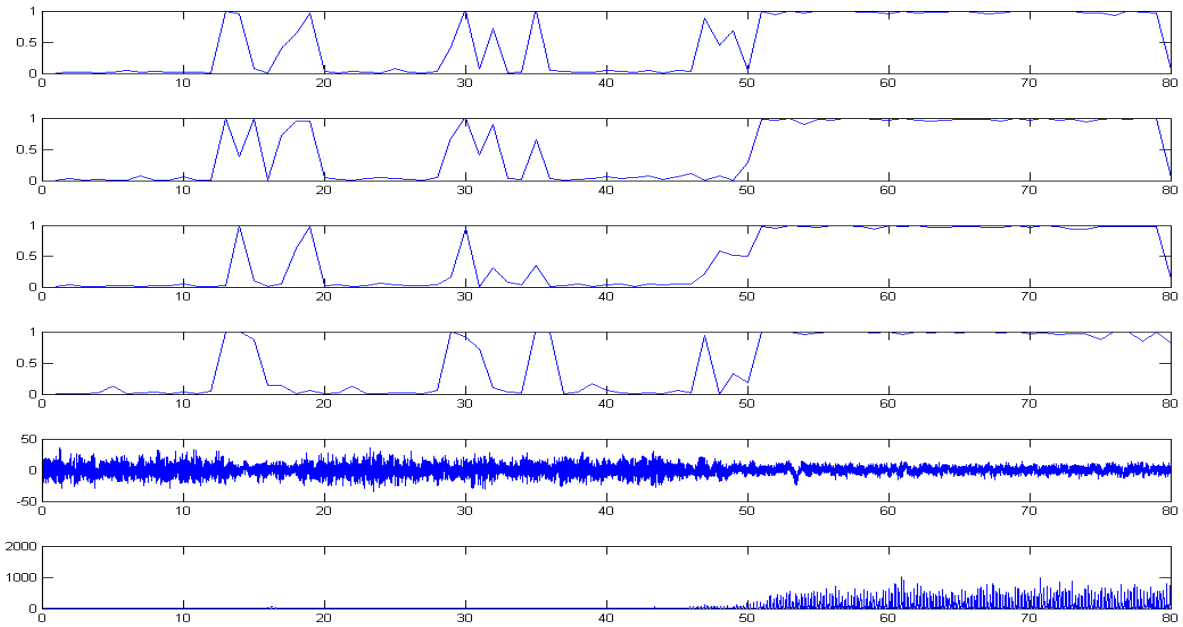

Figure 1: Time plot of the onset of a Parkisonian tremor incident with corresponding artificial neural network indicators.

second point and this can be seen as an indication of the fact that a tremor will shortly occur. Ongoing research is involved with selection of the type and number of inputs to the network, presently these being based on the energy spectrum in different frequency ranges. The networks are also being tested on considerable amounts of resting data, that is long periods of brain activity where no tremors at all actually occur in patients. Clearly the aim is that a network will not give false predictions of tremors.

In fact false positive predictions are not so much of a critical problem. The end result with a false positive is that a stimulation may occur when it is not strictly necessary. In any event no actual tremor would occur, which is indeed a good outcome, however unnecessary energy would have been used – in fact if numerous false predictions occurred the intelligent stimulator would tend toward the present 'blind' stimulator. Effectively the occasional false positive prediction is perhaps not a problem, unless it became a regular occurrence. The good news is that results show that the network can be readily tuned to avoid false positives anyway.

6 GENERAL IMPLANT STUDIES

Some of the most impressive human research to date has been carried out using the microelectrode array, shown in Figure 2. The individual electrodes are only 1.5mm long and taper to a tip diameter of less than 90 microns. Although a number of trials not using humans as a test subject have occurred (Branner and Normann, 2000), human tests are at present limited to two studies. In the second of these the array has been employed in a recording only role (Donoghue et al., 2002), (Donoghue et al., 2004), (Friehs et al., 2004), most notably recently as part of the 'Braingate' system. Essentially activity from a few neurons monitored by the array electrodes is decoded into a signal to direct cursor movement. This has enabled an individual to position a cursor on a computer screen, using neural signals for control combined with visual feedback. The first use of the microelectrode array (Figure 2) will be discussed in the following section as this has considerably broader implications which extend the capabilities of the human recipient.

A key selection point at the present time are what type of implant to employ, as several different possibilities exist, ranging from single electrode devices to multielectrode needles which contain electrode points at different depths to multielectrode arrays which either contain a number of electrodes which penetrate to the same depth (as in Figure 2) or are positioned in a banked/sloped arrangement. A further key area of consideration is the exact positioning of a BCI. In particular certain areas of the brain are, apparently, only really useful for monitoring purposes whilst others are more useful for stimulation.

Actually deriving a reliable command signal from a collection of captured neural signals is not necessarily a simple task, partly due to the complexity of signals recorded and partly due to time constraints in dealing with the data. In some cases however it can be relatively easy to look for and obtain a system response to certain anticipated neural signals – especially when an individual has trained extensively with the system. In fact neural signal shape, magnitude and waveform with respect to time are considerably different to the other signals that it is possible to measure in this situation.

If a greater understanding is required of neural signals recorded, before significant progress can be made, then this will almost surely present a major problem. This is especially true if a number of simultaneous channels are being employed, each requiring a rate of digitization of (most likely) greater than 20KHz in the presence of unwanted noise. For real time use this data will also need to be processed within a few milliseconds (100 milliseconds at most). Further, although many studies have looked into the extraction of command signals (indicating intent) from measured values, it is clear that the range of neural activity is considerable. Even in the motor area not only are motor signals present but so too are sensory, cognitive, perceptual along with other signals, the exact purpose of which is not clear – merely classifying them as noise is not really sufficient and indeed can be problematic when they are repeated and apparently linked in some way to activity.

It is worth stressing here that the human brain and spinal cord are linking structures, the functioning of which can be changed through electronic stimulation such as that provided via an electrode arrangement. This type of technology therefore offers a variety of therapeutic possibilities. In particular the use of implanted systems when applied to spinal cord injured patients, in whom nerve function is disordered, was described in (Warwick, 2004) as having the following potential benefits (among others):

1. Re-education of the brain and spinal cord through repeated stimulation patterns
2. Prevention of spinal deformity
3. Treatment of intractable neurogenic and other pain
4. Assisting bladder emptying
5. Improving bowel function
6. Treatment of spasticity
7. Improvement of respiratory function – assisting coughing and breathing
8. Reduction of cardiovascular maleffects
9. Prevention of pressure sores – possibly providing sensory feedback from denervated areas
10. Improvement and restoration of sexual function
11. Improved mobility
12. Improved capability in daily living, especially through improved hand, upper limb and truncal control

Sensate prosthetics is another growing application area of neural interface technology, whereby a measure of sensation is restored using signals from small tactile transducers distributed within an artificial limb (Fin and LoPresti, 2003). The transducer output can be employed to stimulate the sensory axons remaining in the residual limb which are naturally associated with a sensation. This more closely replicates stimuli in the original sensory modality, rather than forming a type of feedback using neural pathways not normally associated with the information being fed back. As a result it is supposed that the user can employ lower level reflexes that exist within the central nervous system, making control of the prosthesis more subconscious.

One final noteworthy therapeutic procedure is Functional Electrical Stimulation (FES), although it is debatable if it can be truly referred to as a BCI, however it aims to bring about muscular excitation, thereby enabling the controlled movement of limbs. FES has been shown to be successful for artificial hand grasping and release and for standing and walking in quadriplegic and paraplegic individuals as well as restoring some basic body functions such as bladder and bowel control (Grill and Kirsch, 2000). It must be noted though that controlling and coordinating concerted muscle movements for complex and generic tasks such as picking up an arbitrary object is proving to be a difficult, if not insurmountable, challenge.

In the cases described in which human subjects are involved, the aim on each occasion is to either restore functions since the individual has a physical problem of some kind or it is to give a new ability to an individual who has very limited motor abilities. In this latter case whilst the procedure can be regarded as having a therapeutic purpose, it is quite possible to provide an individual with an ability that they have in fact never experienced before. On the one hand it may be that whilst the individual in question has never previously experienced such an ability, some or most other humans have – in this

case it could be considered that the therapy is bringing the individual more in line with the "norm" of human abilities.

It is though also potentially possible to give extra capabilities to a human, to enable them to achieve a broader range of skills – to go beyond the "norm". Apart from the, potentially insurmountable, problem of universally deciding on what constitutes the "norm", extending the concept of therapy to include endowing an individual with abilities that allow them to do things that a perfectly able human cannot do raises enormous ethical issues. Indeed it could be considered that a cochlea implant with a wider frequency response range does just that for an individual or rather an individual who can control the curser on a computer screen directly from neural signals falls into this category. But the possibilities of enhancement are enormous. In the next section we consider how far things could be taken, by referring to relevant experimental results.

7 HUMAN ENHANCEMENT

The interface through which a user interacts with technology provides a distinct layer of separation between what the user wants the machine to do, and what it actually does. This separation imposes a considerable cognitive load upon the user that is directly proportional to the level of difficulty experienced. The main issue it appears is interfacing the human motor and sensory channels with the technology. One solution is to avoid this sensorimotor bottleneck altogether by interfacing directly with the human nervous system. It is certainly worthwhile considering what may potentially be gained from such an invasive undertaking.

Advantages of machine intelligence are for example rapid and highly accurate mathematical abilities in terms of 'number crunching', a high speed, almost infinite, internet knowledge base, and accurate long term memory. Additionally, it is widely acknowledged that humans have only five senses that we know of, whereas machines offer a view of the world which includes infra-red, ultraviolet and ultrasonic. Humans are also limited in that they can only visualise and understand the world around them in terms of a limited dimensional perception, whereas computers are quite capable of dealing with hundreds of dimensions. Also, the human means of communication, essentially transferring an electro-chemical signal from one brain to another via an intermediate, often mechanical medium, is extremely poor, particularly in terms of speed, power and precision. It is clear that connecting a human brain, by means of an implant, with a computer network could in the long term open up the distinct advantages of machine intelligence, communication and sensing abilities to the implanted individual.

As a step towards this more broader concept of human-machine symbiosis, in the first study of its kind, the microelectrode array (as shown in Figure 2) was implanted into the median nerve fibres of a healthy human individual (myself) in order to test *bidirectional* functionality in a series of experiments. A stimulation current direct onto the nervous system allowed information to be sent to the user, while control signals were decoded from neural activity in the region of the electrodes (Gasson et al., 2005:pp 365-375), (Warwick et al., 2003).

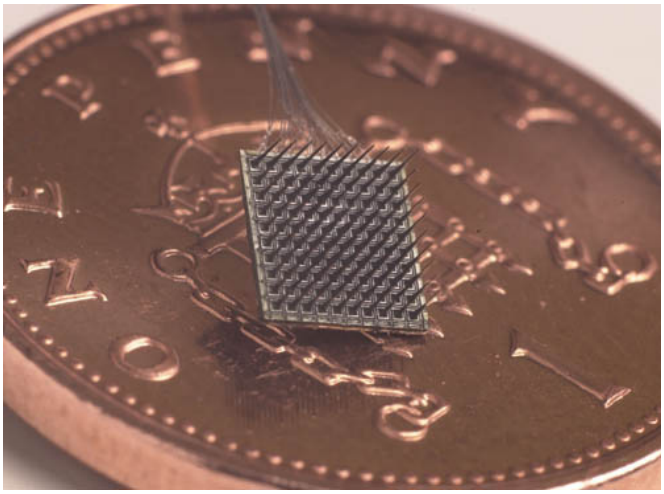

Figure 2: A 100 electrode, 4X4mm Microelectrode Array, shown on a UK 1 pence piece for scale.

In this way a number of experimental trials were successfully concluded (Warwick et al., 2004), (Warwick et al., 2005): In particular:

1. Extra sensory (ultrasonic) input was successfully implemented and made use of.
2. Extended control of a robotic hand across the internet was achieved, with feedback from the robotic fingertips being sent back as neural stimulation to give a sense of force being applied to an object (this was achieved between New York (USA) and Reading(UK))
3. A primitive form of telegraphic communication directly between the nervous systems of two humans was performed.
4. A wheelchair was successfully driven around by means of neural signals.
5. The colour of jewellery was changed as a result of neural signals – as indeed was the behaviour of a collection of small robots.

In each of the above cases it could be regarded that the trial proved useful for purely therapeutic reasons, e.g. the ultrasonic sense could be useful for an individual who is blind or the telegraphic communication could be very useful for those with certain forms of Motor Neurone Disease. However each trial can also be seen as a potential form of augmentation or enhancement for an individual. The question then arises as to how far should things be taken? Clearly enhancement by means of BCIs opens up all sorts of new technological and intellectual opportunities, however it also throws up a raft of different ethical considerations that need to be addressed directly.

8 ON STIMULATION

After extensive experimentation it was found that injecting currents below 80µA onto the median nerve fibers had little perceivable effect. Between 80µA and 100µA all the functional electrodes were able to produce a recognizable stimulation, with an applied voltage of 40 to 50 volts, dependant on the series electrode impedance. Increasing the current above 100µA had no apparent additional effect; the stimulation switching mechanisms in the median nerve fascicle exhibited a non-linear thresholding characteristic.

During this experimental phase, it was pseudo randomly decided whether a stimulation pulse was applied or not. The volunteer (myself), wearing a blindfold, was unaware of whether a pulse had been applied or not, other than by means of its effect in terms of neural stimulation. The user's accuracy in distinguishing between an actual pulse and no pulse at a range of amplitudes is shown in Figure 3.

In all subsequent successful trials, the current was applied as a bi-phasic signal with pulse duration of 200 µsec and an inter-phase delay of 100 µsec. A typical stimulation waveform of constant current being applied to one of the MEA's implanted electrodes is shown in Fig 4.

It was, in this way, possible to create alternative sensations via this new input route to the nervous system. Of the 5 enhancement features mentioned in the previous section, this one will be described, as an example, in further detail. Background information on the other enhancements can be found in a number of references, e.g. (Gasson et al., 2005:pp 365-375), (Warwick et al., 2003), (Warwick et al., 2004), (Warwick and Gasson, 2004).

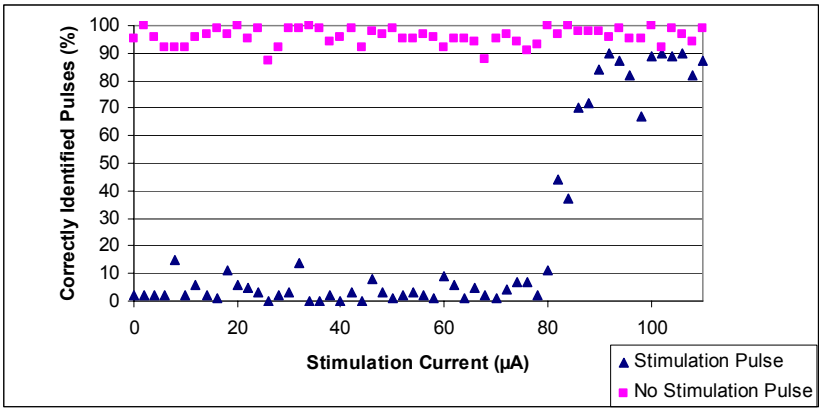

Figure 3: Effect of stimulation amplitude on the number of correctly identified pulses and absence of pulses (over 100 trials).

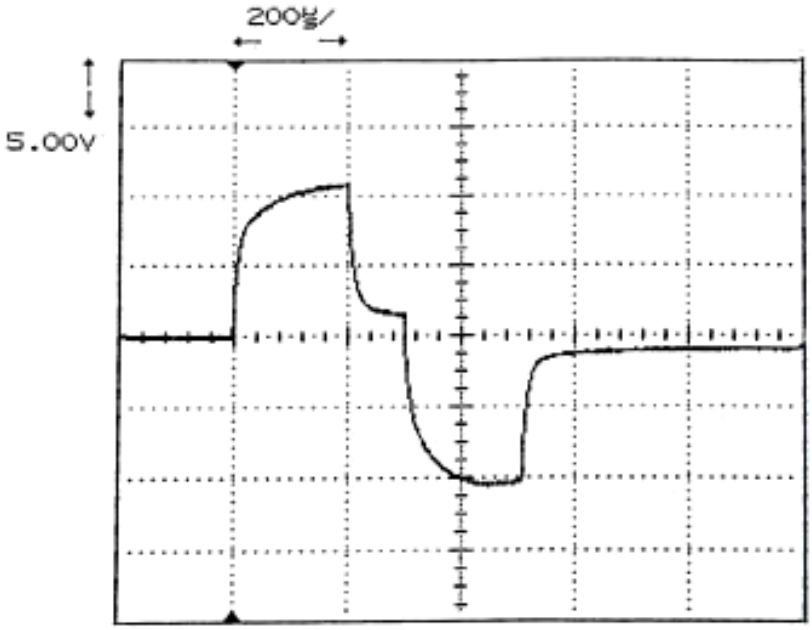

Figure 4: Voltage profile during one bi-phasic stimulation pulse cycle with a constant current of 80µA.

It must be reported that it took 6 weeks for my brain to repetitively recognize the stimulating signals accurately. This time period can be due to a number of contributing factors:

(a) The team had to learn which signals (what amplitude, frequency etc.) would be best in order to bring about a recognizable stimulation.

(b) The recipient's brain had to learn to recognize the new signals it was receiving.

(c) The bond between the recipient's nervous system and the implant was physically changing (becoming stronger).

9 EXTRA SENSORY EXPERIMENT

An experiment was set up to determine if the human brain is able to understand and successfully operate with sensory information to which it had not previously been exposed. Whilst it is quite possible to feed in such sensory information via a normal human sensory route, e.g. electromagnetic radar or infra-red signals are converted to visual, what we were interested in was feeding such signals directly onto the human nervous system, thereby bi-passing the normal human sensory input.

Ultrasonic sensors were fitted to the rim of a baseball cap (see Figure 5) and the output from these sensors, in the form of a proportional count, was employed to bring about a direct stimulation of the nervous system. Hence when no objects were in the vicinity of the sensors, no stimulation occurred, and as an object moved close by so the rate of stimulation pulses being applied increased in a linear fashion up to a pre-selected maximum rate. No increase in stimulation occurred when an object moved closer than 10cm to the sensors.

The ultrasonic sensors were open type piezoelectric ceramic transducers with conical metal resonators and operated at 40 KHz. These were used in a pair, one for transmit and one for receive, to give maximum sensitivity for small and distant objects. The most useful range for the experimentation was found to be 2 – 3m, this being also dependent on the size of object. A simple microcontroller was programmed to perform the echo ranging on the pair of transducers, and provide the range to the first detectable object only. This was translated into a stimulation pulse train, which operated on a single pin of the electrode array. Pins on the array had been tested for their suitability for stimulation by the earlier experimentation in which the recipient identified the presence or absence of stimulation pulse trains at various amplitudes and repetition frequencies.

Figure 5: Experimentation and testing of the ultrasonic baseball cap.

It was found that very little learning was required for the new ultrasonic sense to be used effectively and successfully – merely a matter of 5/6 minutes. This said it must be remembered that it had already taken several weeks for the recipient's brain to successfully, accurately recognize the current signals being injected.

As a result, in a witnessed experiment, the recipient, whilst wearing a blindfold, was able to move around successfully within a cluttered laboratory environment, albeit at a slower than normal walking pace. The sensory input was "felt" as a new form of sensory input (not as touch or movement) in the sense that the brain made a direct link between the signals being witnessed and the fact that these corresponded in a linear fashion to a nearby object.

10 CONCLUSIONS

External input-output interfaces with human and animal brains have been studied for many years. These are sometimes referred to as Brain-Computer Interfaces (BCIs) even though the interface may be external to the (human) body and its sensorimotor mechanism. In this paper an attempt has been made to put such systems in perspective. Emphasis has been placed on such interfaces that can be obtained by means of implanted devices through invasive surgery and actual direct neural connections. In particular a number of trials in this area have clearly shown the possibilities of monitoring, stimulating and enhancing brain functioning.

Although there is no distinct dividing line it is quite possible as far as humans are concerned to investigate BCIs in terms of those employed for direct therapeutic means and those which can have an enhanced role to play. It is clear that the interaction of electronic signals with the human brain can cause the brain to operate in a distinctly different manner. Such is the situation with the stimulator implants that are successfully used to counteract, purely electronically, the tremor effects associated with Parkinson's disease. Such technology can though potentially be employed to modify the normal functioning of the human brain and nervous system in a number of different ways.

The same stimulator, with slightly different positioning, has been shown to elicit feelings of sadness or happiness in the recipient. Given the nature of the intelligent stimulator described here it would appear to be possible to monitor, in real time, a human brain with a computer brain, and for the computer brain to predict when the human is going to feel sad – quite some time before they actually feel sad. In theory a signal could then be injected at

that time to make them feel happy, or at least to stop them actually ever feeling sad in the first place. Maybe this could be regarded as an electronic anti-depressant. There are of course questions about recreational use here – but this would need a deep brain implant which might well prove to be rather too onerous for most people.

Perhaps understandably, invasive BCIs are presently far less well investigated in University experiments than their external BCI counterparts. A number of animal trials have though been carried out and the more pertinent have been indicated here along with the relevant human trials and practice. In particular the focus of attention has been given to the embodiment of grown neural tissue within a technological body. Whilst only 1,000 or so neurons are involved this presents an interesting research area in a number of ways. But once the number of such neurons used increases 1,000 or 1,000,000-fold, it also raises enormous philosophical and ethical issues. For example is the robot 'thinking' and what rights should it have?

The potential for BCI applications for individuals who are paralysed is enormous, where cerebral functioning to generate command signals is functional despite the motor neural pathways being in some way impaired – such as in Lou Gehrig's disease. The major role is then either one of relaying a signal of intention to the appropriate actuator muscles or to reinterpret the neural signals to operate technology thereby acting as an enabler. In these situations no other medical 'cure' is available, something which presents a huge driver for an invasive implant solution for the millions of individuals who are so affected. Clearly though, bidirectional signalling is important, not only to monitor and enact an individual's intent but also to provide feedback on that individual's resultant interaction with the real world. For grasping, walking and even as a defensive safety stimulant, feedback is vital. This paper has therefore focussed on such studies.

Where invasive interfaces are employed in human trails, a purely therapeutic scenario often exists. In a small number of instances, such as use of the microelectrode array as an interface, an individual has been given different abilities, something which opens up the possibilities of human enhancement. These latter cases however raise more topical ethical questions with regard to the need and use of a BCI. What might be seen as a new means of communication for an individual with an extreme form of paralysis or a new sensory input for someone who is blind, opening up a new world for them, can also be seen as an unnecessary extra for another individual, even though it may provide novel commercial opportunities. What is therapy for one person may be regarded as an enhancement or upgrading for another.

Whilst there are still many technical problems to be overcome in the development of BCIs, significant recent experimental results have indicated that a sufficient technological infrastructure now exists for further major advances to be made. Although a more detailed understanding of the underlying neural processes will be needed in the years ahead, it is not felt that this will present a major hold up over the next few years, rather it will provide an avenue of research in which many new results will shortly appear through trials and experimentation, possibly initially through animal studies although it must be recognised that it is only through human studies that a full analysis can be made and all encompassing conclusions can be drawn. Nevertheless the topic opens up various ethical questions that need to be addressed and as such, research in this area should, I believe, only proceed in light of a pervasive ethical consensus.

ACKNOWLEDGEMENTS

The Author would like to acknowledge the considerable assistance and input of the Consultant Neurosurgeons Mr. Peter Teddy, Mr. Amjad Shad, Mr. Ali Jamous and Mr. Tipu Aziz and researchers Iain Goodhew, Mark Gasson, Ben Whalley and Ben Hutt. Ethical approval for the author's research was obtained from the Ethics and Research Committee at the University of Reading, UK and with regard to the neurosurgery aspect, the Oxfordshire National Health Trust Board overseeing the Radcliffe Infirmary, Oxford, UK.

REFERENCES

Branner, A. and Normann, R. (2000) A multielectrode array for intrafascicular recording and stimulation in the sciatic nerve of a cat, *Brain Research Bulletin*, Vol.51, pp.293-306.

Chapin, J.K. (2004) Using multi-neuron population recordings for neural prosthetics. *Nature Neuroscience*, 7, 452-454.

Carmena, J., Lebedev, M., Crist, R., O'Doherty, J., Santucci, D., Dimitrov, D. Patil, P., Henriquez, C. and Nicolelis, M. (2003) Learning to control a brain-

machine interface for reaching and grasping by primates, *Plos Biology*, Vol.1, Issue.2, article number e2.
Dobelle, W. (2000) Artificial vision for the blind by connecting a television camera to the visual cortex, ASAIO J, Vol.46, pp.3-9.
Donoghue, J. (2002) Connecting cortex to machines: recent advances in brain interfaces, *Nature Neuroscience Supplement*, Vol.5, pp.1085-1088.
Donoghue, J., Nurmikko, A., Friehs, G. And Black, M. (2004) Development of a neuromotor prosthesis for humans, Chapter 63 in *Advances in Clinical Neurophysiology, Supplements to Clinical Neurophysiology*, Vol.57, pp.588-602.
Finn, W. and LoPresti, P. (eds.) (2003) Handbook of Neuroprosthetic methods, CRC Press.
Friehs, G., Zerris, V., Ojakangas, C., Fellows, M. and Donoghue, J. (2004) Brain-machine and brain-computer interfaces, *Stroke*, Vol.35, Issue.11, pp.2702-2705.
Gasson, M., Hutt, B., Goodhew, I., Kyberd, P. and Warwick, K. (2005) Invasive neural prosthesis for neural signal detection and nerve stimulation, Proc. International Journal of Adaptive Control and Signal Processing, Vol.19, No.5, pp.365-375.
Gasson, M., Wang, S., Aziz, T., Stein, J. and Warwick, K. (2005) Towards a demand driven deep brain stimulator for the treatment of movement disorders, Proc. 3rd IEE International Seminar on Medical Applications of Signal Processing, pp.16/1-16/4.
Grill, W. and Kirsch, R. (2000) Neuroprosthetic applications of electrical stimulation, *Assistive Technology,* Vol.12, Issue.1, pp.6-16.
Hinterberger, T., Veit, R., Wilhelm, B., Weiscopf, N., Vatine, J. and Birbaumer, N. (2005) Neuronal mechanisms underlying control of a brain-computer interface, *European Journal of Neuroscience*, Vol.21, Issue.11, pp.3169-3181.
Kennedy, P., Bakay, R., Moore, M., Adams, K. and Goldwaith, J. (2000) Direct control of a computer from the human central nervous system, *IEEE Transactions on Rehabilitation Engineering*, Vol.8, pp.198-202.
Kennedy, P., Andreasen, D., Ehirim, P., King, B., Kirby, T., Mao, H. and Moore, M. (2004) Using human extra-cortical local field potentials to control a switch, *Journal of Neural Engineering*, Vol.1, Issue.2, pp.72-77.
Mann, S. (1997) Wearable Computing: A first step towards personal imaging, *Computer*, Vol. 30, Issue.2, pp. 25-32.
Nicolelis, M., Dimitrov, D., Carmena, J., Crist, R., Lehew, G., Kralik, J. and Wise, S. (2003) Chronic, multisite, multielectrode recordings in macaque monkeys, *Proc. National Academy of the USA*, Vol.100, Issue.19, pp.11041-11046.
Penny, W., Roberts, S., Curran, E., and Stokes, M. (2000) EEG-based communication: A pattern recognition approach, *IEEE Transactions on Rehabilitation Engineering*., Vol. 8, Issue.2, pp. 214-215.
Pinter, M., Murg, M., Alesch, F., Freundl, B., Helscher, R. And Binder, H. (1999) Does deep brain stimulation of the nucleus ventralis intermedius affect postural control and locomotion in Parkinson's disease?, *Movement Disorders*, Vol.14, Issue.6, pp.958-963.
Reger, B., Fleming, K., Sanguineti, V., Simon Alford, S., Mussa-Ivaldi, F. (2000) Connecting Brains to Robots: an artificial body for studying computational properties of neural tissues, *Artificial life*, Vol.6, Issue.4, pp.307-324.
Rizzo, J., Wyatt, J., Humayun, M., DeJuan, E., Liu, W., Chow, A., Eckmiller, R., Zrenner, E., Yagi, T. and Abrams, G. (2001) Retinal Prosthesis: An encouraging first decade with major challenges ahead, *Opthalmology,* Vol.108, No.1.
Roitberg, B. (2005) Noninvasive brain-computer interface, *Surgical Neurology*, Vol.63, Issue.3, p.195.
Warwick, K. (2004) I Cyborg, University of Illinois Press.
Warwick, K., Gasson, M., Hutt, B., Goodhew, I., Kyberd, P., Andrews, B., Teddy, P., Shad, A. (2003) The application of implant technology for cybernetic systems. *Archives of Neurology*, 60 (10), pp.1369-1373.
Warwick, K., Gasson, M., Hutt, B., Goodhew, I., Kyberd, P., Schulzrinne, H. and Wu, X. (2004) Thought Communication and Control: A First Step Using Radiotelegraphy, *IEE Proceedings on Communications,* Vol.151, No. 3, pp 185-189.
Warwick, K., Gasson, M., Hutt, B. and Goodhew, I. (2005) An Attempt to Extend Human Sensory Capabilities by means of Implant Technology. Proc. IEEE Int. Conference on Systems, Man and Cybernetics, Hawaii.
Wolpaw, J., McFarland, D., Neat, G. and Forheris, C. (1990) An EEG based brain-computer interface for cursor control, *Electroencephalogr. Clin. Neurophysiol*., Vol.78, pp.252-259.
Pan, S., Warwick, K., Gasson, M., Burgess, J., Wang, S., Aziz, T. and Stein, J. (2007) Prediction of parkinson's disease tremor onset with artificial neural networks", Proc. IASTED Conference BioMed 2007, Innsbruck, Austria, pp.341-345.
Warwick, K. (2007) The promise and threat of modern cybernetics, Southern Medical Journal, Vol.100, Issue.1, pp.112-115.
Warwick, K. and Gasson, M.N. (2004) Practical Interface Experiments with Implant Technology, in "Computer Vision in Human-Computer Interaction", Sebe, N., Lew, M.S and Huang, T.S. (eds.), Lecture Notes in Computer Science, Vol. 3058, pp.7-16.Xie, S., Yang, Z. and Yang, Y. (2004) Brain-computer interface based on event-related potentials during imitated natural reading, International Journal of Psychology, Vol.39, Issue.5-6, Supplement S., p.138.
Yoo, S., Fairneny, T., Chen, N., Choo, S., Panych, L., Park, H., Lee, S. and Jolesz, F. (2004) Brain-computer interface using fMRI: spatial navigation by thoughts, *Neuroreport*, Vol.15, Issue.10, pp.1591-1595.
Yu, N., Chen, J. and Ju, M. (2001) Closed-Loop Control of Quadriceps/Hamstring activation for FES-Induced Standing-Up Movement of Paraplegics, *Journal of Musculoskeletal Research*, Vol. 5, No.3, pp.173-184.

ANALYSIS AND MODELS OF BRAIN EPILEPTIC ACTIVITIES

Fernando Henrique Lopes da Silva
University of Amsterdam, The Netherlands

Abstract: The essence of epilepsy is the sudden occurrence of a qualitative change in the behaviour of neuronal networks of some specific areas of the brain. In general we may assume that neuronal networks possess multistable dynamics. We may simplify this concept considering the case that a neuronal network may display, at least, two dynamical states: an interictal state characterised by a normal on-going neural activity, as revealed in the Eletcroencephalogram of Magnetoencephalogram (EEG, MEG), that may be apparently random, and another one – the ictal state - that is characterised by the sudden occurrence of synchronous oscillations, most commonly with large amplitude. The latter becomes manifest as a paroxysmal change of behaviour and /of the state of consciousness of a patient, i.e. an epileptic seizure. In the terminology of the mathematics of non-linear systems, we may state that a neuronal network behaves as a bistable system with two attractors, to which the system converges depending on initial conditions and on the system's parameters.

We propose schematically that the transition between the normal on-going to the seizure activity can take place according to three basic models: Model I – a transition may occur due to random fluctuations of some system's parameters. These transitions are thus unpredictable. Models II and III – a transition may result from a gradual change of some unstable parameters, either due to endogenous (model II) or exogenous (model III). In these cases the change of parameter values causes a deformation of the attractor resulting in a transition from the basin of the attractor corresponding to the normal state, to the attractor corresponding to the seizure dynamical state. Some experimental findings obtained in different cases of epilepsy, both in human and in animals, are compatible with each of these 3 models. Some examples of these cases are illustrated.

BRIEF BIOGRAPHY

Fernando Henrique Lopes da Silva received his Medical Degree from the University of Lisbon in 1959, got his Ph.D. from the University of Utrecht in 1970, and in 1980 was appointed Full Professor of General Physiology at the Faculty of Science at the University of Amsterdam (since 2002 part of the Swammerdam Institute for Life Sciences). From 1993 to 2000 he was Director of the newly created Institute of Neurobiology of the University of Amsterdam, and member of the Scientific Directorate of the Graduate School Neurosciences Amsterdam. In 2000, when he reached the retirement age of 65, he became Emeritus Professor of the same University, and has at present a free-lance contract with the Swammerdam Institute for Life Sciences.

Since 1970, he supervised a large number of student trainees from different Universities and Faculties: Medical, Biology, Sciences, (Bio-medical) Engineering. Supervised 65 Ph.D. students (up to December 2006).

His research interests are centred on the biophysical aspects of electrical activity of the brain and the functional organization of neuronal networks, namely of the cerebral cortex and the limbic system, with a special interest in the generation and functional significance of brain rhythmic activities. He published more than 220 papers in peer-reviewed journals and contributed Chapters to 10 multi-authored books (of 6 he is co-editor), among which the Handbook "Electroencephalography: Basic principles, clinical applications and related fields", Niedermeyer, E. and Lopes da Silva, F.H. (Eds), published by Lippincott, Williams and Wilkins, Baltimore; 5 Editions: 1982, 1987, 1993, 1998, 2004. In addition he contributed chapters to to the Encyclopedia of Neuroscience (George Adelman, Barry H. Smith. Eds), Elsevier Science, 2003 (3rd edition), to the Encyclopedia of the Human Brain (Ed. V. S. Ramachandran), Academic Press, 2002, and to The Handbook of Brain Theory and Neural Networks (Ed. Michael A. Arbib), The MIT Press, 2003 (2nd edition).

Selection of Scientific Awards

- 1975 He received the Winkler Medal from the Netherlands Association for Neurology for scientific contributions in the field of neurosciences.
- 1985 Elected member of the Royal Netherlands Academy of Arts and Sciences.
- 1990 "Lord Adrian" Lecturer at the 12th World Congress of Electroencephalography and Clinical Neurophysiology in Rio de Janeiro, Brazil.
- 1992 Honorary President of the VIIth European Congress of Clinical Neurophysiology, Budapest, Hungary.
- 1995 Honorary Life Member of The British Society for Clinical Neurophysiology (Formerly The EEG Society), London, United Kingdom.
- 1997 Doctor Honoris Causa of the University of Lisbon (Portugal).
- 1997 Special "Berger" Lecturer at the 14th International Congress of EEG and Clinical Neurophysiology in Florence, Italy.
- 1999 Recipient of the Herbert H. Jasper Award, selected by the American Clinical Neurophysiology Society for his "lifetime of outstanding contributions to the field of clinical neurophysiology.''
- 2000 Recipient of the 'Storm van Leeuwen/ Magnus Prize' of the Dutch Society of Clinical Neurophysiology.
- 2000 Honorary member of the Portuguese Society of Electroencephalography and Clinical Neurophysiology.
- 2002 Recipient of the Ragnar Granit Prize for his work on the field of Bioelectromagnetism.
- 2002 Doctor Honoris Causa of the University of Porto (Portugal).
- 2004 Recipient of the first Prize "Universidade de Coimbra" for a (sic) "person of Portuguese nationality who has made a particular relevant and innovative contribution in the fields of culture or science."

General Honors

- 2000 High Officer of the Order of Santiago da Espada, for outstanding achievements in the field of Science/Art/Literature, awarded by the President of the Republic of Portugal.
- 2001 Knight of the Order of the 'Nederlandse Leeuw' awarded by the Queen of the Netherlands in appreciation for his achievements in science.

FROM THE BENCH TO THE BEDSIDE

The Role of Semantics in Enabling the Vision of Translational Medicine

Vipul Kashyap
Partners HealthCare System, Clinical Informatics R&D, USA

Abstract: Biomedical research and healthcare clinical transactions are generating huge volumes of data and information. At the same time, the results of biomedical research in the form of new molecular diagnostic tests and therapies are being increasingly used in the context of clinical practice. There is a critical need to speed "translation" of genomic research insights into clinical research and practice. In this talk, we will discuss challenges faced by a healthcare enterprise in realizing the vision of Translational Medicine, such as:

- The need to create structured and semantic representations of genotypic and phenotypic data such as clinical observations and molecular diagnostic tests.
- The need for cost-effective and incremental data integration for combining genotypic and phenotypic information at the point of care.
- The need for actionable decision support for suggesting molecular diagnostic tests and therapies in the context of clinical care.
- The need for knowledge update, propagation and consistency to keep abreast of the rapid pace of knowledge discovery being witnessed in the life sciences, a crucial pre-requisite to reduce the cost of knowledge acquisition and maintenance.

Semantics-based approaches to address the above-mentioned challenges, including the applicability of semantic web standard (RDF, OWL, Rules); and issues related to the value proposition of these technologies will be presented.

BRIEF BIOGRAPHY

Vipul Kashyap, PhD is a Senior Medical Informatician in the Clinical Informatics Research & Development group at Partners HealthCare System and is currently the chief architect of a Knowledge Management Platform that enables browsing, retrieval, aggregation, analysis and management of clinical knowledge across the Partners Healthcare System. Vipul received his PhD from the Department of Computer Science at Rutgers University in New Brunswick in the area of metadata and semantics-based knowledge and information management. He is also interested in characterization of the value proposition of semantic technologies in the enterprise context. Before coming to Partners, Vipul has held positions at MCC, Telcordia (Bellcore) and was a fellow at the National Library of Medicine. Vipul has published 2 books on the topic of Semantics, 40-50 articles in prestigious conferences and journals; and has participated in panels and presented tutorials on the topic of semantic technologies. Vipul sits on the technical advisory board of an early stage company developing semantics-based products, and represents Partners on the W3C advisory committee and the HealthCare Information Technology Standards Panel (HITSP).

THE CANCER INFORMATICS ECOSYSTEM

A Case Study in the Accretion of Federated Systems based on Service Oriented Architectures, Semantic Integration and Computing Grids

David Hall
Research Triangle Institute in North Carolina, USA

Abstract: Information technology is playing an increasingly critical role in health and life sciences research due to the profound expansion in the scope of research projects in the post-genomic age. Robust data management and analysis systems are becoming essential enablers of these studies. Driven by funding agency requirements, funding opportunities, and grass roots organizing, efforts are underway to develop standards and technologies to promote large-scale integration of publicly-funded systems and databases including infrastructure developed for individual studies. Predicted benefits include an enhanced ability to conduct meta-analyses, an increase in the usable lifespan of data, a funding agency-wide reduction in the total cost of IT infrastructure, and an increased opportunity for the development of third party software tools. This presentation will critically examine efforts towards developing publicly-accessible interoperable and distributed production systems in the health and life sciences via ontologies, formal metadata, service oriented architectures, and grid computing models with a focus on several projects under the direction of the author in the area of cancer informatics.

BRIEF BIOGRAPHY

David Hall is a Senior Software Project Leader at RTI International based in North Carolina, USA. He leads teams of up to 30 developers implementing computer systems that support large biomedical and biotechnological research enterprises in cancer research, drug discovery, genetic epidemiology, and plant biotechnology. His area of interest is the practical application of bioinformatics and medical informatics methods, technologies, and standards in the development of production software. Particular topics of interest include data visualization, semantic integration, systems integration, and high performance computing. Recent clients include the US National Institutes of Health, GlaxoSmithKline, Syngenta, and Duke University. Data systems developed by David's group manage clinical and research data for nearly one million patients. Applications include data warehouses, metadata registries, workflow systems, high resolution image databases, analytical applications, and web services. David is currently Principal Investigator of the Informatics Support Center for the National Cancer Institute's Breast and Colon Cancer Family Registries. He holds a Ph.D. in Genetics from the University of Georgia and a B.S. in Computer Science from Wake Forest University.

ICT AND PERSONS WITH DISABILITIES
The Solution or the Problem?

Albert M. Cook
Faculty of Rehabilitation Medicine, University of Alberta, Edmonton Alberta, Canada
al.cook@ualberta.ca

Keywords: Assistive technologies, information and computer technologies, persons with disabilities.

Abstract: In order to lead full and productive lives, persons with disabilities need to have the same access to information and communication systems as the rest of the population. Advances in information and communication technologies (ICT) are occurring quickly, and the capability of technologies to meet the needs of persons with disabilities is growing daily. Future developments in assistive technologies (AT) and the successful application of these technologies to meet the needs of people who have disabilities are dependent on exploitation of these ICT advances. AT also involves the development of specialized interfaces such as the brain computer interface (BCI), adaptive interfaces that accommodate for changes in the user's physical skills, cognitive interfaces that allow understanding of the human technology interface by individuals with intellectual disabilities and systems that accommodate for user needs based on environmental sensing (e.g., GPS interfaces) and downloading of profiles to meet specific user needs. Universal Design (or design for all) calls for the design of products and environments to be usable by all people, to the greatest extent possible, without the need for adaptation or specialized design. In the physical world this often means ramps, curb cuts and other adaptations to the built environment to accommodate individuals who have disabilities. In the ICT world the barriers to access are technological, and the goal for ICT universal design is to have an environment with enough embedded intelligence to be easily adaptable to the varying cognitive, physical and sensory skills of a wide range of individual's in order to meet their productivity, leisure and self care needs. If ICT advances are not adaptable enough to be accessible to persons with disabilities it will further increase the disparity between those individuals and the rest of the population leading to further isolation and economic disadvantage. On the other hand, availability of these technologies in a transparent way will contribute to full inclusion of individuals who have disabilities in the mainstream of society.

BRIEF BIOGRAPHY

Dr. Albert Cook is Professor of Speech Pathology and Audiology and currently Dean of the Faculty of Rehabilitation Medicine and Chair of the Health Sciences Council at the University of Alberta. Dr. Cook has worked with interdisciplinary teams to develop assistive devices and to assess the effectiveness of technology being used by persons with disabilities. Dr. Cook is also associated with the I CAN Centre the Glenrose Rehabilitation Hospital. He was formerly Professor of Biomedical Engineering at California State University, Sacramento where he established the graduate program in biomedical engineering and directed it for 12 years. He also served as Co-Director of the Assistive Device Center in Sacramento, California, helping over 500 persons with disabilities to identify and obtain assistive technologies.

He received his Bachelor of Science in Electrical Engineering at the University of Colorado, a Masters in Bioengineering and his doctorate from the University of Wyoming He is a member of Tau Beta Pi, Phi Kappa Phi and Gold Key honorary societies.

Dr. Cook co-authored with Janice Polgar, OTR, Cook and Hussey's Assistive Technologies: Principles and Practice 3nd edition, published in October 2007 by Elsevier. He has co-edited three other textbooks with John Webster and others and has written numerous chapters in rehabilitation and biomedical engineering texts and monographs.

Dr. Cook's research interests include augmentative and alternative communication, biomedical instrumentation and assistive technology design, development and evaluation. His most recent

research has focussed on the use of robotics with young children who have severe disabilities to develop and assess cognitive and linguistic skills. He has US and foreign patents and numerous publications and conference presentations in these areas. He has been principal investigator on research and training grants in augmentative communication, assistive technologies and biomedical engineering.
Dr. Cook is Past-President and Fellow of RESNA, a major professional society for assistive technology practitioners in North America. He has also served in national united States positions in the Institute of Electrical and Electronic Engineers Engineering in Medicine and Biology Society, the American Society for Engineering Education, the Biomedical Engineering Society, the International Society for Augmentative and Alternative Communication and the Association for the Advancement of Medical Instrumentation. Dr. Cook is a registered professional engineer (electrical) in California.

1 ICT AND PERSONS WITH DISABILITIES TECHNOLOGY AND PROGRESS

Societal Progress requires change much of which is accomplished through advances in technology. In his book, *A Short History of Progress*, Ronald Wright *(*2004) points out that this characteristic has been true for millions of years as societies have advanced through greater utilization of technology.

Wright goes on to describe the problems that technology typically creates such as over consumption, environmental ruin, and separation of classes. These problems are amplified for people who have disabilities, and they lead to a gap in the access to work, self care and community participation for persons with disabilities compared to the general population. Since people with disabilities often depend on technologies for societal participation, the lack of availability of accessible technology or the obsolescence of accessible technologies isolates them further. This is an extension of the concept of the "digital divide" that separates people along socioeconomic lines based on their access to ICT. I refer to it as the "disability gap".

2 ADVANCES IN INFORMATION AND COMMUNICATION TECHNOLOGIES (ICT)

The 21st Century is characterized by a continuous move from a machine-based to a knowledge based economy (Ungson & Trudel, 1999). In this shift, the basis of competence is changing to knowledge skills from machine skills. Information currently amounts to 75% of value added to products This will continually increase, and connectivity will be the key to business success. There is also a move from a regional or national scope of business influence to a global scope, in which virtual networks dictate organizational structures.

Key players in business development are becoming communication suppliers with the move from host-based to network based systems. Telephone, cable TV and internet service providers control commercial growth. Along with these changes networks will become more graphically-based moving increasingly from text-based systems. In order to lead full and productive lives, persons with disabilities need to have the same access to this new information and communication system as the rest of the population.

2.1 What Can we Expect from Technology in the Next 20 Years?

The cost of information technology is continually dropping for comparable or increased computing power and speed. There is also a greater understanding of the biological/physical interface for the control of computers. The human computer interface (HCI) is being developed to be more human-like, more user oriented and more intelligent-providing additional capabilities for searching, processing and evaluating information.

There are a number of changes that are likely to occur over the next few years (Applewhite, 2004). There will be an increase in automated transactions between individuals and organizations enabling people to complete all transactions without face-toface interactions. It is expected that we will achieve equalized access to the web and information between the developed and developing world. Embedded systems will dramatically increase with application such as "intelligence in the doorknob" that recognizes the owner and doesn't require key manipulation. We are likely to see much greater

understanding of the biological to physical interface for the control of computers.

2.2 Changes in Mainstream Tech with AT Implications

There are many examples of emerging mainstream technologies with potential for assisting people with disabilities to access ICT systems. A few of these are described in this section.

Display-based assistive technologies present an array of choices for a user to select from (Cook & Polgar, 2007). This often referred to as scanning since the choices are highlighted sequentially and then chosen using some sort of gross movement. One of the problems associated with this approach is that there must be a physical display for making selections. This often requires the overall system to be larger and more bulky or places a display between a user and a communication partner. A new development is a direct retinal display that creates image that overlays view of real object (Lewis, 2004). The retinal display is low powered because it is shined on retina directly. Scanning light into the eye allows the image to overlay an object such as a communication partner's face-enabling eye contact and small size. The scanning array could be the retinal image, since display scans across the retina power levels can be kept low kept low for safety.

Another development is 3-D displays that create a more intuitive view of objects, events and activities (Lewis, 2004). This type of display may be helpful to individuals who have cognitive disabilities. It might also create new challenges for individuals with visual limitations.

Embedded automatic speech recognition is being developed for PDAs because of the need for keyboards with more and more functions and the limitations of very small keyboards (Kumagai, 2004). This feature could be very useful to reduce individuals who have limited hand function or for those who cannot see the keyboard to make entries.

3 MEETING THE ICT NEEDS OF PERSONS WITH DISABILITIES

Over the centuries, our ability to make tools is what distinguishes us as human, but our tools ultimately control us by making us dependent on them (Wright, 2004). This dependence is less optional for people who have disabilities

3.1 Impact of Technology Advances on People who have Disabilities

Technology advances increase the gap between people who have disabilities and those who don't (Wright, 2004). All societies become hierarchical with an upward concentration of wealth (including aggregations of technology tools) that ensures that "there can never be enough to go around", and this disparity contributes to the "digital divide" and the "disability gap". As advances occur more quickly, the gap widens faster and the people who are poor and/or disabled loose out even more completely and faster. This is a characteristic of cultural and societal "progress" over centuries-technology drives change, and creates both positive and negative outcomes in the process

The prognosis is not good for people with disabilities unless there is considerable effort to keep them connected to ICT and thereby to commerce, employment and personal achievement. There two fundamental approaches to this problem (1) make mainstream technologies accessible to people who have disabilities, or (2) design special purpose technologies specifically for people with disabilities. The former approach is referred to as *universal design* or *design for all*. The second approach utilizes *assistive technologies*.

3.2 Implications for Assistive Technologies

Access to ICT for people with disabilities is a significant global problem, and it has major implications for assistive technologies. There is a constant challenge to keep ICT systems accessible to persons who have disabilities as mainstream advances occur and adaptations become potentially incompatible with the new systems. Communication technologies change rapidly, and each change may result in the need to re-design accessible interfaces. We are closer to goal of having assistive technology adaptations available when the mainstream consumer product ships, but there are still many problems with "workarounds" necessary to make mainstream operating system, productivity software and internet access accessible to people with disabilities.

Development and maintenance of access to ICT must be driven by the needs of people with disabilities. Developments which broaden the scope, applicability and usability of the human technology

interface will be driven, at least in part by the needs of people who have disabilities.

The Internet (e-mail and chat rooms) have the advantage of anonymity, and this can be a major benefit to individuals who have disabilities. Because the person's disability is not immediately visible, people who have disabilities report that they enjoy establishing relationships with people who experience them first as a person and then learn of their disability. For example, Blackstone, (1996) describes some of the advantages of e-mail for individuals who have disabilities. Since the receiver of the message reads it at a later time composition can be at a slower speed. The person with a disability can communicate with another person without someone else being present, establishing a greater sense of privacy than situations in which an attendant is required. It is also possible to work form any location-avoiding some transportation problems

3.3 Universal Design

Increasingly, commercial products are being designed to be usable by all people, to the greatest extent possible, without the need for adaptation or specialized design (NC State University, The Center for Universal Design, 1997).

3.3.1 General Principles of Universal Design

Features are built into products to make them more useful to persons who have disabilities (e.g., larger knobs; a variety of display options--visual, tactile, auditory; alternatives to reading text--icons, pictures) are built into the product. This is much less expensive than modifying a product after production to meet the needs of a person with a disability. The North Carolina State University Center for Universal Design, in conjunction with advocates of universal design, have compiled a set of principles of universal design, shown in Box 1. This center also maintains a Web site on universal design (www.design.ncsu.edu/cud).

3.3.2 Universal Design for ICT

In universal design for ICT the barriers are technological rather than political and economic barriers that characterize architectural and commercial product design (Emiliani, 2006). The goal of universal design for ICT is to have an environment with enough embedded intelligence to be easily adaptable. The features of future information services are that there will be no clearly predefined service and little distinction between interpersonal communication and access to information. Services will need to be highly interactive, inherently multimedia, sensory multimodal (i.e., access via auditory or visual means is equally possible). To achieve this cooperation between users or representatives of users is critical in a variety of contexts of use. The overall goal is to have access to information involving communities of users with a wide range of motor, sensory and cognitive skills.

ONE: EQUITABLE USE
The design is useful and marketable to people with diverse abilities.
TWO: FLEXIBILITY IN USE
The design accommodates a wide range of individual preferences and abilities.
THREE: SIMPLE AND INTUITIVE USE
Use of the design is easy to understand, regardless of the user's experience, knowledge, language skills, or current concentration level.
FOUR: PERCEPTIBLE INFORMATION
The design communicates necessary information effectively to the user, regardless of ambient conditions or the user's sensory abilities.
FIVE: TOLERANCE FOR ERROR
The design minimizes hazards and the adverse consequences of accidental or unintended actions.
SIX: LOW PHYSICAL EFFORT
The design can be used efficiently and comfortably and with a minimum of fatigue.
SEVEN: SIZE AND SPACE FOR APPROACH AND USE
Appropriate size and space is provided for approach, reach, manipulation, and use regardless of user's body size, posture, or mobility.

Box 1: Principles of Universal Design From North Carolina State University, The Center for. Universal Design, 1997.

In addition to Universal Design for ICT, access to capabilities of mainstream technologies includes individualized assistive technologies that are easily – customized. This in return requires an increased understanding of the biological/physical interface for the control of assistive technologies and expanded availability of embedded systems networks.

3.4 A Working Definition of Assistive Technologies

The *International Classification of Functioning, Disability and* Health (ICF) is a system developed by the World Health Organization (WHO) that is designed to describe and classify health and health related states. These two domains are described by

body factors (body structures and functions) and individual and societal elements (activities and participation) (WHO, 2001). The ICF recognizes two contextual factors that modify health and health related states: the environment and personal factors (WHO, 2001). Environmental elements include assistive technologies in relation to activities of daily living, mobility, communication, religion and spirituality as well as in specific contexts such as education, employment and culture, recreation and sport (WHO, 2001). Other environmental elements such as access to public and private buildings, and the natural and built outdoor environments, also have implications for assistive technologies.

A commonly used definition of assistive technology is from the Technical Assistance to the States Act in the United States (Public Law (PL) 100-407): ***Any item, piece of equipment or product system whether acquired commercially off the shelf, modified, or customized that is used to increase, maintain or improve functional capabilities of individuals with disabilities.***

3.4.1 Hard and Soft Technologies

Odor (1984) has distinguished between hard technologies and soft technologies. Hard technologies are readily available components that can be purchased and assembled into assistive technology systems. The main distinguishing feature of hard technologies is that they are tangible. On the other hand, soft technologies are the human areas of decision making, strategies, training, concept formation, and service delivery as described earlier in this chapter. Soft technologies are generally captured in one of three forms: (1) people, (2) written, and (3) computer (Bailey, 1997). These aspects of technology, without which the hard technology cannot be successful, are much harder to obtain. Soft technologies are difficult to acquire because they are highly dependent on human knowledge rather than tangible objects. This knowledge is obtained slowly through formal training, experience, and textbooks such as this one. The development of effective strategies of use also has a major effect on assistive technology system success. Initially the formulation of these strategies may rely heavily on the knowledge, experience, and ingenuity of the assistive technology practitioner. With growing experience, the assistive technology user originates strategies that facilitate successful device use. There is a false belief that progress is solely driven by "hard" technological change The gap between the general public and persons with disabilities can only be closed by gains in both soft and hard technologies

3.4.2 Mainstream Technologies to Specially Designed Technologies: A Range of Options

As illustrated in Figure 1, the needs of people with disabilities can be met in a number of ways. Off the shelf "standard" (i.e., mainstream technologies) commercially available devices (especially those designed using the principles of universal design) can often be used by people with a variety of disabilities. For example, standard personal computers designed for the general population are often used by persons with disabilities. Sometimes these need to be modified however, to make them useable. Another type of commercially available device is one that is mass-produced but specifically designed for individuals with disabilities *(special commercially available devices)*. These devices often need to be modified to meet the needs of a specific individual. Our goal is to reduce the amount of modification necessary and to make mainstream technologies as accessible as possible. However, there will always be a portion of the disabled population that will require specifically designed assistive technologies.

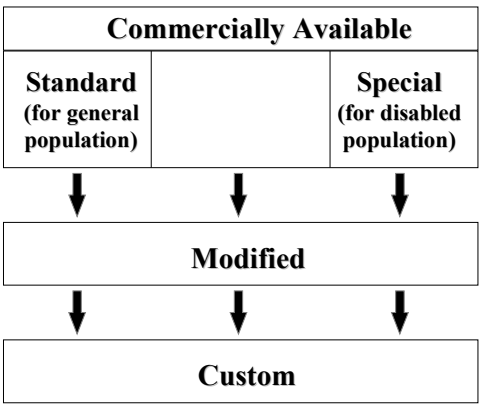

Figure 1: This diagram shows the progression from commercially available devices for the general population and commercially available devices for special populations to modified devices and custom devices. From Cook and Polgar, (2007).

3.5 The Human Technology Interface for ICT

3.5.1 General Concepts

It is estimated that as many as 40 million persons in the United States alone have physical, cognitive, or sensory disabilities (Lazzaro, 1999). The world-wide impact is significantly larger. If these people are to compete on an equal basis with non-disabled individuals, then it is extremely important that the internet be accessible to all. As the internet becomes more and more dependent on multimedia representations involving complex graphics, animation, and audible sources of information, the challenges for people who have disabilities increase. In order for access to the Internet to be useful to people with disabilities, the accessibility approach must be independent of individual devices. This means that users must be able to interact with a *user agent* (and the document it renders) using the input and output devices of their choice based on their specific needs. A **user agent** is defined as software to access Web content (www.w3.org/wai). This includes desktop graphical browsers, text and voice browsers, mobile phones, multimedia players, and software assistive technologies (e.g., screen readers, magnifiers) that are used with browsers. The person with a disability interacts with technology through the Human Technology Interface (HTI) (Cook and Polgar, 2007).

The graphical user interface (GUI) has both positive and negative implications for persons with disabilities. The positive features are those that apply to non-disabled users (e.g., use of icons, recognition rather than recall memory, screen icons for the same task look the same, operations such as opening and closing files are always the same). The GUI is the standard user interface because of its ease of operation for novices and its consistency of operation for experts. The latter ensures that every application behaves in basically the same way. People with motor disabilities may not have the necessary physical (eye-hand coordination) and visual skills to navigate the GUI. Modification of the GUI to allow specialized access (see Figure 1) can also be more challenging for GUI-based operating systems.

As networks are expanded and more devices (e.g., cell phones, PDAs) have open architectures, it will be possible to download profiles, adaptations and special instructions that enable adaptable systems to be developed to meet the needs of people who have disabilities. Some examples are (1) trainable hearing aids that adjust automatically to the environments in which they are used; (2) a "Smart House" that assesses occupants current state and the state of various home utilities to aid with common activities of daily living, provides feedback should residents become disoriented or confused and report medical emergencies automatically; an orientation and direction finding device that senses the current location (via GPS) and gives directions to a desired location for individuals who cannot read maps because of visual or cognitive disabilities.

3.5.2 Access for Motor Impairment

There are a significant number of people who cannot effectively use standard keyboards, mouse controls or switches. It is likely that we will see a much greater understanding of the biological/physical interface for the control of computers in the future (Applewhite, 2004).

One approach that may offer promise is the brain computer interface (BCI). BCI systems may be grouped into a set of functional components including the input device, amplification, feature extraction, feature translation and user feedback (Mason and Birch, 2003). Signals are mathematically analyzed to extract features useful for control (Fabiani, Mcfarland, Walla, and Pfurtscheller 2004). Features or signals that have been used include slow cortical potentials, P300 evoked potential, sensorimotor rhythms recorded from the cortex and neuronal action potentials recorded within the cortex). A typical task for a user is to visualize different movements or sensations or images.

Another approach to cursor control is the use of a digital camera and image recognition software to track a particular body feature to control an on-screen mouse cursor (Betke, Gips and Fleming, 2002). The most easily tracked feature is the tip of the nose, but the eye (gross eye position not point of gaze), lip, chin and thumb have also been used. Non-disabled subjects used this approach and fund that the camera mouse was accurate but slower than a typical hand-controlled mouse. Using an on-screen keyboard the camera mouse was half as fast as a regular mouse in a typing task, but the accuracy obtained was equivalent on each system. More and more computers have built-in cameras, so the camera mouse requires only software to capture the body feature image and interpret its movement as mouse commands. This may lead to wider application of this technique.

There are many other approaches that are used to provide access to and control over technologies for people with severe motor disabilities (Cook and Polgar, 2007) \. These range form keyboards of various type, to automatic speech recognition to mouse and mouse emulators systems to single and multiple switches.

3.5.3 Access for Cognitive Impairment

Cognitive disabilities include a wide range of skills and deficiencies. Learning disabilities typically involve significant difficulties in understanding or in using either spoken or written language, and these difficulties may be evident in problems with reading, writing, mathematical manipulation, listening, spelling or speaking (Edyburn, 2005). These limitations make it increasingly difficult to access complicated Web sites that may include flashing pictures, complicated charts, and large amounts of audio and video data. While there are assistive technologies that are specifically designed to address these areas (discussed later in this chapter), many of the technological tools are useful for all students, and are part of instructional technology (Ashton, 2005). Even the so-called assistive technologies have features (e.g., multimedia, synthetic speech output, voice recognition input) that are useful to all learners.

For individuals with acquired cognitive disabilities due to injury (e.g., traumatic brain injury) or disease (e.g., stroke (CVA) or dementia) changing features such as font size, background/ foreground color combinations, contrast, spacing between words, letters and paragraphs and using graphics can all improve access to screen-based information. Another technological concept for these individuals is a cognitive prosthesis, which is a custom-designed computer-based compensatory strategy that directly assists in performing daily activities[1]. It may also include additional technologies such as a cell phone, pager, digital camera or low tech approaches

Persons with intellectual disabilities have difficulties with memory, language use and communication, abstract conceptualization, generalization and problem identification/problem solving. Characteristics of the HTI that are important for these individuals include simplicity of operation, capacity of the technology to support repetition, consistency in presentation, and inclusion of multiple modalities (e.g., speech, sounds and graphical representations) (Wehmeyer, Smith and Davies, 2005).

An example of technology designed for cognitive needs is the Planning and Execution Assistant and Trainer (PEAT). It is a PDA-based personal planning assistant designed to assist individuals with cognitive disorders due to brain injury, stroke, Alzheimer's disease, and similar conditions (Levinson, 1997). PEAT employs artificial intelligence to automatically generate plans and also to revise those plans when unexpected events occur. PEAT uses a combination of manually entered schedules and a library of stored scripts describing activities of daily living (e.g., morning routine or shopping). Scripts can be used for both planning and for execution. Planning involves a simulation of the activity with key decision points presented and prompts (auditory and visual) supplied necessary to aid the individual through the planning process. The plan to be executed can be either the stored script or a modified script based on the simulation. The PEAT artificial intelligence software generates the best strategy to execute the required steps in the plan (LoPresti, Mihailidis, and Kirsch, 2004). PEAT also automatically monitors performance, and corrects schedule problems when necessary.

3.5.4 Access for Auditory Impairment

Since web pages are a mixture of text, graphics, and sound, people who are deaf may be prevented from accessing some information unless alternative methods are available. The primary approach for thee individual is the use of the Microsoft Synchronized Accessible Media Interchange (SAMI), which allows authors of Web pages and multimedia software to add closed captioning for users who are deaf or hard of hearing. This approach is similar to the use of closed captioning for television viewers. The W3C WAI SMIL (www.w3.org/WAI) is designed to facilitate multimedia presentations in which an author can describe the behavior of a multimedia presentation, associate hyperlinks with media objects, and describe the layout of the presentation on a screen

Trainable hearing aids adjust automatically to the environments in which they are used through access to embedded information networks. This allows automatic adaptation to changing noise levels and environments.

[1] Institute for Cognitive Prosthetics, http://www.brain-rehab.com/ definecp.htm

3.5.5 Access for Visual Impairment

The W3C WAI user agent guidelines are based on several principles that are intended to improve the design of both types of user agents. The first is to ensure that the user interface is accessible. This means that the consumer using an adapted input system must have access to the functionality offered by the user agent through its user interface. Second, the user must have access to document content through the provision of control of the style (e.g., colors, fonts, speech rate, and speech volume) and format of a document. A third principle is that the user agent help orient the user to where he is in the document or series of documents. In addition to providing alternative representations of location in a document (e.g., how many links the document contains or the number of the current link), a well-designed navigation system that uses numerical position information allows the user to jump to a specific link. Finally, the guidelines call for the user agent to be designed following system standards and conventions. These are changing rapidly as development tools are improved.

Communication through standard interfaces is particularly important for graphical desktop user agents, which must make information available to assistive technologies. Technologies such as those produced by the W3C include built-in accessibility features that facilitate interoperability. The standards being developed by the W3C WAI provide guidance for the design of user agents that are consistent with these principles. The guidelines are available on the W3C WAI Web page (www.w3.org/wai).

3.5.6 Other ICT Access

Cellular telephones are becoming more powerful with capabilities approaching that of personal computers. This expanded capability will provide significant advantages for people with disabilities, especially those with low vision or blindness. describes Three changes will be particularly valuable to people who have disabilities:: (1) standard cell phones will have sufficient processing power for almost all the requirement of persons with visual impairments, (2) software will be able to be downloaded into these phones easily, (3) wireless connection to a worldwide network will provide a wide range of information and services in a highly mobile way (Fruchterman, 2003). Because many of these features will be built into standard cell phones the cost will be low and reachable by persons with disabilities. A major advance will occur if the cell phone industry moves away from proprietary software to an open source format providing the basis for a greater diversity of software for tasks such as text-to-speech output, voice recognition and optical character recognition in a variety of languages. Many applications for people with disabilities will be able to be downloaded from the internet. With expanded availability of embedded systems, it will be possible for a user to store their customized programs on the network and download them as needed form any remote location.

Downloading a talking book program into a cell phone can provide access to digital libraries for persons who are blind. Outputs in speech or enlarged visual displays can be added as needed by the user. With a built-in camera and network access a blind person could obtain a verbal description of a scene by linking to on-line volunteers who provide descriptions of images. These applications will depend on the increasing application of universal design in information technology products (Tobias, 2003). These applications include ATMs, cell phones, vending machines and other systems that are encountered on a daily basis (Tobias, 2003).

4 INFRASTRUCTURE FOR FUTURE ACCESSIBILITY

The infrastructure for future accessibility consists of: (1) an expanded, smarter and more available "real" and "virtual" internet, (2) Home automation systems that are smarter and have greater interconnectivity, (3) universal design principles that are applied more widely, (4) alternative approaches for accessing information technologies, and (5) special-purpose assistive technologies.

The Infrastructure for future accessibility will depend on several factors. These include: Web-based virtual systems, home automation, universal design for ICT, alternatives for accessing information technologies and special-purpose assistive technologies. In addition there is n on going need for the development of soft technology tools.

If ICT advances are not adaptable enough to be accessible to persons with disabilities it will further increase the disparity between those individuals and the rest of the population leading to further isolation and economic disadvantage. On the other hand, availability of these technologies in a transparent way will contribute to full inclusion of individuals who have disabilities in the mainstream of society.

5 CONCLUSIONS

The move to the information age offers great promise for persons with disabilities. It also holds great threats for persons with disabilities. Constant vigilance is required to insure that information technologies remain accessible and responsive to the needs of persons with disabilities. The future for persons with disabilities will not be driven by advances in technology, but rather by how well we can take advantage of those advances for the accomplishment of the many tasks of living that require technological assistance

6 SUMMARY

Anticipated changes in technologies coupled with the focus on the social aspects of disability, provide a significant opportunity for major advances in the degree to which individuals with disabilities can participate in all aspects of life, including work, school, leisure and self care.

Technological advances will be particularly important as the percentage of the population that is elderly rises. Concepts from universal design will be important in ensuring that this segment of the population remains active and is able to participate in society. This new group of elderly individuals will also be more experienced with computers and other technologies than their predecessors and they may well demand greater performance and adaptability from both assistive technologies and mainstream ICT (e.g., telephones, internet communication).

The percentage of individuals with long-term disabilities who join the over 65 age group will also increase. These individuals will have been long-term users of assistive technologies, and their experience will have major implications for developments to meet future needs.

While much of what I have described is conjecture, it is based on modest extrapolation from the current state of the art. There are some things that we know with a high degree of certainty. We know that computer systems will be faster, have more memory be smaller and be less expensive for the same or greater functionality. We also know that the communication channel bandwidth will continue to increase allowing much more information and much more sophisticated information processing. Finally, it is clear that people with disabilities will continue to assert their right to fully participate in society.

Technological advances also raise questions for people who have disabilities. The most important of these is whether accessibility will keep pace with technological developments. For example, will assistive technologies for input and output be compatible with the user agents and operating systems of tomorrow. A second major question is whether the needs of persons with disabilities will be a driving force in future technological developments. Will people who have disabilities have to adapt to the existing technologies based on characteristics for non-disabled people or will universal design become a greater reality? In the latter case, adaptations will become less important and accessibility will become the rule rather than the exception.

For people who have disabilities, there are significant implications of emerging information processing technologies. If not closely monitored, these could result in less rather than more access to the new information economy for persons with disabilities. Despite the wider use of universal design principles, there will still be a need for effective assistive technology design and application if individuals with disabilities are to realize the full potential of the new information age.

REFERENCES

Applewhite A: (2004). 40 years: the luminaries. *IEEE Spectrum,* 41(11), 37-58.

Ashton T.M. (2005). Students with learning disabilities using assistive technology in the inclusive classroom, pp. 229-238, in Edyburn D., Higgins K.. & Boone R. (eds.): *Handbook of Special Education Technology Research and Practice,* Whitefish Bay, Wisconsin: Knowledge by Design, Inc.

Bailey, R.W: (1996). *Human performance engineerin.,* ed 2, Upper Saddle River, NJ, , Prentice Hall.

Betke M., Gips J. & Fleming P: (2002). The camera mouse: Visual tracking of body features to provide computer access for people with severe disabilities. *IEEE Trans. Neural Systems and Rehabilitation Engineering,* 10(1): 1-10.

Blackstone S. (1996). The Internet: what's the big deal *Augment Commun News* 9(4):1-5.

Cook A.M. & Polgar J.M. (2007). *Cook and Husey's Assistive Technologies: Principles and Practice*, 3rd ed St. Louis: Elsevier.

Edyburn D.L. (2005). Assistive technology and students with mild disabilities: from consideration to outcome measurement, pp 239-270, in Edyburn D, Higgins K. & Boone R. (eds.): *Handbook of Special Education Technology Research and Practice,* Whitefish Bay, Wisconsin: Knowledge by Design, Inc.,

Emiliani, P.L. (2006). Assistive technology (AT) versus Mainstream Technology (MST): The research perspective. *Tech Disab*, 18, 19-29,

Fabiani G.E., Mcfarland D.J., Wolpaw J.R., & Pfurtscheller G (2004). Conversion of EEG activity into cursor movement by a brain-computer interface (BCI). *IEEE Trans. Neural Systems and Rehab Engr*, 12: 331-338.

Fruchterman J.R: (2003) In the palm of your hand: A vision of the future of technology for people with visual impairments. *J Vis Impair Blindness, 97*(10), 585-591.

Kumagai, J. (2004).Talk to the machine. *IEEE Spectrum,* 39(9): 60- 64.

Lazzaro J.L. (1999). Helping the web help the disabled, *IEEE Spectrum* 36(3): 54-59

Levinson R.L. (1997): The planning and execution assistant and trainer. *J. head trauma rehabilitation*, 12(2): 769-775.

Lewis, J.R. (2004). .In the eye of the beholder*, IEEE Spectrum,* 41(5)24- 28.

LoPresti E.F., Mihailidis A. & Kirsch N. (2004): Assistive technology for cognitive rehabilitation: State of the art. *Neuropsychological Rehabilitation,* 14(1): 5-39.

Mason S.G. & Birch G.E: (2003).A general framework for brain-computer interface design. *IEEE Trans. Neural Systems and Rehab Engr*, 11, 70-85.

Odor P. (1984): Hard and soft technology for education and communication for disabled people, *Proc Int Comp Conf*, Perth, Western Australia,

Tobias J: (2003). Information technology and universal design: An agenda for accessible technology. *J Vis Impair Blindness, 97*(10), 592-601.

Ungson G.R. and Trudel J.D. (1999). The emerging knowledge-based economy. *IEEE Spectrum*, 36(5):60-65.

Wehmeyer M.L., Smith S.J., Palmer SB, Davies D.K. & Stock S.E: (2004). Technology use and people with mental retardation. *International Review of Research in Mental Retardation,* 29: 291-337.

World Health Organization (2001): *International classification of functioning disability and health*-ICF, Geneva, World Health Organization

Wright, RA. (2004). *A Short History of Progress*, Toronto: Anansi Publications.

SHORT PAPERS

PROBABILISTIC WORKPSACE SCAN MODES OF A ROBOT MANIPULATOR COMMANDED BY EEG SIGNALS

Fernando Alfredo Auat Cheeín, Fernando di Sciascio, Ricardo Carelli
Institute of Automatic, National University of San Juan, Av. San Martin 1109-Oeste, San Juan, Argentina
fauat@inaut.unsj.edu.ar, fernando@inaut.unsj.edu.ar, rcarelli@inaut.unsj.edu.ar

Teodiano Freire Bastos Filho
Electrical Engineering Department, Federal University of Espírito Santo, Av. Fernando Ferrari 514, Vitória, ES, Brazil
tfbastos@ele.ufes.br

Keywords: Brain Computer-Interface, Robot Manipulator, Probabilistic Scan Mode.

Abstract: In this paper, probabilistic-based workspace scan modes of a robot manipulator are presented. The scan modes are governed by a Brain Computer Interface (BCI) based on Event Related Potentials (Synchronization and Desynchronization events). The user is capable to select a specific position at the robot's workspace, which should be reached by the manipulator. The robot workspace is divided into cells. Each cell has a probability value associated to it. Once the robot reaches a cell, its probability value is updated. The mode the scans are made is determined by the probability of all cells at the workspace. The updating process is governed by a recursive Bayes algorithm. A performance comparison between a sequential scan mode and the ones proposed here is presented. Mathematical derivations and experimental results are also shown in this paper.

1 INTRODUCTION

Brain Computer Interfaces have got a great impulse during the last few years. The main reasons for this growing are the availability of powerful low-cost computers, advances in Neurosciences and the great number of people devoted to provide better life conditions to those with disabilities. These interfaces are very important as an augmentative communication and as a control channel to people with disorders like amyotrophic lateral sclerosis (ALS), brain stroke, cerebral palsy, and spinal cord injury (Kubler et al.,2001, Wolpaw et al., 2002).

The main point of a BCI is that the operator is capable to generate commands using his/her EEG (electroencephalographic) signals in order to accomplish some specific actions (Wolpaw et al., 2002, Lehtonen, 2003, Felzel, 2001, Millán et al., 2003). Thus, an operator using a BCI can control, for example, a manipulator, a mobile robot or a wheelchair (amongst other devices) without using any muscle. The EEG frequency bands have enough information to build an alphabet of commands in order to control/command some kind of electronic device (Ochoa, 2002). In this paper a BCI, which is controlled through alpha waves from the human brain, is used. Although the EEG signal acquisition/conditioning, which is part of this BCI, was developed in other work of the authors (Ferreira et al., 2006), one of the objectives of this paper is to illustrate its versatility, mainly in terms of the simple algorithms used.

Event related potentials (ERP) in alpha frequency band are used here. Such potentials are ERD (Event Related Desynchronization) and ERS (Event Related Synchronization), well described in the following sections. This BCI has a Finite State Machine (FSM) which was tested in a group of 25 people.

The main contributions of this paper are the scan mode algorithms proposed to allow the user to command a manipulator (Bosch SR-800), based on a probabilistic scan of the robot's workspace. The workspace is divided into cells. Each cell contains three values: its position (x, y) at the robot's workspace plane and a probability value. This value indicates the accessibility of that element. Once a particular cell is accessed, its probability is updated based on Bayes' rule.

This paper is organized as follows: a brief description of the sequential scan mode of the manipulator's workspace is presented in section 2. The probabilistic scan modes proposed are shown in Section 3. Section 4 shows the results for a Montecarlo experimentation, where the probabilistic evolution of the whole workspace and of a specific cell is presented. Section 5 shows the conclusions of this work.

2 SEQUENTIAL SCAN MODE

As a brief introduction, the sequential scan mode of the robot workspace developed in Ferreira et al. (2006) is presented here.

The workspace is previously divided into three main zones as it can be seen in Fig. 1. The system iteratively scans from *zone 1* to *zone 3* until one of them is selected by the user (using EEG signals). Once it is so, the selected zone is scanned row by row until one is selected. Once a row is selected, the system scans cell by cell (switching columns) iteratively inside the selected row. After a cell is selected by the user, the robot reaches the position given by that cell.

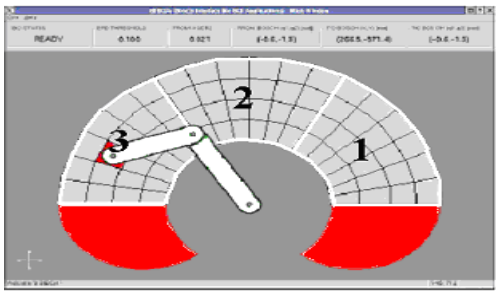

Figure 1: Main zone division at robot's workspace.

3 PROBABILISTIC SCAN MODES

The two probabilistic scan modes shown in this paper are based on Bayes rule for updating probability values of the cells at the manipulator's workspace. The scan modes are shown in the following sections.

3.1 First Approach of a Probabilistic Scan Mode

The first approach of a probabilistic scan mode works as follows:

1. The workspace's resolution is set to 72 cells and can be easily changed, decreasing or increasing this number. The workspace behaves as a *pmd* (probabilistic mass distribution).
2. Each cell has its own initial probability. This value can be previously determined by some heuristic method (for example: if the BCI operator is right-handed, then cells to the right of the workspace will have higher accessing probability than the ones to the left). However, it is also possible to set all cells to a probability near zero, in order to increase or decrease them depending on the times they are accessed by the user. In this work, the first case was adopted.
3. Let *a* and *b* be the higher and lower probabilities cells respectively. Then, the workspace is divided into three zones according to these values. Table 1 shows how division is made. Let $P(C_i \mid G)$ be the probability of cell C_i given a group G to which it belongs.
4. Every zone at the workspace is divided in three sub-zones under the same philosophy presented before. Each one of these sub-zones contains a set of probabilistic weighted cells.
5. The scan mode proceeds as follows:
   I. First, the zone with the highest probability value at the workspace is highlighted. If that zone is not selected by the operator, the second highest probabilistic zone is highlighted. If it is not selected, the highlight passes to the third and last zone. The scan keeps this routine until a zone is selected.
   II. When a zone is selected, the highlight shows first the sub-zone with the highest probability inside the zone previously selected. The scan, in this case, is exactly the same used in the last step.
   III. When a sub-zone is selected, then the scan highlights first the cell with the highest probability of occupancy. If it is not selected, the scan passes to the next cell value. This routine keeps going on until a cell is selected. Once a position is selected, the probability value of the cell, sub-zone, zone and complete workspace is updated. The update of the probabilities values is made by the Bayes' rule.

As it can be seen, the number of cells that belong to a sub-zone or a zone is variable. Then, the organization of the zones at robot's workspace is dynamic. This allows improving the scan mode in

order to access in a priority way to the most frequently used cells.

The probability update of each cell at the workspace is based on the recursive Bayes' rule. Once a cell is reached by the user, its probability value changes according to (1).

Table 1: Workspace's Zones Definitions.

a	highest probability cell value
b	lowest probability cell value
$\left\{c_i : b+\frac{2}{3}(a-b) < P(C_i \mid G) \le a\right\}$	zone 1: the set of all cells which probabilities are the highest of the workspace
$\left\{c_i : (b+\frac{(a-b)}{3}) < P(C_i \mid G) \le (b+\frac{2}{3}(a-b))\right\}$	zone 2: the set of all cells which probabilities are of middle range
$\left\{c_i : b \le P(C_i \mid G) \le (b+\frac{(a-b)}{3})\right\}$	zone 3: the set of all cells with the lower probability of the workspace.

Let C be any cell at robot's workspace and G a set to which that cell belongs. Thus, the updating algorithm is given by,

$$P_k(C \mid G) = \frac{P_k(G \mid C)P_{k-1}(C \mid G)}{P_k(G \mid C)P_{k-1}(C \mid G) + P_k(G \mid \overline{C})P_{k-1}(\overline{C} \mid G)} \quad (1)$$

Though (1) is mainly used in very simple applications (Thrun et al., 2005), it fits as an updating rule for the purpose of this work.

Equation (3) can be re-written in (4), where a scale factor was used.

$$P_k(C \mid G) = \eta P_k(G \mid C)P_{k-1}(C \mid G) \quad (2)$$

According to the Total Probability Theorem (Thrun et al., 2005), η is the scale factor, which represents the total probability of $P(G)$. In (1), $P_{k-1}(C \mid G)$ is the prior probability of a cell given the primary set to which it belongs at time $k-1$. $P_k(G \mid C)$ is the transition probability which represents the probability that a given cell C belong to a set G. Finally, $P_k(C \mid G)$ is the posterior probability -at instant k- of the cell used given the zone to which it belongs.

In order to make sense to the use of the recursive Bayes algorithm, an initial probability value must be given to all cells at the workspace.

Figure 2 shows the evolution of a cell's probability when it is accessed successively by the user.

The cell used in Fig. 2, for example, has an initial value of 0.05 but it is increased each time the cell is accessed by the user. As was expected, the maximum value a cell can reach is one. When this situation occurs, the whole workspace is scaled. This scaling does not change the scan mode because the relative probability information remains without changes, i.e., if a cell p has the maximum probability over all cells, after scaling, p will continue being the cell with the highest weight. A more extended development of this algorithm can be seen at Papoulis (1980). Once the updating algorithm is complete, the scan algorithm is released as described in Section 3.

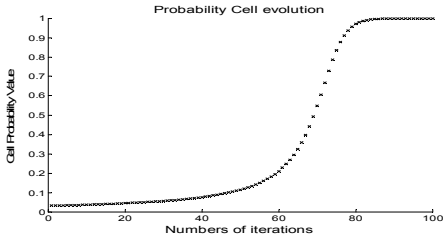

Figure 2: Evolution of Cell's probability when successively accessed.

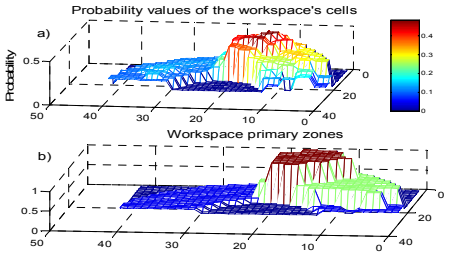

Figure 3: Probabilistic distribution of a workspace for a right-handed user.

Figure 3 shows the workspace's *pmd* for a right-handed user. Fig. 3.a shows the cells probability's value and Fig. 3.b shows the different zones of the manipulator's workspace.

3.2 Second Approach

This second approach investigated in this work is based on the sequential scan mode algorithm. Each zone or sub-zone -as those shown in Fig. 1- has a probability value associated with it. As the workspace is considered as *pmd* then each zone or sub-zone's probability value is calculated as the sum of all probability values of the cells that belong to that group. The scan mode proceeds as follows:

1. The zone with the highest probability is highlighted first; then, the second higher

probability zone is highlighted and then the last zone (see Fig. 1). The highlighting process repeats until the user chooses a zone.

2. Once a zone is chosen, the row with the highest probability -inside that zone- is highlighted. A row of a zone is known as sub-zone. If this sub-zone is not selected by the user after a period of time, the highlight passes to the next higher probability value row. This process is repeated iteratively until a row is selected by the user.
3. Once a sub-zone is chosen, the cell with the highest probability of that sub-zone is highlighted. If it is not chosen after a period of time, the highlight passes to the next higher probability cell. The process continues and if no cell is chosen, it starts from the beginning cell.
4. If a cell is chosen, then its probability is updated according to the Bayes rule (Eq. 3). Then, workspace *pmf*, sub-zone's probabilities and all zone's probabilities are also updated.

The sampling time used in all scan modes is the same one used in Ferreira et al. (2006).

4 EXPERIMENTAL RESULTS

This section is entirely dedicated to compare the three scan types: sequential and probabilistic ones. For this purpose, a Montecarlo experiment was designed (Ljung, 1987). This experiment shows the performance of the three methods by measuring the time needed to reach different cells at the robot's workspace.

4.1 Montecarlo Experiment

The robot's workspace consists of 72 cells. It also can be considered as a 4×18 matrix. According to this, a cell's position is defined by a number of row and a number of column at that matrix. The number of a row and a column can be considered as a random variable. To generate a random position of a cell destination, the following algorithm was implemented.

i. An uniform random source generates two random variables: x and y.
ii. The random variable x is mapped into the rows of the 4×18 matrix workspace.
iii. The random variable y is mapped into the columns of the 4×18 matrix workspace.
iv. When a position is generated, both scan types begin. The time needed to reach the cell is recorded.
v. After the system reaches the position proposed, a next process point generation is settled -the algorithm returns to point i-.

4.2 Mapping Functions

Let f_x be a mapping function such as:

$$f_x : A \to B$$
$$x \to m$$

where,

$$\begin{cases} A = \{x : x \in [0,1) \subset \Re\} \\ B = \{m : m \in \{1,2,3,4\} \subset \aleph\} \end{cases} \quad (3)$$

and let f_y be another mapping function such as:

$$f_y : A \to C$$
$$y \to n$$

where,

$$\begin{cases} A = \{y : y \in [0,1) \subset \Re\} \\ B = \{n : n \in \{1,2,3,...,18\} \subset \aleph\} \end{cases} \quad (4)$$

Equations (3) and (4) show the domain and range of the mapping functions. Finally, the mapping is made according to the following statements.

i. Let δ be the sum of all weights at robot's workspace, that is, $\delta = \sum_{i\in B}\sum_{j\in C} P_{ij}$, where P_{ij} is the probability value of a cell located at the $i-row$ and $j-column$.
ii. Let $x \in A$ be an outcome of the uniform random source for f_x.
   - If $0 \le x < \frac{\sum P_{ij}}{\delta}$ then $f_x(x) = i = 1$. This means that the value of $x \in A$ should be lower than the sum of all cell's values in row one -over δ - to $f_x(x)$ be equal to one.
   - If $\frac{\sum P_{ij}}{\delta} \le x < \frac{\sum P_{ij}}{\delta}$ then $f_x(x) = i = 2$. This means that $x \in A$ should be greater or equal to the sum of all cell's values in row one and lower than the sum of all cell's values in row 2.
   - The same process continues up to the last row, whose expression is: if $\frac{\sum P_{ij}}{\delta} \le x < \frac{\sum P_{ij}}{\delta}$ then $f_x(x) = i = 4$.
   - Each time a cell is selected, the mapping functions vary. It is so because they are

dependent with the probability value of the cells.

- For the mapping over the columns, the procedure is the same, however in this case, the sum is made over the set *B* (four rows).

Concluding, the mapping presented here is dynamic because it is updated each time a cell varies its probability value. For the case implemented in this work (a right-handed user) the initial mapping functions are represented in Figs. 4.a and 4.b. In Fig. 4.b is also possible to see that column 10 has higher probability than column 1. It is also important to see that, if all cells at robot's workspace have the same probability weight, then the mapping functions would be uniform. Thus, each row or column would have the same probability to be generated.

4.3 Montecarlo Simulation Results

The objective of Montecarlo experiments was to test the performance of both scanning methods: probabilistic and sequential ones. The performance is measured in function of the time needed to access a given position. This position is generated by the uniform random source. After 500 trials the mean time needed to access a random position by the first approach of the probabilistic scan was of 20.4 seconds. For the second approach of the probabilistic scan the mean time needed was of 16.8 and for the sequential scan was of 19.8 seconds. The three results are in the same order but the probabilistic second approach of the scan mode requires less time. Consider now only the right side of the workspace, which is, according to Fig. 3, the most accessed side. The mean time of access for all points belonging to the workspace right side is of 8.4 seconds under the first approach of the probabilistic scan instead of 11.3 seconds corresponding to the second approach of the probabilistic scan mode. Under sequential scan, the mean time is of 14.8 seconds. The probabilistic scan mode first approach is 43% faster than the sequential scan for cells over the right side of the workspace while the second approach is 23.7% faster.

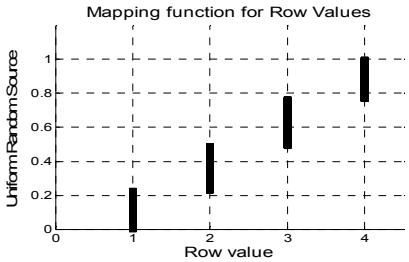

Figure 4.a: Mapping function for the four values of rows.

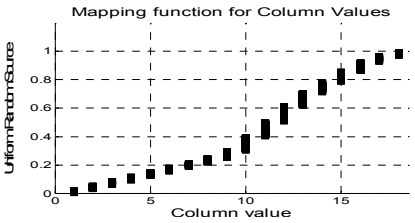

Figure 4.b: Mapping function for the 18 values of columns.

Figure 5 shows how a low probability valued cell in the probability scan first approach evolves after successive callings. The cell passes through the different zones of cells according to its actual probability value. After 240 iterations -or callings-, the cell has passed through three zones and its performance has also been improved as long as its weight. In Fig. 5, one can see that at the beginning, 32 seconds were needed to access that cell.After 240 iterations, only 14 seconds were needed. This time is smaller than the one needed on the sequential scan mode which is of 18 seconds. Fig. 5 also shows when the cell changes zones. Thus, if its probability increases, the cell passes from, for example, *primary zone 2* to *primary zone 1*. Though a cell could be the first in being scanned in the *primary zone 2*, if it increases its value and passes to *primary zone 1*, it could be the last scanned element in this zone. That is the reason of the two time increments in Fig. 5. A cell under the second approach of the probabilistic scan shows similar behavior to the one showed in Fig. 5.

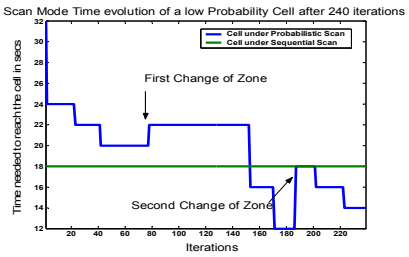

Figure 5: Evolution of a cell access time.

Figure 6 shows the workspace state after 500 iterations generated by the Montecarlo experiment using the first approach of the probabilistic scan. Fig. 6.a shows the probability state of each cell at the workspace while Fig. 6.b shows the new three zones of the scan mode algorithm. One can see that the non-connectivity tends to disappear.

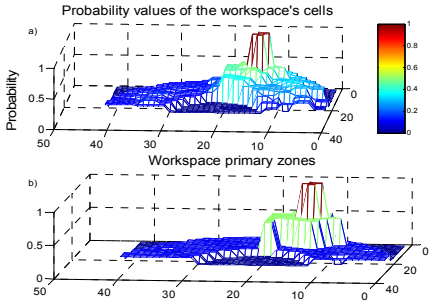

Figure 6: Workspace state after 500 iterations.

On the other hand, Fig. 7 shows the workspace state after the same iterations of Fig. 6 under the second approach of the probabilistic scan, though this scan do not imply a dynamic behavior of the number of cells of the different zones.

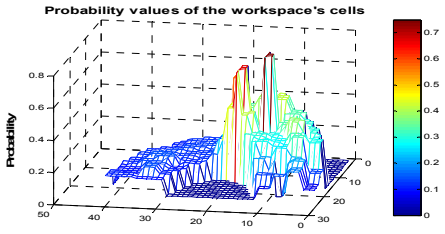

Figure 7: Workspace state after 500 iterations under the second approach of the probabilistic scan mode.

As it can be seen from Figs. 6 and 7, probabilistic distribution of the workspace depends on the type of scan mode used. Both probabilistic scan modes presented in this work show a better performance respect to the sequential scan mode.

5 CONCLUSIONS

The work presented here showed the implementation of two probabilistic scan modes, based on a recursive Bayes algorithm, of a robot manipulator's workspace. A comparison between these methods and a sequential scan mode showed that the probabilistic scan improves the access time of the most frequently accessed cells. Although this system could be implemented in several Human-Machine Interfaces, it was primary designed for a Brain-Computer Interface.

Experimental results show that the time needed to access a specific position at the workspace is decreased each time the position is reached. This is so because the recursive Bayes algorithm implemented updates the probability value of that position once it is reached. A decrement of the access time means that the user of the Interface needs less effort to reach the objective.

In this work, a right-handed workspace distribution case was presented. This case showed that all cells to the right of the middle point -half of the main workspace- have the higher probability and the lower time needed to be accessed.

Finally, it is possible to say that the system learns the user's workspace configuration. It pays special attention to those cells with the highest probability minimizing the time needed to access them.

ACKNOWLEDGEMENTS

The authors thank CAPES (Brazil), SPU and CONICET (Argentina) and FAPES (Brazil), for their financial support to this research.

REFERENCES

Felzel, T., 2001. On the possibility of developing a brain-computer interface (BCI). Technical University of Darmstadt, Darmstadt, Germany, Tech. Rep., (2001).

Ferreira, A., T. F. Bastos Filho, M. Sarcinelli Filho, F. A. Auat Cheeín, J. Postigo, R. Carelli, 2006. Teleoperation of an Industrial Manipulator Through a TCP/IP Channel Using EEG Signals, I*n International Symposium on Industrial Electronics*, Montreal. Proceedings of ISIE2006, v. 1, p. 3066-3071.

Kubler, A., B. Kotchoubey, J. Kaiser, J. R. Wolpaw, and N. Birbaumer, 2001. Brain-computer communication: unlocking the locked, In. *Psychol Bull*, vol. 127, no. 3, pp. 358.75, (2001).

Lehtonen, L., 2003. *EEG-based brain computer interfaces*,. Master's thesis, Helsinky University of Technology, Helsinky, Finl.andia, (2003).

Ljung, L., 1987. *System Identification*, New Jersey: Prentice Hall.

Millán, J., F. Renkens, J. Mouri.ño, and W. Gerstne, 2003. Non-invasive brain-actuated control of a mobile robot, in *Proceedings of the 18th International Joint Conference on Artificial Intelligence*, Acapulco, Mexico.

Ochoa, J. B., 2002. *EEG brain classification or brain computer interface*, Master's thesis, Ecole Polytechnique Federale de Lusanne, Lusanne.

Papoulis, A., Probabilidad, variables alatorias y procesos estocásticos, Barcelona: Eunibar, 1980.

Thrun, S., W. Burgard, D. Fox, Probabilistic Robotics, Massachusetts: The MIT Press, 2005.

Wolpaw, J. R., N. Birbaumer, D. J. McFarland, G. Pfurtscheller, and T. M. Vaughan, 2002. Brain-computer interfaces for communication and control. *Clin Neurophysiol*,6, no. 6, pp. 767.791.

OMNIDIRECTIONAL VISION TACKING SYSTEM BASED ON KALMAN FILTERING AND OMNICAMSHIFT

B. Allart, B. Marhic, L. Delahoche
LTI – IUT Informatique Avenue des facultés – Le Bailly - 80025 Amiens Cedex 1, France
Benjamin.allart@cegetel.net , {bruno.marhic, Laurent.delahoche}@u-picardie.fr

O. Rémy-Néris
CHU of Brest, 5 avenue Foch 29200 Brest, France
olivier.remyneris@chu-brest.fr

A. M. Jolly-Desodt
GEMTEX - 9, rue de l'Ermitage - 59056 Roubaix Cedex 1, France
anne-marie.jolly-desodt@ensait.fr

Keywords: Rehabilitation Robotics, Autonomous platform, wheelchair tracking, CAMSHIFT, Kalman filter.

Abstract: This paper deals with a robotised assistance dedicated for Handicap person. In this paper, we will propose to discus about one of the main functionality of this project: the tracking of the wheelchair from an autonomous mobile platform on which the Manus (c) arm is mounted. To ensure the tracking, we will present a method based on Kalman filter's algorithm that we have upgraded in combination with two Kalman filtering levels. The first level permits an estimation of the wheelchair configuration in its environment and the second is used to compute the mobile platform configuration in connection with its environment. The association of the two filtering processes allows a robust tracking between a mobile target (wheelchair) and a mobile observer (assistive platform). More over, the team project was also composed with a clinical group; hence we present some interesting real-life testing of this technical assistance.

1 INTRODUCTION

Our laboratory works on an assistive prehensile mobile robot project and has to ensure the tracking of a wheelchair from the mobile platform. In this article, we propose an approach to solve the problem known as target motion analysis (TMA). We propose a target tracking filter based on a probabilistic approach with the Kalman Filtering which will be fed by omnidirectional vision sensors and dead-reckoning sensors mounted on the mobile platform. The problem of tracking is classical in the world of robotics. It's generally linked to the data association stage and state estimation. The data association problem is that of associating the many measurements made by a sensor with the underlying states or trajectories that are being observed. It includes issues of validating data, associating the correct measurement to the correct states or trajectories, and initializing, confirming or deleting trajectories or states. The Probabilistic Data Association Filter (PDAF) for single target and the Joint Probability Data Association Filter (JPDAF) (Y. Bar Shalom *et al*, 1988), (Bar-Shalom Y *et al*, 1995) for multiple targets are two inescapable approaches. They are both Bayesian algorithms that compute the probability of correct association between an observation and a trajectory. The general JPDAF framework can be implemented using Monte Carlo techniques, making it applicable to general non-linear and non-Gaussian models (D.Schulz *et al*, 2003).

A second classical paradigm of data association is the Multiple hypothesis tracking (MHT) (S.Blackman, 1986) which permits to represent multimodal distributions with Kalman filters (Y. Bar Shalom *et al*, 1988). It has been used with great effectiveness in radar tracking systems, for example. This method maintains a bank of Kalman filters, where each filter corresponds to a specific hypothesis about the target set. In the usual approach, each hypothesis corresponds to a

postulated association between the target and a measured feature.

For our application, we have chosen to use two Kalman filters to solve the problem of target tracking from a mobile observer.

The originality of this approach in connection with the classical solutions resides in two points:

- Solving the problem of data association with a dedicated image-processing filter (camshift).
- Solving the problem of simultaneous moving of the target and the tracker with two embedded Kalman filters.

The combination of the prior two points contributes to solving the non-linearity problem of the global filter.

Paper Organisation. In the next paragraphs (§1.1, §1.2, §1.3, §1.4), we will mention the specific context of this study, outline the perception system and describe the functionalities of the proposed assistive platform. After that in part 2, we will briefly explain the first tracking method (1TM) based on the iterative algorithm CAMSHIFT with a specific use for omnidirectional images. We also present very original clinical results of the tests made under genuine conditions by disabled people. In the last part (§3), we deal with the multi-level Kalman filtering tracking (second Tracking Method, 2TM). Moreover, in this section, we will describe our Embedded Extended Kalman Filtering (EEKF). Finally (§4), we will conclude with an explanation of the experimental results.

1.1 Context Overview

This project, ARAP (Robotised Assistance for Prehensile Help), came into being from a human synergy, which grew out of a definition of problems faced by peoples of reduced mobility. The idea of robotised assistance for handicapped people followed an observation: there is generally a significant delay between technology, no matter how advanced, and assistance for peoples of reduced mobility. Above all, however, this project meets a social demand, that was defined by patients of reduced mobility confined to the Berck Hopale group (Hospital), who are taking part in this project. An interesting specificity of this project was composing a strongly plural-disciplinary team:

- "Science for the Engineer" skills of the IUT of Amiens (University of Picardie, Jules Verne) have been used for the integration of a system of detection on the mobile platform and for the development of the prototype.
- The "Human and Social Science" team was in charge of the psychological impact of this mobile assisting platform on the end-user.
- The "Clinical group" (the Calvé Centre in Berck-Sur-Mer) used its clinical knowledge of the problem of disability, which will allow an evaluation of the work done.

A lot of work has been carried out in connection with the problems defined by technical assistance. Some of them are describe in (B.Marhic *et al*, 2006).

We have proposed studying the technical, psychological and clinical impact of robotised assistance for persons of reduced mobility by combining a mobile platform with a grasping arm in its usual role as robotics for handicapped persons (robot arm MANUS®).

1.2 Main Perception System

The mobile platform, in other words "the observer", is mounted by the two classical kinds of sensors; *i.e.* the Inner Navigation System (INS) and the External Position System (EPS). The INS are dead-reckoning sensors and the EPS is a stereoscopic omnidirectional vision sensor used in a goniometric mode (figure 2). Moreover, this exteroceptive sensorial system is also used for the target observation (wheelchair) as a "classical" vision system involving the intrinsic properties (colour).

The well-known equation (first order) of "dead-reckoning", considering the figure 1 is given by: $X^m = [x^m, y^m, \theta^m]^T$

$$\begin{cases} x^m(n+1) = x^m(n) + \delta S(n) \cdot \cos(\theta^m(n)) \\ y^m(n+1) = y^m(n) + \delta S(n) \cdot \sin(\theta^m(n)) \\ \theta^m(n+1) = \theta^m(n) + \delta\theta(n) \end{cases}$$

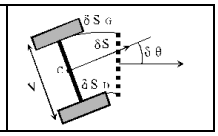

Figure 1: Small movements of the robot during a period.

Stereoscopic Omnidirectional Vision System. Main vision applications in mobile robotics use the classical pinhole camera model. Depending on the lens used, the field of view is limited. Nevertheless, it is possible to enlarge the field of view by using cameras mounted in several directions (H. Ishiguro, S. Tsuji, 1993) but the information flow is very important and time consuming.

We have opted for a catadioptric vision system (figure 2).

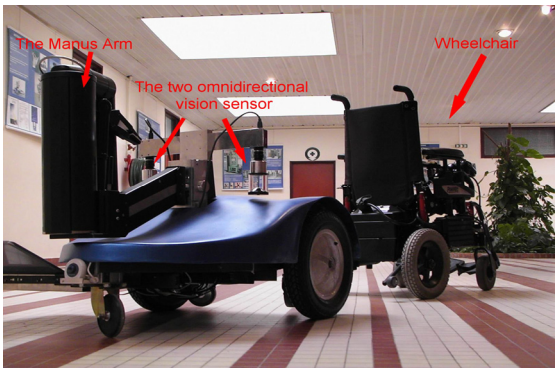

Figure 2: The mobile platform and stereoscopic sensors.

There are many advantages to using an omnidirectional vision sensor. Firstly, in one acquisition, we obtain a full view of the environment without using a sophisticated mechanical system. Secondly, the same system can be used as EPS and also as a "bearing sensor". Finally, even if the visual interpretation of omnidirectional pictures is difficult, it is possible to compute a "classical perspective view" of the scene. The previous functionality is not discussed in this paper.

The figure 3 shows an omnidirectional view of an environment with a wheelchair.

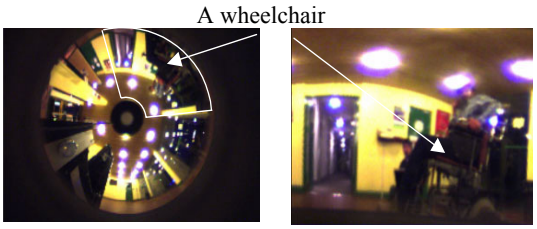

Figure 3: (left) an omnidirectional view of a scene with a wheelchair in the field of view. (right) "un-warped" picture of the white area from the omnidirectional view.

1.3 Main Functional Specificities

Two functional specificities have been integrated into the robotised assistance (ARAP). Firstly (automatic mode), the mobile platform follows the patient's wheelchair whenever the patient does not wish to use it. Secondly, a remote controlled mode for the grasping arm MANUS$^{(R)}$ and for the mobile base, used when the patient wishes to carry out a task involving grasping.

1.4 Scientific Problematic

The two main scientific themes associated with the automatic mode are the tracking and the path planning according to the obstacle avoidance and map building (locally). The coordination of the tracking and of the detection of obstacles is very important for the proper progress of our system.

The block diagram below (figure 4) shows the concomitance between the local map and the tracking phase. These can sometimes give orientation orders to the mobile platform that are contradictory.

In this paper, we focus only on the tracking problem.

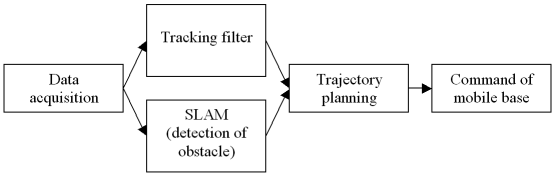

Figure 4: Coordination of tracking and detection of obstacle.

2 1TM: OMNICAMSHIFT

We wished to achieve the greatest possible degree of flexibility regarding the use of this robotic assistance. We therefore did not want to restrict our method to the use of one wheelchair in particular. More over, the wheelchair is not equipped with any particular marker; we have to track it as it is. Thus, in the first stage, our strategy for wheelchair recognition and tracking was based on a specific use of the CAMSHIFT. We have named the calculation of a CAMSHIFT directly into an omnidirectional image "OmniCAMSHIFT". (C. Cauchois *et al*, 2005)

The Continuously Adaptive Mean SHIFT (CAMSHIFT) algorithm (Bradski, 1998), is based on the mean shift algorithm (Comaniciu *et al*, 1997), a robust non-parametric iterative technique for finding the mode of probability distributions including rescaling.

2.1 Initialisation (Target-wheelchair)

Our construction of the model accommodates not only the wheelchair, but also the patient. This is why we turned our work towards an intrinsic model, directly calculated from a stereoscopic colour video signal. The figure below (Figure 5) shows omnidirectional images: they illustrate the extraction of the background and the extraction of the wheelchair. Once the model is computed, a histogram (acts as density function) representation is calculated.

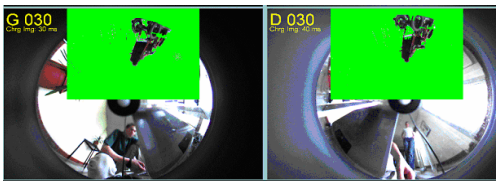

Figure 5: Target Initialisation. Subtraction of the image.

2.2 OmniCAMShift Results

The next figure (Figure 6) shows an example of the OmniCAMShift application.

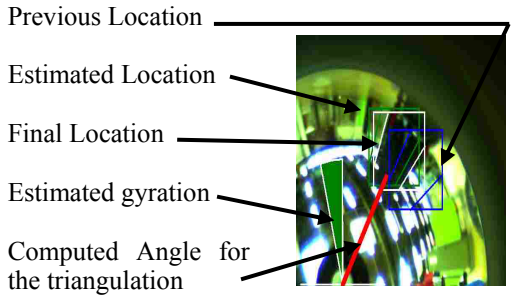

Figure 6: Wheelchair recognition using OmniCAMShift.

Once the wheelchair is identified in the two omnidirectional images, computing the relative position of the wheelchair by triangulation (figure 7) using the two computed angles is easy:

$X^{tri} = [x^{tri}, y^{tri}]^T$

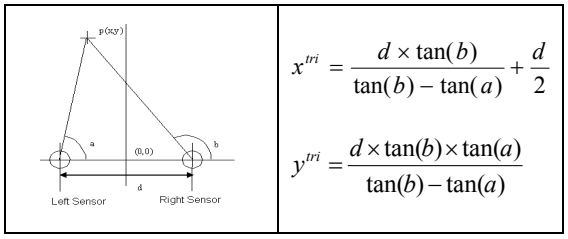

$$x^{tri} = \frac{d \times \tan(b)}{\tan(b) - \tan(a)} + \frac{d}{2}$$

$$y^{tri} = \frac{d \times \tan(b) \times \tan(a)}{\tan(b) - \tan(a)}$$

Figure 7: triangulation by two bearing angles. The referential frame is between the two omnidirectional sensors.

2.3 Evaluation and Clinical Results

As we explained at length, the prototype that we designed is based on an actual social demand. The prototype has thus been tested in a hospital. Unfortunately, the automatic mode, i.e. 1TM: OmniCamShift was not secure enough (loss of target) to be used and tested by handicaped people. The required reliability for wheelchair tracking was too strict to establish an evaluation with tetraplegic subjects in clinical conditions. In a first stage we chose to test the platform with 13 non handicapped subjects placed in the same constrained motor conditions as tetraplegic subjects.

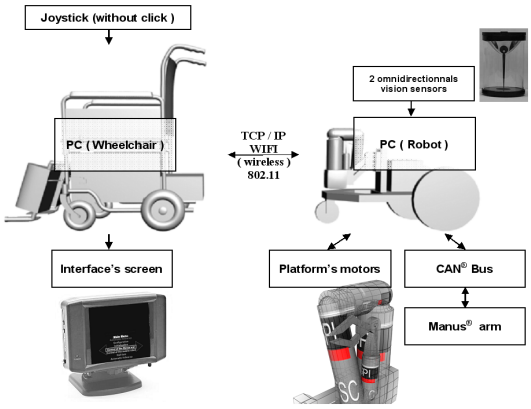

Figure 8: Operation's schema.

However, under laboratory conditions, the mobile platform was able to follow the wheelchair at a low speed and at a distance of 2m without any oscillation in the trajectory (automatic mode). In order to be manually controlled by the end-user, the base has to go around the wheelchair automatically when ordered to, without any prior warning. This intermediary phase corresponds to the transition from the automatic mode to the remote-controlled mode. This transitory trajectory was chosen in a reliable manner based on obstacle avoidance and the platform positioned itself without difficulty in front of the wheelchair in order to start the remote-controlled operation.

Real-life testing has shown that the end-user will encounter no difficulties operating the platform. The main clinical evaluation was dedicated to validate that the end-user can operate the mobile base + robot arm as easily when he is seated in the wheelchair as when he is in bed.

During the grasping operation with a moving base, the time needed to place the base was not significantly different between for 5meters near 84sec (standard deviation, s.d. 40) and 9 meters (105sec s.d. 36). The time needed to accomplish a grasping task was significantly longer when the joystick was driven by the chin (108sec s.d. 24) than by a hand blocked in an orthosis (102sec s.d. 33) or by a digital device (95sec s.d. 25). The difference in distance for the grasping action to be undertaken (between 1, 5 and 9 meters) had a non-significant impact on the outcome, respectively 56sec s.d. 17; 64sec s.d. 17 and 67sec s.d. 25, with a significant difference between 1 to 9 meters. With a fixed base and randomly presented at either 90° or 45° to the subject, the average time needed to grasp showed a

significant increase between conditions (respectively 61sec s.d. 18 and 141sec s.d. 56). No significant difference was found during the task combining the movement of the base and the grasping of an object, no matter if the patient was in the wheelchair or in bed, nor if the object was on the ground or on a table. However, the change in distance from 5 meters to 9 meters increased significantly the average grasping time from 102sec s.d. 56 to 151 s.d. 80.

In short, the results presented by this research project show that whether feasible, the time for grasping with a mobile platform increases considerably with the distance and with the base orientation in comparison to the patient place. Grasping with a mobile robot seems to be a solution to a wider demand than that originally targeted by the first studies into the use of robotic assistance. As there are many people, other than from tetraplegic people, who are bed-ridden, a far wider target-group can benefit from the use of robotic assistance.

However, the evaluation also proved that the wheelchair tracking by a mobile platform had its limitations and an actual use in an environment outside of the laboratory is very complicated. This necessitated the implementation of new software elements. A part of this future improvement is discussed in the next part of this article.

3 2TM: KALMAN FILTERING

For solving the problems of target loss presented above, we add at the previous tracking method Kalman filtering. That way, we can pinpoint some detection errors that weren't detected before (divergence of the OmniCamShift).

3.1 Problem Formulation

The target, i.e. the wheelchair, located at coordinates (x^f, y^f) in the world frame, moves with a constant velocity. The state vector is defined by: $X^f = \begin{bmatrix} x^f & y^f \end{bmatrix}^T$.

The discrete-time state equation for this problem can be written as:

$$X^f_{n+1} = \begin{bmatrix} 1 & 0 & 0 \\ 0 & 1 & 0 \end{bmatrix} \times X^m_{n+1} + X^{f/m}_{n+1} + v_{n+1} \qquad (1)$$

Where $X^m_{(n+1)}$ is defined figure1 and $v_{(n+1)}$ is centred Gaussian white noise v(n+1) ~ (0, Q) with Q = σ.I_2, here σ is a scalar and I_2 is the 2x2 identity matrix. The superscript $^{f/m}$ indicates the position of the wheelchair in relation to the mobile platform.

We assume that during the prediction stage the relative movement between the wheelchair and the mobile platform remains constant:

i.e. $X^{f/m}_{(n+1)} = X^{f/m}_{(n)}$. This classical target-observer geometry is depicted in the figure 9.

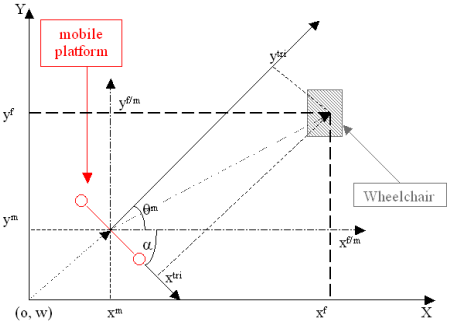

Figure 9: Target-observer geometry.

3.2 First Level of Filtering

We use the dead-reckoning data (INS) to compute the observer state, *i.e.* our mobile platform state (step 1: the prediction stage); the non-linear equation 8. Afterwards, the relative position X^{tri} of the wheelchair in connection with our mobile platform is computed by triangulation (figure 7) of data provided by the two omnidirectional vision sensors.

The equation (2) enables us to obtain the state vector $\hat{X}^f = \begin{bmatrix} \hat{x}^f & \hat{y}^f \end{bmatrix}^T$ which gives us the position of the wheelchair in the environment (World frame), based on the addition of two vectors $\vec{X}^m$ and $\vec{X}^{f/m}$.

$$\begin{bmatrix} \hat{x}^f \\ \hat{y}^f \end{bmatrix} = \begin{bmatrix} 1 & 0 & 0 \\ 0 & 1 & 0 \end{bmatrix} \times \begin{bmatrix} x^m \\ y^m \\ \theta^m \end{bmatrix} + \begin{bmatrix} \cos(\alpha) & -\sin(\alpha) \\ \sin(\alpha) & \cos(\alpha) \end{bmatrix} \times \begin{bmatrix} x^{tri} \\ y^{tri} \end{bmatrix} \qquad (2)$$

where : $\alpha = 90° - \delta\theta^m$. The previous vector $\hat{X}^f = \begin{bmatrix} \hat{x}^f & \hat{y}^f \end{bmatrix}^T$ is computed outside the filter; $\hat{X}^f$ is used as the measurement in the observation equation (step 2: update Stage) defined as follow:

$$\hat{X}^f = H_n \times X^f_n + w_n \qquad (3)$$

where $w_{(n)}$ is a zero-mean white Gaussian noise.

The observation matrix $H_{(n)}$ of the filter becomes the matrix identity. The observation stage is thus linear. The diagram below (figure 10) summarises this process. Some actual results are shortly shown in the figure 11. This figure represents the position of our mobile platform and the wheelchair in a real scenario. The result obtained was satisfactory for a

straight trajectory but insufficient during the phase where the mobile platform turned, due to errors of dead-reckoning and the non-repositioning of the mobile platform. The state vector estimation $\hat{X}^f$ is highly dependant of the of dead-reckoning vector $\vec{X}^m$; thus if an error occurs on $\vec{X}^m$, it appears on $\hat{X}^f$. This method is not efficient.

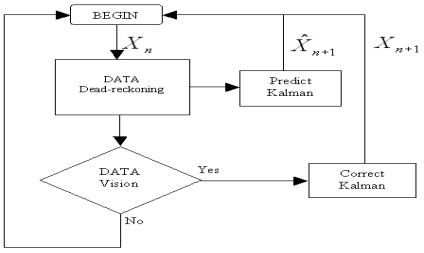

Figure 10: Filter's algorithm.

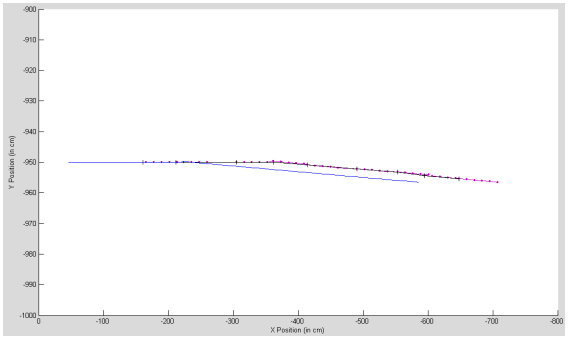

Figure 11: First filter results. (In blue the mobile platform position, in purple the estimated wheelchair position and in black the real wheelchair position).

So, to resolve this new problem and to make our application robuster, we add a second level of Kalman to this filter, which then deletes this imperfection. We have named this second filter the Embedded Extended Kalman Filter (EEKF).

3.3 Second Level: EEKF

We now propose to fully estimate the platform state vector ("the observer") by a classical EKF. Thus, this method requires knowledge of the environment's landmarks (EPS). We will be able to determine, with precision, the position of our mobile platform and thus be able to re-inject the platform position in the first Kalman loop.

For indoor application, these landmarks are walls, doors, objects, angles which one will be able to detect in an omnidirectional image using segmentation processing. Therefore, it is necessary for us to know the map of the environment to be able to match the omnidirectionnal image primitive to the known landmarks (doors and windows) of the environment (see figure 12). In order to extract the landmarks' angles of the ominidirectionnal picture, we compute a Deriche-Canny filter before applying a classical Hough transform algorithm.

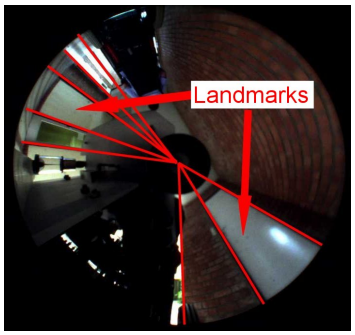

Figure 12: Segmentation and landmarks in an omnidirectional image.

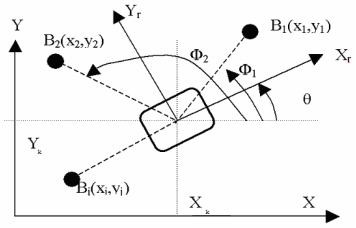

Figure 13: Relation between landmarks and mobile platform.

For this process, the equation of observation of the extended Kalman filter is as follows. The vector of observation is:

$$z_k^* = \begin{bmatrix} 1_k^\tau \\ 2_k^\tau \\ . \\ . \\ n_k^\tau \end{bmatrix} + v_k = h(X_k, k) + v_k \quad (4)$$

where i_k^τ, which contains the azimuths angles, is the layer of $i^{ème}$ landmark B_i of co-ordinates (x_i, y_i) i the world landmark in the moment k. And v_k is a measurement noise, presumably white and Gaussian.

The exact position of the beacon B_i is expressed according to the state vector X_k of the system as follows:

$$i_k^\tau = \arctan\left(\frac{y_k - y_i}{x_k - x_i}\right) \quad (5)$$

The matrix of the Jacobian of the vector function H is, in the case of measurements of absolute angle:

$$H_k = \begin{bmatrix} -(y_k - y_1)/_1 d_k^2 & -(x_k - x_1)/_1 d_k^2 & 0 \\ . & . & . \\ -(y_k - yn)/_n d_k^2 & -(x_k - x_n)/_n d_k^2 & 0 \end{bmatrix}_{X_k = \hat{X}_{k/k-1}} \quad (6)$$

where d is the distance between the landmark and the mobile platform.

We add this second Kalman filter before the correction of the first Kalman filter as can be seen in the graphic figure 14.

The result of this add-on is a reposition of the mobile platform in the environment reference (see figure 13). This better knowledge of the base location also allows us to have a better estimation of the wheelchair. Moreover, the update stage of the first level Kalman filter is now achieved by data from both the triangulation and the platform location (second level Kalman filter).

Moreover the errors induced by the dead-reckoning such as skids and slips, errors of quantification and others, are taken into account in an improved way. This improvement stems from our multi-level Kalman filter that performs a more accurate location.

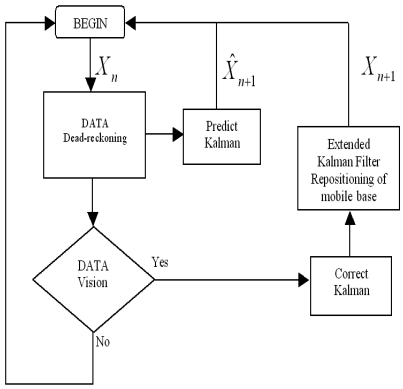

Figure 14: New process of filtering.

We can see that the second filter corrects the dead-reckoning as seen in figure 15, represented by the arrow. Here it is a big error because the wheelchair is suddenly turning.

As we can see in the figure 16, the result of our process follows the curve well, which our system did not manage to do before.

Figure 17 shows us the error in X and Y of your system. These results are given by the matrix of variance/covariance and allows us to see that our system tracks the target with the precision as expected. This way we can confirm the importance and the need of our second Kalman filter.

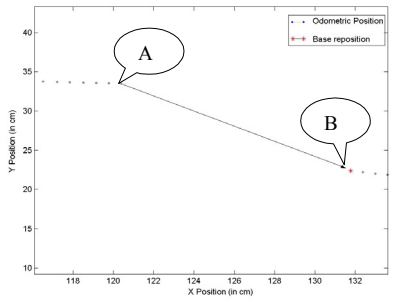

Figure 15: repositioning of the mobile platform. A: dead-reckoning prediction location; B: EKF estimation.

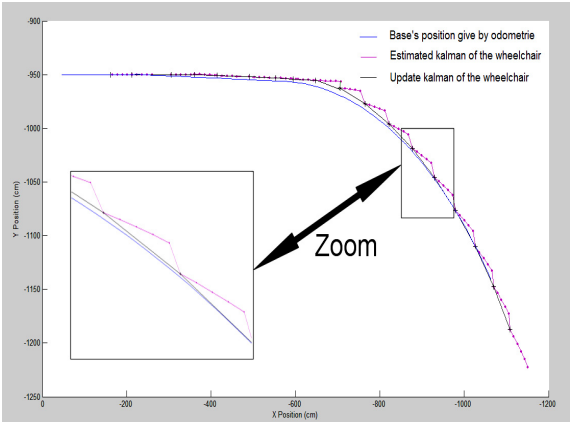

Figure 16: System in a straight trajectory following in a curve.

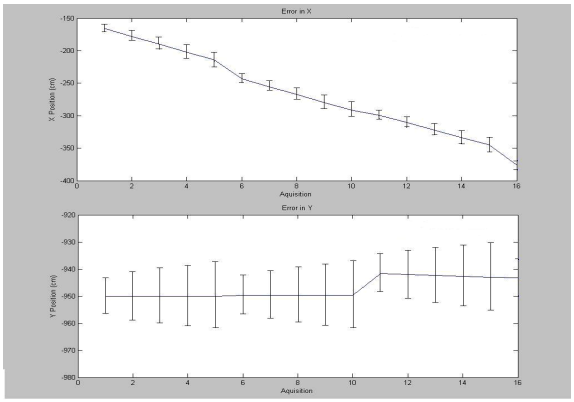

Figure 17: Error of our wheelchair's system in X and Y.

4 CONCLUSIONS

In this article, we studied a target tracking application dedicated to an assistive platform for the disabled. The aim was to track a wheelchair with a mobile platform mounted with a grasping arm

(MANUS®). We propose an approach based on an association of two Kalman filtering levels. We have named this architecture the EEKF. The first level permits to estimate the wheelchair configuration. The second is used to compute the mobile platform configuration in connection with its environment. We have shown that the second level increases the precision of the configuration estimation of the wheelchair in the platform frame. The use of the identity matrix in the first stage of the Kalman filtering allows us to solve the problem of the non-linearity of the system due to the triangulation. However, our paradigm integrates a strong coupling of the camshift algorithm and the Kalman estimation state. This new target tracking approach shows that it is possible to compensate the loss of tracking by the camshift, whilst continuing to track.

This paradigm can be considered as a contribution to solving the problem of TMA (target & tracker). The robustness of the filtering process is very important because it is used in a clinical context. Future works will study the integration of a supplementary layer based on a particle filter.

Moreover, in this paper we have presented some original results concerning the clinical tests. These tests have permitted to evaluate the impact of the remote controlled mode of this assistive platform. The results seem to be encouraging. The automatic mode will also be evaluated in the near future.

REFERENCES

Y. Bar Shalom et T. E. Fortmann, "Tracking and data association", Academic Press, 1988.

Bar-Shalom Y, Xiao-Rong Li, Multitarget-Multisensor Tracking: Principles and techniques, 1995.

D.Schulz, W. Burgard, and D. Fox, “People tracking with mobile robots using sample-based joint probabilistic data association filters” International Journal of Robotics Research, vol 22, no. 2, 2003.

Blackman S., Multiple-Target Tracking with Radar Applications, Artech House, 1986.

B. Marhic, L. Delahoche ,F. de Chaumont, and O. Remy-Néris, “Robotised Assistance for Persons of Reduced Mobility: résumé of a project”, ICOST’2006, Ireland.

H. Ishiguro, S. Tsuji “Applying Panoramic Sensing to Autonomous Map Making a Mobile Robot” in Proc, Int. Conf. on Advanced Robotics, pp127-132, November 1993.

G. R. Bradski. Computer video face tracking for use in a perceptual user interface. Intel Technology Journal, Q2 1998.

D. Comaniciu and P. Meer. Robust analysis of feature spaces: Color image segmentation. In International Conference on Computer Vision and Pattern Recognition, pages 750-755, San Juan, Puerto Rico, 1997.

C. Cauchois; F. de Chaumont, B. Marhic, L. Delahoche, M. Delafosse : ”Robotic Assistance: an Automatic Wheelchair Tracking and Following Functionality by Omnidirectional Vision”. IEEE/RSJ Int. Conf. on Intelligent Robots and Systems, (IROS 2005). Pp :2397 – 2402, 02-06 Aug. 2005.

A RECONFIGURABLE SYSTEM FOR MOVEMENT REHABILITATION AND DIAGNOSTICS WITH FES

Piotr Kaczmarek, Andrzej Kasiński, Marek Kraft and Przemysław Mazurkiewicz
Poznań Univeristy of Technology, Insitute of Control and Information Engeenering, Piotrowo 3a, 60-395 Poznań, Poland
Piotr.Kaczmarek@cie.put.poznan.pl, Andrzej.Kasinski@cie.put.poznan.pl

Keywords: Electrical stimulation, rehabilitation, movement restoration, instrumentation.

Abstract: The architecture of a custom originally designed FES system is described. The system is built from off-the-shelf and cusom components to obtain a target functionality. List of potential applications is provided. Some tasks have been already tested in laboratory and clinical conditions. Hardware specification of proprietary components is given and interfacing issues are addressed.

1 INTRODUCTION

Motion restoration through the appropriate functional electrostimulation (FES) of a neuro-muscular system is an interesting perspective. Still, the investigations are continued at the level of a single joint as well as that of a limb. The most interesting problem is to evaluate how the electrical stimulation program translates into an efficient and controlled elementary motion. Commercially available functional stimulators can be divided in 2 groups: stimulators for clinical research (like the S88 from Grass Teledyne), daily-use electrical stimulators for rehabilitation and functional electrical stimulation systems used in neurophysiological research (like NeuroTrac, Compex Motion, ODFS, Parastep)(Keller et al., 2002; Taylor et al., 1999). In principle all of these stimulators provide the possibility to alter the stimulation pulse frequency, amplitude and duration. In most cases (S88, NeuroTrac, ODFS, Parastep) these parameters are controlled manually by the user. Only the most advanced stimulators, like Compex Motion, allow to control the parameters by means of a closed loop control based on data coming from a number of sensors (switches, force sensors, EMG sensors). Most common approach is a simple event-triggered stimulation for a certain amount of time with the parameters set by the therapist (ie. in ODFS stimulators the stimulation sequence is triggered by a heel-switch). All of the above mentioned stimulators lack the capability of optimizing the shape of the single stimulation pulse, leaving only various square or trapezoid pulse combinations at the therapist disposal.

Many research institutes try to determine the influence of stimulation parameters on the muscle contraction, the fatigue effect, as well as the long-term effects generated in the muscles subjected to persistent stimulation (this refers to the regeneration process as well as to side effects). The experiments are aimed at investigation of physiological properties of the muscles both of healthy and of disabled subjects (Chizeck et al., 1999). An interesting issue is to reveal the optimal stimulation pattern for the application in the FES systems (Breen et al., 2006). So far the optimization process was restricted to the selection of the stimuli train frequency (Chou et al., 2005), or the pulse width and amplitude. The influence of the stimulating pulse shape on the contraction force has not been studied yet. Moreover, research results of the experiments concerning the pulse shape influence on the muscle contraction are not clear (Bennie et al., 2002).

Both movement restoration and rehabilitation processes are evaluated upon apparent effects. Such effects can be used as a feedback for the FES control algorithm, however it is desirable to quantify the effects, which are of different character. First apparent effect is the response of neuro-muscular system under stimulation on its own. The neuro-muscular system excitation level can be judged on the basis of the electromyographic signals (EMG) being the response to

the electrostimulation. In movement restoration experiments however, it is necessary to measure and to analyze the EMG of the particular muscles contributing to the movement (Kutch and Buchanan, 2001). Moreover, it might be desirable to use a multi-channel transcutaneus electrode to support the decomposition of the EMG signal for studying the propagation of a single action potentials and motor point localization, or to analyze the signals in more detailed way. In order to get a better image of the stimulation effects there might be also required to partially estimate the state of a biomechanical system from additional physiological signals such as electroneurograms (ENGs)(Sinkjaer et al., 2003) or mechanomyograms (MMGs) (Kaczmarek et al., 2005; Orizio et al., 2003) which better reflect the senso-motor system activity as well as changes of the muscle geometry, respectively.

However, these signals reflect the intermediate effects of electrostimulation, but the target result (the final effect) is the motion of a limb or at a lower level, the motion of a joint under study. There are two interesting aspects of the motion evaluation - the static aspect, related to the force generated by a joint at a certain perceived level of the EMG activity while correlated with joint configuration (angle), and the second, which is related to the resulting motion dynamics. The investigation of the first aspect is performed by the simultaneous recording of EMGs of the appropriate muscle and the resulting force being directly recorded with the tensometric device, while the joint is locked at a particular angle. For the second aspect, it is necessary to acquire simultaneously the signals of the generated force, EMGs, the joint-angle rotation signal and the task-space acceleration signal due to the resulting dynamic motion of the limb.

This would be possible under the condition that one disposes of a fully programable electrostimulator with a necessary number of outputs, of a measurement system running during stimulation (a multichannel EMG signal acquisition and a processing system) and of a measurement system to evaluate the biomechanical effects of the FES (an instrumented exoskeletal device - the orthosis). In this paper we describe such a custom system, which has been built from modules and list examples of applications of that system to the rehabilitation and diagnostics procedures.

2 THE SYSTEM ARCHITECTURE

The schematic outline of the complete system is shown in fig. 1. The main control and sensors readout tasks are performed by the embedded 3,5” PC. The

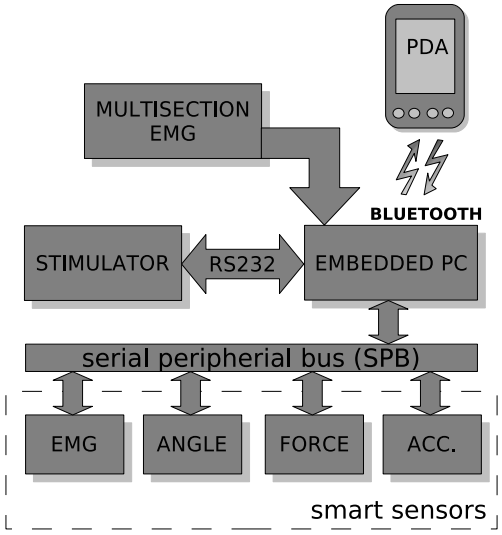

Figure 1: The block diagram of the FES system.

PC is equipped with a Intel Celeron 400MHz processor, 256MB RAM and 4GB CompactFlash card. The configuration of the system involved in a particular task is open in a sense, that the use of a simple serial peripheral bus (SPB) and of a specially designed communication protocol enables the user to connect a number of intelligent sensors (like accelerometers, goniometers, tensometers, point EMG sensors) to form a distributed measurement system, enabling tailoring of the system configuration to the particular task at hand. These distributed sensors perform all the measurement, preprocessing and data forming operations on-site. This allows to reduce the influence of various environmental interferences on measurements. The availability of sensor data enables the system to perform real-time closed loop control of joints by proper muscles stimulation depending on this data. The embedded PC is equipped with a multichannel A/D converter PCM-3718HG. This converter is used to measure the data from a multi-section EMG electrode. The PC is also fitted with the Bluetooth wireless interface. This enables remote control (for example by exchanging stimulation programs during rehabilitation), the visualization of a system state and sensor readouts (usable in biofeedback applications). For simple therapeutic programs at the patient bed it is possible to control the system by a palmtop.

2.1 Electrostimulator

The stimulator unit has the ability to perform stimulation through four independent channels. This enables independent stimulation of different muscle groups. The control circuit consists of a microcontroller and a 4-channel, 8-bit digital to analog converter (DAC).

Such the system setup enables the user to define the pulse shape, frequency, amplitude and other parameters (i.e. number of stimuli, initial delay, pulse train profile and modulation frequency) independently for each stimulation channel. The output stage consists of a voltage controlled current source, which can source a current of up to 60 mA and can work with voltages up to 400 Vpp, which is important in the case of the transcutaneous stimulation. The high voltage stage is galvanically separated from the control circuit. Control and programming of the device can be performed on-line via RS232, SPI or I2C interface. In that way the described device let the therapist to define flexibly the movement-restoration or rehabilitation requirements to each individual patient and to the particular task.

2.2 Orthosis and its Instrumentation

The orthosis is a skeleton enabling the force and position sensors attachment. Fig. 2 presents the exoskeleton of the ankle joint, which is one of the most important joints for balancing and locomotion tasks. The orthosis enables to perform static measurements (during an isometric contractions), as well as dynamical acquisitions during walking or balancing. It is equipped with the angle sensor i.e. an incremental encoder of 0.05 deg resolution and with the force sensor based on a planar-beam force sensor with a full-bridge strain gage. The system is capable of measuring a torque generated by a dorsi as well as a plantar flexion during isometric contractions for variable ankle joint angles in the range between -10 and 10Nm. The mechanical solution of the force sensor allows to obtain the force, that is always perpendicular to the sensor beam and independent on the ankle joint angle. The orthosis controller has a 10-bit AD converter with a variable input gain. This let the user to select appropriate gain depending on the performed test and the torque value. Moreover, the controller performs signal processing tasks such as a signal filtering and sampling with rate up to 4kHz, evaluation of the absolute angle of the joint and data buffering. The communication and data transfer to the Embedded PC is performed via SPB. Moreover, during locomotion or balancing tests, 3D accelerometric sensors can be fixed to the exoskeleton. The accelerometric sensor is equipped with a microcontroller and a 10bit AD converter, moreover it has 3 digital inputs enabling to connect the additional switches (foot switches or limit switches) or other discrete triggering elements. The smart sensor can operate in three modes, selected by the user via SPB. The first one is the data acquisition mode, where raw data is transmitted to the embedded PC. The second is the data processing mode, enabling the estimation of the velocity and of the position and the signal filtering. The third is the events detection or a fuzzification mode, which is used for fuzzy logic control algorithm. The sensor in such a mode evaluates the system state from the accelerometric signals and digital input state according to the given set of fuzzy rules.

The use of registered signals is the following. 3D acceleration signal together with goniometric signal let to reconstruct the position and the motion trajectory independently. This enables to analyze the kinematic effects of the electrostimulation and to discover pathological deficits. The tensometric subsystem gives the opportunity to evaluate the contraction force at a single joint. Thus not only the kinestatic evaluation is possible but also dynamics of the movement can be studied.

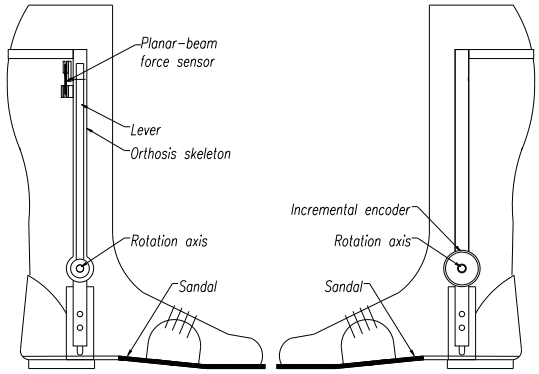

Figure 2: Instrumented Orthosis of the ankle joint.

2.3 EMG Acquisition Subsystem

Multichannel EMG. Important part of the presented system is an EMG electrode (Fig 3). The electrode consists of 9 rectangular AgCl contacts surfaces placed of a distance of 5 mm and with the contact surface size of 10x1[mm]. Multichannel EMG signal acquisition system is modular, where every module is connected to a single acquisition channel. It consists of an instrumental amplifier, analog high-pass Butterworth filter (f3dB=10Hz), low-pass Butterworth filter (f3dB=1000Hz) and a final amplifier stage giving the total gain within the range $1000 \div 2000$. Acquired signals are collected by a PCM-3718HG card connected to the embedded PC.

Point-like EMG Smart Sensor. Smart EMG sensor is a device with analogue and digital parts. The analog part is similar to that described in a previous section. However, the contact surfaces (electrodes) are integrated with the PCB of the analog subsystem.

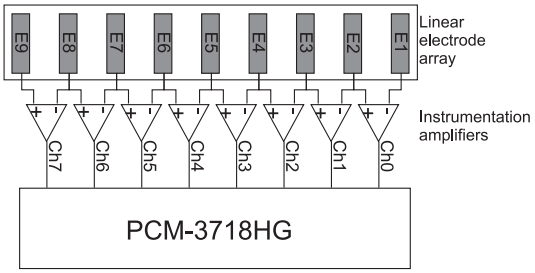

Figure 3: Linear electrode array for multichannel EMG.

The digital part consists of microcontroller with a 10-bits AD converter. Its main role is the acquisition of the analog EMG signal, buffering and basic preprocessing such as evaluation of the RMS value. The sensor can operate in two modes. In the first, the raw data are transmitted via SPB to the master controller, in the second mode only the results of processing are transmitted. The sensor is designed to be placed directly over a tested muscle in order to reduce noise and artefacts. Additionally, all IC chips can work in the shutdown mode for protecting the sensor amplifiers from damage due to the high-voltage stimulation.

3 APPLICATIONS OF THE SYSTEM

3.1 Research Tasks

As far the system has been used in 4 research tasks focused on the FES issues.

Stimulus Waveform Optimization. The system restricted to the stimulator, the force sensor and the EMG sensors has been used to evaluate the influence of the stimuli shape on the muscle contraction dynamics, and comfort level. The experiments were performed on a group of healthy volunteers and subjects with movement deficits. Within this study the biphasic stimuli with inter-phase interval (IPI) have been tested. 24 stimulus waveforms have been taken into account. They are combination of a pulse widths (50, 100, 175, 250us) and the inter phase intervals (0, 50, 250, 500, 1000, 2000us). The preliminary results suggest that the contraction force recorded during stimulation depends not only on the pulse amplitude, width and frequency, but also on the IPI. The contraction force has increased significantly with increase of the IPI. Additionally decrease of the pain sensation side-effects was reported. The results suggest, that the modification of the pulse shape seems to be an alternative for the the commonly used force control techniques such as a pulse-width, amplitude or frequency modulation.

Evaluation of the EMG-force Relationship. Using the instrumented orthosis and exoskeletons one is limited to apply the FES system only in the clinics. Therefore it is essential to built the portable FES with feedback based on measured physiological signals. This is necessary in order to evaluate or estimate the force and the joint configuration. In this study, the maximal voluntary contraction force and the EMG signal have been recorded while varying the ankle joint angle. It was observed, that for a medial gastrocnemius muscle the maximal force increases with increase of the dorsi flexion, however the RMS value of the recorded EMG signal significantly decreases, which may suggest the decrease of the muscle activity level. This phenomenon demonstrates that the for the force estimation at a gastrocnemius muscle from the EMG signal, the simultaneous estimation of the ankle joint orientation is required. This effect did not occurred for tibialis anterior muscle.

Evaluation of the Fuzzy Rules for a Fuzzy Logic Controller for Movement and Balancing Tasks. The efforts are made to create a fuzzy sets describing the phase of gate cycle during locomotion from 5 accelerometric sensors located at lower limbs and the trunk as well as from EMG sensors. This could enable to estimate the mass center position changes during locomotion or balancing tasks. The smart sensors are powerful enough to perform simple classification tasks and enable easy testing and evaluation of the rules.

Developing of the FES Control Algorithms. Using the Embedded PC with Linux on-board as the system supervisor enables an easy development and testing of various control algorithms based on fuzzy logic, neural networks or classical control. Moreover, the standard, well known and powerfull tools and libraries can be used for the application developing and testing. The distributed intelligent sensors may be reconfigured to work in a given control mode delivering a appropriate feedback signals.

3.2 Diagnostics Tasks

The diagnostics tasks refer to the potential application of the system in the clinical field. In the presented system it is possible to perform the electrophysiological as well as kinematics test, which may support the diagnosis. Moreover, such system could be used for

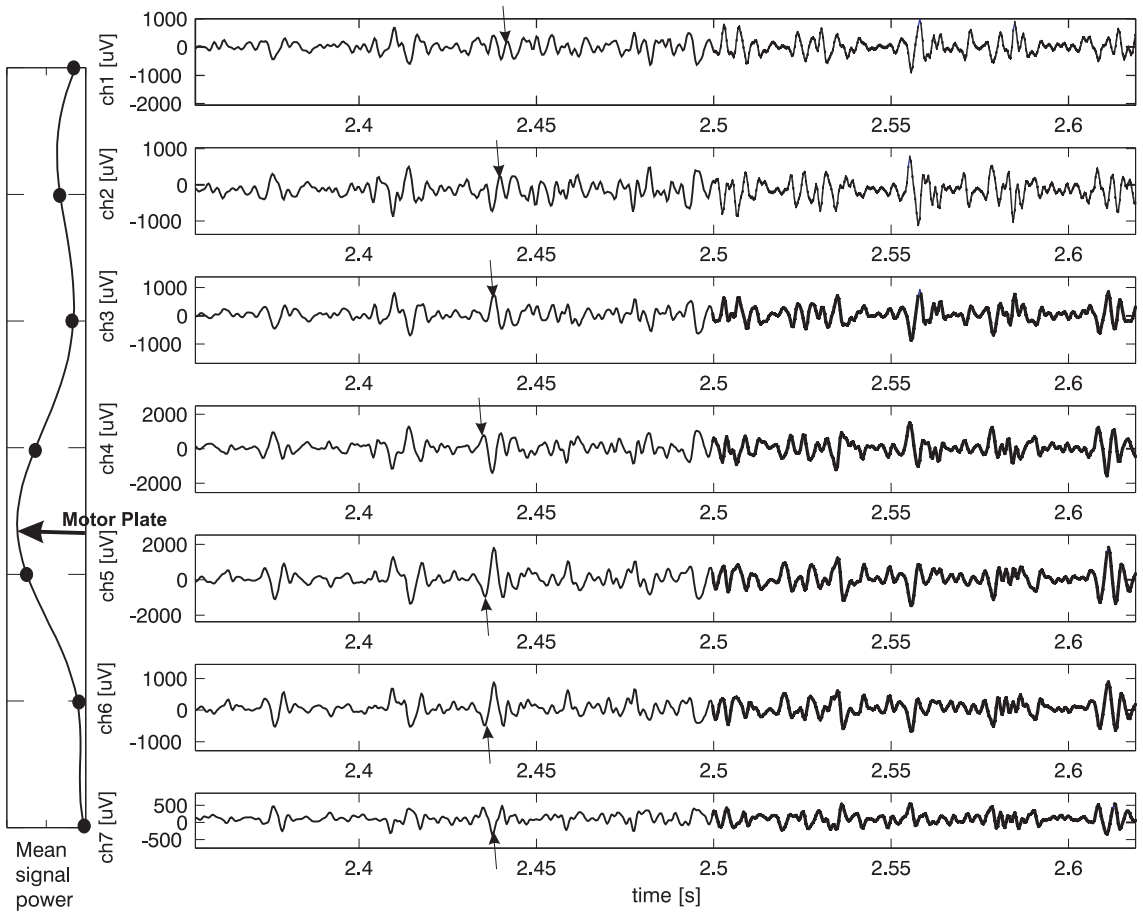

Figure 4: The multichannel EMG signals recorded from a tibialis anterior muscle with 8-point linear electrode array. A selected Action Potential (AP) propagating through the muscle has been marked with the arrows. The mean EMG signal power has also been computed. The black dots denote the mean signal power of the particular EMG channels. The maximum of the mean signal power between the channels ch4 and ch5 denotes the motor point localization.

selecting the individually optimized stimulation treatment.

Multisection EMG. Signals recorded with the multichannel EMG signal acquisition system have been used to estimate the conduction velocity of motor unit's action potentials (AP). This can be achieved by a special technique based on analysis of the APs having similar shape and being recorded in neighbouring channels. Selected AP generated by a single MU has been marked in Fig. 4. The AP propagation velocity can be computed on the basis of measured delay of the AP observed in particular channels and known distance between electrode points. Additionally, the system allows to localize neuromuscular junction in a particular muscle. It has been shown that signal parameters such as AVR or mean frequency (Fmnf) of the signals recorded at given points located along the tested muscle, can indicate the localization of the innervation zone. The motor point can be localized in two ways: the first is localization based upon the maximum signal power and the second is the AP phase inversion. The phase inversion can be seen in Fig 4 where the AP marked with the arrows is inverted in the channels ch5, ch6 and ch7. The motor point localization is important for an appropriate stimulation electrodes placement in FES application as well as a linear array-electrode placement in the signal decomposition task. The main purpose of the decomposition task is to estimate a discharge time of a particular motor unit during a voluntary contraction. In contrary to the decomposition systems of the intracellular EMG signals, decomposition of the multichannel surface EMG signals does not require to use needle electrodes which is an advantage. Multichannel recordings may compensate for the lower selectivity and give a deeper insight into the motor units activity. These information can be used in more sophisticated algorithms to improve the overall performance. The smart EMG sensors can be used during walking tasks in order to

analyze the muscles synchronization issues. Two sensors located over 2 antagonistic muscles can discover their synchronization during contractions. Moreover, the information from these sensors can be used in control algorithms.

System Identification. The estimation of the system state only from physiological sensors or the determination of fuzzy sets must be adjusted to the individual subject. Moreover, the optimal control algorithm for the FES controller must be selected. The system is capable to perform tests enabling to work out the force-EMG relationship for each subject. It is possible to prepare a set of tests which enable semi-automatic calibration of the sensors system.

The Stimuli Optimization. The stimulation experiments revealed the variability of the excitability level for the same stimulation procedure. The variability is dependent on the pathology but also on the individual features of the subject. Therefore, the stimulation waveforms and stimulus shapes should be selected individually. It was observed, that the stimulation let to divide the subjects into few groups. The system let to perform tests enabling classification of the subject to the particular group.

3.3 Rehabilitation Tasks

Repetitive Exercises with or without Stimulation Support. The aim of such a treatment is to increase the maximum contraction force, or to increase a range of motion. A subject can observe the actual force level, the EMG amplitude, or the joint angle on the screen, and to try to follow the reference trajectory as set by the therapist. Moreover it is possible to use the stimulation in order to compensate partially for the error between the reference and the actual trajectory.

Restoration of Movement Functions for the Physically Disabled Subject. The main aim of the presented system is to develop a daily-use FES system for the restoration of movement functions with a minimal number of sensors. The system is potentially capable to operate in closed feedback loop mode with sensors and stimulation sequences configured individually by therapist on the basis of the identification tests results. However, to obtain satisfying results with this application further investigations and development of control algorithm is necessary.

ACKNOWLEDGEMENTS

The work was partially supported by the Polish Ministry of Education and Science, project no. 1445/T11/2004/27.

REFERENCES

Bennie, S. D., Petrofsky, J. S., Nisperos, J., Tsurudome, M., and Laymon, M. (2002). Toward the optimal waveform for electrical stimulation of human muscle. *Eur J Appl Physiol*, 88(1-2):13 – 19.

Breen, P. P., O'Keeffe, D. T., Conway, R., and Lyons, G. M. (2006). A system for the delivery of programmable, adaptive stimulation intensity envelopes for drop foot correction applications. *Med Eng Phys*, 28(2):177 – 186.

Chizeck, H. J., Chang, S., Stein, R. B., Scheiner, A., and Ferencz, D. C. (1999). Identification of electrically stimulated quadriceps muscles in paraplegic subjects. *IEEE Trans Biomed Eng*, 46(1):51 – 61.

Chou, L.-W., Ding, J., Wexler, A. S., and Binder-Macleod, S. A. (2005). Predicting optimal electrical stimulation for repetitive human muscle activation. *J Electromyography Kinesiology*, 15:300–309.

Kaczmarek, P., Celichowski, J., and Kasiński, A. (2005). Experimentally verified model of mechanomyograms recorded during single motor unit contractions. *J Electromyogr Kinesiol*, 15(6):617 – 630.

Keller, T., Popovic, M., Pappas, I., and Müller, P. (2002). Transcutaneous functional electrical stimulator "compex motion". *Artificial Organs*, 26(3):219–223.

Kutch, J. J. and Buchanan, T. S. (2001). Human elbow joint torque is linearly encoded in electromyographic signals from multiple muscles. *Neurosci Lett*, 311(2):97 – 100.

Orizio, C., Gobbo, M., Veicsteinas, A., Baratta, R. V., Zhou, B. H., and Solomonow, M. (2003). Transients of the force and surface mechanomyogram during cat gastrocnemius tetanic stimulation. *Eur J Appl Physiol*, 88(6):601–606.

Sinkjaer, T., Haugland, M., Inmann, A., Hansen, M., and Nielsen, K. D. (2003). Biopotentials as command and feedback signals in functional electrical stimulation systems. *Medical Engineering & Physics*, 25(2003):45 – 96.

Taylor, P. N., Burridge, J. H., Wood, D. E., Norton, J., Dunkerly, A., Singleton, C, and Swain, I. D. (1999). Clinical use of the odstock drop foot stimulator - its effect on the speed and effort of walking. *Arch Phys Med Rehabil*, 80:1577 – 1583.

METROLOGICAL CHARACTETIZATION OF A CYCLE-ERGOMETER

Bocciolone Marco, Comolli Lorenzo
Department of Mechanical Engineering, Politecnico di Milano, Via La Masa 34, 20156 Milano, Italy
marco.bocciolone@polimi.it, lorenzo.comolli@polimi.it

Molteni Franco
Valduce Hospital, Villa Beretta Rehabilitation Center, Via N.Sauro 17, Costamasnaga (LC), Italy
francomolteni@libero.it

Keywords: Cycle-ergometer, wireless data transmission, mechanical measurements, data analysis, rehabilitation.

Abstract: A cycle-ergometer has been instrumented with suitable strain gauges to obtain metrological qualified measurements of the left and right leg torque. A wireless device has been used to transmit in real-time the gathered signals to the acquisition PC. Advantages are to give to doctors and physiotherapists a diagnostic tool, to analyze the cycling pattern of the patients and to monitor the improvements during rehabilitation. The real-time measures are also suitable input data for the Functional Electrical Stimulation (FES). All the analysis was conducted with a particular attention to spinal cord injured patients, who are characterized by highly asymmetric cycling: yet, this measurement setup, by independent measurement of right and left torques, can be used successfully also in this particular situation. An explanation of the measuring principles and a set of first results are given, that show the potentiality of the setup.

1 INTRODUCTION

The present work is aimed at the metrological characterization of a commercial cycle-ergometer, used in clinical and private field, for the rehabilitation of people who need a motor therapy. The device shows on a display the mean value of clinical parameters: subject's motor power, angular velocity, energy, right and left leg unbalance. Those values are computed using electrical quantities from the motor and the unbalance supposes that one of the legs is not opposing a relevant resistance to the motion. These average measurements proved to be quite accurate on healty subjects, but problems could arise in the unbalance measurement expecially with strongly asymmetric spinal cord injured patients. Indeed, in the standard device, the unbalance is computed by splitting the revolution in half; but in asymmetric patients one of the legs typically has a bigger resistance during flexure respect to extension (e.g. due to spasticity, contracture or joint limitation), that could lead to systematic errors. The proposed measurement of indipendent left and right torques would solve the problem. An introduction to the devices can be found in (Comolli et al., 2005).

Moreover the average data on the display are not saved. To give specialists a better idea of the rehabilitation of a patient, a recording and tracking of the data should be done, together with an *a-posteriori* appropriate data analysis to quantify the improvements of the treatment.

Another advantage of having a real time measurement setup is to provide a proper input to a Functional Electrical Stimulation (FES) system such as that in (Ferrante et al., 2005 and 2006).

2 CYCLE-ERGOMETER INSTRUMENTATION

The employed cycle-ergometer provides the mean value of the above parameters by using measurement techniques and data processing that, in particular working situations (typically asymmetries), could give unreliable information. In order to overcome those limitations and to have instantaneous information, an independent measurement system has been designed and developed, using mechanical

sensors. Such system provides the following quantities:

- **bending moments (M_b) and radial forces (F_r)** of right and left cranks: through two Wheatstone full-bridges each made up of electrical resistance strain gauges;
- **angular crank position (θ)**: through optical encoders (Gföhler et al., 2001; Mimmi, Pennacchi & Frosini, 2004) drawn with white and black sectors on the main wheel (see Appendix for additional solutions).

Strain gauges are sensors suitable for superficial strain measurements. To measure the bending moments and radial forces, the gauges must be positioned in the appropriate position and direction on the crank, and must be connected on a Wheatstone full-bridge electrical circuit (made of 4 strain gauges) so that the voltage output is made proportional only to the selected quantity. An analysis of the strains present on the crank, subject to a generic force on the pedal axis, and the application of the basic laws of the theory of elasticity, will lead to the conclusion that for the measurement of the bending moment the sensors must be positioned near the crank axis, where the strain is larger, two on the upper and two on the lower surfaces, with the sensing direction along the crank longer dimension. The radial forces can be measured with two opposite strain gauges with the sensing direction along the crank longer dimension in a position corresponding to the smaller section; but to complete the Wheatstone bridge, two more strain gauges are necessary and they will be positioned transverse to the former so that they will sense transverse strain.

The positions on the Wheatstone bridge of each group of 4 strain gauges are selected such that compensation of radial forces and bending moments are achieved respectively in the bridges apt to measure the bending moment and radial force. Moreover temperature compensation is achieved automatically by means of auto-compensated strain gauges for the crank material (steel) and also thanks to the full-bridge properties. In this specific application, the locations of strain gauges are shown in Figure 4, with the numbers corresponding to specific positions on the Wheatstone bridge, according to the conventions of Figure 12. A detailed description of the applied methods can be found in Doebelin, 2003, Hoffmann, 1989 and Cigada, Comolli and Manzoni, 2006.

The strain gauge bridges are conditioned through a four-channel wireless device, which allows to transmit the signal from the rotating shaft to the acquisition system. This solution was selected after also considering slip rings and capacitive coupling (Mimmi et al., 2004), both of which required too much additional space.

The selected components are very compact: the wireless device is mounted on the left side crank inside a metal protection box (Figure 1); the connections between the sensors located on the right and left side of the device are realized by means of a multi-core cable passing through the crank axis (Figure 2). The power supply is given by an internal hi-capacity rechargeable battery that provides up to 9 h working time. The transmitted data are then converted in analog signals and acquired with a traditional DAQ board.

Figure 1: The strain gauge wireless acquisition device is inside the blue box, mounted on the left crank.

Figure 2:The right crank with the strain gauges wires passes through the axis to be connected to the wireless device that is on the other crank.

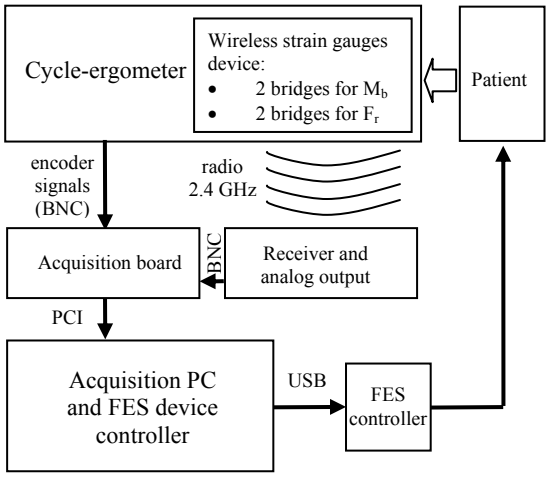

Figure 3: Scheme of the measuring chain and feedback on the patient.

3 MEASURED QUANTITIES

The measurement setup was designed and developed in order to identify the torque T as a combination of the bending moment M_b and the radial force F_r (Figure 4).

Known all the dimensions of the crank, the torques T are given by:

$$T_R = M_{b,R}\frac{b}{d} - F_{r,R}\frac{e(b-d)}{d}$$
$$T_L = M_{b,L}\frac{b}{d} - F_{r,L}\frac{e(b-d)}{d} \quad (1)$$

where b, d, e are the dimensions shown in Figure 4, and L and R pedex are respectively referred as the left and right leg.

The instantaneous total power P_{tot} can be computed, known the angular velocity $\dot{\theta}$ measured by the encoder, as:

$$P_{tot} = (T_R + T_L)\cdot\dot{\theta} \quad (2)$$

Moreover the mean energy per revolution can be computed as:

$$E_{m,tot} = \int_{t1}^{t2} P(t)\cdot dt \quad (3)$$

where t is the time and t_1 and t_2 are the instants of start and end of a revolution.

The unbalance U, a very significant quantity for asymmetric patients, can be computed as:

$$U = \frac{E_{m,R} - E_{m,L}}{E_{m,tot}} \quad (4)$$

where a positive value of U mean an unbalance toward the right leg that is more powerful.

Another useful quantity is the jerk J, i.e. the rate of change of angular acceleration, which shows the fluidity of the motion (Schot, 1978 and Teulings et al., 1997). Absolute jerk is defined as the third derivative of angular position, while a more interesting parameter is J_{std}, the standard deviation of jerk computed per revolution:

$$J = \dddot{\theta}$$
$$J_{std} = \sqrt{\frac{1}{(t_2 - t_1)}\int_{t1}^{t2}(J - \bar{J})^2\,dt} \quad (5)$$

where $\bar{J}$ is the mean jerk in one revolution.

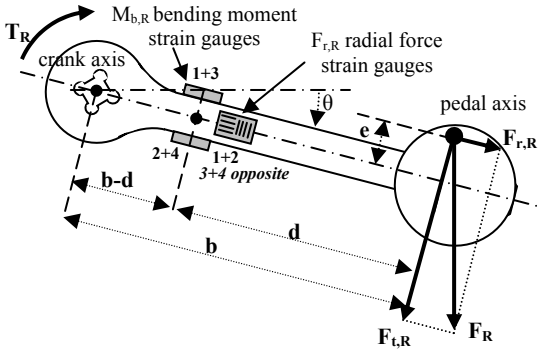

Figure 4: Scheme of the positioning of strain gauges on the right crank. For the strain gauges numbering conventions, see Figure 12.

4 FIRST RESULTS

The identification of the motor strategy of a patient and the comparison with healthy subjects (or with the same patient before rehabilitation) is fundamental to diagnose a pathology and verify the progress. The modified cycle-ergometer gives to the doctors and physiotherapist many information: in the following some examples.

Figure 5 shows a spinal cord injured patient cycling with the help of FES. Such a patient can cycle also without FES because the cycle-ergometer is motorized and maintains a minimum speed. But the muscles of the insane leg would never make any work and may loose mass. FES permits also the use

of those muscles and therefore let them grow in size, even if the patient cannot control them.

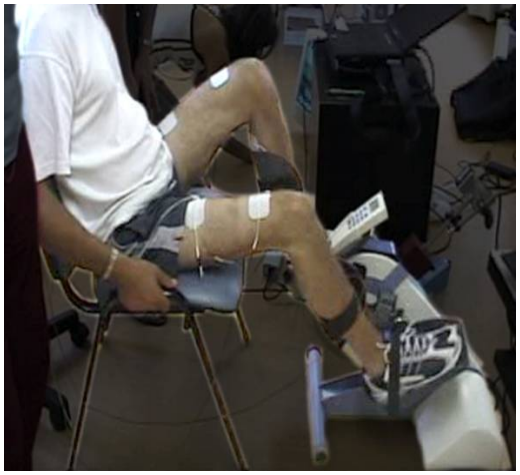

Figure 5: A spinal cord injured patient cycling with the help of FES.

Figures 6-9 show an example of data that can be retrieved from the measuring system. A healthy subject was asked to cycle in different conditions, such as active (time 0-15 s), passive (15-40 s), active (40-58 s, various powers), only right leg (58-68 s) and only left leg (68-82 s).

Figure 6 shows the angular position and the three derivatives that are necessary to compute all the subsequent quantities.

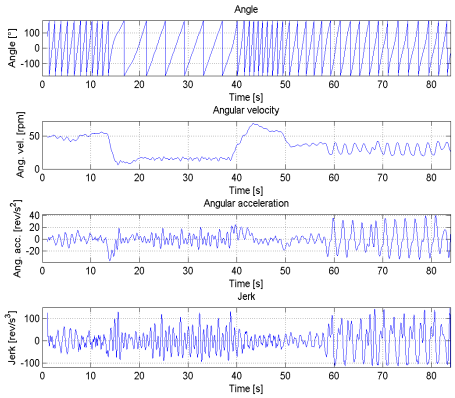

Figure 6: Angle and derivatives from cycling data of a healthy subject in different operating conditions.

In Figure 7 the standard deviation of jerk per revolution was computed; this quantity has relevant information: particularly the higher jerk is obtained when only one leg is used, this is due to the higher speed variations. Values up to 20 rev/s^3 are normal for healthy subjects during normal cycling with a high cycling resistance, while small values such as 2 rev/s^3 can be obtained with small resistance (not shown).

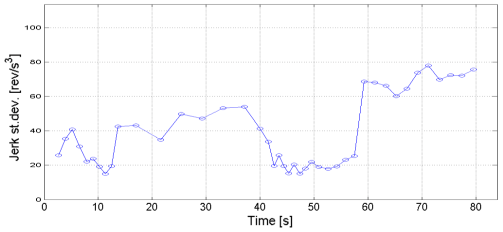

Figure 7: standard deviation of jerk per revolution: the biggest values are at right when only one leg was used.

The raw measurements would lead to instantaneous torque and power plots (not shown), with left, right and total components. Those information are interesting but highly difficult to analyze. A better solution has been found in re-phasing and averaging the torque values from some adjacent revolutions. Some examples will be shown ahead.

Average power and energy per revolution are shown in Figure 8, and give a good idea of the cycling conditions.

Figure 9 shows the percent unbalance and the total energy produced by the patient from the start of the test. Here also very small unbalance will build up and will be easily visible at the end of the test.

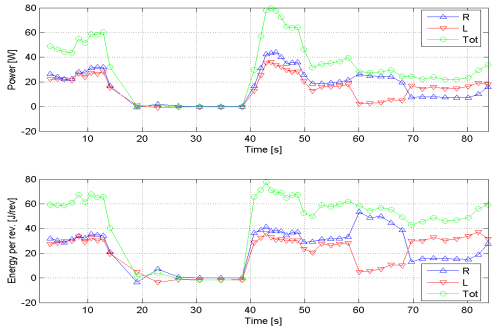

Figure 8: Average power and energy per revolution.

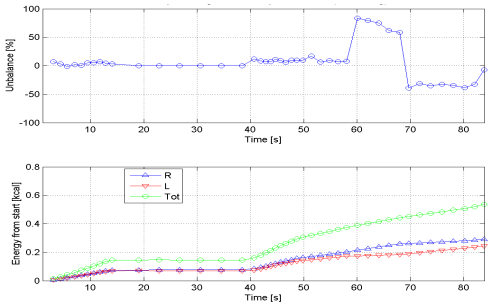

Figure 9: Unbalance and total energy from the start of the test.

A better way to evaluate the torque produced by the patient is to re-phase the torque signals and compute the median value in a number of revolutions. The median torque (along with percentiles) shows a

better waveform of the cycling and allows a better comparison between healthy and non healthy subjects and between the same patient before and after the rehabilitation. Figure 10 shows the torque from a healthy subject, while in Figure 11 the same subject was asked to use only the right leg. The zero crank angle is set at the maximum flexion of the left hip.

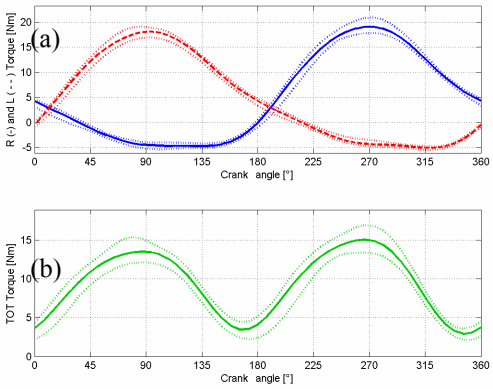

Figure 10: Median torque from a healthy subject actively cycling: (a) the left (dashed) and right (solid) components, (b) total torque that show nearly symmetric peaks. In dotted line the 5th-95th percentiles.

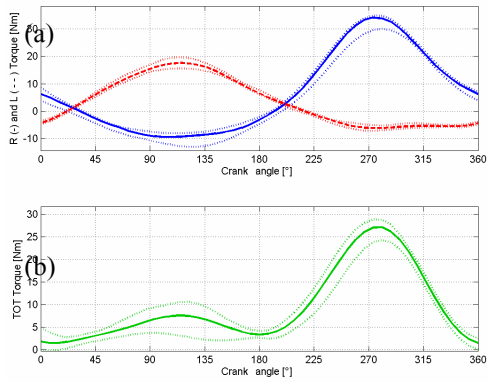

Figure 11: Same as the previous figure but related to an healthy subject, asked to cycle only with the right leg; the curves show highly asymmetric peaks.

The situation of a healthy subject asked to cycle only with the right leg simulates only one of the many possible cases of pathologic patients, where one of the legs is very weak but not completely passive. Indeed a healthy subject is unable to perform a true passive pedaling, as shown in Figure 11(a), where the left leg curve (dashed) is nearly flat in the angular range 270-360°, indicating that the weight of the leg is unconsciously partially compensated.

5 CONCLUSIONS

The paper deals with the design and the realization of a measurement system able to measure relevant quantities of the cycling, such as the torque (left, right and total), power, energy, unbalance and jerk.

The experimental tests involved both healthy subjects and spinal cord injured patients. Examples of the obtained measurements had been shown extensively in the figures. The results obtained up to now allowed the doctors and physiotherapists to have at their disposal additional and metrological qualified information, useful for diagnostic purposes and for checking the effects of the rehabilitation.

ACKNOWLEDGEMENTS

This work was supported by the Fondazione Cariplo in the framework of the research program HINT@Lecco. Authors would like to acknowledge Mauro Rossini (Villa Beretta Rehabilitation Center) for his helpful discussion.

REFERENCES

Comolli, L., Cantatore, A., Zappa, E., Bocciolone, M., Molteni, F., 2005. HINT@LECCO project: metrological characterization of a cycle-ergometer,. In *SIAMOC 05, 6th Congress of the Italian Society of Movement Analysis in Clinics.*

Ferrante, S., Pedrocchi, A., Gioia, M., Ferrigno, G., Molteni, F., 2005. HINT@LECCO project: FES cycling optimization and first clinical experiments of on patients. In *SIAMOC 05, 6th Congress of the Italian Society of Movement Analysis in Clinics.*

Ferrante, S., Pedrocchi, A., Ferrigno, G., Molteni, F., 2006. Experimental campaign of FES cycling on hemiplegics: first results. In *SIAMOC 06, 7th Congress of the Italian Society of Movement Analysis in Clinics.*

Gföhler, M., Angeli, T., Eberharter, T., Lugner, P., Mayr, W., Hofer, C., 2001. Test Bed with Force-Measuring Crank for Static and Dynamic Investigations on Cycling by Means of Functional Electrical Stimulation. *IEEE Transactions On Neural Systems And Rehabilitation Engineering,* Vol. 9, No. 2, June 2001, pp. 169-180.

Mimmi, G., Pennacchi, P., Frosini, L., 2004. Biomechanical Analysis of Pedalling for Rehabilitation Purposes: Experimental Results on Two Pathological Subjects and Comparison with Non-pathological Findings. *Computer Methods in Biomechanics and Biomedical Engineering,* Vol. 7, No. 6, Dec. 2004, pp. 229-345.

Doebelin, E.O., 2003. *Measurement Systems*, McGraw-Hill, 5th edition.
Hoffmann, K., 1989. *An introduction to measurements using strain gauges*, Hottinger Baldwin Messtechnik GmbH, 1st edition.
Cigada, A., Comolli, L., Manzoni, S., 2006. *Estensimetria Elettrica*, CittàStudi Edizioni, 1st edition.
Schot, S.H., 1978. Jerk: The time rate of change of acceleration, *American Journal of Physics,* Nov. 1978, Vol. 46, Iu. 11, pp. 1090-1094.
Teulings, H.L., Contreras-Vidal, J.L., Stelmach, G.E., Adler, C.H., 1997. Parkinsonism Reduces Coordination of Fingers, Wrist and Arm in Fine Motor Control, *Experimental Neurology*, Vol 146, pp. 159-170.

APPENDIX

For the crank angle measurement, a traditional encoder solution was chosen using a photo-reflective sensor coupled with a yet-present encoder drawn on the main cycle-ergometer wheel. Another two solutions have been also investigated.

The first solution was an inclinometer able to measure the bending of a beam with a small mass at the extreme, by means of strain gauges. The inclinometer has been positioned on the crank and have a nearly cosinusoidal output dependent on the angular position. The measured bending moment is proportional to the tangential acceleration a_t of the mass, which can be computed as:

$$a_t = g\cos\theta + \ddot{\theta}\rho \qquad (6)$$

where g is the acceleration of gravity and ρ is the distance of the mass from the crank axis (see Figure 12). After the realization of an inclinometer with a small ρ value (Figure 13), the measurements showed that the angular acceleration term can be neglected and so the signal is actually a cosinusoid.

Another consideration is about the thickness of the beam that should not be too thin, this because a high natural frequency is desirable; but also not too thick because the bending must be measurable. The output signal was gathered with the same strain gauge wireless device used for moments and forces measurements, then it is filtered and analyzed to find the unknown angle. To solve the two solutions ambiguity of the arccosine function, the first derivative was considered: a negative value indicate that the solution is in the first or second quadrant.

Another studied solution takes advantage of a cam positioned on the crank axis (Figure 12); the distance of the cam to a fixed point on the cycle-ergometer was measured by means of a laser triangulation transducer. The resulting signal is nearly cosinusoidal and can be analyzed in the same way of the inclinometer one. In fact the signal is of this kind:

$$r(\theta) = -e_c\cos\theta + \sqrt{R^2 - e_c^2\sin\theta} \qquad (7)$$

where r is the distance from the crank axis of a point on the cam surface that cannot rotate with it, e_c is the cam eccentricity and R is the cam radius. With the proper selection of the dimensions, the cosinusoid approximation can give as low as ±5° errors, as in the realized cam.

All the described measurement solutions were successfully used and proved to be of interest when no simpler alternatives are possible.

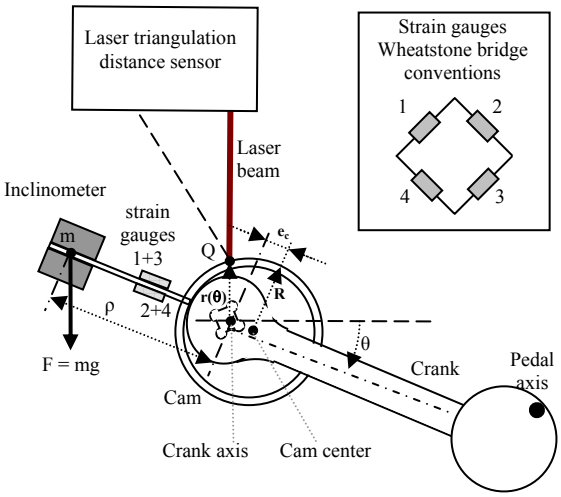

Figure 12: Scheme of the inclinometer and the cam mounted on the crank.

Figure 13: The adopted inclinometer.

MEASURING THE FORCES APPLIED TO A VIRTUAL REALITY LAPAROSCOPIC SURGICAL SIMULATOR WITH QUANTUM TUNNELLING COMPOSITE SENSORS

I. W. Mack, K. McMenemy, R. S. Ferguson
The Queen's University of Belfast, Belfast, United Kingdom
iw.mack@ee.qub.ac.uk, k.mcmenemy@ee.qub.ac.uk, r.ferguson@ee.qub.ac.uk

S. Potts, A. Dick
The Royal Belfast Hospital for Sick Children, Belfast, United Kingdom
sr.potts@tesco.net, alistair.dick1@ntlworld.com

Keywords: Laparoscopic simulator, low cost, PIC microcontroller, quantum tunnelling composite, force feedback.

Abstract: Abdominal surgery performed by laparoscopy requires a very high degree of skill in the surgeon. This skill level can only be acquired through practice and training. However, a virtual reality (VR) training simulator commands a high price. There is no reason for a VR simulator to be expensive, as a modern personal computer can produce high-quality graphics. If all that was required was good graphics, every surgeon could have a training tool within their laptop computer. What is missing is suitable low-cost human interface hardware – the equivalent of the computer game 'joystick'. This paper presents a design for a low cost device to address this issue. In order to provide force feedback, the forces exerted on the surgical instruments have to be measured by sensors mounted at various points. The sensors are constructed from quantum tunnelling composite pills which measure the pressure applied to them by the surgeon. The force feedback is produced by small direct current motors. The low cost design has been tested by both specialist laparoscopic surgeons and non surgical personnel to assess its benefits in training at different levels of expertise. A preliminary qualitative report is given which documents the findings from these initial tests.

1 INTRODUCTION

Laparoscopic, or minimally invasive, or keyhole surgery is well established among surgeons as a technique used to carry out surgery through small incisions as compared to larger incisions required for traditional surgery. However, while a singer, for example, can practice before a concert, a surgeon does not always have available the means to sharpen his/her skills before performing an operation.

The quality of the training equipment to which a surgeon has access largely depends on the amount of money a hospital has available for that purpose. At the low cost end of the market, a plastic box with a fabric top represents the body, with holes through which real surgical instruments are pushed to operate on rubber body parts. A camera looks through the side of the box and displays the 'operation' on an ordinary video monitor.

At the top end of the market the laparoscopic surgical trainer can be a pair of pseudo surgical instruments with force feedback and virtual reality software running on a computer which displays a depiction of the inside of a virtual patient and VR tool tips. The LapVR system from the Immersion Corporation allows the surgeon to learn essential skills through virtual reality training. The VEST systems from Select-IT VEST Systems AG allow for training in gall bladder removal and surgery in gynaecology. The SurgicalSim Education Platform from Simsurgery can be used for a wide range of training scenarios including trocar placement, camera navigation, suturing and knot tying.

VR training systems like these, and the one shown in Figure 1, can cost many thousands of dollars. However, the cost of such simulators need not be prohibitive, as personal computer (PC) game technology can deliver excellent, high quality, real time interactive 3D graphics that can easily meet any

requirements of a VR laparoscopic simulator. If it was only an issue of graphics, then every surgeon could have a training and practicing tool on their laptop PC. It is suitable human interface hardware, the equivalent of the computer game 'joystick' or 'flight simulator yolk' that is missing.

Figure 1: A VR laparoscopic surgery application displaying a representation of the abdomen and two simple instruments.

When interacting with a 3D virtual environment the experience not only depends on the type of device used to provide the human interaction, but also on external factors such as feedback, whether this is visual, audio or tactile. Other factors also have to be considered, such as the number of degrees of freedom of the user interaction device, as well as subjective and ergonomic aspects. For example, (Kontarinis and Howe, 1995) demonstrated that high frequency vibrations played a significant role in manipulation tasks. (Lindeman, Sibert and Hahn 1999) showed that adding passive-haptic feedback to precise manipulation tasks appreciably improved user performance. (Lindeman, Templeman, Sibert and Cutler, 2002) demonstrated that adding vibrotactile feedback to visual and auditory feedback improved the user experience of virtual environments.

Force reflecting interfaces such as the PHANTOM Desktop Device from Sensable Technologies provide useful feedback, but their utilization is limited by their cost and the fact that it is difficult to customize them to fulfill a specific task.

Vibrating motors, like the ones in mobile telephones, can be used to provide low-cost vibrotactile feedback as demonstrated by (Cheng, Kazman and Robinson, 1996). Indeed vibration elements have been attached to a standard computer mouse by (Hughes and Forrest, 1996) to provide tactile feedback.

This research reflects the belief that integrated tactile and visual feedback must be implemented in surgical simulators. The visual feedback is readily available in real time and at low cost using advanced computer graphics. The tactile feedback is much more difficult to integrate into the simulator at low cost. This paper aims to resolve this issue by documenting the development of a low cost haptic device for use in a surgical simulator. Following on from this introduction, section 2 will outline the basic design of the mechanical hardware. Sections 3 and 4 describe the electronic system and interface protocols. The quantum tunnelling sensors are introduced in section 5 and section 6 illustrates how the concept was initially tested. Section 7 will then present conclusions from our work to date.

2 THE SURGICAL TOOLS

This section outlines the design and development of low-cost haptic devices for interaction with a surgical simulator.

2.1 The Mk1 Surgical Instruments

The hand grips, and spatial positions used in the pseudo-instruments, were constructed to match dimensions taken from actual surgical instruments. The instruments (the surgical tools) were mounted on pillars attached to a base. They could rotate from the horizontal to point down by 45 degrees, and from facing forward to point inwards by 45 degrees.

These instruments had no electronics attached, as they were produced solely to verify that the measurements taken had been translated into an accurate 3D model. Following initial field trials it was decided to make some alterations to the position of the pillars because, during an operation the tool-tips mostly remain within a 4cm diameter spherical volume. These changes had the advantage of allowing more space at the tool-tip end to mount some electronics in the Mk2 instruments.

2.2 The Mk2 Surgical Instruments

From our earlier research, Mack, Ferguson, Potts and McMenemy (2006), and discussions with practicing surgeons it was decided that each joystick or surgical tool should have six degrees of freedom. That is, they should allow for movement in the X, Y and Z axes, rotation about the Z-axis, rotation of the

tool-tip about the Z-axis, and the opening and closing of the tool-tip. A Binary-Coded Decimal (BCD) thumbwheel switch was used to simulate the actual method of rotating the tool-tip. Five small rotary potentiometers were used to detect movement in the X, Y and Z axes, rotation about the Z axis and the opening and closing of the tool-tip.

For increased stability the instruments were mounted on a heavy wooden base as shown in Figure 2.

Figure 2: A pair of Mk2 instruments mounted on a wooden base.

3 THE USB INTERFACE

This section outlines the design and development of the Universal Serial Bus (USB) which was chosen to interface the instruments to the PC.

3.1 The Electronics

The 16C765 USB microcontroller from Microchip was selected for the interface because Microchip's MPLAB and Crownhill's Proton Development Suite provide a stable and comprehensive Integrated Development Environment (IDE). The PICs are cheap and employ re-usable re-programming technology, and require little in the way of additional external components to implement a working circuit. They have low power requirements and can therefore draw their power from the Universal Serial Bus itself.

Members of the Human Interface Device (HID) Class such as USB keyboards and mice are low-speed devices, and use interrupt data transfer.

The maximum possible transfer rate of data for this combination is 8 bytes per 10 milliseconds. This is quite sufficient for joysticks and similar devices such as the custom-made Mk2 pseudo surgical instruments because each surgical instrument's interface has only to send 6 bytes of data, one byte for each potentiometer and one byte for the thumbwheel switch on the pseudo surgical instrument.

The PIC was initially configured as a Human Interface Device without force feedback for the Mk2 joystick. Descriptor details for a HID device can be found in our earlier paper (Mack et al., 2006).

With the addition of force feedback, each interface would have to send force data to the PC and receive force feedback data from the PC. It was apparent that a HID class interface could not handle the data rates required. For a Mk3 joystick another method would have to be found to send and receive larger data bursts.

Other classes of USB devices were investigated to determine if any would be suitable for use in a force feedback interface. The Communications Device Class (CDC) specification from USB.org indicated that it could be used for bulk data transfer.

However, the 16C765 could only operate as a HID class device, so the 18F4550 was selected as it could operate as a Communications Class Device.

A PCB very similar to the one used for the Mk2 joysticks was designed for the new microcontroller on the Mk3 joysticks. Two of these circuit boards are required, one for each surgical instrument, and are mounted underneath the base of the instrument.

3.2 The PIC Descriptors

The Universal Serial Bus interface uses a serial protocol, and depending on how it is configured, can be low, full or high speed. The maximum data rates are 800 bytes per second for low speed, 1.2 Megabits per second for full speed and 53 Megabits per second for high speed.

When a USB interface is connected to a PC a procedure called enumeration takes place. During enumeration the interface must send descriptors to the PC which completely define the USB device's capabilities and how the device will be used.

If a USB device can be incorporated into a standard USB device class then there is a good chance that it can be made to work using the standard device drivers included with the Windows operating system. Configuring the interfaces as members of the Communication Device Class results in a twofold advantage. Firstly, the Proton+ compiler is able to use customizable descriptors provided by Microchip which allows the Communications Device to emulate RS232 serial protocol over a USB connection. Secondly, the device enumerates as a COM port on the PC and allows the use of a standard Windows device driver to establish communications with the device.

Although the descriptors define the interfaces as standard COM ports, this is only used as a convenient way to input data to and output data from the PC application via the Universal Serial Bus.

Details of the descriptors used in the Mk2 and Mk3 surgical instruments are explained in detail in internal documents entitled, "Descriptors required for a HID USB Interface", and, "Descriptors required for a CDC USB Interface", respectively.

4 THE PIC PROGRAM

However, to have any purpose, the USB devices must each run an application program.

The surgical instruments were originally developed without force feedback, and only fed position information to a Windows VR application, which can be seen in Figure 1. A different PIC application was developed for use with an experimental rig to test the setup for force feedback in one degree of freedom.

The data flow for one degree of freedom can be seen in Figure 3. The force feedback in the surgical instruments will be provided by small DC motors, which will provide a more tactile feel for the surgeon. A potentiometer at each pivot point provides position data. The force exerted by the user is measured by the use of pressure sensors produced from Quantum Tunnelling Composite (QTC) pills manufactured by Peratech.

Excluding the thumbwheel switch input, which is not suitable for force sensing or force feedback, four sets of data are required for the operation of each degree of freedom. Position data has to be sent from the joystick to the PC application, as does data regarding the force exerted by the user in two directly opposing directions. Force feedback data has to be sent from the PC application to the pseudo surgical instruments.

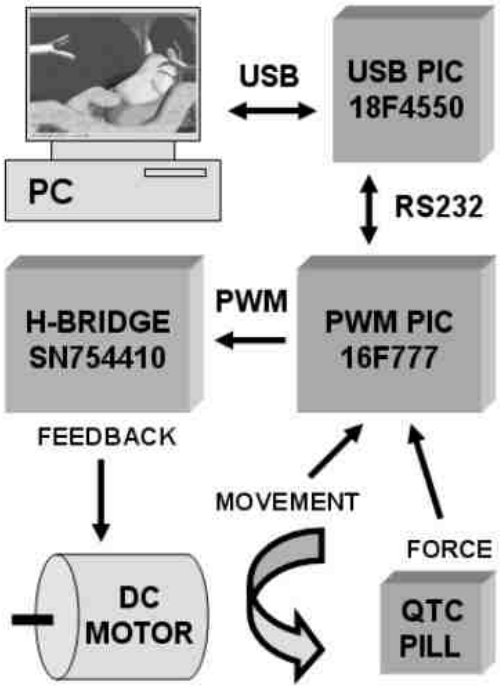

Figure 3: Data flow for one degree of freedom.

Small DC motors have been used in the development process. The motors have to operate in both forward and reverse, and this can be achieved by the use of an H-bridge circuit. The motor torque can be controlled by using Pulse Width Modulation (PWM) to vary the average current. A motor can be controlled by varying the duty cycle and/or the frequency of the PWM pulse train applied to it. Some PICs, such as the 16F777 used here, have hardware PWM channels which allow the pulse train to be produced in the background while the program is executing other instructions.

It was decided to produce separate modules which could control three degrees of freedom, with each module being controlled by a 16F777 PIC. The PIC also has the nine Analogue-To-Digital (A/D) converters required to sample three position and six force sensors. Each module sends data to the USB interface PIC and receives data from it to control the torque on three force feedback motors.

At this stage of the research it was decided to work on only one degree of freedom on one surgical instrument.

The applications for the USB and 16F777 module PICs were written in Basic and compiled using the Proton Development Suite.

5 THE QTC SENSORS

When deformed, Quantum Tunnelling Composites transform from a near perfect insulator to a conductor similar to metal. This transformation can be as a result of compression, stretching or twisting the composite.

Each QTC pill is sandwiched between two electrodes, and the user force applied perpendicularly to the flat face of the pill, as shown in Figure 4.

The circuit for measuring user force is a simple potential divider with the sensor in series with a current limiting resistor. Under no pressure the sensor appears open circuit, while under pressure it appears short circuit.

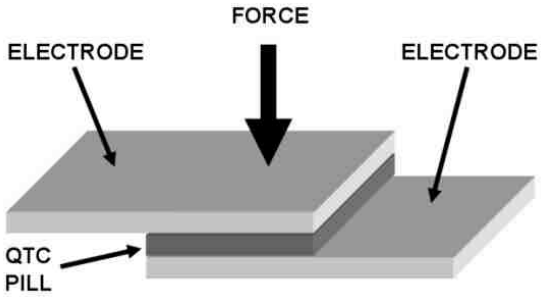

Figure 4: A QTC sandwich sensor.

6 TESTING THE CONCEPT

Figure 5 shows the rig used to evaluate the force feedback setup. For the sake of clarity it is shown before wiring.

A simple front-end program, written in Visual Basic (VB) is used to control and display the output from the experimental test rig.

Figure 5: The force feedback test rig.

Four bytes of data specify the motor behaviour. The application program allows forward or reverse motion to be selected. It is also possible to interactively control the PWM signal sent to the motor through the simulated RS232 protocol over the USB interface to the 18F4550 PIC. The 18F4550 sends the data to the 16F777, to configure the H-bridge and hence control the DC motor, thus providing force feedback.

The tests proved that a single personal computer could act as output generator for force specification and simultaneously acquire and act upon signals from the pressure sensors in real-time.

7 CONCLUSIONS

This paper presented a design for, and practical realization of, a low-cost laparoscopic surgical training tool that offers the possibility of incorporating force sensing through the novel use of quantum tunnelling composite force sensors.

Several electronic interfaces have been developed, culminating in a fully implemented USB design that emulates a traditional PC COM port. A test rig for a one degree of freedom force feedback axis has been produced which sends position and force data via one of these USB interfaces to a driver program in a host PC. Data from the driver program has been returned to the test rig to control a force feedback motor. It is the ultimate aim of this research to have twelve such motors controlled in the final version of the surgical instruments.

Two instruments give a surgeon the opportunity to practice realistic procedures, and our design offers the possibility of highly accurate force sensing and feedback in the future. The tight interaction between force sensing and feedback afforded by the quantum tunnelling sensors will alleviate some of the problems that arise in conventional haptic rendering applications, for example the need for a very high sampling rate in the servo loop.

When combined with the realistic graphics that current Graphics Processing Unit (GPU) based rendering hardware offers it will be possible to offer a very effective training package that could be made widely available.

Two surgeons and two non-specialists tested the Mk2 instruments in conjunction with the virtual reality software and they were very favourably received. Both groups found the instruments easy to use, with the surgeons able to perform simulated surgery on a gall bladder. With force sensing, force feedback and collision detection algorithms, surgeons will be able to practice realistic surgical procedures with a good level of authenticity.

The development of force feedback systems that are actually used by surgeons requires close

teamwork between medical staff and researchers. It is hoped that the development of this VR trainer will result in a laparoscopic simulator which will be acknowledged by the medical profession and lead to an enhancement in the safety of patient care.

The original aim of making a pair of low-cost pseudo surgical instruments for a VR laparoscopic simulator is well on the way to a successful conclusion. The component cost of the Mk2 instruments is approximately 0.4% of the cost of the Virtual Endoscopical Surgery Training (VEST) simulator without force feedback from Select-IT VEST Systems AG. The Mk3 training instruments, when they have force sensing and force feedback implemented will have a projected component cost of 1.1% of the cost of the VEST force feedback system. While our costs do not include the cost of manufacturing the instruments they compare very favourably with commercial equipment. Indeed we could include a laptop computer with pre-installed laparoscopic simulation software, which could also be used independently as an ordinary PC, and still cost only 1.5% and 1.7% of the commercial non force feedback and force feedback systems respectively.

REFERENCES

Cheng, L.-T., Kazman, R., & Robinson, J. (1996). Vibrotactile Feedback in Delicate Virtual Reality Operations. *Paper presented at Fourth ACM International Conference On Multimedia.* Boston, MA.

Hughes, R., & Forrest, A. (1996). Perceptualisation Using a Tactile Mouse. *Paper presented at Visualization '96.* San Francisco, CA.

Kontarinis, D., & Howe, R. (1995). Tactile Display of Vibratory Information in Teleoperation and Virtual Environments. *Presence: Teleoperators and Virtual Environments, 4*(4)*,* 387-402.

Lindeman, R., Sibert, J., & Hahn, J. (1999). Towards Usable VR: An Empirical Study of User Interfaces for Immersive Virtual Environments. *Paper presented at ACM CHI '99.* Pittsburgh, PA.

Lindeman, R., Templeman, J., Sibert, J., & Cutler, J. (2002). Handling of Virtual Contact in Immersive Virtual Environments: Beyond Visuals. *Virtual Reality*; *6*(3), 130-139.

Mack, I.W., Ferguson, R.S., Potts, S., & McMenemy, K. (2006). Adding tactile realism to a virtual reality laparoscopic surgical simulator with a cost effective human interface device. *Paper presented at Electronic Imaging 2006.* San Jose, CA.

FORCE MEASUREMENT DURING GAIT THERAPY ASSISTED BY A ROBOTIC TREADMILL

The Case of Lokomat®

M. Bocciolone, M. Lurati, M. Vanali
Department of Mechanical Engineering, Politecnico di Milano, Via La Masa 34, Milano, Italy
marco.bocciolone@polimi.it, massimiliano.lurati@polimi.it, marcello.vanali@polimi.it

F. Molteni
Valduce Hospital, Villa Beretta Rehabilitation Center, Via N. Sauro 17, Costamasnaga (LC), Italy
francomolteni@libero.it

Keywords: Gait analysis, assisted gait, rehabilitation, force measurement, data analysis, controlled orthosis.

Abstract: The present paper deals with force measurement during gait therapy assisted by a special robotic treadmill with driven robotic orthoses that guide inferior limbs movements. The objectives, the measurement setup and the results are presented. This work has been carried out in order to gather data necessary to begin the analysis and the design of a new ankle motion device. The presented results also show how these measurements can be useful in gait parameters assessment and patient's muscle activity level.

1 INTRODUCTION

Nowadays mechanical measurements give a valid and important aid in the rehabilitation field, both for the design of specific devices and for the development of suitable data analysis techniques. Different types of sensors can be fixed on the rehabilitation machines (Comolli et al., 2005), and particular wearable sensors allow to perform the measurements directly on the patient's body, e.g. the acceleration of body segments during gait (Zijlstra, 2003). Mechanical measurements can be useful to properly set-up the rehabilitation device parameters or to evaluate the patient's conditions during rehabilitation sessions (Melis et al., 1999).

This paper deals with force measurements applied to the case of locomotion therapy assisted by a specific robotic treadmill, the Lokomat®. This is a rehabilitation device composed of a driven robotic gait orthosis that guides the patient's legs on a treadmill while a desired percentage of the body weight is sustained by a special support system. The patient is sustained while his hips, thighs, knees and legs are actively guided during the entire gait cycle, therefore reproducing a physiologic movement. The feet are instead passively pulled with a spring-belt system: consequently ankles and feet follow non "natural" trajectories and do not reproduce the actual human walking. The foot sustainment is strictly necessary to avoid the patient to stumble. Even if this eventuality wouldn't represent a danger for the patient's health because of the presence of suitable security devices, it would cause the system emergency stop to avoid the patient to fall, thus interrupting the rehabilitation session. The growing interest around this topic and the study of possible solutions are the starting point of the present work. The internal forces exchanged between the patient and the Lokomat® have been measured in order to analyze the mechanical behaviour of the utter system (human and mechanical), and to investigate the forces transmission from the suspension system to the ground and vice versa. This knowledge is the basis to upgrade the ankle motion system allowing a better control and a more physiological ankle movement. This paper describes the design of the tests, the experimental set-up and the obtained results. The analysis of the results has allowed to get information about the patient's working conditions. The achieved data have also been the inputs in order to design an innovative prototype device able to control the ankle motion (Bucca et al., 2008). The possibility of the patient's conditions evaluation and the rehabilitation parameters assessment have been therefore investigated in the paper.

Force measurements during patients' rehabilitation sessions have been performed using suitable transducers (load cells) expressly built and calibrated. These have been installed between the patient and the Lokomat® frame. The body weight sustaining force and the left/right foot pulling force have been measured during the assisted gait, both for an healthy subject and for an actual patient.

2 MEASUREMENT SETUP

This paragraph describes in detail the measurement setup, the installed sensors and the Lokomat® system.

The Lokomat® rehabilitation device (Figure 1) is essentially composed by three parts:

1. a hip support system that sustains a desired percentage of the patient's weight;
2. two electrically driven leg orthoses;
3. a passive spring-belt system that pulls and drives the feet.

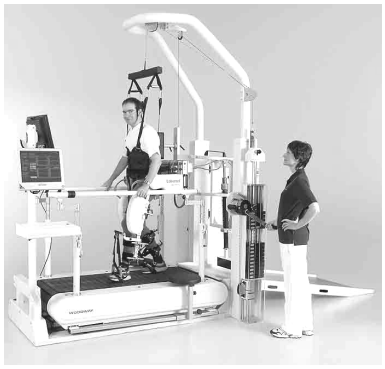

Figure 1: view of Lokomat® (with the courtesy of Hokoma, from website www.hocoma.ch).

The body weight support system allows the therapist to set the counterweight that sustains the patient during the gait, accordingly to the medical directions. This parameter setup is crucial because it influences the rehabilitation session effectiveness and therefore the patient's progresses. During the gait the patient is submitted to dynamic forces, which have been measured and analyzed using suitable techniques. In order to perform this goal, a specific load cell (diameter 90 mm, thickness 5 mm, depth 30 mm, output sensitivity 7.69 mV/N) has been installed between the cable and the pin that pull the system frame (Figure 2). In the following it will be referred as the sensor N. 5.

Because of the main interest toward the feet pulling system, other transducers have been installed to measure the involved internal forces. Four load cells (diameter 45 mm, thickness 2 mm, depth 20 mm, sensitivity 20 mV/N), have been inserted between the springs and the belts that pull up the feet. Sensor N. "1" and "2" have been installed on the left side, "3" and "4" on the right one (Figure 3).

All the load cells are not commercial products but have been designed and realized for this specific application. The transducers incorporate an aluminium cell ring as the elastic element. Four strain gauges, located as shown in Figure 4, are used as sensors able to measure the strains due to the force (extension or compression) acting along a diameter.

Figure 2: sensor number 5.

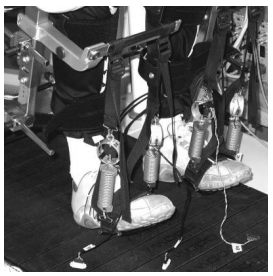

Figure 3: sensors number 1-2 (left leg), 3-4 (right leg).

The strain gauges are connected in a full Wheatstone Bridge. The arrangement allows the thermal compensation. The bandwidth is 0-20 Hz.

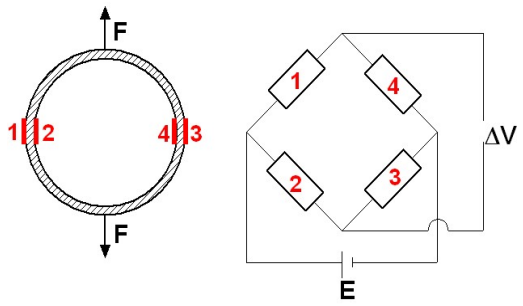

Figure 4: mechanical and electrical design of the load cells.

All the output voltage signals have been acquired with a National Instruments Acquisition System, using a 12 bit PCMCIA DAQ card and a notebook for data storing.

3 TEST DESCRIPTION

Several tests have been carried out in two different conditions:

1. during the gait of a 65 kg healthy person, with no specific pathology (it will be referred as the *"normal"* condition);
2. during the gait of a patient with a specific motor disability.

In the first case (healthy subject) different speed and counterweight conditions have been tested, and are listed below:

- gait speed of 1.5 km/h and 2 km/h;
- counterweight of 20 kg and 35 kg;
- active and passive gait: in the active session the subject was asked to walk in normal conditions, therefore using his muscles at 100% and contrasting the Lokomat® resistance; in the passive session he was asked not to use his muscles, being completely transported and guided by the Lokomat® orthoses.

In the second case (real injury condition) a Spinal Cord Injury (SCI) patient has been monitored during a usual rehabilitation session. Because of the specific pathology he was almost unable to use the left leg but not the right one. Considering that the patient used to have his gait sessions at 2 km/h with 40 kg of counterweight, two different speed parameters have been tested (1.5 km/h and 2 km/h), and he was asked to walk both passively and actively. In order to prevent negative effects on the patient's rehabilitation sessions, only the usual 40 kg counterweight has been tested.

4 RESULTS

This paragraph presents the results obtained in the most meaningful tests for both test conditions.

4.1 "Normal" Conditions

A first effective analysis can be performed analyzing the data obtained from the sensor N. 5 (the one measuring the body sustaining dynamic force).

Figure 5 shows the force time histories 30 s long, measured in the following conditions:

a) subject standing and suspended;

b) subject walking suspended;

c) subject walking leant with 35 kg counterweight;

d) subject walking with 20 kg counterweight.

The measured forces, except obviously the case of standing subject (a), present a periodic shape due to the alternate left and right foot contact.

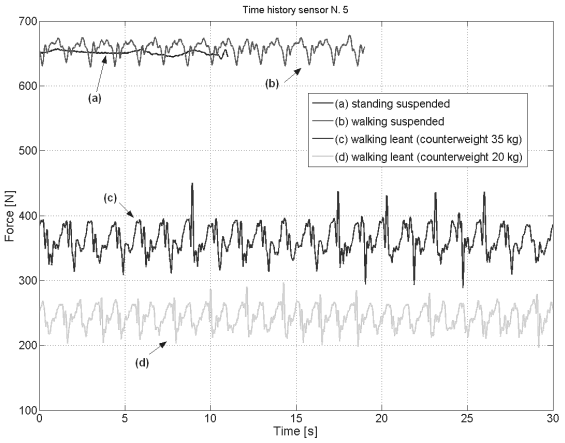

Figure 5: measured body sustaining force in different test conditions.

A characteristic force waveform can be observed in a step cycle, considering for example a 10 s long time interval, in the case of subject walking at 1.5 km/h with a counterweight of 35 kg (Figure 6).

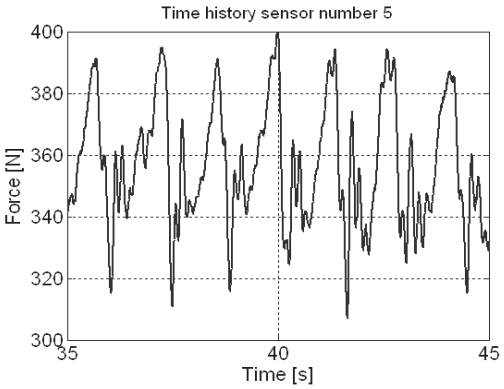

Figure 6: body sustaining force - time history.

The subject has a left (or indifferently right) foot contact in 2.7 s and therefore a foot contact in 1.35 s. The lowest force values are exhibited at the foot contact instant while the highest when the foot rises. The time-history analysis allows to evaluate the actual load variations. In this case the measured mean value is 359 N, with minimum and maximum values equal to 310 N and 400 N. It has therefore been calculated that the subject has sustained an

average weight of 275 N (~28 kg), with a minimum of 235 N (~24 kg) and a maximum of 324 N (~33 kg). The analysis in the frequency domain (using DFT techniques) is useful to identify the dynamic component parameters. Figure 7 shows the force amplitude spectrum: there is a main component at 0.7 Hz (correspondent to the feet contact frequency at a speed of 1.5 km/h) and other lower multiple components.

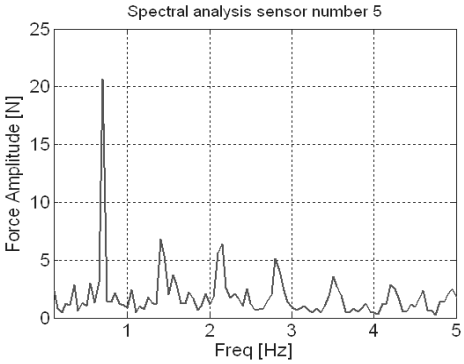

Figure 7: body sustaining force - amplitude spectrum.

Table 1 contains the numeric results for all test conditions, in terms of mean, max and min values and peak to peak amplitude.

Table 1: measured body sustaining force (mean, max, min, peak-to-peak values) for 35 kg and 20 kg counterweight.

	35 kg	**20 kg**
Mean value	359 N	242 N
Max value	400 N	265 N
Min value	310 N	215 N
Peak-to-peak	90 N	50 N

The analysis of the data acquired by the cells installed over the feet (sensors N.1 to N.4), gives some important indications about the subject's real activity during the gait. Table 2 presents the numeric results, comparing the suspended and the leant subject conditions, both for left and right leg.

Table 2: numerical results for left/right foot pulling force.

	Suspended patient		**Leant patient**	
	Right	**Left**	**Right**	**Left**
Peak-to-peak	30 N	25 N	105 N	110 N

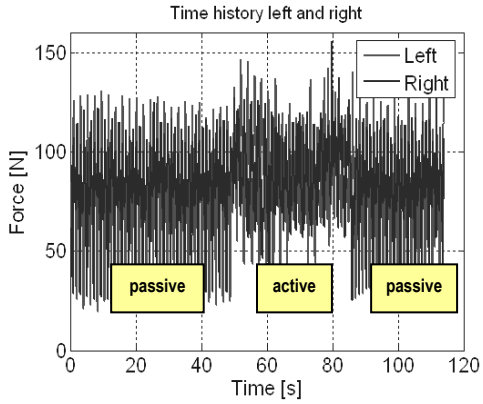

Figure 8: left and right foot pulling force (comparison between active and passive zones).

In this case the mean values are not meaningful because of their dependence on the static tension the therapist gives preparing the patient. The dynamic components are instead indices of the subject's muscle activity. The peak-to-peak value grows from 30 N to 105 N for the right leg and from 25 N to 110 N for the right, showing a strong increment of the forces needed to sustain the feet when the subject walks leant on the treadmill respect to the suspended case.

The comparison between the time histories of the active and passive sessions shows a significant difference in the measured forces, being useful for the subject's work evaluation (Figure 8).

4.2 SCI Patient Gait

The previous analyses, performed in the case of an healthy subject, have been applied to the case of a SCI patient. The considered patient is affected by an asymmetric left/right motor disability, and therefore well suits a study case.

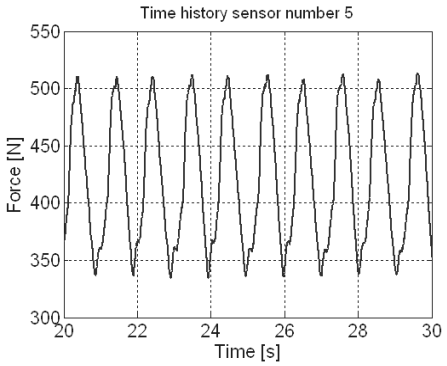

Figure 9: time history (body sustaining force).

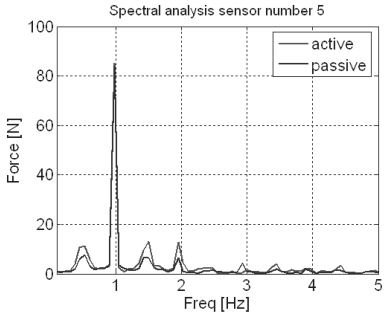

Figure 10: spectral analysis (body sustaining force).

The body sustaining force time history (Figure 9) shows a more regular signal waveform, confirmed by the spectral analysis (Figure 10), where the main spectral component (associated to the foot contact frequency) is more marked if compared with the normal case. Comparing the active and passive session spectra, it can be observed that the secondary dynamic components tend to become lower in the passive case, but when the patient tries to walk actively a little increase appears (like the "normal" gait case, where multiple components are well marked).The analysis in the time domain has pointed out significant differences in the measured sustaining force depending on the patient's speed gait: the mean, max and min values of the aliquot part of the weight sustained by the patient himself are respectively 147 N, 59 N, 226 N for speed of 2 km/h. In the case of speed of 1.5 km/h the values are 127 N, 29 N, 226 N. The first case (2 km/h) is the usual rehabilitation condition for the patient: he seems therefore able to realize a more fluent gait supporting a higher load.

The analyses of the time histories of the feet sensors are useful to obtain indications about the patient's muscular activity (Figure 11).

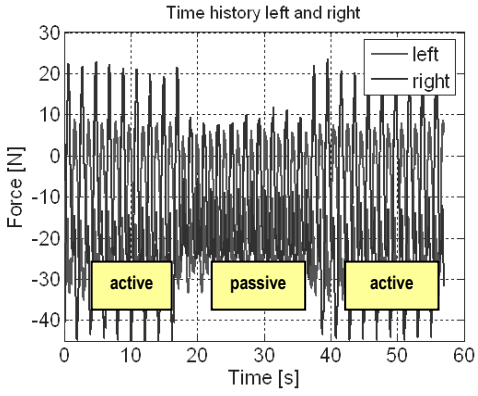

Figure 11: left and right foot pulling force (comparison between active and passive zones).

The calculation of the standard deviation of the forces, index of the dynamic forces exchanged between the patient and the orthosis, shows an increment related to the patient gait efficiency (Table 3, Table 4).

Table 3: feet pulling force values for 2 km/h speed.

2 km/h	**Passive**	**Active**	**Increment**
Right	12.3 N	19.8 N	+61%
Left	12.6 N	14.1 N	+12 %

Table 4: feet pulling force values for 1.5 km/h speed.

1.5 km/h	**Passive**	**Active**	**Increment**
Right	12.1 N	19.9 N	+64%
Left	12.8 N	16.3 N	+27 %

In agreement with the patient's pathology the results has pointed out a significant difference between active and passive sessions only for the right leg, with an increment of 61% and 64% respectively for 2 and 1.5 km/h, while 12% and 27% for the left leg.

5 DISCUSSIONS AND CONCLUSIONS

Measurement chains able to gather the forces during gait therapy assisted by a robotic treadmill have been designed and settled-up. Results have pointed out that these measurements can help doctors and therapists in the patient's assessment and the rehabilitation parameters set-up. The obtained results have also been the starting point for the study of an ankle motion system improvement.

The actual load sustained by the patient during assisted gait is a fundamental parameter. The proper value is different for each patient, depending on the physical condition and the specific pathology. A too high value may be detrimental to the patient, while a too low value may be inappropriate, raising the patient's recovery time length. The measurement of the actual load, and especially of the dynamic load variations, for sure very important to this aim, has been performed and the results analyzed.

Beside this, the knowledge of the involved internal forces can help the therapist in the rehabilitation session evaluation, allowing to properly set-up all the parameters, as the gait speed and the session time length.

The very good results obtained in the present work provide the basis for future developments aimed to the real diagnostic possibilities. Additional experimental tests will be carried out in order to

consider a greater number of patiens, thus validating the obtained results and estimating the associated uncertainty levels.

The authors think that the measured internal forces are associated to the actual muscular activity of the patient. Therefore the next step in this research field will be the correlation between the measured forces and the results coming from the electromyography of lower-limb muscles during walking, in order to validate the presented results. The possibility of the patient's assessment based on force measurements is very interesting, giving a lot of advantages as low cost and ease of carrying out.

ACKNOWLEDGEMENTS

Authors wish to thank Mauro Rossini (Villa Beretta Rehabilitation Centre) for his helpful discussion.
This work was supported by the Fondazione Cariplo in the framework of the research program HINT@Lecco.

REFERENCES

Zijlstra, W., 2003. Assessment of spatio-temporal gait parameters from trunk accelerations during human walking*, Gait and Posture* Vol. 18, 1-10.

Bucca, G., Bezzolato, A., Bruni, S., Molteni, F., 2008. A mechatronic device for the rehabilitation of ankle motion, *BIODEVICES 2008 Conference, Funchal, Madeira*.

Comolli, L., et al, 2005. Metrological characterization of a cycle-ergometer, *6th Congress of the Italian Society of Movement Analysis in Clinics*.

Melis, E.H., et al, 1999. *Analysis of assisted-gait characteristics in persons with incomplete spinal cord injury, Spinal Cord*, Vol. 37, Issue 6 pp. 430-439.

INSTRUMENTATION AND LABVIEW BASED CONTINUOUS PROCESSING FOR CHEST PHYSIOTHERAPY

Luc Marechal, Christine Barthod, Gérard Gautier, Jacques Lottin
Laboratory SYstems and Materials for MEchatronics (SYMME),University of Savoie, BP80439, Annecy-le-Vieux, France
luc.marechal@univ-savoie.fr, christine.barthod@univ-savoie.fr

Jean Claude Jeulin
Réseau Bronchiolite de Haute Savoie (RB74), 8 avenue de champ fleuri 74600, Seynod, France
jc.jeulin@free.fr

Keywords: Force Sensing Resistor Sensors, Motion Sensors, LabVIEW, Continuous Processing, Infant Chest Physiotherapy.

Abstract: Infant chest physiotherapy (CPT) has never been the purpose of any assessed scientific study although it is widely used for newborn babies suffering from bronchiolitis. It is thus compulsory to quantify the limits of the gesture to obtain the expected effect. In this paper, we present original instrumented gloves designed to perform measurements during the CPT act on babies to characterize the gesture. Associated electronics and software were specially developed with LabVIEW for data acquisition, continuous processing and analysis of the characteristic parameters. The measuring system and its readout electronics were calibrated. A drive to do measurement with babies in real situation validates the principle of the system. The analysis of the results highlights relevant parameters for typical phases of the CPT act.

1 INTRODUCTION

As the demand for clinical or medical instrumentation design increases rapidly, the techniques and methods used to convert medical and physiological information to electrical signals grow too. Quantitative responses must be relevant to allow a better understanding of the medical or clinical analysis through computer interfaces. In surgery or physiotherapy for example, the characterization of the gesture for a medical or a clinical act is more and more required (Davidson, 2002). The need of standard quantitative definition of chest physiotherapy gesture expressed by physiotherapists is at the beginning of our study. Hardly any study concerning the characterization of infant chest physiotherapy technique has been achieved. This paper presents the method and the system for the characterization of the physiotherapist gesture when performing chest physiotherapy act on newborn babies. First a chest physiotherapy technique is rapidly described in order to explain the need of practitioners regarding the definition and characterization of their gesture. We present the implementation of force and displacement sensors on innovative instrumented gloves that we designed to record the characteristic parameters of the gesture. In a second part, the study of the different components of a computer based measuring system is detailed. In particular, the acquisition system, the readout electronics, the acquisition program and important details of the coding are presented. Finally, measurement results are proposed, showing the reliable capability of the system to give a scientific definition of the gesture.

2 MEASURING SYSTEM

2.1 Medical Context

Bronchiolitis is an acute disease of the respiratory tract that affects young babies. In French-speaking European countries, the two consensus conferences, held in 1994 and 2000, concerning the management of bronchiolitis in infants have widely recommended the use of chest physiotherapy in order to provide care (ANAES, 2000). These techniques aim at generating forced respirations in order to improve bronchial pulmonary exchanges. More particularly in France, the forced expiration maneuver used is the Increase

of Expiratory Flow technique (IEF). IEF technique is a thoracic-abdominal movement generated by the hands of the physiotherapist on the infant's chest. The infant being lain on a table, the physiotherapist places one hand on the thorax close to the neck and the other hand on the abdomen. The "thoracic hand" presses uniformly with its cubital part whereas the "abdominal hand" has a global support. The applied pressure sequences must be synchronized with the infant free respiratory cycle.

2.2 Assesment of Needs

These last years, due to management with the IEF technique, results have shown an improvement of the clinical evolution of babies' health preventing many of them from reaching the critical state of the hospitalisation (Postiaux et al., 2006). Consequently, the CPT act is more and more used and the efficiency of this physiotherapy technique is now currently admitted in France. Although the IEF technique requires a good know-how, the physiotherapist has an empiric approach and relies his practicing on his own perception. He adapts and controls the magnitude and the frequency of the gesture versus the sound of the infant respiratory system and his own sense of touch. A qualitative protocol for the IEF technique has been defined (Fausser et al., 2002) but no quantitative definition has been made. The demand is then twofold: on one hand, to prove the efficiency of the gesture for validating the technique; on the other hand, to characterize the gesture to enhance learning and create didactical situations.

2.3 Implementation of Force and Displacement Sensors

As it was decided to quantitatively define the basic gesture of the IEF technique, technical discussions between instrumentalists and expert physiotherapists, about the practical knowledge for doing the efficient gesture, allowed to choose its physical parameters to record. So, specific instrumented gloves were designed to measure during the CPT act (Maréchal et al., 2007): the space displacement of the physiotherapist hands, and the distribution of the force applied by the hands on the infant's chest. A third relevant parameter consisting of the sound of the infant respiratory system has to be taken into account too. Thus, the measurement system should neither modify the physiotherapist's gesture nor being cumbersome or disturbing for the infant.

Since the force measurement system must be thin, flexible and painless for the baby, and because the force applied by the practitioner is as well quasi-static as dynamic, Force Sensing Resistor sensors (FSR) from Interlink Electronics were chosen. FSR are polymer thick film (PTF) devices which exhibit a decrease in resistance with an increase in the force applied to the active surface (Interlink, 2004). After an exhaustive comparative study of different sensors, we have chosen the most appropriate one as far as their size and cost are the lowest, for equivalent technical properties. Such sensors have already been used for biomedical devices (Morris et al., 2006).

The FSR sensors are glued on a cotton glove by an adhesive band (supplied by 3M). What is innovative with such gloves is the location of the sensors. Investigation of the contact between the physiotherapist hands and the infant body has been led so that we can characterize it. The contact shapes have been determined after several tests according to the referent physiotherapist, so that the most interesting pressures applied during the IEF act can be seen and measured. Regarding hygiene and medical environment, a thin medical latex glove is worn over the instrumented glove so that the sensors are not directly in contact with the skin of the toddler.

Besides, the measurement of the position of the hands of the physiotherapist is performed thanks to a six-degree of freedom electromagnetic tracking device, the Flock of Birds (FoB, from Ascension Technology). It is composed of one transmitter and two receivers. Each receiver is placed on a cotton glove on the upper side of the back of each hand. Manufacturer claims that the system accuracy is 1.8 mm and 0.5° RMS for position and orientation respectively within a working range of $\pm$ 1.2 m in any direction. No conductive material must be present near the system because interferences produce significant error measurement (LaScalza et al., 2003). This system is suited to our application because the transmitter is placed 30 cm far from the head of the baby and the displacement of the hands doesn't exceed 5 cm in each direction.

2.4 Signal Conditionning

Preliminary trials were made with the referent physiotherapist in order to determine the range for our application. Then, we designed the FSR signal conditioning according to the manufacturer's advices among suggested electrical interfaces.

For a force-to-voltage conversion, the FSR device is the input of a current-to-voltage converter. In the shown configuration (Figure 1), the output voltage is inversely proportional to the FSR resistance. An output swing of 0 V to 10 V is desired to enhance the sensitivity of the measurement system. Vref is set to -

5 V. It is to be noticed that a variation of the reference voltage would lead to a variation of the output voltage. The supply voltage should be constant. Hence, a precision voltage reference, the AD584, was chosen for that purpose. The current through the FSR should be limited to less than 1 mA/cm^2 of applied force, to prevent from damaging the sensor. Rg value of 15 kΩ was chosen to limit the current and maximize the output voltage range. Moreover, the risk of electronic noise is avoided with these sensors because the value of resistance in the feedback loop is high enough. This circuit is simple, easy to implement, reliable and costless.

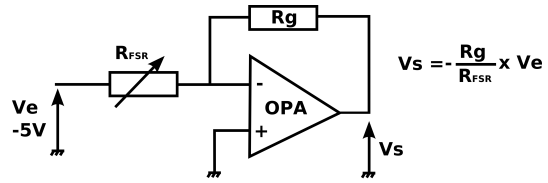

Figure 1: FSR associated electronics.

3 DATA ACQUISITION AND PROGRAMMING

FSR sensors voltage responses are acquired using a NI-9205 DAQ card and NI cDAQ-9172 compact chassis for USB interface communication. It features a 32 single-ended analog inputs with a sampling rate up to 250 ksamples per second. Figure 2 is a block diagram of the system. The program is written in Graphical programming using National Instrument LabVIEW version 7.1 since dataflow language is well adapted for application with parallel tasks. Sampling rate was chosen at 200 Hz for each sensor. This has been defined after tests and recordings of the CPT act: observation of the gesture pointed out important variations lasting about 100 ms. In order to have enough samples to acquire and plot the signals, we chose a resolution of 5 ms which is well adapted to have enough accuracy.

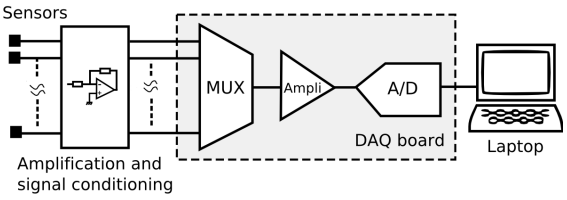

Figure 2: Acquisition block diagram.

3.1 Continous Processing (Figure 3)

In the aim to display the measurements when the gesture is being performed, we decided to process the signals on-the-fly during their acquisition. The length of the trial, up to several minutes, and the number of signals (fifteen) increase rapidly the amount of the collected data. Regarding these parameters, the recording of the data must be done throughout the measurement. The DAQ board performing the acquisition stocks the samples in its circular memory. The Ni DAQmx driver ensures the continuous transfer of the digitized data to the computer memory. The reading of the samples is done block by block with the LabVIEW program by the Analog Input (AI) Read routine returning data from the buffer. This high level priority routine is expensive in terms of performance. As a matter of fact, for slow frequency rate acquisition when AI Read is called, data might not be all present in the buffer. So, AI Read will wait for data to be available. This waiting time from a priority task involves heavy performance cost. To remedy this, Châlons recommends an optimisation of the computer resources when a continuous processing is desired (Châlons, 2001). In order to acquire and process a continuous amount of data, we used a new programming technique in our code which stands for a call of the AI Read routine only when needed. To do so, a variable is used to indicate the number of analog input data remaining in the buffer. The new version of the DAQ driver NI-DAQmx 8.3 makes easier the programming by using a simple Read property node that returns the state of the buffer. This frees enough resources to activate other asynchronous tasks that are less time critical such as display and file storage, and allows continuous display.

This solution is low cost to perform ”real time” acquisition and display, in comparison to Real Time hardware modules. The program runs on a conventional Laptop PC, Pentium M CPU at 1.6 GHz with 512 MB RAM under Windows 2000. Any reasonably current PC should be compatible with our measurement system. The program has been tested and shown to operate reliably.

3.2 Monitoring and Visualization

Before each trial, a user friendly interface enables the user to supply information about the management of the patient. Sex, age, size, weight and pathology are also asked. A text box is dedicated to comments and evolution of the clinical state. All information are saved in a result file detailed further. While gesture is performed by the physiotherapist, waveform plot dis-

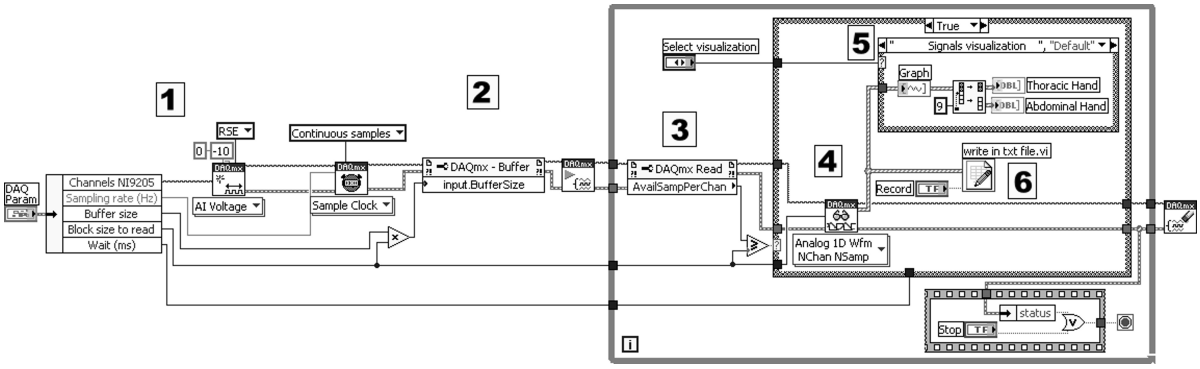

Figure 3: Structure of the LabVIEW acquisition program: (1) acquisition configuration; (2) definition of buffer size; While loop: (3) reading buffer state; (4) reading of samples by AI read routine if the buffer is fulfilled; (5) graphical display update and (6) file storage when AI read routine is not solicited.

plays signals issued from each sensor in ”real time”. The monitoring screen is presented Figure 4.

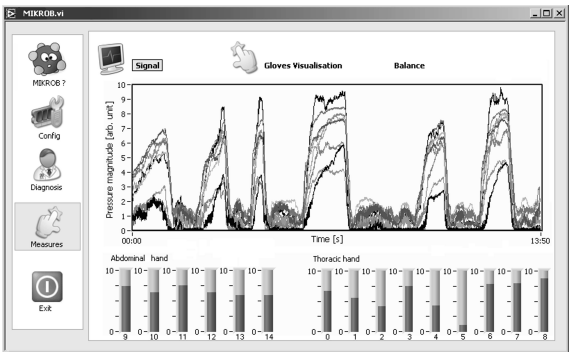

Figure 4: Monitoring screen.

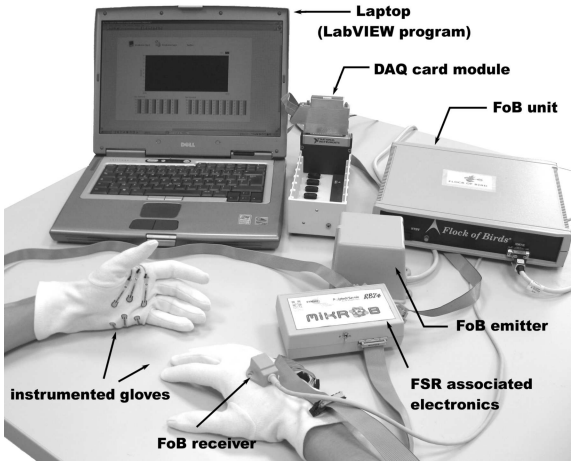

Figure 5: Whole measuring system.

Simultaneously to force measurements, the trajectories of the hands are recorded with the FoB sensors located on the gloves. The whole system is presented Figure 5.

3.3 File Output

For each trial the program saves the data in a *.txt file. Spreadsheet file format compliant for common software such as Microsoft Excel or OpenOffice Calc was not chosen because they have a limitation of 65536 rows. The file contains the values of the output data of the fifteen sensors versus the time, for each measurement. It also contains the acquisition parameters: measurement rate, trial start and end times. The average size of the result files is of 10 MB which is acceptable in comparison with actual disk space capabilities.

4 FIRST RESULTS

4.1 Calibration System Validation

Calibration of FSR devices before use is of inevitable occurrence. Calibration curves supplied by the manufacturer are carried out with the sensor placed between two rigid materials. However, it is worthwhile noting that the response of this kind of sensor depends on the nature and shape of the contact. Consequently, FSR sensors should be calibrated in the same situation as the use. Former studies focused on measuring forces developed by the human hand when gripping objects (Nikonovas et al., 2004). In this work, Nikonovas used FSR sensors between human hand tissues and stiff surface, nevertheless calibration was not made in the conditions of their use. Besides, Castro (Castro and CliquetJr, 1997) placed small rigid

plates over and under the active area of the sensor to improve its behaviour during use, but for calibration the force was applied thanks to a small sphere. Regarding our application, the contact is between human hand tissues and human body tissues. Pertaining to the work of Castro, in order to enhance FSR response, we thought to insert plates on both sides of the sensors, but we can't mount them on rigid substrates since they could injure the infant during the CPT act. For use and calibration, we also tried to insert the sensors between different flexible substrates such as thin layers of polymer materials or silicones but it had no relevant effect on sensor response.

A specific workbench is implemented to calibrate the sensors in order to be in a situation closest as possible as between hand covered by cotton material and body (Figure 6). A plate of metal covered with a polymer layer realises the distribution of the applied force. We made comparative calibration to highlight the impact of the substrate. Dead loads in range of 0.1 kg to 1 kg were applied to the active surface of each sensor. With the same applied force but with different implementations, the sensor's response is strongly different. Figure 7 shows the calibration curves for the same sensor; alone (a) and implemented on the glove (b). In the end, keeping in mind that the stiffness of the hands of two physiotherapists may be very different, we decided to calibrate the sensor with identical impementation for all measurements. So, we use the static calibration curve obtained with the bench described before, the FSR being implemented on the cotton glove and covered with a medical glove.

However, the calibration gives the part-to-part repeatability but is not able to provide the absolute force magnitude during the measurement on newborn babies.

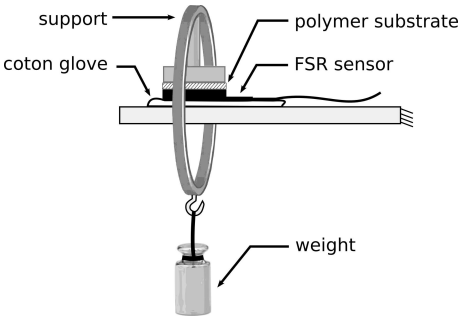

Figure 6: Calibration System.

4.2 Measurement Results

The measurement with the whole system was performed in a physiotherapist consulting room from January to March 2007. The study was managed taking into account a population of 25 infants aged from 5 to 7 months suffering from bronchiolitis. This random trial was performed by the same expert physiotherapist, J.C. Jeulin.

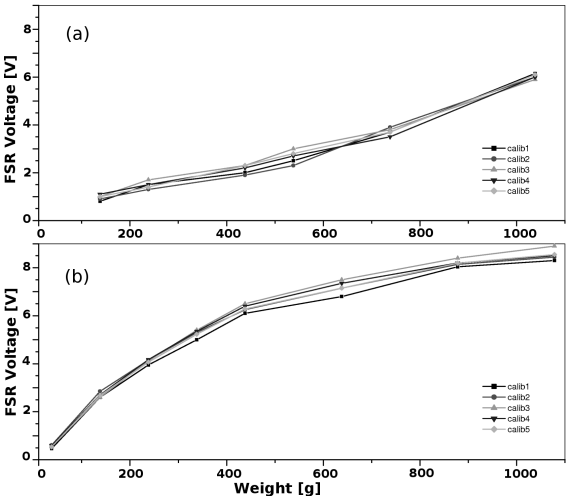

Figure 7: FSR calibration curves: (a) alone; (b) implemented on the glove.

Figure 8(a) shows the sensors responses acquired on the thoracic hand glove during two compressions on the chest of a 5-month-old infant, for a sequence of the gesture called "fast IEF". The FSR responses evolve synchronously. They are repeatable since the rising time of the applied pressure and the magnitude of the forces remain constant for each sensor in each compression. The displacement of the thoracic hand in the direction perpendicular to the table plane during one compression of a "fast IEF" is reported on Figure 8(b). These first results are consistent with the gesture qualitatively described as the referent one by the expert.

5 CONCLUSIONS

The measuring system, designed and created to record hands applied pressures and displacement during the act, has been validated. The choice of the sensors and their implementation respect the medical environment. Specific calibration according to the use has been achieved. Low cost portable hardware is used to acquire sensors signals. Custom optimized software has been developed with LabVIEW to process and display the data as in real time. The first results obtained are reproducible and consistent with the expert sensations. Our ongoing work in the framework

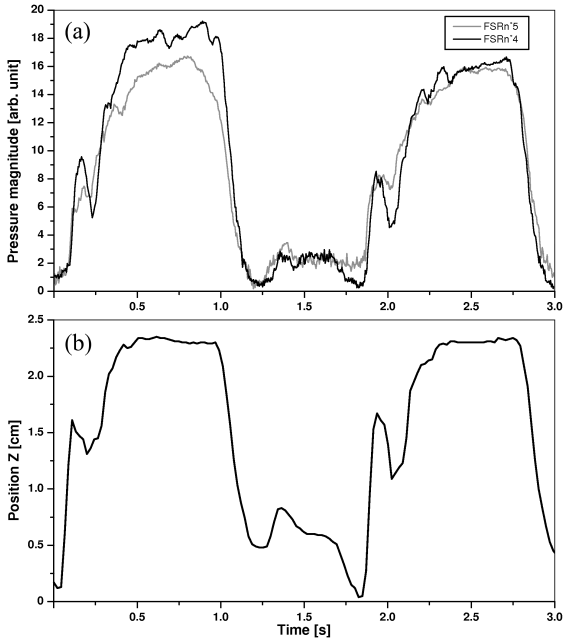

Figure 8: (a) Pressure (two FSR) and (b) displacement (FoB) responses of sensors on the thoracic glove.

of CPT enables quantitative investigations of the gesture.

ACKNOWLEDGEMENTS

Authors thank Laboratory Ampère (Lyon, France), for lending us one Flock of Birds device, and the Assemblée des Pays de Savoie for funding this project.

REFERENCES

ANAES (2000). Consensus conference of management of bronchiolitis in infant. *Arch.Ped2001*.

Castro, M. and CliquetJr, A. (1997). A low-cost instrumented glove for monitoring forces during object manipulation. *IEEE Trans. Rehab. Eng.*, 5(2):140–147.

Châlons, J. (2001). Acquisition and processing, daq-sc-01-jmc-a40119. *SAPHIR*. www.saphir.fr.

Davidson, K. (2002). Airway clearance strategies for the pediatric patient. *Respir Care*, 47(7):823–830.

Fausser, C., Breheret, V., and Lopes, D. (2002). Augmentation du flux expiratoire (afe) et tolérance. *KS*, (428):21.

Interlink (2004). Force sensing resistor integration guide. *Interlink Electronics*.

LaScalza, S., Arico, J., and Hughes, R. (2003). Effect of metal and sampling rate on accuracy of flock of birds electromagnetic tracking system. *Journal of Biomechanics*, 36(1):141–144.

Maréchal, L., Lottin, J., Barthod, C., Gautier, G., Goujon, L., and Jeulin, J. (2007). Instrumented gloves for gesture characterization during chest physiotherapy act on babies. In *8th International workshop on Research and Education in Mechatronics*, Tallin, pages 171–176.

Morris, S., LaStayo, P., Dibble, L., Musselman, J., and Raghavendra, S. K. D. (2006). Development of a quantitative in-shoe measurement system for assessing balance: sixteen-sensor insoles. In *28th IEEE EMBS annual International Conference*, New York, pages 6041–6044.

Nikonovas, A., Harrison, A., Hoult, S., and Sammut, D. (2004). The application of force-sensing resistor sensors for measuring forces developed by the human hand. *Proc Inst Mech Eng*, 218(2):121–126.

Postiaux, G., Dubois, R., Marchand, E., Denay, M., Jacquy, J., and Mangiaracina, M. (2006). Chest physiotherapy in infant bronchiolitis: a new approach - ncpt including elpr-expiration lente prolongée and tp-toux provoquée. *Kinesither. Rev.*, (55):35–41.

AUGMENTED COMANIPULATION IN ROBOTIC SURGERY

B. Cagneau, D. Bellot, G. Morel,
Institut des Systèmes Intelligents et Robotique, 18 route du Panorama, 92265 Fontenay Aux Roses, France
{*cagneau,bellot,morel*}*@robot.jussieu.fr*

N. Zemiti
TIMC-IMAG Laboratory, 38706 La Tronche Cedex France
nabil.zemiti@imag.fr

G. D'Agostino
Università Federico II di Napoli, Facoltà di Ingegneria dell'Automazione, Corso Umberto I, 80138 Napoli, Italy
gianluca82@gmail.com

Keywords: Force control, robotic surgery, cobotic, augmented comanipulation.

Abstract: This paper presents a control scheme for augmented comanipulation with force feedback in robotic surgery. This approach aims at increasing the surgeon's dexterity. The surgeon manipulates a handle mounted on the robot which manipulates the instrument. The control law ensures that the instrument applies on the organ the same forces that the surgeon applies on the handle but decreased by a scale factor. As a consequence, the robotic device provides the surgeon with an augmented sensation of the interaction forces between the instrument and the organ. The proposed control law does not require any knowledge of the environment. This control scheme is proven stable thanks to a passivity study. Indeed, passivity analysis is a useful tool for the stability analysis of a robot interacting with an unknown environment. Experimental results are presented on a robot dedicated to minimally invasive surgery.

1 INTRODUCTION

In the context of robotic surgery, the surgeon and the medical staff have to interact with the robot. Depending on the surgical task, the degree of cooperation can be really different. Simple tasks may be realized by the robot, in an autonomous way, under the surgeon's supervision. For example, the surgeon defines the desired positions via an interface and the robot moves to these positions. However more complex tasks require the surgeon's judgment and, thus, cannot be performed autonomously by the robot. These tasks require that the robot works in cooperation with the surgeon. The surgeon's skills are thus improved as the robot increases his dexterity. To do so, one of the possibilities is robot's force control. For instance, in minimally invasive surgery, a robotic device could be used in order to display manipulation forces back to the surgeon. Indeed, since the instruments are manipulated through a trocar and because of the friction in the trocar, the surgeon looses the sensation of the interaction forces between the instrument and the organ and his dexterity is thus reduced. An other application of force control that could increase the dexterity of the surgeon is force scaling. Indeed, for precise manipulation tasks, a robotic device could provide the surgeon with an augmented sensation of the interaction forces between the instrument and the organ.
Comanipulation appears to be a good solution to overcome these problems. Comanipulation is a direct interaction between the surgeon and the robot: the instrument is manipulated simultaneously by the surgeon and by the robot. The main difference between comanipulation and teleoperation is that no master arm is needed to impose displacements to the robot. So the complexity and the cost of a comanipulation system may be lower since it involves only one mechanical system. Moreover, the use of a comanipulation system may be more intuitive for the human operator.
Different approaches have been studied concerning the comanipulation. Some systems are able to impose virtual constraints to the surgeon's gesture which restrain the tool into a delimited area of the task-space

and forbid the access to critical zones.

For example, in (Schneider et al., 2000), the system *PADyC* has been presented. The clinical results obtained with this system concern pericardial puncture. It consists to remove pathological liquid from the pericardium using a needle. *PADyC* can be used under different control modes corresponding to the degree of autonomy the surgeon wants. The robot is controlled with a velocity loop and it imposes constraints on the surgeon to prevent damages on the surface of the heart. These constraints are computed with respect to the relative position between the needle and the percutaneous access. Indeed, a model of the operation's area is created during a pre-operative phase. This model is then used to derive the constraints field. Here no force control is used to perform the operation.

In (Jakopec et al., 2003), the *Acrobot* system is used to assist the surgeon during an operation of knee replacement. The main feature of this system is to impose virtual constraints on the surgeon when he/she cooperates with the robot. When the task has been defined with the planning software, the manipulator is able to move freely the robot to the operations area. If the surgeon moves the tool outside the defined path, the robot applies forces on the user to modify the current trajectory. It has been clinically proven that the preparation of bones surfaces are more accurate comparing to a classical operation. Once again, no force control is performed with this system.

Moreover, some systems can exploit a measure of forces. Therefore, there is no need to use models of contacts to obtain the measure of distal forces. It is also possible to derive constraints which are directly based on the forces applied by the surgeon on the organs.

In (Kazanzides et al., 1992), a force controller is used so that the surgeon can guide the robot. The surgical tool is attached below a force sensor mounted on the robot's wrist. The force controller uses the measured forces to provide the reference to an inner velocity control loop. When the desired force is null, any applied force on the instrument causes the robot to move in the direction of this force. So, the surgeon can guide the robot by holding the tool.

In the same manner, the *Surgicobot* system (Kochan, 2004) allows the surgeon and the robot to manipulate the same drilling instrument for maxillofacial interventions. The surgeon can freely move the instrument except in some predefined space where the robot generates restrictive forces in order to prevent the surgeon from moving the instrument too close to vital nerves.

In (Taylor et al., 1999), (Kumar et al., 2000) and (Roy et al., 2002) augmented comanipulation approaches are presented: the surgeon holds a handle mounted on the robot and the robot manipulates the instrument in a way such as it exerts on the organ the same force that the surgeon applies on the handle, but scaled-down. Three different control laws using an inner position/velocity control loop are compared in (Roy et al., 2002). The best results are obtained with an adaptive control law involving the estimation of the environment's compliance. However, when the contact with the environment is lost, the estimation becomes problematic. Another disadvantage of this control law is that it requires differentiation of the force applied by the surgeon on the handle which is a noisy signal.

Even if benefits presented in the above references are important (e.g. gesture's accuracy or the increase of system's safety), none of these systems allow the surgeon to feel an amplified version of the distal forces acting between the tool and the organ.

In this paper, we present a control scheme for augmented comanipulation with force feedback. The main advantages of this control law is that it does not require any knowledge of the environment nor differentiation of a noisy signal. This approach is an extension of previous works (Zemiti et al., 2006) realized in our laboratory.

The first part of this paper is devoted to the proposed control law for augmented comanipulation. This control scheme is proven stable thanks to a passivity study in the second part. Experimental results with a robot dedicated to minimally invasive surgery are presented in the last part.

2 AUGMENTED COMANIPULATION

2.1 Principle of the Approach

We present, hereafter, a robotic device in order to assist the surgeon for accurate manipulation tasks requiring human judgment and involving small interaction forces between the surgical tool and the organ. Therefore, the proposed device allows an augmented comanipulation. It is a comanipulation system because the surgical instrument is held simultaneously both by the surgeon and by the robot. We call it augmented because the robot is controlled in such a way that the surgeon is provided with an amplified sensation of the interaction forces between the instrument and the organ. As a consequence, the instrument applies on the organ the same forces that the surgeon would apply in a transparent mode but decreased by a

scale factor. This device can also filter the surgeon's tremor in order to increase the accuracy of the task. This approach supposes that the reference forces provided by the surgeon and the interaction forces between the instrument and the organ may be measured separately. Therefore a handle equipped with a force sensor (force sensor 2) is mounted on the instrument (see figure 1). The surgeon manipulates this handle and the force sensor 2 measures the forces applied by the surgeon on the instrument at point O_2. The force sensor 1 measures the forces applied by the organ on the instrument at point O_1. The data provided

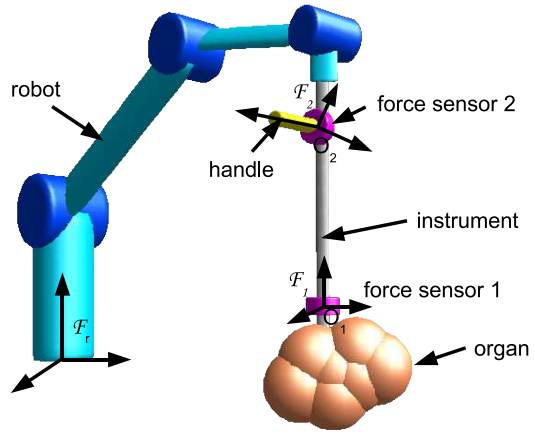

Figure 1: Setup for augmented comanipulation.

by the force sensor number i are wrenches applied on point O_i and expressed in the basis of frame $\mathcal{F}_i$ linked to the sensor. In order to be compared these wrenches have to be expressed in the same point and in the same basis. As the transformations between the basis linked to frames $\mathcal{F}_i$ and the basis linked to the fixed robot base frame $\mathcal{F}_r$ are supposed to be known, we choose to express the wrenches in the basis linked to the frame $\mathcal{F}_r$. So, from the data provided by the force sensor 1, we can compute $-w_e$ the wrench applied by the organ on the instrument at point O_1 and expressed in frame $\mathcal{F}_r$. From the data provided by the force sensor 2, we can compute $-w_s$ the wrench applied by the surgeon on the instrument at point O_2 and expressed in frame $\mathcal{F}_r$. Note that w_e and w_s are respectively the wrench applied by the instrument on the organ at point O_1 and the wrench applied by the instrument on the surgeon at point O_2. Assuming that the transformation between the frame $\mathcal{F}_1$ and the frame $\mathcal{F}_2$ is known, we can compute the wrench $-w_u$ applied by the surgeon on the instrument at point O_1 in $\mathcal{F}_r$: $-w_u = \mathbf{T_{12}}(-w_s)$ with

$$\mathbf{T_{12}} = \begin{bmatrix} \mathbf{I_3} & \mathbf{0_3} \\ -[O_2O_1]_\times & \mathbf{I_3} \end{bmatrix}$$

where $[O_2O_1]_\times$ denotes the skew symmetric matrix associated with the vector from O_2 to O_1 expressed in the basis of frame $\mathcal{F}_r$. However, in future work, it will be interesting to compute this transformation with a calibration process. In the Section 4, we assume that the mechanical design is precise enough to have a good estimation of this transformation.

With these notations, as detailed in subsection 2.3, the aim of the proposed approach is to control the robot such that $w_u = -\frac{1}{\beta} w_e$ where $\beta \in]0;1]$ i.e. the surgeon feels the forces applied by the organ on the instrument, $-w_e$, amplified by a scale factor $\frac{1}{\beta} > 1$. The proposed control scheme is presented in the following subsection.

2.2 Proposed Control Scheme

The robot dynamics is modeled by the general form:

$$\mathbf{M}(q)\ddot{q} + C(q,\dot{q})\dot{q} + \Gamma_v\dot{q} + G_g(q) = \tau - \tau_e - \tau_u \quad (1)$$

where $q \in \mathbb{R}^n$ denotes the joint positions, $\mathbf{M}(q)$ is the positive definite symmetric inertia matrix, $C(q,\dot{q})\dot{q}$ is a vector grouping the Coriolis and centrifugal joint torques, $\Gamma_v\dot{q}$ is a vector grouping the dissipative joint torques, $G_g(q)$ is a vector grouping the gravity joint torques, τ is the command vector for joint torques. $-\tau_e$ and $-\tau_u$ are the joint torques corresponding respectively to $-w_e$ and $-w_u$ i.e. $-\tau_e = \mathbf{J^t}(q)(-w_e)$ and $-\tau_u = \mathbf{J^t}(q)(-w_u)$ where $\mathbf{J}(q)$ is the Jacobian matrix of the robot at point O_1, expressed in the basis of $\mathcal{F}_r$.

At the lowest level of the controller, a proportional velocity feedback is used in order to partially linearize the robot dynamics:

$$\tau = -\mathbf{B}\dot{q} + \widehat{G_g}(q) + \widehat{C}(q,\dot{q})\dot{q} + \tau_c \quad (2)$$

where $\mathbf{B}$ is a symmetric positive definite matrix of feedback gains, τ_c is the new command vector for the joint torques, $\widehat{G_g}(q)$ and $\widehat{C}(q,\dot{q})\dot{q}$ are estimated values of $G_g(q)$ and $C(q,\dot{q})\dot{q}$. Therefore, the model (1) becomes:

$$\mathbf{M}(q)\ddot{q} + \mathbf{B}\dot{q} = \tau_c - \tau_e - \tau_u \quad (3)$$

The proposed control scheme is presented on figure 2.

In this figure the Jacobian matrix $\mathbf{J}(q)$ is noted $\mathbf{J}$. This control scheme introduces notations defined as follow:

- $C_\tau(s)$ is a Proportional-Integral torque compensator at the joint level such that:

$$\mathbf{C}_\tau(s) = \mathbf{K_p} + \frac{\mathbf{K_i}}{s} \quad (4)$$

where $\mathbf{K_p} \in \mathbb{R}^{n\times n}$ and $\mathbf{K_i} \in \mathbb{R}^{n\times n}$ are symmetric, positive definite matrices.

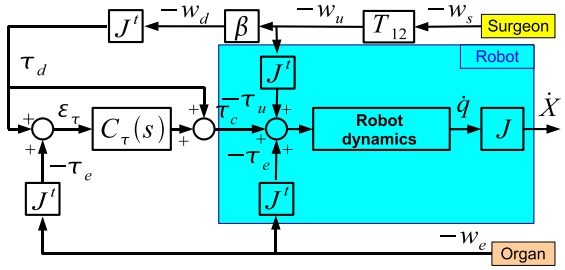

Figure 2: Augmented Comanipulation force control scheme in joint space.

- $\dot{X}$ is the 6-component vector grouping the coordinates of the rotational and linear velocity of the instrument at point O_1 with respect to frame $\mathcal{F}_r$, expressed in the basis of $\mathcal{F}_r$.

In the sequel the following assumption will be used :

Assumption 1 *The matrix* $\mathbf{J}(q)$ *is of full rank n*

This assumption means that the robot is not in a singular configuration.

2.3 Equilibrium

The stability of the control scheme 2 will be proved in the following section. So, assuming that this control scheme is stable, as the controller $\mathbf{C}_\tau(s)$ involves an integral term, the torque error ε_τ will be null at the equilibrium. So, at the equilibrium:

$$\tau_d - \tau_e = 0 \tag{5}$$

As the stable low-pass filter $G(s)$ has a steady-state gain equal to 1, at the equilibrium, $\tau_d = \mathbf{J}(q)^t \beta(-w_u)$. Thus (5) leads to :

$$\mathbf{J}(q)^t \left((-w_u) + \frac{1}{\beta}(-w_e) \right) = 0 \tag{6}$$

If $n = 6$ i.e. if we consider a 6 joints robot, the matrix $\mathbf{J}(q)$ is square. Moreover, according to assumption (1), this matrix is of full rank. Therefore, it can be deduced from equation (6) that:

$$w_u = \frac{1}{\beta}(-w_e) \tag{7}$$

Suppose that we choose $\beta = 1$. Then, equation (7) can be written:

$$w_u = (-w_e) \tag{8}$$

It means the wrench w_s sensed by the surgeon at point O_2 is such that its expression at point O_1, w_u, is equal to the wrench $-w_e$ applied by the organ on the instrument expressed at point O_1. Thus the surgeon manipulates the instrument in a transparent way i.e. the surgeon senses the wrench w_s as if he/she were manipulating a zero mass instrument without any friction.
Similarly, if $\beta \in]0;1[$, equation (7) means that the wrench w_s sensed by the surgeon is an amplified version, by the scale factor $\frac{1}{\beta} > 1$, of the wrench that he would sense in a transparent manipulation. Let's remark that (7) can be written $w_e = \beta(-w_u)$. It means that the wrench applied by the instrument on the organ at point O_1 is the wrench applied by the surgeon at the same point, reduced by the scale factor β.

If $n < 6$, $\mathbf{J}^t(q) \in \mathbb{R}^{n\times 6}$ is not square. Thus it cannot be deduced from (6) that the wrench error $\varepsilon_w = (-w_u) + \frac{1}{\beta}(-w_e)$ is zero. The wrench error ε_w is not necessarily zero but belongs to the null space of $\mathbf{J}^t(q)$. An equilibrium is obtained between w_u and $\frac{1}{\beta}(-w_e)$.

3 PASSIVITY

In the proposed approach, the robot interacts with its environment. The stability of the control loop depends not only on the robot dynamics but also on the environment dynamics. However we cannot assume for a known model for the environment. Therefore, a useful tool for the stability analysis of the proposed control loop is passivity analysis since this study does not require any environments model. Thus, whatever could be the contacts (robot-organ / robot-surgeon), the passivity analysis ensures that the system remains stable. The principle of a passivity study is presented in the following subsection

3.1 Principle

Let consider an LTI system with an input u, an output y, such that $y = \mathbf{T}(s)u$ with $\mathbf{T}(s)$ a real rational transfer matrix. This system is passive if and only if $\mathbf{T}(s)$ is positive real. In turn, positive realness can be checked by the following property (Anderson and Vongpanitlerd, 1973):

Property 1 *Let* $s_k = \sigma_k + j\omega_k$, $k \in \{1..m\}$, *denote the m poles of all the elements* $T_{ij}(s)$ *of* $\mathbf{T}(s)$, *and let* $j\omega_l$, $l \in \{1..p\}$, *denote the* $p \leq m$ *pure imaginary poles of all the elements* $T_{ij}(s)$ *of* $\mathbf{T}(s)$. *The transfer* $\mathbf{T}(s)$ *is Positive Real if, and only if:*

1. $\forall k \in \{1..m\}, \sigma_k < 0$;
2. $\forall l \in \{1..p\}$, $j\omega_l$ *is of multiplicity 1, and the associated residue matrix* $\mathbf{K}_l$ *is hermitian, positive*

semidefinite (PSD). The matrix $\mathbf{K}_l$ *can be computed as:*

$$\mathbf{K}_l = \lim_{s \to j\omega_l} (s - j\omega_l)\mathbf{T}(s) \text{ , if } \omega_l \text{ is finite}$$
$$\text{and:} \quad \mathbf{K}_l = \lim_{s \to \infty} \frac{\mathbf{T}(s)}{s} \text{ , if } \omega_l \text{ is infinite}$$

Note that a zero of $T_{ij}(s)$ *is considered as a pole at the infinity.*

3. $\mathbf{T}^t(-j\omega) + \mathbf{T}(j\omega) = \mathbf{T}^*(j\omega) + \mathbf{T}(j\omega)$ *is PSD, for any* $\omega \in \mathbb{R} - \{\omega_l, l \in \{1..p\}\}$. ■

Let, now, consider an LTI system with two different inputs u_1 and u_2 provided by two different environments, and assume that this system is described by: $y = \mathbf{T_1}(s)u_1 + \mathbf{T_2}(s)u_2$. This system is passive if and only if $\mathbf{T_1}(s)$ is positive real and $\mathbf{T_2}(s)$ is positive real.

3.2 Passivity of the Modified Force Control Scheme

3.2.1 Modeling, Linearized Robot Dynamics

The robot controlled by the control scheme depicted on figure 2 is a system whose output is $\dot{X}$. This system has two inputs $-w_u$ and $-w_e$ provided by two different environments, respectively the surgeon and the organ. So, in order to study the passivity of this system we first have to compute the transfer matrix $\mathbf{Y_u}(s)$ between $-w_u$ and $\dot{X}$ and the transfer matrix $\mathbf{Y_e}(s)$ between $-w_e$ and $\dot{X}$. This computation supposes that the system is linear. Therefore, in order to study the passivity of the proposed control scheme, we linearize the robot dynamics (3) by assuming that the robot evolves in a neighborhood of a given joint configuration q_0 so that we can set $\mathbf{M} = \mathbf{M}(q_0)$ constant. The resulting linearized model writes:

$$\dot{q} = \mathbf{Y_r}(s)(\tau_c - \tau_u - \tau_e) \quad \text{with} \quad \mathbf{Y_r}(s) = (\mathbf{M}s + \mathbf{B})^{-1} \tag{9}$$

where s is the Laplace complex variable. Moreover, under the assumption that the robot evolves in a neighborhood of a given joint configuration q_0, we can set $\mathbf{J} = \mathbf{J}(q_0)$ constant. Then, we get the following model:

$$\dot{X} = \mathbf{Y_u}(s)\,(-w_u) + \mathbf{Y_e}(s)\,(-w_e) \tag{10}$$

where:

$$\begin{cases} \mathbf{Y_u}(s) &= \mathbf{J}\mathbf{Y_r}(s)\,[\mathbf{I_n} + \beta\,(\mathbf{C}_\tau(s) + \mathbf{I_n})]\,\mathbf{J^t} \\ \mathbf{Y_e}(s) &= \mathbf{J}\mathbf{Y_r}(s)\,[\mathbf{I_n} + \mathbf{C}_\tau(s)]\,\mathbf{J^t} \end{cases}$$

3.2.2 Passivity Study

The system (10) is passive if and only if the matrices $\mathbf{Y_u}(s)$ and $\mathbf{Y_e}(s)$ are positive real. As $\mathbf{J}$ is supposed to be of full rank (Assumption 1), this condition is equivalent to the positive realness of the matrices $\mathbf{Y_{u,2}}$ and $\mathbf{Y_{e,2}}$ defined as follow:

$$\begin{cases} \mathbf{Y_{u,2}} &= \mathbf{Y_r}(s)\,[\mathbf{I_n} + \beta\,(\mathbf{C}_\tau(s) + \mathbf{I_n})] \\ \mathbf{Y_{e,2}} &= \mathbf{Y_r}(s)\,[\mathbf{I_n} + \mathbf{C}_\tau(s)] \end{cases} \tag{11}$$

Equations (11), (9), and (4) lead to :

$$\begin{cases} \mathbf{Y_{u,2}} = (\mathbf{M}s + \mathbf{B})^{-1}\left[\mathbf{I_n} + \beta\mathbf{K'_p} + \frac{\beta\mathbf{K_i}}{s}\right] \\ \mathbf{Y_{e,2}} = (\mathbf{M}s + \mathbf{B})^{-1}\left[\mathbf{I_n} + \mathbf{K_p} + \frac{\mathbf{K_i}}{s}\right] \end{cases} \tag{12}$$

where $\mathbf{K'_p} = \mathbf{K_p} + \mathbf{I_n}$.

We first derive conditions ensuring the positive realness of $\mathbf{Y_{u,2}}(s)$. The poles of $\mathbf{Y_{u,2}}(s)$ are $s_1 = 0$ and the poles of $\mathbf{Y_r}(s)$. The poles associated to $\mathbf{Y_r}(s)$ are the solutions of $\det(\mathbf{M}s + \mathbf{B}) = 0$ i.e. the eigenvalues of $-\mathbf{M}^{-1}\mathbf{B}$. As far as $\mathbf{M}$ and $\mathbf{B}$ are symmetric positive definite matrices, the eigenvalues of $-\mathbf{M}^{-1}\mathbf{B}$ are negative real.

In order to check the second condition of property 1, we compute the residue $\mathbf{K_1}$ associated to pole $s_1 = 0$. We get:

$$\mathbf{K_1} = \lim_{s \to s_1} s\mathbf{Y_{u,2}} = \beta\mathbf{B}^{-1}\mathbf{K_i}$$

As $\beta > 0$, we deduce the following condition for the passivity of the control scheme:

$$\mathbf{B}^{-1}\mathbf{K_i} \geq 0 \tag{13}$$

The third condition of property 1 consists in checking, for any $\omega \in \mathbb{R} - \{0\}$, the positive semidefiniteness of the matrix$\mathbf{H_1}(j\omega)$ defined as follow:

$$\begin{aligned} \mathbf{H_1}(j\omega) &= \mathbf{Y_{u,2}}(j\omega) + \mathbf{Y_{u,2}}^t(-j\omega) \\ &= (j\omega\mathbf{M} + \mathbf{B})^{-1}\left[\mathbf{I_n} + \beta\mathbf{K'_p} + \frac{\beta\mathbf{K_i}}{j\omega}\right] \\ &+ \left[\mathbf{I_n} + \beta\mathbf{K'_p} + \frac{\beta\mathbf{K_i}}{-j\omega}\right](-j\omega\mathbf{M} + \mathbf{B})^{-1} \end{aligned} \tag{14}$$

because $\mathbf{K'_p}$, $\mathbf{K_i}$, $\mathbf{M}$ and $\mathbf{B}$ are symmetric.

Positive semidefiniteness of $\mathbf{H_1}(j\omega)$ is equivalent to positive semidefiniteness of $\mathbf{H_2}(j\omega)$ defined as follow:

$$\begin{aligned} \mathbf{H_2}(j\omega) &= \tfrac{1}{\beta}(j\omega\mathbf{M} + \mathbf{B})\mathbf{H_1}(j\omega)(-j\omega\mathbf{M} + \mathbf{B}) \\ &= \left[\tfrac{1}{\beta}\mathbf{I_n} + \mathbf{K'_p} + \frac{\mathbf{K_i}}{j\omega}\right](-j\omega\mathbf{M} + \mathbf{B}) \\ &+ (j\omega\mathbf{M} + \mathbf{B})\left[\tfrac{1}{\beta}\mathbf{I_n} + \mathbf{K'_p} + \frac{\mathbf{K_i}}{-j\omega}\right] \end{aligned} \tag{15}$$

We get:

$$\mathbf{H_2}(j\omega) = \mathbf{R_1} + \mathbf{R_2} + j\omega\,\mathbf{Im_1} + \frac{j}{\omega}\mathbf{Im_2} \tag{16}$$

where:

$$\begin{aligned}\mathbf{R_1} &= (2/\beta)\mathbf{B}\\ \mathbf{R_2} &= \mathbf{K'_p B} + \mathbf{B K'_p} - (\mathbf{K_i M} + \mathbf{M K_i})\\ \mathbf{Im_1} &= \mathbf{M K'_p} - \mathbf{K'_p M}\\ \mathbf{Im_2} &= \mathbf{K_i B} - \mathbf{B K_i}\end{aligned}$$

The hermitian matrix $\mathbf{H_2}(j\omega)$ must be PSD in order to ensure passivity. Thus its real part has to be PSD and its imaginary part has to be null. Therefore, the following conditions have to be satisfied for any $\omega \in \mathbb{R} - \{0\}$:

$$\mathbf{R_1} + \mathbf{R_2} \geq 0 \tag{17}$$

$$\omega \mathbf{Im_1} + \frac{1}{\omega}\mathbf{Im_2} = 0 \tag{18}$$

Thus, condition (18) is equivalent to:

$$\begin{cases} \mathbf{R_1} + \mathbf{R_2} \geq 0 \\ \mathbf{Im_1} = 0 \\ \mathbf{Im_2} = 0 \end{cases} \tag{19}$$

To summarize, the matrix $\mathbf{Y_{u,2}}(s)$ and thus $\mathbf{Y_u}(s)$ is positive real if and only if the following conditions are satisfied:

$$\begin{cases} \mathbf{B^{-1} K_i} \geq 0 \\ \mathbf{Im_1} = 0 \\ \mathbf{Im_2} = 0 \\ \mathbf{R_1} + \mathbf{R_2} \geq 0 \end{cases} \tag{20}$$

As far as positive realness of $\mathbf{Y_{e,2}}(s)$ is concerned, with a similar reasoning we deduce that the first and the second condition of property 1 are satisfied if and only if $\mathbf{M^{-1} B} > 0$ and $\mathbf{B^{-1} K_i} \geq 0$. It can be noticed in equations (12) that the expression of $\mathbf{Y_{e,2}}(s)$ is similar to the expression of $\mathbf{Y_{u,2}}(s)$ when $\beta = 1$ and $\mathbf{K'_p}$ is replaced by $\mathbf{K_p}$. Therefore, we deduce from equations (19) and (17) that the third condition ensuring the positive realness of $\mathbf{Y_{e,2}}(s)$ is satisfied if and only if:

$$\begin{cases} \mathbf{M K_p} - \mathbf{K_p M} = 0 \\ \mathbf{K_i B} - \mathbf{B K_i} = 0 \\ \mathbf{B} + \mathbf{K_p B} - \mathbf{K_i M} \geq 0 \end{cases} \tag{21}$$

The equations (20) and (21) lead to the following conditions for the passivity of the proposed control scheme:

$$\begin{cases} \mathbf{B^{-1} K_i} \geq 0 \\ \mathbf{M K_p} - \mathbf{K_p M} = 0 \\ \mathbf{K_i B} - \mathbf{B K_i} = 0 \\ (\frac{1}{\beta}\mathbf{I_n} + \mathbf{K'_p})\mathbf{B} - \mathbf{K_i M} \geq 0 \end{cases} \tag{22}$$

with $\mathbf{K'_p} = \mathbf{K_p} + \mathbf{I_n}$.

4 EXPERIMENTS

The aim of these experiments is to show that it is possible to provide force feedback to the surgeon thanks to proposed control scheme. Furthermore, for different values of the gain β, we will verify that the system remains stable. Experimental setup will be briefly described and benefits of augmented comanipulation will be evaluated experimentally.
Note that, in the rest of the paper, the used joint torque compensator gains and the values of $\mathbf{B}$ and β were chosen in such a way that the conditions given in 22 are verified.

4.1 Experimental Setup

The robot MC^2E (French acronym for *compact manipulator for endoscopic surgery*) is a Kinematically Defective Manipulator (KDM) which means that it has fewer joints than the dimension of the space in which its end-effector evolves. It is specially suited for minimally invasive robotic surgery applications(Zemiti et al., 2007). With $n = 4$ joints and a spherical structure, this robot provides 4 degrees of freedom (DOFs) at the instrument tip.

The Figure 3 shows how the mechanical constraint

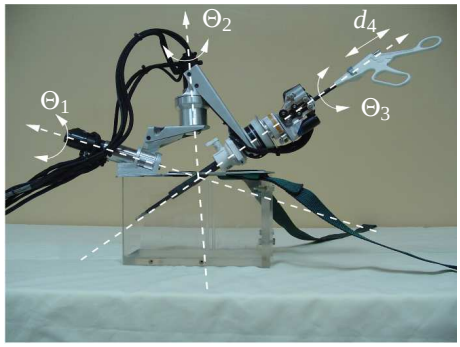

Figure 3: MC^2E can comanipulate an instrument with a surgeon, and measures wrenches that are applied either by the surgeon, or at the instrument tip.

is created. The lower part of the robot is dedicated to the orientation of the instruments. The upper part allows translation and rotation of the instrument along its own axis.

Since the 4 axis coincide, there is a fulcrum point which allows the insertion of the trocar into the patient's body. This mechanical structure is clearly adapted to Mini Invasive Surgery. Traumatisms are reduced because translations through the fulcrum point are not allowed.

Apart from its compactness, the main feature of this robot is that it offers a possibility for force

measurement in MIS. Namely, MC^2E can measure the distal organ-instrument interaction with a 6-axis force-torque sensor placed outside the patient. Thus, it is subject to much less sterilization constraints. Remarkably, due to the special mounting of the force sensor, these measurements are not affected by the disturbance forces and torques arising from the interaction between the trocar and the instrument.
It is important to mention that the control scheme that we have detailed in Section 2 can be used in other fields of interest and not only in laparoscopic surgery. For example, it is possible to improve surgeon accuracy during otologic surgery. The forces applied during such kinds of interventions are very low. Therefore, it should be useful to provide an amplified version of these forces thanks to force feedback.
The new control scheme presented in section 2 indicates that the robot interacts with two different environments (the organ and the surgeon). This configu-

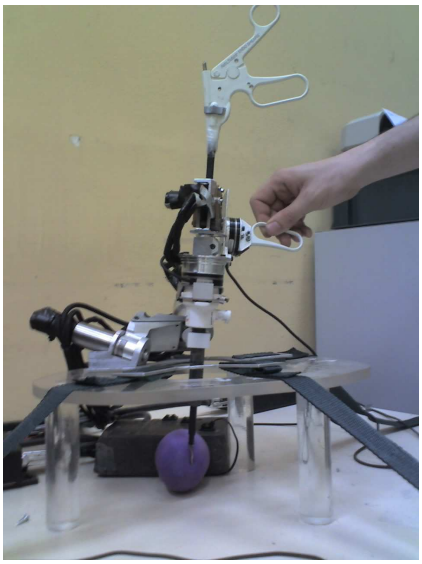

Figure 4: Experimental Setup.

ration is shown on figure 4. It needs a second force sensor to measure forces between the robot and the surgeon. Therefore to measure forces applied by the surgeon, a second force sensor has been added on the robot. Due to difficulties to fix it directly on the handle, it has been deported on the second axis of MC^2E. This particular disposition was the quickest way to provide force feedback to the manipulator. However, the same disposition is not adapted to transmit forces along instrument's axis. In order to overcome this problem, next step will be to modify existing experimental setup to exploit each of the robot's DOF.

4.2 Experimental Results

The figure 5 shows how the gain β has been modified during the experiment. $\beta = 1$ is a particular value

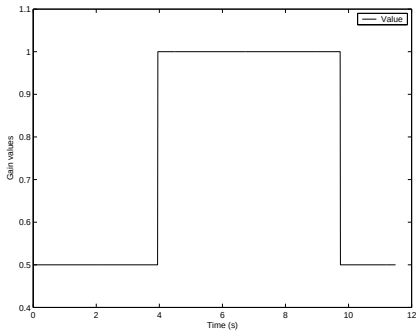

Figure 5: Gain values vs. time.

for which torques measured on the organ are equal to torques applied by the manipulator. When setting $\beta = 0.5$, torques applied on the organ should be decreased by a factor 2.
The figure 6 depicts torque measurements. It allows to compare torques applied on the organ, torques provided to the controller and torques applied on the manipulator. This result demonstrates that the proposed

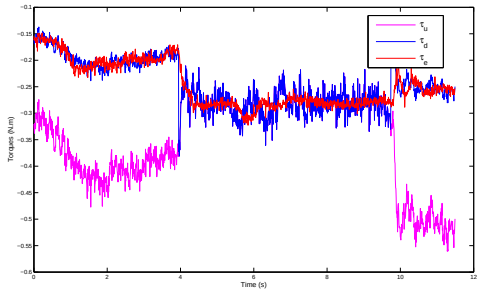

Figure 6: Torque values vs. time.

control scheme allows a reduction of the torques applied on the organ. At $t = 10s$, β is switched from 1.0 to 0.5. One can notify that torques applied on the organ almost remain the same but torques applied by the surgeon are amplified. Therefore, to apply the same efforts on the organ, the surgeon must amplify forces acting on the robot. This result satisfies equation (7).
The figure 7 shows that the system remains stable for different values of gains. Furthermore, it demonstrates that good performances can be achieved with the controller which has been proposed in section 2. Error appearing on Figure 7 is mainly due to noise on measurement. However, one can notice that there are some error peaks on this plot. This phenomenon is due to the modification of the force feedback gain

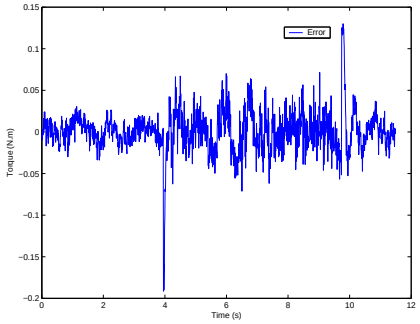

Figure 7: Torque error vs. time.

during experiments. In practice, if a fixed value of β is used, these peaks would not appear.

5 CONCLUSIONS

This paper presents a modified version of a force control scheme. In the context of comanipulation, it is possible to provide force feedback to the manipulator by modifying torques reference. In order to obtain such results, a second force sensor is necessary to distinguish manipulator and environment forces.

Robots kinematic has been used to deal with torques equilibrium. In other words, using a gains matrix allows reduction of forces acting on the environment and amplification of forces acting on the manipulator. Experiments have been conducted to show efficiency of the proposed control scheme.
Moreover, a formal proof of passivity has been established. It ensures stability of the system whatever could be contacts between the robot and its environment.

In future work, in-vivo experiments will be conduced. Even if experiments are satisfying with actual experimental setup, it should be modified to exploit the last 2 DOFS. A new handle seems to be the easiest way to use existing robot.

ACKNOWLEDGEMENTS

Barthélemy Cagneau would like to acknowledge Clara Lord for her contribution to this work. Scientific and technical discussions have been very useful to improve the quality of this paper.

REFERENCES

Anderson, B. D. and Vongpanitlerd, S. (1973). *Network Analysis and Synthesis -A Modern Systems Theory Approach-*. Englewood Cliffs, N.J. , Prentice-Hall.

Jakopec, M., Baena, F., Harris, S., Gomes, P., Cobb, J., and Davies, B. (2003). The hands-on orthopaedic robot acrobot: Early clinical trials of total knee replacement surgery. *IEEE Transactions on Robotics and Automation*, 19(5):902–911.

Kazanzides, P., Zuhars, J., Mittelstadt, B., and Taylor, R. H. (1992). Force sensing and control for a surgical robot. In *Proceedings of the IEEE International Conference on Robotics and Automation*, pages 612–617.

Kochan, A. (2004). A cobotic solution for surgical applications. *Industrial Robot: An International Journal*, 31:478–480.

Kumar, R., Berkelman, P., Gupta, P., Barnes, A., Jensen, P. S., Whitcomb, L. L., and Taylor, R. H. (2000). Preliminary experiments in cooperative human/robot force control for robot assisted microsurgical manipulation. In *Proceedings of the IEEE International Conference on Robotics and Automation*, pages 610–617.

Roy, J., Rothbaum, D. L., and Whitcomb, L. L. (2002). Haptic feedback augmentation through position based adaptive force scaling: theory and experiment. In *Proceedings of the IEEE/RSJ International Conference on Intelligent Robots and Systems*, pages 2911–2919.

Schneider, O., Troccaz, J., Chavanon, O., and Blin, D. (2000). Padyc: a synergistic robot for cardiac puncturing. In *Proceedings of the IEEE International Conference on Robotics and Automation*, pages 2883–2888.

Taylor, R., Jensen, P., Whitcomb, L., Barnes, A., Kumar, R., Stoianovici, D., Gupta, P., Wang, Z., deJuan, E., and Kavoussi, L. (1999). A steady-hand robotic system for microsurgical augmentation. *International journal of robotics research*, 18:1201–1210.

Zemiti, N., Morel, G., Micaelli, A., Cagneau, B., and Bellot, D. (2006). A passive formulation of force control for kinematically constrained manipulators. In *Proceedings of the IEEE International Conference on Robotics and Automation*, pages 2238–2243.

Zemiti, N., Morel, G., Ortmaier, T., and Bonnet, N. (2007). Mechatronic design of a new robot for force control in minimally invasive surgery. *IEEE/ASME Transactions on Mechatronics*, 12(2):143–153.

NEW DEVELOPMENT ON SHAPE MEMORY ALLOYS ACTUATORS

Roberto Romano
Instituto de Pesquisas Tecnológicas do Estado de São Paulo and Telecommunications and Control Department
Escola Politécnica da Universidade de São Paulo, São Paulo, Brazil
rromano@ipt.br

Eduardo Aoun Tannuri
Instituto de Pesquisas Tecnológicas do Estado de São Paulo and Mechatronics Engineering Department
Escola Politécnica da Universidade de São Paulo, São Paulo, Brazil
eduat@usp.br

Keywords: Modeling, shape memory alloy, actuator, robotics, sliding mode control.

Abstract: The present paper presents the development of a mechanical actuator using a shape memory alloy with a novel cooling system based on the thermo-electric effect (Seebeck-Peltier effect). Such a method has the advantage of reduced weight and requires a simpler control strategy as compared to other forced cooling systems. A complete mathematical model of the actuator was derived, and an experimental prototype was implemented. Several experiments are used to validate the model and to identify all parameters. A robust and nonlinear controller, based on sliding-mode theory, was derived and implemented. Experiments were used to evaluate the actuator closed-loop performance, stability, and robustness properties. The results showed that the proposed cooling system is able to improve the dynamic response of the actuator.

1 INTRODUCTION

Shape Memory Alloys (SMAs) consist of a group of metallic materials that demonstrate the ability to return to some previously defined shape or size when subjected to the appropriate thermal procedure. The shape memory effect occurs due to a temperature and stress dependent shift in the materials crystalline structure between two different phases called Martensite and Austenite. Martensite, the low temperature phase, is relatively soft whereas Austenite, the high temperature phase, is relatively hard. The change that occurs within SMAs crystalline structure is not a thermodynamically reversible process and results in temperature hysteresis. SMAs have been used in a variety of actuation applications. The key feature of this material is its ability to undergo large seemingly strains and subsequently recover these strains when a load is removed or the material is heated. SMA actuators have several advantages such as excellent power to mass ratio, maintainability, reliability, and clean and silent actuation. The disadvantages are low energy efficiency due to conversion of heat to mechanical energy, inaccurate motion control due to hysteresis, nonlinearities, parameter uncertainties, difficulty in measuring variables such as temperature and the slow response due to the thermal process evolved in the working principle.

To operate quickly, the SMA must be cooled rapidly. Some researchers have proposed static methods, in which the SMA wires are continually cooled by means of an air stream (Tanaka and Yamada, 1991). In a similar way, Furuya and Shimada (1990) used a cooling system based on water immersion. In such case, cooling time was reduced in 10 times compared to a non-cooled wire. However, the power consumption of such actuator has increased by a factor of 20, since in the heating phase it is necessary much more power to compensate the heat that is lost by the cooling system. Golbert and Russel (1995) used a mobile metallic heat sink and a complex mechanism guaranteed that the sink was only in contact to the wire being cooled, which minimizes the power consumption of the actuator and increases its dynamic behavior. Asada and Mascaro (2002) developed an actuator with a cooling system based on flowing water around the wire. A complex

system guarantees that water flows only when wire must be cooled. The dynamic response of the actuator is expressively better, and the power consumption is also acceptable.In order to increase the dynamic characteristics of SMA actuators, keeping a simple mechanical and electrical design, the present work proposes a novel cooling system based on thermoelectric effect (Seebeck-Peltier effect). A complete mathematical model of the actuator is derived and an experimental prototype is used to validate the model and identify all parameters. A sliding-mode control is also derived and some preliminarily results of its application in the experimental system are obtained and discussed.

2 EXPERIMENTAL SET-UP

An experimental prototype of the SMA actuator, cooled by a thermoelectric element, was built. It was used to validate the mathematical model and to evaluate the control algorithm. Figure 1 shows a simple scheme of the actuator. The thermoelectric tablet is assembled in a heat sink and a small blower is also used to dissipate the heat. The SMA wire is attached to the structure, by means of an electric connector C1. The other end of the wire is attached to the intern pulley (radius r1=0.45cm). A 40g load is supported by a wire connected to the external pulley (r2=4.5cm). The length of the SMA wire is 15cm, and its typical 4.0% deformation is amplified by a factor 10. So, it is expected a 6cm elevation of the load, which is equivalent to a 76^0 pulley rotation. Such rotation is measured by a potentiometer directly attached to the pulley axis.

Figure 2 shows a picture of the actuator. The signal conditioning module is composed by a constant current amplifier that supplies up to 1A the electric current to heat the SMA wire and by a voltage amplifier/filter connected to the potentiometer.

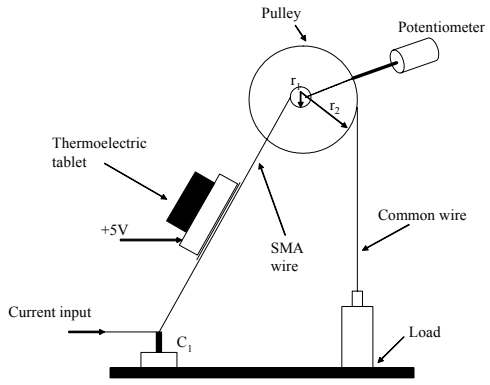

Figure 1: Diagram of the SMA actuator.

The module is connected to a computer (Pentium 100MHz) by mean of a 10bits AD/DA board. The thermoelectric tablet is constantly powered by a 5V tension.

A Matlab/Simulink software was used to acquire and process the data from the potentiometer, and to send the command to the current that must be imposed to the SMA wire. Such software is flexible, and several control algorithms can be easily implemented. Furthermore, all graphical and mathematical tools provided by Matlab/Simulink can be used. The interface with AD/DA board was developed by means of a low-level code included in the software.

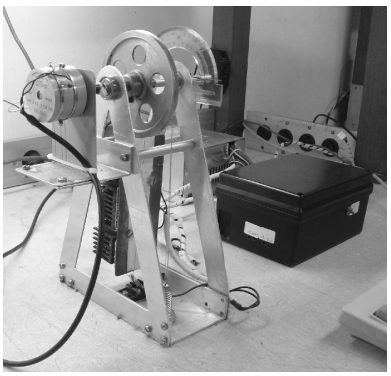

Figure 2: Picture of the actuator.

3 MATHEMATICAL MODEL

The model developed in the present work is based on the formulations proposed by Ikuta, Tsukamoto and Hirose (1991); Grant, Hayward and Lu (1997); Ashrafiuon and Elahinia (2002), Hoder, Vasina and Solc (2003) and Dutta and Ghorbel (2005). It is composed by a thermal model, a phase transformation model and a description of the mechanical properties and dynamics of the system (Figure 3).

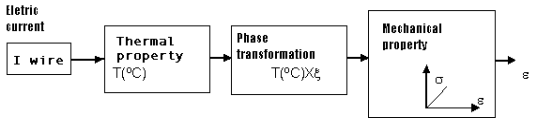

Figure 3: SMA actuator model.

The main variables used in the model are:

i – electric current in the SMA wire (A)
T – SMA wire temperature (ºC)
ξ - martensite fraction (0 a 100%)
σ - mechanical stress in the SMA wire (N/m^2)
ε - deformation (strain) of the SMA wire ($\Delta L/L$)

3.1 Thermal Model

Thermal model was base on the system shown in Figure 4 in which the SMA wire touches the thermoelectric element. The temperature of the element is considered to be constant, equal to 15 ^{0}C.

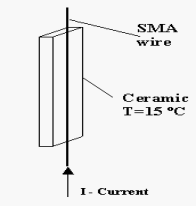

Figure 4: SMA wire and cooling element.

Considering several simplification hypothesis (Grand, Hayward and Lu, 1997), the thermal model can be written as (thermomechanical coupling is also not included since the deformation rate of the SMA wire is small, and such effect becomes important for fast or highly oscillatory deformations):

$$m.c_p.\frac{dT}{dt} = i^2.R - h.A.(T - T_{amb}.) - C.(T - T_p) \qquad (1)$$

In the previous equation, T_p is the temperature on the surface of the cooling element (15^{o}C), T_{amb} is the ambient temperature (considered to be 20^{o}C), h is the natural convection coefficient per unity length of SMA wire (in W/m^2 ºC/m) and C is the conduction coefficient per unity length (in W/ ºC/m). Furthermore, technical specifications of the SMA wire Flexinol FLX 00870, 0.008'', 70ºC) are given by (Dynalloy, 2005):

m - mass per unity length (2.10^{-4} Kg/m)
c_p - specific heat (837 J/Kg.K)
R - electrical resistance per unity length (32Ω/m)
A - external area per unity length (6.28.10^{-4} m^2/m)
d -diameter (2.10^{-4}m)

The parameters h and C are very difficult to estimate, since they depend on several variables. A rough estimation of such parameters, based on the theory exposed in Incropera and Witt (1998), are C = 0.4 W/^{o}C/m and h=6.55 W/m^{2}ºC/m. In the sequel, an identification procedure will be used to obtain values closer to the real ones.

3.2 Phase Transformation

During heating, occurs the transformation between Martensite (M) to Austenite (A), and during the cooling phase, the opposite transformation occurs. Basic equations that model such transformations, as a function of temperature, are given below (Ikuta, Tsukamoto and Hirose, 1991):

$$\xi = \frac{\xi_m}{1 + \exp\left[\frac{6.2}{Af - As}\left(T - \frac{As + Af}{2}\right)\right]} \quad \text{(heating)}$$

$$\xi = \frac{1 - \xi_A}{1 + \exp\left[\frac{6.2}{Mf - Ms}\left(T - \frac{Ms + Mf}{2}\right)\right]} + \xi_A \quad \text{(cooling)} \qquad (2)$$

where As and Af are the initial and final temperature of austenite transformation respectively; Ms and Mf are the initial and final temperature of martensite transformation respectively, ξ_m is the highest martensite fraction during cooling and ξ_A is the initial value of martensite fraction during cooling. Typical values are As=68ºC, Af= 78ºC, Ms=52ºC and Mf= 42ºC (Dynalloy, 2005). However, such values may present variations up to ±15^{o}C, and an identification procedure will be applied to evaluate the correct values for the wire used in the experimental actuator. Phase transformation is shown in Figure 5, and the hysteresis gets evident (Holder; Solc and Vasina, 2003).

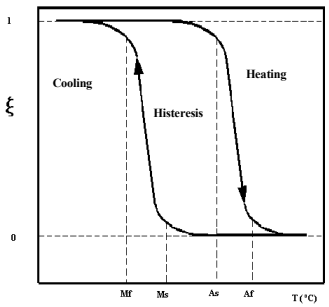

Figure 5: Phase transformation plot.

3.3 Mechanical Properties and Dynamics

Mechanical properties of shape memory alloys are obtained by means of a multiple layer model. The austenite phase is characterized by an elastic behavior. The martensite phase presents a behavior that seems to be plastic, deformed by a small stress (Ikuta, Tsukamoto and Hirose, 1991). So, for ξ= 0 (full austenite), the stress-strain relation is given by:

$$\sigma_A = E_A.\varepsilon \qquad (3)$$

where σ_A is the mechanical stress in the austenite portion of the alloy and E_A is the austenite Young's Modulus. In the other way, when ξ = 1 (full martensite), the stress-stain relation is given by:

$$\begin{aligned} \sigma_m &= E_m.\varepsilon \quad \text{if} \quad |\varepsilon| \le |\varepsilon_{my}| \\ \sigma_m &= E_m.\varepsilon_{my} \quad \text{if} \quad |\varepsilon| > |\varepsilon_{my}| \end{aligned} \qquad (4)$$

E_m is the martensite Young's Modulus , ε_{my} is the martensite maximum elastic deformation, σ_m is the maximum stress in the martensite. The martensite mechanical behavior is illustrated in the fig. below:

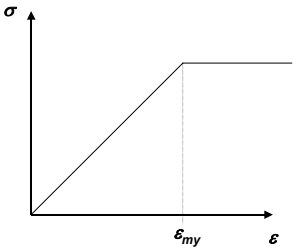

Figure 6: Martensite mechanical behaviour.

Considering then the case with 0<ξ< 1, the stress-strain relation is given by:

$$\sigma = \xi.\sigma_M + (1-\xi).\sigma_A \Rightarrow \begin{cases} \varepsilon = \dfrac{\sigma}{\xi.E_M + (1-\xi).E_A} & \text{for} \quad |\varepsilon| \le |\varepsilon_{my}| \\ \varepsilon = \dfrac{\sigma - \xi.Em.\varepsilon_{my}}{(1-\xi).E_A} & \text{for} \quad |\varepsilon| > |\varepsilon_{my}| \end{cases} \quad (5)$$

The dynamics of the actuator is now considered. A simplified diagram of the actuator and the main forces are shown in the Figure 7, where the coordinate *x* represents the position of the load.

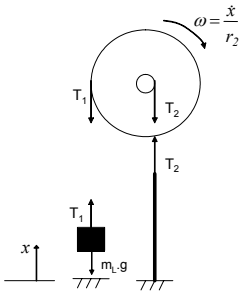

Figure 7: Diagram of the actuator and main forces.

The traction T_1 holds the load, T_2 is the traction acting on the SMA wire and ω is the angular velocity of the pulley. So, being *J* the moment of inertia of the pulley and m_L the mass of the load, using the basic laws of Mechanics one obtains:

$$-T_1.r_2 + T_2 r_1 = J.\frac{\ddot{x}}{r_2} \quad ; \quad -m_L g + T_1 = m_L.\ddot{x} \quad (6)$$

Traction T_2 may be estimated using a linear spring analogy. Figure 8 shows the wire in three possible states. In the austenite phase, the "spring" presents its initial length l_0. In the martensite phase, the wire reaches its maximum length l_{wire}, that correspond to the situation in which the load position is x=0. The difference between l_0 and l_{wire} is approximately 4% of the l_{wire}. In an intermediate phase, the "spring" elongation Δl is given by $4\%.l_{fio} - x/n$.

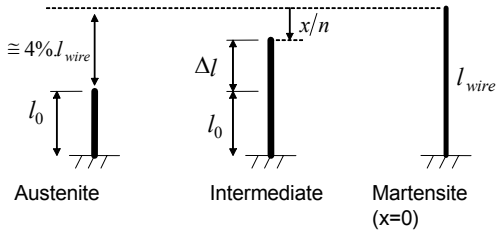

Figure 8: Spring analogy.

So, the traction is given by $T_2 = K.\Delta l = K.(0{,}04.l_{wire} - x/n)$, where K is the equivalent stiffness coefficient of the wire. Including a damping term, the equation of motion of the actuator becomes:

$$\left(J/r_2^{\,2} + m_L\right).\ddot{x} + c.\dot{x} + K/n^2.x = -m_L g + (0.04 l_{wire} K)/n \quad (7)$$

The stiffness coefficient K may be evaluated using (5). Assuming elastic behavior, being A_{wire} the sectional area of the wire, one obtains:

$$\sigma = \left[\xi.E_M + (1-\xi).E_A\right]\varepsilon \quad \text{or}$$

$$\frac{T_2}{A_{wire}} = \left[\xi.E_M + (1-\xi).E_A\right]\frac{\Delta l}{l_0} \quad (8)$$

Finally, considering that martensite stress will be higher than its elastic limit, it may be assumed that it will present a full plastic behavior, with a very small stiffness. So, E_M may be excluded from (8), resulting the approximation:

$$K = \left[(1-\xi).E_A\right]\frac{A_{wire}}{l_0} \quad (9)$$

4 PARAMETER IDENTIFICATION

Thermal parameters *C* and *h*, as well as the transformation temperatures (*Ms*, *Mf*, *As* and *Af*) must be accurately evaluated using a proper experimental procedure. A ramp excitation was induced in the wire, inducing a displacement of the load, as shown in Figure 9.

Using an optimization algorithm based on Quadratic Sequential Programming (SQP), the model parameters were adjusted in order to make the model to recover the measured position accurately. The following parameters were obtained,: *C*=0.255 W/ºC/m, *h*=7 W/m²ºC/m, Ms = 66ºC , Mf = 34ºC As = 53ºC, Af = 93ºC. The comparison between the measured position ant that obtained by the model simulation is given in Figure 10. A good accuracy of the model is verified.

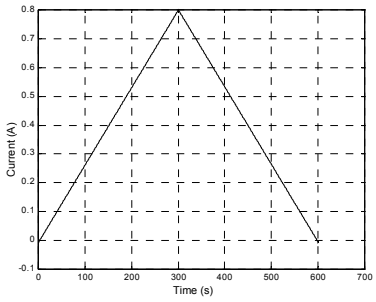

(a)

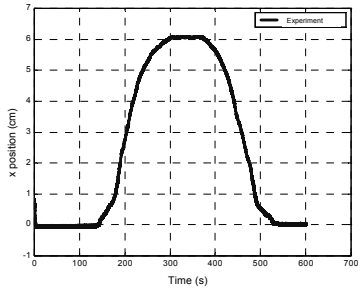

(b)

Figure 9: (a) Current ramp excitation; (b) Position of the load.

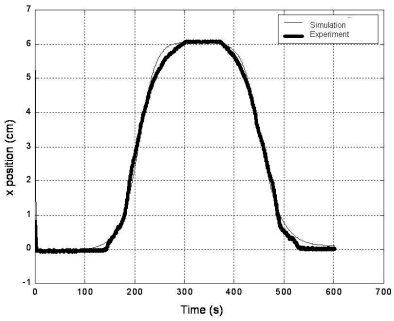

Figure 10 Comparison between simulation and experimental results

5 CONTROL SYSTEM DESIGN

In order to apply the sliding mode control to the SMA actuator, the model previously developed must be adapted, following the formulation exposed in Slotine and Li (1991). After some algebraic manipulation using (1) and (2), the dynamics of phase transformation can be written as:

$$\dot{\xi} = f(\xi) + b(\xi).u \tag{10}$$

with:

$$f(\xi) = \frac{-a}{\xi_0 mc_P}\left(\xi_0(\xi-k)-(\xi-k)^2\right)\left(hAT_{amb} + cT_P - (hA+c)\left(\frac{1}{a}\ln\left(\frac{\xi_0}{\xi-k}-1\right)+b\right)\right)$$

$$b(\xi) = \frac{-a}{\xi_0 mc_P}\left(\xi_0(\xi-k)-(\xi-k)^2\right)R \;;\; u = I^2$$

and

$$\begin{cases} a = \dfrac{6.2}{A_f - A_s}; b = \dfrac{A_s + A_f}{2}; \xi_0 = \xi_M; k = 0 \text{ if } \dot{T} > 0 \\ a = \dfrac{6.2}{M_s - M_f}; b = \dfrac{M_s + M_f}{2}; \xi_0 = 1 - \xi_A; k = \xi_A \text{ if } \dot{T} < 0 \end{cases}$$

Using (1) and (9), the dynamics of the motion can also be written as:

$$I\ddot{x} + c\dot{x} + \frac{K_0(1-\xi)}{n^2}x = -m_L g + \frac{K_0(1-\xi)}{n}\Delta \tag{11}$$

With $I = \left(J/r_2^{\,2} + m_L\right)$; $K_0 = E_A\, A_{wire}/l_0$ and $\Delta = 0.04 l_{wire}$. In equations (10) and (11), the variable x is measured, but the variable ξ must be estimated. This may be done considering a quasi-static approximation to (11), making $\dot{x} = \ddot{x} = 0$, that results:

$$\hat{\xi} = 1 - \frac{m_L g}{K_0\left(\dfrac{\Delta}{n} - \dfrac{x}{n^2}\right)} \tag{12}$$

Differentiating (11), and using (10), one obtains the SMA model adequate to apply sliding mode control, as proposed by Slotine and Li (1991):

$$\dddot{x} = f(\mathbf{x}) + b(\mathbf{x}).u \tag{13}$$

with $\mathbf{x} = \left(\xi \quad x \quad \dot{x} \quad \ddot{x}\right)^T$,

$$f(\mathbf{x}) = \frac{-c}{I}\ddot{x} - \frac{K_0(1-\xi)}{In^2}\dot{x} + \left(\frac{K_0 x}{In^2} - \frac{K_0\Delta}{In}\right)f(\xi)$$

and $b(\mathbf{x}) = \left(\dfrac{K_0 x}{In^2} - \dfrac{K_0\Delta}{In}\right)b(\xi)$.

So, the control action $u = i^2$ is given by:

$$u = \frac{1}{\hat{b}(\mathbf{x})}\left(-\hat{f}(\mathbf{x}) + \dddot{x}_d - 2\lambda\ddot{\tilde{x}} - \lambda^2\dot{\tilde{x}}\right) - K_{SM}\,sat(s/\phi) \tag{14}$$

with $s = \ddot{\tilde{x}} + 2\lambda\dot{\tilde{x}} + \lambda^2\tilde{x}$. $\hat{f}(\mathbf{x})$ and $\hat{b}(\mathbf{x})$ are the best estimates of the functions in model (13), considering the approximate values for the parameters and the estimate of the variable ξ given in (12). x_d is the desired position of the actuator load (set-point), λ is a positive constant related to the cut-off frequency of the closed-loop system, ϕ is the boundary layer thickness to avoid control chattering and K_{SM} is a control gain related to the modeling and parameter estimation errors. A detailed description of the control design may be found in Slotine and Li (1991).

6 EXPERIMENTAL RESULTS

The control logic previously developed was applied to the experimental prototype, and the performance

of the closed loop system could be evaluated. Figure 11 shows a reference step of 2.5cm applied at t=10s. Control parameters are λ=40; ϕ=1,6 and K_{SM}=64. The 5% settling time obtained is 0,23s, and the maximum overshoot is 0,6%.

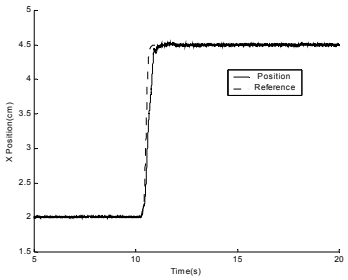

Figure 11: Step response of the SMA actuator.

A harmonic set-point was applied to the actuator, with amplitude of 1cm and periods of 20s and 5s (Figure 12. It can be seen that, despite a small oscillation around the set-point, the system follows the reference with good accuracy. Tests with decreasing periods indicated a 0.69Hz cut-off frequency, despite of a 0.37Hz obtained with a conventional PID controller. Finally, a cooling disturbance was applied, created by a computer cooler fan directed toward the SMA wire (Figure 13). The robustness of the controller can be verified, by comparing the response with the open-loop response.

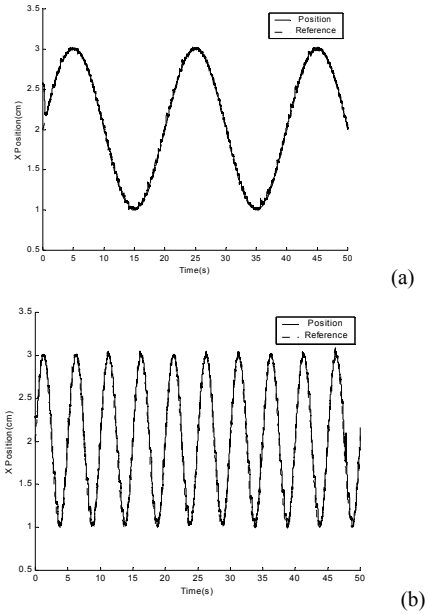

Figure 12: Harmonic set-point response of the SMA actuator (cm amplitude). (a) 20s; (b) 5s period

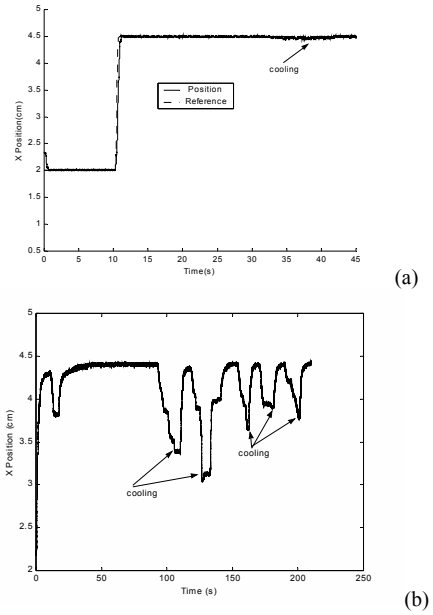

Figure 13: Cooling disturbance response of the SMA actuator (a) closed-loop; (b) opened-loop

7 CONCLUSIONS

A novel SMA actuator was proposed, using the thermoelectric effect for cooling the SMA wire. An experimental prototype was built, and a mathematical model was developed. The model parameters were adjusted by means of an experimental identification procedure. The validated model was then used to design a sliding mode controller. Such controller is able to deal with model and parameter uncertainties, and also with non-linear effects. Closed-loop preliminary results obtained in the experimental set-up showed that the proposed actuator presents a good dynamic response and low sensibility to disturbs of load and ambient cooling. So it is recommended in application with SMA devices.

ACKNOWLEDGEMENTS

The authors would like to express their gratitude for the IPT (Institute for Technological Research - São Paulo, Brazil) for supporting this research and for CNPq (National Council for Scientific and Technological Development), Research Process Number 484232/2006-1.

REFERENCES

Asada, H.H. and Mascaro S., 2002, “Wet Shape Memory Alloy Actuators”, MIT Home Automation and Healthcare Consortium, Phase 3 Final Report, Boston, USA.

Ashrafiuon, H. and Elahinia H.M., 2002, “Nonlinear Control of a Shape Memory Alloy Actuated Manipulator”, ASME Journal of Vibration and Acoustics, Vol. 124, pp.566-575.

Dutta, S.M. and Ghorbel, F.H., 2005, "Differential Hysteresis Modeling of a Shape Memory Alloy Wire Actuator," IEEE/ASME Transactions on Mechatronics, Vol. 10, Issue 2, April , pp. 189-197.

Dynalloy, Inc., 2005, “Flexinol – Wire specifications”. Available at: http:// www.dynalloy.com. Acess: 20 Dec. 2005.

Furuya, Y. and Shimada H., 1990, “Shape Memory Actuator for Robotic Applications, Engineering Aspect of Shape Memory Alloys”, Butterworth-Heinemann, London, pp 338-355.

Gorbet, B.R. and Russel A.R., 1995, “Improve the Response of SMA Actuators”, IEEE International Conference on Robotic and Automation, Vol. 3, May, pp. 2299-2303.

Grant, D., Hayward V. and Lu A., 1997, “Design and Comparison of High Strain Shape Memory Alloy Actuators”, International Conference on Robotic and Automation, Albuquerque, New Mexico, 260-265.

Hoder K., Vasina, M. and Solc F., 2003, “Shape Memory Alloy- Unconventional Actuators”, International Conference on Industrial Technology ICIT, Maribor, Slovenia, pp. 190-193.

Ikuta K., Tsukamoto M. And Hirose, S., 1991, “Mathematical Model and Experimental Verification of Shape Memory Alloy for Designing Micro Actuator”, Proc. of the IEEE on Micro Electromechanical Systems, an Investigation of Microstructures, Sensors, Actuators, Machines, and Robots, pp.103-108.

Incropera, P.F. and Witt, D.P.D., 1998, “Fundamentos de transferência de calor e de massa”, 4 ed., Rio de Janeiro, LTC (In Portuguese).

Slotine, J.J.E. and Li, W., 1991, “Applied nonlinear control”, Englewood Cliffs: Prentice –Hall, USA.

Tanaka,Y. and Yamada Y., 1991, “A Rotary Actuator Using Shape Memory Alloy for a Robot, and Analysis of the Response with Load”, IEEE/RSJ International Workshop on Intelligent Robots and Systems IROS ’91, Osaka, Japan, pp1163-1168.

A VERSATILE ROBOTIC WHEELCHAIR COMMANDED BY BRAIN SIGNALS OR EYE BLINKS

André Ferreira, Daniel Cruz Cavalieri, Rafael Leal Silva
Teodiano Freire Bastos-Filho and Mário Sarcinelli-Filho
Department of Electrical Engineering, Federal University of Espirito Santo
Av. Fernando Ferrari, 514, 29075-910, Vitória-ES, Brazil
tfbastos@ele.ufes.br

Keywords: Wheelchair control, Human Machine Interfaces (HMI), Biomedical Signal Processing.

Abstract: A system allowing a person with severe neuromotor disfunction to choose symbols in a Personal Digital Assistent (PDA) using electroencephalography (EEG) or electromyography (EMG) is implemented onboard an electrical wheelchair. Through this system the user is able to elicit personal needs or states, like sleep, thirst or hunger; to write texts using an alpha-numeric keyboard and to command a robotic wheelchair. The EEG patterns used are event-related synchronization and de-synchronization (ERS and ERD, respectively) occurring in the alpha band of the signal spectrum captured in the occipital region of the head, while the EMG patterns are eye-blinks. The results so far obtained with the system developed, in indoor and outdoor environments, are quite satisfactory. This paper describes the system so far implemented and shows some experimental results associated to it.

1 INTRODUCTION

The use of biological signals intentionally generated by impaired people can contribute to improve their life-quality, providing augmentative communication capabilities and autonomy of movement (Wolpaw et al., 2002; Millán et al., 2003). The development of a Human Machine Interface (HMI) that considers myoelectric (EMG) or electroencephalographic (EEG) signals is here described. Such an HMI acquires the myoelectric or electroencephalographic signals of an impaired individual in order to recognize a short set of easily voluntarily generated patterns, which are associated to a group of previously defined tasks. Such an interface has been used in connection to robotic devices (Ferreira et al., 2006; Frizera-Neto et al., 2006), and is currently being used to allow an individual to control a robotic wheelchair and to communicate with other people, as it is shown hereinafter.

To the extent of the authors' knowledge, just two works using EEG to command a wheelchair have been published so far (Tanaka et al., 2005; Rebsamen et al., 2007). In (Tanaka et al., 2005) the processing unit is off board the wheelchair, a high number of EEG electrodes (thirteen) is used, and the recognition rate associated to the brain signal may be as low as 20%. In (Rebsamen et al., 2007) the focus is the navigation of the wheelchair (no communication support is included), and a high number of electrodes (fifteen) is used. The system here developed, by its turn, uses only three EEG electrodes, is quite easy to use, presents a high recognition rate, and is more versatile, since it allows selecting between two communication channels (EEG or EMG). Besides allowing commanding the wheelchair, the system here described provides other useful functions, as it is shown in Section 4. It was tested in indoor and outdoor environments, with quite satisfactory results.

The current structure of the proposed HMI and the way it interacts with the impaired individual and the wheelchair are shown in Figure 1. The signal acquired by the electrodes connected to the face/head of the impaired individual are conditioned and quantized through a high-resolution A/D converter. After being read by a computer, such a signal is filtered through a bandpass digital filter whose pass band spans from 1 to 30 Hz, when using the EMG option, or from 8 to 13 Hz, when acquiring EEG signal (the alpha band). Features of interest extracted from such signals are then delivered to a classifier that identifies if the impaired individual wishes or not to select a symbol shown on the screen of the Personal Digital Assistant (PDA) as illustrated in Figure 1. If yes, the communication interface shown in the figure asks the PDA for the information necessary and sends it to the next module, which is responsible for generat-

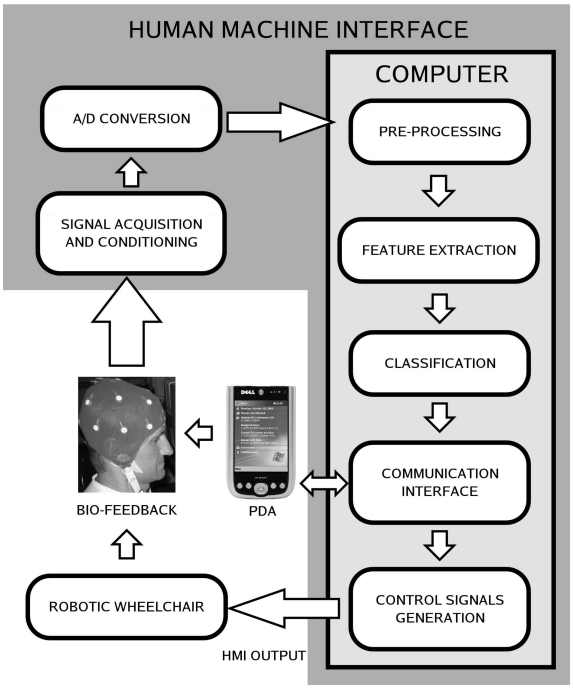

Figure 1: The structure of the proposed HMI.

ing the necessary control actions so that the robotic wheelchair executes the task the impaired individual has chosen. The feedback is closed through the operator (bio-feedback), as shown in the figure.

The description of the system so far implemented is completed in Section 2. The data acquisition system and the techniques used in the EMG and EEG processing module are presented in Section 3. In the sequel, a description of the functionalities included in the graphic interface programmed in the PDA is presented in Section 4. The experimental results are presented in Section 5 and are discussed in Section 6, which highlights the conclusions of the work as well.

2 HARDWARE STRUCTURE

Figure 2 illustrates the hardware embedded on the wheelchair. Encoders and ultrasonic sensors are functional, while the others are under development. The motors are controlled by a low-level controller programmed on a MSP430 microcontroller (Texas Instruments, Inc.), which receives commands of angular and linear velocities from a mini-PC onboard the wheelchair. The signal acquisition system and the PDA are connected to the PC through a parallel and a serial port, respectively.

Two electronic boards, a signal conditioning one and a quantization one, compound the signal-acquisition system. The signal acquisition board has two input channels and a third electrode used as the reference for the signal amplifier. A high-pass filter with cut-off frequency of 0.1 Hz avoids the saturation of the amplifiers due to the continuous voltage caused by the coupling between the electrodes and the skin. A fourth order low-pass Butterworth filter with cutoff frequency of 32 Hz limits the spectrum of the acquired signal and attenuates 60 Hz artifacts (electromagnetic induction), some contaminating noise and disturbances generated by muscles movements, electrodes displacement, etc. Such a board also embeds a Body Driver circuit to reduce 60 Hz artifacts (Webster, 1998).

The second part of the acquisition system is a quantization board based on the AD7716 analog to digital converter. The main features of such a chip are a resolution correspondent to 22 bits, four A/D channels, and a low-pass digital filter with a cutoff frequency selectable among 36.5 Hz, 73 Hz, 146 Hz, 292 Hz and 584 Hz. The sampling rate used for the EEG signal is 140 Hz, so that the cutoff frequency of such a low-pass filter has been set to 36.5 Hz. The digital signal thus obtained is then sent to the high level hardware.

After receiving the acquired data delivered by the data acquisition board, the onboard CPU (mini-ITX) is responsible for pre-processing them, extracting the desired features, classifying them and generating the control signals associated to the recognized pattern. Figure 2 illustrates how the hardware pieces are connected.

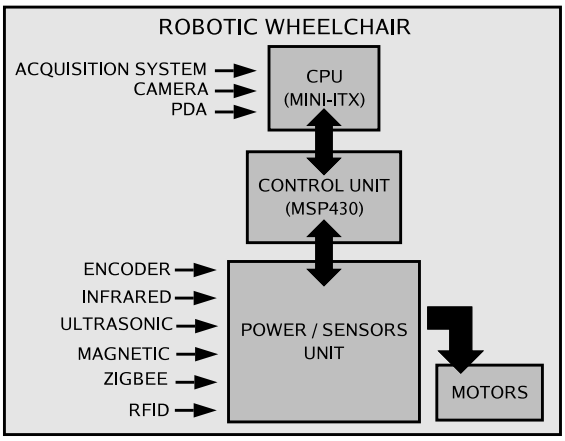

Figure 2: The hardware structure of the system developed.

3 RECOGNIZING SIGNAL PATTERNS

3.1 Through Processing EEG

Event-related Synchronization and Desynchronization (ERS and ERD, respectively) are the EEG patterns searched for in this work. They are characterized by meaningful changes in the signal energy in specific frequency bands. An energy increase is associated to an ERS, while an energy decrease is associated to an ERD (Pfurtscheller and da Silva, 1999). The frequency band used to detect these patterns is the alpha band (8-13 Hz) and, thus, the digitized signal is filtered by a FIR filter with such a pass band.

The EEG signal is acquired in the occipital region of the user's head, with electrodes in the positions O_1 and O_2 (regarding the 10-20 International System of Figure 3) and the reference in the right ear.

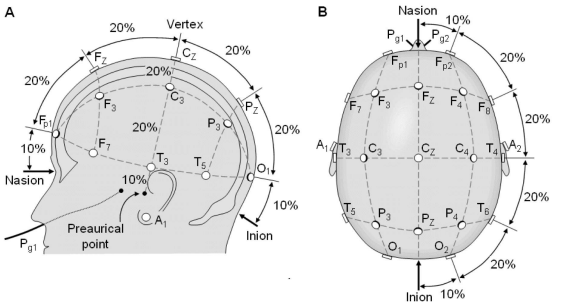

Figure 3: The 10-20 International System.

A user whose eyes are open (under visual stimulus or concentrated) keeps the alpha rhythm in a low energy level. When he/she closes the eyes (with no visual stimulus or relaxed), there is a great energy increase in the alpha rhythm, characterizing an ERS. The variance of the filtered EEG signal allows detecting these energy changes, as observed in Figure 4.

The second graphic in Figure 4 is generated regarding a moving window filled with $N = 280$ samples (N is empirically determined) of the filtered EEG signal (x_k), for which the mean value and the variance are, respectively, $\mu = \frac{1}{N}\sum_{k=1}^{N} x_k$ and $\sigma^2 = \frac{1}{N}\sum_{k=1}^{N}(x_k - \mu)^2$.

The variance thus obtained is the input of a threshold-based classifier, whose function is to detect if the user wishes or not to select a symbol presented in the PDA screen. Case yes, a request is sent to the PDA through a serial line, and it informs which symbol has been selected. Knowing that, the mini-ITX calculates the necessary control signals to accomplish the chosen task and sends it to the actuation module (MSP430).

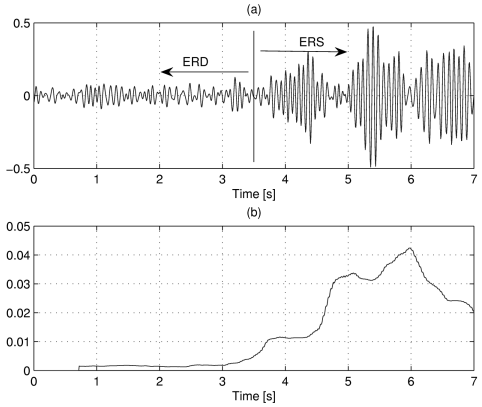

Figure 4: (a) Filtered EEG signal with ERD and ERS. (b) Variance increase during an ERS.

3.2 Through Processing EMG

The objective here is to recognize the presence of an eye-blink (Figure 5) in the Myoelectrical signal (MES) acquired on the user's face, for selecting symbols presented in the PDA screen.

The samples of a given MES can be considered as a random variable, whose variance represents an averaged measure of the variability or activity of the signal about its mean (Rangaraj, 2002), as shown in Figure 6. Such indicator of signal activity was used to control the robotic wheelchair with good results, as it is indicated in Table 1. Four individuals tested the capability of choosing an icon in the PDA screen through the variance associated to the MES signal. They should blink an eye to select an icon they were asked to select. As shown in Table 1, the accuracy obtained by using the MES variance as the indicator of activity was very high, thus justifying to use

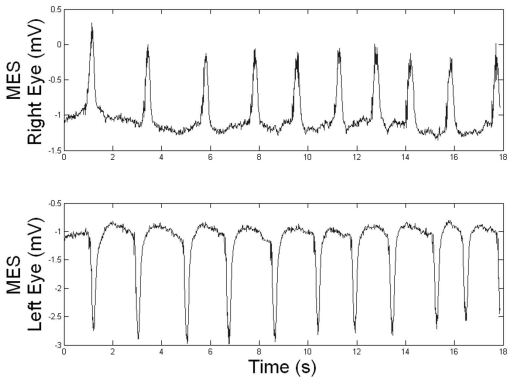

Figure 5: Myoelectrical signal associated to eye-blinks.

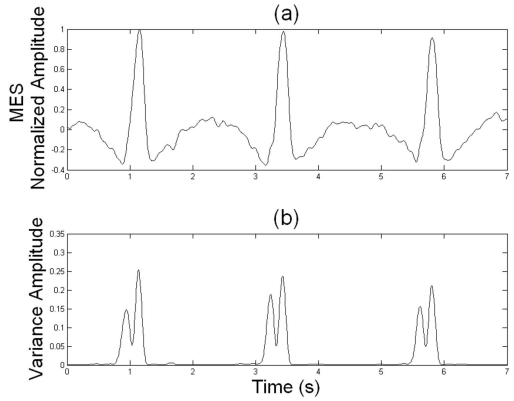

Figure 6: (a) MES of an ordinary individual (male, 25 years). (b) Signal variance.

such an indicator. Each individual was asked to select 15 icons, each one associated to a movement of the wheelchair. The calculation of the variance of the MES is performed in the same way used for the EEG signal (Subsection 3.1), after normalizing the signal amplitude. A threshold-based classifier was used again.

However, according to (Kreifeldt, 1974) the myoelectrical signal is better described as a stochastic random process, for its average and variance vary along time. Thus, it is necessary to use more robust systems to process MES, to take into account its stochastic behavior. In (Hudgins et al., 1993) it is shown that such signal presents a deterministic characteristic in the first 200 ms after a muscular contraction. Due to the nature of the MES, it is reasonable to expect meaningful changes in the value of the parameter describing a particular pattern from one individual to other. Other aspects, like changes in the position of the electrodes and body-weight fluctuations, will produce changes in the signal patterns along time (Hudgins et al., 1993). Thus, a classifier based on an artificial neural network (ANN) was trained to accommodate the expected individual differences and, as well, to accept slow variations in the values associated to the patterns to be recognized.

The neural network is trained using three back-propagation algorithms: Bayesian Regularization (BR), Resilient Back-propagation (RP) and Scaled Conjugate Gradient (SCG) (MathWorks, 2000). A

Table 1: Results for controlling the wheelchair with basis on the indicator of activity.

Individual	# of Tests	# of Errors	Rightness
A	15	0	100 %
B	15	0	100 %
C	15	1	93.3 %
D	15	0	100 %

Table 2: The ANN's implemented and the training algorithms.

Training Algorithm	Input Layer	Hidden Layer	Output Layer	Error (%)
BR	20	4	3	0.6
BR	20	6	3	0.5
BR	20	8	3	0.6
BR	20	10	3	0.6
RP	20	4	3	0.3
RP	20	6	3	0.6
RP	20	8	3	0.3
RP	20	10	3	0.5
SCG	20	4	3	0.8
SCG	20	6	3	0.5
SCG	20	8	3	0.3
SCG	20	10	3	0.3

total of 210 pre-processed sequences of facial MES correspondent to right-eye blinks, 210 pre-processed samples of facial MES correspondent to left-eye blinks, and 210 sequences of random noise, resulting in 630 sequences of signal samples, were used for training and validating the neural networks tested. For each one of these three sets of samples, fifty percent were used for training and fifty percent were used for validation. The results are shown in Table 2. A hidden layer with 4 to 10 neurons resulted in a very good accuracy in classifying the three patterns of interest, knowing left-eye blink, right-eye blink and noise (no blink). The error presented in Table 2 is the sum of the errors during training and validation.

The ANN configurations showing the best performances in Table 2 were tested, now regarding 252 new test signals, from which 84 corresponds to left-eye blinks, 84 corresponds to right-eye blinks and 84 corresponds to noise sequences (no blinks). The results obtained when classifying them are presented in Table 3, and show that the use of the artificial neural network as a classifier for the patterns searched for in the MES resulted in a high rate of rightness. In particular, the classifier currently implemented in the system here addressed is an artificial neural network having 20 neurons in the input layer, 4 neurons in the hidden layer and 3 neurons in the output layer, whose training algorithm is the Resilient Back-propagation.

Table 3: Results of testing the best ANN's in Table 2.

Training Algorithm	# of Neurons in the Hidden Layer	Success Rate (%)
BR	6	98.4
RP	4	99.6
SCG	10	98.4

4 SELECTING AN OPTION ON THE PDA SCREEN

The PDA (Figure 1) is installed onboard the wheelchair in such a way that it is always visible for the impaired individual seated on it. It provides a graphic interface containing the possible options for the operator, including the pre-programmed movements of the wheelchair, a virtual keyboard for text edition, and symbols to express some basic needs or feelings of the impaired individual, such as to sleep, drink, eat, feel cold, heat, etc. For all these cases, a specific option is selected using a procedure to scan the rows and columns in which the icons are distributed on the PDA screen (once the desired screen is presented). A voice player confirms the option chosen, providing a feedback to the user and allowing the communication with people around as well, either through EMG or through EEG signals.

The operator selects symbols presented on the PDA screen, which are distributed in a form that resembles a matrix, assisted by an automatic scanning system. Each row of the matrix of symbols remains pre-selected for a while, until the operator confirms the choice. After selecting the row, the process is repeated, now regarding the columns of that row. For tasks like controlling the wheelchair or asking for specific external help, this scanning system is quite suitable.

Figure 7 illustrates the `STATE` and `TEXT` screens. The first one is designed to support interpersonal communication. It presents options to the operator in order to elicit emotions, personal states or some basic needs. Although the options of this screen can be expressed by using the `TEXT` screen, this mode is much faster, mainly in emergencies, such as to complain about pain. The `TEXT` mode provides a communication channel to the operator, allowing the selection of letters and numbers through a virtual keyboard, whose sounds are echoed to speakers. Although being a low bit-rate communication process, it provides a way to elicit words via artificial voice when the patient does not have this capacity anymore.

The screen `MOVEMENT` provides to the operator a set of symbols corresponding to movements of the robotic wheelchair. The options are shown in Figure 8, and represents actions sent directly to the wheelchair motors. The first command starts the movement of the wheelchair and the next one, it does not mind where the automatic scan is, stops the wheelchair. For safety, only successive short back-displacements are allowed, because of the null visibility in such a movement. Through the screen `CONTROLLER`, option currently being developed, the user will be able to choose a place in a structured environment, and the wheelchair will be guided to that place by an automatic control system. This screen is shown in Figure 8.

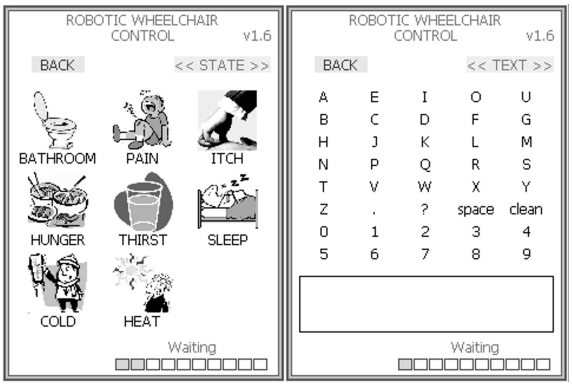

Figure 7: Software `RWCC: STATE.` and `TEXT` screens.

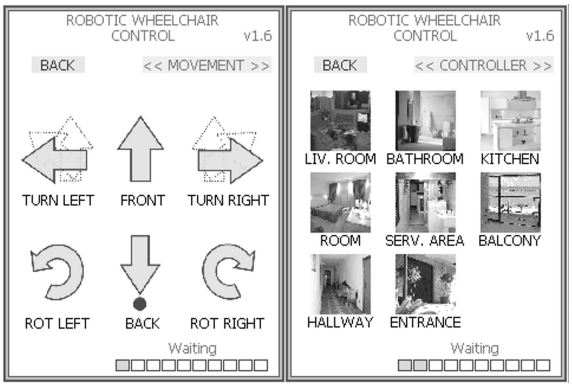

Figure 8: Software `RWCC: MOVEMENT.` and `CONTROLLER` screens.

5 EXPERIMENTS

A user testing the wheelchair in an indoor environment (left) and in an outdoor environment (right), using the EEG signal option of the developed HMI, is presented in Figure 9. The preparation of the user to operate the system consists of cleaning the regions where the electrodes should be connected (the O_1 and O_2 positions in the head and the right earlobe) and, then, a special gel is applied between the electrode and the user's skin, for impedance-matching.

A meaningful group of users tested their capability of using the system, and the result was that all of them were capable to command the wheelchair and to communicate with people around it.

The analysis of the EEG signal in the alpha band, and of its variance as well, shows very clearly when

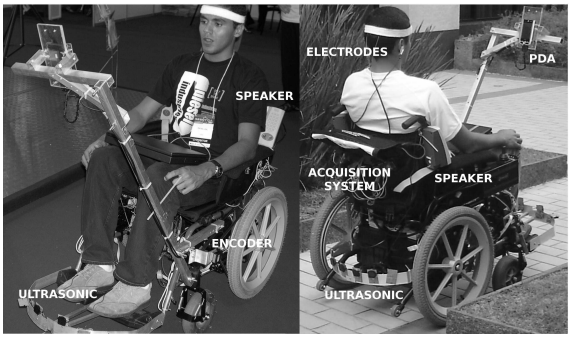

Figure 9: Testing the system prototype.

the user closes his/her eyes, generating an ERS (the signal variance exhibits a great increase, as shown in Figure 4). This indicates that the user wishes to select the option currently highlighted in the PDA screen. An important aspect, regarding the detection of the changes in the signal variance, is that an adjustable hysteresis-zone is included in the threshold-based classifier in order to increase the system robustness, thus avoiding false ERS/ERD detection.

6 CONCLUSIONS

The HMI so far developed was tested in indoor and outdoor environments, with quite satisfactory results, according to the statements of the users who operated the prototype during the tests.

The acquisition system allied to the PDA has proven to be quite efficient for choosing commands to the wheelchair using EMG or EEG signals. A minimum knowledge about the HMI and a very quick training is required to operate the whole system.

However, it is worthy to mention that so far the developed HMI has not been tested by people with severe neuromotor disabilities, which is the next step of this work.

The ANN used in the analysis of MES has demonstrated a very good capability to find the desired patterns in such signals. The feedforward topology with back-propagation training algorithm, having two active and one hidden layers, allowed a satisfactory rate of classification rightness.

The easiness of electrode-placing (for both EMG and EEG options), the simplicity of the graphical interface running in the PDA and the easiness to adapt the system to a commercial electrical wheelchair are the major advantages of the HMI here developed, when taking into account the final users of this assistive technology.

ACKNOWLEDGEMENTS

The authors thank CAPES, a foundation of the Brazilian Ministry of Education (Project 150(07)), FAPES, a foundation of the Secretary of Science and Technology of the State of Espirito Santo (Process 30897440/2005), and FACITEC/PMV, a fund of the Vitoria City Hall for supporting Scientific and Technological Development, for their financial support to this research.

REFERENCES

Ferreira, A., Bastos-Filho, T. F., Sarcinelli-Filho, M., Cheein, F. A., Postigo, J. F., and Carelli, R. (2006). Teleoperation of an industrial manipulator through a TCP/IP channel using EEG signals. In *Proceedings of the International Symposium on Industrial Electronics (ISIE 2006)*, pages 3066–3071, Montreal, Canada.

Frizera-Neto, A., Celeste, W. C., Martins, V. R., Bastos-Filho, T. F., and Sarcinelli-Filho, M. (2006). Human-machine interface based on electro-biological signals for mobile vehicles. In *Proceedings of the International Symposium on Industrial Electronics (ISIE 2006)*, pages 2954–2959, Montreal, Canada.

Hudgins, B., Parker, P., and Scott, R. N. (1993). A new strategy for multifunction myoelectric control. *IEEE Transactions on Biomedical Engineering*, 40:82–94.

Kreifeldt, J. G. (1974). A signal-to-noise investigation of nonlinear electromyography processors. *IEEE Transactions on Biomedical Engineering*, 21:298–308.

MathWorks (2000). Neural network toolbox users guide.

Millán, J., Renkens, F., Mouriño, J., and Gerstner, W. (2003). Non-invasive brain-actuated control of a mobile robot. In *Proceedings of the 18th International Joint Conference on Artificial Intelligence*, Acapulco, México.

Pfurtscheller, G. and da Silva, F. H. L. (1999). Event-related eeg/meg synchronization and desynchronization: basic principles. *Clinical Neurophysiology*, 110(11):1842–1857.

Rangaraj, M. R. (2002). *Biomedical Signal Analysis*. Wiley Interscience, New York.

Rebsamen, B., Burdet, E., Guan, C., Zhang, H., Teo, C. L., Zeng, Q., Laugier, C., and Ang Jr., M. H. (2007). Controlling a wheelchair indoors using thought. *IEEE Intelligent Systems*, 22:18–24.

Tanaka, K., Matsunaga, K., and Wang, H. (2005). Electroencephalogram-based control of an electric wheelchair. *IEEE Transactions on Robotics*, 21:762–766.

Webster, J. G. (1998). *Medical Instrumentation. Application and Design*. John Wiley & Sons, Inc., New York, 3 edition.

Wolpaw, J. R., Birbaumer, N., McFarland, D. J., Pfurtscheller, G., and Vaughan, T. M. (2002). Brain-computer interfaces for communication and control. *Clin Neurophysiol*, 113(6):767–791.

NEUROLAB: A MULTIMODAL NETWORKED EXOSKELETON FOR NEUROMOTOR AND BIOMECHANICAL RESEARCH

A. F. Ruiz, E. Rocon, F. Brunetti, L. Bueno, J. C. Moreno and J. L. Pons
Bioengineering Group, Instituto de Automatica Industrial, Ctra. Campo Real km 0.200, Madrid, Spain
afruiz@iai.csic.es

Keywords: Biorobotics, Biomechanical Devices, Exoskeletons, Health Monitoring Devices.

Abstract: NeuroLab refers to an experimental platform designed to enhance studies in human movement and neuromotor control. The platform comprises a robotic exoskeleton and some other stand-alone devices. All of these components have communication capabilities integrated in hardware and can work cooperatively taking advantage of a networked architecture. A set of experiments have been conducted with NeuroLab. The objective of the trials was to use mechanical perturbations to identify the viscous-elastic properties in human elbow joint and to correlate such mechanical impedance with the electromyographic information of muscles associated to the joint, during a postural task and in a rest position. In each condition, a pseudo-random torque perturbation was applied directly to the arm and to the forearm by mean of an upper limb powered exoskeleton. The angular kinematics (velocity and position), kinetics (torque) and the muscular activation patterns (EMG) in the two main muscles (biceps and triceps brachii) intervening in the elbow flexion-extension movement were recorded.

1 INTRODUCTION

Human movement and neuro-motor control is a very complex research field due mainly to the complexity of the involved mechanisms and the difficult access to the components of the overall system. Due to these reasons, the research community tries to exploit all kinds of valid information (EMG, EEG, kinetics and kinematics) relating to movement planning and execution in order to understand this complex system and to develop new aids in the medical robotics field.

One common and generally-accepted approach to understanding and modelling the human motor system is to monitor and analyse movement-related data during different motor task. A common approach to understand the dynamics of the motor control system is to independently manipulate the mechanical conditions of each joint while acquiring the biomechanical signals and the generated bio-potentials while the human motor system adapts to those new applied conditions.

In this scenario, a set of tools attached to the human body is required. In NeuroLab, there are independent devices that communicate with each other, based on a Personal Area Network (PAN) concept. Each device has a specific function and helps to address the overall goal of the platform. The NeuroLab integrates several devices in a global architecture. The main goals of NeuroLab are:

1. Study of human movement in subjects with motor disorders such as pathological tremor or spasticity. The information provided by the platform during the execution of specific motor tasks can be used as a tool to diagnose and assess motor disorders, (Rocon et al., 2007).
2. Study of neuro-adaptative strategies for learning and training of specific motor patterns through the application of selected force-fields to the upper limb. This application could potentially be of considerable impact in patients suffering of cerebral injuries, (Krebs et al., 1998).
3. Validation of neurophysiological models of human motor control in upper and lower limbs. This will help to gain a better understanding of the integration of the sensory information and the under-

lying mechanisms for generation of motor commands.

4. Study of human body behaviour under external loads. The load application is the basis for several technical aids to compensate functional disability.
5. Exploration of new communication channels in human-robot interfaces. This is potentially feasible through the use of EMG and EEG information to control wearable robots, (Rosen et al., 2001), (Pfurtscheller et al., 2002).
6. Assessment and quantification of human upper limb parameters, e.g. mechanical impedance. These parameters are considered important for understanding of the control mechanisms of the human joints, the generation of control signals, the execution of movements and the adaptation under changing conditions.

This paper aims at describing the design and the development of a platform to enhance research in several fields. The next section presents each device concept of the NeuroLab system. Next, a set of experiments which are being conducted with such platform in order to model the human motor control at the upper limb will be described. The experimental methods and preliminary results are presented in section 3. Finally, the section 4 discusses future work with NeuroLab.

2 PLATFORM DESCRIPTION

The platform (see figure 1), is composed of modules and devices that provide several capabilities: an upper limb robotic exoskeleton, an EMG module, a Biomechanical Monitoring module, and an EEG module. It can further be expanded with other peripherals. A software platform is defined to manage the system, e.g. setup the experiments and acquire data. Safety and reliability were priority considerations in the development.

The powered exoskeleton and the devices can communicate with each other using a CAN-based network and specific protocols. Each element of the platform provides several services which can be requested by other devices. There are therefore different primitives in the upper layers of the protocol, for instance to retrieve the data acquired by a module or to control a joint of the exoskeleton.

The robotic device is an upper limb exoskeleton which allows the mechanical conditions of each limb joint to be manipulated independently, (Ruiz et al., 2006). The networked platform enables combined measurement of biomechanical variables (kinematics and kinetics variables) and biopotentials, such as electromyography (EMG) and electroencephalography (EEG).

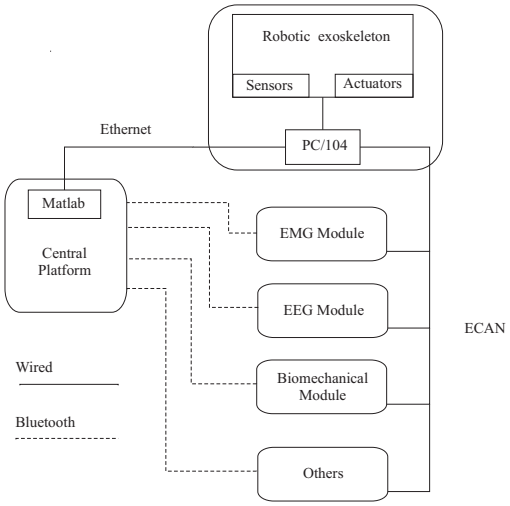

Figure 1: Layout of the NeuroLab system. Different modules can connect to a base station using Bluetooth. At the same time, all the modules are part of the wearable-robot network, called BioNET.

2.1 Robotic Exoskeleton

The upper limb robotic exoskeleton in NeuroLab spans the human elbow and wrist joints, (Rocon et al., 2007). The sensors (gyroscopes, potentiometers and force sensors) measure the biomechanics of the arm. Using this data, limb movements, motor tasks and several postures can be assessed under different mechanical conditions.

Maxon Motor EC 45 Flat continuous current have been selected as actuation device, which is a very light, small DC motor without brushes that adapts to orthotic applications. In order to match the speed and the torque of the DC motor to the application requirements, a gearbox was necessary for the system. This was done via a harmonic drive. In particular, the drive selected for the application was the HDF-014-100-2A. The actuator system configured in this way can apply a maximum torque of 8 N.m.

The exoskeleton is controlled following an impedance control strategy which includes a position feedback loop. The goal of the controller is to modify the apparent Human–Robot impedance.

NeuroLab has a real-time target computer system (xPC Target) to control the exoskeleton. Control is implemented using the MatLab Real-Time suite by

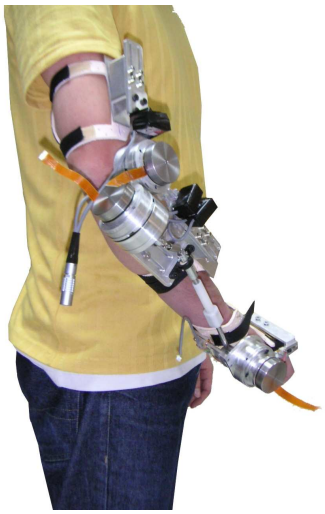

Figure 2: Upper limb robotic exoskeleton. The device spans the human elbow and wrist joints.

MathWorks, Inc. This environment provides mathematical libraries making it easy to implement control strategies. The algorithm can be coded in C-language and compiled in an executable application.

2.2 EMG Module

Measurements supplied by electromyography (EMG) provide a valuable information regarding physiology and muscle activation patterns. This information describes the forces that will be generated by the muscles and the timing patterns of the motor commands. It can be also used to assess the response of the human motor system to external dynamic conditions or perturbations.

The EMG module allows for acquisition of data on four muscle groups. Since the EMG signal is very small ($50\mu V$- $5mV$), it may be affected by interference from other biological and environmental noise sources, e.g. movement artifacts, electric noise and muscle noise among others, (DeLuca, 1997). In order to minimise the effects of noise, the EMG module amplifies and filters the raw EMG signals before they are digitalized.

Additionally, a battery is used to power the EMG acquisition module in order to reduce 50 Hz harmonics (power-line noise). In the light of international safety regulations regarding electronic devices connected to human beings, several topics were addressed in connection with electric isolation of the EMG module. In particular, galvanic isolation using a wide-band, unity-gain isolation amplifier was implemented in the EMG Module.

2.3 Biomechanical Monitoring Module

This module uses inertial sensors to acquire kinematic and kinetic information on the system. This was the first smart module developed, so further details are given. The modular approach of NeuroLab enables the use of the different devices in many different applications.

The Biomechanical monitoring comprises the following logical components:

- *The controller.* This uses a TMS320F2812 DSP Texas Instrument, which is powerful enough to run all the signal processing algorithms. The clock frequency is up to 150 MHz. The DSP includes several communication interfaces.
- *The Sensor Set.* Two inertial sensors can be connected to the controller using a SPI interface. Each sensor consists of a set of three gyroscopes, three accelerometers and three orthogonally-mounted magnetometers (see figure 3).
- *The Data Logging block.* An ATMega32 microcontroller is used to manage a SD card. The microcontroller implements a FAT16 file system. Using basic commands, the controller can store the data of the sensors in a non-volatile memory.
- *Communication block.* The communication block includes four different communication interfaces for networks. The first is the SPI, which is embedded in the DSP and is used to communicate with the sensors and the data logger. The second block comprises a Bluetooth module for wireless communication with a base station for real-time monitoring. The third interface is a CAN port provided by the DSP. It can be attached to the NeuroLab BioNET using simple CAN drivers. The last interface is an USB port for data transfer and real-time monitoring. The Biomechanical Monitoring Module can be connected to the central platform (Figure 1) using Bluetooth or USB.
- *Power supply.* This is based on an Ion-Lithium battery with a capacity of 900 mAh. The module uses the USB connection to charge this battery.

2.4 EEG Monitoring Module

EEG can be used to study movement planning and to control wearable robots, (Wolpaw et al., 2002). The development of portable EEG module for research purposes is not a trivial task. Noisy environments and movement artifacts affect the quality of the EEG signals. Moreover, EEG signal processing techniques are usually complex and require a powerful platform

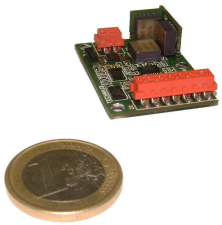

Figure 3: Inertial sensor that include 3 gyroscopes, 3 accelerometers and 3 magnetometers.

to execute these algorithms. Even relatively simple algorithms can require a powerful platform as usually the EEG is acquired using arrays with more than 10 electrodes.

Early developments of EEG Monitoring Module have been based on a PC/104 computer platform. A special amplification board was designed following the safety requirements for devices directly connected to the human body. This board is aimed to amplify 16 channels with variable gain amplifiers and a bandwidth that spans from 0.1 to 80 Hz. The board also has a notch filter centered on 50 Hz to compensate for 50 Hz line noise. This board is connected to the PC/104 through a data acquisition board. The acquisition of the EEG is aimed to use a 512 Hz frequency, minimizing distortion due to acquisition. The CAN connectivity is achieved through the use of an external CAN board attached to the PC/104 platform.

The EEG monitoring module can provide EEG logging through the use of a hard drive connected to the PC/104 board. Other services of the module comprises the identification of patterns related to the movement planning and imagination to be used as a control signal to the robot. This module also uses the xPC target platform (from MatLab, Inc.) used to control the robotic exoskeleton. This software platform was chosen due to the mathematical tools already implemented and for its flexibility.

2.5 BioNET

The purpose of NeuroLab is to integrate several different devices in order to study Human-Robot interaction (both cognitive and physical) and the human neuromotor system using non-invasive techniques. In view of the wide range of profiles and applications of the system, a distributed modular approach was selected to implement the proposed concepts.

A network of smart devices was identified as the optimum solution to achieve the goal. The network is called BioNET and is CAN-based. The work package includes the development of several network protocols including service discovery, synchronisation, and priority management mechanisms among others. A table describing the device, its services and its parameters, is stored in the device itself. This concept is similar to TEDS, used in IEEE P1451.3.

Current research efforts are aimed to develop the monitoring and rehabilitation profiles for the network.

3 EXPERIMENTAL METHODS

Many studies have approximated the dynamic behaviour of human body segments such as upper and lower limbs and their joints as a mechanical impedance, (Hogan, 1984), (Dolan et al., 1993), (Tsuji et al., 1995), (Zhang and Rymer, 1997). The mechanical impedance in this context can be defined as the dynamic relation between small force and position variations.

Using the platform described, NeuroLab, a set of experiments are being conducted to estimate the properties of the human elbow joint impedance and to determine viscoelasticity–EMG relationships. This is supported for the fact that the EMG information can be also used to assess the response of the human motor system to external dynamic conditions or perturbations. In literature, several studies have used electromyography in biomechanical analysis and human joint torque estimation, (Clancy and Hogan, 1997).

To start with experiments on this topic, a system for measuring arm impedance is required. Thus, the robotic exoskeleton is set up as a mechanical measurement system to get reference measurements for correlation with EMG–signals. The robotic device applies torque perturbations to the subject's arm. Sensors of robotic device deliver the necessary data to compute the mechanical impedance.

The human arm and their articulations could be modelled as a mechanical impedance in terms of inertia (I), viscosity (B) and elastic stiffness (K), using a linear second order model (Equation 1), (Dolan et al., 1993).

The parameters in the model that represent the dynamic behaviour of the human neuromusculoskeletal system are non-linear and vary highly depending on factors such as torque bias and posture, (Kearney and Hunter, 1990). Therefore, experiments that fit the data to an impedance of a second-order linear-model must specify an operating point. The operating point consists of constant posture, constant force, and non-fatiguing contractions over a particular task. The ensemble of linear models estimated over a range of operating conditions may be thought of as defining a quasistatic model of arm dynamics and can be defined by the following linear equation:

$$F(t) = I\frac{\partial^2 X(t)}{\partial^2 t} + B(\delta)\frac{\partial X(t)}{\partial t} + K(\delta)X(t) \quad (1)$$

where F(t) and X(t) represent the force and the displacement, respectively, and δ defines the operating point of the system.

According to Equation 1, inertial component remain constant and viscous and stiffness components (B and K) are functions.

3.1 Protocol

Four healthy subjects participated in the experiments. Subjects were instrumented with surface EMG electrodes according to the SENIAM recommendations, (http://www.seniam.org). Two muscles agonist-antagonist involved in the elbow joint movement were measured: the flexor (biceps brachii) and extensor (triceps brachii long head) muscles.

Subjects wore a robotic exoskeleton on its right arm allowing elbow flexion and extension in the vertical plane. Shaft joint on the device was aligned with subject elbow joint, and the device was attached to its upper arm and forearm. The elbow was flexed making an angle of 90 degrees.

The trials consisted of an intentional postural task. In each trial a pseudo-random torque perturbation was applied directly to arm and forearm by the upper limb powered exoskeleton.

The duration of each trial was 10 seconds. The subject was asked to maintain the position while the mechanical perturbation was applied. Three repetitions were chosen for each experimental session and the signals were sampled at 1 kHz for biomechanical variables (kinetics and kinematics) and for the electromyographic signals (sEMG).

3.2 Data Analysis

Kinematics and kinetics data were filtered using a 4^{th} order Butterworth low-pass filter with a cut-off frequency of 10 Hz.

The toolbox *System Identification Toolbox* of Matlab have been used to accomplish the modelling process. In particular, the function *armax* was used to fits the parameters of the linear second-order model to the structure of ARMAX (*Auto-Regressive Moving Average with eXogenous inputs*), based on a prediction error method.

Surface EMG signals were rectified (full-wave) and the envelope of the signals extracted using a low-pass filter with a cut-off frequency of 10 Hz. A 5^{th} order Butterworth filter for this purpose was adopted. The RMS (*Root Mean Square*) value was used as index to quantify amplitude of EMG signals as defined by Equation 2. In the correlation procedure, the RMS value was the considered variable.

$$RMS = \sqrt{\frac{1}{n}\sum_{i=1}^{n} x_i^2} \quad (2)$$

where x_i is value voltage in i^{th} sample, n is number of samples in segment.

The RMS value represent the root square of the mean power of the EMG signal for a specific time period.

The linear equation that relates EMG amplitude and the variation of angular position to the variation in the generated torque by the joint might be modelled as Equation 3.

$$\Delta T = I \cdot \Delta\ddot{\theta} + B(\hat{s}_e, \hat{s}_f) \cdot \Delta\dot{\theta} + K(\hat{s}_e, \hat{s}_f) \cdot \Delta\theta \quad (3)$$

where $\hat{s}_e$ and $\hat{s}_f$ are the amplitude estimation of EMG signals for muscles flexor and extensor, respectively. $\Delta\theta$ is the variation in angular position and ΔT is the variation of torque generated by the joint.

3.3 Results

Figure 4 represents the estimated parameters of mechanical impedance and its mean and standard deviation for one subject. Each sample of x-axis in figure represents a trial, in order to evaluate the repeatability. Each trial magnitude was the mean of estimated values of a set of two-second windows of the recorded data.

Several quantitative information have been reported in literature mechanical impedance of human elbow joint, (Zhang and Rymer, 1997). The parameters obtained in the experiments carried out are similar to those values.

Correlating EMG–signals with the computed mechanical impedance can be considered as a function of EMG-activity, according to Equation 3. Currently, this functional relation has being found out.

4 CONCLUSIONS AND FUTURE WORKS

NeuroLab is based on an upper limb robotic exoskeleton with which specific force profiles can be applied. It establish a real multimodal interaction between the user and the powered exoskeleton through a set of

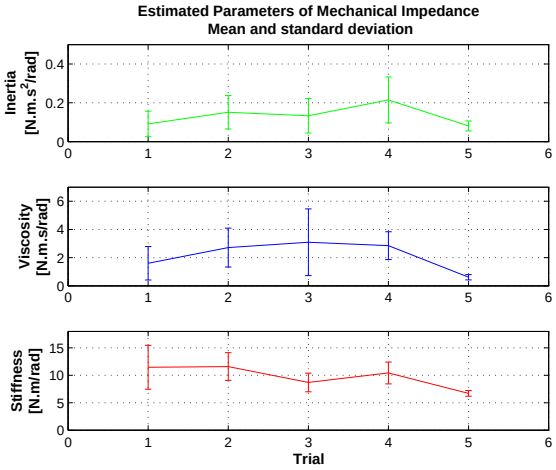

Figure 4: Mean and standard deviation of estimated parameters, for inertia (top), viscosity (middle) and stiffness (bottom).

smart devices. With the networked platform, several different experiments can be configured to explore the human neuromotor system and to study the human movement.

In the platform, there are independent devices that communicate with each other, based on a Personal Area Network (PAN) concept. Each device has a specific function and helps to address the overall goal of the platform.

The system can be used in a wide range of applications. The results obtained with NeuroLab provide valuable information for robotics, modelling of the human motor system, rehabilitation programs in health care, training programs and biomechanics.

Lately, several studies are being conducted with NeuroLab. The experiments presented in the paper aim to estimate the properties of the human elbow joint impedance and to obtain the viscoelasticity–EMG relationships. System identification is achieved by perturbation analysis, using an external perturbation application that produces changes in the dynamics of system and EMG patterns.

The presented method to estimate the mechanical impedance of the human arm is suitable to be used in a clinical setting, e.g., with people with stroke undergoing robotic rehabilitation for a paralyzed arm, (Palazzolo et al., 2007).

Future work includes a quantitative analysis, processing and correlation of the acquired signals (bioelectric and biomechanical signals), based in Equation 3. Currently the EEG Monitoring Module is being validated and integrated in the system presented.

REFERENCES

Clancy, E. A. and Hogan, N. (1997). Relating agonist-antagonist electromyograms to joint torque during isometric, quasi-isotonic, nonfatiguing contractions. *IEEE Transactions On Biomedical Engineering*, 44(10):1024–1028.

DeLuca, C. J. (1997). The use of surface electromyography in biomechanics. *Journal of Applied Biomechanics*, 13(2):135–163.

Dolan, J. M., Friedman, M. B., and Nagurka, M. L. (1993). Dynamic and loaded impedance components in the maintenance of human arm posture. *IEEE Transactions on Systems, Man and Cybernetics*, 23(3):698–709.

Hogan, N. (1984). Adaptive control of mechanical impedance by coactivation of antagonist muscles. *IEEE Transactions On Automatic Control*, 29(8):681–690.

Kearney, R. E. and Hunter, I. W. (1990). System identification of human joint dynamics. *Critical Reviews on Biomedical Engineering*, 18:55–87.

Krebs, H. I., Hogan, N., Aisen, M. L., and Volpe, B. T. (1998). Robot-aided neurorehabilitation. *IEEE Transaction On Rehabilitation Engineering*, 6(1):75–87.

Palazzolo, J. J., Ferraro, M., Krebs, H. I., , Lynch, D., Volpe, B. T., and Hogan, N. (2007). Stochastic estimation of arm mechanical impedance during robotic stroke rehabilitation. *IEEE Transaction On Neural Systems and Rehabilitation Engineering*, 15(1):94–103.

Pfurtscheller, G., Muller, G., and Korisek, G. (2002). Mental activity hand orthosis control using the eeg: a case study. *Rehabilitation*, 41(1):48–52.

Rocon, E., Belda-Lois, J. M., Ruiz, A. F., Manto, M., and Pons, J. L. (2007). Design and validation of a rehabilitation robotic exoskeleton for tremor assessment and suppression. *IEEE Transactions on Neural Systems and Rehabilitation Engineering*, 15(3):367–378.

Rosen, J., Brand, M., Fuchs, M., and Arcan, M. (2001). A myosignal-based powered exoskeleton system. *IEEE Transaction On Systems, Man and Cybernetics - Part A: Systems and Humans*, 31(3):210–222.

Ruiz, A. F., Forner-Cordero, A., Rocon, E., and Pons, J. L. (2006). Exoskeletons for rehabilitation and motor control. In *Proceedings of the IEEE International Conference on Biomedical Robotics and Biomechatronics (BioRob)*.

Tsuji, T., Morasso, P. G., and Ito, K. (1995). Human hand impedance characteristics during maintained posture. *Byological Cybernetics*, 74(1):475–485.

Wolpaw, J. R., Birbaumer, N., McFarland, D. J., Pfurtscheller, G., and Vaughan, T. M. (2002). Brain-computer interfaces for communication and control. *Clinical Neurophysiology*, 113:767–791.

Zhang, L. Q. and Rymer, W. Z. (1997). Simultaneous and nonlinear identification of mechanical and reflex properties of human elbow joint muscles. *IEEE Transactions On Biomedical Engineering*, 44(12):1192–1209.

MECHATRONIC SYSTEM FOR TRANSURETHRAL RESECTION TRAINING

Ángel Asensio, Alejandro Ibarz, Jose Ignacio Artigas, Álvaro Marco
Javier Casas and Roberto Casas
Instituto de Investigación en Ingeniería de Aragón, Universidad de Zaragoza, María de Luna 1, Zaragoza, España
{aasensio,aibarz, jiartigas, amarco, rcasas}@unizar.es

Keywords: Transurethral resection, TUR, endoscopic operation.

Abstract: Training the residents who start with endoscopic operations remains a challenge. This paper describes an electromechanical system developed for learning the transurethral resection (TUR) technique. This system can be easily set and cleared up in a classroom, and consists of a supervisor's workbench with a wireless sensing device, connected to several trainees' workbenches with motorised devices. These devices have a resectoscope mounted on an electromechanical structure that is able to reproduce all the movements of an actual endoscopic operation of the prostate.

1 INTRODUCTION

Transurethral resection (TUR) is an endoscopic surgical technique that makes it possible to extract tissue from the prostate in mitigating or corrective operations. It is performed by means of a resectoscope, consisting of a thin cannula that includes an endoscopic lens system and contains a tiny wire loop acting as an electro-scalpel, and operated from the exterior.

Nowadays, video-surgery has simplified TUR training, becoming a common practice among many urologists. However, no urologist hesitates to consider learning this technique difficult and time-consuming. Mere vision of the moving endoscopic image is not enough to acquire the reflexes, manual skill, and mental agility necessary to cope with the recurring occasions in which only solid practical experience will make it possible to handle the situation, and conclude the operation successfully (Pycha, 2003).

Traditional training for novel surgeons is carried out by first explaining the techniques with endoscopic images, to later begin performing very simple operations, directly in the operating theatre.

Work has been done on support for training in endoscopic techniques, and there have also been efforts to devise manipulators for motorised operations guided by the surgeon (Kerfoot, 2004; Gettman, 2003; Katz, 2003; Ottensmeyer, 2000; Ballaro, 1999; Gomes, 1999). However, these systems have certain problems, such as lack of tactile feedback, and their high cost for generalised use in training. Their main objective is to automate operations, not to perform exact imitations of the movements of a surgeon. Our system achieves a great precise reproduction of the movements of an expert surgeon, at a much lower cost.

Another difference with the mentioned line of work is that our proposal aims at low-cost robot systems, specific for this operation, capable of capturing the movements of the resectoscope and reproducing them both in real time and recorded.

For this, we have devised an easy to set and clear up lecture room, practical for use at hospitals. The room has a sensing workbench connected to a computer, and several motor workbenches linked by Bluetooth. All these workbenches are able of reproducing the movements of a hand at the degrees of freedom of the resectoscope. A video monitor shows images of an operation. The sensing workbench senses the movements performed upon it, and the motor workbenches are able of reproducing these movements.

The solution we present in this paper is cost-effective, and has been successfully tested by experienced surgeons. First we detail the specific goals pointed out by the users, which guided us in the design of the solution presented; Next, we analyze in depth each block of the final system.

2 SYSTEM GOALS

The aim of our system is to aid learning of a complex technique of endoscopic surgery, transurethral resection, in order to improve the skill of surgeons and reduce risks for patients. We try to offer a lecture room that permits training in techniques as they are currently performed, in such a way that its structure allows inclusion of more data, and with feasible installation in hospitals (easily set and cleared up in multipurpose halls).

Thanks to the system's modular structure, several different teaching modes are possible:

1. Real time teaching mode: The trainer operates the sensing workbench and movements are repeated in the hands of trainees by means of the motor workbenches. The trainer's explanations can be underlined by videos played on the computer.
2. Recording mode: The trainer watches an endoscopic video on the computer, and simultaneously performs the corresponding movements with the sensing workbench. The movement pattern is stored in the computer, and a video of the operation with embedded information on positions is generated. This video will be used later to control motor workbenches without the presence of the trainer.
3. Recorded teaching mode (without the presence of the trainer): The computer plays a pre-recorded video that controls the motor workbenches.
4. Trainee assessment without trainer: A video is played and trainee operates the sensing workbench; movements are stored in the control board of the sensing workbench. Once the test has ended, data are sent to the trainer's computer, and they are checked against the movement pattern of the expert surgeon.

The technical requirements we have had to deal with are the following:

– The workbenches must reproduce movements with the same degrees of freedom that the surgeon has during an actual operation. The initial hypothesis is that the urinary tract sphincter is fixed in space, which leads us five degrees of freedom. The correctness of this hypothesis and the validation of the movement replicator have been checked during the research actions performed by the group.

– Another very important requirement is synchronization of the endoscopic video playing with the movements of the resectoscope.

– To ensure portability, we envisage a radiofrequency workbench data communications structure using Bluetooth (Anastasi, 2003). Bluetooth chips available on the market managed from a microcontroller based system have been used. Both the hardware and the firmware have been original developments aimed at the present final application.

– One last goal is to allow collection of actual movements data in the operating theatre. In this scenario it is not possible to modify the instruments available to the surgeon, nor interfere with his movements. To achieve this, we propose a new method for sensing and capture of the movement of the resectoscope in the operating theatre, based on ultrasound.

3 DESCRIPTION OF THE ENVIRONMENT

3.1 Basic Scenarios

Next we briefly describe the structure of a possible lecture room. It should be pointed out that some systems share certain common blocks, so these will be described only once.

3.1.1 Trainer's Workbench

Its role is that of a general coordinator, and it comprises several clearly distinct subsystems (Figure 1).

The resectoscope or instrument to be used by the medical personnel is mounted on a mechanical system that allows mobility as if an operation were being performed. For this, three turns (coordinate axes) and two sweeps (cannula and resection loop) are allowed. The trainer will introduce the sequence of movements using this workbench. A set of position encoders capture kinetics directly, or by means of the corresponding transmission ratios.

A digital system based on a Field Programmable Gate Array (FPGA) has been developed for data collection tasks, management of communications, motor device control and memory management. Previous developments were based on microcontroller solutions, but the large number of inputs-outputs and the need for concurrence recommended migration to programmable logic devices. The use of FPGA allows for modular and flexible design, which eases the integration of the various subsystems developed.

A Bluetooth device in this workbench acts as a master of the wireless communications system. It is possible to control a complete network, commanding the various devices and modes, and at the same time the various flows of information.

Acting as a central server, the trainer's workbench relies on computer equipment offering various functions: It controls reproduction of the TUR operation video; it allows storage of movement patterns for later analysis or repetition; and it manages communications and state of the devices in the lecture room by means of Bluetooth linking via electronic system.

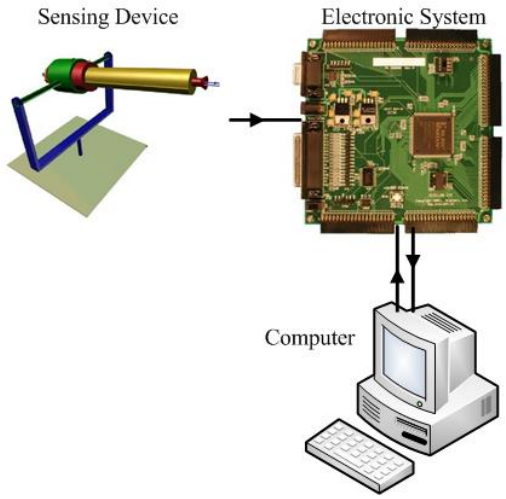

Figure 1: Trainer's workbench.

3.1.2 Trainee's Workbench

The mechanical structure is similar to that of the trainer's workbench (Figure 2). It includes the electromechanical devices allowing reproduction of movements. The student holds the device and feels the movement to be performed. The device retains the position encoders, making available a process of auto-calibration without the need of supervision by the user. A Bluetooth device acts as a slave in the network managed by the trainer's workbench.

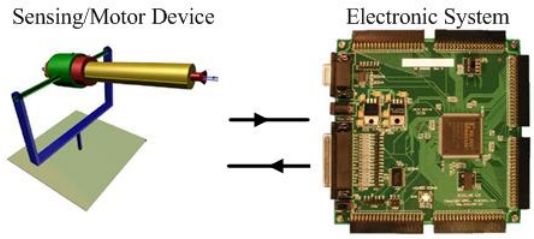

Figure 2: Trainee's workbench.

3.1.3 Installation in Operating Theatre

Figure 3 shows the block diagram of the installation in operating theatre. Encoder-based position capture is not possible in the operating theatre, since the set of instruments cannot be modified (figure 4). We have therefore developed a novel positioning technique based on ultrasound (US) pulses, with the aim of applying it to the capture of the movements performed by the surgeon on the resectoscope in the operating theatre. In this way, it will be possible to document fragments of actual operations with the video information, movements, and other parameters that may be considered relevant. We should point out that the training video is obtained by an endoscopic camera during the operation. Later on, and as a previous step to its use in the training system, it is processed by the computer system.

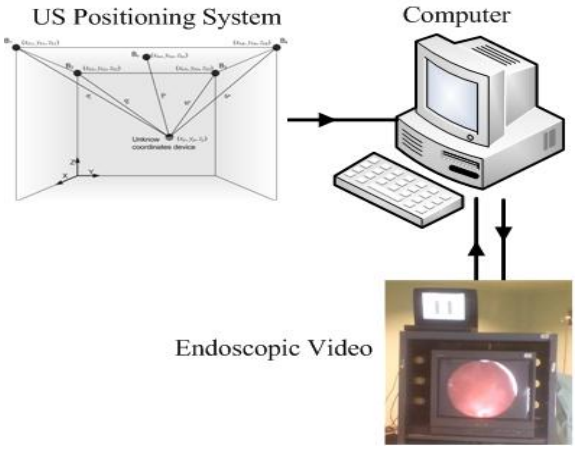

Figure 3: Installation in operating theatre.

3.2 Mechatronic System

Initially, the typical movement of the resectoscope in an operation was studied. Considering the results, to express the movement as parameters, the following hypothesis is adopted: "The point of the resectoscope oppressed by the sphincter is considered still, and this point does not vary throughout the operation".

To all practical effects, it is considered as the origin of the coordinates of the mechanical system. On the basis of this hypothesis, the conclusion reached is the need to design a mechanical system allowing three angular movements, one forward movement for the cannula, another for the cutting-loop, and two for the switches of irrigation and coagulation. To sum up, seven coordinates are used to define the state of the device at a given moment. Four of them reflect the point in space where the end of the resectoscope is, another the state of the cutting loop, and the remainder refer to the state of the switches the resectoscope is equipped with (generally pedal-operated).

According to the explanation offered, the mechanical system should allow the movements detailed in Figure 4.

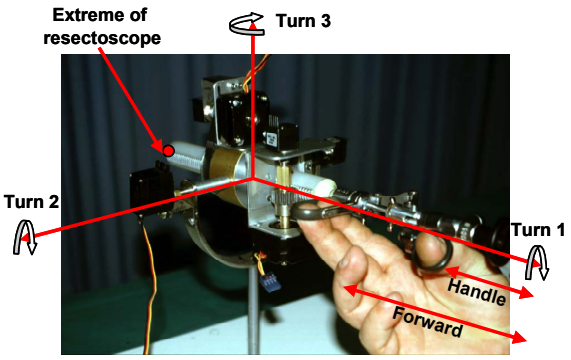

Figure 4: Kinetic diagram of the resectoscope.

The final system has been the result of several different prototypes. At the moment of designing the mechanical system, we have two different kinds of devices:

Sensing device: Conveniently equipped with encoders in order to capture the movements performed with it.

Motor device: Fitted with servo-motors to reproduce movement. In the design phase, this device is also equipped with sensing elements in order to carry out calibration and performance measurements.

The present design is capable of completely valid mobility. The sensing workbench can most realistically imitate any type of operation. Both the sensing and motor workbenches share a similar design, so that they may or may not include motors and sensors, that they may have the required functionality on the basis of a single development. The mechanical similarity between them likewise eases the generation of movements from the stored kinematics.

Various alternatives have been checked for movement generation, among which we could feature step-motors and servo-motors. The latter presents suitable speed-torque characteristic curves, which together with their simple handling have made them the chosen solution. Different kinds of movement must be generated, angular for the three coordinate turns, and longitudinal for the cannula and resection movements. In order to achieve linear movements, mechanical transmission chains have been designed, based on the turning of the servo-motor.

The measurement of the three angular movements is performed with angular encoders. The linear movements are indirectly measured from the electromechanical rotation system. In this way we can use the same kind of sensor for the different movements, with all the advantages of uniformity and simplicity. Specifically, the encoder chosen will be of the digital type and incremental.

Once the mechatronic system implemented, the performance, both kinetic (speed, accelerations, movement ranges and sensitivity) and dynamic (torque) of the system was tested. For this, automated tests have been devised to check the step and ramp response of each motor device.

Finally, several tests were carried out by the medical team, with the goal of simulating the different kinds of movements that actual operations might require. Two models were simulated: cystoscopy (inspection) and resection (operation), as well as a mixed model including various types of movement. On the basis of these tests, we can state that our system correctly replicates a model operation.

3.3 Synchronization

In the system, various temporal distortions may appear, which can generically be grouped as two different sets of problems:

– Data delay: An ideal design in the FPGA will make this negligible in the context of the time intervals operated with.

– Loss of synchronization and regularity between video frames and mechanical positions: Critical aspect. The computers might be unable to send the movement data in a totally regular and predictable way while it reproduces a video or is handling other processes.

Different alternatives have been checked: synchronization by means of video subtitles, real-time operative systems, and modulation in audio channel.

The solution finally adopted is based on use of the video's audio channel. To include the digital information of positions on an analog audio signal, Manchester encoding has been chosen. It has been decided to encode and send the sampling number corresponding to each video frame, rather than all the data for each frame. A Hamming code with distance 4 is applied, to minimize environmental noise. This strategy will make it possible to detect up to three bit errors, and correct up to one bit. The frame under the Hamming format is Manchester encoded and modulated upon the audio channel. Both processes have been carried out with Matlab. The final application generates an audio file containing the sampling numbers, spaced the exact

time needed. This file is included in the video, so that we have a video with exact time marks indicating a sampling number. In normal use, an audio channel carries the frame number we are at, and the other channel may include trainer's comments.

Before the use of a trainee's workbench, a massive download of positions in each motor system is performed from the computer to the local FPGA. During the video playing, the time marks are extracted and the local memory is searched for the associated positions.

3.4 Computer System

The computer system presents two layers. One of them is opaque to a certain degree for the end user, and collects the data of the different blocks and integrates them. Also, it calculates the kinematics of the resectoscope during the operation, using the obtained data from the ultrasound location system. Finally, it generates the movement references for the device, synchronized with the endoscopic video.

The computer system has another aspect, intended for the end user in the training context. A simple and friendly user interface is offered for interaction in the lecture room (Figure 5). It includes a video player and a manager of the various operation modes that the trainer may request. The more tedious tasks, such as Bluetooth node management and processes with data files have been completely automated.

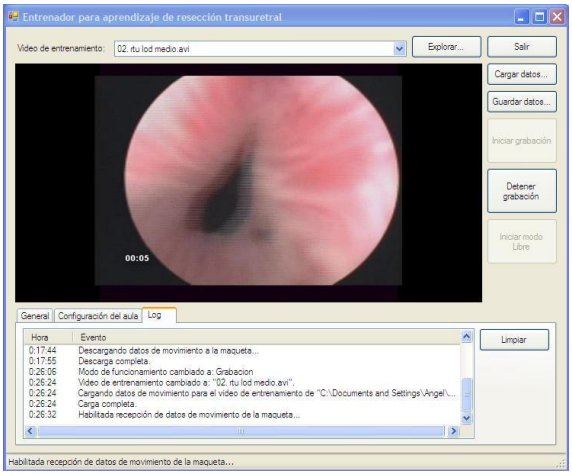

Figure 5: Computer system. User interface.

4 OPERATING THEATRE POSITIONING

It is interesting to see how different data are obtained in the operating theatre, such as the endoscopic video of the operation and the actual in situ trajectory followed by the resectoscope. Obtaining the endoscopic video is possible with commercial equipment, so we will concentrate on the analysis of the problems regarding highly accurate location. The different alternatives allowing a sufficiently exact positioning were analyzed, with the main focus on optical, radiofrequency and ultrasound solutions. Several aspects, such as economy and environmental constraints pointed to ultrasound positioning as the ideal method.

Through high precision positioning by ultrasound waves, it is possible to locate an object within a given volume with a tiny error margin, simply and quickly, without any necessary physical contact with the point to be referenced (Fukuju, 2003; Casas, 2004; Mahajan, 2001; Prigge, 2000). The initial idea was to obtain a system allowing capture of the position of the resectoscope during an actual operation in the operating theatre; the system should therefore have very restrictive features.

In the case of our application, there are certain key aspects defining the location system, due to the characteristics of work in an operating theatre.

The range of the system must agree with the dimensions of the operating theatre (in our case, up to 3.5 metres).

Given the need for a precise reading of the kinematics and of the position of the resectoscope, the positioning refresh rate must be as high as possible. It has been possible to obtain up to twenty references per second.

In order to achieve millimetric errors in the position of the resectoscope, it was necessary to analyze other factors of the design: the possibility of background noise, disadjustment of probes, environmental factors (temperature and humidity), and reflected ultrasound waves due to reflecting surfaces.

The probes of the emitter modules (Figure 6) are joined to the resectoscope in fixed positions. Three probes are usually necessary in order to later infer the position and direction of the instrument from them.

The receiving probes will be attached to the ceiling of the operating theatre in positions with known coordinates, with the necessary precision to later give references for the emitting probes in the

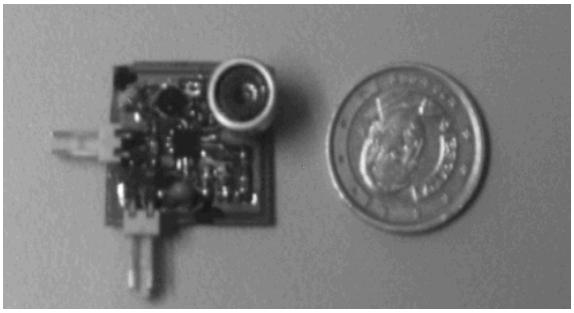

Figure 6: Emitter probe.

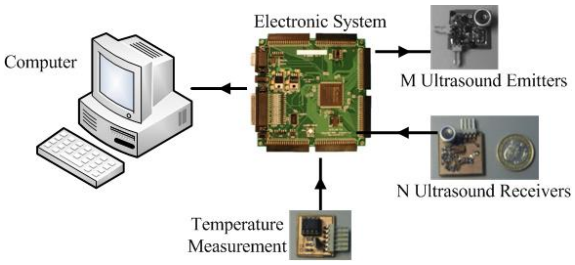

Figure 7: Precision positioning block diagram.

space. A redundant number of probes make possible to minimize the effects of occlusions.

The system includes the blocks shown in figure 7.

The control system will send a signal to the corresponding emitter modules, to generate the ultrasound pulse train, and simultaneously the time-of-flight of the ultrasound waves to the receiver modules will be measured. During the time-of-flight of the ultrasound pulses a measurement of the temperature will be obtained, to compensate the data. The features and pattern of the pulse trains generated are critical for the system. Their generation is based on a self-interference strategy, in which the optimum phase and counter-phase periods have been obtained analytically and empirically. In the receiver, filtering is an equally delicate process, articulated around a second order Rauch filter followed by a high speed comparator.

The receiver modules will send the received signal, filtered and conditioned, to the FPGA, which will capture and process the data in order to calculate the times-of-flight of each emitter-receiver pair, as well as reliability indicators of each measurement for their later processing. Once all of the data have been processed, it will send all the information obtained to the computer together with the temperature measurement. The computer will calculate the distances between each of the emitter-receiver pair.

After obtaining the distances between emitter and receiver probes, the coordinates of the emitter probes are calculated by an algebra resolution

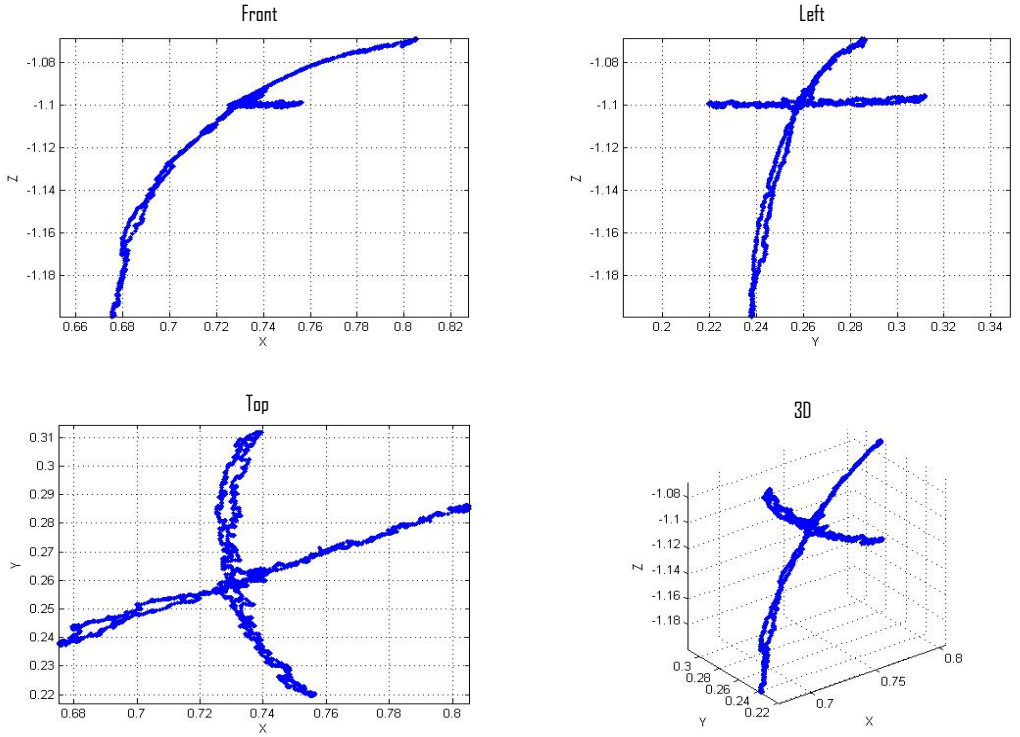

Figure 8: Positions of the end of the resectoscope.

method (Casas, 2004) and a solution filtering algorithm based on the least median of squares (Casas, 2006). Once the positions of the emitter probes have been obtained, the trajectory of the resectoscope is obtained as well.

In order to verify the system, an experiment set-up has been designed with the motor workbench managed by the computer system in auto-calibration mode. Figure 8 illustrates the results obtained. It shows the position of an emitter probe located at the end of the resectoscope. An emitter transducer is attached to the mock up, which moves using a predefined pattern. With three receivers, the results are very accurate (few millimetres), and even the bounces and oscillations of the mechanical system itself can be detected.

5 CONCLUSIONS

Training surgery residents who start with endoscopic operations remain a challenge. This paper has described an electromechanical system developed for learning the TUR technique. It consists of a trainer's workbench with a wireless sensing device connected to several trainees' workbenches with motorised devices. These devices have a resectoscope mounted on an electromechanical structure able to reproduce all the movements of an actual endoscopic operation.

The system has several operating modes that will make it possible to:

– Reproduce the movements of an expert surgeon in the hand of the trainee.

– Reproduce the pre-recorded movements of an actual operation in the hand of the trainee.

– Assess the level reached by the student before participation in any operations or in solving problems requiring a certain degree of experience.

As a complement, a millimetrically accurate, ultrasound-based positioning system has been developed. This will be mounted on a resectoscope in order to capture the movements performed in an real operation. The management software of the training room allows easy integration of these data with the endoscopic video, to rely on an adequate operations database.

What remains is to assess this tool in the practical conditions of training urology residents in the use of medical equipment, which will doubtless offer most interesting data regarding the use or need for modifications of the global system.

ACKNOWLEDGEMENTS

This work has been partially supported by the Spanish Ministry of Science and Technology under CICYT project numbers TIC2003-07766 and TIN2006-15617-C03-02

REFERENCES

Anastasi, G., Bandelloni, R., Conti, M., Delmastro, F., Gregori, E. Mainetto, G., 2003. Experimenting an Indoor Bluetooth-based Positioning Service. ICDCSW'03, Proc. of the 23rd Int. Conf. on Distributed Computing Systems Workshops, 480-483.

Ballaro, A., Briggs, T., Garcia-Montes, F., MacDonald, D., Emberton, M., Mundy, A.R., 1999. A computer generated interactive transurethral prostatic resection simulator. The Journal of Urology, 162 (5), 1633-1635.

Casas, R., 2004. BLUPS: Bluetooth and Ultrasounds Positioning System. Doctoral Dissertation, University of Zaragoza.

Casas, R., Marco, A., Guerrero, J.J., Falcó, J., 2006. Robust Estimator for Non-Line-of-Sight Error Mitigation in Indoor Localization. EURASIP J. Applied Signal Processing, vol. 2006, article ID 43429, 1–8.

Fukuju, Y., Minami, M., Morikawa, H., Aoyama, T., 2003. DOLPHIN: An Autonomous Indoor Positioning System in Ubiquitous Computing Environment. Proc. of the IEEE Workshop on Software Technologies for Future Embedded Systems, 53-56.

Gettman, M.T., Hoznek, A, Salomon, L, Katz, R, Borkowski, T, Antiphon, P, Lobontiu, A, Abbou, C.C., 2003. Laparoscopic radical prostatectomy: Description of the extraperitoneal approach using the Da Vinci robotic system. The Journal of Urology, 170 (2 Pt 1), 416-419.

Gomes, M.P.S.F., Barret, A.R.W., Timoney, A.G., Davies, B.L., 1999. A computer-assisted training/monitoring system for TURP structure and design. IEEE Trans. Information Technology in Biomedicine, 3 (4), 242-251.

Katz, R, Nadu, A, Olsson, L.E., Hoznek, A, De La Taille, A, Salomon, L, Abbou, C.E., 2003. A simplified 5-step model for training laparoscopic urethrovesical anastomosis. The Journal of Urology, 169 (6), 2041-2044.

Kerfoot, B.P., Baker, H, Volkan, K, Church, P.A., Federman, D.D., Masser, B.A., De Wolf, W.E., 2004. Development of validated instrument to measure medical student learning in clinical urology: A step toward evidence based education. The Journal of Urology, 172 (1), 282-285.

Mahajan, A., Walworth, M., 2001. 3-D Position Sensing Using the Differences in the Time-of-Flights from a

Wave Source to Various Receivers. IEEE Trans. Robotics and Automation, 17 (1), 91-94.

Ottensmeyer, M., Ben-Ur, E., Salisbury, K., 2000. Input and Output for Surgical Simulation: Devices to Measure Tissue Properties in vivo and a Haptic Interface for Laparoscopic Simulators. MMVR'2000, Proc. of Medicine Meets Virtual Reality, IOS Press, 236-242.

Prigge, E., How, J., 2000. An Indoor Absolute Positioning System with No Line of Sight Restrictions a Building-Wide Coverage. ICRA'00, Proc. IEEE Int. Conf. on Robotics and Automation, 2, 1015-1022.

Pycha, A., Lodde, M., Lusuardi, L., Palermo, S., Signorello, D., Galantini, A., Mian, C., Hohenfellner, R., 2003. Teaching transurethral resection of the bladder: Still a challenge?. Urology, 62 (1), 46-48.

SYNCHRONIZATION ISSUES IN SURGICAL TRAINING

Álvaro Marco, Héctor Gracia, Ángel Asensio, Carlos Guallart
José Ignacio Artigas and Roberto Casas
Instituto de Investigación e Ingeniería de Aragón (TecnoDiscap group), Universidad de Zaragoza
María de Luna 1, Zaragoza, España +34976762627
amarco@unizar.es, hgracia@unizar.es, aasensio@unizar.es, carlosguallart@gmail.com
jiartigas@unizar.es, rcasas@unizar.es

Keywords: Synchronization, Training systems, Wireless sensor networks, Video.

Abstract: Surgical training systems allow novel surgeons to acquire the required skills to successfully carry out an operation without harming a real patient. These systems emulate the situation of a real operation, replicating the information gathered by sensors, movements of the surgeon, patient response, etc. All this information must be synchronized to provide an experience to the novel surgeon as closest to reality as possible. A special case of information synchronization is when using video images from the operation. In this paper, we analyze these synchronization issues —video, movements, sensors, etc. — and show a particular case that bring all together: an endoscopic video-surgery learning system.

1 INTRODUCTION

Endoscopy or tele-surgery, are medicine techniques that require a special skill from surgeons, as they have not a direct vision of what they are doing. Learning these techniques is supported by training systems that allow the surgeon to acquire the required skills to successfully carry out an operation without harming a patient.

(Ballaro et al. 1999) propound a training system where the surgeon manipulates synthetic images of a prostate. (Gomes et al. 1999) and (Kumar et al. 2002) improve it by providing a tactile feedback of the manipulation with an artificial prostate. (Chen and Marcus, 1998) offers also a feedback with an adapted resectoscope, analyzing the anatomic tissues virtually touched and generating the opposing force.

To properly emulate real situations where the surgeon can be involved, it is necessary to collect a lot of data from different sensors in real operations. Besides that, surgical training is often supported by use of pre-recorded video images (Gambadauro and Magos, 2007).

Although most of training systems offering haptic feedback use virtual simulations instead of real video, augmented reality systems combining these videos with graphics images systems provide a better simulation environment (Botden et al. 2007). Real videos can be used for training with motorized mock-ups driving surgeon's hands while playing video-images of the operation, reproducing the movements displayed in the video. Obviously, it is needed that the information used to drive them to a position is synchronized with the related frames of the video.

In this paper, we discuss some synchronization issues we have faced during the development of a video-surgery learning utility, which implements also a wireless-synchronization between classroom workbenches.

Next section outlines the learning utility and its synchronization issues, which are discussed in sections three and four. Section five details synchronization integration in the classroom and its operation, and finally, conclusions are presented.

2 VIDEO-SURGERY LEARNING TOOL

Our application consists on a classroom for training surgeons on prostatic surgery, whose system layout is presented in figure 1, and consists of several mock-ups. All the mock-ups are wireless connected, which allows an easy deployment and configuration of the classroom.

One of them —master—, includes a motion monitoring system which extracts all the movements the instructor surgeon makes; this one is called sensing mock-up. The others —slaves—, transmit these previously recorded movements to the practice surgeon so he can first learn the instructor movements and, after that, be evaluated by comparing his movements with the ones made by the instructor; this ones are called motor mock-up.

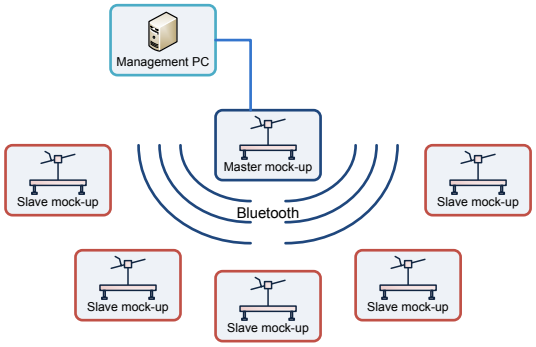

Figure 1: Video-surgery classroom. Master mock-up is video-synchronized and slave mock-ups are wireless-synchronized.

In order to get a real-like feedback, a big video display is used. At this moment, it seems clear there is heavy need of synchronization for this system, so video and captured instructor movements are correctly recorded and, this way, the learning and evaluation processes are synchronized with the video displayed.

It is also necessary to propagate this synchronization through the different motor mock-ups so all of them reproduce the movements at the same time the action is being taken at the video they see.

In short, we can group synchronization in two terms:

a) *Video-synchronization*, between the pre-recorded images and the surgeon's movements.
b) *Wireless-synchronization* between the mock-ups.

In the next sections, these synchronization issues are discussed in deep.

3 VIDEO SYNCHRONIZATION

In this case, a little misalignment between images and movement —below several milliseconds— is admissible, but playing must be fluid and without cuts that will hinder learning. If the training system core runs in a PC, a possibility for synchronizing surgeon's movements with video is to play the video in the PC, and to stream the movement information to the mock-up —through a serial port, by TCP/IP…—, but common multi-task Operating Systems (OS) can lead to cuts or undesired delays, so a real-time OS will be needed to do that.

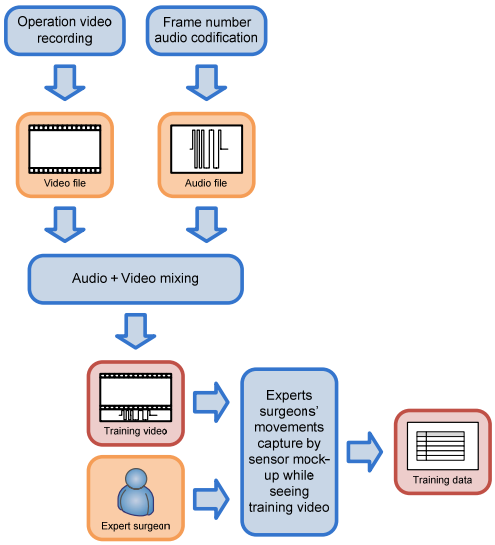

Figure 2: Block diagram for video synchronization. Expert surgeon's movements are captured and time-stamped with the corresponding frame number of the operation video.

To properly synchronize the video and the data, we decide to integrate the data directly into the video stream. AVI file formats allow integrating multiple streams into the same file (e.g. the video, audio, subtitles, chapters… of a movie). A possibility is to integrate a data stream with the movement information like a "subtitle", but we need also to extract that information and to stream it to the mock-ups, outside the PC, which can lead to an "asynchronous playing". The easiest way to avoid that is recurring to the audio channel. Audio is send by the OS to the sound card, and is synchronized with the video, so if we code our data in the audio track, the mock-ups can listen to the sound card and get the data synchronously with the video. Moreover, we could record the file in a DVD and play the video on a DVD player without the need of a PC.

In addition to that, there is another big issue about how to compound the operation information and the video images to get a synchronized training data set. If all the information of the operation is obtained "online", while the operation is carried out, as all the sensors must be synchronized, the training data set can be generated directly.

However, if the information related to the surgeon's movements cannot be real-time acquired,

an offline synchronization is required. The way to do this is that an experimented surgeon, while seeing the video images, replicates the movements over a sensor mock-up. That mock-up captures the movement information, and synchronizes it with the video.

Again, streaming the movement data to or from a PC can lead to a bad synchronization. The ideal solution would be to directly record the movement data on the audio track of the video, but this is not trivial. Fortunately, there is an easiest method. Strictly, we don't need to extract the data directly from the video, and it's enough by knowing the timestamp of the video, or the frame number.

For the movement data capture, we have coded the frame number of the video in the audio track, and the sensor mock-up listen to the video the expert surgeon is viewing. When the capture starts, the surgeon reproduces the movements displayed on the operation, and the mock-up store them together with the frame numbers listened. This way, we obtain a training data set where each frame of the video has synchronized information relative to the movements of the expert surgeon.

3.1 Frame Number Codification

To code the frame number into the audio track, we have generated an audio wave with a Manchester code, suitable for binary data transmissions. The data rate will be constrained by the audio characteristics and the sound card hardware. With a sampling frequency of 44.100 Hz, and using two samples to codify each bit (one sample for both high and low part of the wave), will give us a maximum data rate of 22.050 bps, but resulting sound wave cannot be correctly played by every sound card. A safer ratio of six samples per bit allows 7.350 bps, enough to codify more than 200 frame numbers per second with 32 bits resolution.

Frame number codes must be placed in the audio wave at the exact moment the frame is displayed in the video, which can be easily done with any video editing tool. To prevent errors when decoding the audio wave, a hamming code of distance three is also applied to the frame number.

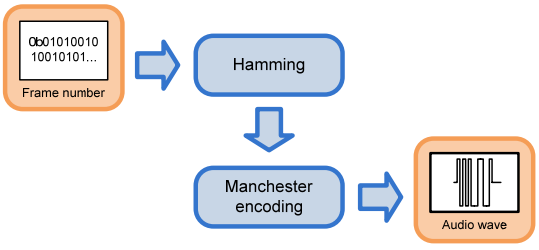

Figure 3: Frame number codification.

4 WIRELESS COMMUNICATION AND SYNCHRONIZATION

Once we have established synchronization between video and movements on the master mock-up, this synchronization must be propagated to the slave mock-ups, so we need that they are wireless synchronized. Every mock-up calculates its local time basing on its own oscillator, and these timings tend to diverge one from another. This is caused by the lack of precision on their oscillators, as there can be errors from 20 ppm to 100 ppm. The more time they keep running their clocks free, the bigger the misalignment will be.

This is a familiar matter on wireless sensor networks. Creating a common temporal reference using wireless communication capabilities has been widely studied keeping in mind the energy, cost and size limitations of the devices used in wireless sensor networks (Sivrikaya and Yener, 2004). The regular clock corrections needed to keep wireless networks synchronized are usually performed by exchanging reference messages time-stamped with the reference time. The more accurate that timestamp is the higher accuracy the synchronization achieves. Some protocols that achieve high synchronization accuracy with a reduced traffic load are the TMSP —Timing-sync Protocol for Sensor Networks— (Ganeriwal et al., 2003) or the FTSP —Flooding Time Synchronization Protocol— (Maróti et al., 2004). Their main advantage is that they can gain access to the MAC layer, so they can precisely timestamp messages when they pass through the lower layers.

According to the time-analysis performed by Maróti et al, the most problematic delays when transmitting messages over a wireless link are those from the send, receive and access processes (see figure 4). Besides bigger than propagation time, they are not deterministic, so they have a big influence on synchronization accuracy.

This way, methods which can access to MAC layer and precisely timestamp messages, such as TMSP or FTSP, can achieve a high accuracy. However, the use of standard wireless hardware such as ZigBee or Bluetooth —as in our case— to ease deployment, block access to lower layers, preventing from a precise timestamp.

Figure 4: Times on sending, accessing, propagating and receiving reference messages. Propagation time is negligible versus send, access or reception times.

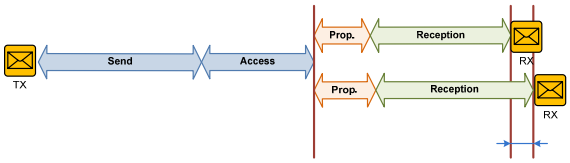

Figure 5: Misalignment on reception time. The non deterministic times on the sender side are eliminated.

In order to reduce as much as possible the uncertainties in this process, a receiver-receiver synchronization scheme is used. There is a common time reference for every member of the network, which is propagated through all the mock-ups using a broadcast message sent by the network coordinator (whose local hour is taken as the global time). After that, each mock-up receives this global hour and thus, can correct its own clock with the just received information.

With this receiver-receiver message synchronization method, medium access time variation is avoided (fig.5), so the biggest part of the non-deterministic error is eliminated. This method compares the local hours when the master mock-up and the different slaves receive the same message, so they can refer their local time to the master global time and hence, correct it. This is possible, because the uncertainty associated with the time involved in sending the message affects the same way both receivers, and so, doesn't have influence on the overall timing error. The propagation can be assumed as equal for the two nodes (because the distance is not significant enough to cause a measurable time difference in the propagation of a radio signal).

Thus, synchronize the clock of the mock-up i implies estimate and compensate its clock skew s_i and offset k_i. The most used procedure to perform these adjustments is broadly described in literature (Sivrikaya et al. 2004, Maróti et al. 2004, Elson et al. 2002, Cox et al. 2005). There is a reference clock which all the mock-ups will be synchronized to (t_r). A sync-point is defined as a pair of timestamps collected at the same time t_k in the reference node and in the node that want to be synchronized: $\{t_i^k, t_r^k\}$. Once each mock-up stores several sync-points at different instants, the offset (k_i*) and slope (s_i*) differences with the reference are calculated using linear regression:

$$s_i^* = \frac{\sum_k \left(t_r^k - \bar{t}_r\right)\left(t_i^k - \bar{t}_i\right)}{\sum_k \left(t_r^k - \bar{t}_r\right)^2}, \qquad (1)$$

$$k_i^* = \bar{t}_i - s_i^* \bar{t}_r .$$

This way, every node can estimate the global time (tr*) from its local clock:

$$t_r^* = \frac{t_i - k_i^*}{s_i^*}. \qquad (2)$$

Table 1 shows the results obtained when using the below described process to correct local times using Bluetooth and ZigBee technologies compared to other synchronization methods.

By these resynchronizations, clocks can be kept with a misalignment considerably lower than the precision required to cover our timing correction goals. The response time of the mock-up kinematics is considerably bigger than 1 ms, so achieving this misalignment between the different mock-up clocks is more than enough for this application.

Table 1: Misalignment on reception time. Results obtained by using different synchronization methods.

Sync Method	Average	Worst case
Sender – Receiver		
Zigbee (Motes-2.4GHz) *[Cox 2005]*	14.9 µs	61.0 µs
TPSN (Motes-916MHz) *[Ganeriwal 2003]*	16.9 µs	44.0 µs
FTSP (Motes-433MHz) *[Maróti 2004]*	1.4 µs	4.2 µs
Receiver – Receiver		
RBS (Motes) *[Elson 2002]*	29.1 µs	93.0 µs
RBS (Bluetooth)	4.5 µs	18.0 µs
RBS (ZigBee)	22.2 µs	52.0 µs

5 CLASSROOM INTEGRATION

Once we know how to perform video-synchronization and wireless-synchronization, it is time to integrate them into the classroom. In the layout shown in figure 1, the sensor mock-up — master— is connected to the PC, which controls video playing. The mock-ups form a Bluetooth piconet that allows communicate them and keep them synchronized with an absolute error below 1 millisecond, small enough for the classroom requirements.

For synchronizing the data with the video, we have generated an audio file in Matlab, containing a frame number every 10 milliseconds, and mixed it with the video containing the images of the operation for training. In the configuration of the mock-ups, it is possible to set an amount of frame

numbers to drop out when decoding audio, reducing the effective frame rate.

There are two basic operating modes: capture and playing. Combinations of them allow recording movements of the expert surgeon and reproducing them for training the novel surgeon, capturing movements of the novel surgeon for evaluating, guiding, etc.

In the capture mode, the surgeon reproduces the movements related to the video sequence. The sensor mock-up receives the audio in the training video, and decodes the frame numbers, which are periodically distributed. When a frame number is decoded, the mock-up captures the values of the position encoders and stores them together with the frame number. When the capture ends, the mock-up sends the data to the PC, where can be saved as the training data file related to the video, or be evaluated with a previously stored data.

In the playing mode, all the motor mock-ups previously store the training data, and wait for the start command from the sensor mock-up. When the PC starts video, the sensor mock-up decode the first frame number, and timestamp it with the global hour. Then, it broadcasts that information to the motor mock-ups, which can compute the timestamp for the next frames, and synchronize playing.

The sensor mock-up periodically broadcast frame-time pairs for prevent errors, and when there is an unexpected value in the frame number sequence, which means a change in the video playing (pausing the video for an explanation, advance the video, looping some technique… etc.).

6 CONCLUSIONS

In this paper we have discussed two different synchronization issues we have faced during the development of a video-surgery learning utility.

Video synchronization was performed by a cost effective and simple method recurring to the audio channel. It allows accurate synchronization without the need of a complex system. Even it is possible to eliminate a PC by using a dedicated video player and controlling playing from the sensor mock-up.

Wireless synchronization between mock-ups was also analyzed using a similar criterion of wireless sensors networks. We use a synchronization protocol over Bluetooth (we also tested ZigBee with similar results) that largely achieves our requirements. The method avoids accessing the lower layers of the protocol while performing similar accuracy as others that use the MAC layer.

With the strategies described in this article, we conclude in a surgical training classroom in which images displayed will be correctly synchronized with the sensor information and the mock-up movements, so the novel surgeons can acquire the needed skills in a real-like environment without harming any patient. This is obtained at low cost by using off-the-shelf components to build up this surgical classroom.

ACKNOWLEDGEMENTS

This work has been partially supported by the Spanish Ministry of Science and Technology under CICYT project numbers TIC2003-07766 and TIN2006-15617-C03-02.

REFERENCES

Ballaro, A., et al., 1999. A computer generated interactive transurethral prostatic resection simulator. In *Journal of Urology*, 162 (5), pp. 1633-1635.

Gomes, M.P.S.F., et al., 1999. A computer-assisted training/monitoring system for TURP structure and design. In *IEEE Trans. Information Technology in Biomedicine,* 3 (4), pp. 242-251.

Kumar, P.V.S., et al., 2002. A computer assisted surgical trainer for transurethral resection of the prostate. In *Journal of Urology*, 168 (5), pp. 2111-2114.

Chen, E., Marcus, B., 1998. Force feedback for surgical simulation. In *Proceedings of the IEEE*, pp. 524-530.

Gambadauro, P., Magos, A., 2007. Digital video technology and surgical training. In *European Clinics in Obstetrics and Gynaecology*, 3 (1), pp. 31-34.

Botden, S.M.B.I., et al., 2007. Augmented versus Virtual Reality Laparoscopic Simulation: What Is the Difference? In *World Journal of Surgery*, 31 (4), pp. 764-772.

Sivrikaya, F., Yener, B., 2004. Time Synchronization in Sensor Networks: A Survey. In *IEEE Network*. 18 (4), pp. 45-50.

Ganeriwal, S., et al., 2003. Timing-sync protocol for sensor networks. In *Proceedings of the 1st International conference on Embedded networked sensor systems*, pp. 138-149.

Maróti, M., et al., 2004. The flooding time synchronization protocol. In *Proceedings of the 2nd international conference on Embedded networked sensor systems*, pp. 39-49.

Elson, J. et al., 2002. Fine-Grained Time Synchronization using Reference Broadcasts. In *Proc. 5th Symp. Op. Sys. Design and Implementation*, pp. 147–163.

Cox, D. et al., 2005. Time Synchronization for ZigBee Networks. In *Proceedings of the 37th Southeastern Symposium on System Theory (SSST2005)*, pp. 135–138.

QUANTUM CASCADE LASERS FOR BIOSENSING APPLICATIONS

Pietro Regoliosi
Lehrstuhl für Nanoelektronik, Technische Universität München, Arcistrasse 21, 80333 Munich, Germany
INFN – Sezione di Trieste, Via A.Valerio 2, 34127 Trieste, Italy
regoliosi@tum.de

Andrea Vacchi
INFN – Sezione di Trieste, Via A.Valerio 2, 34127 Trieste, Italy
andrea.vacchi@ts.infn.it

Giuseppe Scarpa, Paolo Lugli
Lehrstuhl für Nanoelektronik, Technische Universität München, Arcistrasse 21, 80333 Munich, Germany
scarpa@tum.de, lugli@tum.de

Keywords: Nanotechnology, optical biosensors, infrared spectroscopy, quantum cascade lasers.

Abstract: Quantum cascade lasers represent nowadays a mature technology to obtain laser sources in the medium and far infrared region (up to THz). Several advantages with respect to other coherent sources make this kind of lasers particularly attractive: the emission frequency can be selected by properly designing the growth structure, the emission wavelength is tunable with a very good precision and a high optical power in the IR range can be emitted in a spot of small size. These properties make them suitable for several applications, including gas spectroscopy in the IR range. In this work we introduce different types of quantum cascade lasers and we provide a description of their performances and properties, showing that they are suitable candidates for biosensing applications.

1 INTRODUCTION

In recent years, the first realization and the further development of quantum cascade lasers (QCL) (Faist, 1994; Hofstetter, 2001; Pfügl, 2003; Faugeras, 2005)) have provided reliable, powerful and tunable sources for the IR region, whose wavelength emission can be selected along a wide range by properly designing the constituting layered structure. Therefore, possible applications of such a source have been already explored in different fields of IR spectroscopy, like environmental monitoring (McManus, 2005), medical diagnostics (Roller, 2002), atomic spectroscopy (Vacchi, 2006), plasma diagnostics (Röpcke, 2006). QCL look quite profitable, since they could provide a compact and unique source also in the IR region, avoiding the requirement to use sophisticate and complicate laser systems.
In the present work, we present the development and testing of QCL sources designed to be used in atomic spectroscopy, with the aim to describe the characteristics which make them usable also for other applications. In Section 2 we describe the peculiar structure of quantum cascade lasers and we introduce the lasers tested in order to define the achievable performances.

In Section 3 it is presented the experimental setup which allowed us to perform the measurements aimed to define the lasers characteristics: the results are shown in Section 4. Finally, in Section 5 a discussion of the possible applications of QCL in the field of biosensing is provided taking into account the obtained results and presenting some of the worldwide already running activities.

2 DEVICES UNDER TEST

In conventional semiconductor lasers light is generated by stimulated emission across band-gap

(inter-band emission); in the case of QCL radiation is generated by intersubband transitions across designed energy gap inside the same band (intra-band emission). Thus the emission transition can be designed by mean of band-structure engineering, i.e. by choosing the thickness of the different layers of the materials composing the active region of the device. A scheme of the basic principle is shown in Figure 1.

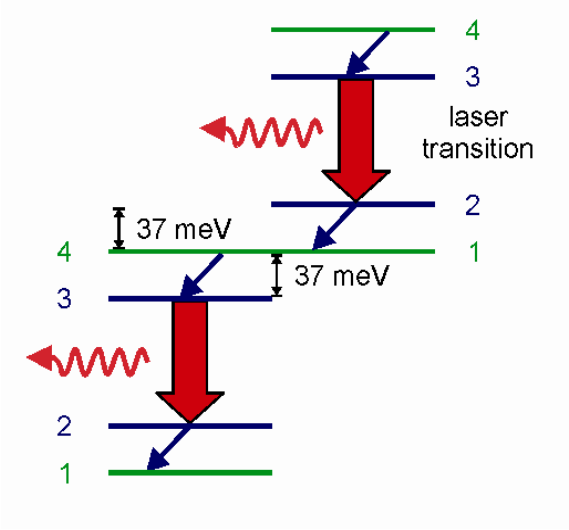

Figure 1: Scheme of the principle of an injectorless QCL.

The QCL structures we designed have been thought for high power and reduced instability in the laser pulse. The scheme is called bound-to-continuum (Pfügl, 2003): the upper laser state is a bound one as in the basic case of QCL structure, while the lower state is spread on a continuum of state, which helps the laser emission, the fast injection of the following active layer and thus inversion of the population. The optimal structure as derived by simulations is presented in Figure 2.

Three different groups of lasers have been designed and fabricated with a lattice matched technique in order to avoid strain problems (morphological defects). The different designs aimed to check the possibility to span the emission over a wider range around 7μm.

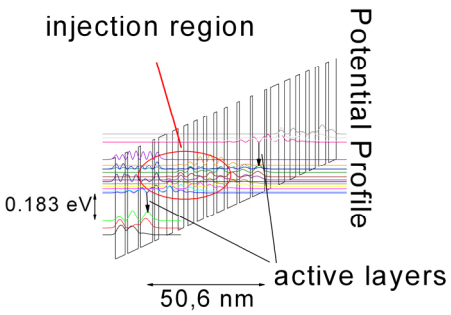

Figure 2: Bound-to-continuum scheme for a QCL with injection region.

Such kind of lasers are basically Fabry-Perot structures, thus expected to have multimode emission (i.e., to emit with several different near peaks). For spectroscopy purposes, single-mode, narrow linewidth lasers with well-defined, precise tunability can be required. In order to achieve these goals, QCL are fabricated with a periodic structure built in the cavity (Figure 3). This periodic variation of the refractive index or of the gain leads to a certain amount of coupling between the back- and forth-travelling waves. The coupling becomes strongest if the periodicity is an integer multiple of half the laser wavelength in the cavity. Because feedback occurs along the whole cavity and not only on the mirrors, these devices are called distributed feedback lasers (DFB). They show usually an excellent single-mode behaviour, can be precisely tuned with temperature or current, and deliver a reasonable amount of output power. In order to test the DFB monomode behaviour, we commissioned such a structure from Alpes Lasers SA, Switzerland, with specification able to match our structures.

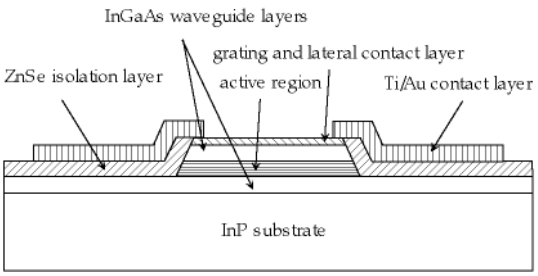

Figure 3: Scheme of the distributed feedback structure, with the grating superimposed to the active region (from University of Neuchatel).

3 EXPERIMENTAL SETUP

The lasers are fixed on the cold finger of a cryostat, whose chamber can be evacuated and cooled down to a temperature as low as liquid nitrogen temperature (77K). The emitted light is coupled out of the cryostat through a CaF window (more than 90% transmission in the 2-9 μm range), then collimated and focused on a IR detector by two parabolic reflectors (equivalent f/# ~ 3.9). The measurements are performed by applying a pulsed voltage on the QCL, and reading out the optical power on the detector by mean of an oscilloscope.

In case of spectral measurements, the focused beam has been coupled to the input of a monochromator, and the detector has been positioned at the output of the monochromator itself. We performed both power and spectral measurements at different temperature, in order to define the achievable power and the possible tuning of the laser emission. A scheme of the whole setup is depicted in Figure 4.

In order to perform both the kind of measurements in the same time, it has been explored another possible setup, by mean of inserting a ZnSe beam splitter in the optical path. The beam splitter divides the emitted light in two parts: one is focused directly on a photo detector to measure the optical power, the other is coupled with the monochromator for a contemporaneous spectral measurement. The configuration is also able to provide an online feedback on the drifting of the emission wavelength, which shows to be useful in case of spectroscopy measurements.

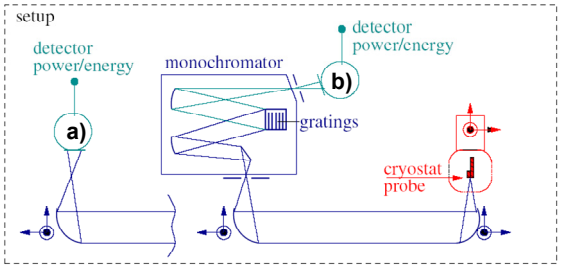

Figure 4: Setup for the optical power measurements: (a for power estimation, b for spectral measurements).

4 RESULTS

In Figure 5 an example of the I-V characteristics of our set of lasers is shown as a function of the temperature together with the corresponding emission peak powers. The measurements gave the idea of the achievable power: more than 1W at cryogenic temperatures; about half of such power is still present at room temperature. The laser could be operated up to 400K. Considering that the laser facet has an area of about 60-100 μm^2, it corresponds to a power density of 10^6 W/cm^2 if the whole power is perfectly focused. The amount of power allows the lasers to be exploited in spectroscopy of gas, for example by mean of absorption measurements.

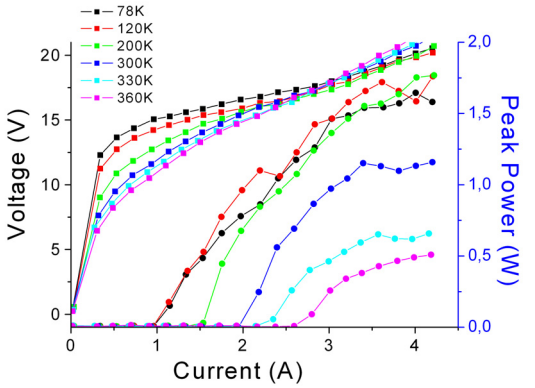

Figure 5: I-V curves and peak power of QCL of our set of laser in the range between 77K and 360K.

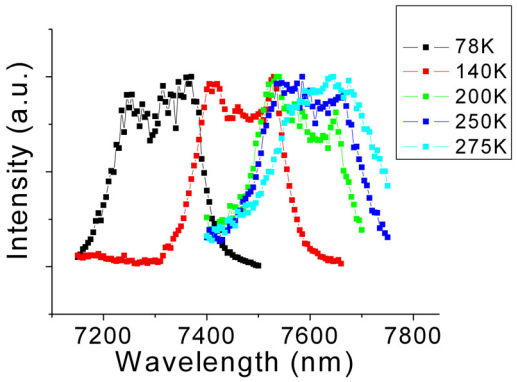

Figure 6: QCL Spectra between 78K and 275K.

The corresponding spectra for one of the three groups of lasers are shown in Figure 6 as a function of the temperature. Due to the high emitted power, it is possible to observe fine structures: none of the spectra could be optimally fit with a simple Gaussian curve, due to the expected multimode emission. The convoluted spectra have widths spanning from 70 nm to about 150 nm. Taking into account all the three groups, the overall range that is possible to span with such lasers is very wide, from 6900 nm up to 7800 nm, demonstrating the possibility to tailor the structure in order to span a desired wavelength range. This feature is another important one in terms of spectroscopy application,

since it could allow to scan wide spectral ranges with a limited number of different devices.

In order to define the achievable tunability, we performed studies on the DFB structure: since it emits in monomode behaviour, its tunability is more well defined. The power achievable with the DFB structure is lower than the one emitted by our structures (even if still about 1W at cryogenic temperatures). However the emission is clearly monomode in a certain range of temperatures as it is possible to estimate from the measurements shown in Figure 7 and it is tuneable with very nice precision by mean of changing the voltage applied by the pulser. Figure 8 reports the study of the tunability, performed at 90K: the peak wavelength increases with increasing voltage (due to the increase of the temperature of the active region), and the behaviour is linear. The achievable tunability is as low as (30±1) pm/V around the emission, and the estimation is limited by the resolution of the spectrometer (the actual width of the laser line should be as narrow as 5 pm).

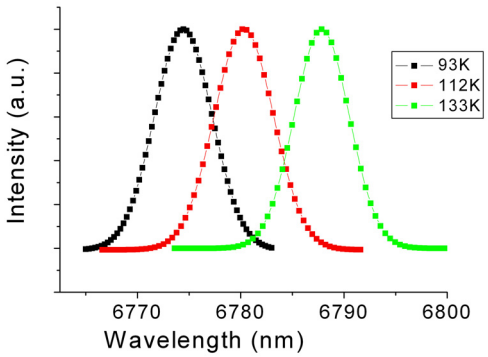

Figure 7: Monomode emission of DFB structure and its shift with the temperature.

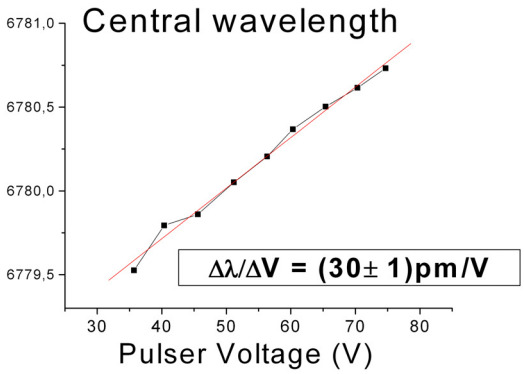

Figure 8: Linear fit of the variation of the central emission wavelength as a function of the pulser voltage.

The very nice achievable precision is a feature strictly required for atomic spectroscopy, where the fine definition of the transition energies is quite important, but it can be also exploited in general spectroscopy.

5 QCL FOR BIOSENSING

The presented results describe the achievable performances with a QCL source: high IR power localized in the space, spanning on a very wide range of wavelengths or with monomode emission depending on the chosen structure, providing the availability of fine tuning by mean of very precise temperature changes. All these properties look profitable for spectroscopy in the IR region, and they can be applied as well to biosensing applications.

Indeed, most of the chemical species have distinctive absorption lines in the range between 3 and 20 μm (500 – 4000 cm^{-1}), due to the vibration modes of the most important organic bonds (see the panel in Figure 9). For example, the QCL structures presented so far emit around 7 μm which means about 1425 cm^{-1} (they have been designed in order to provide sources for atomic applications), thus they could be used to detect the C-H bending in the alkanes. Moreover as mentioned above it is possible to choose the emission wavelength only by changing or using different materials without modifying the achievable performances.

Therefore, molecular detection in terms of vibrational spectroscopy is possible, and it is currently under development. Most of the activities is oriented on the utilisation of DFB structures, since spectroscopic applications usually require single mode operation. The laser emission is collimated and focused in a gas cell (usually a tube terminated with antireflection coated windows), which provides both the volume where the absorption takes place and a way to increase the optical path of the radiation and thus to increase the sensitivity of the system. The method has been explored with different kinds of laser to detect different gases, like CO_2 and H_20 (640 cm^{-1}, Kosterev, 2002), C_2H_4 and NH_3 (1000 cm^{-1}, Weidmann, 2004), NO (1920 cm^{-1}, Weber, 2002), providing detection limit down to < 1ppbv, which could be already exploited in medical diagnostics. Recently, more sophisticated approaches as the off-axis integrated cavity output spectroscopy (OA-ICOS) have been applied to deeply investigate the achievable sensitivity (Bakhirkin, 2006). Another explored way to realize QCL-based gas sensors has made use of photonic bandgap fibers, which are able to transmit radiation in the IR range. The QCL emission is coupled into

the fiber using a coupling cell: a sensor able to detect C-H stretch band of ethyl chloride gas has been realized in this way (975 cm^{-1}, Charlton, 2005). THz lasers, which have higher wavelengths, have been used for gas phase spectroscopy (Hübers, 2006).

For laser spectroscopy of larger molecules with broad absorption features narrow linewidth is not required, but it is more important to be able to tune the emission over a wide wavelength range. In this case, the bound-to-continuum structures we presented provide the required broad spectrum (the lower state of the transition is a relatively broad continuum). The fine tuning is achieved by mean of the utilization of an external cavity configuration: the emission of the laser is collimated and reflected off a diffraction grating so to create a resonant cavity. The first order diffraction from the grating provides the laser feedback, while the output of the

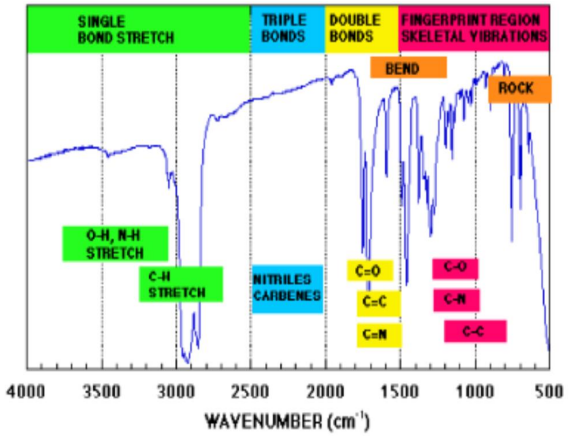

Figure 9: Absorption regions in the infrared.

external cavity is obtained by the zeroth order. The tunability is provided by moving and rotating the grating with piezo actuated positioners. The method has been proved to be fruitful (Wysocki, 2005) and it is currently exploited for measuring absorption spectra of large molecules, like Freon (around 1150 cm^{-1}, Phillips, 2007).

Another idea which can be exploited comes from the realization of surface-emitting quantum cascade micro cavity lasers: the active region of the laser is covered with a patterned surface, like a photonic crystal. The presence of the crystal provides both feedback for the laser action and a selection of the polarization of the emitted light (Colombelli, 2003). This structure could allow also the possibility to allocate defects on the photonic crystal which can absorb chemical species: the change in emission due to the absorption of molecules can be monitored as a change of the laser emission and the whole would perform as a compact and sensitive biosensing device.

6 CONCLUSIONS

QCL present themselves as reliable sources for IR range: they provide high optical IR power, their emission can be tailored to span a selected range and by mean of a superimposed grating it could be made monomode. The emission is also tuneable with very fine precision, either intrinsically by changing the laser temperature or externally by using a coupled diffraction grating Their performances make them suitable for a series of application, since most of the molecular species present distinctive absorption lines in the medium infrared.

Different methods to realize QCL-based biosensor have been already tested or are currently in development, principally in the field of the gas sensing for medical diagnostics applications or environmental control: several substances have been already proved to be detectable through the utilization of QCL based sensing devices, which start to provide significant and interesting results.

Such a development is a very interesting field which looks to be double faced. From one side a new class of biosensors could profit of the unique properties of QCL in the IR range: the versatility of such structures could allow a very wide range of design and applications. On the other hand the study of such sensors could provide a further push to the design and development of even more efficient QCL structures properly aimed to better match the requirements of biosensor field.

ACKNOWLEDGEMENTS

The present work has been performed in cooperation with the SISTER project of the AREA Science Park of Trieste, Italy.

REFERENCES

Faist J. (1994) ‘Mid-infrared field-tunable intersubband electroluminescence at room temperature by phonon-assisted tunneling in coupled-quantum wells’, *Applied Physics Letters*, vol. 64 no. 9, February, pp. 1144-1146.

Hofstetter D. (2001) ‘High temperature operation of distributed feedback quantum-cascade lasers at 5.3 μm’, *Applied Physics Letters*, vol. 78 no. 4, January, pp. 396-398.

Pflügl C. (2003) 'High-temperature performance of GaAs-based bound-to-continuum quantum-cascade lasers', *Applied Physics Letters*, vol. 83 no. 23, December, pp. 4698-4700.

Faugeras C. (2005) 'High-power room temperature emission quantum cascade lasers at □=9 □m', *IEEE Journal of Quantum Electronics*, vol. 41, no. 12, December, pp. 1430-1438.

McManus J.B. (2005) 'A high precision pulsed quantum cascade laser spectrometer for measurements of stable isotopes of carbon dioxide', *Journal of Modern Optics*, vol. 52 no 16, November, pp. 2309-2321.

Roller C. (2002) 'Simultaneous NO and CO_2 measurements in human breath with a single IV-VI mid-infrared laser', *Optics Letters*, vol. 27 no.2, January, pp. 107-109.

Vacchi A. (2006) 'Steps towards the development of a QCL laser for muH experiments', *Book of Abstract*s, International Conference on Precision Physics of Simple Atomic Systems, Venice, Italy, p. 33.

Röpcke J. (2006) 'Application of mid infrared tuneable diode laser absorption spectroscopy to plasma diagnostics: a review', *Plasma Sources Science and Technology*, vol.15, October, pp. S148-S168.

Kosterev A. (2002) ' Chemical sensing with pulsed QC-DFB lasers operating at 15.6 □m', *Applied Physics B*, vol. 75, August, pp. 351-357.

Weidmann D. (2004) 'Monitoring of ethylene by a pulsed quantum cascade laser', *Applied Optics*, vol. 43, June, pp. 3329-3334.

Weber W. (2002) 'Using a wavelength-modulated quantum cascade laser to measure NO concentrations in the parts-per-billion range for vehicle emissions certification', *Applied Spectroscopy*, Vol. 56, June, pp. 706-714.

Bakhirkin Y. (2006) 'Sub-ppbv nitric oxide concentration measurements using cw thermoelectrically cooled quantum cascade laser-based integrated cavity output spectroscopy', *Applied Physics B*, vol. 82, November, pp. 149-154.

Charlton C. (2005) 'Midinfrared sensors meet nanotechnology: Trace gas sensing with quantum cascade lasers inside photonic band-gap hollow waveguide', *Applied Physics Letters*, vol. 86, May, 194102.

Hübers H.-W. (2006) 'High-resolution gas phase spectroscopy with a distributed feedback terahertz quantum cascade laser', *Applied Physics Letters*, vol. 89, August, pp. 061115.

Wysocki G. (2005) 'Widely tunable mode-hop free external cavity quantum cascade laser for high resolution spectroscopic applications', *Applied Physics B*, vol. 81, September, pp. 769-777.

Phillips M. (2007) 'External cavity quantum cascade laser for quartz tuning fork photoacoustic spectroscopy of broad absorption features', *Optics Letters*, vol. 32, May, pp. 1177-1179.

Colombelli R. (2003) 'Quantum cascade surface-emitting photonic crystal laser', *Science*, November, pp. 1374-1377.

RAPID FINITE STATE MACHINE CONTROL OF INDIVIDUAL DNA MOLECULES IN A NANOPORE

Noah A. Wilson, Robin Abu-Shumays, Elizabeth Koch, Seico Benner and William B. Dunbar
Dynamics and Control Laboratory, Computer Engineering and Biomolecular Engineering
University of California, Santa Cruz, CA, 95064 USA
{*noahness, roabu*}*@soe.ucsc.edu, kochel@carleton.edu,* {*sbenner, dunbar*}*@soe.ucsc.edu*

Keywords: Nanopore, single molecule control, finite state machine.

Abstract: This paper demonstrates feedback voltage control of individual DNA hairpin molecules captured in a nanopore. A finite state machine is used to program voltage control logic, executed on a field-programmable gate array, for rapid detection and regulation of hundreds of DNA hairpins, one at a time. Prompt voltage reduction is used for extension of the dwell time of DNA hairpins in the nanopore. Then, voltage reversal after a preset dwell time is used for automated expulsion of molecules prior to hairpin unzipping. The demonstrated control authority of single molecular complexes captured in the nanopore device is an integral part of our ongoing research for direct monitoring and control of enzyme-bound biopolymers.

1 INTRODUCTION

Nanopore sequencing is based on electrophoretically driving a singe-stranded DNA (ssDNA) or RNA molecule through a nano-scale pore (Deamer and Branton, 2002). The potential of this technology is high-speed, high throughout sequential identification of all nucleotides in any single DNA or RNA molecule. Many research groups are now exploring and developing biological and solid-state nanopores to achieve low-cost, high throughput nanopore-based sequencing (Rhee and Burns, 2006), in addition to other single molecule sensing applications (Dekker, 2007).

In the biological nanopore setup, a planar lipid bilayer is created across a 20 μm teflon aperture in a KCl solution. A single α-hemolysin protein channel is inserted into the planar lipid. The channel (pore) is 15 nm in length and varies in diameter. The cis-opening of the pore is 2.6 nm wide, opening to a 3.6 nm vestibule before narrowing to a limiting 1.5 nm width at the beginning of the stem. The remainder of the stem up to the trans-opening is 2 nm wide. The vestibule is large enough for double-stranded DNA (dsDNA) to enter, but the limiting stem is just wide enough for ssDNA to pass through. Across the bilayer, AgCl electrodes are used to apply a potential that produces an ionic current through the pore. The field created by this voltage pulls the negatively charged phosphate backbone of the ssDNA or RNA through the pore, passing from the cis side to the trans side of the pore with the trans-side voltage positive. As molecules translocate, the pore becomes partially blocked by the translocating molecule, causing an momentary drop in current. These translocation events can be characterized by the amplitude of the blockade current and the time the molecule spends in the pore, defined as the dwell time.

We use DNA oligomer that is 79 nucleotides total in length, with a 20 base pair hairpin (20 bphp). The hairpin is formed by the 3' end folding over and annealing on itself resulting in a 20 base pair region. The hairpin is thus the double-stranded segment, with the single-stranded segment 35 nucleotides long (4 unpaired bases in the doubled-stranded end loop). Upon capture of the ssDNA end, the hairpin enters the pore vestibule and remains until the hairpin is unzipped. A schematic of the nanopore system and an example 20 bphp translocation event is illustrated in Figure 1.

Regarding the resolution limits of ionic current measurements, homopolymers of ssDNA and block copolymers of RNA are distinguishable based on the measurable differences in the blockade current amplitude or kinetics (Akeson et al., 1999). However, translocation rates are too fast (up to 2 nucleotides/μsec, (Akeson et al., 1999)) to identify individual nucleotides in heterogeneous single-stranded polymers using existing biological nanopores (Dekker, 2007). In this paper and other

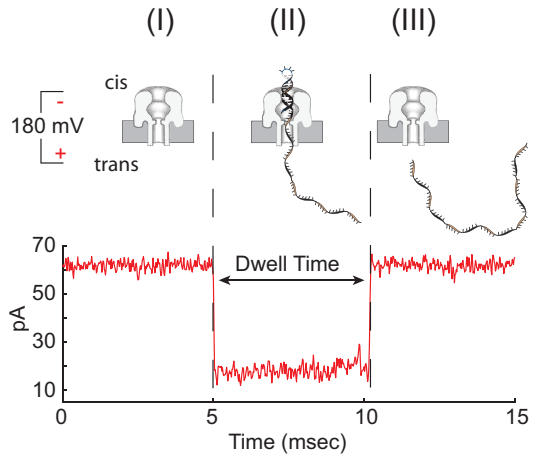

Figure 1: Schematic of nanopore and DNA, and plot of representative ionic current signal during a 20 bphp DNA translocation event under 180 mV applied potential. (I) At 180 mV, KCl ions pass through the open channel resulting in ∼64 pA current. (II) Upon capture of the single-stranded end of the DNA molecule into the cis opening of the pore, the flow of ions is reduced to ∼20 pA. (III) After ∼5 msec, the voltage unzips the hairpin, causing ssDNA to pass through the pore into the trans chamber, completing the measured blockaded event. The duration of the event is referred to as dwell time.

studies (Vercoutere et al., 2003; Mathe et al., 2004), DNA with single and double stranded segments is used to increase the dwell time of nucleotides in the pore (0.5–10 ms, depending on applied voltage and dsDNA segment length). Another approach is to use DNA-binding proteins (enzymes) to increasing the nucleotide dwell time in the pore. This is being pursued at UCSC as part of the $1000/mammalian genome project (Golovchenko, 2005). Under an applied voltage, the ssDNA end of enzyme-bound DNA is captured in the nanopore, with the enzyme residing on top of the nanopore being too large to translocate through it. Binding of enzymes to DNA in this configuration has been shown to increase the dwell time of DNA in the nanopore by up to two orders of magnitude (up to 200 msec). Recently, kinetics of Escherichia coli exonuclease I binding to ssDNA has been quantified using voltage ramps for nanopore-based force spectroscopy (Hornblower et al., 2007). The voltage field force exerted on the ssDNA causes it to dissociate from the enzyme after several milliseconds before translocating. The time-to-dissociation in turn can be correlated to enzyme binding rate constants.

In (Benner et al., 2007), the interaction of DNA with the Klenow fragment (KF) of Escherichia coli DNA polymerase I was explored. In the absence of KF, capture and subsequent unzipping of 20 bphp at constant 180 mV reveals blockades with 20 pA mean amplitude and 4 msec median dwell time. Addition of KF and the dNTP complementary to the DNA template base in the KF catalytic site yielded a substantial increase in blockade dwell times (110 msec median lifetime for dGTP), attributable to ternary (DNA-KF-dGTP) complexes. Closer investigation of such blockades revealed a two-step pattern in greater than 97% of the blockades, the first step at 24 pA mean amplitude, and the second (terminal) step at 20 pA mean amplitude lasting 4ms consistent with the hairpin kinetics alone. It was demonstrated that the transition from step one to two resulted in dissociation of KF from DNA first, followed by hairpin dropping into the pore vestibule until unzipping occurred. As a initial effort at voltage control of enzyme-bound DNA, we demonstrated efficient automated detection of individual ternary complexes (< 3 msec), based on the characteristic 24 pA amplitude, and truncation of the blockade time by voltage reversal after 20 ms (Benner et al., 2007)).

This paper presents an extension of the control results presented in (Benner et al., 2007). Specifically, we demonstrate automated detection and manipulation of DNA hairpins. Rapid detection (< 2 msec) is based on computing a filtered mean amplitude of the ionic current in real time, and monitoring the mean relative to an amplitude range consistent with DNA hairpin blockades (20 ± 2.8 pA). Upon detection, two methods of voltage control are demonstrated. In method 1, dwell time extension is achieved by prompt voltage reduction, with the reduced voltage applied until the hairpin unzips. A voltage for capture increases the number of molecules examined, and the reduced voltage post-capture increases the dwell time to, in principle, facilitate sequencing. In particular, extending the life of DNA hairpins in the pore increases the time within which a terminal base identification could be acheived using machine learning methods (Vercoutere et al., 2003). In method 2, voltage reduction is applied for a preset time (10 msec) followed by voltage reversal to expel the molecule prior to hairpin unzipping. This demonstrates our control authority to aggregate the dwell times of hundreds of blockade events. Additionally, it complements our prior work (Benner et al., 2007), confirming our ability to detect DNA-enzyme blockades and DNA hairpin blockades. Confirmation of our ability to discern between each blockade type in real time is part of our ongoing work. Ultimately, nanopore-based characterization of enzyme dynamics will require direct detection and control of multiple DNA conformations relative to the enzyme, and direct control of enzyme-free DNA is a prerequisite toward developing

this capability.

Direct control of ssDNA in a nanopore has been demonstrated (Bates et al., 2003), in which detection of DNA is based on monitoring the raw amplitude relative to a threshold level. Voltage level changes, comparable to those employed in this paper, were commanded to explore the zero and low voltage effects on ssDNA-pore interactions. In contrast to thresholding the raw ionic current amplitude, the windowed amplitude mean calculation we have used here filters the current noise. Additionally, detection depends on the mean remaining within a preset amplitude range ($<$ 6 pA in spread) for multiple consecutive comparisons. Alternative methods for single molecule sensing and manipulation include optical tweezers and atomic force microscopy (Bustamante et al., 2003). For example, optical trapping has been used to sequence DNA by attaching a processive enzyme to a polystyrene bead (Abbondanzieri et al., 2005), (Greenleaf and Block, 2006). At present, greater spatial and temporal resolution of single DNA molecule polymerization has been achieved than with nanopores. However, these methods generally require more preparative steps, and far fewer molecules can be analyzed over a common time period.

2 CONTROL LOGIC SETUP

The nanopore system is setup in a 0.3 M KCl solution. A patch-clamp amplifier, Molecular Devices AxoPatch 200B, regulates the applied voltage and measures the ionic current through the channel. The data are recorded using the Molecular Devices Digidata 1440A digitizer, sampled at 50 kHz and low-pass filtered at 5 kHz with a four-pole Bessel filter. The voltage control logic is programmed using a finite state machine (FSM) within LabVIEW 8 software. The FSM logic is implemented on a field-programmable gate array (FPGA) hardware, National Instruments PCI-7831R. An FPGA is a reconfigurable hardware platform that permits fast measurement and voltage reaction times (1 μsec output sample time). An FSM is a logic construct where program execution is broken up into a series of individual states (Gill, 1962). Each state has a command associated with it, and transitions between states are a function of system measurements. Measurements of the pore current are processed and passed to the FSM as inputs. Changes in the FSM control logic are done as necessary, then re-compiled and re-routed to run on the FPGA. This achieves a balance between speed and flexibility, by enabling the system to react to events on the order of a microsecond, while also allowing for the control logic to be reconfigured as necessary between experiments.

Blockade events, quantified by the blockage current and dwell time, can be detected and monitored in real time using the FSM/FPGA. A mean filter applied to the incoming current signal on the FPGA removes a large portion of the peak-to-peak noise. Specifically, every 5.3 μsec, the FPGA samples the ionic current and computes a windowed mean amplitude based on the previous 0.75 ms of signal. Every 0.2 ms, the FPGA tests if the mean is within 20$\pm$2.8 pA (17.2 to 22.8 pA range). The basis for choosing this range is that $\sim$20 pA is the median amplitude for DNA 20 base pair hairpin events at 180 mV, as shown in the experimental results below. If the mean enters and remains within this range for four consecutive tests, the FSM logic diagnoses the blockade as a DNA hairpin event. The *nominal detection time*, between DNA translocation event and diagnosis of the event, is 2.0 ms; 0.75 ms for the windowed mean to first enter the 17.2 to 22.8 pA range, and 0.6 ms for three more confirmed tests, and 0.65 ms of delay[1].

3 EXPERIMENTS AND RESULTS

In our first experiment, the objective was to efficiently detect individual DNA hairpin events, and increase the blockade dwell time by lowering the applied voltage from 180 mV to 150 mV upon detection. This is referred to as **dwell time extension control**. Next, we sought to aggregate the extended blockade dwell times, by expelling the DNA using voltage reversal of -50 mV after 10 ms at 150 mV. This is referred to as **dwell time aggregation control**. The motivation was to increase the nominal hairpin dwell time, and expel the molecule before unzipping the hairpin. A typical 20 bphp event at constant 180 mV voltage is shown in Figures 1 and 2aI. The probability histogram of the base 10 logarithm of dwell time (Figure 2aIII, blue) is unimodal, with median dwell time of 2.8 ms. The median amplitude of the event plot in Figure 2aII is 20.9 pA with an interquartile range (IQR) of 1.7 pA. Only 6% of events are in the subset range of 13-18 pA (2aIII, yellow). For the same experiment at constant 150 mV voltage (data not shown), the events cluster around a median amplitude of 15 pA and 87% of 150 events are in the 13-18 pA range. Thus, under extension and aggregation control for which the voltage is reduced to 150 mV for all detected events, a larger

[1]Certain inefficiencies in FPGA signal routing into the sampling loop caused the additional 0.65 ms of delay in the reaction time. By bringing global signals inside the sampling loop, the delay has recently been eliminated, reducing detection time to 1.35 ms.

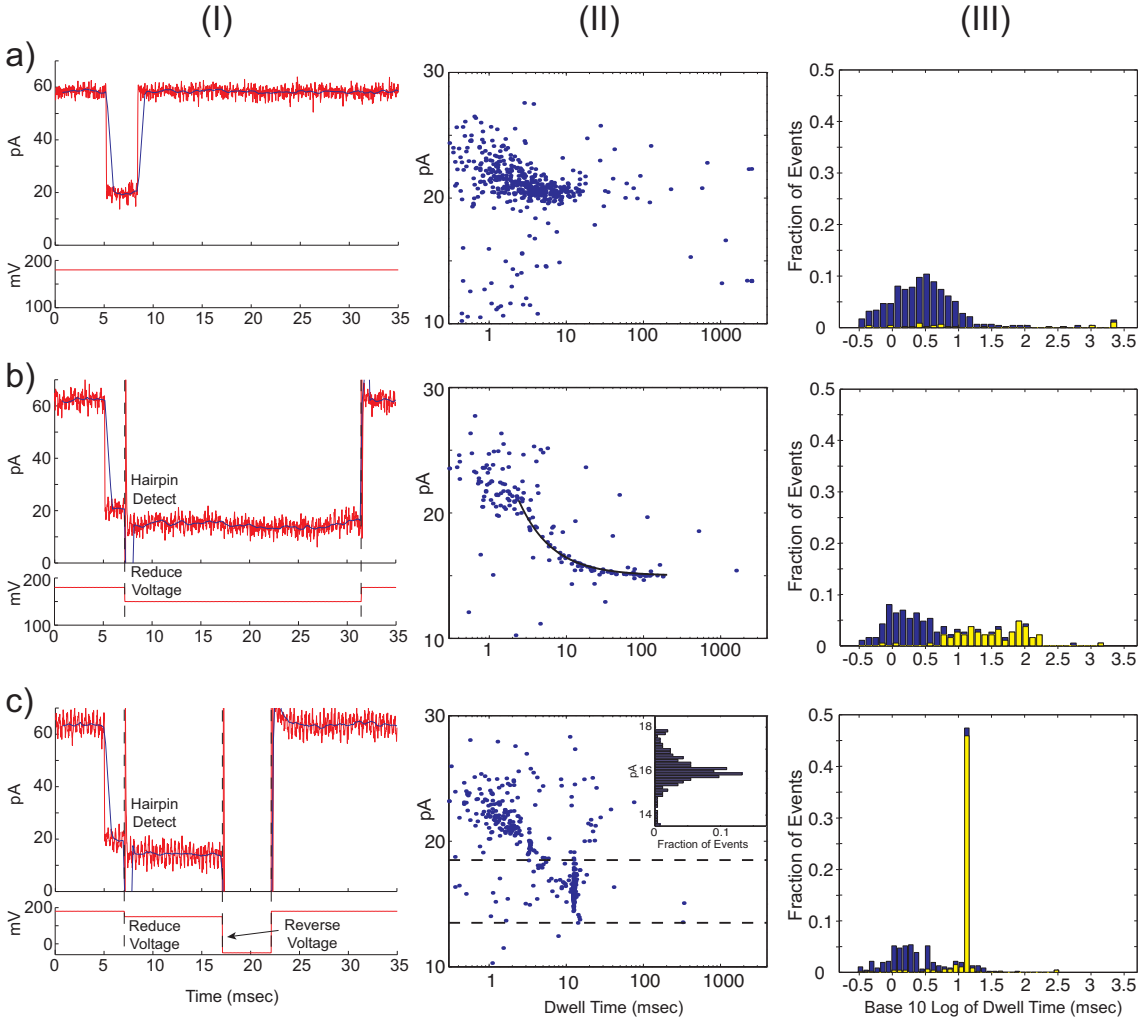

Figure 2: Regulation of 20 bphp dwell time using FSM control. (I) The red current signals are low-pass filtered at 5kHz, the blue signal is a mean filtered current, and the red voltage signal is the commanded voltage. Typical events and corresponding voltage signals under a) constant 180 mV voltage, b) dwell time extension control, and c) dwell time aggregation control. (II) Event plot of DNA events, showing average amplitude vs. dwell time for each event (point). Equation (1) (line) fit to events in bII), and amplitude histogram for events within 13-18 pA (dashed line) range in cII). (III) Probability histograms of the base 10 logarithm of dwell time for all events (blue), and for subset of events in 13-18 pA range (yellow).

percentage of blockades should have a mean amplitude within the 13-18 pA range.

3.1 Dwell Time Extension (Figure 2b)

Upon diagnosis of a DNA hairpin event using the mean filtered current, the command voltage is reduced to 150 mV until the hairpin unzips and the DNA translocates through the pore. Using 180 mV for capture results in more events than 150 mV, while reducing to 150 mV extends the life of the hairpin. Dwell time extension is useful for terminal base-pair sequencing by machine learning methods (Vercoutere et al., 2003). After each translocation, the FPGA resets the voltage to 180 mV. A representative event is shown in Figure 2bI. The event plot (Figure 2bII) pattern shows that events faster than the nominal diagnosis time of 2.0 ms are unaffected by extension control, and events with longer dwell times converge to the ∼15 pA mean amplitude as expected. The concave trend is also consistent with an equation for event's mean amplitude vs. dwell time. In particular, for an event at 21 pA (median amplitude at 180 mV) for 2.4 ms [2], and at 15 pA (median amplitude at 150 mV) for

[2]Step changes in voltage induce a capacitive transient, and the transient at the end of each event is ∼0.4 ms for changing from 150 mV to 180 mV. Thus, 2.4 ms at 21 pA is 2.0 ms of detection time and 0.4 ms of transient time. While

x ms, an approximate mean amplitude $\bar{I}$ is

$$\bar{I} = \frac{2.4 * 21 + 15 * x}{2.4 + x}. \quad (1)$$

When $x \approx 24$ ms, as in Figure 2bI, $\bar{I} = 16$ pA. Equation (1) closely matches the mean amplitude vs. dwell time data (Fig. 2bII). Also, the fraction of events within the subset range 13-18 pA increased to 41%, as shown in the yellow histogram overlaid on the blue probability histogram (Fig. 2bIII).

3.2 Dwell Time Aggregation (Figure 2c)

The objective was to aggregate the dwell times of the extended events by applying 150 mV for 10 ms upon diagnosis of a hairpin event, followed by voltage reversal of -50 mV for 5 ms. The reversal time of 5 ms is known to be sufficient to clear the DNA from the channel, prepping the pore for the next event. Aggregation control would imply a measure of control over the distribution of the events, in addition to temporal control of individual molecular events. A representative event is shown in Figure 2cI. As before, the event plot (Fig. 2cII) pattern shows that events faster than the nominal diagnosis time of 2.0 ms are unaffected by aggregation control. Within the subset range of 13-18 pA, the median amplitude is 16 pA with 0.7 pA IQR (amplitude histogram shown in Fig. 2cII). The 16 pA median is consistent with (1), since for $x = 10.0$ ms, $\bar{I} = 16$ pA. Also in the subset range, and the median dwell time is 12.4 ms with 0.1 ms IQR. The low IQR indicates a high degree of control over the distribution of events that extend to at least 10 ms at 150 mV. The median dwell time of 12.4 ms is commensurate with 2.0 ms of detection time, 10 ms at 150 mV, and 0.4 ms due to a transient that is included at the end of each event resulting from voltage reversal[3].

Summary statistics for the histograms in Figure 2III are reported in Table 1.

In (Mathe et al., 2004), the authors characterize hairpin unzipping at a set of constant voltages by fitting a curve to an unzipping probability data profile. Specifically, for an unzipping time t at voltage V, the unzipping probability is the fraction of events with dwell time less than t, divided by the total number of events[4]. For a set of t values, the unzipping probability data profile is shown in Fig. 3 for our experiments at 180 mV constant, under extension control, and at 150 mV constant. As in (Mathe et al., 2004), we fit a line to the data, revealing a characteristic unzipping time τ_u^V for constant voltage V. For amplitude range 10-30 pA and dwell time range 0.3-500 ms, it is revealing to compare the median dwell times with the fitted τ_u^V constants. For $V = 180$ mV, the median is 2.6 ms and $\tau_u^{180} = 4.2$ ms. For $V = 150$ mV, the median is 25.2 ms and $\tau_u^{150} = 39.4$ ms. We observe that data trimming has a significant affect over the quality of the fit to the data, and consequently over the value for τ_u^V. In contrast, the median does not vary as much, suggesting a sensitivity of τ_u^V to outliers, in addition to the fitting method used. For example, for a dwell time range of 0.3-4000 ms at $V = 150$ mV, the median is

Table 1: Summary statistics for Figure 2III.

Figure No.	No. of Events	Median Dwell Time (ms)	IQR (ms)
2aIII[a]	472[b]	2.8	4.2
2bIII[c]	76[d]	31.6	62.0
2cIII[c]	256[e]	12.4	0.1

[a] Blue histogram, for events within 10 to 30 pA range.
[b] 6% (27 events) within subset 13-18 pA range.
[c] Yellow subset histogram, for events within 13-18 pA range.
[d] 41% of the 187 events within 10 to 30 pA range.
[e] 55% of the 466 events within 10 to 30 pA range.

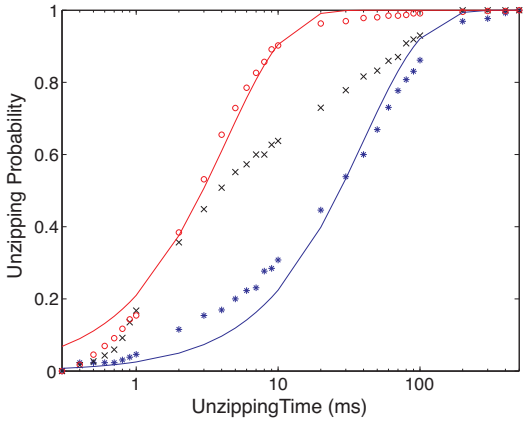

Figure 3: Unzipping probability data profile, defined as fraction of events with dwell time less than each unzipping time t, and line $1 - \exp[t/\tau_u^V]$ fit to profile for constant voltages $V = 180$ mV (red) and $V = 150$ mV (blue). Characteristic unzipping time constant τ_u^V at constant voltage V is generated by fit. Symbols: $\circ$ for $V = 180$ mV, $\times$ for extension control (transitions from 180 mV to 150 mV), and $*$ for $V = 150$ mV.

the 0.4 ms transient varies in amplitude, assuming 21 pA is sufficient for line fitting.

[3] The transient due to the 180 mV to 150 mV change is included within the 10 ms waiting time under aggregation control.

[4] The authors formulate an alternative but equivalent definition for unzipping probability.

34.9 ms (+ 9.7) and $\tau_u^{150} = 55.7$ ms (+ 16.3). Careful selection and analysis of statistical models appropriate for our data (with outliers always present) is part of our ongoing work.

4 CONCLUSIONS

We have shown that single DNA hairpin molecules captured in a biological nanopore can be detected and reacted to using a finite state machine implemented on a field-programmable gate array. The dwell time of such translocation events can be extended to gain more signal, which can in turn be analyzed offline using machine learning methods to yield terminal base-pair specific signatures. The signatures can then be used for real-time identification of terminal base pairs. Additionally, the finite state machine is capable of ejecting a molecule from the pore after it has been detected but prior to unzipping the hairpin. Rapid DNA hairpin detection ($<$ 2 msec) relied on a mean filtered amplitude, which was required to remain within a preset amplitude range ($<$ 6 pA in spread) for multiple consecutive threshold comparisons. The method will be tuned to differentiate DNA-enzyme blockades from DNA alone blockades in real time as part of our ongoing work. Ultimately, nanopore-based characterization of enzyme dynamics will require direct detection and control of multiple DNA conformations relative to the enzyme, and direct control of enzyme-free DNA is a prerequisite toward developing this capability.

ACKNOWLEDGEMENTS

E. Koch was supported by a Summer Undergraduate Research Fellowship in Information Technology, funded by NSF under grant CCF-0552688. The work was also supported in part by NHGRI under grant K25 HG004035-01. We thank K. Lieberman and M. Akeson for their help in preparing the paper.

REFERENCES

Abbondanzieri, E., Greenleaf, W., Shaevitz, J., Landick, R., and Block, S. (2005). Direct observation of base-pair stepping by RNA polymerase. *Nature*, 438(24):460–465.

Akeson, M., Branton, D., Kasianowicz, J., Brandin, E., and Deamer, D. (1999). Microsecond time-scale discrimination among polycytidylic acid, polyadenylic acid, and polyuridylic acid as homopolymers or as segments within single RNA molecules. *Biophysical Journal*, 77:3227–33.

Bates, M., Burns, M., and Meller, A. (2003). Dynamics of DNA molecules in a membrane channel probed by active control techniques. *Biophysical Journal*, 84:2366–2372.

Benner, S., Chen, R. J., Wilson, N. A., Abu-Shumays, R., Hurt, N., Lieberman, K. R., Deamer, D. W., Dunbar, W. B., and Akeson, M. (2007). Sequence-specific detection of individual DNA polymerase complexes in real time using a nanopore. *Nature Nanotechnology*. advanced online publication, DOI 10.1038/nnano.2007.344.

Bustamante, C., Bryant, Z., and Smith, S. B. (2003). Ten years of tension: single-molecule DNA mechanics. *Nature*, 421:423–427.

Deamer, D. and Branton, D. (2002). Characterization of nucleic acids by nanopore analysis. *Acc. Chem. Res.*, 35:817–825.

Dekker, C. (2007). Solid-state nanopores. *Nature Nanotechnology*, 2:209–215.

Gill, A. (1962). Introduction to the theory of finite-state machines. *McGraw-Hill*.

Golovchenko, J. (2005). Electronic sequencing in nanopores. The $1000/mammalian genome project, NHGRI R01 HG003703-03.

Greenleaf, W. J. and Block, S. M. (2006). Single-molecule, motion-based DNA sequencing using RNA polymerase. *Science*, 313:801.

Hornblower, B., Coombs, A., Whitaker, R., Kolomeisky, A., Picone, S., Meller, A., and Akeson, M. (2007). Single-molecule analysis of DNA-protein complexes using nanopores. *Nat Methods*, 4(4):315–317.

Mathe, J., Visram, H., Viasnoff, V., Rabin, Y., and Meller, A. (2004). Nanopore unzipping of individual dna hairpin molecules. *Biophysical Journal*, 87:3205–3212.

Rhee, M. and Burns, M. (2006). Nanopore sequencing technology: research trends and applications. *Trends in Biotechnology*, 24:580–6.

Vercoutere, W., Winters-Hilt, S., DeGuzman, V., Deamer, D., Ridino, S., Rodgers, J., Olsen, H., Marziali, A., and Akeson, M. (2003). Discrimination among individual watson-crick base pairs at the termini of single DNA hairpin molecules. *Nucleic Acids Research*, 31:1311–8.

NOVEL FIELD-EFFECT CONTROLLED SINGLE-WALLED CARBON NANOTUBE NETWORK DEVICES FOR BIOMEDICAL SENSOR APPLICATIONS

Udo Schwalke
Institute for Semiconductor Technology and Nanelectronics, Darmstadt University of Technology
Schlossgartenstrasse 8, 64289 Darmstadt, Germany
schwalke@iht.tu-darmstadt.de

Keywords: Carbon nanotube (CNT), carbon nanotube field-effect sensor (CNTFES), carbon nanotube field-effect transistor (CNTFET), functionalization, virus-detection, integrated circuit, CMOS, hybrid CNT-CMOS integrated circuit, atomic force microscopy (AFM).

Abstract: In this position paper we propose a novel method for the realization of carbon nanotube field-effect sensors (CNTFESs) which will most likely have a strong impact on the next-generation of sensors. CNTFESs are ideally suitable for biomedical sensor applications due to their excellent inherent properties such as ultra small size, high specific surface area and extremely high sensitivity. CNTFESs are based on carbon nanotube field-effect transistors (CNTFETs) which are optimized for sensor applications. We have succeeded to develop a simple, reproducible fabrication process to grow individual CNTs and CNT-networks directly within the specified device area. No tedious manual manipulation and alignment of the CNTs is necessary. Electrical results of the fabricated fully functional CNTFETs are presented and the use of these devices as single-walled CNT-based field-effect controlled sensors for virus detection is discussed.

1 INTRODUCTION

Carbon nanotubes (CNTs) are hollow cylinders of graphene with a diameter of approximately 1 nm and lengths up to 100 µm. Multi-walled carbon nanotubes (MWNTs) consist of several concentrically arranged cylinders of graphene and were observed for the first time in 1991 (Iijima 1991). MWNTs are always metallic with very good conductivity. Single-walled carbon nanotubes (SWNTs), however, can be either metallic (m-SWNTs) or semiconducting (s-SWNTs) depending on the arrangement of the carbon atoms within the hexagonal network, i.e. their chirality.

Since 1998 (Martel 1998; Bezryadin 1998) it is known that s-SWNTs can be used to realize carbon nanotube field-effect transistors (CNTFETs) which are promising candidates for future nanoelectronic applications to replace Si-CMOS. Furthermore, only a change in the charge state is needed to alter the device characteristics via the field effect (i.e. just by the presence of the charge and not via current flow), so that extremely sensitive sensors are feasible, i.e. carbon nanotube field-effect sensors (CNTFESs).

In addition, the inner and outer surface of the single-walled CNT is equal to the whole tube itself and thus the CNTFES will be extremely sensitive to the immediate environment, i.e. ideally suited for biomedical sensor applications. In fact, excellent electronic response properties of CNTFETs to their chemical (Someya 2003) and biological (Staii 2005) environments have been demonstrated already. The response times of CNT-sensors are at least one order of magnitude faster than those based on solid-state sensors. CNT-based nanosensors have the advantages that they are thousands of times smaller than even MEMS sensors and consume much less power. Therefore, CNT-based nano-sensors are highly suitable as implantable sensors. Apart from their small size, semiconducting SWNTs operate at room temperature with a sensitivity as high as 10^3 (Kong 2000). This enables them to perform better in many of the biomedical sensing applications.

Currently CNTFETs and CNTFESs are fabricated and investigated by several research groups. However, the fabrication processes used are often complicated, including both separate growth (Barreiro 2006) and tedious manual manipulation of

the CNTs (Kong 200; Someya 2003; Staii 2005). Obviously, commercial large scale integration remains a major challenge to the realization of CNT-based nanoelectronics and nanosensor technology as well.

At our institute we have developed a novel process to overcome the limitations of manual fabrication of CNTFETs and hence CNTFESs as well (Rispal 2006; Rispal 2007; Schwalke 2007). Our group has succeeded to develop a simple, reproducible fabrication process to grow individual SWNTs and SWNT networks as wells in order to fabricate fully functional CNTFETs and single-walled CNT-based field-effect controlled sensors.

In this position paper we will first present a brief summary of our research results on CNTFETs and subsequently discuss the use of this technology for possible biomedical CNT-based sensor applications.

2 RESULTS AND DISCUSSION

2.1 CNTFET & CNTFES Fabrication

The process is based on chemical-vapor-deposition (CVD) growth of CNTs using an aluminum/nickel 'sacrificial' catalyst which transforms itself after CNT growth into a high-k dielectric (i.e. Al_xO_y) covered with dispersed Ni-nanoclusters (Rispal 2007). SWNTs are grown uniformly across the wafer surface and subsequently contacted with palladium for S/D contacts and the Si-substrate acts as a gate electrode as illustrated in Fig. 1. The process contains neither complicated manipulations of the SWNTs nor multi-step lithography and is Si-CMOS compatible. We choose the in-situ growth method because it appears the most practical approach for future use in high-volume fabrication of advanced integrated nano-sensors at low cost.

For the development of this novel process we have extensively used atomic force microscopy (AFM) for process control and to optimize the CNTFET fabrication technology as well. The role of the Al/Ni films as "sacrificial" catalyst to stimulate SWNT growth is evident from the AFM images of Fig. 2 where the SWNTs always start to grow from a Ni-cluster and extend on the SiO_2. With topographic AFM the SWNTs with a diameter of approximately 1 - 2 nm are clearly detectable on smooth thermally grown SiO_2. Examples of simple CNT network structures are shown in Fig. 3.

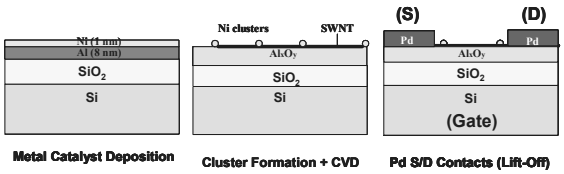

Figure 1: Process flow of CNTFET and CNTFES fabrication based on CVD with sacrificial catalyst.

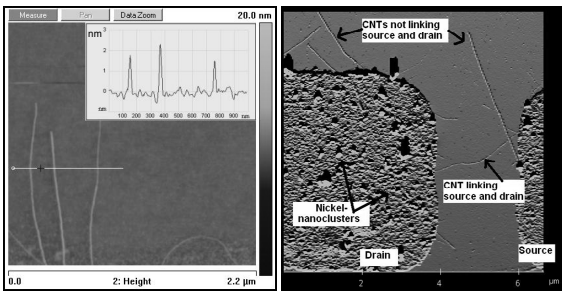

Figure 2: AFM scan of SWNTs with a diameter of approximately 1 to 2 nm on test structure (left). Top view of CNTFET/CNTFES with CNT connecting source and drain electrodes (right).

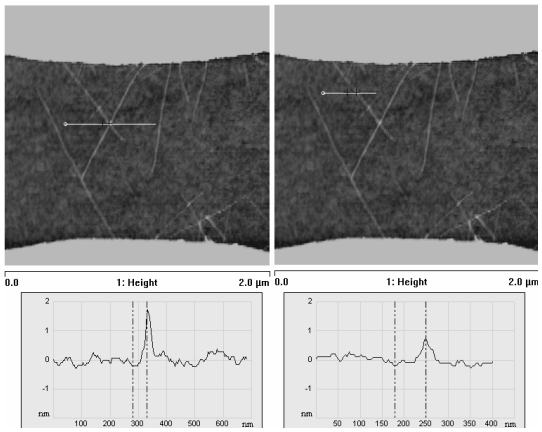

Figure 3: Example of CNT network structures with cross-over points.

2.2 Electrical CNTFET Device Characteristics

Once the electrical connection with the S/D contacts is established, the electrical characteristics of the CNTFETs can be obtained as shown in Fig. 4. In a CNTFET the electric field applied via the gate electrode modulates the charge carrier density in the nanotube and thus the current between the source (S) and drain (D) electrodes. Figure 4 shows the measured drain-current (Ids) as a function of the gate voltage (Vgs) which is swept between positive and negative values. Our fabricated devices are fully

functional and the drain-current is well controlled by the gate voltage. Similar to conventional MOSFETs, the CNTFET device can be properly turned on and off. In fact, the on/off current ratio is in the 10^5 range and exceeds the values of previously published "hand made" CNTFETs (Martel 1998; Bezryadin 1998). The transistor characteristic is unipolar and PMOS-like, i.e. a negative gate bias is required for turn-on.

The gate controlled drain current shown in Fig. 4 exhibits a strong hysteresis effect which is well reproducible. It has been found (Rispal 2007) that the hysteresis is caused by trapped charges and the related charge transfer at the interface between the gate dielectric and s-SWNT. With respect to CNT-sensor applications, the hysteresis effect confirms that any attached charges will have clearly detectable signatures on the device characteristics of

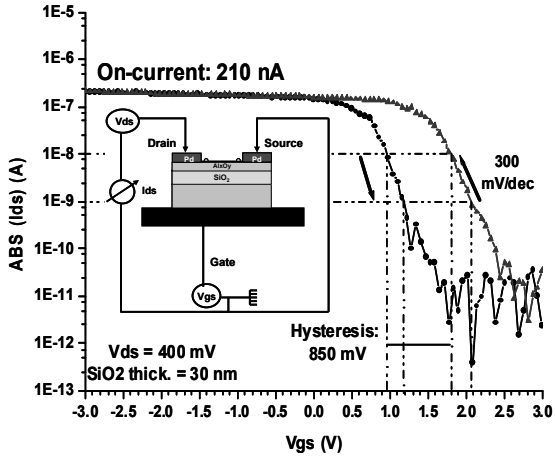

Figure 4: Measured transfer characteristics of fabricated CNTFET device structure. In this example the CNTFET contains just one s-SWNT. Device characteristics of CNTFETs containing multiple SWNTs (CNT-network) are similar, except for the increased drain current drive (Ids) proportional to the number of SWNTs in parallel.

CNTFETs. Since only the change in the charging state will be needed to alter the device characteristics via the field effect, extremely sensitive sensors are feasible.

These CNTFET devices form the basis of the technology platform of the proposed nano-sensors for biomedical applications.

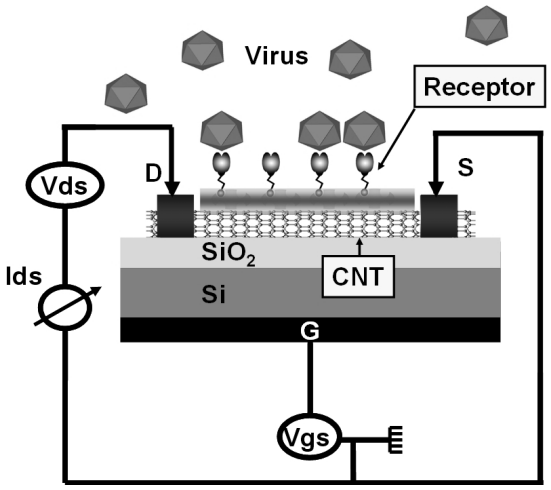

Figure 5: Illustration of proposed CNTFET-sensor for virus detection. The semiconducting single-walled CNT is functionalized with a suitable receptor to allow selective bonding via its protein. Extremely sensitive sensors for virus detection are feasible, since any change in the charging state introduced by the virus will alter the device characteristics via the field-effect.

3 PROPOSAL: BIOMEDICAL CNTFES

Taking advantage of the above mentioned hysteresis effect which we observe in our CNTFET devices, extremely sensitive nano-sensors (i.e. CNTFES) well suitable for biomedical applications can be realized. For example, the detection and identification of single viral particles may be possible using functionalized CNTFETs as sensors as illustrated in Fig. 5: The binding of a virus to a suitably functionalized s-SWNT will measurably affect the gate-dependent electrical current-voltage characteristics of the s-SWNT via charge transfer between the CNT and the virus. The virus detection is thus performed electronically via the CNTFET (cf. Fig. 4) which will alter its electrical device characteristics in presence of a virus. The sensitivity can be enhanced further by using CNT-networks (cf. Fig. 3) or array structures with multiple SWNTs. Furthermore, complete electronic integrated sensor circuits based on hybrid CNT-CMOS technology are envisioned which will perform data analysis on-chip (smart biosensors).

However, the main challenge for the realization of this biomedical sensor will be the proper functionalization of the CNT in order to be highly selective to the desired type of virus. This knowledge is outside of the scope of our own

expertise (nanoelectronics). For a successful realization of these biomedical nano-sensors additional expertise from the biochemical and biomedical area is needed through collaborations with experts from the respective fields via research projects (e.g. EU FP7). In these projects we will provide the CNTFET-sensor devices and will be able to perform all necessary electrical characterization.

4 CONCLUSIONS

In this position paper we have proposed a novel method for the fabrication of carbon nanotube field-effect sensors (CNTFESs). These nano-sensors are ideally suitable for biomedical sensor applications due to their excellent inherent properties such as ultra small size, high specific surface area and extremely high sensitivity. Results have been presented on the novel fabrication process to grow individual CNTs and CNT-networks directly within the specified device area. This is the most practical approach for future use in high-volume fabrication of advanced integrated nano-sensors at low cost since tedious manual manipulations and alignment procedures of CNTs are obsolete. As a proof of concept electrical results on the fabricated fully functional CNTFETs suitable for sensor applications have been presented.

We are offering the biomedical device community our CNT-sensor technology in order to realize next-generation of nano-sensors within a joint project and to evaluate their potential in biomedical applications.

REFERENCES

Barreiro, A., et al., 2006, Applied Physics A, 82 (4), 719
Bezryadin, A., et al., 1998, Phys. Rev. Lett., 80, 4036.
Iijima, S., 1991, Nature, 354, p. 56-58
Kong, J., et al., 2000, Science 287, 622
Martel, R., et al., 1998, Appl. Phys. Lett., 73, 2447.
Rispal, L., et al. 2006, Japanese J. Appl. Physics, 45, 3672
Rispal, L., et al. 2007, *International Conference on Solid State Devices and Materials (SSDM2007),* Tsukuba, Japan.
Schwalke, U., 2007, ECS Transactions, 10, in print.
Someya, T. et al., 2003, Nano Lett. 3, 877
Staii, C., et al., 2005, Nano Lett. 5, 1774

SCREEN-PRINTED SENSOR FOR CHLORIDE QUANTIFICATION IN SWEAT FOR EARLY DETERMINATION OF CYSTIC FIBROSIS

Javier Gonzalo-Ruiz*, Roser Mas, F. Javier Muñoz
Centro Nacional de Microelectronica (CNM-IMB-CSIC), Campus UAB,08193 Bellaterra, Barcelona, Spain
**Javier.gonzalo@cnm.es*

Rafael Camero
Técnicas Científicas para Laboratorio (TECIL), C\Lope de Vega, 99-101,08005 Barcelona, Spain

Keywords: Screen-printed electrodes, choride detection, potentiometric sensor, sweat test, cystic fibrosis.

Abstract One-use screen-printed sensor capable to generate sweat and measure the chloride concentration is presented. Sweat is induced by iontophoresis, pilocarpine is forced to get into de skin and stimulate the sweat glands. Chloride concentration is measured by potentiometry. The performance of the devices has been tested by means of reproducibility studies. Finally, the application of these sensors in several volunteers has been carried out. Errors less than 10% have been obtained in real samples.

1 INTRODUCTION

Cystic fibrosis (CF) is a inherited chronic disease that affects the lungs and digestive system(Davis, 1993). Life expectancy of people with cystic fibrosis is between 30 and 40 years (Doering et al., 2007). Early diagnosis of CF is important, newborn screening can lead to fewer hospitalizations; minimized the symptoms, nutritional benefits (Rosenstein, 1998) and potentially better lung function throughout early childhood (Wang et al., 2002).

There is a close correlation between increased concentration of chloride and sodium in sweat and the presences of the disease (Rockville, 1974). Chloride concentration in sweat less than 40 mmol dm-3 is defined as normal but over 60 mmol dm-3 is indicative of CF. People showing values between 40 – 60 mmol dm-3 are considered as population in risk of CF. The sweat test offers a rapid diagnosis and permits a early CF determination (Warwick et al., 1990, Warwick et al., 1986).

The Gibson-Cooke sweat test (Gibson and Cooke 1959) is accepted as the most discriminatory test for diagnosis of CF. This method is based on iontophoretic sweat test. Pilocarpine is a reagent with the capacity to stimulate sweat glands (Katzung 2004). Sweat is collected either upon a gauze square or filter paper, and then the chloride presents on the sample is analyzed on a laboratory. This test involves multiple steps for collection and analysis of sweat sample, and requires prescribed procedures for each step and high level of quality control.

In this work, the development and test of four electrodes configuration sensor, fabricated by thick film technology, with the capacity to generate sweat and measure chloride ion is presented. Two electrodes were used for sweat generation. Pilocarpine is immobilised over the cathode electrode using a hydrogel matrix, and applying a small current (iontophoresis), this reagent is forced to get into the skin in order to induce sweat (Davis, Wilson et al. 2005; Ortuno, Rodenas et al. 2007).

The other electrodes, working as ISE format, measure the chloride concentration in sweat by potenciometry. Both electrodes were made of Ag/AgCl ink. One acts as working electrode. The other one was cover with KCl-containing membrane in order to realise the miniaturized reference electrode. The organic matrix consist of KCl-containing poly(2-hydroxyethl methacrylate) (pHEMA) membrane (Simonis, Dawgul et al. 2005).

The performance of the reference electrode as well as these sensors was checked by their reproducibility and the response in different synthetic solutions of chloride. Finally, these devices were tested in several volunteers. The chloride concentrations obtained were compared with the results achieved by a common method used by the hospitals.

2 EXPERIMENTAL

2.1 Reagents, Equipment and Software

Analytical grade chemicals were used. All the solutions were prepared from ultra pure deionised water (DI) (18 MΩ cm).

Polyvinyl alcohol (PVA) powder (Mowiol 28-99, Flucka, Steinheim, Germany), pilocarpine (Advanced instruments Inc., Norwood, USA) and sodium nitrate (Advanced instruments Inc., Norwood, USA) solutions were used to develop the hydrogel matrix for iontophoresis process.

To fabricate pHEMA solution the adequate amount of 2-hydroxyethl methacrylate (Aldrich, Steinheim, Germany), ethilenglicol (Flucka, Steinheim, Germany) Tripropylene glycol diacrylate (TPGDA) (Aldrich, Steinheim, Germany) and Benzyldimethyl-ketal (irgacure 651) (Ciba, Basel, Switzeland) were mixed.

Potassium chloride (KCl) (Flucka, Steinheim, Germany) solutions were used on the fabrication, storage and test of the fabricated sensors.

Homemade equipment was developed in order to integrate current application and chloride measurement. Sweat chloride analyzer (Advanced instruments Inc., Norwood, USA) was used to contrast the measurements achieve with the homemade electrodes.

2.2 Electrode Preparation

2.2.1 Screen-printed Electrode Fabrication

A DEK 248 screen-printing system (DEK, UK), screen polyester mesh and polyurethane squeegees were used to fabricate the electrodes. Sequential layer deposition has been performed on a polyester substrate (0.15mm thickness). First, a layer of silver ink (Electrodag 418 SS) was deposited to define the conductive paths. Over these paths, a layer of Ag/AgCl ink (Electrodag 6037SS) was deposited to form the electrodes. A drying cycle (80º/30 min + 120º/5 min) was subsequently applied (Gonzalo-Ruiz et al., 2007). Finally, a piece of polyester substrate was used to prevent the conducting paths form the solution.

These designs are made up of two parts, sweat generator made up of the two external electrodes (28.2 mm^2) and potentiometric sensor composes of both internal electrodes (7.0 mm^2) (Fig.1).

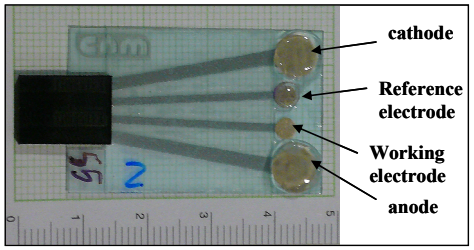

Figure 1: Picture of screen-printed sensor.

2.2.2 Electrode Modification Procedure

In order to fabricate the sweat generator, a hydrogel formulation containing polyvinyl alcohol (PVA) and pilocarpine was developed to entrap this drug over the cathode surface.

Aqueous solution of 17% by weight of PVA was prepared by adding a calculated amount of dry PVA powder into a mixing vessel and slowly dissolving it in water. The temperature of the solution was raised to 98 – 100 ºC during 15 minutes with continuous stirring of the mixture. It was then transferred to pattern and frozen at -10 ºC during 24h. Each pattern had a diameter of 6.2 mm, bit bigger than the electrode, and a thickness of 2 mm. The cured hydrogel samples were immersed, overnight, in a solution of 0.5% by weight of pilocarpine. These pieces were stuck on the cathode surface.

Hydrogel sample saturated with sodium nitrate solution (1% by weight), fabricated in the same way described above, was adhered onto the anode surface.

Sensing part is composed by two electrodes fabricated with Ag/AgCl ink. The surface of the electrode which acts as working one were not modified because of the high selectivity of this material to chloride ion activity (Ives and Janz, 1961).

In the case of reference electrode, it is necessary keep constant the chloride activity over the electrode. In order to do this, the surface was

modified with KCl containing matrix based on photocurable hydrogel. 80% of HEMA, 1,4% of ethilenglicol, 14,6% of TPGDA and 4% of irgacure solution (0.11gr l^{-1} in EtOH)were mixed. 25% of 1 mol dm-3 of KCl solution was added to the mixture. Using an O ring seal, a drop of HEMA-containing solution was deposited on top of AgCl layer, which will act as reference electrode, and it was irradiated with UV light for 4.30 min to polymerise HEMA to pHEMA.

The electrode was stored over night and a glassy pHEMA layer was obtained. Before measuring, the sensor was immersed in 3 mol dm^{-3} of KCl solution.

3 RESULTS AND DISCUSSION

3.1 Potentiometric Sensor Test

First, the performance of the potentiometric sensor in synthetic samples was tested by its reproducibility. The potentiometric response of six different electrodes was checked. Calibration curves in the concentration range 0.01–0.1 mol dm^{-3} of KCl were carried out (Fig. 2). The slopes of these calibrations were used to evaluate the sensor reproducibility. The residual standard deviation (RSD) was 8.02 % (n=6 α= 0.05).

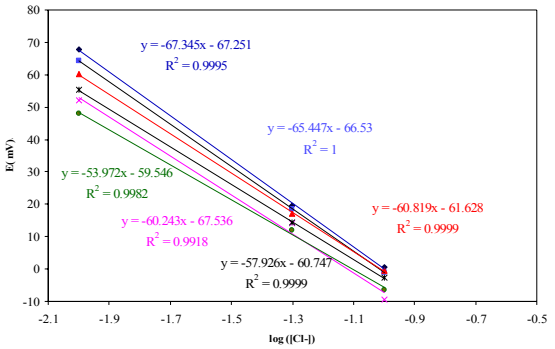

Figure 2: Calibration curves recorded to estimate the sensor reproducibility.

3.2 Application in Real Samples

These devices were used to chloride determination in sweat.

First, the sensor was stuck over the skin (Fig. 3), and then a current between 1 and 1.2 mA was applied during 10 min between the cathode and the anode to force the pilocarpine to get into the skin. Current over 1.2 mV may cause burns. After 10 min waiting, the skin started sweating. The sensing part recorded potential values which can be related to chloride concentration by a calibration curve.

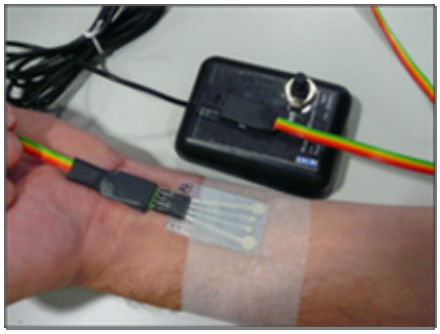

Figure 3: Picture of a sensor during measurement.

Chloride concentration was measured in six volunteers using 1-use screen-printed sensors (SPS). The results were compared with the values achieved by a common method (CM) used by the hospitals.

Table 1 shows the results obtained, as it can be seen, good agreement with the common method was obtained.

Table 1: Chloride concentrations obtained by two different methods in 6 volunteers.

Volunteer	[Cl] (SPS) (mmol dm^{-3})	[Cl] (CM) (mmol dm^{-3})	Error (%)
1	55.5	58	4.3
2	52.7	50	-5.4
3	60.1	56	-7.4
4	60.2	58	-3.9
5	56.8	58	1.9
6	74.5	70	-6.4

4 CONCLUSIONS

We have demonstrated that it is possible to develop a device capable to induce sweat and measure chloride concentration. The potentiometric sensor reaches acceptable values of reproducibility (8.02%) These sensors were applied in 6 volunteers with satisfactory results, using a rapid and low cost methodology for cystic fibrosis detection.

ACKNOWLEDGEMENTS

The authors would like to acknowledge funding from the Spanish Ministry of Science & Education via the MICROFIBROSIS (PET2005-0849) project.

REFERENCES

Davis, P. B. (Ed.) (1993) *Cystic fibrosis,* Marcel Dekker, cop., New York.

Davis, S. L., Wilson, T. E., Vener, J. M., Crandall, C. G., Petajan, J. H. and White, A. T. (2005) *Journal of Applied Physiology,* 98, 1740-1744.

Doering, G., Elborn, J. S., Johannesson, M., de Jonge, H., Griese, M., Smyth, A., Heijerman, H. and Grp, C. S. (2007) *Journal of Cystic Fibrosis,* 6, 85-99.

Gonzalo-Ruiz, J., Alonso-Lomillo, M. A. and Munoz, F. J. (2007) *Biosensors & Bioelectronics,* 22, 1517-1521.

Ives, D. J. and Janz, G. J. (1961) *Reference Electrodes, Theory and Practice*, New York.

Katzung, B. G. (Ed.) (2004) *Basic and Clinical Pharmacology, 9th ed.*

Ortuno, J. A., Rodenas, V., Garcia, M. S., Albero, M. I. and Sanchez-Pedreno, C. (2007) *Sensors,* 7, 400-409.

Rockville (Ed.) (1974) *Guide to Diagnosis and Management of Cystic Fibrosis,* Cystic Fibrosis Foundation.

Rosenstein, B. J. (1998) *Clinical in Chest Medicine,* 19, 423-441.

Simonis, A., Dawgul, M., Luth, H. and Schoning, M. J. (2005) *Electrochimica Acta,* 51, 930-937.

Wang, S. S., O'Leary, L. A., FitzSimmons, S. C. and Khoury, M. J. (2002) *The Journal of Pediatrics* 141, 804-810.

Warwick, W. J., Hansen, L. G. and Werness, M. E. (1990) *Clinical Chemistry,* 36, 96-98.

Warwick, W. J., Huang, N. N., Waring, W. W., Cherian, A. G., Brown, I., Stejskallorenz, E., Yeung, W. H., Duhon, G., Hill, J. G. and Strominger, D. (1986) *Clinical Chemistry,* 32, 850-853.

BIOINTERFACES BASED ON IMMOBILIZED BORONIC ACID WITH SPECIFITY TO GLYCATED PROTEINS

Jan Přibyl and Petr Skládal
National Center for Biomolecular Research, Masaryk University, Kotlářská 2, Brno, Czech Republic
pribyl@chemi.muni.cz, skladal@chemi.muni.cz

Keywords: Glycated hemoglobin, aminophenylboronic acid, biosensors, quartz crystal microbalance, heterogeneous affinity assay, microtitre plate.

Abstract: Development of bioanalytical assays for determination of glycated hemoglobin content in blood samples is reported. First, a combined biosensor setup for determination of total and glycated hemoglobin content was successfully developed and tested. The effect of various operating parameters, such as ionic strength, flow rate and instrumental set-up was optimized. The total hemoglobin content was analyzed by measuring of absorbance of the hemoglobin-cyanide derivative at 540 nm. Only one standard (calibrator), diluted in various proportions, was necessary for the method calibration. The full range of HbA_{1c} content (4 to 15 %) presented in blood can be analyzed. Only 1 µl of blood was required for analysis. The developed method was successfully evaluated for analysis of blood samples collected from diabetic patients. Next, the heterogeneous affinity assay performed in a microtitre plate with an immobilized boronic acid is described. This assay is based on ELISA (Enzyme-Linked Immunosorbent Assay) principle; however stable chemiselective ligand is used in this case. The content of glycated hemoglobin is determined according to its peroxidase activity after attachment to immobilized boronic acid derivative; the total hemoglobin concentration is measured as an absorbance at 405 nm.

1 INTRODUCTION

Diabetes mellitus is a group of diseases characterised by high levels of blood glucose resulting from defects in insulin production, insulin action, or both. Diabetes can be associated with serious complications and premature death. Diabetes was the sixth leading cause of death in USA in 2000. (National Diabetes Information Clearinghouse, http://diabetes.niddk.nih.gov). The steps to control the disease and lower the risk of complications should be taken. In this way, blood and urine glucose analysis, cholesterol reduction and blood pressure control should be mentioned. Analysis of glycated hemoglobin (HbA_{1c}) helps to monitor the long-term progression of diabetes without influence of the short-term fluctuations of blood glucose. The fraction of HbA_{1c} is usually indicated as percentage of its presence in the total hemoglobin content. The content of glycated hemoglobin in blood should substitute the term "glycemia"; values lying under 7% indicate good health state of patient and effective practicing of the proposed therapy (Marshall and Barth, 2000).

Glycated hemoglobin (GHb) refers to a series of minor hemoglobin components which are stable adducts formed by reaction of hemoglobin primary aminogroups with various sugars. Hemoglobin HbA_{1c} is a stable glucose adduct to the N-terminal group of the β-chain of HbA_0. In current opinion, concentration of the hemoglobin variant HbA_{1c} is considered to be the only specific and stable indicator of long-term diabetes progress. Neither the whole glycated fraction of hemoglobin (HbA_1) nor fructosamine can be any longer used in the disease diagnosis.

A wide range of methods for analysis of the glycated hemoglobin (either HbA_1 or HbA_{1c}) has been reported recently. However, only few of them were based on biosensor approach and mostly the chromatographic approaches were employed. From the area of biosensor development, especially two concepts should be mentioned. The first one was based on selection of ligands from the hexapeptide combinatorial library for binding the glycated terminus of hemoglobin β-chain; thus found hexaptides exhibited high specifity and stability (Chen et al., 1998). However, only the preliminary study was performed, additional testing of this

affinity molecules and integration to some analytical method (e.g. affinity chromatography) is essential for correct evaluation. A monolayer of boronic acid conjugate with 11-mercaptoundecaonic acid immobilised on the surface of gold nanoclusters was used as recognition element in another study (Valina-Saba et al., 1999). An easy approach was reported, when the precipitation reaction between boronic groups on the particle surface and glycated protein (horse-radish peroxidase) was visible. Unfortunately, the application for determination of HbA_{1c} content in whole blood, which is rather complex mixture, was not tested.

Boronic acid shows ability to bind covalently to either 1,2- or 1,3-diols and thus forms five- or six-membered cyclic esters. 3-aminophenylboronic acid (APBA) binds in this way to the *cis*-diols of saccharides, glycated proteins or nucleic acids (Pickup et al., 2005). The formation of a boronate ester is usually described as a two step reaction; the planar boron group initially reacts with hydroxyl (pH>7.0 is essential) to form tetrahedral boronate anion, which subsequently binds reversibly to the positively charged carbon atoms in the diol-containing structure (Ito et al., 2003). This kind of ester formation designates boronic acid and its derivatives to be used as the affinity recognition elements in variety of applications, such as construction of sensors for saccharides with piezoelectric (Lau et al., 2000) and surface plasmon resonance (Kugimiya and Takeuchi, 2001) transducers or fluorescent (Kataoka et al., 1995) detection. Boronic acid derivatives immobilized in the matrix of columns have formed the basis of a new field of chromatographic techniques designated for analysis and separation of sugars and glycated proteins. This area is commonly known as boronate affinity chromatography (Bongartz and Hesse, 1995).

The aim of presented study was to continue our previous attempts with boronate-modified sensors for sugars (Přibyl and Skládal, 2005) in order to develop an innovative, easy to handle and cost effective but reliable biosensor set-up with high stability and reproducibility for determination of glycated hemoglobin in blood samples. The designed system contains two parts, one performs the analysis of HbA_{1c} using a piezoelectric sensor modified with phenylboronic acid, and the second one is designed for a photometric determination of total Hb. The absolute concentration of these blood components differs in each sample. The percentage of HbA_{1c} presence will be determined as a ratio of these two concentrations; $(conc_{HbA1c}/conc_{Total\ Hb})$ x 100%.

Another interesting method for detection of glycated hemoglobin is reported, too. This bioanalytical method called AHA (Affinity Heterogeneous Assay) employs microtitre plates consisting of the wells covered with aminophenylboronic acid. The AHA assay allows determination of total hemoglobin as well as glycated fraction of hemoglobin in blood samples, similarly as the biosensor based method.

2 EXPERIMENTAL

2.1 Chemicals and Reagents

Chemicals were obtained from Sigma (St. Luis, USA) and used as received without any further purification. Microtitre plates with chemically reactive surface (NUNC Immobilizer Amino) were from Nunc (Copenhagen, Denmark).

The special solutions were prepared, stored and used as officially recommended (International Committee for Standardization in Haematology, 1978) for analysis of total hemoglobin content in blood samples.

2.2 Instrumentation

Measurements with the piezoelectric biosensor were performed using 10 MHz, AT-cut quartz crystals (ICM, Oklahoma City, OK, USA) with gold-coated smooth quartz discs (electrode area, 0.8 cm^2).

In the center of the system, there was placed a PMMA-made flow-trough cell (internal volume 10 μl) from NanoQ (Brno, Czech Rep.) with the piezoelectric biosensor mounted between two silicon rubber O-rings. The cell was supplied with flowing liquid via two stainless steel tubes (i.d., 0.5 mm). Sensor was connected to MultiLabPlus instrument (MultiLab) combining oscillator with high resolution frequency counter.

Handling of liquids and samples was performed by the FIAlab 3500b instrument (Alitea, Seattle, WA, USA).

Optical part for determination of total hemoglobin content was located in front of the biosensor cell. The detector consisted of a Z-type flow-trough absorption cell (optical path, 10 mm) supplied with flowing liquids trough the Teflon tubing and standard visible light source and optical fibre spectrophotometer from Ocean Optics (Dunedin, FL, USA).

2.3 Immobilization Procedure

2.3.1 Affinity Biosensor Fabrication

Matrix based layer was prepared when 2% solution of polyethylene imine (PEI) in methanol (3 μl) was used to activate the gold surface. The APBA layer was attached through the glutaraldehyde linker (8%, 8 hours, 4 ^{o}C) In the last step, the recognition layer was stabilised by the reduction of Schiff bonds with 10 mg/ml solution of sodium borohydride (2 hours).

The thiocompound-APBA conjugates were prepared in order to modify the gold biosensor surface with a monolayer of boronate groups. In the first step, the carboxygroup of mercapto-terminated (on the opposite side of chain) acids was activated with carbodiimide (3 hours, 99 ^{o}C). Conjugation of aminophenylboronic acid to bellow mwntioned thiocompounds was performed during the next step: DTSP, 11-MUA, 16-mercaptohexadecanoic acid and lipoic acid (3 hours, 99 ^{o}C). Final products exhibited light-yellow color and were stored at -20 ^{o}C prior use.

A monolayer of boronic groups was prepared, when the freshly cleaned gold electrodes were incubated with 15 μl of the conjugate for 24 hours at laboratory temperature in a closed chamber.

Gold surface modified with 11-mercaptoundecanoic acid and the freshly cleaned gold electrode were used as reference surfaces. For comparison of binding specifity to the matrix-modified surfaces, the polyethylene imine layer was attached to the piezosensor.

2.3.2 Specific Modification of Microtitre Plate

The 'Amino Immobilizer' microtitre plate from Nunc shows ability to bind covalently any molecule containing primary aminogroup. 10 mg/mL solution of aminophenylboronic acid (APBA) in 50 mM carbonate buffer pH=9.5 was used to cover the microtitre plate with boronic groups. The solution of APBA was kept overnight under ambient temperature in order to cover the wells of plate with boronic groups. After 4-times repeated washing (PBS pH=7.4), the unreacted surface group were saturated with glycine (25 mg/mL in PBS buffer pH=7.4) during 2 hours reaction performed under ambient temperature. After thorough washing with PBS, the plates were dried in the air stream of ambient temperature (4 hours). Such modified plates can be long-term stored in a well sealed box (4 ^{o}C) without any significant loosing of their binding activity.

2.3.3 Biosensor Setup - Measuring Procedure

A similar protocol was used for all experiments:

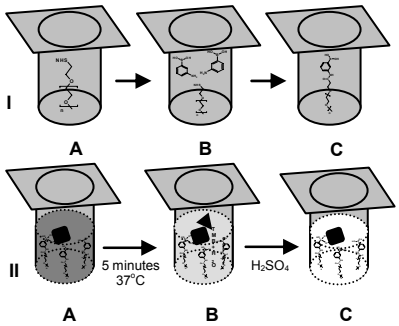

Figure 1: I – Immobilization of the APBA molecule to the activated surface of microtitre plate (A, activated surface; B, APBA solution added; C, APBA-modified surface. II – Procedure of total and glycated hemoglobin determination in boronic acid modified plate (A, well filled with diluted blood sample – total hemoglobin determination during binding of GHb to the surface; B, peroxidase activity of bound GHb is used to oxidase a substrate; C, reaction stopped and the overall activity measured).

after 5 min of the base-line signal stabilisation with the carrier buffer, the flow of sample - glycated hemoglobin dissolved in the carrier buffer (alternatively supplied by sorbitol solution) followed for 7 min. For the next 7 min, the flow cell was washed with the carrier buffer in order to equilibrate the signal (non-specifically adsorbed molecules dissociated from the biosensor surface). Injection of 200 mM aquatic solution of HCl for 120 seconds disintegrated the complex formed between glycated hemoglobin and monolayer of boronic acid groups; complex [GHb-matrix immobilized APBA] dissociated spontaneously. Washing with working buffer for a few minutes followed (new base-line stabilization) prior performing the next measuring cycle.

2.3.4 AHA Analysis

Another way of determination of total hemoglobin in blood samples is, comparing to the previously employed conversion to a cyanomethemoglobin, its conversion to alcalic hematin. The carbonate buffer pH=9.0 was used for this purpose, when the blood samples were diluted 400-times in this medium, the most of hemoglobin molecules was converted to the hematin. This can be quantified by measuring of absorbance at 405 nm. Moreover, the alcalic pH is an optimal value to support the affinity interaction between the boronic group and GHb in a solution.

The blood solution (in a carbonate buffer) was left to interact with the surface immobilized boronic groups for 60 minutes, at ambient temperature, in a closed box. The total hemoglobin content was quantified as change of A_{405} during 20 minutes following the reagent addition. Afterwards, the wells were washed 4-times with PBS buffer pH=7.4 and the peroxidase substrate solution, containing 0.075% hydrogen peroxide and 105 ug/mL of tetramethylbenzidine in 50 mM acetate buffer pH=4.5 (solution freshly prepared before each experiment). The enzymatic reaction releasing intensive blue color was left to proceed for 5 minutes in a dark box heated to 37 ^{o}C. The reaction was stopped by addition of 50 uL of 1 M H_2SO_4 solution to each well. The color of solution in wells turns yellow immediately. The amount of the enzymatic reaction product was measured as absorbance at 405 nm in a microtitre plate reader.
The absorbance of the whole blood solution corresponds to a total hemoglobin in a sample, the enzymatic activity of bound hemoglobin (measured as A_{405} in a next step) is proportional to a glycated hemoglobin content. The percentage of GHb presence in the total hemoglobin can be easily calculated by simple dividing of those two values.

3 RESULTS AND DISSCUSSION

3.1 Biosensor based Experiments

The amount of boronic groups deposited on the surface of piezoelectric sensors was first monitored during the immobilisation procedure. The deposited mass was calculated according to Saurbray equation from the difference of resonant frequency during deposition. These results indicate that the highest amount of boronic groups was coupled to the biosensor surface via 3,3′-Dithiodipropionic acid di(N-hydroxysuccinimide ester (DTSP), 11-mercaptoundecanoic acid (11-MUA) and mainly inside the polyethylene imine structure.

However, the evidence of optimal affinity for samples containing glycated hemoglobin provided the comparative experiments. Within those, the eight types of prepared biosensors with either specific or reference surfaces were consequently mounted into the flow-trough cell and the response to GHb sample (410 μg/ml, constant concentration) was monitored. The experiments were done in duplicate with each sensor; the equal scheme of experiment was used in all cases. The lowest response provided the Gold-PEI-GA-APBA sensor (together with the appropriate reference one). Therefore these were tested for their ability to bind sorbitol (low molecular compound containing vicinal diol group) in concentration of 10 mg/ml (in phosphate buffer pH=9.0). Response of the specific sensor (229.6 Hz) together with the reference one (19.8 Hz) showed correctness of theoretical predictions. Low density of boronate groups presented on the top of PEI-matrix (low affinity to glycated hemoglobin) allowed only low binding of glycated hemoglobin. Moreover, the difference between specific and non-specific response (66.5 vs. 44.6 Hz, respectively) was the next, and probably main, reason to exclude the PEI-GA-APBA recognition layer from further use in GHb analysis.

As it was commonly considered the boronic acid-diol interaction is not substantially affected by ionic strength of environment. However, most recent publications (Zhong et al., 2004) indicated a substantial increase of boronate affinity to diol group in low ionic strength solutions (co-solute concentrations up to 0.25 M). Determination of the ionic strength effect on glycated hemoglobin interaction with immobilised boronic groups was not the principal aim of our study. However, the examination of influence of the used various reagents on interaction were carried out prior to the final analysis. The ionic strength of tested reagents proceeded from 0.9 to 84.3 mM (Modified Drabkin reagent and 50 mM phosphate buffer, respectively), pH was in range 7.4 - 9.6. Low ionic strength, i.e. use of Modified Drabkin Reagent, supports the affinity interaction. This result well correlates with findings of other authors.

The biosensor Gold-MUA-APBA and the previously optimized conditions (peristaltic pump; flow rate of 100 μl/min; Modified Drabkin reagent as the working medium and the 2 min regeneration of sensing surface with 200 mM HCl) were used in all calibration experiments. The presented method shows the advantage of calibration using only one standard solution – blood sample with defined content of glycated hemoglobin. After dilution in various proportions, thus obtained standards were used for calibration. The response of the piezoelectric biosensor as well as photometric sensor was increasing with increasing concentration of glycated and total Hb, respectively. The percentage of glycated hemoglobin was calculated as the glycated hemoglobin / total Hb ratio (x 100%). Both values (glycated and total hemoglobin concentration, respectively) were taken from the calibration curves, constructed as the response of biosensor and photometric sensor to concentration of glycated and total hemoglobin, respectively. The biosensor can not be calibrated only using samples containing various percentage of glycated hemoglobin, the

amount of total hemoglobin should be considered, too.

A blood sample of diabetic patient with high content of glycated hemoglobin (14.3%; determined by the ion-exchange HPLC) was used for calibration of our setup. The set of six samples for calibration of analyser was prepared by dilution of blood with the Modified Drabkin reagent in the following sequence: 300, 375, 500, 600, 1000 and 2875-times. Thus prepared samples were placed to the autosampler and after 15 min of preincubation (including the base-line stabilisation) were consequently measured. The combined calibration graph was constructed using the responses of photometric and piezoelectric sensors in the time 5 min (Fig. 2).

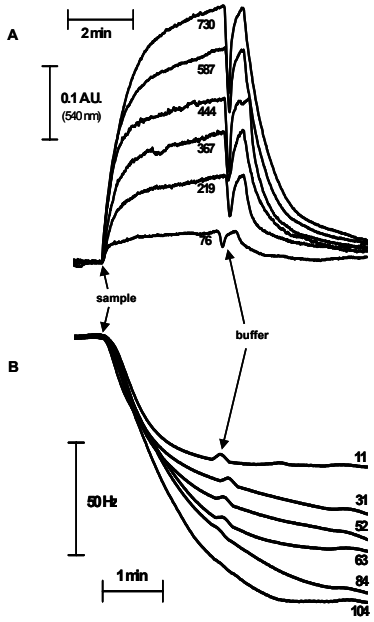

Figure 2: Calibration of a combined setup, upper curves show absorbance changes due to the different hemoglobin content in samples, the curves below were recorded as a result of binding of various concentration of glycated hemoglobin.

3.2 AHA Experiments

The AHA method was optimized according its ability to bind glycated hemoglobin. Buffers of various pH (7 and 9, respectively) were used to maximize the surface affinity to GHb. Although there was found higher adsorption of glycated hemoglobin at pH=7, the next experiment showed the low specifity of binding at this pH. On the other hand, use of buffer of pH=9.0 provides quite a lower capacity of the surface, however, the binding is highly specific (Fig. 3). The reference surface, covered only with glycine, was employed to compare specifity of binding.

In the further experiments the assay was calibrated by use of hemoglobin standard solution (total Hb calibration) and blood sample (with known GHb content, determined by a standard method), both diluted in various ratio in order to get at least five points in a calibration graph. The total hemoglobin assay provided a linear response in range 10 – 1000 μg/mL; the GHb analysis can be performed in the concentration range varying between 10 and 40 μg GHb/mL.

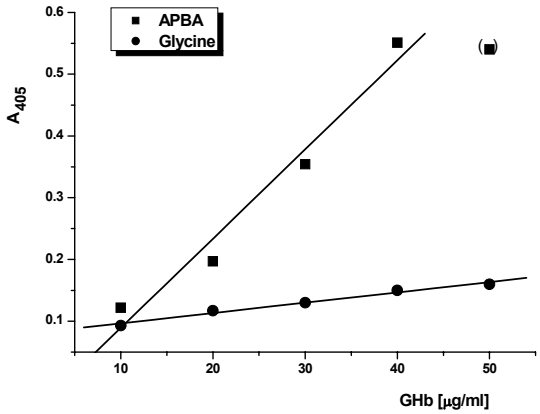

Figure 3: Measured enzymatic activity as result of binding of glycated hemoglobin to reference (modified with glycine) and specific surface (modified with aminophenylboronic acid, APBA). Experiments performed at pH=9.0.

4 CONCLUSIONS

Two methods for analysis of hemoglobin A_{1c} are presented. First, a combined biosensor for determination of glycated and total hemoglobin in blood is reported. The amount of total hemoglobin is measured in flow-through photometric sensor, concentration of the glycated fraction is subsequently monitored by its binding to the APBA-modified piezoelectric biosensor (higher content cause higher damping of resonant frequency).

The other method is based on ELISA principle (AHA, Affinity Heterogeneous Assay) in either direct or indirect arrangement. Boronic acid derivative, capturing the glycated fraction of hemoglobin, is immobilized on the surface of the microtitre plate. Amount of glycated hemoglobin is visualized by measuring of its peroxidase activity. Total hemoglobin concentration is measured photometrically at 405 nm.

Both methods present promising approach in diagnosis of glycohemoglobin. The first one presents fully automatic, low-cost instrument, the other one offers the possibility to monitor simultaneously HbA_{1c} content in 96 blood samples within a relatively short time (2 hours).

Possible use of those methods in routine analysis of blood samples and their comparison with conventional methods (HPLC) was shown, too.

ACKNOWLEDGEMENTS

The work was supported by the grant no. KJB401630701 of the Grant Agency of the Czech Academy of Science.

REFERENCES

Bongartz, D., Hesse, A., 1995. Selective extraction of quercetrin in vegetable drugs and urine by off-line coupling of boronic acid affinity chromatography and high-performance liquid chromatography. J. Chromatogr., B. 673, 223-230.

Chen, B., Bestetti, G., Day, R.M., Turner, A.P.F., 1998. The synthesis and screening of a combinatorial peptide library for affinity ligands for glycosylated hemoglobin. Biosens. Bioelectron. 13, 779-785.

International Committee for Standardization in Haematology, 1978. Recommendations for reference method for hemoglobinometry in human blood (ICSH Standard EP 6/2: 1977) and specifications for international hemoglobincyanide reference preparation (ICSH Standard EP 6/3: 1977). J. Clin. Pathol. 31, 139-143.

Ito, H., Kono, Y., Machida, A., Mitsumoto, Y., Omori, K., Nakamura, N., Kondo, Y., Ishihara, K., 2003. Kinetic study of the complex formation of boric and boronic acids with mono- and diprotonated ligands. Inorg. Chim. Acta 344, 28-36.

Kataoka, K., Hisamitsu, I., Sayama, N., Okano, T., Sakurai, Y., 1995. Novel sensing system for glucose based on the complex formation between phenylborate and fluorescent diol compounds. J. Biochem. 117, 1145-1147.

Kugimiya, A., Takeuchi, T., 2001. Surface plasmon resonance sensor using molecularly imprinted polymer for detection of sialic acid. Biosens. Bioelectron. 16, 1059-1062.

Lau, O.W., Shao, B., Lee, M.T.W., 2000. Affinity mass sensors: determination of fructose. Anal. Chim. Acta 403, 49-56.

Marshall, S.M., Barth, J.H., 2000. Standardization of HbA_{1c} measurements: a consensus. Ann. Clin. Biochem. 37, 45-46.

Pickup, J.C., Hussain, F., Evans, N.D., Rolinski, O.J., Birch, D.J.S., 2005. Fluorescence-based glucose sensors. Biosens. Bioelectron. 20, 2555–2565.

Přibyl, J., Skládal, P., 2005. Quartz crystal biosensor for detection of sugars and glycated hemoglobin, Anal. Chim. Acta 530, 75-84.

Valina-Saba , M., Bauer , G., Stich , N., Pittner , F., Schalkhammer T., 1999. A self assembled shell of 11-mercaptoundecanoic aminophenylboronic acids on gold nanoclusters. Mat. Sci. Eng. C 9, 205-209.

Zhong, H., Li, N., Zhao, F., Li, K., 2004. Determination of proteins with Alizarin Red S by Rayleigh light scattering technique. Talanta 62, 37–42.

A MINIMALLY INVASIVE MICROWAVE HYPERTHERMIC APPLICATOR WITH AN INTEGRATED TEMPERATURE SENSOR

Guido Biffi Gentili and Mariano Linari
Department of Electronic and Telecommunications, University of Florence, Via S. Marta 3, 50139 Firenze, Italy
guido.biffigentili@unifi.it, mariano.linari@unifi.it

Keywords: Interstitial microwave applicator, endocavitary, hyperthermia, temperature sensor.

Abstract: In the field of microwave hyperthermia and thermo-ablation, the use of minimally invasive applicators is recognized as a very promising means for the treatment of small, early stage, cancer lesions because a very thin applicator can be easily introduced inside the body and precisely directed towards a deep seated tumour using the most advanced 3D imaging techniques and surgical stereo-navigation. Minimally invasive applicators have been successfully employed for the treatment of bladder carcinoma and brain tumours but the accurate temperature monitoring of the heated tissue volume still remains an open problem. In this paper we propose a new minimally invasive applicator, integrating a low-cost metallic wired temperature sensor. The miniaturised endocavitary applicator consists of a asymmetric isolated dipole operating at 2.45 GHz. The very slim shape of the applicator allows to easily insert it into the lesion through a soft plastic tube (catheter) while a temperature sensor, properly embedded in the applicator body, measures the tissue temperature at the interface with the catheter surface. An electromagnetic analysis based on the Finite Integration Technique (FIT) and experimental verifications over a tissue sample proved that a coaxial choke, enclosing the temperature sensor wires, allows localize the heating pattern in a restrict volume while drastically reducing measuring artefacts due to the perturbing effects induced by the probe leads.

1 INTRODUCTION

Microwave endocavitary and interstitial hyperthermia has been widely investigated in the past decades as localised thermal therapy for cancer treatment. Many thin applicators have been developed and used in therapeutic applications with valuable results. Most of them are essentially constituted of an insulated monopole, dipole or helix feed through a thin coaxial cables. However several technical solutions (Turner, 1986; Tumeh and Iskander, 1989; Camart *et al.*, 1996; Lin and Wang, 1987; Cerri *et al.*; 1993; Saito *et al.*, 2000) have been proposed in order to localize the heating in a restrict area of tissue around the tumour and to avoid accidental and unwanted hot spots in the healthy tissue.

The effectiveness of a microwave thermal therapy depends not only on the radiative properties of the applicator used but also on the reliable and accurate temperature control during the therapeutic treatment. Impedance tomography, microwave radiometry, magnetic resonance imaging (MRI) and also methods based on ultrasounds are very attractive non-invasive temperature-monitoring techniques. Despite these promising prospects, up till now a very accurate measure of depth tumours temperature can be obtained only by invasive techniques, because only thermocouples, thermistors or optical fibres sensors seem to give the required measuring accuracy, spatial resolution and real-time response. Temperature monitoring by invasive sensors is common practice in the hyperthermic treatments. Usually, very thin probes are separately inserted in the tissue near the antenna and moved ahead and back in order to better estimate the effective heating pattern. In that case only optical fibre sensors could be employed because metallic wired probes located near the antenna strongly interact with the radiating element, producing uncontrollable electromagnetic fields distortion and false temperature readings.

When the tumour is at its early stage a single applicator can be employed to heat the small volume of the lesion by inserting it as sketched in Figure 1.

In this case it is advantageous to integrate the temperature sensor directly in the applicator body in order to avoid additional traumas in the patient and to simplify the hyperthermic treatments itself.

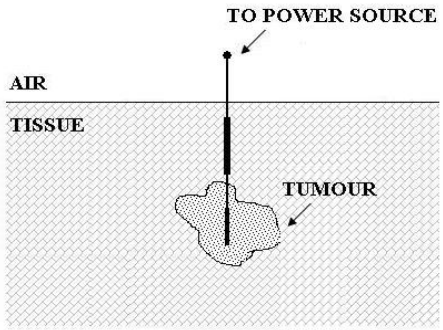

Figure 1: Single applicator heating a small tumour.

When lesions are more extended in volume an array of applicators could be required to uniformly heat the tumor, as sketched in Figure 2.

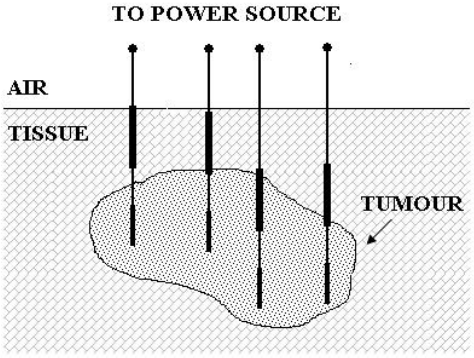

Figure 2: Array of applicators heating a medium-sized tumour.

Also in this case applicators with integrated temperature sensors can be usefully employed because the temperature distribution inside the tumor volume can be numerically estimated starting from the point measurements taken in correspondence of each radiating element, by combining tomography algorithms and bio-heat equation.

From the mechanical and structural point of view it is not difficult to integrate a very thin fiber-optic probe inside the core of the applicator without altering its original diameter. It is worth to note, however, that fiber-optic sensors are very expensive and delicate devices and thus not properly suited for the production of a rugged mono-use applicators, as required for the routined clinical practice.

Another sensor that is practically unaffected by the strong EM fields existing near the antenna is the Bowman thermistors (Bowman, 1976) because its high resistance leads can not carry significant RF currents. Unfortunately also this sensor type is delicate and expensive to be fabricated.

Ordinary low-cost and sturdy thermometric sensors, as thermocouples and thermistors, use high conductance metallic leads for the connection to the measuring unit. Unfortunately, when they are placed too close to the applicator body, metallic wires cause unwonted electromagnetic (EM) interferences. In these cases dangerous and uncontrolled hot spots in the tissue can occur, as well erroneous (or very noisy) temperature readings.

This work suggests a novel technique for integrating a low-cost wired temperature sensor inside the body of a minimally invasive Microwave Hyperthermic Applicator (MHA) without perturbing the radiated fields.

2 METHODS

2.1 Applicator Design

The proposed interstitial/endocavitary MHA, depicted in Figure 3, essentially consists of a coaxial asymmetric dipole type antenna, radiating in the biological tissue through an insulating tube (catheter).

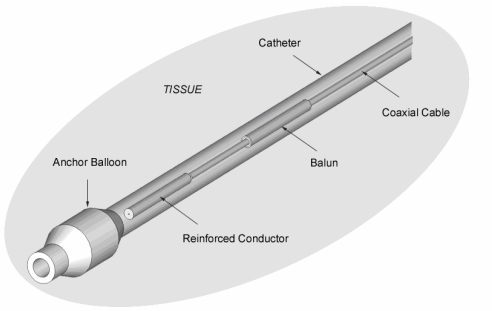

Figure 3: Microwave Hyperthermic Applicator (MHA) (length: 65 mm; thickness: 2 mm) working at 2.45 CHz.

In order to avoid unwanted heating of the healthy tissue, a coaxial balun has been introduced to block the back currents flowing on the surface of the coaxial feeding line (Longo *et al*., 2003). The diameter of the radiating upper arm of the dipole has been properly increased to improve the matching of

the MHA input impedance to the tissue (Jones *et al.*, 1988; Biffi Gentili *et al.*, 1995). Thank to its very thin shape (65 mm in length and 2 mm in thickness) the coaxial applicator can be easily introduced inside a small catheter (3-4 mm in diameter) and subsequently inserted into the lesion. The position of the applicator can be fixed *in loco* using an anchor balloon.

Starting from this basic applicator configuration, a wired temperature probe (thermocouple or thermistor) has been successively introduced into the catheter inside the balun as depicted in Figure 4.

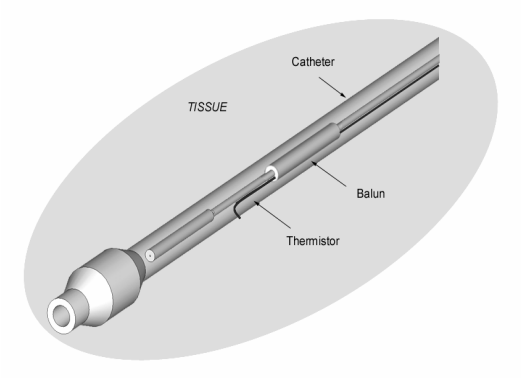

Figure 4: MHA with a temperature probe embedded inside the insulator of the coaxial choke.

The temperature sensitive tip of the probe is embedded in the catheter body in order to measure the temperature of the tissue at the interface with the catheter itself, where higher temperatures are expected. Miniature (SMT) chip inductors can be also inserted close to the sensing tip of the probe to isolate it from the radiating conductors of the coaxial applicator.

2.2 Numerical Analysis

Electromagnetic full-wave analysis has been employed to investigate the Specific Absorption Rate (SAR) distribution produced by the applicator and the perturbations due to the closeness of the metallic wires of the temperature probe. EM fields have been calculated with a time domain Finite Integration Technique (FIT) (CST Studio Suite, 2006) in a three-dimensional spatial domain constituted by a muscular tissue volume including the MHA model.

Perfect Matched Layers (PML) boundaries condition (Berenger, P. 1994) have been used in order to limit the computational domain to 140 × 60 × 60 mm^3 volume. However the thin profile of the applicator and the high permittivity of the human muscle tissue ($\varepsilon_r = 52 - j13$ @ 2.45 GHz) required a very little mesh size (< λ/50 at 3 GHz) which made heavy the computation load. EM simulations, performed in the 2 to 3 GHz frequency range, run for 2 hour with an Intel Pentium III @1GHz with 1.5 GB RAM memory

2.3 Experimental Set-up

Different types of soft material phantoms with the same dielectric properties of human tissue have been experimented upon in the recent years to investigate SAR and temperature distribution produced by microwave applicators. An accurate phantom should closely represent the electromagnetic properties of the human body in the frequency range of interest and it should be easy to prepare and to handle.

When small volume of tissue are involved in the heating process, true biological tissue sample as a suine liver or a chicken breast appear more suitable to investigate power deposition near the applicator.

In our case the realized MHA prototype has been tested by using chicken breast. The prototype, ending with a SMA male connector, is connected to a microwave source working at 2.45 GHz, capable of a maximum power of 300 W continuous (CW) or pulsed. The input and reflected power of the MHA is monitored by a power meter connected to a bidirectional coupler while the temperature, measured by a thermocouple or a thermistor, is acquired by an A/D converter, recorded in a data file and simultaneously displayed on a PC monitor for the real-time direct control of the heating process.

3 RESULTS AND DISCUSSION

In order to accurately define the heating pattern volume and avoid unpredictable field distortion or undesirable tissue overheating, back currents flowing on the surface of the coaxial feeding line and currents induced on the metallic wires of the thermocouple was blocked by a common coaxial balun. As a result, at the 2.45 GHz operative frequency, the power deposition in the tissue is confined within a small well defined ellipsoidal volume wrapping the radiating section of the applicator body as shown in Figure 5.

As expected, numerical simulations evidence a focusing point of the EM fields near the sensing tip of the sensor that could be responsible of a localised hot spot and temperature overestimation. In order to reduce this unwonted spot, miniaturised chip inductors have been properly inserted in series to the leads of the temperature sensor near the tip to block any RF current flowing in the sensing element. In

our EM model we used lumped inductive elements with an inductance of 1 nH and we compared numerically this solution (Figure 6c) with the reference cases where the tip was kept floating (Figure 6a) or short circuited to the external coaxial conductor of the applicator (Figure 6b) that schematizes the applicator shown in Figure 5.

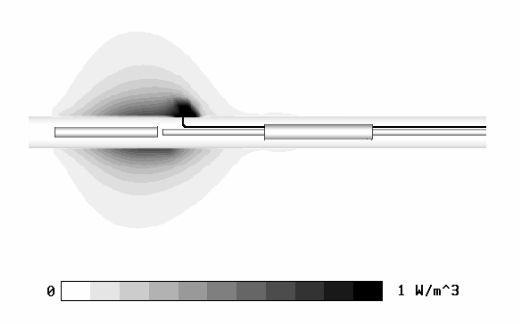

Figure 5: Normalized SAR distribution of a MHA with a temperature probe embedded inside the insulator of the coaxial choke.

If a thermistor is used as temperature sensing element instead of a thermocouple, the sensor tip is constituted by a semiconductor with conductivity ranging between 10^{-2} and 10^{-4} S/m. In both cases the simulation result of Figure 6c shows that the insertion of the micro-chokes practically eliminates the arising of hot spots near the sensing termination and therefore drastically reduces temperature measuring errors.

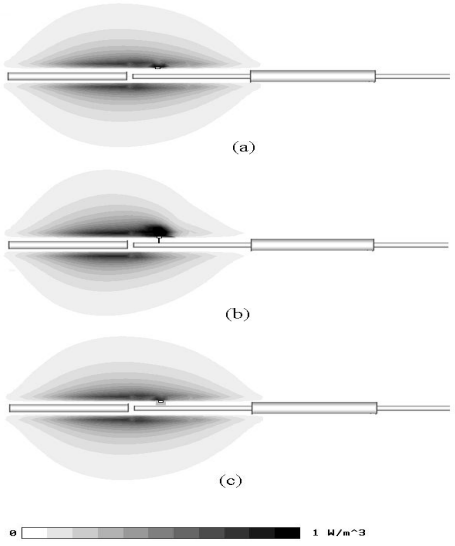

Figure 6: Normalized SAR distribution of a MHA with the integrated temperature probe: (a) floating tip (ideal case), (b) tip short circuited to the coaxial conductor (worst case), (c) tip RF isolated with inductors (actual case).

At a radial distance of 5 mm from the applicator, in the direction of maximum radiation, SAR is less than 50 % of the maximum value calculated at the surface of the catheter and reduces to 90 % at a distance of 10 mm. This confirms that the applicator can be used both for hyperthermic treatments of small tumours ad also for thermo-ablation surgery, depending on the maximum applied power and time. It is worth to note that the device can tolerate 30 W CW or average power and up 150 W pulsed power without any damage or excessive self-heating.

The MHA input matching is also numerically calculated in the frequency range from 2 to 3 GHz, in absence of the thermocouple and in presence of a temperature sensor with the probe close to the applicator and the metallic leads embedded into the coaxial balun. In both cases a reflection coefficient less than -20 dB is assured at the 2.45 GHz working frequency as shown in Figure 7.

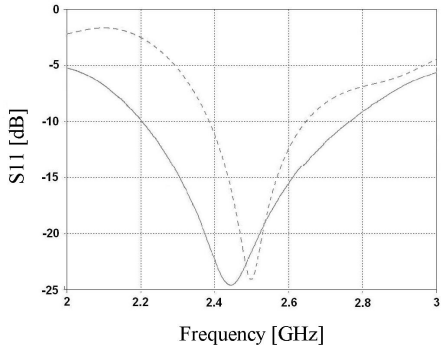

Figure 7: Input reflection parameter vs. frequency of the MHA with (continuous line) and without the integrated temperature probe (dotted line).

Power distribution in the tissue was experimentally evaluated by applying 20 W continuous microwave power to the MHA over a period of about 15 minutes (Figure 8) and a pulse power of 60 W for 10 seconds. The results are in good agreement with the numerical predictions and proved that the induced heating pattern in the biological medium assumes the typical ellipsoidal shape around the applicator radiating end. The overall dimension of the ellipsoidal heating pattern clearly depends on the so called *thermal-dose*, i.e. on the quantity of the EM energy delivered to the medium. It is also evidenced that the metallic sensor tip (thermocouple or thermistor) do not produces a local hot spot, authorizing us to state that an accurate temperature monitoring can be obtained. This was afterward confirmed through a measure made with an auxiliary fiber-optic temperature sensor. Using the integrated

sensor, the temperature at the interface between the catheter and the tissue can be carefully monitored during the microwave heating process because not significant self-heating of the sensor has been observed. Figure 9a shows the evolution of the temperature vs. time when 20 W CW power is applied for 15 minutes at the input of the applicator, while Figure 9b depicts the thermal response of the medium to a 10 second pulse of 60 W peak power.

It is worth note that the increase of the temperature is very fast in both cases because the chicken breast used as phantom for our heating experiments is not perfused by the blood and therefore the thermal response of the tissue is determined only by its thermal conductivity.

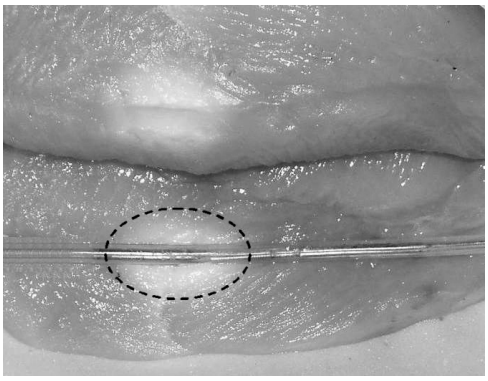

(a)

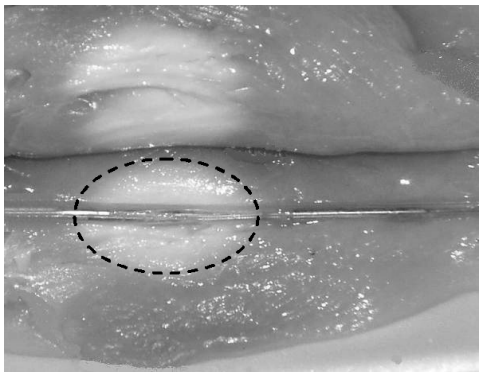

(b)

Figure 8: Thermal pattern in a splitted chicken tissue obtained by applying 20 W CW power to the MHA for 15 minutes (a) and 20 minutes (b) respectively.

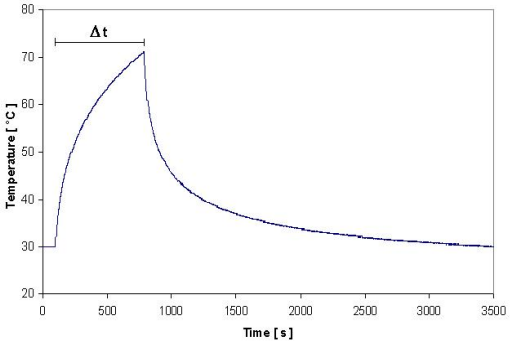

(a)

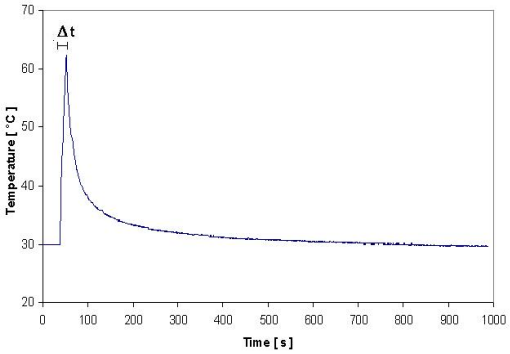

(b)

Figure 9: Temperature evolution at the tissue/applicator interface obtained by applying 20W CW input power to the MHA for 15 minutes (a) and a 10 second pulse of 60W peak power (b).

4 CONCLUSIONS

The proposed minimally invasive MHA integrates a very cheap temperature sensor and therefore it is very suited for the mass-production of mono-use devices. The integration of the radiating element and the temperature sensor inside the same applicator case allows to heat a small tissue volume (target) and to measure the temperature accurately at the same time. Due to the use of a simple coaxial balun the microwave energy is confined around the applicator body reducing the risk of accidental overheating of healthy tissue close to the tumour. The thermistor (or the thermocouple junction) peeps out from the catheter surface in the point where the EM field, and hence the temperature, reaches the maximum. Temperature in deeper zone of the tissue surrounding the applicator can be extrapolated by mathematical models based on the bio-heat equation (Pennes, 1948) if the EM and thermal parameters of the tissue are known.

Multiple applicators (arrays) with integrated temperature sensors could be used in order to treat larger tissue volumes and more accurately estimate the temperature distribution through the combined application of bio-heat equation and tomography algorithms.

The pliability of the miniaturized coaxial cable and of the associated silicon catheter make easier the insertion of the applicator using the natural way of the body or minimally invasive surgical procedures.

Many coaxial applicators for hyperthermic treatments show a heating pattern characterized by a typical tear drop shape. The implementation of a coaxial choke in the MHA investigated in this paper reduces appreciably the drop tail and allows to precisely localize the tissue volume involved during the microwave treatment. Moreover the high degree of miniaturization due to the availability of miniaturized coaxial cable to use in medium-high power applications (dimensions about 1-2 mm in diameter are easily available), permits to extend the clinical applications of this minimally invasive applicator. Hyperthermic treatments of bile-ducts in cancer therapy, impracticable in the past for the restrict dimensions of the ducts, could be possible nowadays as well other delicate surgical interventions that require high precision and reduced invasivity.

The originality of this MHA, from an engineering point of view, lies in the peculiar integration of the metallic wires of a low cost temperature sensor inside of the choke body without perturbing the SAR distribution.

The invasivity of the clinical hyperthermic or thermo-ablation treatment is highly reduced using this type of applicator because in fact no separated insertions for temperature probes, no additional external electrodes as for RF treatments or any other kind of devices are required. Therefore many deep-seated tumors (e.g. certain brain, liver, gastrointestinal or gynaecological tumours), could be effectively and easily treated with the proposed MHA.

The integrated temperature sensing element permits to accurately monitor the maximum temperature reached into the tissue and it can be used to close the control loop of a specific microwave hyperthermic or ablative process by defining the appropriate thermal-dose to be administered to the lesion.

By monitoring the temperature in time domain, very useful data on blood perfusion rate, thermal conductivity and specific heat could be directly extrapolated by the bio-heat transfer equation and used to construct more complex and realistic biological tissue models. As well thermal properties difference between healthy and pathological tissue could be relieved in order to extrapolate diagnostic information.

REFERENCES

Turner, F., 1986. Interstitial equal-phased arrays for EM hyperthermia. *IEEE Trans. Microwave Theory Tech.*, vol. 34, no. 5, pp. 572-578.

Tumeh, A.M., Iskander, M.F., 1989. Performance comparison of available interstitial antennas for microwave hyperthermia. *IEEE Trans. Microwave Theory Tech.*, vol. 37, no. 7, pp. 1126-1133.

Camart, J.C., Despretz, D., Chive, M., Pribetich, J., 1996. Modeling of various kinds of applicators used for microwave hyperthermia based on the FDTD method. *IEEE Trans. Microwave Theory Tech*., vol. 44, no. 10, pp. 1811-1818.

Lin, J.C., Wang, Y. 1987. Intertitial microwave antennas for thermal therapy. *Int. J. Hyperthermia*. vol. 3, no. 1, pp. 37-47.

Cerri, G., De Leo, R., Primiani, V.M. 1993. Thermic endfire' interstitial applicator for microwave hyperthermia. *IEEE Trans. Microwave Theory Tech.*, vol. 41, no. 6, pp. 1135-1142.

Saito, K., Hayashi, Y., Yoshimura, H., Ito, K., 2000. Heating characteristics of array applicator composed of two coaxial-slot antennas for microwave coagulation therapy. *IEEE Trans. on Microwave Theory and Techniques*, vol. 48, no. 11, pp. 1800-1806.

Bowman, R.R. 1976. A probe for measuring temperature in radio-frequency-heated material. *IEEE Trans. on Microwave Theory and Techniques*, pp. 43-45.

Longo, I., Biffi Gentili, G., Cerretelli, M., Tosoratti, N., 2003. A Coaxial Antenna with Miniaturized Choke for minimally Invasive Interstitial Heating. *IEEE Trans. on Biomedical Engineering*, vol. 50, no. 1, pp. 82-88.

Jones, K., Mechling, J.A., Trembley, B.S. 1988. SAR distributions for 915 MHz interstitial microwave antennas used in hyperthermia for cancer therapy. *IEEE Trans. on Biomedical Engineering*, vol. 35, no. 10, pp. 851-857.

Biffi Gentili, G., Leoncini, M., Trembly, B.S., Schweizer S.E. 1995. FDTD Electromagnetic and Thermal Analysis of Intertitial Hyperthermic Applicators. *IEEE Trans. on Biomedical Engineering*, vol. 42, no. 10, pp. 973-980.

CST Studio Suite 2006, Computer Simulation Technology GmbH, D-64289 Darmstadt, Germany.

Berenger, P. 1994. A perfectly matched layer for the absorption of electromagnetic waves. *J. Computat. Phys*. vol. 114, no. 2, pp. 185-200.

Pennes, H.H. 1948. Analysis of tissue and arterial blood temperatures in the resting human forearm. *J. Appl. Physiol*. vol. 85, no. 1, pp. 93-122.

MICROCOMPUTERIZED SYSTEM TO ASSESS THE PERFORMANCE OF INFANT INCUBATORS

Mário Anderson de Oliveira, Maurício Campelo Tavares
Institute of Biomedical Engineering, Federal University of Santa Catarina, campus trindade
88040 – 970, Florianópolis, SC, Brazil
Laboratory of Biomedical Engineering, Catholic University of Pelotas, campus I, number: 412
Félix da Cunha 109C, 96010-000, Pelotas, RS, Brazil
mandersoneee@gmail.com, mtavares@ucpel.tche.br

Raimes Moraes
Department of Electrical Engineering, Federal University of Santa Catarina, 88040 – 900, Florianópolis, SC, Brazil
raimes@eel.ufsc.br

Keywords: NBR IEC 601.2-19 (1999), Bluetooth, neonate incubators, clinical engineering, assessment.

Abstract: This work presents a system based on a microcomputer to assess the performance of infant incubators in a semi-automatic manner. It carries out the tests described by the section 8 of the NBR IEC 601- 2-19 (1999). The developed electronic circuit acquires data from the sensors using a microcontroller. A set of sensors are used: five for temperature, one for humidity and one for air flow. The sampled data is sent to the PC via Bluetooth. The software running on the PC manages the data sampling, as well as guides the user through the test procedure by means of messages and sound alerts at the end of each stage. The sampled data is shown on the screen and also stored in a database that can be remotely accessed. The results are presented on a graph where the measurements (temperature, humidity and air flow) performed during the whole test can be seen. The procedure to calibrate the sensors and an infant incubator assessment carried out with the developed system is presented.

1 INTRODUCTION

There is a high percentage of mortality associated to low birth weight newborns (Ministério da Saúde, 2002). These neonates have an immature thermal control mechanism, preventing them to keep constant their body temperature (Gonzáles, 2001). The infant incubator (InI) aims to provide a thermo-neutral environment where the infant does not exchange heat, consuming a minimum amount of oxygen. This environment is obtained by controling the temperature, humidity and air flow. Inside the InI, the infant has a reduced metabolism that helps its healthier and faster growth (Ministério da Saúde, 2002). Therefore, InIs shall be periodically checked to assure that they offer a suitable environment to the neonate.

This work describes a system developed to assess the InI performance according to the Section 8 of the NBR IEC 601-2-19 (1999).

To evaluate the InI performance, the standard demands measurements of the following parameters: air temperature at five different points, relative humidity and air velocity. The temperature sensors are placed at five points 10 cm above the mattress surface (A, B, C, D and E) as shown in Figure 1.

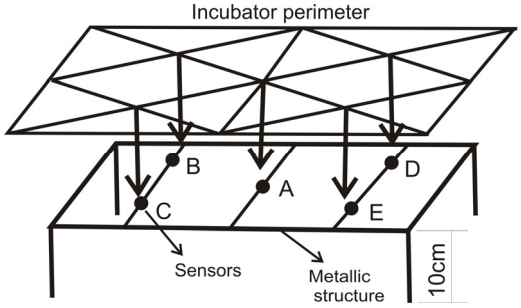

Figure 1: The NBR IEC 601-2-19 demands temperature measurements at 5 different points (10 cm above the mattress surface): A, B, C, D and E. A metallic structure is used to hold the sensors at the required positions.

2 MATERIALS AND METHODS

The performance testing required by the standard is relatively difficult to be carried out manually, being desirable to automate it. Thus, a microcontrolled system was developed to automatically sample InI data that are sent to a microcomputer (Figure 2).

The developed system consists of 5 modules: sensors, acquisition, communication, control software and database.

The remote control software running on a PC communicates with the acquisition module to require samples from the sensors placed into the InI.

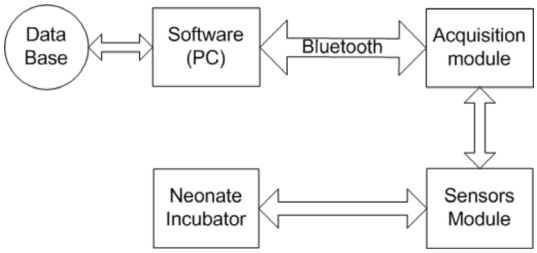

Figure 2: The developed system has five modules: sensor, acquisition, communication (Bluetooth), control software and database.

2.1 Sensors Module

The sensors are placed into the InI as shown by the Figure 1.

The sensor SHT75 (Sensirion Inc) is used to measure the Incubator Temperature (temperature at the point A of Figure 1) and the relative humidity (RH). It measures temperature in a range from -40 to 123.8°C and RH from 0 to 100%RH. For temperature, the SHT75 has a typical accuracy of ±0.5°C and resolution of 0.01°C. For humidity, typical accuracy of ±1.8%RH and resolution of 0.03%RH.

The measurements executed by the SHT75 are available in digital format via the 2-wire protocol. This is a bi-directional protocol, allowing the sensor to receive commands as well.

To measure the temperature at the other points (B, C, D and E), 4 TMP05 (Analog Devices) sensors are used. The TMP05 measures temperature in a range from -40 to 123.8°C with a typical accuracy of ±0.5°C and resolution of 0.01 °C.

The TMP05 sensors can be connected in cascade, establishing a net. Thus, only two microcontroller pins are needed to acquire the temperature measurements from the sensors: one generates a start pulse and the other receives the PWM signal.

The sensor F900 (Degree Controls Inc.) is used to measure the air velocity in the InI. It has a linear output voltage for a range from 0.15 to 2m/s with a typical accuracy of ±0.05m/s and resolution of 0.05m/s.

2.2 Acquisition Module

The acquisition module contains the microcontroller ADuC841 (Analog Devices) that has the following characteristics: 8052 core, 20 MIPS, 8 ADC channels (12 bits), 2 DAC channels (12 bits), 3 timers/counters (16 bits) and serial communication interfaces (UART, I2C and SPI).

The ADuC establishes serial communication with the SHT75 and TMP05 to get the humidity and temperature measurements. Its ADC samples the F900 voltage output to figure the air velocity out.

These measurements are sent to the PC when demanded by the control software.

2.3 Communication Module

The Bluetooth module implements wireless link between the acquisition module and the PC. To provide a communication range up to 100 meters, a KC-11 unit (KCWirefree) is connected to the acquisition module and a KC-210 is inserted into the PC USB port.

A virtual serial port driver is used by the control software to communicate with the KC-210.

2.4 Control Software Module

About 6 hours are necessary to carry out the measurements required by the NBR IEC 601-2-19 (1999). To simplify the task, a control software was developed for WindowsOS® in Borland C++ Builder.

At 20 second intervals, the software demands a new set of measurements. For that, an ASCII command is sent to the acquisition module. After receiving the command, the microcontroller communicates with the sensors to get the measurements that are sent back to the PC. The received data are presented on the PC screen and stored into a database.

Besides managing the measurements, the developed software guides the user through the testing procedure by means of messages and sound alerts at the end of each stage. The software displays messages on the PC screen asking the user to change the InI settings or the mattress position. After doing so, the user shall click the OK button of the message

box. Then, the software keeps executing the measurements.

2.5 Database

The database (DB) was developed with PostgreSQL 8.0, a free software object-relational database management system (Matthew and Stones, 2005). The implemented DB has two entry tables, one registers the equipment identification key; the other stores the measurements carried out during the InI testing.

3 SENSORS CALIBRATION

The F900 and SHT75 sensors are individually calibrated. They both have calibration certificate. The F900 is supplied with its calibration curve. The SHT75 has calibration coefficients programmed into its internal memory.

The TMP05 sensors were calibrated using the SHT75 as reference since there was no other traceable reference sensor with better accuracy and resolution available in this laboratory.

To calibrate the four TMP05 sensors, they were placed together with the reference sensor into a container with low heat transmission walls. The air inside the container was heated up to 60ºC and then, the heat source was turned off. During the air cooling, 17 sets of temperature measurements were obtained for each sensor within the range from 25 to 41ºC. For each sensor, a third order polynomials was fitted to the experimental data to correct the systematic error observed with respect to the reference sensor. These polynomials are used by the software running on the PC to reduce the measurement errors.

To evaluate the described calibration, 3 measurements were executed for 13 different temperatures within the calibrated range to find out the resultant errors. This procedure was repeated for each sensor.

For each sensor, the systematic error (bias) and the random error (repeatability) were surveyed.

As example of the result achieved with this sensor calibration procedure, the Figure 3 shows the curves obtained for the sensor to be placed at the point E (Figure 1). This one presented the larger errors (about ± 0.5ºC) within the InI operating range (32 to 36ºC).

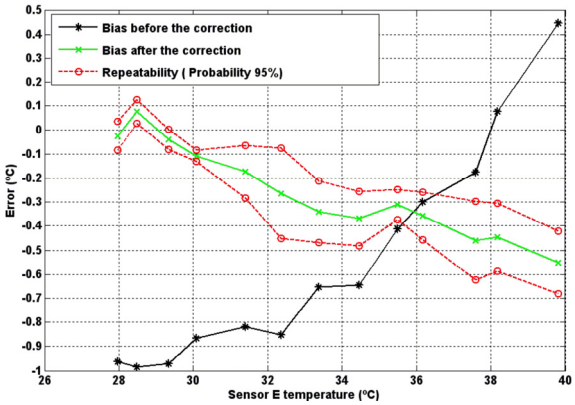

Figure 3: Measured error curve versus temperature is plotted for the sensor E. It is also shown the systematic error (before and after the application of the polynomial adjustment) and the random error.

4 RESULTS

To evaluate the performance of the developed system, assessment of an InI was carried out.

At the end of test, the results are stored in the DB. The results can be consulted on text format or graphically visualized. In text format, statements on the standard conformance are presented as shown in Figure 4.

For ethical reason, since the developed system was not certificated by an accredited laboratory, reference to the model and manufacturer of the InI as well as the health institution to which it belongs are omitted.

In the graph, the behaviour of the measured parameters (Incubator Temperature, RH and the air velocity) during the whole test can be observed.

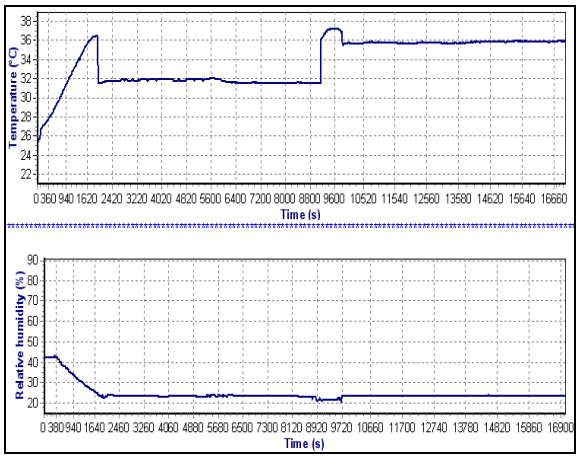

Figure 4: Incubator temperature measured during the assessment. Relative humidity and air flow curves are also presented in the graphical report.

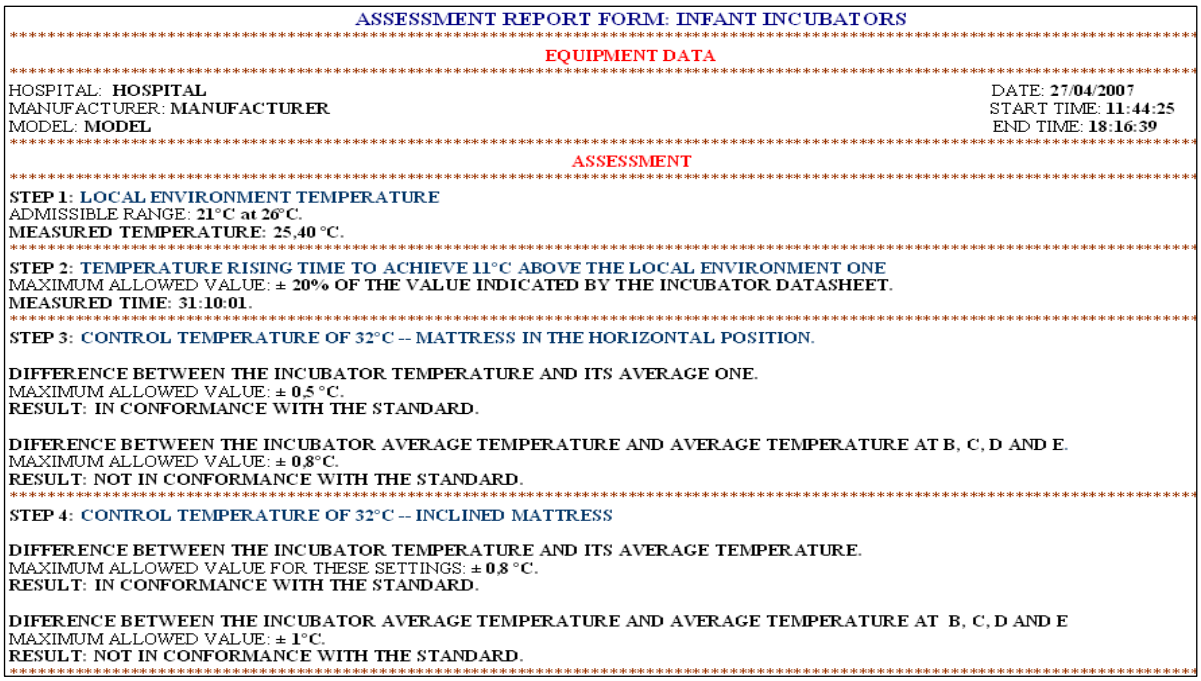

ASSESSMENT REPORT FORM: INFANT INCUBATORS

EQUIPMENT DATA

HOSPITAL: **HOSPITAL**
MANUFACTURER: **MANUFACTURER**
MODEL: **MODEL**
DATE: **27/04/2007**
START TIME: **11:44:25**
END TIME: **18:16:39**

ASSESSMENT

STEP 1: LOCAL ENVIRONMENT TEMPERATURE
ADMISSIBLE RANGE: **21°C at 26°C.**
MEASURED TEMPERATURE: 25,40 °C.

STEP 2: TEMPERATURE RISING TIME TO ACHIEVE 11°C ABOVE THE LOCAL ENVIRONMENT ONE
MAXIMUM ALLOWED VALUE: **± 20% OF THE VALUE INDICATED BY THE INCUBATOR DATASHEET.**
MEASURED TIME: 31:10:01.

STEP 3: CONTROL TEMPERATURE OF 32°C -- MATTRESS IN THE HORIZONTAL POSITION.

DIFFERENCE BETWEEN THE INCUBATOR TEMPERATURE AND ITS AVERAGE ONE.
MAXIMUM ALLOWED VALUE: **± 0,5 °C.**
RESULT: IN CONFORMANCE WITH THE STANDARD.

DIFERENCE BETWEEN THE INCUBATOR AVERAGE TEMPERATURE AND AVERAGE TEMPERATURE AT B, C, D AND E.
MAXIMUM ALLOWED VALUE: **± 0,8°C.**
RESULT: NOT IN CONFORMANCE WITH THE STANDARD.

STEP 4: CONTROL TEMPERATURE OF 32°C -- INCLINED MATTRESS

DIFFERENCE BETWEEN THE INCUBATOR TEMPERATURE AND ITS AVERAGE TEMPERATURE.
MAXIMUM ALLOWED VALUE FOR THESE SETTINGS: **± 0,8 °C.**
RESULT: IN CONFORMANCE WITH THE STANDARD.

DIFERENCE BETWEEN THE INCUBATOR AVERAGE TEMPERATURE AND AVERAGE TEMPERATURE AT B, C, D AND E
MAXIMUM ALLOWED VALUE: **± 1°C.**
RESULT: NOT IN CONFORMANCE WITH THE STANDARD.

Figure 5: Part of the report generated by the developed system.

5 CONCLUSION

The developed system does not comprise a sound level meter. The sound measurements required by the standard are relatively simple to be made. Equipments available in the market can be employed to this end, having a layout that allows their use in other applications.

The maximum uncertainties in the temperature measurements (taking into account the propagation of the reference sensor uncertainty: ±0.3ºC) obtained with the sensors B, C, D and E are ±0.4 ºC, ±0.5 ºC, ±0.5 ºC and ± 0.61 ºC, respectively.

Assessment of InIs according to the NBR IEC 601-2-19 standard can be performed by the developed system in a semi-automatic manner, since the user has to change the InI operating settings during the test. Throughout the procedure, the control software beeps at the end of each stage and shows messages on the PC screen. These messages ask the operator to adjust the InI settings before performing the next set of measurements.

The control software and the used communication protocol have proven to be suitable and robust during the InI assessment.

The report generated at the end of the assessment points out the InI conformance with respect to the NBR IEC 601-2-19 requirements.

It shall be noted that all the tests carried out with an InI are stored in a same DB, allowing a better follow-up of its performance along its lifetime.

For instance, the number of corrective maintenance underwent by a given InI model can be very useful to the managers when considering the purchasing of new equipments.

ACKNOWLEDGEMENTS

The authors thank the CNPq for financial support (507363/2004-3).

REFERENCES

Ministério da Saúde, 2002. *Manual do curso de humanização do recém – nascido de baixo peso. Método Canguru* - Série A: Normas e Manuais Técnicos Nº 145. Brasília. 1nd edition.

Gonzaléz, L. H., 2001. *Termoregulación em Recién Nacido. In: Servicio Neonatalogia. Servicio Neonatalogia.* Hospital Clinico Universidad de Chile. Chile. 1nd edition. p. 34-40.

NBR IEC 601-2-19, 1999. *Equipamento Eletromédico Parte2: prescrições particulares para segurança de incubadoras para recém-nascidos RN*, Rio de Janeiro. ABNT.

Matthew N, Stones R., 2005. *Beninning databases with PostgreSQL*. Aprress. 2nd edition.

A NOVEL APPROACH FOR SIMULATING A BIO-CONTAMINATION PROCESS

Gerard Chalhoub, Antonio Freitas and Michel Misson
LIMOS-CNRS, Network and Protocols Team, Blaise Pascal University
B.P. 86, 63172 AUBIERE CEDEX, France
chalhoub@sancy.univ-bpclermont.fr, freitas@sancy.univ-bpclermont.fr, misson@sancy.univ-bpclermont.fr

Keywords: Simulation, CSMA/CA, bio-contamination, Ad-hoc, WLAN.

Abstract: The phenomenon of bio-contamination in a population of individuals being contaminated in a near by near physical, viral or bacterial contact could be compared by analogy with a near by near exchange of "atomic" data between mobile entities of an ad hoc network. Would the tools of wireless communication engineering then make it possible to contribute in the modeling of a bio-contamination process? Does the use of CSMA/CA in order to share the "contamination medium" make it possible to simulate this process of contagion? To establish the limits of the analogy, we consider the most unfavorable case, the systematic contamination of proximity. A susceptible mobile becomes contaminated if it passes near a contaminant mobile at a distance lower than the contamination distance. Simulations under NS2 highlight the effect of the overall radiation compared to the power used for emitting the atomic data representing the virus and reveal an optimal frequency of atomic data diffusion in the case of a population with strong geographical density moving in confined environment.

1 INTRODUCTION

The symbolic system and the vocabulary used in part(a) of figure 1 give the impression that it is an ad-hoc wireless communication system between entities moving according to a certain trajectory and a given speed. A mobile emits or receives information by means of an antenna characterized by the range of an electromagnetic radiation. This exchange of data takes place only if the receiver is within range from the transmitter, more precisely the distance traveled by the signal, is lower than a given threshold.

Let us suppose now that this range does not concern the distance at which the mobiles can exchange information but the distance of a contamination by air following a cough, a sneeze, or simply breathing, between individuals during an ordinary day. Part (b) of figure 1 shows that the entity A (the contaminant) contaminates the entities B then C which become in their turn contaminators.

The question put here is the following one: can the engineering of the wireless networking be usable to include (represent) a process of bio-contamination? More precisely, prototyping using light wireless communicating equipments, or simulating using simulators developed for the wireless communications like OPNET and NS2, can be of a certain utility to model a process of contagion?

The most important criteria that affect a contagion process identified by (Shane C. St. John, 1997) were:

- The probability of infection.
- The probability of recovery.
- The number of encounters between individuals which depends on: the density of the population and the dynamic degree of that population.
- The initial number of infected individuals.

Each one of these parameters can be associated with a step of the modulation process using simulation tools like OPNET and NS2 (G. Chalhoub, A. Freitas & M. Misson, 2007). Let us consider the probability of infection: a susceptible individual touched by a contaminant is considered infected with a probability of infection P. In the

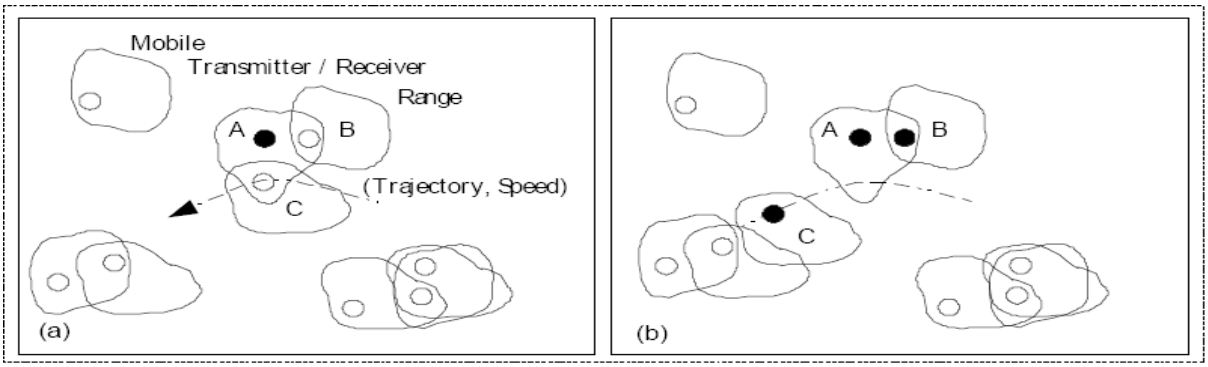

Figure 1: Wireless Communications / Bio-contamination process.

context of a network modulation process, the transition from susceptible to infected will not take place unless the susceptible individual receives a contaminant message with a certain probability of success (figure 2). In this article we are considering a systematic contamination (P=1).

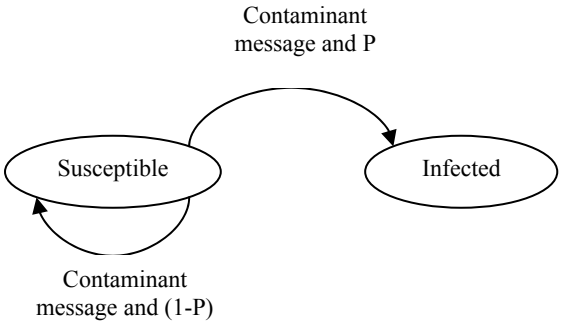

Figure 2: Susceptible becomes infected.

2 ASSUMPTIONS

If we consider the cough or the sneeze as means of contamination by air between individuals, the analogy with a wireless networking will result in the diffusion on the radio medium of a frame containing atomic data. Nevertheless, we make the assumption in this article that the contamination is regarded as succeeded, if this information is received with no errors by one or more other entities.

For an individual the support of viral transmission, the air, is always available. A cough or a sneeze of an individual can be contaminant even if other individuals have an activity which coincides in time at the same place. In that sense the activities of contamination are rather cumulative. Here we see a limit with our analogy arising. In a WLAN several simultaneous emissions cause a superposition of signals, a collision, which makes impossible the deciphering of information (with the exception of the capture effect). In this case, the contention-based access methods implement an arbitration which will try to order the access to the medium. Data to be transmitted will then undergo a random delay. The access method CSMA/CA is today the most “popular” method in the field of the WLAN (ANSI/IEEE Std 802.11, 1999), (IEEE Std 802.15.4™-2003)…, and will be detailed in part 3 of this article.

In the case of a contamination caused by coughing or sneezing, the recurrence of the events is about a few seconds. This recurrence is not really periodic but, nevertheless, we can consider it as a "Burst" activity like it is illustrated in figure 3. Although T_1 and T_2 are not periodic, the time t separating 2 messages in a "Burst" transmission can be considered as a pseudo periodic activity.

While transposing this activity in a wireless networking domain with the CSMA/CA method, the density of traffic representing the information of contamination will be easily assured by the MAC layer (G. Chalhoub, A. Freitas & M. Misson, 2007). This approach differs from the stochastic model based on the cellular automata used by (H. Situngkir, 2004).

This leads us now to consider a contamination only due to proximity. Any susceptible individual who is near a contaminated person, at a distance lower than the distance of contamination, becomes contaminant himself. We will call this model of contamination by proximity, the geometrical model.
In the context of wireless networking, the contaminated entity must broadcast atomic information of contamination. Our objective is thus to answer the following question: compared to the geometrical model, which is the optimal frequency of broadcasting the contamination data, with CSMA/CA as the access method, in a context of

strong density of individuals and a contamination by proximity?

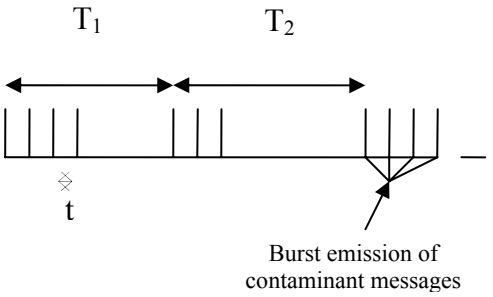

Figure 3: Burst activity.

3 CSMA/CA AND THE SHARED MEDIUM

The basic principle of CSMA consists in listening to the medium before emitting when a station has a pending (ready to be emitted) frame (Chen, 1994). On the discharge of the medium the station applies a method to manage the possible competition with other stations. In the case of the CA (Collision Avoidance) method the stations draw a back-off period to desynchronize the potential candidates.

The detection of an activity on the network is carried out by the measurement of the power of the received electromagnetic radiation. If this measurement is higher than the fixed threshold for the noise, the medium is regarded as being busy.

In the case of WiFi, the contention resolution mechanism is governed by the 802.11 standard specifications (ANSI/IEEE Std 802.11, 1999). For the DCF (Distributed Coordination Function) mode a station having a pending frame may begin to access only when the radio channel is sensed Idle. That is the case when the PHY layer performs a "Clear Channel Assessment (CCA)" which returns "IDLE" as the value of the CCA Indicator. This is the case when the energy level received is lower than a threshold very often estimated at - 95 dBm (value given by the suppliers of WiFi interface). It is this value which is passed in parameter (CSThresh: Carrier Sense Threshold) for a simulation by NS2 (Wu Xiuchao, n.d.) and which creates a little polemic for a simulation by OPNET (S. Roy, H. Ma, R. Vijayakumar & J. Zhu, 2006). Let us consider a signal received with a power Pr higher than the Carrier Sense Threshold, it allows to identify the fact that the channel is indeed busy but it is not a sufficient condition so that the information transported by the signal can be suitably interpreted. For that it is necessary that the receiver has a Margin of Decoding (MD) which depends on the modulation used for the transmission (Intersil Data Sheet HFA3861B, 2001). For example, it is admitted that in the case of a WiFi network the decoding of a frame with 11 Mbps requires that the energy of the signal received be higher than - 82 dBm. It is the value which is passed via the RXThresh parameter in a NS2 simulation. This obviously implies that the area in which the signal is perceived as higher than - 95 dBm is much larger than the zone of reception. If we illustrate that by a mechanism of contamination by cough simulated using an access method of the type CSMA/CA, a person who coughs prevents from coughing people whom it does not reach!

This is illustrated in the parts (a) and (b) of figure 4. The most external disc represents the surface in which the CCA indicator has the value BUSY, the disc delimited by -82 dBm corresponds to the surface in which the reception is done with an acceptable error rate.

Regardless of the nature of the medium, at a short distance from the transmitter, it is standard to consider that the law of dispersion of energy is in $1/D^2$.

If we know the transmission power, it will possible then to deduce the received power at the security (or contamination) distance which we introduced. Thus for a transmission power of 20 dBm the power hoped at 2 meters is - 26 dBm. It is what corresponds to the smallest disc of part (b) of figure 4.

In the same way by adjusting the power of transmission to -36 dBm, the threshold of reception of -82 dBm corresponds to the distance of contamination. This is represented by the part (c) of figure 4.

At this stage we can discuss the effect of the Clear Channel Assessment (CCA). A transmission with 11 Mbps and a power of - 36 dBm has an impact which goes well beyond a disc of 2 meters because of the CCA which covers a surface with a power higher than - 95 dBm. By reducing the power of emission we also reduced considerably the surface of carrier sensing. Using NS2 we will evaluate the effects of reducing the power of transmission, on the simulation of the process of contagion.

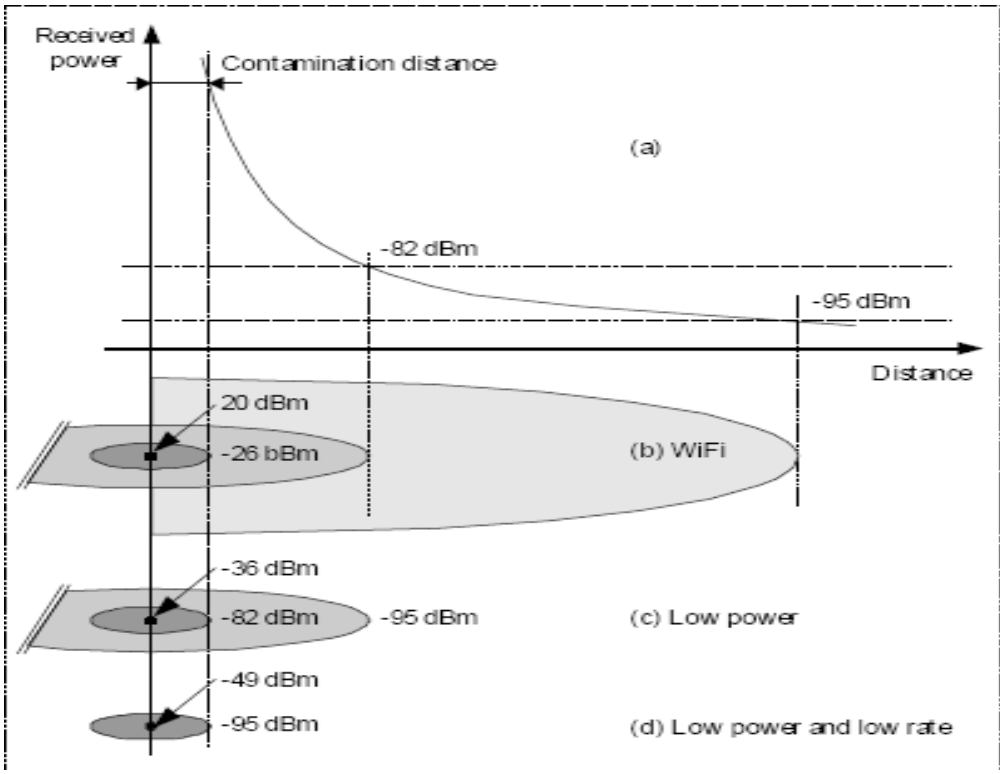

Figure 4: CSMA and thresholds.

4 SIMULATIONS

The object of this paper is to study if the choice of the access method CSMA/CA exploited to broadcast atomic information at a given frequency is an acceptable way to model a process of contamination by contact.

4.1 The Reference Taken for a Contamination by Contact

In our approach of simulation we considered that the ideal case was given by a geometrical approach of the problem, i.e. at any moment (in fact every 10 ms) we calculate for each contaminated station the distance which separates it from its neighbors. So if for a neighbor of a contaminant, this distance is lower than the threshold of contamination, this neighbor becomes also contaminated.

The choice of the frequency of this calculation depends on the velocity of the mobiles: the latter being at a maximum of 2 m/s this gives us a maximum error of 4 cm on the calculation of the distance between mobile if calculation is made every 10 ms. By this geometric calculation we obtain a number of mobiles contaminated throughout the simulation time that we will indicate thereafter like the result of the geometrical model. This result will represent an asymptote for those which are obtained by any other way.

4.2 The Simulation Assumptions

In this paper we chose to illustrate the results of a contamination modeled by CSMA/CA and to compare them with the results of the geometrical model for two configurations of mobiles which correspond to the same initial rate of contamination.
- The First simulation: 100 mobiles in a surface of 20 X 20m² with only one mobile contaminated at the beginning of simulation
- The Second simulation: 400 mobiles in a surface of 40 X 20m² with 4 mobiles initially contaminated.

In these two cases two frequencies of broadcasting (2 and 10 Hz) and two powers of transmission (20 and - 36dBm) are studied.

All simulations were made for 20 scenarios of nodes distribution and the curves displayed later on represent the averages of the number of nodes contaminated during these 20 simulations. Each simulation represents an evolution of the contagion

during 20 s, the number of contaminated mobiles is calculated every 0,2 s. All nodes are randomly moving within the simulated area with a maximum speed of 2 m/s.

4.3 Analysis of the Effects of the Transmission Power

In the case of the first simulation one can note that the power of transmission does not have much influence because the curves obtained for 20 dBm and - 36 dBm are very close (Figure 5). The frequency of broadcasting at 10 Hz makes it possible to approach the geometrical model much more clearly.

While multiplying by 2 the geographical density of the nodes and by considering the same density of contaminant (4 nodes initially contaminated), a diffusion made with a limited power gives results that approach more the geometrical model than those done using the usual power of Wifi.

The simulation results:

With our assumptions everything takes place during the first seconds of simulation. Figure 6 shows clearly how reducing the transmission power improves the propagation by reducing the effect of CSMA/CA on the delay of the diffusion in an area with a dense population.

4.4 Examining the Effects of the Frequency of Diffusion in Low Power Transmission

Another factor which has also a big part in determining the effect of CSMA/CA is the frequency of diffusion. Our goal is to approach the geometric model which gives us a representation of an almost continuous contagion. Hence, one can think of increasing the frequency of the broadcasting of the contamination frames, that means increasing the offered load on the network and reaching the limits of the effectiveness of such an access method (Chen, 1994). We can thus suppose that there exists, for a given density of mobile stations, an optimum frequency of transmission, and that's what we will try to find by simulation.

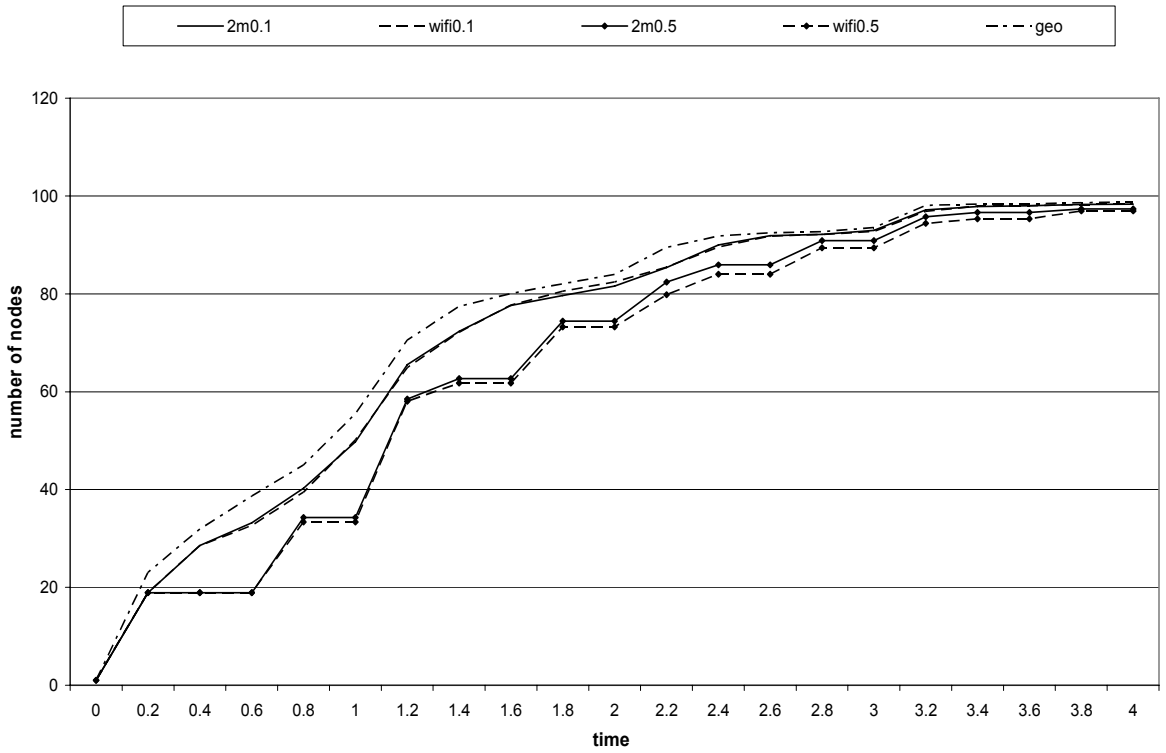

Figure 5: Low density contamination.

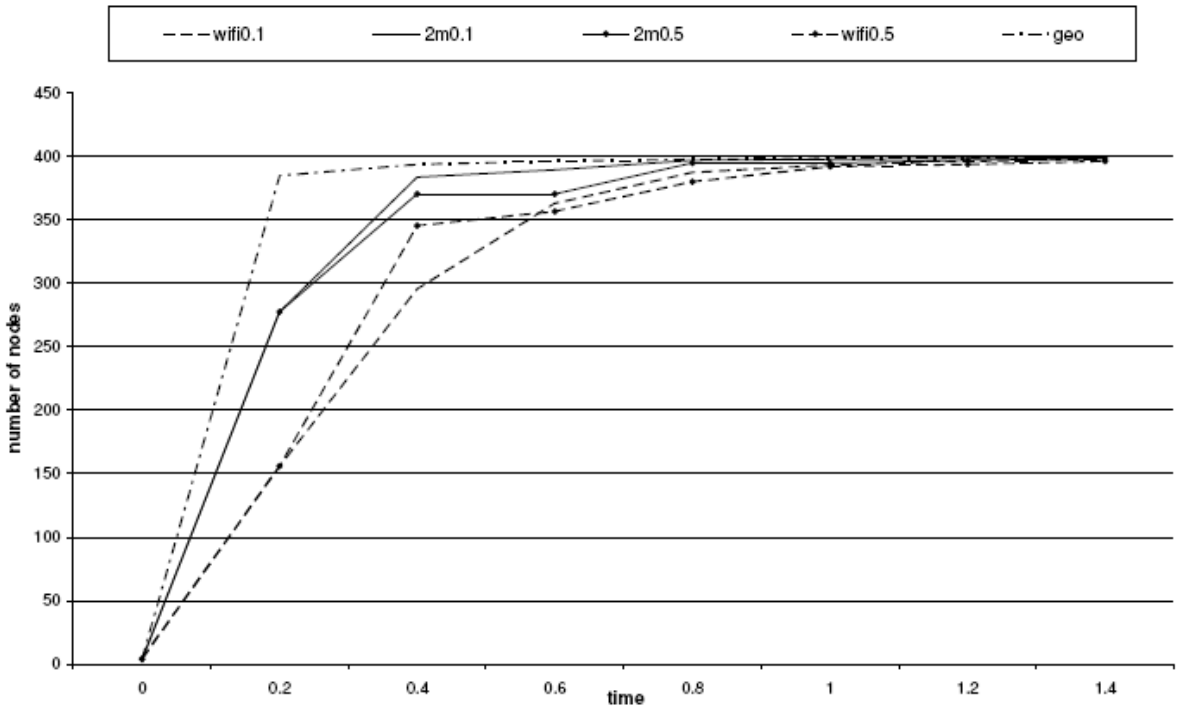

Figure 6: High density contamination.

We tested several frequencies using the previous model by using a low power transmission (- 36 dBm). For frequencies of broadcasting going from 0.5 to 200 Hz, we will consider the average of 20 simulations, to calculate the number of contaminated nodes. Each simulation lasts 20 seconds and gives a value every 0,2 second, we will thus have 100 values per frequency. These 100 values will be compared with those corresponding to the same moment, given by the geometrical model to identify a difference: "an error" between the theoretical contamination given by the geometrical model and that approached by CSMA/CA.

Let M be the average of these 100 differences between the two corresponding values for each frequency of transmission, we thus obtain the following curve (Figure 7):

We can notice that with a frequency of diffusion between 10 and 20 Hz the average number of contaminated nodes is 0.5 node less when compared to the ideal number given by the geometric model. We can clearly identify 3 different zones illustrated by that curve. In the first zone we are under-loading the network using frequencies between 0.5 and 4 Hz for emitting contaminant messages and not being able to produce the same result given by the geometric model, which is easily explained by the fact that we are missing some encounters due to the mobility of the individuals that cross into each other without being able to exchange contaminant messages. By increasing the frequency beyond 20 Hz we are overloading the network and the effect of CSMA/CA causes a delay on the transmitted messages which prohibit some individuals to emit and therefore miss some encounters. We determined effectively an optimal frequency of diffusing contaminated messages in a continuous way which, for our assumptions of simulation, varies between 10 and 20 Hz.

5 CONCLUSION AND PERSPECTIVES

CSMA/CA and simulators for the wireless networks are original assets to simulate processes like a contamination by contact. We have just shown that by adjusting the transmission power and the frequency of the access to the medium, it is possible to simulate with a simulator like NS2 the way in which a virus is propagated in a mobile human being community.

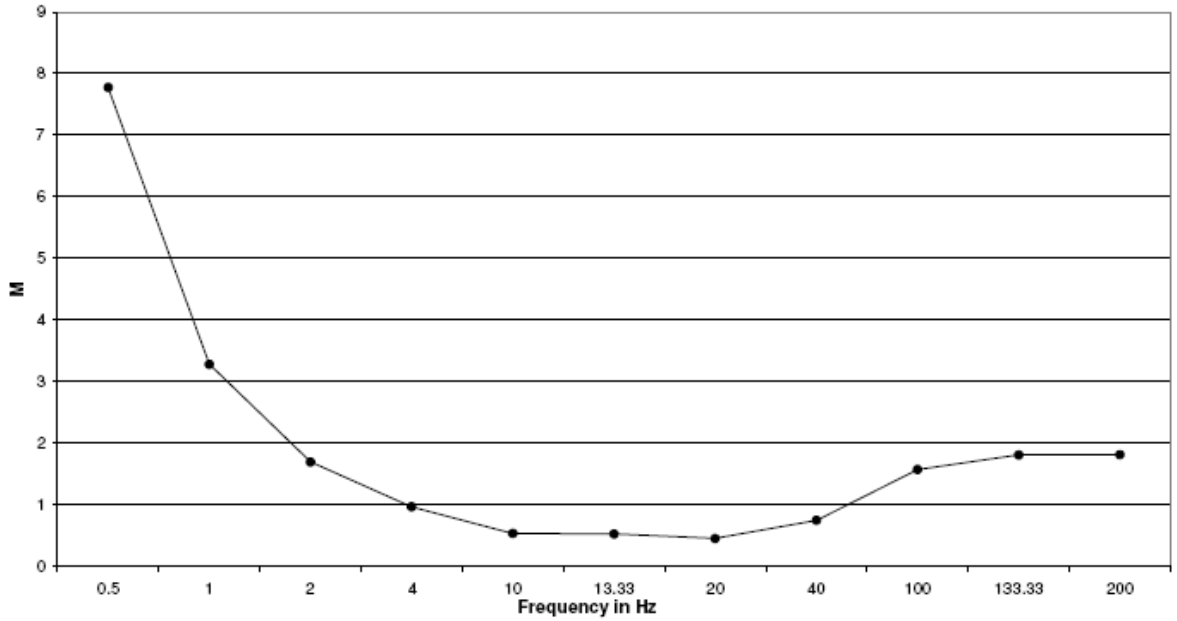

Figure 7: Frequency effect.

To approach more the real nature of a contamination by proximity, the action of the contaminant radiation of a node must be limited to the distance of contamination. It would be interesting to study next the effect of the bandwidth which finishes the surfaces dilemma between the zone of carrier sensing and that of a good reception. In the case of a 1 Mbps transmission these two surfaces are overlapping which brings us even closer to the geometrical model (part (d) of figure 4).

Following a meeting, that took place June 2007, with a group of doctors who were interested in our work, we will improve our simulation model by defining individual profiles which define the personal biological characteristic of each individual (degree of vulnerability, being immunized or not, and time needed to be recovered…), and by applying the "burst" activity to emit the contaminant messages instead of the continuous emission. Having a virus profile with all its characteristics will also help us build a specific transmission behavior that will reproduce the virus' nature.

REFERENCES

ANSI/IEEE Std 802.11, 1999 Edition (R2003)

G. Chalhoub, A. Freitas & M. Misson, 2007. *Using Wireless Networking Simulation Tools and Technics to model a bio-contamination process –First Approach-* Unpublished internal report of the N&P Team LIMOS.

Hokky Situngkir, 2004. *Epidemiology Through Cellular Automata* .WPF2004 Bandung Fu Institute.

IEEE Std 802.15.4™-2003.

Intersil Data Sheet HFA3861B 2001. *Direct Sequence Spread Spectrum Baseband Processor*.

Kwang-Cheng Chen, 1994. *Medium Access Control of Wireless LANs for Mobile Computing.*

S. Roy, H. Ma & R. Vijayakumar, J. Zhu, 2006. *Optimizing 802.11 Wireless Mesh Network Performance Using Physical Carrier Sensing.* University of Washington Electrical Engineering Technical Report.

Shane C. St. John, 1997. *Population Dynamics in spatially explicit lattice epidemic models.* AAT 1385006.

Wu Xiuchao, n.d.. *Simulate 802.11b Channel within NS2.*

PATIENT SIMULATOR APPLIED TO AUDITORY EVOKED POTENTIALS, ELECTROCARDIOGRAPHY AND ELECTRONYSTAGMOGRAPHY

M. Tavares, C. Richter
Biomedical Engineering Laboratory, Catholic University of Pelotas, Rua Felix da Cunha 412, Pelotas, Brazil
mtavares@ucpel.tche.br, richter@ucpel.tche.br

R. Moraes
Electric Eng. Department, Federal University of Santa Catarina, Campus Universitário Trindade, Florianópolis, Brazil
raimes@eel.ufsc.br

T. Oliveira
PDI, Contronic Sistemas Automaticos Ltda.,Rua Rudi Bonow, 275, Pelotas, Brazil
tiago.rockembach@contronic.com.br

Keywords: Simulator, AEP, ECG, ENG, electro-medical equipments maintenance.

Abstract: This paper describes an electronic device, named SimPac I, developed to simulate auditory evoked potentials of short, middle and long latencies, ECG and electronystagmography signals. It uses sampled waveforms in order to better reproduce real physiologic AEPs. The simulator is based on the ADuC841 microconverter, a device with an 8052-like core, FLASH memory and two 12-bit DACs. SimPac I is portable and easy to operate, and it is very useful for calibration of AEP, ECG, ENG and VENG systems during manufacture and maintenance. The simulator can also be used to support development and testing of DSP algorithms intended to filter and/or average the above mentioned signals. As a result, examples of several waveforms generated by SimPac I are shown.

1 INTRODUCTION

The auditory evoked potentials (AEP) play a fundamental role in the audiology practice. The capacity of capturing electric potentials generated in response to acoustic stimulations resulted in many relevant applications to the oto-neurologist (Katz, 1999). AEPs are classified in agreement with its latency. Potentials of short latency occur in up to 10 ms after the auditory stimulation. Middle latency potentials occur between 10 ms and 100 ms after the stimulus, and long latency potentials are registered after 100 ms from the stimulus. Short latency AEPs are known by the acronyms BAEP – Brainstem Auditory Evoked Potentials, BERA – Brainstem Electric Response Audiometry or ABR - Auditory Brainstem Response (Chiappa, 1997). The electrocochleography (EcochG), used for cochlear evaluation, is also considered a short latency AEP. ABR is used for evaluation of the brainstem integrity and also for objective audiometry. Middle latency evoked potentials are identified with the acronyms MLR or MLAEP (Middle Latency Auditory Evoked Potential). MLAEP is indicated to evaluate dysfunctions that could commit the hearing pathways located between the brainstem and the primary cortex.

P300 and MMN (Mismatch Negativity) are the most used long latency AEPs in the clinical practice. P300 presents a positive peal around the 300 ms latency and using it makes it possible to obtain, in only one test, information about the activity of the transition thalamus-auditory cortex, the own auditory cortex, about the hippocampus, hearing attention and cognition. P300 is elicited through a "rare paradigm", in which a few "rare" stimuli happen randomly in a series of "frequent" stimuli. The difference between both can be the intensity or the frequency. The MMN test uses also rare and frequent stimulus, but the result reflects the central processing capacity (Caovilla, 2000).

ECG is certainly the most known bioelectric signal generated by the human body. That signal is captured and analyzed for use in clinical diagnosis, surgical accompaniment and rehabilitation. Several types of ECG simulators exist, able to simulate changes in amplitude, heart beat frequency and many types of arrhythmias (Prutchi and Norris, 2005). They find application in the project of new monitors and in the preventive and corrective maintenance.

The perfect corporal balance is very important for the living organism orientation in the environment. That balance widely depends on the vestibular system, which acts in cooperation with the visual system to maintain the vision focus during head movements. The cerebral system that makes it possible is known as vestibulo-ocular reflex (VOR). The electric evaluation of VOR is done through the electronystagmography exam (ENG) or by its variant, the vector-electronystagmography (VENG) (Castagno et al., 1994). The evaluation of ENG/VENG is based on the registration and analysis of the nystagmus, that is, the reflex ocular movements which happen when the labyrinth receive caloric or rotational stimuli.

The proposed Patient's Simulator was called SimPac I and incorporates the technological solutions used in the previously developed prototype SPEA (Freitas et al., 2006). SimPac I has the purpose of serving as a tool for development, validation, adjustment and maintenance of AEP, ECG and ENG/VENG equipments.

2 MATHERIALS AND METHODS

SimPac I is able to generate in two channels all of the short, middle and long latency AEP waveforms mentioned in the introduction. The morphology of those signals was shown in a previous paper (Freitas et al., 2006). Real signals of AEP were scanned to obtain 500 samples for each one, and after they were digitally processed in order to ensure the use of whole the dynamic range of the 12-bit D/A converters present in the simulator. Figure 1 contains the blocks diagram of SimPac I. The main hardware component is the microconverter (μC) ADuC841 (Analog Devices, 2003), whose CPU is compatible with Intel's 8052, modified to execute instructions to 20 MIPS peak. The simulator does not require external memories, since it uses only the μC internal program FLASH and internal RAM. ADuC841 is responsible for waveforms generation using DDS technique (Digital Direct Synthesis), starting from the sample tables stored in FLASH memory (Grover and Deller, 1999). Energy is provided by four NiMH 1.2V batteries, or by 5 V external source. The microconverter requires 5 V supply while the analog circuits are supplied by a symmetrical voltage of ±5 V. Those voltages are generated by a circuit which combines boosts with switching capacitors and inverters. The complete power circuit uses two chips LM2621 (National), one ADM8660 (Analog Devices) and one ICL7662 (Maxim), including also a soft starter commanded by μC. User's interface was remodeled regarding SPEA. The rotary encoder and the push-buttons were substituted by a membrane keyboard and a graphic liquid crystal display (GLCD) with 8 kpixels. The GLCD driver is made by the μC itself, through the ports P0 and P2.

The effective AEP simulated signal generation depends on an external request, since the averaging operation demands synchronism between auditory stimuli and electric signal acquisition. That external event consists of applying a voltage border in the "external trigger" input. The direction of the border, rise or fall, can be programmed in the simulator.

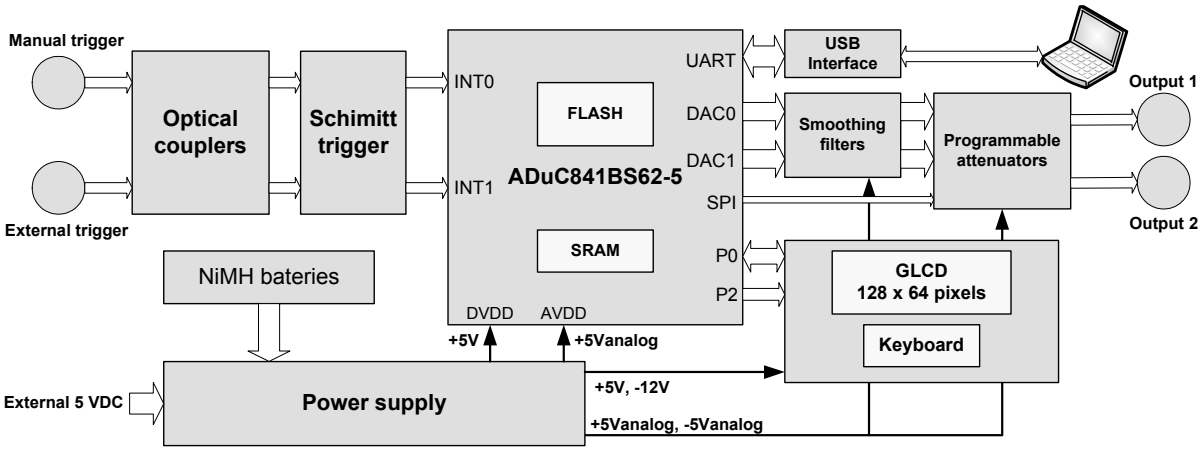

Figure 1: SimPac I blocks diagram.

For test and continuous type signals generation, a button named "manual trigger" was included. In any trigger type, manual or external, the pulse passes through a Schmitt trigger circuit that gives to the µC an interrupt signal free from bouncing.

Manual trigger causes the INT0 core interrupt, while external trigger causes the INT1 core interrupt.

The D/A conversion rate is set by an internal µC timer, which is reprogrammed in agreement with the selected signal to be generated. Each D/A output is followed by a conditioning circuit that filter (low-pass reconstruction) and reduce the signals to the real voltage levels observed in the human body signals. The amplitude adjustment is made by an attenuator of 120 dB in range and 0.5 dB in resolution, programmed through the µC SPI port.

2.1 Software

When the equipment is turned on, the software exhibits a greeting message in GLCD, which is followed by the main menu. Starting from that menu the user can select the signal to be simulated. For each signal, a specific sub-menu is exhibited allowing adjustment of parameters as frequency, amplitude, heart rate, angular velocity and others. When the generation of a signal associated with the external trigger is requested, the first task is to program the reference timer with the corresponding value for the signal's sample rate. In the interrupt INT1, the timer is trigged and its service routine is responsible for the DDS signal generation. EcochG, ABR, MLR and LLR are reproduced in the same way: at each INT1 interrupt, a finite loop transfers the samples stored in FLASH memory to the D/A converters. The software routine which generates P300 and MMN signals alternate the reproduction of frequent and rare signals, stored in different tables, to simulate the physiologic response to stimulation. From each INT1 interrupt, the software establishes which signal should be generated. The signals generation sequence is established through an oddball table also stored in FLASH. For generation of the ECG signals, the start is given by the manual trigger button. The timer defines the D/A conversion rate and the different heart beat frequencies are simulated varying the pause among two groups of complex P-QRS-T and the T duration itself. For ENG signals the technique is similar to that of ECG, however the variations of angular velocity are simulated changing the sweeping step of the tables recorded in FLASH memory. The parameters used on the SimPac I software regarding signal characteristics are presented in Table 1. The different combinations of periods and D/A conversion rates are obtained programming the reference timers prior to starting the generation of each signal.

The SimPac I embedded software was developed in C language with aid of the µC/51 V1.20.04 programming tool (Wickenhaeuser, 2005). After the code compilation, the software was downloaded to the program FLASH memory using WSD 6.7 (Analog Devices), and tests were made, which are showed in next section.

Table 1: Main characteristics of simulated signals.

Signal	Amplitude	Period/frequency	D/A Rate
EcochG	0.5 µV typical	5 ms	100 ksps
ABR	1 µV typical	10 ms	50 ksps
MLR	3 µV typical	50 ms	10 ksps
LLR	5 µV typical	500 ms	1 ksps
P300	5 µV typical	500 ms	1 ksps
MMN	5 µV typical	500 ms	1 ksps
ECG	0.5-1-2 mV	30-60-120-240 BPM	500 sps
ENG	0.1-0,5-1-2 mV	1-125 degrees/s	500 sps
Sine	0.5-1-2-10 mV	0.05-0.1-10-50-60-100 Hz	500 sps
Square	0,5-1-2-10 mV	0,05-0,1-10-50-60-100 Hz	500 sps

3 RESULTS

The ADuC841 was welded on the LQFP-to-DIL adapting board showed in Figure 2, developed to facilitate the access to the microconverter pins.

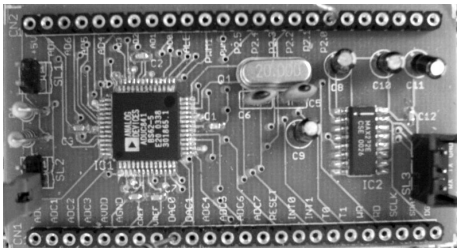

Figure 2: Adapter board from LQFP to DIL used in the prototype, evidencing the ADuC841 µC and the serial download interface to internal FLASH.

The other prototype components were mounted on a universal pre-drilled board, and the whole circuit was conditioned in a plastic box (Phoenix Mecano/BOPLA), as it can be observed in Figure 3. SimPac I prototype was exhaustively tested with a commercial AEP equipment (Contronic, 2007), presenting all AEP signals with synchronism, amplitude and timing as expected.

Figure 3: SimPac I layout.

Some of these signals are presented through the software ATC Plus version 2.1.59 (Contronic, 2007a), and they are shown in Figures 4 through 6. It is possible to note the perfect repetition of the AEP signals generated by SimPac I.

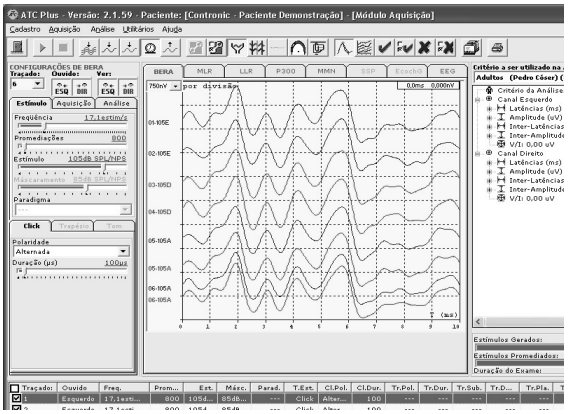

Figure 4: Simulated ABR.

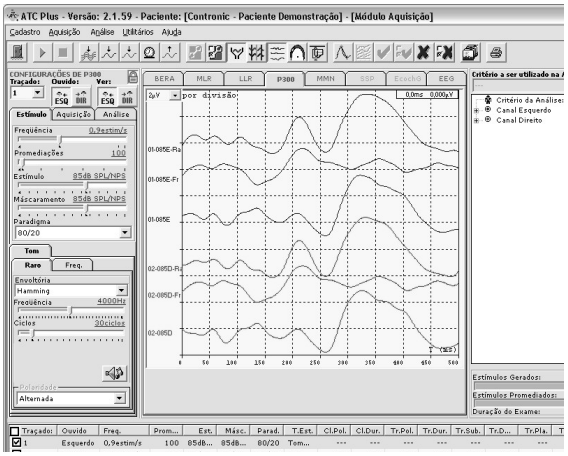

Figure 5: Example of simulated rare, frequent and resulting P300 signals.

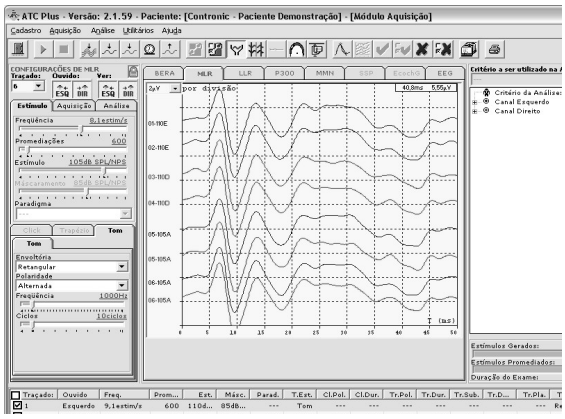

Figure 6: Simulated MLR (with VEMP) signal.

In Figures 7 and 8 some ECG and ENG signals from SimPac I can be seen, which were registered directly from the DAC outputs with the aid of a Rigol DS5102MA oscilloscope. These simulated ENG signals are being used in another project for validation of automatic algorithms intended to calculate the slow component of angular velocity of positional, caloric and rotary nystagmus.

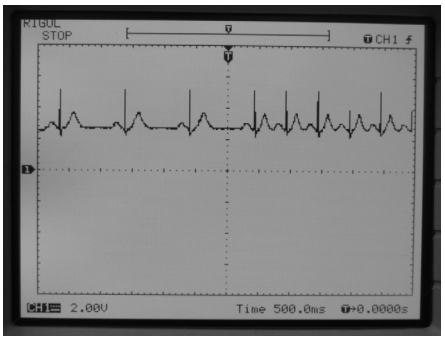

Figure 7: Simulated ECG signal at 60 and 120 BPM.

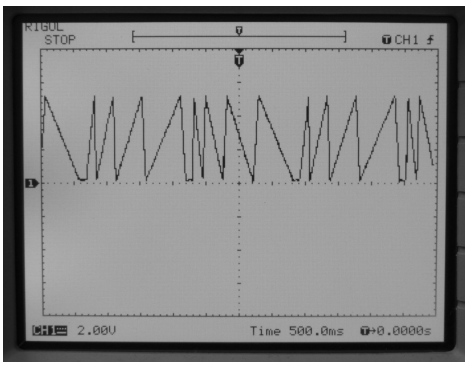

Figure 8: Simulated ENG at several angular velocities, clockwise and counter clockwise.

4 DISCUSSION

SimPac I carried out all the expected basic functions. Several improvements were made regarding the previous prototype (SPEA): ECG and ENG signals, inclusion of performance signals intended to be used on amplifiers and filters verification (sine and square), inclusion of optical isolation in the external trigger input, new user interface using GLCD, function keyboard and soft starter. A circuit for USB communication was added to make easy the future inclusion of new signals to simulate.

For next version we intend to add a white noise generator to simulate the EEG signal in which the auditory evoked potential is immersed. That characteristic will allow extension of the tests of AEP equipments to the averaging quality.

Some simulators in the market generate waveforms through complex mathematical formulas, demanding digital signal processors for its implementation. SimPac I generates the waveforms from samples tables by DDS, and the execution can be made through a simple microconverter. The SimPac I main advantages are: the generation of signals that resemble those observed on biological systems, however with known amplitudes and latencies; the generation of signals with excellent repeatability; the substitution of the patient or volunteer during the development of medical equipments; and also in development, the elimination of undesired factors of difficult control, such as the electrode-skin impedance, other bioelectric signals like spontaneous EEG or EMG, and electromagnetic interference.

5 CONCLUSIONS

In this work we demonstrated the viability of creating an equipment intended to simulate AEPs of several types, ECG, ENG and performance test signals. SimPac I simulated signals were verified through a commercial system for AEP acquisition and a digital oscilloscope, showing reliability and precision in the requirements of synchronism, amplitude, timing and repetition. The use of this simulator can facilitate the software development and validation for processing AEP, ECG and ENG, as well as the hardware adjustment in production, and the preventive and corrective maintenance of electro-medical equipments.

ACKNOWLEDGEMENTS

The authors thank to Brazilian Agency CNPq by the financial support under the grants 507363/2004-3, 310611/2005-9, 120005/2007-7 and 310058/2007-4 (DTI and ITI scholarships) and also to the designer Leonardo de Jesus Furtado by the SimPac I layout project.

REFERENCES

Analog Devices, 2003. *MicroConverter 12-bit ADCs and DACs with Embedded High Speed 62-kB Flash MCU*. Analog Devices Inc. Norwood.

Caovilla, H. H., 2000. *Audiologia Clínica.* Atheneu. São Paulo.

Castagno, L.A., Tavares, M.C., Richter, C.M. et al., 1994. Sistema Computadorizado de Eletronistagmografia e Vectonistagmografia "UCPel/Castagno" (Versão 3.0). *Anais do IV CBIS*, pp 26-31.

Chiappa, K. H., 1997. *Evoked Potentials in Clinical Medicine*. Third Ed.. Lippincott-Raven Publishers. Philadelphia.

Contronic, 2007. *Manual do Usuário - Módulo de Aquisição de Sinais Bioelétricos – MASBE – Rev. 4*. Contronic. Pelotas.

Contronic, 2007a. *Manual do Usuário - ATC Plus - Software para Audiometria de Tronco Cerebral – Build 2.1.X – Rev. 4*. Contronic. Pelotas.

Freitas, G.M., Oliveira, T.R, Moraes, R. e Tavares, M.C., 2006. Simulador de Potenciais Evocados Auditivos de Curta, Média e Longa Latência Baseado em Microconversor. *Anais do CBEB 2006*, v 1, pp 1224-1227.

Grover, D.; Deller, J. R.; 1999. *Digital Signal Processing and the Microcontroller*. Motorola University Press/Prentice Hall PTR. New Jersey.

Katz, J., 1999. *Tratado de Audiologia Clínica*, Ed. 4. Manole. São Paulo.

Prutchi, D., Norris, M., 2005. *Design and Development of Medical Electronic Instrumentation.* Wiley. New Jersey.

Wickenhäeuser, 2005. *uC/51 V1.20.04 User´s Manual*. Wickenhäeuser Elektrotechnik. Karlsruche.

DESIGN OF A PC-BASED PATIENT SIMULATOR FOR TESTING AND CALIBRATION OF ELECTROMEDICAL DEVICES USING LABVIEW

Pedro Pablo Escobar, Gerardo Acosta
INTELyMEC, Fac. of Engineering, UNCPBA University, Del Valle Av. 5737, Olavarría, Argentina
pescobar@fio.unicen.edu.ar; ggacosta@fio.unicen.edu.ar

Marcos Formica
Fac. of Bioengineering, UNER University, Ruta 10, Km. 11, Oro Verde, Paraná, Argentina
mformica@bioingenieria.edu.ar

Keywords: Patient simulation, testing, calibration, education, electromedicine.

Abstract: Modern digital biomedical devices need a testing and calibrating equipment to asses its functional state with the appropiate technology, so patient simulators have become an essential tool for maintenance and biomedical engineers. An interactive virtual instrument was developed in Labview for simulation of healthy and pathological conditions to test biomedical devices which acquire, register and store temporal evolution of human physiological variables. In this article we present some details of the design and implementation of a simple pc-based patient simulator using Labview, in order to obtain a low cost solution for teaching and practical purposes.

1 INTRODUCTION

Medical science relay for decades on biomedical devices that technology developed continuously, such as ECG, EEG and others which had very limited features at the beginning and were relatively expensive. As the years went by, we found that these devices were reducing their size, enhancing capabilities, adding new features and changing the visualization and registration ways (Neer, 2003).

On the last two decades, biomedical devices have had a vertiginous evolution which brought a lot of new features including non-invasive signal acquisition, data-processing, automation and others; but also brought the necessity of calibrating them and verify its functional state with an appropriate technology (Bronzino, 1995). Then, patient simulators for biomedical devices broke into the market and nowadays they have become an essential tool for biomedical and maintenance engineers on every health institutions worldwide.

With the constant advance of technology, not only biomedical devices but also simulators incorporated new capabilities and connectivity improvements. In spite of these evident advantages, simulators have a high cost, especially for hospitals and health centres in developing countries, situation that sometimes turns them into prohibitive and makes impossible the proper maintenance of the devices, because of the lack of adequate evaluation instrumental.

There is a bunch of interesting commercial solutions available in the market, from many manufactures, but most of them are designed for specific medical applications so they can simulate a set of parameters for these applications in particular, for example, an ECG patient simulator for testing ECG biomedical devices. The cost of any of these analysis tools is high and this led us to design our own tool using resources available at the university labs and a moderated investment on technology, with the main objective of develop a double purpose device: a patient simulator and a teaching tool.

Teaching of Electromedicine is often based on the integration of electronic and physiological knowledge applied to the comprehension of how a device works and why is it malfunctioning. It is remarkable that patient simulators are extremely useful for teaching and practicing electromedicine anywhere, and for all the people who use and maintain modern medical devices.

On our laboratories, the main obstacle for testing and calibrating different kinds of electromedical

devices is the lack of a versatile and economic tool to simulate many diverse physiological conditions, normal and pathological, in order to measure the output range values and verify that they meet manufacturer's specifications (Del Aguila, 1994).

Nowadays, it is a reality to acquire, digitalize, process and visualize data by means of a personal computer with the help of programming software for instrumentation and measurement. Moreover, it is also possible to integrate a wide variety of medical devices into a wireless network (Chronaki, 2006).

In this brief article we present the design and implementation of a simple PC-based patient simulator using Labview® for the graphic user interface, in order to obtain a low cost solution for testing medical devices.

2 DESIGN

2.1 Requirements and Considerations

The main goal was to create a versatile tool for testing and calibrating biomedical devices, suitable for both practical and educational purposes. We chose *Labview® v8.0* for the programming environment because it is available for several computer platforms such as Linux, Windows, Palm PC, etc, (Wang, 2003) and because its excellent connectivity with the outside world through DAQ modules, I/O and networks protocols which make it a great tool to perform computer-based experiments like acquisition, control, instrumentation and quick engineering solutions development (Wells, 1997).

Our needs consisted on developing an interactive virtual instrument (VI) for simulation of healthy or pathological conditions in order to test different biomedical devices. The VI also must have capabilities for acquiring, registering and storing temporal evolution of physiological variables like biopotentials, respiratory frequency, pulse oximetry, temperature and others (Kheir, 1995) sensed by these devices in order to make a testing signals repository available at any time in the computer hard disk or any other non volatile storage system.

We consider the design of a VI with a simple user interface but with full capability to interact with six different medical devices available at the lab as educational modules: a *bi-directional vascular Doppler* (frequency and beat noises); an *incubator* (room and skin temperatures); an *external peacemaker* (frequency and amplitude); an *electrocardiograph;* a *neonatal cardiac monitor* and a *cardiac monitor* (signal shape and frequency).

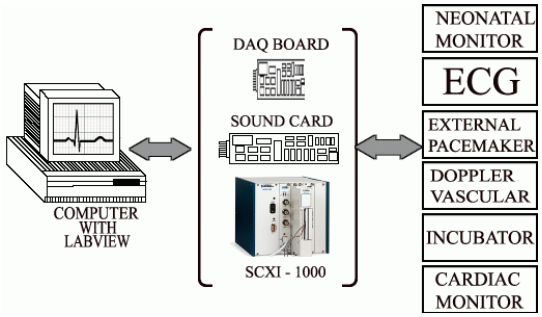

Figure 1: General system connection.

2.2 Design of the Patient Simulator

The first version was designed choosing a physical model for each device and selecting the basic parameters we wanted to control from the user interface. Then, the mathematical models were built to simulate different signal conditions varying some parameters of the differential equations while others remained constant or stable (Zeigler et al., 2000). Each parameter was controlled by a graphical component of the VI's front panel (e.g. a slider or a knob). The signals generated by the mathematical model could be stored in an excel sheet or a text file, creating this way a repository of signals that allowed us to test the devices mentioned before, and then re-define the model if necessary (Dorf, 1998).

A second version was developed to overcome some limitations of the first one, and to simplify the design. In this case, mathematical models were replaced by a repository of signals acquired by different methods. This version provides two main modalities: simulation and testing. Simulation allows for sending signals from the computer to a device, and testing allows for acquiring signals from a device.

Figure 1 shows the general system overview for this second version. It can be seen that the Virtual Instrument we developed can interact with all the devices through three different interfaces: a *multipurpose DAQ Board* that we designed and built, the *PC sound card*, and the *SCXI-1000 DAQ* device form National Instruments. Details of each will be provided ahead.

2.3 Simulation Modality

This modality is not applicable for all the devices, for example the incubator or the external pacemaker. As it was introduced on the previous section, the signals for the simulations of the cardiac monitors (adult an neonatal) and the ECG device were obtained in an "offline" fashion and stored locally on the hard drive. For example, a wide variety of

normal an pathological cardiac signals were scanned from ECG traces and processed using the open source software *Engauge Digitizer® v4.12* which converts an image file into a bidimensional array of numbers (X,Y), that can be read on the screen and stored in a text file or a spreadsheet (Salatino et al, 2007). Figure 2 shows a capture of the software during a digitalisation process of an ECG signal and the numeric output file format.

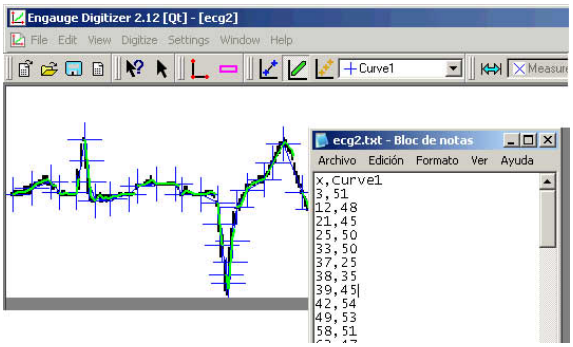

Figure 2: ECG signal digitalisation process using *Engauge Digitizer v4.12.*

In our case, sample signals were selected in order to cover a wide variety of cases like regular rythms, tachycardia, arrhythmias, idioventricular rythms, wandering pacemakers, conduction defects, infarcts, anomalous waves, fibrillation, coronary diseases and others (Lopez et al, 2005).

Sound signals from the bi-directional vascular Doppler were acquired connecting its audio output to the Line-in input of the PC sound card.

All kind of signals were located in a signal repository on the hard disk and used for simulation without the need of a patient, and also for testing and calibrating the devices.

2.4 Testing Modality

In this modality, we wanted to test the functional state of a particular device by sending a stored signal to it and checking the values it is sensing. The signal is represented on a chart and compared in shape and values with the signal on the monitor.

For achieving this, the virtual instrument has some features for interfacing with a medical device, as we mentioned before. Because of the nature of the signals the devices can handle, we needed to implement different interfacing ways. One of the ways we proposed was using a SCXI-1000 DAQ chassis from National Instruments with its respective modules: 1200, 1161, 1122; and the 1302 accessory. The chassis can connect to the computer through its serial or paralell port. The second alternative was a multipurpose DAQ board that was designed and built here in our lab. The third, the PC sound card. For each of them, the digital simulation signal is converted to analogical output by these interfaces and used to stimulate the biomedical devices.

In the case of the external pacemaker, it wasn't able to visualize the stimulating spikes on the device because it is old and it has no display. So, testing was accomplished using a virtual oscilloscope library for Labview 5.1 or superior available on Internet. The test of the incubator was performed by means of thermistor with a conditioning circuit and also a traditional bulb thermometer, in order to compare the evolution of temperature with the one that the device's probe sensed.

3 RESULTS

3.1 The Virtual Instrument

Once we determined all the requirements for each device, the virtual instrument was programmed and named *SIMPAC*, version 1.0. Figure 3 shows the VI graphical user interface (GUI).

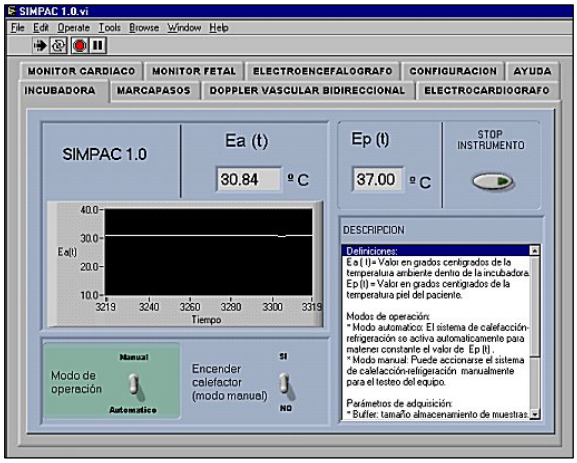

Figure 3: The SIMPAC v1.0 Virtual Instrument GUI.

The GUI was designed as simple as possible; it contains a tab for each device and the controls and indicators for the required parameters. There were included two extra tabs; one for the help and the other for a configuration utility which allows for configuring the serial communication, the buffer size, sampling frequency and other settings.

In figure 4 we can see the Labview design window, showing the graphical code of the incubator sub VI.

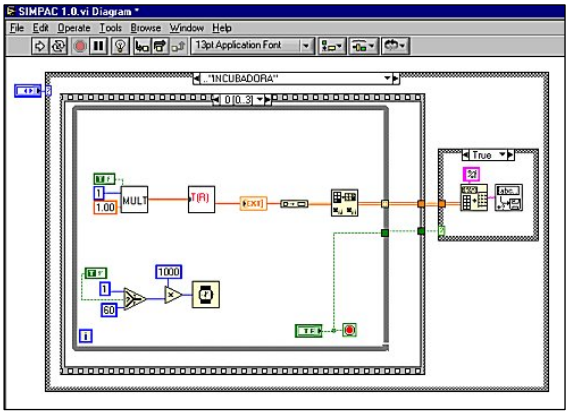

Figure 4: Design view of the incubator Sub VI.

3.2 The Multipurpose DAQ Board

Some modern devices come equipped with a PC interface, generally a RS232 protocol or a GPIB488 connector. Other older devices do not come equipped for interfacing a PC but it is possible to build a low cost specific board in order to replace a paper registration system or similar, with a PC which can acquire, show, store and process information sensed by these devices.

A multipurpose board was designed in our lab for a previous work and used here as another alternative for interfacing biomedical devices with the virtual instrument on the PC. In this case, the VI (master) commands the start and stop of the acquisition, and also handles the occurrence of possible errors.

The PC establishes communication via RS232 with an 8-bit microcontroller (MCU, slave) 68HC08, that read the sensors and send data to the PC. The MCU provides the A/D converting module (ADC) with 8 multiplexed channels and a full-duplex serial asynchronous communication module (SCI). The signals of the sensors are applied to the ADC inputs of the MCU through a voltage follower with high impedance and unitary gain.

Signal conditioning is made using the MAX232 IC, which adapts voltage levels between the MCU and the PC. Communication is made at 9600 bps baud rate with a format of 1 Start bit, 8 data bits, 1 Stop bit and no parity bit. Other baud rates and transmission formats were tested but we chose the mentioned above because of its simplicity and because it is a MCU common configuration.

3.3 Simulation and Testing

Six devices were connected to the virtual instrument for testing or simulation. In the case of the cardiac monitors, all were tested using the signals repository. This modality show great usefulness because it allows for comparing signals displayed on the charts of the VI with the others on the monitors.

Taking advantage of the fact that any common PC has integrated a 16-bit sound card, we connected the audio output of the vascular Doppler device (*Fetal monitor*) to the "Line-in" input of the sound card. Labview provides all necessary drivers to handle the incoming data from the sound card, to plot the signal shape and frequency spectrum in real time and also record the signals into a file. This allows for recovering signals at any time and to perform cuantitative and qualitative assesments of the signal like beat noises, frequency, amplitude, etc.

The incubator was tested by comparing the temperature sensed by the room electrode and skin electrode against a thermistor (with a conditioning circuit) and also a mercury bulb thermometer. We could see that the room electrode wasn't working properly and its values were almost 5° centigrades far from the real temperature. Figure 5 shows the incubator VI during a test.

Figure 5: Working with the incubator Sub VI.

The electrocardiograph's capabilities were enhanced when it was connected to the virtual instrument. It delivers the amplified signals of the electrical activity of the heart, with the respective derivations, to the A/D converter of the MCU and then taken to the PC for processing. The PC allows for displaying all derivations simultaneously and also for making a vectorial sum of each derivation in order to build a 3D graph of the cardiac vector, performing a vectocardiography, a feature that is not available on modern ECG devices. The Labview ECG VI can also work as a Holter device registering ECG signals and storing them.

4 CONCLUSIONS

Basic simulators used for medical training are useless for testing and calibrating electromedical devices. The need of a simple and powerful tool and the avalability of new programming technologies motivated us to develope our own tool with the students of the last year.

A PC-based patient simulator was designed and built with minimum investment in comparison with the commercial solutions available in the market. It took only a standard PC with Windows 98 (for Labview v5.1 or v6.1) or Windows XP (for Labview v8.0) as the operating systems to run the programming environment. Three alternatives were used to interface Labview and biomedical devices: a 16-bits sound card, a SCXI-1000 DAQ device (with 1200, 1161 and 1122 modules and the 1302 accessory) and a multipurpose DAQ board designed and built at our laboratories.

Six different biomedical devices were connected to the virtual instrument, which can work in two modalities: simulation and testing. Both modalities were acomplished succesfully.

One of the problems found was the limited numbers of digital outputs of the DAQ device. This turns into a limitation when we want to test an ECG device using more than 6 derivations. Other limitations found were dued to the few parameters selected for each device. Further versions of the patient simulator will overcome these limitations and add more devices in a closer future, such as new VI's for mechanical ventilation devices, EEG, electronic sthetoscopes, tensiometers, biostimulators and others (Murita et al, 2004).

The patient simulator is not fully developed yet, but this partial success has encouraged us to continue this way in order to improve the capabilities of SIMPAC v1.0.

The secondary goal or this work, education and training, was fully achieved. Teaching has been traditionally based on concept transmission; however, in practical careers like electromedicine or bioengineering most of the time it is necessary to integrate basic and clinical science concepts with electronics to improve critical analysis of real life working situations. Simulations are used to visualize real world dynamic processes in classes and to enhance students' knowledge.

Labview shown to be a powerful tool and an excelent resource for building human-machine interfaces, taking advantage of the great connectivity it provides by different means. Testing capabilities were of great practical relevance.

The designed patient simulator is a low cost, very useful tool, developed entirely as an original work.

REFERENCES

Bronzino, J.D. (Editor in chief), 1995. *The Biomedical Engineering* Handbook. CRC Press.

Del Aguila, C. 1994. *Electromedicina*. Ed. Hispano Americana.

Chronaki, Catherine E. *Facilitating telemedicine: plug and play of different ECG devices.* CMI-HTA, Institute of Computer Science, Foundation for Research and Development - Hellas, Heraklion, Greece.

Wang, J.Y.-Z. *LabView in Engineering Laboratory Courses.*Frontiers in Education, 2003. FIE 2003. 33rd Annual Volume 2, Issue , 5-8 Nov. 2003 Page(s): F2E - F13 Vol.2

Wells, K.K.; Travis, J. 1997. *Labview for everyone-Graphical Programming Made Even Easier*. Prentice Hall.

Kheir, N.A. (editor) 1995. *Systems Modelling and Computer Simulation*. Marcel Dekker, Inc.

Zeigler, B.P., Praehofer, H., Kim, T.G. 2000. *Theory of Modelling and Simulation*. Academic Press.

Dorf, R.C., Bishop, R.H. 1998. *Modern Ccontrol Systems*. Addison Wesley Longman.

Salatino, D.R., Puglesi, A., Bernasconi, M.S. *Desarrollo de Software y Adecuación de Hardware para Adquisición y Procesamiento de Señales Electrocardiográficas y Vectocardiográficas.* Proceedings of Escuela Argentina de Microelectrónica, Tecnología y Aplicaciones: Regular Papers, Vol. 1, No. 1, pp. 62-65, July 2007.

López, N. M., Echenique, A.M., di Sciascio, F. *Modelo y Simulación del Sistema Cardiovascular. Mecanismos de regulación*. XV Congreso Argentino de Bioingeniería. 2005.

Murita, K., Shiraishi, Y., Sato, S. *Making Eeg Output On Human Patient Simulator.* Surgical Center. 2004 IEEE International Workshop on Biomedical Circuits & Systems.

EFFICIENT EVALUATION OF THE INFLUENCE OF ELECTRIC PULSE CHARACTERISTICS ON THE DYNAMICS OF CELL TRANS-MEMBRANE VOLTAGE

N. Citro, L. Egiziano, P. Lamberti and V. Tucci
Dept. of Electrical and Information Engineering, University of Salerno, Via ponte don Melillo, Fisciano (SA), Italy
ncitro@unisa.it, legiziano@unisa.it, plamberti@unisa.it, vtucci@unisa.it

Keywords: Electroporation, Trans-Membrane Voltage, Design Of Experiments, Response Surface Method, Hodgkin-Huxley model.

Abstract: This paper aims at presenting a systematic approach for evaluating the effects induced on the dynamics of the Trans-Membrane Voltage of a biological cell by the characteristics of the non-ideal (trapezoidal) applied electric pulses. The proposed methodology is based on a combined use of the Design of Experiments (DoE) and Response Surface Methodology that allows to put in evidence the self and mutual effects produced by the characteristic parameters of the pulse (slew rate, the total duration of the impulse and its amplitude) on the time evolution of the Trans-Membrane Voltage (TMV). In particular, the effects on the max instantaneous value of the TMV are analysed: its qualitative behaviour vs. the considered parameters, the combination of parameters leading to the highest amplitude and the most influencing parameter are identified with an efficient search based on an optimal set of numerical trials. The analysis concerning the dependence of the max value of TMV on the pulse parameters is performed by considering either a basic Hodgkin-Huxley (HH) circuit or a modified one taking also into account the electroporation phenomenon.

1 INTRODUCTION

An externally applied electrical field pulse determines fast structural modifications of the plasma membrane of biological cells. This phenomenon, known as electro-permeabilization or electroporation has been proposed as an efficient tool to interact with biological materials in several applications. An irreversible electroporation has been used in biology for the decontamination of water and in food processing for the nonthermal killing of harmful microorganisms (Joshi et al., 2004). On the other side, a transient membrane permeabilization has been proposed in medicine for gene therapy, cancer chemotherapy, drug delivery, etc. (Sukharev, et al., 1992, Weaver 2000). In fact, the application of a pulsed electric field has been shown to improve the uptake of drug with respect to conventional methods (Hofmann, et al. 1999). The most remarkable phenomena associated to electroporation are linked to the formation of pores in the lipid bilayer membrane and the growth of their dimensions. The opening of these gateways allows the transport of ions and water-soluble species through the membrane (Beebe et al., 2001, Neumann et al., 1989).

In order to study how the characteristics of the externally applied electric field pulses influence the cell dynamics, either field or circuit-based models approaches have been used (Miller and Henriquez, 1988, Heida et al., 2002). The field-based models, although allowing very detailed determinations of the relevant quantities, require great efforts in modelling the different cellular subsystem and in performing the computations by suitable numerical schemes (FEM, BEM, etc.) in time domain. The circuit-based models are less accurate but more flexible and easy to manage. Moreover, a straight association of the electrical quantities to the biological transport phenomena can be achieved. The lumped parameters circuits employed to represent a small patch of the biological cell can be derived from the so called Hodgkin-Huxley (HH) model after their seminal work concerning the conduction and excitation of nerve membranes (Hodgkin and Huxley, 1952). In this model the membrane is represented by a capacitance, the ionic channels as linear or nonlinear conductances and the voltage generators are linked to the so called Nernst

equilibrium potential, determined by the ratio of the specific ionic concentrations inside and outside the cell. An improved model, where a voltage controlled current generator takes into account the electroporation phenomenon, has been recently proposed (Citro and Tucci, 2006).

The circuit approach is adopted in a large number of papers in order to perform an easy and efficient analysis of the modifications of the cell response to either the variations of the circuit parameters (Citro et al, 2005), or those associated to the input voltage and current characteristics (Bilska, DeBruin, Krassowska, 2000). However, in most cases the identification of the parameters ranges, in which the variability of the response is studied, seems to be carried out with rather naïve criteria.

For this reason, in this paper a systematic approach based on the Design of Experiments (DoE) and Response Surface Methodology (RSM) is used in order to evaluate the most influencing parameters on the dynamics of Trans-Membrane Voltage (TMV) of a cell subjected to a non ideal pulse field modelled by means of a trapezoidal voltage pulse *v(t)*. The slew rate (*dv/dt*), the total duration of the impulse t_{hold} and its amplitude V_{max} are considered as factors of influence. In particular, the effects induced on the maximum value of TMV are studied. The combination of parameters which determines the highest amplitude of TMV and the most influencing parameter (i.e. the max value of the applied pulse) are identified by a suitable choice of tests. The adopted approach, whose efficiency relies in the limited number of proper numerical trials needed, allows also to put in evidence the qualitative behaviour of the TMV vs. the considered parameters. A HH circuit, in which the electroporation phenomenon may be taken into account by a voltage controlled current generator, is considered. The obtained results concerning the TMV dynamics favourably compare with those obtained by other researchers (DeBruin and Krassowska, 1999, Kotnik and Miklavcic, 2006, Vasilkoski et al., 2006). After a brief description of the adopted circuit model in Sect. 2, the application of the DoE is presented in Sect.3. In Sect. 4 the results obtained by RSM are discussed and in Sect. 5 the main conclusions are drawn.

2 CIRCUIT MODEL

The analysis is carried out for the modified HH circuit shown in Figure 1 which mimics the behaviour of a cell membrane patch subjected to a trapezoidal voltage pulse. The circuit takes also into account the behaviour of the biologic solution outside the cell (the parallel C_{ext}-g_{ext}) and the internal cytoplasm (the parallel C_{cyt}-g_{cyt}).

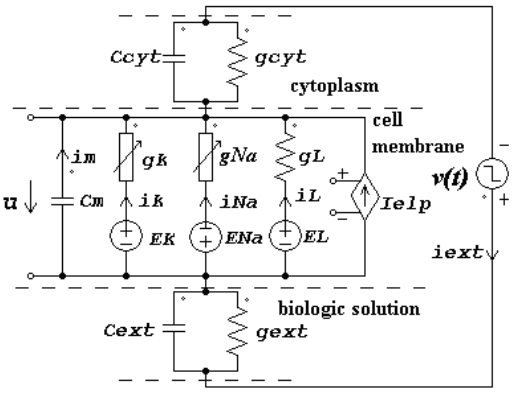

Figure 1: Modified HH circuit.

The details of the model are discussed in (Citro and Tucci, 2006). Here we just summarise the main aspects. The Kirchhoff current law applied to the circuit of Figure 1 gives:

$$C_m \frac{du(t)}{dt} = i_{ext}(t) - \left[I_{elp}(t) + i_L(t) + i_K(t) + i_{Na}(t)\right] \qquad (1)$$

In fact the total ionic current is given by four contributions. The first three contributions (leaking channel current i_L, sodium channel current i_{Na}, potassium channel current i_K) are the same of the basic HH circuit and therefore g_L is a constant value whereas g_{Na} and g_K are non linear time dependent conductances such that $g_{Na} = g_{Na,\max} \cdot m^3 \cdot h$ and $g_K = g_{K,\max} \cdot n^4$ where m, n and h are nonlinear variables describing the activation or inactivation of the channels and given by a first order non linear differential equation (Hodgkin and Huxley, 1952). The fourth is the electroporation current, given by a voltage controlled current source $I_{elp}=N \cdot i_{elp}$ where i_{elp} is the current through a single pore and N is the pore density governed by the Smoluchowsky-equation:

$$\frac{dN(t)}{dt} = \alpha e^{(u(t)/V_{ep})^2}\left(1 - \frac{N(t)}{N_0} e^{-q(u(t)/V_{ep})^2}\right) \qquad (2)$$

where *u(t)* is the Trans-Membrane Voltage (TMV), N_0 is the pore density for *u(t)*=0 and α, V_{ep} and q are suitable constants (DeBruin and Krassowska, 1999). By using the characteristic equation of the

membrane capacitance it results that the dynamic evolution of the TMV and the different ionic currents can be determined by evaluating at each time step a non linear differential equation system in 5 unknowns u, m, n, h, N:

$$\mathbf{Y} = \left[u(t), m(u,t), n(u,t), h(u,t), N(t)\right]^T$$

$$\begin{cases} \dfrac{d\mathbf{Y}}{dt} = \mathbf{f}\left(t, m, n, h, u, N\right) = \mathbf{f}\left(t, \mathbf{Y}\right) \\ \mathbf{Y}\big|_{t=0} = \mathbf{Y}_0 \end{cases} \tag{3}$$

In Table 1 the values adopted for the different quantities appearing in (1)-(3) are reported.

Table 1: Values of the parameters adopted in the model.

g_L	$g_{Na,max}$	$g_{K,max}$	g_{cyt}	g_{ext}
0.3 mS/cm^2	120 mS/cm^2	36 mS/cm^2	24 S/cm^2	24 S/cm^2
u_0	E_L	E_{Na}	E_K	V_{ep}
0 mV	49.39 mV	55 mV	72 mV	258 mV
C_{cyt}= C_{ext}	C_m	N_0	q	α
14.166 nF/cm^2	1 μF/cm^2	$1.5\cdot10^5$ 1/cm^2	2.46	100 cm^{-2}ms^{-1}

The numerical system (3) has been solved by using the commercial software FlexPDE.

3 DOE METHOD FOR THE BEST SET OF PARAMETERS

Design of Experiments (DoE) is a well known technique adopted in experimental or numerical campaigns. It allows the minimisation of the number of tests intended for the identification of the most relevant factors affecting the behaviour of a system. DoE methods allow to ascertain the relative importance of the different parameters and get indications on their interactions. In our case the characteristics of the trapezoidal electric pulse depicted in Figure 2 applied to the HH circuit represent the degrees of freedom considered in our application of DoE. The values of the parameters are chosen in suitable ranges reported in Table 2 according to those suggested in other works (Joshi et al., 2004, Kotnik and Miklavcic, 2006).

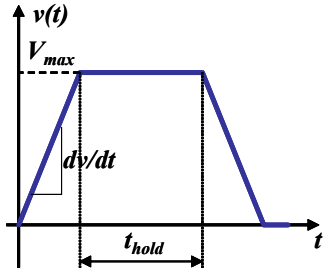

Figure 2: Shape and relevant parameters of the applied electrical pulse.

In order to have an effective but not too heavy scan of the possible range of the parameters space, we choose 9 distinct levels for the slew rate, and 3 for both t_{hold} and V_{max}.

Table 2: Parameters considered for the DoE and their levels.

Parameter	encoding	Number of levels	range values
dv/dt [V/ns]	X1	9	[0.25,34.30]
t_{hold} [ns]	X2	3	[11.0;280.0]
V_{max} [V]	X3	3	[10.0; 60.0]

The total number of experiments for a full factorial design would be 9*3*3=81 points in the parameters space, i.e. the compact D defined as $D = \left[X1_{\min}, X1_{\max}\right] \times \cdots \times \left[X3_{\min}, X3_{\max}\right] \subset \Re^3$. Each experiment is a vector $\underline{X}$=(X1,X2,X3)$\in D$. However, since some combinations of parameters are unfeasible (as for example, when t_{hold} is lower than the sum of rise and fall time), the design matrix results in a reduced set of experiments which in our case is equal to 57. As a response Y, we consider the maximum value of the TMV with (Y_{elp}) or without electroporation (Y_{nelp}):

$$Y = \max_t u\left(t, \underline{X}\right) \tag{4}$$

The design of experiments plot (dex scatter plot) (NIST/SEMATECH, 2006), also known as main effects plot, reported in Figure 3 allows to put in evidence the most influencing factors and the best choice for the setting parameters. In this Figure the values of the response Y_{elp} are reported in correspondence of a fixed level of a given parameter, whereas the other two are varied from the min (-) to the max (+) value of the corresponding range.

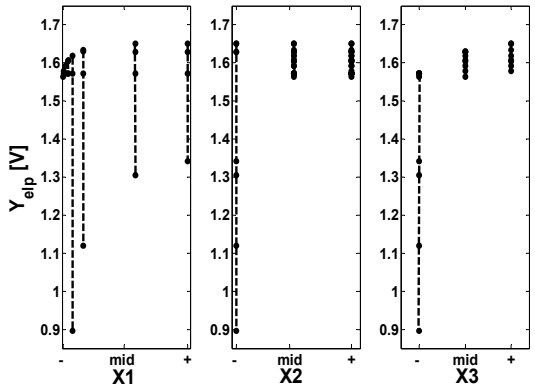

Figure 3: Three factors - dex scatter plot of Y_{elp}.

In a dex scatter plot a factor can be considered as principal one if, when scanning its variability range from the min to the max value, it produces a significant change in the response. By analyzing the Figure 3 we can observe that X3 appears to be a principal factor. In fact, we have a great excursion in the response for the min of X3 whereas the responses are concentrated in a small interval for both the mid point value and for the max of X3. Furthermore, the values of the response increase as X3 increases. Also for X2 an effect similar to X3 in terms of excursion in the responses is evident: a great excursion for the min of X2, whereas the responses are concentrated in a small interval for its midpoint and max level. Indeed, the ranges of Y_{elp} when X2 is fixed at its second or third level are nested, with the third including the second: this implies a lower dependence of the response with respect to that due to X3 and a second order dependence. Instead the amplitude of the response due to changes in the X1 levels does not exhibit sensible variations. A low shift in the maximum value corresponds to a limited first order influence of this factor. Moreover, the factors combination allowing the max value in the response is achieved when X1=max, X2=midpoint, X3=max, as evidenced in the following paragraph.

4 APPLICATION OF THE RESPONSE SURFACE METHOD

The Response Surface Method (RSM) allows to get quantitative information on the dependence of the response on the considered factors. In order to perform such an analysis, the results of the numerical simulations are interpolated on a response surface. In particular, the response surface can be obtained by considering a second order model representing an hyper-surface in a 4-dimensional space:

$$y = \beta_0 + \sum_{i=1}^{k} \beta_i x_i + \sum_{i=1, j \le i}^{k} \beta_{ij} x_i x_j \qquad (5)$$

where y is the desired response (i.e. the maximum value of the simulated TMV), k is the number of the parameters, x_i (i=1,.., k) represents the i-th factor, β_i and β_{ij}, (i,j=1,.., k) denote the effect of i-th factor and the mutual interaction of i-th and j-th factor respectively. By using the previous 57 combinations of the parameter levels we obtain the RSM coefficients, summarized in Table 3 .

Table 3: RSM coefficients at a confidence level of 99%.

Factor	**1**	**X1**	**X2**	**X3**	**X1²**
effect	969.820	13.122	4.374	8.890	-0.155
Factor	**X2²**	**X3²**	**X1·X2**	**X1·X3**	**X2·X3**
effect	-0.008	-0.054	-0.035	0.032	-0.019

In order to graphically show the correlation among the response and the factors, we use the MATLAB® function RSTool which allow to interactively plot the response (either in presence or in absence of electroporation) as a function of one parameter at a time while letting the remaining two fixed. In Figure 4 we compare the responses with (Y_{elp}) and without (Y_{nelp}) the electroporation generator in the circuit of Figure 1.

The results in Figure 4 show that there is a linear dependence of the TMV maximum with respect to X1 and X3, whereas it is of quadratic type for X2. These behaviours are evident for the responses obtained either in absence of the electroporation phenomenon (Y_{nelp} in the upper part of Figure 4) or in presence of it (Y_{elp} in the lower part of Figure 4).

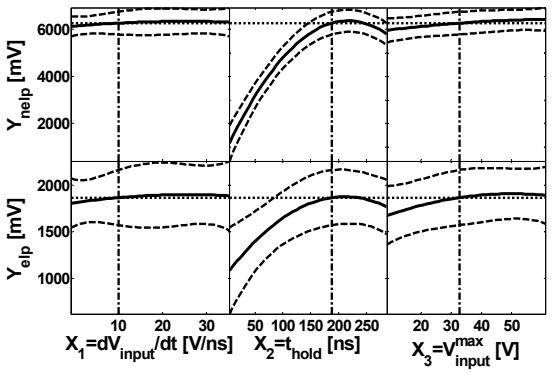

Figure 4: Behaviour of the responses as a function of one parameter at a time while the remaining two are fixed.

Moreover, since the shapes of the curves remain the same in these two cases, it is possible to state that the behaviour is not influenced by the electroporation phenomenon, but it is mainly dictated by the non-linear conductances of the ionic channels, i.e. the common part of the circuit. By looking at the values of the response, it is evident that, according to similar results obtained by other research groups (DeBruin and Krassowska, 1999), the maximum of the TMV is three times greater in the basic HH model than that obtained when electroporation is taken into account. In Figure 5 the resultant maximum of the responses Y_{elp} is depicted, where we have set X1=34.3V/ns, X2=120.7ns X3=60V corresponding to the Best Parameters Set (BPS=(X1*,X2*,X3*)), as previously obtained by the DoE approach. Such a combination gives Y_{elp}=1.77V. As found also by using DoE, the most influencing factors are X3 and X2 because they give rise to the greater variation of the response.

The effectiveness of the BPS identification procedure based on RSM is checked by evaluating the real TMV peak value in correspondence of the BPS from the circuital model described by the equation system (3). Firstly we note that the time evolutions depicted in Figures 6-7 are characterised by a change of the shape similar to that found by other researchers (Vasilkoski et al., 2006) for similar values of t_{hold} and dv/dt. The plots depicted in Figure 6 show the time evolutions of TMV for the BPS (thin continuous line) and for other combinations of the parameters. In particular, the other three curves are obtained for X1=X1*, X2 set to its min value and three different values of X3 (including X3*). We obtain for the BPS the highest actual peak value of TMV equal to 1.65V. Such a value exhibits a small discrepancy of about 7% to the value (1.77V) obtained by means of the RSM. Better accordance may eventually be achieved by adopting a polynomial Response Surface of higher order. We also note that the two solid curves corresponding respectively to BPS (thin line) and that obtained for (X1*,X2$_{min}$,X3*) (thick line) overlap in the first part and are characterised by the same peak value, since the applied stress during the rising front, i.e. the main cause influencing the peak, coincides. Moreover, a decrease of X3 determines a sensible decrease in the peak value of TMV.

The effects induced in the response by varying X1 and X3 and keeping constant the pulse duration t_{hold} to its min value (X2$_{min}$=11ns) can be appreciated by comparing the plots of Figure 6 and 7. In particular, we observe that the same reduction of V_{max} (from X3=60V to X3=35V) associated to a reduction of the slew rate (from X1=34.3V/ns to X1=19.9V/ns) does not lead to appreciable differences in the peak value of the TMV, as shown by the two leftmost curves of Figures 6 and 7. On the other side, a reduction in the slew rate (X1=5.7V/ns in Figure 7) for the lowest level of V_{max} (X3=10V) induces a significant change in either the peak value or the shape of the TMV dynamics.

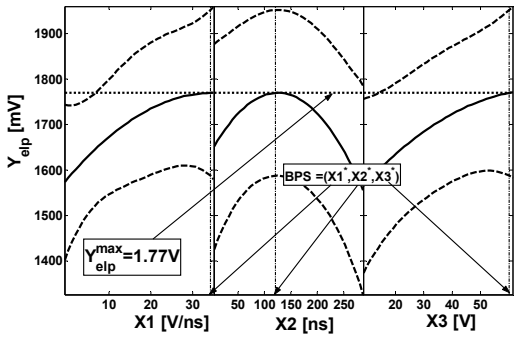

Figure 5: Identification of the BPS for the response Y_{elp}.

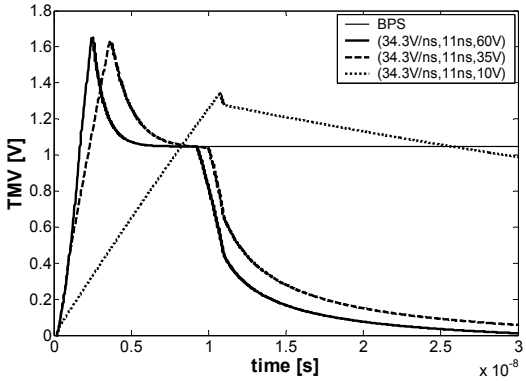

Figure 6: Time evolutions of TMV. BPS=(34.3V/ns, 120.7ns, 60V). The parameters values corresponding to the other curves are reported in the insert.

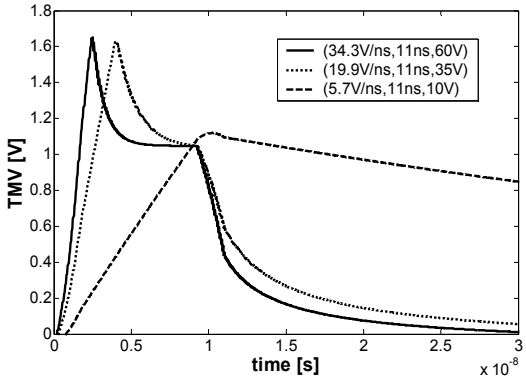

Figure 7: Time evolutions of TMV. The parameters values corresponding to the curves are reported in the insert.

5 CONCLUSIONS

A systematic approach based on the combined use of Design of Experiments and Response Surface Methodology has been applied for evaluating the effects induced on the dynamics of the Trans-Membrane Voltage of a biological cell by the characteristics of the applied electric pulses. The proposed methodology is applied to a lumped parameter circuit, subjected to a trapezoidal pulse. The combined use of DoE and RSM allows to reliably identify the parameters set leading to the highest peak value of the TMV. The parameters which show the greatest influence are the max value of the applied pulse and the slew rate whereas the response is almost insensitive to the pulse duration. The proposed approach can be easily extended in order to study the effects of the pulse characteristics on the response of more complex circuit models taking into account also the internal cell structures (nucleus, organelles, etc), such as those describing the cell behaviour to ultrashort, high-intensity pulses for intracellular manipulation.

ACKNOWLEDGEMENTS

This work has been carried out with the financial support of ex MURST 60% funds of the University of Salerno.

REFERENCES

Beebe S.J.,. Buescher E.S, Schoenbach K.H., "Intracellular effect of ultrashort electrical pulses," *Bioelectromagnetics*, vol. 22, pp.440–448, 2001.

Bilska, A.O., DeBruin, K.A., Krassowska W. 2000, Theoretical modelling of the effects of shock duration, frequency and strength on the degree of electroporation, *Bioelectrochemistry*, 51, 2000, 133-143.

Citro, N., Tucci, V. 2006. A detailed analysis of the electrical dynamics of the Hogkin-Huxley cellular model including electroporation. *Proc. of the 4th Int. Workshop on Biological Effects of Electromagnetic Fields*. ISBN/ISSN: 960-233-173-9, Vol. 2: 853-860.

Citro, N., De Vivo, B., Spagnuolo, G., Tucci, V. (2005), "Range Analysis of Biological Cells Subjected to Pulsed Electric Fields", *Conf. on Electrical Insulation and Dielectric Phenomena,* 10.1109/ CEIDP.2005.1560732, pp. 511-514.

DeBruin, K.A., Krassowska W., 1999. Modelling Electroporation in a Single Cell. I. Effects of Field Strength and Rest Potential. *Biophysical Journal*. 77: 1213-1224.

Heida, T., Wagenaar, J. B. M., Rutten, W. L. C., Marani, E. 2002. Investigating Membrane Breakdown of Neuronal Cells Exposed to Nonuniform Electric Fields by Finite-Element. Modeling and Experiments. *IEEE Trans. On Biomedical Engineering*. 49-10:1195-1203.

Hodgkin, A.L., Huxley, A.F. 1952. A quantitative description of membrane current and its application to conduction and excitation in nerve. *Journal of. Physiology*. 117: 500-544.

Hofmann, G. A., Dev, S. B. Dimmer, S., Nanda G. S. 1999. Electroporation therapy: a new approach for the treatment of head and neck cancer, *IEEE Trans. On Biomedical Engineering*. Volume: 46, Issue: 6, 752-759.

Joshi, R.P., Hu, Q., Schoenbach, K.H. 2004. Modeling studies of cell response to ultrashort, high-intensity electric fields-implications for intracellular manipulation. *IEEE Transactions on Plasma Science*. Vol. 32, issue 4, part II: 1677- 1686.

Joshi, R.P., Hu, Q., Schoenbach, K.H. 2004. Energy-landscape-model analysis for irreversibility and ist pulse-width dependence in cells subjected to a high-intensity ultrashort electric pulse. *Physical Review E 69*, 051901.

Koyamada, K., Sakai, K., Itoh, T. 2004. Parameter Optimization Technique Using The Response Surface Methodology. *Proc. of the 26th Annual Int. Conf. of the IEEE EMBS* San Francisco, CA, USA Sept. 1-5.

Kotnik, T., Miklavcic, D. 2006. Theoretical Evaluation of Voltage Inducement on Internal Membranes of Biological Cells Exposed to Electric Fields. *Biophysical Journal*. 90:480-491.

Miller, C. E., Henriquez, C.S. 1988. Three Dimensional Finite Element Solution for Biopotential: Erythrocyte in an Applied Field. *IEEE Transaction on Biomedical Engineering*. Vol. 35, No. 9: 712-718.

Neumann, E., Sowers E., and Jordan C. A., *Electroporation and Electrofusion in Cell Biology*. New York: Plenum, 1989.

NIST/SEMATECH e-Handbook of Statistical Methods, http://www.itl.nist.gov/div898/handbook/

Sukharev, S. I., et al. 1992,. Electroporation and electrophoretic DNA transfer into cells. The effect of DNA interaction with electropores. *Biophys. J.* 1992, 63(5): 1320–1327.

Vasilkoski, Z., Esser, A. T., Gowrishankar, T. R., Weaver, J.C. 2006. Membrane electroporation: The absolute rate equation and nanosecond time scale pore creation. 2006. *Physical Review E 74*. 021904.

Weaver, J.C. 2000, Electroporation of cells and tissues, *IEEE Transactions on Plasma Science*, 2000, Vol. 28, Issue: 1, 24-33.

POLYMER MEMS SYSTEM FOR MEASURING THE MECHANICAL MODULUS OF A BIOLOGICAL CELL

Wenyue Zhang[1], Markus Gnerlich[1], Yaohua Sun[1], Gaoshan Jing[1], Jonathan J. Paly[2]
Arkady Voloshin[2,3] and Svetlana Tatic-Lucic[*1,2]
[1]*Sherman Fairchild Center, Electrical & Computer Engineering Department*
[2]*Bioengineering Program*
[3]*Department of Mechanical Engineering & Mechanics, Lehigh University, Bethlehem, Pennsylvania 18015, USA*
** svt2@lehigh.edu*

Keywords: Cell mechanics, mechanical modulus, MEMS, polymer, dielectrophoresis.

Abstract: The measurements of the mechanical modulus of biological cells are critical to studies of pathophysiology and the research for an effective treatment. This research has developed a rapid and cost effective technique in order to measure the Poisson's ratio and mechanical modulus of a live biological cell by utilizing microelectromechanical system (MEMS) techniques in a biological application. The design, fabrication, and characterization of a polymer-based MEMS system that integrates a V-shaped electrothermal actuator array and a cell-positioning system in a single microelectronics chip are presented here. This BioMEMS device compressed a NIH3T3 fibroblasts cell and caused up to 25% mechanical strain.

1 INTRODUCTION

Osteoporosis is a pubic health problem that affected more than 44 million Americans in 2004, most of them are women and/or seniors (U.S. Department of Health and Human Services, 2007). This age-related disease results in bones that lack the ability to respond to dynamic mechanical stimulus, which is required for the bones in the human musculoskeletal system to maintain proper osteogenesis (Fritton, McLeod, and Rubin, 2000). Since several properties of bone cells, such as adaptation (Caillot-Augusseau, Lafage-Reoust, Soler, Pernod, Dubois, and Alexander, 1998) and the cytosolic calcium response to fluid flow (Donahue, Zhou, Li, and McCauley, 1997), have been proven to decrease as a function of age, biologists hypothesize that the biomechanical properties of osteoblasts (bone-formation cells) change as a function of age, and this change could be a contributing factor to the pathogenesis of osteoporosis (You, Yellowley, Donahue, Jacobs, 1999).

However, this hypothesis has not been carefully examined due to the limitations of current measurement techniques, such as atomic force microscopy (AFM), which tests the mechanical properties of one small portion of the cell, and can only test one cell at a time. Testing cells one-by-one is too time-consuming and expensive to be commonly practiced in biological research, which relies on statistical studies that require surveying a large number of cells. As a result, the mechanism underlying the pathophysiology of osteoporosis is still unknown.

To improve the public health condition, it is absolutely necessary to develop efficient techniques to measure cell's mechanical properties. Recently, several MEMS devices have been applied to biological researches, such as a MEMS-based force sensor (Yang and Saif, 2006), and a frequency depedent electrostatic actuator (Scuor, Gallina, Panchawagh, Mahajan, and Sbaizero, 2006). Compared to these single crystal silicon and polysilicon devices, polymer devices have several advantages, such as: less possibility of damaging live cells when making physical contact due to the low Young's modulus of polymers; lower cost (Elderstig and Larsson, 1997); and lastly, the ability to operate in liquids if an electrothermal actuation mechanism is used (the heat is insulated due to the low thermal conductance of polymers). This paper reports a polymer-based MEMS system for measuring the mechanical properties of a live cell.

2 METHODOLOGY

To measure the mechanical modulus of a biological cell, a BioMEMS device was designed and fabricated (Figure 1). In a 2.2 x 2.5 mm^2 single chip, a polymer **e**lectro**t**hermal **a**ctuator (ETA) array (1) is to compress a live cell agaist a fixed wall (2), and report associated forces and displacements during the compression. In addtion, a cell positioning system (dielectrophoresis quadrupole electrodes (3)) is used to trap a cell at a desired location, and a set of scale bars (4) is used to calibrate the optical measuring system.

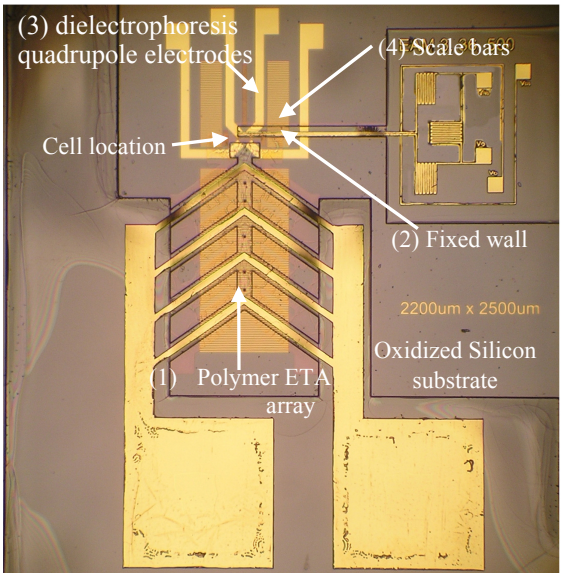

Figure 1: Optical image of a fabricated BioMEMS device for measuring the mechanical modulus of a biological cell.

Four experimental steps need to be done before obtaining the mechanical properties of a cell: (a) characterizing the actuator displacement as a function of input electrical power; (b) determining the reaction force between the actuator and the cell; (c) recording the force versus deformation curve for the cell; (d) fitting the curve with equation (1), which which was based on the derived Hertz contact model (Timoshenko and Goodier, 1970):

$$F = \left(\frac{2\sqrt{2d}E}{3\pi(1-\nu^2)} \right) \Delta d^{\frac{3}{2}} \qquad (1)$$

where F was the applied force to a cell, Δd was cell deformation, E was compressive modulus of the cell, d was the diameter of a cell, and ν was the Poisson's ratio of the cell. The fitted parameter reveals the mechanical modulus of the cell.

3 MEMS DEVICE FABRICATION

Fabrication of the MEMS devices utilized surface micromachining techniques. The processing flow has been described in detail previously (Zhang, 2007), and will be briefly summarized here (Figure 2). The starting materials are oxidized 3-inch diameter silicon wafers. First, a metal layer of 80 nm platinum was patterned using lift-off process (Figure 2a). A 20 nm titanium layer preceding this conductive layer was used to increase the adhesion wherever metallization was present. Second, a 5 µm thick sacrificial photoresist (AZ P4620, Clariant, New Jersey) was applied to create an air gap (Figure 2b). Third, a thick negative tone photoresist (SU-8, product #: 2015, Microchem, MA) was used for a structural layer (Figure 2c). Next, the second metal layer of 80 nm gold (with the same adhesion layer) was patterned on top of the structural polymer (Figure 2d). Finally, the whole structure was immersed in AZ 400T photoresist stripper (Clariant, New Jersey) at room temperature to release the polymer device (Figure 2e).

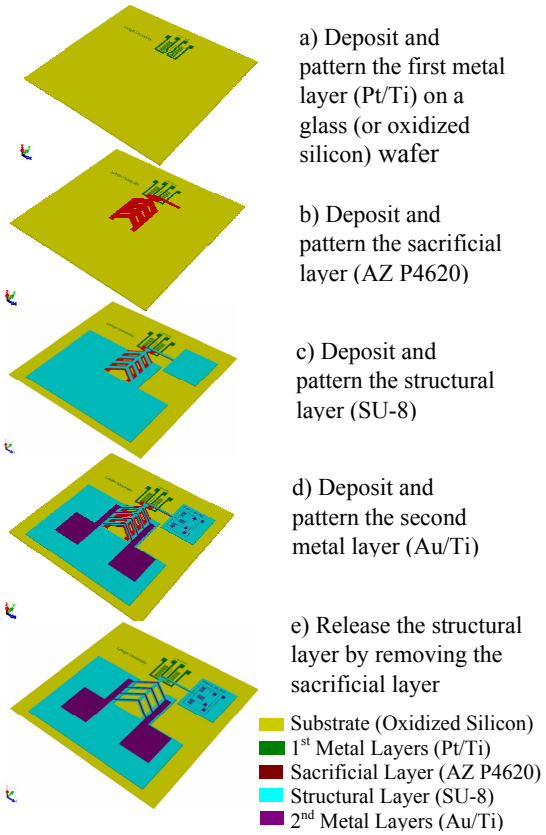

Figure 2: Fabrication process flow for the BioMEMS device for measuring the mechanical modulus of a biological cell.

3.1 Effects of UV/Ozone Treatment

A UV/Ozone cleaner was used to clean the substrates and harden the sacrificial pattern (AZ P4620). Without this step, the sacrificial pattern was destroyed during the spin-coating of the structural SU-8 polymer (Figure 3) by centrifugal forces and/or solvent diffusion. During the UV/Ozone treatment, the deep UV light (in ranges of 185 nm to 254 nm wavelength) hardened the thick sacrificial photoresist (Allen, Foster, and Yen, 1982) while the heat generated by the UV lamps added additional cross-linking. Therefore, the sacrificial patterns can maintain their shapes after SU-8 patterning. We used polymer sacrificial materials because it was too difficult to selectively remove a metal sacrificial layer with the pre-patterned Pt/Ti layer on the substrate.

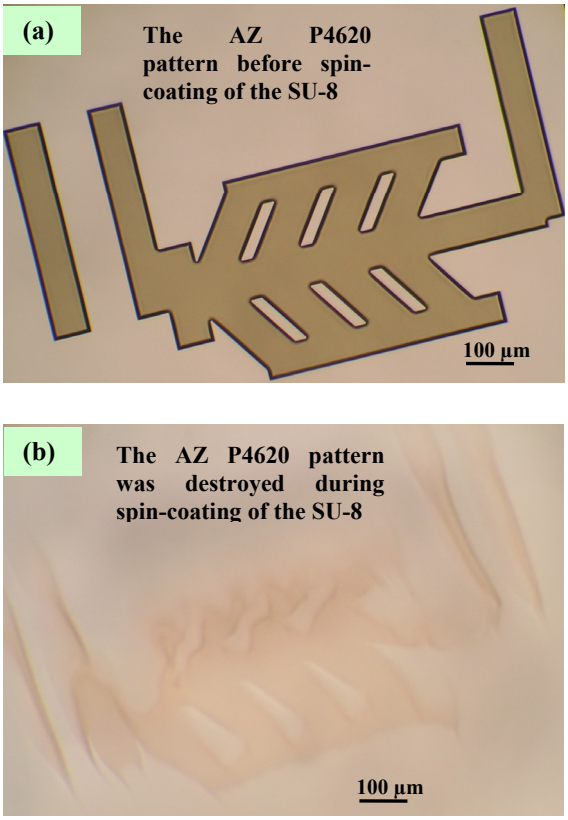

Figure 3: Optical images of the sacrificial patterns (a) before and (b) after spin-coating a transparent structural layer. These sacrificial patterns did not have UV/Ozone treatment and were destroyed.

One more benefit of an UV/Ozone treatment was reduction of gas bubbles in the resist. During the UV exposure of SU-8, the underlying AZ P4620 that had not been previously exposed also absorbed UV radiation. Then, gases due to photoresist outgassing in UV light (Kunz, 2004) were trapped by the SU-8 layer, which causes gas bubbles formation (Figure 4).

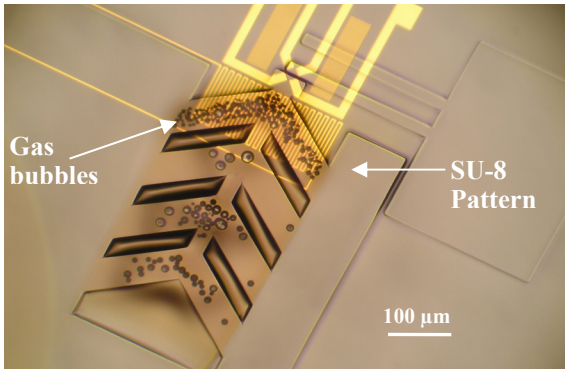

Figure 4: Optical image of gas bubbles that appeared the post exposure baking after UV exposure of the structural layer (SU-8).

Short UV/Ozone treatment (3 to 4 minutes) was applied to solve the gas bubbles problem and resulted in a sacrificial pattern hard enough to resist physical and chemical damage (Figure 5), but still able to be removed at the end of processing.

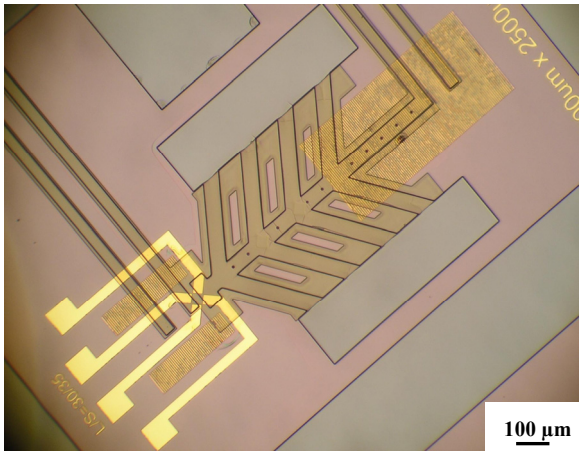

Figure 5: Optical image of a fabricated device. After selecting the proper UV/Ozone treatment time, the sacrificial patterns keep their shapes after SU-8 patterning. (This image was taken after developing the SU-8 layer but before the second metal layer formation).

4 RESULT & DISCUSSION

High frequency (800 KHz, sinusoidal) AC voltages were applied to these BioMEMS devices to avoid electrolysis, which generates a large amount of gas in liquids (Selvaganapathy, Leung Ki, Renaud, and

Mastrangelo, 2002). The actuator displacement as a function of input electrical power was recorded (Figure 6) when operation in NIH3T3 fibroblasts cell medium. The maximum displacement was 4 µm when power was RMS 750 mW. After exceeding the maximum value, the displacement decreased due to the out-of-plane deformation of the polymer V-shaped electrothermal actuator array.

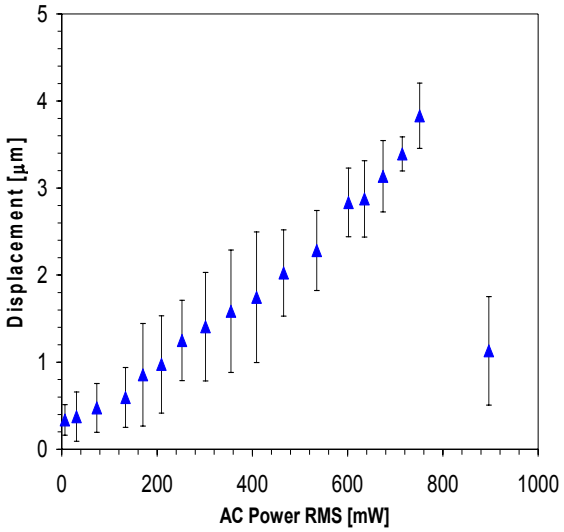

Figure 6: Experimental data of the BioMEMS ETA arrays' displacement as a function of input AC power.

The lab experiments started with immersion of the BioMEMS device into the cell medium. Cells were transferred to the device using a micropipette. First, a cell was trapped at the centre of the dielectrophoresic quadrupole electrodes after applying an AC voltage (10 $V_{p\text{-}p}$, 1 MHz, sinusoidal) to them (Figure 7a). Next, the actuator was moved towards the cell, and it compressed the cell up to 4 µm (Figure 7b). The diameter of the cell under test was measured to be 16 µm. This means that the BioMEMS devices can mechanically stimulate the cell in 25% strain, which is double the minimum requirement (10% strain) of mechanical stimulation to a cell (You, Cowin, Schaffler, and Weinbaum, 2001).

When the cell was under compression, orthogonal extension was observed as well. Currently, the displacement resolution was ±0.5 µm. Next, the spring constant of the polymer ETA was calibrated using a nanoindenter (TriboScope, Hysitron Inc.). Finally, the compressive modulus of the NIH3T3 fibroblast cell can be extracted from these measurements. In order to extract reliable mechanical modulus, we are currently working on improving the resolution of this method.

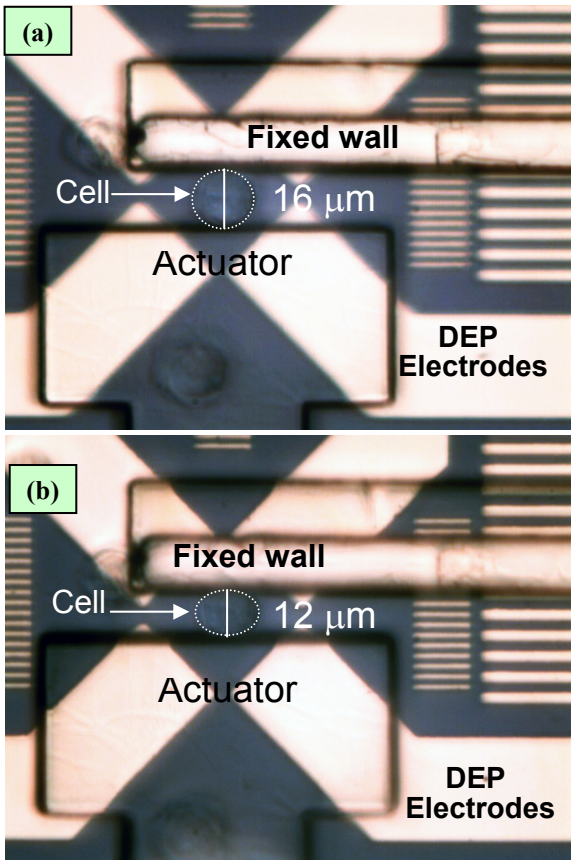

Figure 7: Optical images of: (a) a cell being trapped at the centre of dielectrophoresic quadrupole electrodes, and (b) the cell being compressed by the actuator after being powered up. (Outline of the cell is for better visibility.).

5 CONCLUSIONS

The measurements of the mechanical properties of biological cells are critical to improve the public health condition. This research focuses on the design, fabrication, and characterization of a MEMS system to measure the compressive modulus of a live biological cell. This MEMS-based system has realized three basic functions: (1) trapping a cell to a designed area before testing; (2) applying forces to a cell, and (3) sensing the forces and displacements during the compressing. The device was able to compress a cell up to 25% mechanical strain in a cell medium. The measurements of mechanical properties are limited by the current displacement resolution and the improvements are under investigation.

REFERENCES

Allen, R., Foster, M., Yen, Y.-T., 1982. Deep U.V. Hardening of positive photoresist patterns. *J Electrochem. Soc.,* 128, 1379.

Caillot-Augusseau, A., Lafage-Reoust, M.-H., Soler, C., Pernod, J., Dubois, F., Alexander, C., 1998. Bone formation and resorption biological markers in cosmonauts during and after a 180-day space flight (Euromir 95). *Clin. Chem.* 44(3), 578-585.

Donahue, H. J., Zhou, Z., Li, Z., McCauley, L. K., 1997. Age-related decreases in stimulatory G protein-coupled adenylate cyclase activity in osteoblastic cells. Am. J. Physiol. 273, E776-E781.

Elderstig, H., Larsson, O., 1997. Polymeric MST-high precision at low cost. *J. Micromech. Microeng.,* 7, 89-92.

Fritton, S. P., McLeod, K. J., Rubin, C.T., 2000. Quantifying the strain history of bone: spatial uniformity and self-similarity of low-magnitude strains. *J. Biomechanics.* 33 (3), 317-325.

Kunz, R. R., 2004. Photoresist outgassing: a potential Achilles heel for short wave-length optical lithography? in *Proc. of SPIE*, 5376, 1-15.

Scuor, N., Gallina, P., Panchawagh, H. V., Mahajan, R. L., Sbaizero, O., 2006. Design of a novel MEMS platform for the biaxial stimulation of living cells. *Biomed. Microdevices*, 8, 239-246.

Selvaganapathy, P., Leung Ki, Y.-S., Renaud, P., Mastrangelo, C. H., 2002. Bubble –free electrokinetic pumping. *J. Microelectromech. Syst.,* 11(5), 448-453.

Timoshenko, S.P. and Goodier, J.N., 1970. Theory of Elasticity. 3rd ed. New York: McGraw-Hill Publishing Company. 409-415.

U.S. Department of Health and Human Services, (2007). Bone Health and Osteoporosis: A Report of the Surgeon General. Retrieved July 9, 2007, from http://www.surgeongeneral.gov/library/bonehealth/factsheet2.html

Yang, S., Saif, T., 2006. MEMS based sensors for the study of indentation response of single cells. in *Tech. Dig. of MEMS 2006*, Istanbul, Turkey, 20-23.

You, J., Yellowley, C. E., Donahue, H. J., Jacobs, C. R., 1999. Physiological levels of substrate deformation are less stimulatory to bone cells compared to fluid flow, In *American Society of Mechanical Engineers, Bioengineering Division (Publication) BED*, 43, 161-162.

You, L., Cowin, S. C., Schaffler, M. B., Weinbaum, S., 2001. A model for strain amplification in the actin cytoskeleton of osteocytes due to fluid drag on pericellular matrix. *J. Biomechanics*. 34 (11), 1375-1386.

Zhang, W.-Y., 2007. Design, Modeling, Fabrication and Characterization of a MEMS Device for Measuring the Mechanical Compliance of a Biological Cell. *Ph.D. Dissertation*, Lehigh University, 2007.

MEASUREMENT OF CELL FORCES USING A POLYMER MEMS SENSOR

Nicholas Ferrell, James Woodard and Derek Hansford
Department of Biomedical Engineering, Ohio State University, 1080 Carmack Rd. 270 Bevis Hall, Columbus, OH, USA
ferrell.61@osu.edu, woodard.12@osu.edu, hansford.4@osu.edu

Keywords: Polymer MEMS, cell forces, microfabrication.

Abstract: Cellular mechanics are responsible for execution and regulation of a number of cell functions. Mechanical forces generated within the cytoskeleton are transmitted via transmembrane linkages to the underlying substrate. Measurement of these forces could lead to a wealth of additional information about the role of cell mechanics in regulating cell function and signal transduction. Here we describe the design, fabrication, and testing of a polystyrene cantilever beam array for measuring forces generated by WS1 human skin fibroblasts. Finite element analysis was used to guide the design of a compound cantilever beam. Sensors were fabricated from polystyrene to provide a well-studied and biocompatible surface for cell attachment. Soft lithography based techniques were used for microfabrication of the sensors. Cells were placed on four and eight probe cantilever sensors and deflection of the probes was measured optically during attachment and spreading of the cells. The device was successfully used to measure time varying mechanical forces generated by fibroblast cells.

1 INTRODUCTION

Mechanical forces generated by adherent cells play an important role in execution and/or regulation of a host of cellular processes. When anchorage dependent cells attach to a surface, forces generated in the cytoskeleton are transmitted to the underlying substrate via transmembrane protein linkages. These mechanical forces are involved in controlling cell functions including adhesion, morphology, and motility (Galbraith and Sheetz, 1998; Chicurel et al., 1998) as well as apoptosis (Chen et al., 1997) and wound healing (Wrobel et al., 2002) among others. Measurement of mechanical forces generated by adherent cells could provide additional insight into the basic role of cell mechanics in regulating cell function. In addition, monitoring time dependent cell mechanics could lead to new routes of cell-based sensing focused on mechanical changes in the cell brought about by externally applied chemical or mechanical stimuli.

Several devices have been utilized for observing and measuring cellular forces. Some of the first approaches involved growing cells on deformable elastic substrates, which wrinkled in response to mechanical forces (Harris et al., 1980; Beningno and Wang, 2002). More recently, microfabrication techniques have been used to fabricate force measurement devices. This is an attractive approach due to the ability to make precise structures on the same size scale as biological cells. Galbraith and Sheetz (1997) used micromachined silicon cantilevers to measure localized forces generated by fibroblasts. Single cantilevers with one direction of motion were used, thus limiting the ability to measuring forces directed along the axis of the cantilever or determine the direction of the force. Soft lithography based microfabrication techniques (Xia and Whitesides, 1998) have also been used to fabricate devices for measuring cell forces (Tan, et al., 2003). In this case, elastic poly(dimethylsiloxane) (PDMS) pillars acted as vertical cantilevers. Cells were grown on top of the pillars and deflections were measured and used to calculate the force on each pillar.

Our approach to measurement of cell forces involves the use of a polystyrene cantilever array with a compound beam design. The compound beam allows the forces to be measured in all directions, thus allowing calculation of both the force magnitude and direction. The choice of polystyrene as the structural material also has a significant impact on the function of the device. Polystyrene is

a well-characterized biocompatible material that is used ubiquitously in cell culture applications. In addition, it is well know that the stiffness of the substrate can significantly affect the mechanical behaviour of cells (Lo et al., 2000, Choquet et al., 1997). Most devices to date have been fabricated from relatively flexible (silicone rubber) or relatively stiff (silicon) materials. In this case we use a materials with intermediate stiffness.

The device consists of a four or eight probe cantilever array fixed to a glass substrate at the base of the beams. The ends of the beams were designed to provide adequate surface area for cell spreading. The fixed post at the center of the device was included to provide a location for initial cell attachment as well as provide a fixed reference point for probe deflection analysis. As the cell attaches to the beams and exerts forces, the deflection of each cantilever is measured optically over time to give spatially and temporally resolved measurement capabilities.

2 MATERIALS AND METHODS

2.1 Device Fabrication and Characterization

Devices were fabricated using sacrificial layer micromolding as described in (Ferrell et al., 2007). A water-soluble sacrificial layer was first patterned by photolithography and reactive ion etching. A layer of poly(vinyl alcohol) (PVA) was dissolved in water to a final concentration of 10% (wt/wt). The PVA solution was spin coated on 18 mm glass coverslips at 1000 rpm. A protective layer of poly(methyl methacrylate) (PMMA) was then spin coated on top of the PVA. The PMMA layer protected the PVA from the developer in the upcoming photolithography process. Photolithography was then used to pattern an etch mask on the PVA/PMMA films. Reactive ion etching in an O_2 plasma was used to removed both the PVA and PMMA in the unmasked regions. The remaining photoresist and PMMA layers were then removed by sonication in acetone, leaving only the patterned PVA.

A PDMS mold of the device was fabricated by replica molding (Xia and Whitesides, 1998) of a photolithographically patterned master. The PDMS mold was spin coated with a solution of polystyrene in anisole (7.5% wt/wt). The polystyrene was removed from the raised portions of the mold by contact with a glass slide heated to 200 ºC. The remaining polystyrene was left in the recessed portion of the mold. The mold was aligned with the sacrificial layer and heat (120 ºC) and pressure (75 psi) were used to transfer the device onto the sacrificial layer. The device was then annealed at 115 ºC for 15 minutes to improve adhesion of the anchor regions and remove any residual stress in the beams.

The thickness of each device was characterized using a stylus profilometer. The thickness range for the above processing parameters was 1.31-1.75 μm.

2.2 Design and Simulations

Finite element simulations (ANSYS) were used to guide the design of the cantilever beam. The beam was designed to give reasonable x,y deflection response while still conforming to the geometrical constraints of the devices circular configuration. The deflection plot for a 5 nN force applied to an area at the end of the cantilever beam at 10º increments from 0º to 360º is shown in Figure 1.

An ideal beam response would be a circular deflection profile with no offset between the direction of the beam deflection and the force direction. The plot shows a slight offset. The plot also shows that the beam is stiffer in the 90º and 270º directions compared to the 0º and 180º directions. This leads to slightly less sensitivity to forces in those general directions, but the overall response of the beam is adequate for the application described here.

2.3 Cell Culture and Image Acquisition

The cells used in this study were WS1 human skin fibroblasts (ATCC). Cells were cultured in Minimum Essential Medium, Eagle (ATCC) supplemented with 10% fetal bovine serum and 1% penicillin-streptomycin. Cells were cultured at 37ºC in a 5% CO_2 atmosphere. To obtain cells for measurements, cells were detached from T75 tissue culture flasks using .25% trypsin-EDTA.

Prior to performing measurements, the devices were modified by a brief exposure to O_2 plasma in a reactive ion etcher to make the surface more hydrophilic and improve cell attachment. Devices were fixed to a PDMS coated petri dish. The PDMS coated dish allowed fixation of the device without the use of a chemical adhesive. The devices were placed in cell culture medium to dissolve the sacrificial layer. After complete dissolution of the

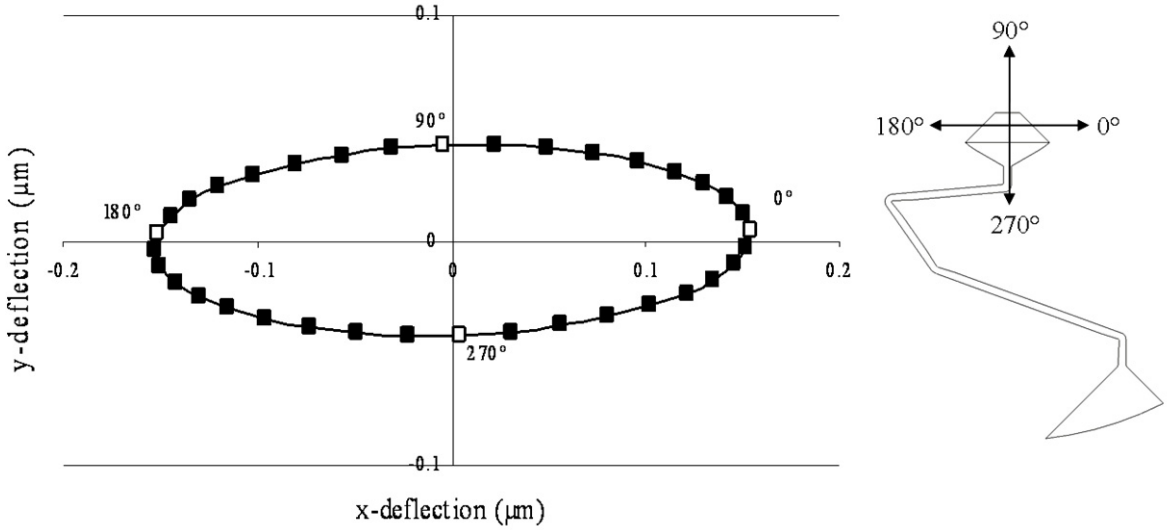

Figure 1: Deflection plot for the compound cantilever beam with a 5 nN applied load.

PVA layer, the medium was aspirated and fresh medium was added and aspirated three times to remove the majority of the dissolved PVA. 20 ml of fresh medium without cells was added to the petri dish. A few drops of cell suspension were then added to the dish. This provided a low cell density and minimized the likelihood of having multiple cells on a single device.

Measurements were performed on an inverted microscope (Nikon TS100) with a custom stage incubator. The incubator consisted of an acrylic enclosure with the temperature regulated at 37ºC and supplied with 5% CO_2. A manual micromanipulator (World Precision Instruments) with a 2μm inner diameter glass micropipette was used to position a single cell on the center region of sensor. Cells were moved onto the device with the microscopy in phase contrast mode to allow better visualization. A 6.6 megapixel CCD camera (Pixelink) was set to capture images at 30 second intervals for the duration of the experiment. For analysis, the phase contrast filter was removed and brightfield images were captured to facilitate easier edge detection.

2.4 Image Analysis and Force Calculation

Images were analysed using NIH Image J software (download available at http://rsb.info.nih.gov/ij/). The x,y position of the end of the probe as well as a fixed point on the device were determined prior to cell attachment. The x,y displacement of the end of each the cantilever was then monitored over time. The x,y position of the fixed point was also monitored to determine and correct for image shift. After determining the magnitude and direction of the cantilever deformation, the force magnitude and direction were calculated based on the finite element simulations.

3 RESULTS AND DISCUSSION

Scanning electron micrographs of the four probe sensor prior to removal of the sacrificial layer are shown in Figure 2. Figure 2(a) shows the entire device with the anchor region at the outer perimeter of the device. The close-up of the center of the device shows the four adhesion pads as well as the fixed post.

The force versus time plots for two different experiments are shown in Figure 3 (a,c). The plots show the force magnitude for each of the four probes. Figure 3(a) shows that force is exerted on each of the four probes. The graph also indicates that the cell adhered to the sensor relatively quickly after being placed on the device. Figure 3(c) shows that force is only exerted on three of the four probes and the magnitude of the force is significantly higher for probes 1 and 3 compared to probe 4. This is likely due at least in part to a smaller adhesion area on probe 4 as compared to probes 1 and 3. This could be a result of off center cell attachment and spreading. In addition, Figure 3(c) shows that there is a period of time prior to cell attachment with no force generation. The plot clearly shows the onset of

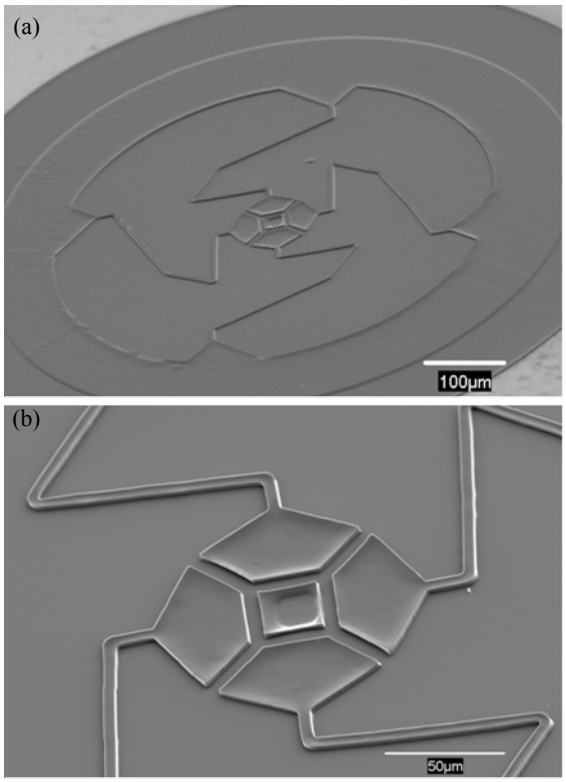

Figure 2: SEM micrographs of the cell force sensor.

cell attachment and force generation for each of the probes. Probe 2 showed no force/deflection response attributed to cell mechanics. The data is included to show the noise in the measurement and analysis system.

The angle of the force vectors are shown in Figure 3(b,d). The boxes highlight that most of the forces are oriented around 90º or toward the center of the devices. This is expected given the nature of the forces. In figure 3(d) the random orientation of the angle prior cell attachment and for probe 2 are due to noise.

Figure 4 shows optical phase contract micrographs of the cantilevers corresponding to the force and direction plots in Figure 3 (a,c). The force vectors for each probe are overlaid on the images. The images show the changes in the both the magnitude and direction of the deformation at 0, 30, 37.5, and 50 minutes.

4 CONCLUSIONS

A novel force sensor was designed and fabricated for measurement of mechanical forces generated by fibroblast cells. The sensor was designed with the aid of finite element simulations of the sensor behavior. The device was fabricated from polystyrene using a soft lithography based fabrication procedure. Force magnitudes and directions were measured using WS1 skin fibroblast and show the ability to measure variation in the cell mechanics over time.

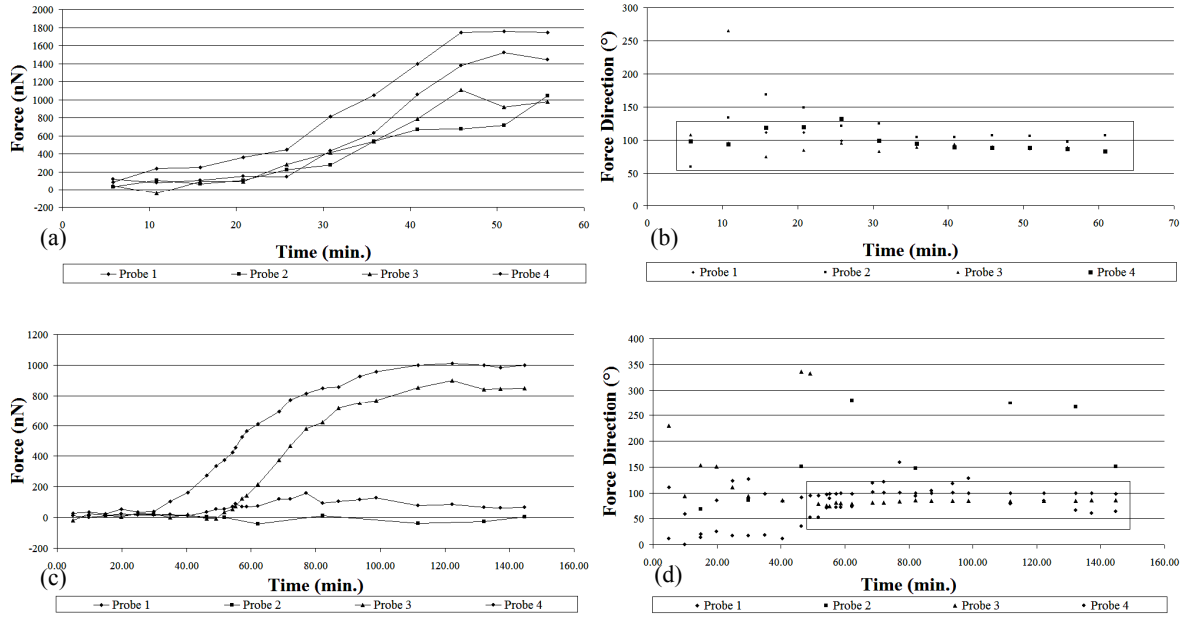

Figure 3: (a,c) Force magnitude versus time for two separate experiments. (b,d) Force direction corresponding to the forces in (a,c). The boxes highlight that the majority of the forces are oriented in the direction toward the center of the structure.

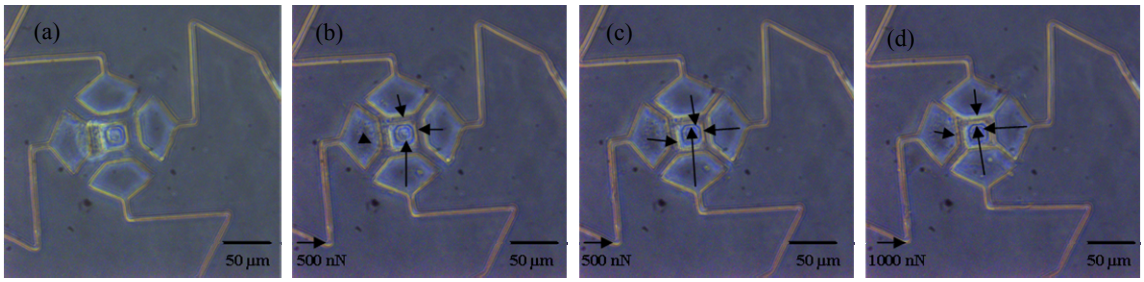

Figure 4: Phase contract micrographs with vector force overlays at (a) 0 min. (b) 30 min. (c) 37.5 min. and (d) 50 min. Note the difference in the force vector scale in (d).

ACKNOWLEDGEMENTS

The authors would like to thank Derek Ditmer and Paul Stefan at the Ohio Nanotech West Laboratory for technical assistance. We also thank Derek Ditmer and Landon McCaroll for assistance with image analysis.

REFERENCES

Beningo, K.A., Wang, Y., 2002. Flexible substrata for the detection of cellular traction forces. *Trends in Cell Biology*, 12, 79-84.

Chen, C.S., Mrksich, M., Huang, S., Whitesides, G.M., Ingber, D.E., 1997. Geometric control of cell life and death. *Science*, 276, 1425-1428.

Chicurel, M.E., Chen, C.S., Ingber, D.E., 1998. Cellular control lied in the balance of forces. *Current Opinions in Cell Biology*, 10, 232-239.

Choquet, D., Felsenfeld, D.P., Sheetz, M.P., 1997. Extracellular matrix rigidity causes strengthening of integrin-cytoskeletal linkages. *Cell*, 88, 39-48.

Ferrell, N., Woodard, J., Hansford, D., 2007. Fabrication of polymer microstructures for MEMS: sacrificial layer micromolding and patterned substrate micromolding. *Biomedical Microdevices*, 9, 815-821.

Glabraith, C.G., Sheetz, M.P., 1998. Forces on adhesive contacts affect cell function. *Current Opinions in Cell Biology*, 10, 566-571.

Galbraith, C.G., Sheetz, M.P., 1997. A micromachined devices provides a new bend on fibroblast traction forces. *PNAS*, 94, 9114-9118.

Harris, A.K., Wild, P., Stopak, D., 1980. Silicone rubber substrata: a new wrinkle in the study of cell locomotion. *Science*, 208, 177-179.

Lo, C., Wang, H., Dembo, M., Wang, Y., 2000. Cell movement is guided by the rigidity of the substrate. *Biophysical Journal*, 79, 144-152.

Tan, J.L., Tien, J., Pirone, D.M., Gray, D.S., Bhadriraju, K., Chen, C.S., 2003. Cell lying on a bed of microneedles: an approach to isolate mechanical force. *PNAS*, 100, 1484-1489.

Wrobel, L.K., Fray, T.R., Molloy, J.E., Adams, J.J., Armitage, M.P., Sparrow, J.C., 2002. Contractility of Single Human Dermal Myofibroblasts and Fibroblasts. *Cell Motility and Cytoskeleton.*, 52, 82-90.

Xia, Y., Whitesides, G.M., 1998. Soft lithography. *Angew. Chem. Int. Ed.*, 37, 550-575.

MICROWAVE DIELECTRIC SPECTROSCOPY OF LOW-VOLUME FRACTION HUMAN CANCER CELLS EMBEDDED IN COLLAGEN GELS

Experimental Feasibility Study with an Open-ended Coaxial Probe

Stéphane Egot-Lemaire*, Pierre-Olivier Bagnaninchi*, Jacek Pijanka*
Josep Sulé-Suso** and Serguei Semenov*
*Institute for Science and Technology in Medicine,*Keele University and **University Hospital of North Staffordshire*
Guy Hilton Research Center, Thornburrow drive, Stoke-on-Trent, U.K.
s.j.egot-lemaire@pmed.keele.ac.uk; s.semenov@pmed.keele.ac.uk

Keywords: Cancer cells, SK-MES cell line, Collagen gels, Volume fraction, Dielectric spectroscopy, Complex permittivity, Open-ended coaxial probe, Microwaves.

Abstract: This paper addresses and demonstrates the feasibility for microwave dielectric spectroscopy to detect small volume fractions of SK-MES lung cancer cells embedded in collagen gels with an open-ended coaxial probe. Measurements were performed on the frequency range 200 MHz – 2 GHz. For all the cell volume fractions tested (1.4%-4.4%), a significant difference in complex permittivity was observed between composite gels (containing cells) compared to gels alone. Statistically significant changes were especially found in the real part of the permittivity, which decreased consistently when the volume fraction increased.

1 INTRODUCTION

The dielectric properties of biological tissues and cells have been widely investigated for many decades (Foster, 1996; Gabriel 1996). They are characterized by the so-called complex permittivity, expressing the polarization response of a material in the presence of a time-varying applied electric field. Measuring its complex response as a function of the field frequency is referred to as dielectric spectroscopy (DS).

The difference in the dielectric properties between various biological tissues is exploited in electromagnetic tomography techniques, such as biomedical microwave imaging, a promising imaging modality (Tofighi, 2001; Semenov, 2003; Fear, 2005). One of its particular interests is the ablility to detect tumours (Hagness, 1998; Bulyshev, 2001; Shao, 2005; Bindu, 2006). Indeed malignant tissues have mainly been found to have significantly different dielectric properties than the corresponding normal tissues regarding both the real and the imaginary parts of the complex permittivity (Chaudary, 1984; Surowiec, 1988; Smith, 1986; Joines, 1994; Sha, 2002). In this regard, DS studies related to cancer have mostly dealt with bulk tissues. In these kinds of studies bulk tissues are either investigated *in vitro* or *in vivo* which have both disadvantages. *In vitro* studies have mostly investigated non-living tissues. Moreover it is difficult to deal with *in vivo* human tissues mainly because surgery is needed, and it does not necessarily give information at cell level.

On the contrary, working on cell culture samples is a good alternative way to get a better biophysical knowledge of living cells. In this regard, a number of DS experiments have been carried out on various types of cell suspensions. The most commonly investigated cell suspensions, whatever the volume fraction (ranging from a few percent to roughly 70%), have logically been blood samples (Lisin, 1996; Chelidze, 2002; Bordi 2002; Jaspard, 2003; Treo, 2005) and yeast suspensions (Claycomb, 2002). A few of them have especially focused on measuring the dielectric properties of white blood cancer cells in suspension which were shown to be also different from those of normal cells (Polevaya, 1999; Ermolina, 2001). Furthermore, *in vitro* cell culture samples embedded in microporous scaffolds have also been successfully investigated for tissue engineering purposes (Bagnaninchi, 2003 and 2004).

The method was proved to be a good way to monitor cell growth and differentiation in scaffolds used in tissue engineering. The aforementioned studies dealing with cell culture samples were shown to be able to retrieve cell signature. This term refers to the dielectric properties of the main cell compartments, such as membrane, cytoplasm but also nucleus. These so-called cell signatures were shown to be distinct for different cell lines or types. This property allows for cell separation of cancer cells from normal cells by dielectrophoresis (Gascoygne, 1997). In these different studies, measurements have covered different parts of the frequency spectrum, extending from the extremely low frequencies to the lower part of the microwave range depending on the measurement method used.

The motivations of the present study are mainly threefold. The first aim would be to get a better biophysical understanding of the differences in dielectric properties between epithelial lung cancer cells and the corresponding normal ones. Secondly, DS could also be used as a method to analyse the response and effectivnesses of various anti-cancer treatments such as chemotherapy drugs on *in vitro* cell culture samples. Some authors have already used DS in the radio and microwave frequency range to do so (Santini, 1991 and 1995; Hübner 2005; Duncan, 2006). Thirdly, this study is a preliminary step to investigate the capability of DS to be used on intraoperative tissue biopsies for on-line assessment of tissue resection effectiveness.

To address these issues, our approach is an adjunct approach of cell suspensions and allows to have an *in vitro* realistic biological 3D model for living lung epithelial cells. As a relatively dense matrix, a collagen gel is a good model for investigation. Collagen is the major component of the natural extracellular matrix (Pietrucha, 2005) and has already been used in other biomedical studies involving similar lung cancer cell culture samples (Yang, 2004). We used low volume fractions of cells in order to have an *in vitro* system that could detect small number of cells so this could have the clinical application of detecting tumours when they are still small enough to undergo radical treatment.

This paper deals with the preliminary investigation of the dielectric properties of lung cancer cell samples embedded in collagen gels in the lower part of the microwave range (UHF). The cells in question belong to a human epithelial lung cancer cell line, namely SK-MES cell line. This paper especially addresses the feasibility of distinguishing low-volume fraction of these cells from the matrix in which they are embedded in this part of the frequency spectrum.

The first section describes in details the materials and experimental set-up used and the second section gives and discusses some obtained results.

2 MATERIALS AND METHODS

We mainly conducted 6 different experiments, on 6 different cell volume fractions: 1.4%, 1.9%, 2.7%, 3.2%, 3.8%, 4.4% corresponding respectively to about 4, 5.3, 7.4, 9, 10.6, 12.3 million cells per gel. They were counted with the aid of a grid-counting chamber (Hycor Kova Glasstic). The volume fraction was estimated by supposing the cells are spherical. Their diameter (mean: 18 μm ± standard deviation: 2.2 μm) was measured on a slide with a light microscope with a computerized ruler.

For each of the 6 experiments, two sets of 7 collagen gels were prepared and measured. The first set did not include any cells and the second set included the same volume fraction of SK-MES cells for a given experiment.

2.1 SK-MES Cell Culture

SK-MES cells (ECACC, UK) were cultured in 175 cm^2-cell culture flasks and incubated at 37°C and 5% CO_2. Each culture vessel contained complete culture medium composed of high-glucose Dulbecco's Modified Eagle's Medium supplemented by 10% volume of foetal calf serum and other standard components according to the provider's instructions and previous studies (Yang, 2004).

2.2 Collagen Gels Preparation

Collagen type I gels were prepared according to the supplier's (BD Biosciences) instructions. To ensure the viability of SK-MES cells reported in (Yang, 2004), the concentration of collagen was 1.5 mg/mL.

Cells were added and mixed with the gel at a temperature of 4°C when collagen is in liquid form. Gels were allowed to set by incubation at 37°C for 3 hours.

Each gel was prepared in a cylinder well and had a diameter of 19 mm and a height of 3 mm. These dimensions are justified in the next section. Therefore each gel had a volume of 0.85 mL.

2.3 Experimental Set-up

2.3.1 Experimental Material

Dielectric spectroscopy was performed using a vector network analyser (model 8753E, Agilent Technologies) operated on the frequency range 200 MHz – 2 GHz connected to a flanged open-ended coaxial probe (dielectric probe, Agilent model 85070) via a coaxial cable.

The complex permittivity of the sample is actually deduced by calculation from the measurement of the complex reflection coefficient at the tip of the probe. Indeed the reflection coefficient is linked to the impedance or admittance seen at the tip of the probe, which is itself directly related to the complex permittivity of the sample by a suitable model (implemented by Agilent's software).

In theory, the model supposes that the sample is semi-infinite (i.e. covers a half space) isotropic and homogeneous. In practice, if the sample is not homogeneous (our case), the result is an average value weighted by the pattern of intensity of the electric field (which is highest at the centre of the probe tip). Besides, the sample is always of finite size. In the probe supplier's data sheet, the diameter of the sample must be at least that of the probe, and its minimal thickness is given by a simple formula related to the permittivity, which in our case yields about 2.5 mm. This is in good agreement with values found in scientific papers to measure biological tissues with probes of similar dimensions (Semenov, 2000; Hagl, 2003). Indeed, some researchers have shown that measurement errors are small when the sample thickness is at least as big as the outer conductor radius of the probe (Fan, 1990; De Langhe, 1994; Hoshina 2001), which is 1.5mm in our case. We therefore decided to prepare 3mm-thick collagen gels.

Nevertheless, a small sample size can be problematic in the microwave range especially when its permittivity is high and its losses relatively low, because cavity resonances could occur. This phenomenon explained by electromagnetic cavity theory has been pointed out by some investigators using the same kind of probe (Grant, 1989; De Langhe, 1994; Sheen, 1999). To avoid potential resonance effects, we chose 2 GHz as the upper frequency (until which we did not observe any resonance effect).

Besides, the frequency range of the probe using a network analyser and the supplier's software is guaranteed from 200 MHz to 20 GHz. As a result, we chose the frequency range 200 MHz – 2 GHz.

As shown in Figure 1, gel samples were actually put onto the probe and fitted its dimension, as the outer diameter of the probe flange is 19mm. Several attempts were made to measure the gels from the top with the probe upside down (compared to Figure 1), but the repeatability of the measurement was very poor. Moreover, the gels measured from the top got squashed. On the contrary, putting the gel onto the probe keeps its integrity and allows for a good control of the contact between the gel and the probe, and improves the repeatability of the measurement.

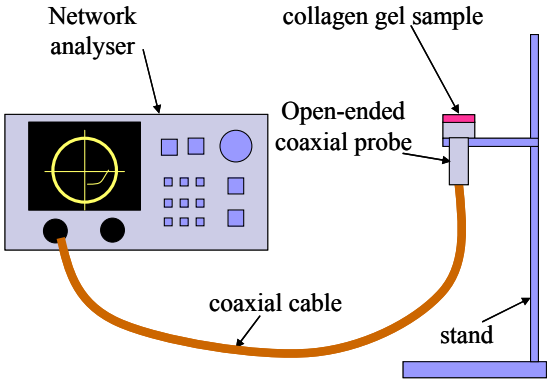

Figure 1: Diagram of the experimental set-up.

2.3.2 Experimental Method

For each experiment, 7 gels with cells, and 7 gels without cells ('controls') were made and measured. Each gel was measured 7 times in order to address the repeatability issue. Prior to measurement, the system was calibrated using a standard procedure, in which the standards are air, a short circuit and deionised water. The latter was measured in a 250 mL beaker to avoid resonance phenomena, in accordance with (Blackham, 1997).

The measurement method was as follows. The wells containing the gels were taken out of the incubator and placed in a water bath at 37°C. Each gel was then put onto the probe, which was at room temperature. To achieve as good repeatability as possible, a few minutes were necessary to get very stable results. On the one hand, while the gels cool down towards room temperature, we observed that the real part of the permittivity ε' increased slightly, and the imaginary part ε'' decreased slightly on the whole chosen frequency range. On the other hand, when left several tens of minutes at room temperature, they start to dry out and we observed that ε' started to decrease and ε'' started to increase on the whole chosen frequency range. Measurements were taken at the time when the two aforementioned

phenomena compensate each other. Thus, excellent repeatability was achieved: at the very most, the fractional error (standard deviation divided by the mean of 7 measurements on the same gel) was 0.25% for ε' and 1% ε''. If measurements are taken before stabilization, these figures become respectively 0.6% and 2.5% at the very most.

3 RESULTS AND DISCUSSION

The measurement reproducibility was assessed for each volume fraction tested by calculating the fractional error (standard deviation divided by the mean, both calculated on 7 gels measured 7 times, i.e. on 49 measurements) as a function of frequency. At the very most, it reached 0.9% for ε' and 5% for ε''. The latter was higher in the lower part of the explored frequency range, where the conductivity is particularly high. However, it could reach 3.3% around 2 GHz.

For all the cell volume fractions tested, a significant difference in permittivity was observed between composite gels (containing cells) compared to gels alone. An example of result for a volume fraction of 4.4% is given on Figure 2 in the complex plane (Cole-Cole diagram).

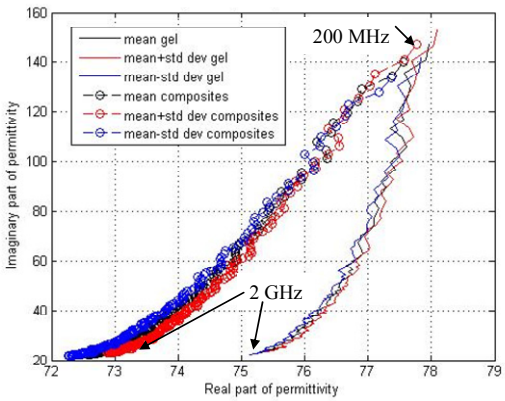

Figure 2: Comparison composite gels / pure gels in the complex plane (mean +/- standard deviation: data obtained on 7 gel samples of each type); volume fraction: 4.4%.

The real part ε' was found to be lower when the gels contained cells rather than when they did not (cf. Figure 3), and also to consistently decrease with the cell volume fraction. A statistically significant difference between composites and pure gels was found for all volume fractions. This was demonstrated by a two-tailed Student's t-test (p-value lower than 0.05 or even 0.01 on the major part of the frequency range). Moreover, the difference in real part between two adjacent volume fractions was also found to be statistically significant by a two-tailed t-test despite the close proximity of the observed variations. It is in good agreement with (Bagnaninchi, 2004) stating that a variation of 0.5% volume fraction is detectable for low cell volume fractions. The p-values were even lower for differences in volume fractions greater than 1%.

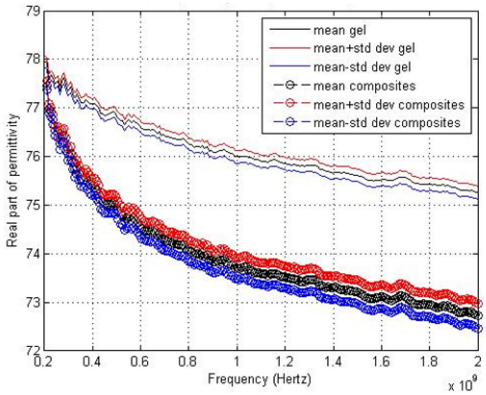

Figure 3: Comparison composite gels / pure gels. Real part of permittivity (mean +/- standard deviation: data obtained on 7 gel samples of each type); volume fraction: 4.4%.

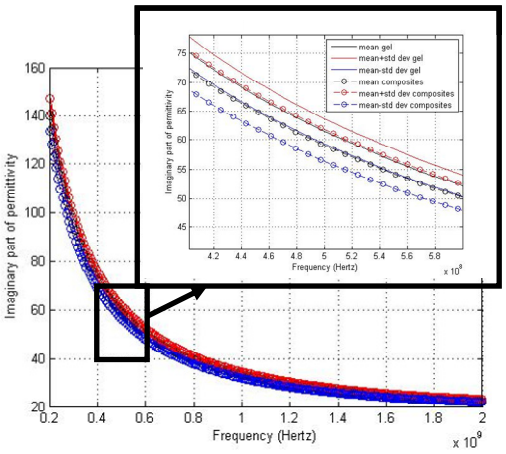

Figure 4: Comparison composite gels / pure gels for the imaginary part of permittivity (mean +/- standard deviation: data obtained on 7 gel samples of each type); volume fraction: 4.4%.

Regarding the imaginary part of the permittivity, a group of 3 experiments (out of 6) showed an increase in ε'' when comparing composites and pure gels, and the 3 others showed a decrease (when considering the means). A two-tailed t-test proved that 2 variations among them were not statistically

significant (one in each group; p>0.1 and 0.3), an example of which is shown on Figure 4.

This result about the imaginary part ε'' can be commented on qualitatively as follows. This suggests that ε'' of the composite gels could actually be of the same order of magnitude as ε'' of pure gels because the reproducibility fractional error on ε'' (which could reach 5% in the lower frequencies) is not negligible. As gels are quite conductive, ε'' is a sensitive parameter whose variability is not negligible.

Quantitatively we did some modelling to explain why ε'' of the composites gels can either be a bit lower or higher than ε'' of pure gels. We used effective medium approximations commonly utilised with biological cells, such as Maxwell-Wagner or Looyenga equations (Bordi, 2002; Asami, 2002). A composite gel is considered as an effective medium in which cells are inclusions. A basic single-shell cell model, modelling the membrane and cytoplasm by their respective permittivities and conductivities was implemented. The latter were varied even beyond their commonly accepted values: the permittivity of the membrane and the cytoplasm were respectively varied from 2 to 30 and from 30 to 70. The simulation easily shows that for small volume fractions, the conductivity of the cytoplasm is decisive: if it is lower (respectively greater) than the one of pure gel, ε'' is lower (respectively greater) for composite than for pure gel. Thus, owing to the variability of the cytoplasm properties, ε'' of composites gels can be a bit lower or higher than ε'' of pure gels. Hence, the conductivity of the cytoplasm of the measured SK-MES cells could be of the same order of magnitude as that of the measured gels.

Another study (Bagnaninchi, 2003) carried out on the same frequency range but with macrophages put inside chitosan scaffolds filled with a similar ionic culture medium (RPMI) showed different results. The addition of cells induced an increase in ε' and a decrease in ε''. However, the effective dielectric behaviour depends on the particular dielectric properties of each type of cells and of the surrounding media. The former constitute the next step of the study.

4 CONCLUSIONS - PROSPECTS

This study has proven the feasibility of detecting small volume fractions of lung cancer cells embedded in collagen gels by microwave dielectric spectroscopy. The real part of the permittivity was found to decrease with the presence of cells. The imaginary part did not significantly show a consistent variation.

The prospects of this study are mainly threefold. Firstly, further suitable modelling should be developed to try to retrieve cell signature and properties. Secondly, similar experiments should be carried out with the corresponding normal lung epithelial cells and results compared to this study. Thirdly, other DS experiments should also be tried to analyse the response and effectivnesses of various anti-cancer treatments such as chemotherapy drugs on *in vitro* cell culture samples.

ACKNOWLEDGEMENTS

This work was partially supported by Maxime Hanss Prize (BBSRC – Alliance Française).

REFERENCES

Asami K., 2002. "Characterization of heterogeneous systems by dielectric spectroscopy". *Progr. in Polym. Sci.*, 27.

Bagnaninchi P-O et al., 2003. "Towards On-Line Monitoring of Cell Growth in Microporous Scaffolds: Utilization and Interpretation of Complex Permittivity Measurements". *Biotech. Bioeng*, 84, 3.

Bagnaninchi P-O et al., 2004. "Complex Permittivity Measurement as a New Noninvasive Tool for Monitoring In Vitro Tissue Engineering and Cell Signature Through the Detection of Cell Proliferation, Differentiation, and Pretissue Formation". *IEEE Trans. on Nanobioscience*, 3, 4.

Bindu G. et al., 2006. "Active Microwave Imaging For Breast Cancer Detection". *Prog. In Electromagnetics Research*, *PIER 58*.

Blackham D.V., Pollard R.D., 1997. "An Improved Technique for Permittivity Measurements Using a Coaxial Probe". *IEEE Trans. Instrum. Meas.*, 46, 5.

Bordi F. et al., 2002. "Dielectric spectroscopy of erythrocyte cell suspensions. A comparison between Looyenga and Maxwell-Wagner-Hanai effective medium theory formulations". *J. Non-Cryst. Sol.*, 305.

Bulyshev A.E. et al., 2001. "Computational Modeling of Three-Dimensional Microwave Tomography of Breast Cancer". *IEEE Trans. Biomed. Eng.*,48, 9.

Chaudhary S.S. et al., 1984. "Dielectric Properties of Normal & Malignant Human Breast Tissues at Radiowave & Microwave Frequencies". *Indian J. Biochem. and Biophys.*, 21.

Chelidze T., 2002. "Dielectric spectroscopy of blood". *J. Non-Cryst. Sol.*, 305.

Claycomb J.R. et al., 2002. "Nonlinear Dielectric Spectroscopy of Living Cell Suspensions". *2nd joint EMBS/BMES Conference*, Houston, USA.

De Langhe P. et al., 1994. "Design Rules for an Experimental Setup Using an Open-Ended Coaxial Probe Based on Theoretical Modelling". *IEEE Trans, Instrum. Meas.*, 43, 6.

Duncan L. et al., 2006. "Assessment of the dielectric properties of drug sensitive and resistant leukaemic cells before and after ion channel blockers using dielectrophoresis". *NSTI-Nanotech 2006*.

Ermolina I. et al., 2001. "Study of Normal and Malignant White Blood Cells by Time Domain Dielectric Spectroscopy". *IEEE Trans. Dielectrics and Electrical Insulation*, 8, 2.

Fan S. et al., 1990. "Static analysis of an Open-Ended Coaxial Line Terminated by Layered Media". *IEEE Trans, on Instrum. Meas.*, 39, 2.

Fear E.C., 2005. "Microwave Imaging of the Breast". *Tech. Cancer Res. Treatm.*, 4, 1.

Foster K.R., Schwan H.P., 1996. "Dielectric properties of tissues" *in C. Polk, E. Postow: Handbook of Biological Effects of Electromagnetic fields*, CRC, Boca Raton, FL.

Gabriel S. et al., 1996. "The dielectric properties of biological tissues: I. Literature survey - II. Measurements in the frequency range 10 Hz to 20 GHz - III. Parametric models for the dielectric spectrum of tissues". *Phys. Med. Biol.*, 41.

Gascoyne P. R. C. et al., 1997. "Dielectrophoretic separation of cancer cells from blood". *IEEE Trans. on industry applic.*, 33, 3.

Grant J.P. et al., 1989. "A critical study of the open-ended coaxial line sensor technique for RF and microwave complex permittivity measurements". *J. Physics E: Sci. Instrum.*, 22.

Hagl D.M. et al., 2003. "Sensing Volume of Open-Ended Coaxial Probes for Dielectric Characterization of Breast Tissue at Microwave Frequencies". *IEEE Trans. Microw. Theo. Tech.*, 51, 4.

Hagness S.C. et al., 1998. "Two-dimensional FDTD analysis of a pulsed microwave confocal system for breast cancer detection: Fixed-focus and antenna array sensors". *IEEE Trans. Biomed. Eng.*, vol. 28.

Hoshina et al., 2001. "A Numerical Study on the Measurement Region of an Open-Ended Coaxial Probe Used for Complex Permittivity Measurement". *IEEE Trans. Magnetics*, 37, 5.

Hübner Y. et al., 2005. "Parallel measurements of drug actions on Erythrocytes by dielectrophoresis, using a three-dimensional electrode design". *IEE Proc. Nanobiotechnol.*, 152, 4.

Jaspard F. et al., 2003. "Dielectric properties of blood: an investigation of haematocrit dependence". *Physiol. Meas.*, 24.

Joines W.T. et al., 1994. "The measured electrical properties of normal and malignant human tissues from 50 to 900 MHz". *Med. Phys.*, 21, 4.

Lisin R. et al, 1996. "Time domain dielectric spectroscopy study of human cells. I. Erythrocytes and ghosts". *Biochim. Biophys. Acta*, vol. 1280.

Pietrucha K., Marzec E., 2005. "Dielectric properties of the collagen–glycosaminoglycans scaffolds in the temperature range of thermal decomposition". *Biophys. Chemistry*, 118.

Polevaya Y. et al., 1999. "Time domain dielectric spectroscopy study of human cells. II. Normal and malignant white blood cells". *Biochim. Biophys. Acta*, 1419.

Santini M.T. et al., 1991. "Effects of lonidamine on the membrane electrical properties of Ehrlich ascites tumor cells". *FEBS*, 291, 2.

Santini M.T. et al., 1995. "A dielectric Relaxation Study on the Effects of the Antitumor Drugs Lonidamine and Rhein on the Membrane Electrical Properties of Ehrlich Ascites Tumor Cells". *Anticancer Res.*, 15.

Semenov S.Y. et al., 2000. "Microwave Spectroscopy of Myocardial Ischemia and Infarction. I. Experimental Study". *Ann. Biomed. Eng.*, 28.

Semenov S.Y. et al., 2003. "Microwave Tomography for Detection/Imaging of Myocardial Infarction. I. Excised Canine Hearts". *Ann. Biomed. Eng.*, 31.

Sha L. et al., 2002. "A review of dielectric properties of normal and malignant breast tissue". *IEEE SoutheastCon conference*, Columbia SC, USA.

Shao W. et al., 2005. "UWB Microwave Imaging for Breast Tumor Detection in Inhomogeneous Tissue". *27th Conf. IEEE EMBS.*

Sheen N.I., Woodhead I.M., 1999. "An Open-ended Coaxial Probe for Broad-band Permittivity Measurement of Agricultural Products". *J. Agricult. Eng. Res.*, 74.

Smith S.R. et al., 1986. "Dielectric properties of VX-2 Carcinoma Versus Normal Liver Tissue". *IEEE Trans. Biomed. Eng.*, 33, 5.

Surowiec A.J. et al., 1988. "Dielectric Properties of Breast Carcinoma and the Surrounding Tissues". *IEEE Trans. Biomed. Eng.*, 35, 4.

Tofighi M.R., Daryoush A.S., 2001. "Near field microwave brain imaging". *Electron. Lett.*, 37, 13.

Treo E.F. et al., 2005. "Hematocrit Measurement by Dielectric Spectroscopy". *IEEE Trans. Biomed. Eng.*, 52, 1.

Yang Y. et al, 2004. "Monitoring of lung tumour cell growth in artificial membranes". *Biosensors and Bioelectronics*, 20.

A 2.4 GHZ WIRELESS ELECTRONIC SHIRT FOR VITAL SIGNALS MONITORING

J. P. Carmo[1], P. M. Mendes[2], C. Couto[2] and J. H. Correia[2]
[1] *Polytechnic Institute of Braganca, Campus Santa Apolonia, 5300, Braganca, Portugal*
jcarmo@ipb.pt
[2] *University of Minho, Dept. Industrial Electronics, Campus Azurem, 4800-058 Guimaraes, Portugal*

Keywords: Wireless electronic shirt, wireless sensors networks, RF CMOS transceiver.

Abstract: This paper presents a wireless sensor network for wireless electronic shirts. This allows the monitoring of individual biomedical data, such as the cardio-respiratory function. The solution chosen to transmit the body's measured signals for further processing was the use of a wireless link, working at the 2.4 GHz ISM band. A radio-frequency (RF) CMOS transceiver chip was designed in the UMC RF 0.18 μm CMOS process. The power supply of the RF CMOS transceiver is of only 1.5 V, thus it can be supplied by a single coin-sized battery. The receiver has a sensibility of -60 dBm and consumes 6.2 mW. The transmitter delivers an output power of 0 dBm with a power consumption of 15.6 mW. Innovative topics concerning efficient power management was taken into account during the design of the RF CMOS transceiver.

1 INTRODUCTION

Today, the link between textiles and electronics is more realistic than ever. An emerging new field of research that combines the strengths and capabilities of electronics and textiles into one: electronic textiles, or e-textiles is opening new opportunities. E-textiles, also called smart fabrics, have not only wearable capabilities like any other garment, but also have local monitoring and computation, as well as wireless communication capabilities. Sensors and simple computational elements are embedded in e-textiles, as well as built into yarns, with the goal of gathering sensitive information, monitoring vital statistics, and sending them remotely (possibly over a wireless channel) for further processing (Marculesco *et al*, 2003).

The e-shirt's goal is the monitoring of the cardio-respiratory function. This makes it able to recognize qualitatively and quantitatively the presence of respiratory disorders, both during wake and sleep-time in free-living patients with chronic heart failure, providing clinical and prognostic significance data.

In wireless sensors networks, the continuous working time of sensorial nodes are limited by its average power consumption (Mackensen *et al*,2005). To optimise the power consumption, it was designed a RF CMOS transceiver for the operation in the 2.4 GHz ISM band. It was used the UMC RF 0.18 μm CMOS process in the design. This process has one poly and six metal layers, allowing the use of integrated spiral indutors (with a reasonable quality factor), high resistor value (a special layer is available) and the low-power supply of 1.5 V. The use of this technology, allows the development of a complete system-on-a-chip (SOC), with the additional advantage to be supplied by a single 1.5 V coin-sized battery. Moreover, in order to optimize power consumption, the RF CMOS transceiver design predicts the use of control signals. With these control signals it is possible to enable and disable all the subsystems of the transceiver. These signals allows, e.g., to switch off the receiver when a RF signal is being transmitted, to switch off the transmitter when a RF signal is being received, and allows the transceiver to enter to sleep when RF signals are neither being transmitted, nor being received.

2 TRANSCEIVER DESIGN

Figure 1 shows the architecture of the RF CMOS transceiver, which consists of a receiver, a

transmitter, an antenna-switch and a frequency synthesizer.

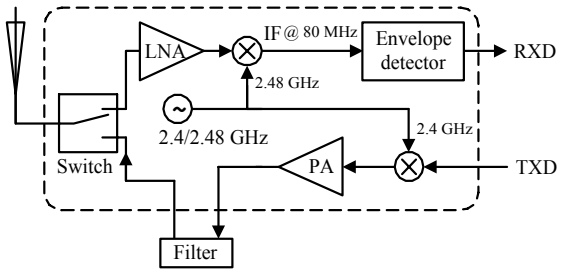

Figure 1: The block diagram of the RF CMOS transceiver.

The receiver adopts a direct demodulation, by means of heterodyne detection. It is enough to achieve a bit error probability less that 10^{-6} with a sensibility of -60 dBm, in a transmitted power of 0 dBm using Amplitude Shift Keying (ASK) modulation. These specifications makes the RF CMOS transceiver suitable for short range applications.

2.1 Receiver

Figure 2 shows the receiver's front-end schematic. The amplified RF signal at the output of the low-noise amplifier (LNA) is directly converted to an intermediate frequency (IF) with a double-balanced downconversion mixer, followed by a low-pass filtering. The final downconversion to the baseband is made by means of envelope detection.

The low-noise amplifier (LNA) is the first gain stage in the receiver path. In a LNA, the signal must be amplified as much as possible, with a small signal-to-noise ratio (SNR) decrease. This is achieved with the best noise figure (NF). The LNA is an inductively degenerated common source amplifier. This makes the input impedance at 2.4 GHz equal to 50 Ω, for matching with antenna-switch (Yao, 2007). The LNA is putted in the sleeping mode, by cutting the current in the polarization stage. The same principle applies to the all subsystems of the transceiver. The downconversion to the IF uses a double-balanced switched transconductor mixer (Klumperink, 2004). The advantage is that the switching stage is directly connected to the power rails, requiring a less voltage headroom. This simplifies the switching process and has a slightly bigger conversion gain. Moreover, this topology also eliminates the presence of the strong carrier at the output, producing only odd harmonics of the local oscillation frequency. The signal at the output of the low-pass filter enters an envelope detector. The 80-MHz IF frequency is produced from the 2.4 GHz RF and from the 2.48 GHz local frequency.

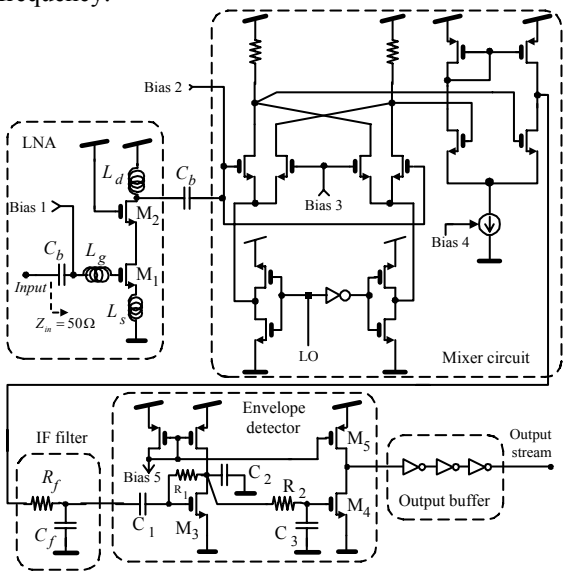

Figure 2: The schematic of the receiver.

2.2 Transmitter

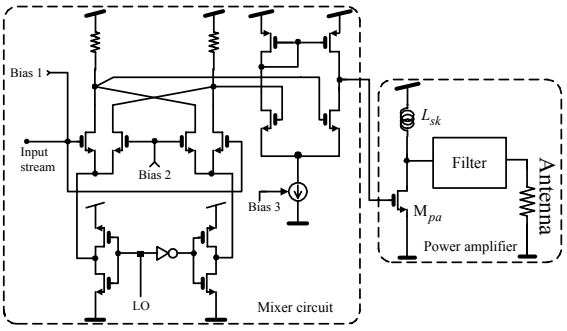

Figure 3: The schematic of the transmitter.

Figure 3 shows the schematic of the RF CMOS transmitter. The mixer used in the frequency upconversion is of the same type of the previous mixer used in the frequency downconversion. The main differences are on the MOSFET's sizes. The RF signal is further amplified by a power amplifier, which provides a transmitted signal with an appropriated output power. The upconversion mixer generates the RF signal, from the input bitstream and from a 2.4 GHz local generated frequency. The external filter follows the power amplifier, and removes the spectral components around the 2.4 GHz carrier frequency while adapts it to the impedance of the antenna.

2.3 Frequency Synthesizer

As depicted in Figure 4, the PLL has a reference generator circuit with a crystal based oscillator at 20 MHz, followed by a phase-frequency difference circuit (PFD) without dead zone, a current steering charge pump (CP) and a third order passive filter. The passive section output is connected to the VCO, which generates the desired frequencies of 2.4 GHz or 2.48 GHz. These frequencies must be divided by 120 or by 124 and connected to the PFD again, closing the loop. The frequency division ratio is selected by the one bit control signal 120/124. This selects the value of the frequency to be connected to the mixer, in order to make the up or the down-conversion operation.
The division by 120/124 in the feedback path is done with a cascade constituted by one half divider implemented with a true single phase clock (TSPC) logic, one divider by 30/31 (digitally selected by the signal 120/124), followed by a toggle flip-flop to ensure a duty-cycle of 50% at the PFD input. The TSPC logic was used to overcome the impossibility to implement the first toggle flip-flop with static logic in this technology. It is required a rail-to-rail input to work properly. Moreover, at these frequencies, the power consumptions are lowest compared with the SCL logic (Pellerano *et al*, 2004). The ratios of 30 and 31 were achieved with the use of frequency dividers by 2/3 with modulus control.

3 WIRELESS ELECTRONIC SHIRT

Like any other every-day garment piece, the wireless electronic shirt (WES) will be lightweight, machine washable, comfortable, easy-to-use shirt with embedded sensors. To measure respiratory and cardiac functions, sensors are plugged into the shirt around patient's chest and abdomen. The WES also uses small sizes and compact modules, made with microsystems, containing the 2.4 GHz RF CMOS transceiver, the electronic of control and processing, and the interfaces to make the connections to the sensors. These modules have also an associated antenna and are supplied by a coin-sized battery. The size-reduction achieved with these modules, make them suitable to be easily plugged in the WES, according the interest of the medical doctors.
Conventional applications of electronic shirts uses wires to connect the sensors to a central unit, and then to make the RF communication to the external base-station (Marculescu *et al*., 2003). An interesting application and an easy way to implement wireless buses, is using modules able to communicate between them and between the base-station.

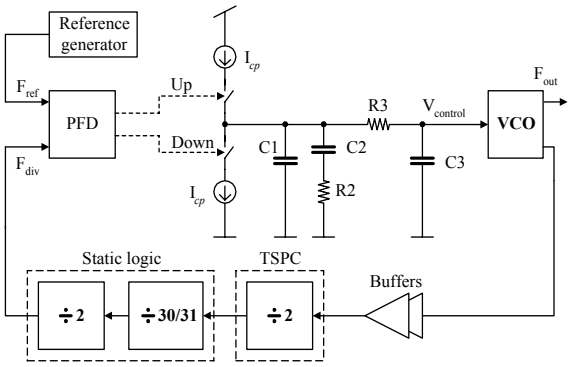

Figure 4: The structure of the PLL.

A single channel measures heart rate and an inductive elastic band will be used for monitoring the respiratory function.
It is used a bending sensor to monitor the shoulders positions, that suffers changes in the electrical resistance when it is bent. As this sensor is bent the resistance gradually increases. When the sensor is bent at 90 degrees, its resistance will range between from the 30 kΩ up to the 40 kΩ. It was also used an elastic band to measure the changes in thoracic circumference due to respiration. The transducer contains an variable inductance, used indirectly to measure the changes in thoracic circumference. The device should be placed around the body at the level of maximum respiratory expansion. This level will change between erect and supine positions. At maximum inspiration the belt should be stretched almost to maximum extension, making its inductance minimum. As shown in the Figure 5, the PLL reference oscillator is reused, to generate the 20 MHz sinusoidal signal, required for this circuit. The variations in the inductance, changes the attenuation for the 20 MHz signal, in the first *RL* low-pass of first order filter. Thus, the attenuation increases with the decreasing of the thorax perimeter. This filtered signal is further amplified, before a second low-pass filtering, to eliminate noise and spurs generated in the 20 MHz oscillator. Then, a peak detector gets the amplitude of the 20 MHz processed signal. This amplitude is a low-frequency signal, and it is converted to the digital domain, using a ΣΔ analog-to-digital converter (ADC) of first order, with an output with resolution of eight bits. This allows the recording of respiratory changes with maximum sensitivity and linearity.

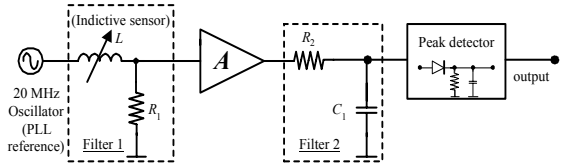

Figure 5: The block diagram of a signal conditioning used in the measure of the respiratory function.

It is shown in Figure 6, a photo of the patient wearing an WES ready to plug the RF modules. It can be seen the three connections for heart-rate respiratory function.

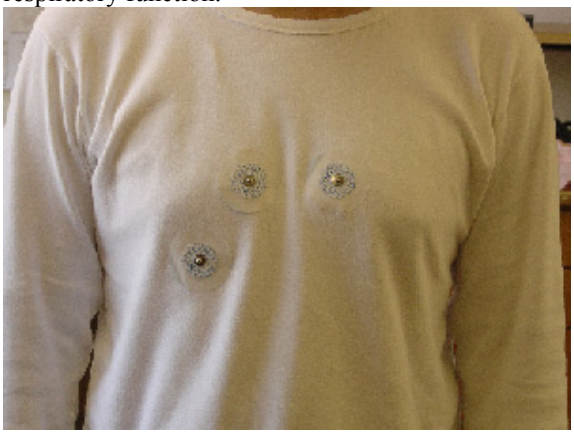

Figure 6: A photo of the patient wearing a electronic shirt ready to plug the RF modules.

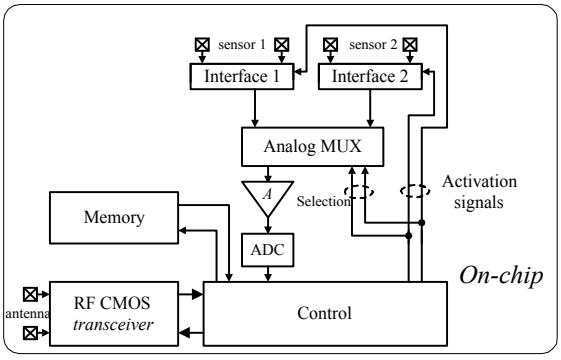

Figure 7: Block diagram of the microsystems used in the plug-and-play modules of the WES.

In WES, the sensor interfaces, data processing, the wireless interface and antenna are integrated in the same microsystem (Figure 7) by Multi-Chip-Module (MCM) techniques. The wireless communication is between the base-station and the multiple processing elements placed in the shirt. The main advantage is to allow the positioning of the sensors where we like. The sensors can also be removed from the shirt, either when the sensors are no more need or when the shirt is to be cleaned and washed. This wireless bus introduces the concept of plug-and-play in textiles.

4 CONCLUSIONS

The simulations of the RF CMOS transceiver, shown a total power consumption of 6.2 mW for the receiver (1.5 mW for the LNA 3.2 mW for the downconversion mixer, and 1.5 mW for the envelope detector). For the transmitter, it was observed the power consumptions in the following blocks: 5.3 mW in the upconversion mixer and 10.3 mW in the PA. The transmitter delivers a maximum output power of 1.08 mW with a total power consumption of 11.2 mW. These characteristics fulfill the requirements for short-range communications for using the 2.4 GHz ISM band.

The main goal of the WES, is improving the monitoring of the cardio-respiratory function, by using devices which reduces healthcare costs and facilitates the diagnostic while at the same time preserving the mobility and lifestyle of patients.

REFERENCES

Mackensen, E., *et al*, 2005, Enhancing the lifetime of autonomous microsystems in wireless sensor actuator networks (WSANs), in Proceedings of the XIX Eurosensors, TC4, pp.1-2, Barcelona, Spain.

Klumperink, E., *et al*, 2004, A CMOS switched transconductor mixer, IEEE Journal of Solid-State Circuits, Vol. 39, No. 8, pp. 1231-1240.

Marculescu, D., *et al*., 2003, Electronic Textiles: A Platform for Pervasive Computing, Proceedings of the IEEE, Vol. 91, No. 12, pp. 1995-2018.

Pellerano, S., *et al*, 2004, A 13.5 mW 5-GHz frequency sinthesizer with dynamic logic frequency divider, IEEE Journal of Solid-State Circuits, Vol. 39, No. 2, pp. 378-383.

Yao, T., *et al*, 2007, Algorithmic design of CMOS LNAs and PAs for 60-GHz radio, IEEE Journal of Solid-State Circuits, Vol. 42, No. 5, pp. 1044-1057.

PERSONAL DIALYSIS USING A WEB-BASED, PORTABLE SYSTEM

C-PAK (Carry-on Pulse Artificial Kidney)

Jung Chan Lee, Wook Eun Kim, Ki Moo Lim, Jeong Chul Kim
Interdisciplinary Program in Medical and Biological Engineering Major, Seoul National University, Seoul, Korea
ljch@snu.ac.kr, wekim@bme.snu.ac.kr, anzuk7@snu.ac.kr, jckim80@snu.ac.kr

Byoung Goo Min
Department of Biomedical Engineering, Seoul National University, Seoul, Korea
bgmin@snu.ac.kr

Keywords: Hemodialysis, Hemofiltaration, Artificial Kidney, Web-based Remote Monitoring.

Abstract: While the number of patients suffering from acute and chronic renal failure has been steadily increasing every year, the mortality rate is not improving. For the purpose of improvement on the quality of life and mortality of renal disease patients, we employ the hemofiltration principle to treat the end-stage renal disease patients. Hemofiltration equipment can be installed without additional plumbing and electrical power construction; operated only with several pre-packaged fluid bags without a huge water treatment facility. This paper describes the development of portable renal treatment equipment based on hemofiltration treatment, Carry-on Pulse Artificial Kidney (C-PAK), and reports the results of animal test using the equipment. The web-based remote monitor/control system for C-PAK is introduced also. We expect that our portable hemofiltration device for chronic renal failure patient would be an alternative for conventional hemodialysis machine and a solution to home renal treatment.

1 INTRODUCTION

While the number of patients suffering from acute and chronic renal failure has been steadily increasing every year, the mortality rate is not improving. According to the USRDS (United States Renal Data System), 20% of the inpatients to intensive care unit of hospitals suffer from acute renal failure. The mortality of renal disease patients with other complications has reached 50-80%. Because the number of patients increases over 6% by annually, we expect the population of renal failure to nearly double in 10 years. However, the number of nurses and physicians who treat the increasing number patients is already insufficient. (Rayner, 2000)

The dramatically increasing number of renal disease patients will be a financial burden to the medical insurance. Nowadays, a patient who is treated with in-center renal treatments costs US$68,400 per year in the United States. (McFarlane, 2002, Mohr, 2001)

Athough renal replacement treatment have been developed for a long time after Kolff introduced the hemodialysis in 1943, patients with end-staged renal disease have an average life expectancy of only 5 years and their quality of life is extremely poor. (Jaber, 2004)

For the purpose of improvement on the quality of life and mortality of renal disease patients, we employ the hemofiltration principle to treat the end-stage renal disease patients. Several researchers have already reported their clinical results of this convective treatment. However, simple replacement of conventional hemodialysis or peritoneal dialysis is meaningless. We expect that the patients suffering from end-stage renal failure will be able to choose the flexible treatment method and schedule. Also the patient should be treated with the renal treatment wherever and whenever upon patient's request. A drastic switch from in-center conventional dialysis policy to home renal treatment is necessary. Instead of standardized renal treatment with fixed dose, a treatment with adequate dose for each patient must

be employed with personalized renal treatment equipments.

Hemofiltration, the filtration of the native kidney, has improved the clearance of intermediate-sized molecules that are insufficiently removed by hemodialysis. In particular, beta2-microglobulin, which causes hemodialysis-related amyloidosis within several years of hemodialysis treatment, can be removed effectively by hemofiltration treatment. In addition, hemofiltration treatment is strongly associated with better cardiovascular stability. Moreover, comparison studies supported the claims of reduced mortality of end-staged renal disease patients given hemofilration treatment. (Jaber and Zimmerman, 2004)

Hemofiltration equipment can be installed without additional plumbing and electrical power construction; operated only with several pre-packaged fluid bags without a huge water treatment facility.

In this paper, we describe the development of portable renal treatment equipment based on hemofiltration treatment, Carry-on Pulse Artificial Kidney (C-PAK), and report the results of animal test using the equipment. We also introduce the web-based remote monitor/control system for C-PAK.

2 METHODS

2.1 Design of Portable Hemofiltration System

C-PAK is designed for hemofiltration treatment. C-PAK consists of the control panel, the driving panel, the disposable set and the electrical power/control unit. (Figure 1-2)

The control panel includes several function keys and a colour touch screen. All operation is available using pop-up menu on the touch screen. The function keys are used in unexpected case, i.e. when the touch screen is not working correctly. During the treatment, the blood flow rates, the replacement flow rates, the effluent flow rates, the replacement fluid remains, the effluent volume, the total treatment time, and the remaining treatment time are displayed on touch screen.

The driving panel consists of four pumps, several sensors, and a safety gadget. Pump unit includes the dual pulsatile blood pump, the replacement fluid pump, the effluent fluid pump, and the anti-coagulation pump. The sensor unit includes the blood detector, the air-bubble detector, the access pressure sensor, the pre-filter pressure sensor, the return pressure sensor, the effluent pressure sensor, the blood leak detector, the replacement fluid weight, and the effluent fluid weight. The safety gadget is the tube clamp.

The electrical power/control unit consists of the power supply, the several motor drivers, and the main controller including the microprocessor. During the treatment, the main controller manages several motor drivers, calculates the remained treatment time according to the received data from each sensor and then sends the data and graphs to display on the touch screen. Especially, maintaining the body water balance between the replacement fluid and the effluent is the most important role of the main controller.

Figure 1: Design of C-PAK.

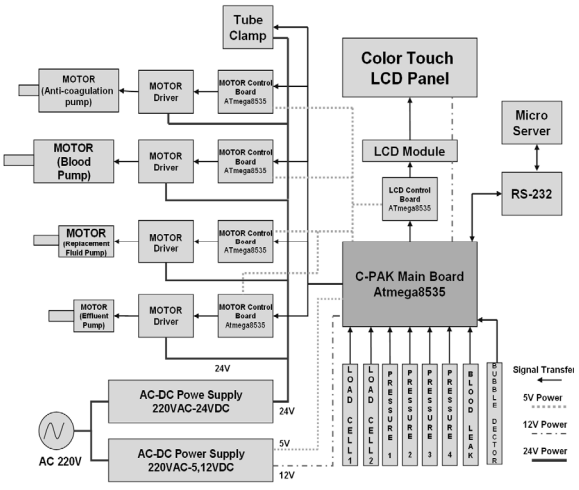

Figure 2: Structure of C-PAK.

2.2 Animal Tests of Portable Hemofiltration System

Animal tests (N=13) were prepared to estimate the treatment efficacy of C-PAK. The ligations of renal artery of mongrel dogs weighing 31.77±2.53 kg were performed to induce the renal failure. After ligation surgery, blood urea nitrogen (BUN) concentrations were measured at 12-hr interval. When BUN exceeds 60 mg/dl, the animal was treated with hemofiltration treatment. The venovenous catheters were inserted into the jugular vein for vascular access. The dual pulsaltile blood pump could maintain the blood flow rates at 100-150 ml/min during hemofiltration treatment and the blood flow rates were monitored by ultrasonic flow meter.

The bloods were sampled at 1-hr interval. When the exchange volume was achieved, last blood sample was collected and the test was terminated. BUN, creatinine, electrolytes, packed cell volume (PCV), fibrinogen (FIB), total protein (TP), red blood cell (RBC), white blood cell (WBC), glucose, activated partial thromboplastin time (aPTT), and prothrombin time (PT) were measured from blood sampling.

All measured parameters were expressed as means ± standard deviation. The adequate efficacy line was defined as Kt/V>0.40 for daily renal treatment.

2.3 Web-based Remote Monitor/Control System for Portable Hemofiltration System

Web-base remote monitor/control system forms a network to connect the patient, his or her medical personnel, and C-PAK.. Embedded system with ARM processor is developed as micro sever, and a communication protocol organizes the network between the micro severs and the main server. Without any restriction of time and place, the medical personnel can access to the main server to monitor the treatment status of the patient and the device in order to send prescriptions with adequate dose for the patient via micro sever. Also, patients can connect to the main servers to check the treatment efficacy and the prescriptions transferred from their medical personnel. (Figure 3-5)

Main server is working with Redhat Linux 9.0 (Red Hat, Inc.) as operating system with Apache/Tomcat server for web service and with MySQL server for database service. Micro server which is directly connected to C-PAK sends the status of both patient and device to the main server through network.

Micro sever is designed with Net+50 system (NetSilicon, Inc.) based on ARM7 processor and Ethernet controller. ThreadX (Express Logic, Inc.) is employed as an embedded real-time operating system (RTOS) of micro server. RS-232 port of C-PAK was employed for a connection of C-PAK with micro server.

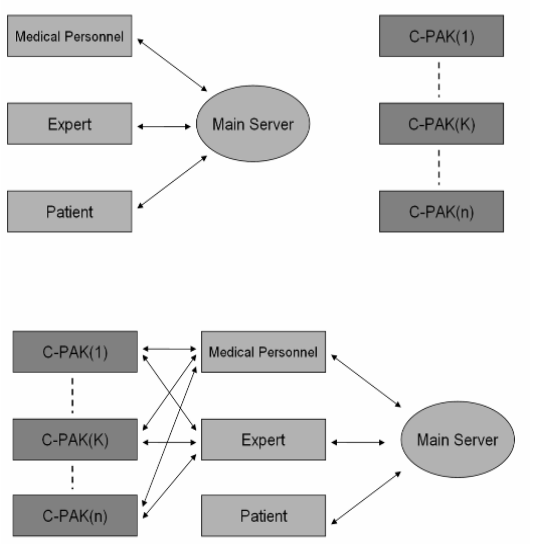

Figure 3: Network structure of web-based monitor-control system for portable hemofiltration system.

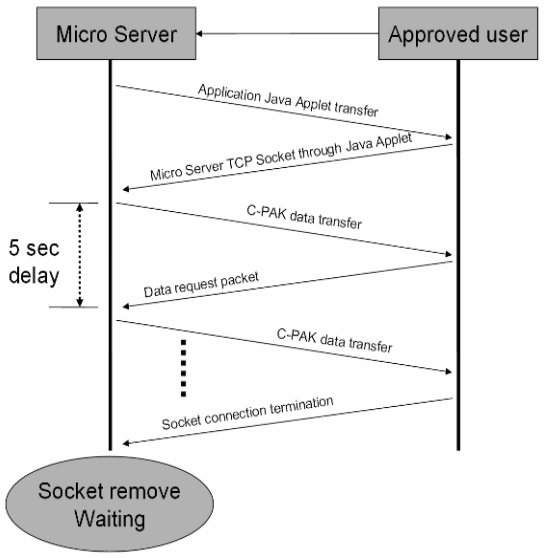

Figure 4: Data transfer protocol between micro server and main server.

3 RESULTS

The prototypes of C-PAK were manufactured and in total of 13 animal test cases were performed using C-PAK. Treatment time was 221 ± 41 min, and achieved exchange volume was 8.98 ± 2.79 l. Kt/V was 0.40 ± 0.14.

The web-based remote monitor/control system was built with a main server and micro servers. C-PAK was connected to a micro server via RS-232 connection. Although web-based remote monitor/control system could not be tested during animal tests, the monitored data transferring test and the remote control test were successfully performed with virtual treatment environment.

System One (NxStage Medical, Inc.) is the only commercialized hemofiltration device for home use. However, our device can meet lighter weights (less than 15kg) than System One (about 35kg).

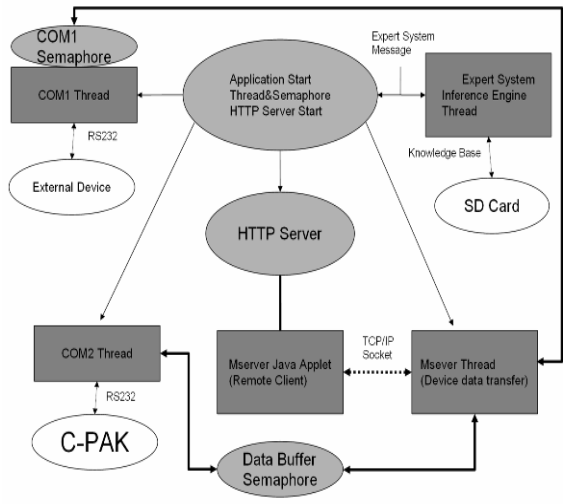

Figure 5: Data transfer scheme of micro server.

4 CONCLUSIONS

C-PAK achieved the sufficient treatment efficacy for daily renal treatment in animal tests. The web-based remote monitor/control system will be integrated into the home/portable hemofiltration system.

We expect that our portable hemofiltration device for chronic renal failure patient would be an alternative for conventional hemodialysis machine and a solution to home renal treatment.

REFERENCES

Rayner, H., Pisoni, R., Bommer, J., Canaud, B., Hecking, E., Locatelli, F., Piera, L., Bragg-Gresham, J., Feldman, H., Goodkin, D., Gollespie, B., Wolfe, R., Held, P., Port, F., 2000. Mortality and hospitalization in haemodialysis patients in five European countries:results from the Dialysis Outcomes and Practice Patterns Study(DOPPS). *Nephrol Dial Trasnplant*.

McFarlane, P., Pieraatos, A., Redelmeier, D., 2002. Cost savings of home nocturnal versus conventional in-center hemodilysis. *Kidney Int.*

Mohr, P., Neumann, P., Franco, S., Marainen, J., Lockridge, R., Ting, G., 2001. The case for daily dialysis: Its impact on costs and quality of life. *Am J Kidney Dis.*

Jaber, B., Zimmerman, D., 2004. Rationale and experience with short daily hemofiltration. *Semin Dial.*

MAGNETIC COUPLING ANALYSIS OF A TET POWER DELIVERY SYSTEM

Thushari Dissanayake, David Budgett
Bioengineering Institute,University of Auckland, 70 Symond Street, Auckland, New Zealand
t.dissanayake@auckland.ac.nz, d.budgett@telemetryresearch.com

Aiguo Patrick Hu
Department of Electrical and Computer Engineering,University of Auckland, 3 Grafton Road, Auckland, New Zealand
a.hu@auckland.ac.nz

Keywords: TET, inductive power transfer, power efficiency, coupling coefficient, mutual inductance.

Abstract: This paper presents a comparative study of methods to determine the coupling coefficient between primary and secondary coils used in a transcutaneous energy transfer system designed for powering implantable biomedical devices. A coupling analysis covering typical misalignments between coils is presented using an analytical model, a simulated model and practical experimental measurements. The simulated model shows good agreement with the experimental measurements. The performance of the system is characterised by carrying out a loss analysis to compute the power efficiency of the system for different misalignment situations. It was established that variable coupling affects the maximum power transfer capacity but has a low impact on the power efficiency for coil separations of less than 30mm.

1 INTRODUCTION

Many implantable biomedical devices require electrical energy for operation. Two common methods of supplying power are using an implantable battery or by having a percutaneous lead from the implant to an external power supply (N. de N. Donaldson 1983). The downsides of these methods are the limited life span of the battery and the potential risk of infection associated with wires through the skin. Inductively coupled power transfer (ICPT) technology enables transfer of power across the skin without direct electrical connectivity. This form of transcutaneous energy transfer (TET) is illustrated in figure 1. The primary coil is located outside the body and generates an electromagnetic field. This time varying field penetrates the skin and induces currents and voltages in the implanted secondary coil which can be used to derive power for the biomedical device.

In high power applications such as left ventricular assist devices (LVADs), the TET coils are located in areas of soft tissue where the coupling conditions are highly variable. Normal patient posture changes or differences in fitting the external parts relative to the internal parts are likely to result in changes to the alignment of the primary and the secondary coils and their relative coupling (John C. Schuder 1971). The coupling between two coils can be represented by their mutual inductance. The definition of mutual inductance is given by Neumann's double integral formula

$$M_{ij} = \frac{\mu_o}{4\pi} \oint\oint \frac{ds_i \cdot ds_j}{R_{ij}} \tag{1}$$

Where μ_o is the permeability of free space, ds_i and ds_j are elements of two coils and R_{ij} is the magnitude of the distance from ds_i to ds_j. This demonstrates that the mutual inductance is a function of the coil geometries and the distance between them (F.C Flack 1971). A more intuitive representation of coil coupling is given by the coupling coefficient, k, defined by:

$$k = \frac{M}{\sqrt{L_1 L_2}} \tag{2}$$

Where L_1 and L_2 are the self inductances of the primary and the secondary coils respectively (C. M. Zierhofer 1996). The coupling coefficient will equal

1 for perfect coupling between two coils and zero for no interaction.

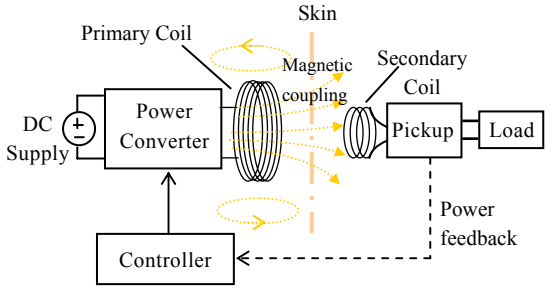

Figure 1: Block diagram of a TET system.

Knowing the coupling coefficient between two coils under a range of orientations is valuable for accessing their ability to transfer sufficient power to the load. This information can be used to guide the design process for primary and secondary coils. The coupling between primary and secondary coils has been categorised into three components:

a) Separation: coils are axially aligned with a separation gap (usually occupied by skin and fat). For an abdominal TET site, this gap is estimated to be within the range of 10 to 30mm.
b) Displacement: where the separation gap between the coils is constant, but their centres are displaced by a distance *x*. Typical range of displacement is estimated to be +/-20mm.
c) Rotation: the primary coil is tilted off-axis with respect to the secondary coil by an angle α.

It is vital to meet the power requirements of the implantable load at various coil orientations, and to not cause excess heating inside the implantable device. Power efficiency is also a valuable element in TET systems as the freedom of the patient is restricted by the weight and duration of the external battery pack they must carry (Hochmair 1984). This paper provides a comparative study of the coupling coefficient and power efficiency of a TET system for various coil coupling conditions.

2 COUPLING ANALYSIS

Three methods of determining the coupling coefficient between primary and secondary coils are presented. The first is an analytical method based on models established by Soma et. al. (Mani Soma 1985). This approach enables calculation of coupling coefficients for a variety of geometrical offsets between two single turn coils. The second method is a finite element approach using JMAG Studio 8.0 to model the coil geometries and numerically solve for the magnetic flux density and coupling coefficient. Finally, physical coils are constructed and the coupling coefficient measured experimentally.

The coil geometry used in the analytical model is considerably simplified in order to provide a tractable closed form solution. This model assumes that the coils are a single turn so that other dimensional data (i.e. internal and external radius) of the coils are ignored. The average radius between the internal and external radius is used in these calculations. The self inductance of L_p and L_s in this instance is taken to be the inductance of a single turn coil. For the simulated model, the coil geometry used is the same as the experimental physical coils.

2.1 Analytical Model

To derive the analytical model, the orientation between the primary and secondary coils needs to be defined. Adopting the same misalignments as used by Soma (Mani Soma 1985), the following three misalignment conditions are considered:

2.1.1 Axially Aligned Separation

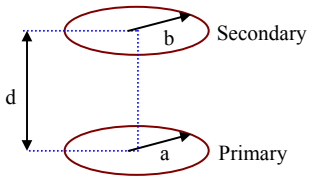

Figure 2: Axially aligned separation.

Figure 2 illustrates the orientation of the coils when they are axially aligned. The distance d represents the minimum separation between the two coils. The characterisation of mutual inductance in this orientation is given by equation 3.

$$M_F = \mu_0 \sqrt{ab} G(s) \tag{3}$$

Where

$$G(s) \equiv \left(\frac{2}{s} - s\right) K(s) - \frac{2}{s} E(s) \tag{4}$$

K(s) refers to the complete elliptic integral of the first kind,

$$K(s) = \int_0^1 [(1-t^2)(1-st^2)]^{-\frac{1}{2}} dt \tag{5}$$

And E(s) is the complete elliptic integral of the second kind,

$$E(s) = \int_0^1 [(1-t^2)^{\frac{1}{2}}(1-st^2)]^{-\frac{1}{2}} dt \quad (6)$$

The variable s, defines the mathematical relationship between the primary and the secondary coils. The formula for s is given by

$$s \equiv \sqrt{\frac{4ab}{(a+b)^2 + d^2}} \quad (7)$$

2.1.2 Lateral Displacement

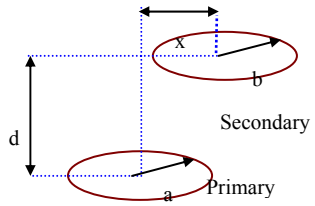

Figure 3: Lateral displacement.

Lateral displacement with parameter x is illustrated in figure 3. Given that x<b in practical situations, the mutual inductance for lateral displacement can be defined by equation 8. G(s) in this equation is also determined by equation (4).

$$M_L = \frac{\mu_0 ab}{\sqrt{a(b+x)}} G(s) \quad (8)$$

Where s becomes

$$s \equiv \sqrt{\frac{4a(b-x)}{(a+b-x)^2 + d^2}} \quad (9)$$

2.1.3 Angular Rotation

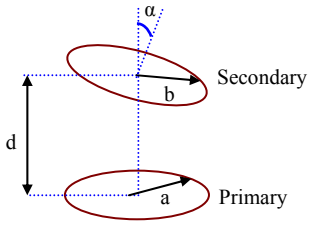

Figure 4: Angular rotation.

Figure 4 demonstrates angular rotation about the z axis. In this analysis, misalignments up to 25° are considered. The value of s used to calculate M_A is taken to be the average value of s_{min} and s_{max}. The formulas used for evaluation of M_A are as follows

$$M_A = \frac{\mu_0 \sqrt{ab}}{\sqrt{\cos a}} G(s_{avg}) \quad (10)$$

Where s_{avg} is

$$s_{avg} = \frac{s_{\min} + s_{\max}}{2} \quad (11)$$

s_{min} and s_{max} are given by

$$s_{\min} \equiv \sqrt{\frac{4ab\cos a}{a^2 + b^2 + d^2 + 2ad\sin a + 2ab\cos a}} \quad (12)$$

$$s_{\max} \equiv \sqrt{\frac{4ab\cos a}{a^2 + b^2 + d^2 - 2ad\sin a + 2ab\cos a}} \quad (13)$$

2.2 Simulated Model

The use of numerical simulation alleviates many of the geometrical simplifications that were used in the previous analytical model. JMAG was used to simulate the coupling relationship between the primary and the secondary coils. Figure 5 illustrates the mesh created for two coils for an axially aligned orientation with 15mm separation. The mesh contained 1435 nodes and 6982 elements. Calculating the magnetic field generated took 6 seconds running on a 3.3GHz PC.

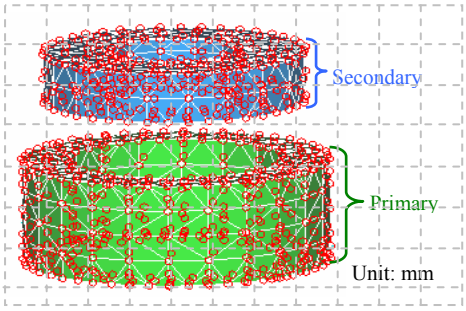

Figure 5: Mesh of primary and secondary coils generated in JMAG – axially aligned.

The coils were defined by the number of turns, physical dimensions, and ESR (Equivalent Series Resistance). Within JMAG, an external circuit was produced to represent the two coils and a sinusoidal current was injected into one of the inflow faces of the primary coil. The secondary coil was shorted to obtain the short circuit current and equation 14 was used to calculate the mutual inductance of the coil for various orientations.

$$M = \frac{I_{sc}}{I_p} L_2 \quad (14)$$

Where I_{sc} is the short circuit rms (Root Mean Square) current in the secondary winding, L_2 is the secondary inductance, and I_p is the primary rms current. Figure 6 shows the magnetic field density contours for a 20mm laterally displaced secondary coil with a separation of 10mm. The magnetic field in the secondary coil is at its highest on the edge facing the primary and gradually drops off to zero on the face furthest from the primary.

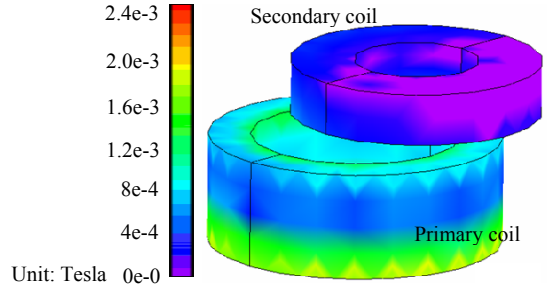

Figure 6: Magnetic field distribution when the secondary coil is laterally displaced by 20mm for a separation of 10mm

2.3 Experimental Measurements

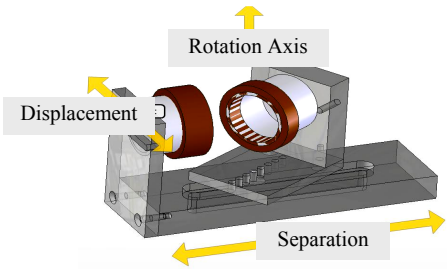

Figure 7: CAD model of physical test rig used to hold primary and secondary coils in known physical orientation.

A test rig was built (see figure 7) to accurately locate the primary and secondary coils at known orientations. The rig allows fixing of the secondary coil in all three misalignments discussed in the previous section. Equation 15 was used for determining the coupling coefficient between the coils.

$$k = \sqrt{1 - \frac{L_{ps\_shorted}}{L_{ps\_open}}} \qquad (15)$$

Where $L_{ps\_shorted}$ is the primary inductance when the secondary is shorted, and L_{ps_open} is the primary inductance when the secondary is open, which is equal to the primary coil inductance L1. At the same time as acquiring coupling coefficient measurements, the efficiency of power transfer was also measured for the whole TET system. The efficiency was computed as the ratio of the power delivered to the medical device over the power drawn from the external battery source supplying the TET system.

3 COUPLING AND EFFICIENCY RESULTS

The first evaluation considered a pair of coils with a very simple geometry which could be accurately represented using all methods. Both coils used a single winding and figure 8 illustrates the effect on the coupling coefficient when the lateral displacement is increased from 0 to 20 mm at 10mm separation. The lines ka, ks and kp corresponds to the coefficient of coupling from the analytical model, simulated model and experimental measurements respectively. As expected the coupling coefficient drops as the lateral displacement increases, and all three methods produced consistent results. Similar consistency is seen for axial alignment and angular rotation cases.

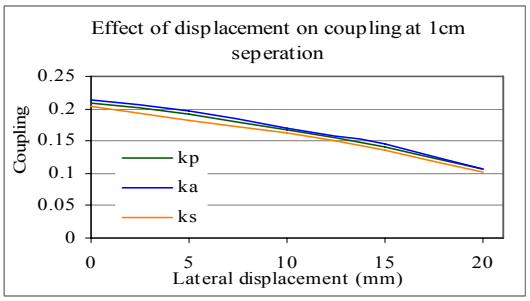

Figure 8: The effect of lateral displacement on coupling at 10mm separation.

However, practical TET coils will not consist of single turns, and they will have bulk which can be characterised by internal and external radius and also a physical height. Physical coils were constructed with a self inductance of 30.4µH for the primary and 8.75µH for the secondary coil.

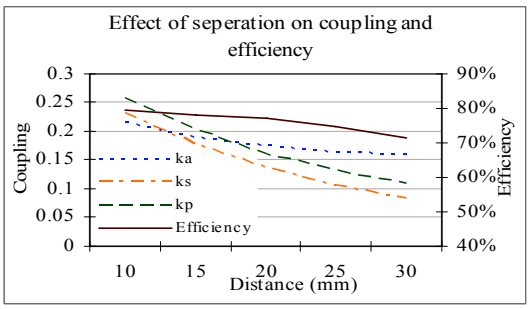

Figure 9: Effects of separation between coils on coupling and efficiency when the coils aligned axially.

The three methods of evaluating the coupling coefficient were implemented using genuine physical parameters, and the results are shown in figure 9. With the coils aligned axially, the coupling coefficient decreases as the separation increases. The simulated coupling coefficients have a mean deviation of 16% from the experimental results. However, the analytical results are far away. This is illustrating the effects of the physical bulk of the coils. The efficiency of the power transfer is also shown in figure 9. The coupling coefficient drops at a greater rate than the efficiency. This is illustrating that, although the coupling coefficient may be low, good power efficiency can still be achieved.

Figure 10 illustrates the effects of displacement on coupling and efficiency when the coils are separated by 10mm and 20mm. Again, the simulated and practical coupling coefficients are fairly similar (with a mean deviation of 9.5%), while the analytical model significantly under estimates the practical result at 10mm separation. However at 20mm separation, the analytical coupling coefficient is in much better agreement with the simulated results. This suggests that for lateral displacement at larger separations, the magnetic coupling for the physical coils is reasonably well represented by idealised coils. The effect of lateral displacement on efficiency was very small (efficiency dropped from 79% to 77% for 20mm lateral displacement) at 10mm separation. Efficiency drops more rapidly down to 72% at 20mm separation.

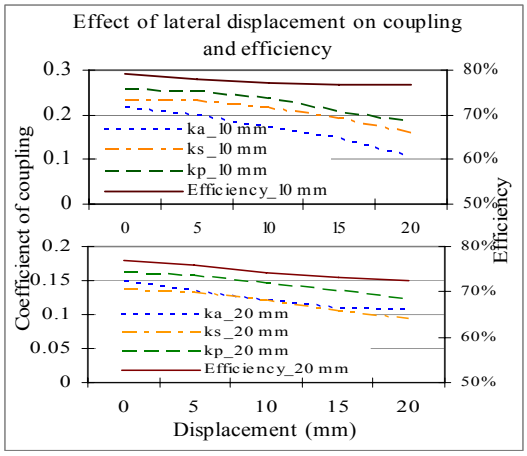

Figure 10: Effects of displacement on coupling and efficiency for coil separations of 10mm and 20mm.

The impact of rotational misalignment on coupling was similar to the lateral displacement case. The simulation result underestimated the practical coupling for both 10mm and 20mm separation however it was within a mean deviation of 14.76% of the experimental measurements.

4 DISCUSSION

The maximum power transfer of a TET system refers to the maximum power that can be transferred from primary to secondary coil disregarding the losses associated with the components in the circuit. The maximum power that can be transferred by a current-fed push-pull resonant converter TET system has been derived by Si et. al. (Ping Si 2007) using mutual inductance between the primary and secondary coils. This relationship is shown in equation 16 as a function of the coupling coefficient.

$$P_{\max} = \frac{\pi k V_{dc}}{8 f \sqrt{L_p L_s}} V_{in} \qquad (16)$$

Where L_p and L_s are the primary and secondary coil inductances, k is the coupling coefficient, P_{max} is the maximum power transfer, V_{in} is the DC input voltage, V_{dc} is the output voltage at the load and f is the system resonant operating frequency.

Equation 16 is based on the assumption that high order harmonic components are negligible and the dc current is continuous at the pickup. These assumptions are reasonable for practical circuits. Equation 16 shows that for given primary and secondary circuits, the maximum power transfer capacity of a TET system is proportional to the coupling coefficient. Good coupling can increase the maximum possible power transfer from primary to secondary coils. However, in terms of the power efficiency, from the previous results shown in section 3, it is clear that coupling does not have a dramatic effect. This is a very important feature of the system, meaning it is possible to achieve high power efficiency for a loosely coupled TET system.

During the power transfer process, there is little power loss in the air gap between the primary and the second coils. Therefore the coupling coefficient is not sensitive to the overall power efficiency of the system. However with low coupling, high magnetic strength is required to deliver the same amount of power, so the required current and/or voltage use to generate the field needs to be higher, resulting in a higher loss in the drive circuits. To further understand the power efficiency issue, the power losses in each component of the TET system was identified.

The loss components were measured from the TET system and are presented in figure 11. The total power loss between the input and output of the system was also measured, and the difference

between the sum of the identified primary and secondary losses, and the actual total losses measured are presented as "Other" in figure 11. The experiment was conducted under a constant load of 10W, and the input power to the TET system was adjusted accordingly for each alignment configuration to maintain the output power to be constant.

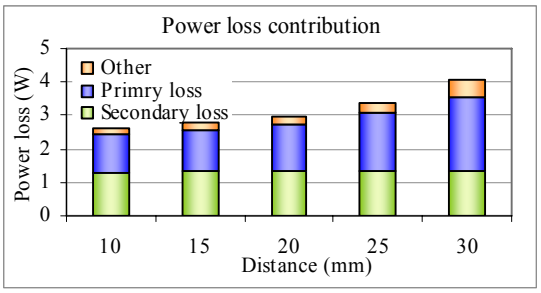

Figure 11: Loss contributions for fully aligned case when delivering 10W to a load.

Figure 11 shows that the total power loss increases when the separation between the coils is larger. However the power loss at the secondary power circuit is more or less the same due to the same load and circuit operating condition. This means no additional losses are occurring at the secondary even when the coupling is poorer. Thus there is no complication of temperature rise and risk of tissue damage.

The increase in total system loss is mainly from the primary power circuit due to the need for higher coil currents to compensate when the air gap separation is larger. A higher strength magnetic field is needed thus the current in the primary coil and its tuning capacitor has to be higher, resulting in higher losses. In this circuit losses in other parts of the primary converter such as dc conduction losses and switching losses also increase at the same time due to the increased dc voltage at the input. However, they are relatively small because the dc current of the primary converter is relatively small compared to the ac resonant current. Therefore (Equivalent Series Resistance) ESR values for the primary coil and tuning capacitor are important parameters to consider in designing an efficient TET system.

5 CONCLUSIONS

Three methods of determining the coupling coefficient for specific coil orientations covering the typical range of TET coils suitable for supplying 10W of power are presented in this paper. The analytical method was shown to be valid for idealised coil configurations although it could not be used to model the actual experimental setup accurately. Numerical simulation gave a superior match with experimental results, and is appropriate for assessing different coil designs efficiently.

The coupling coefficient is a major factor determining the maximum power transfer capacity of a TET system. However, it does not determine the system power efficiency. Power losses at the implant were shown to be largely constant. Therefore there is no additional heat and temperature rise when the coupling becomes poorer. A small overall power efficiency drop was caused mainly by the ESR losses in the primary circuit. With a maximum coil separation of 30mm, the variation in coupling coefficient reduced the overall power efficiency from approximately 80% to 70%.

REFERENCES

C. M. Zierhofer, E. S. H. (1996). "Geometric approach for coupling enhancement of magnetically coupled coils." IEEE transactions on biomedical engineering 43: 708-714.

F.C Flack, E. D. J., D. M. Schlapp (1971). "Mutual inductance of air-cored coils: Effects on design of radio-frequency coupled implants." Medical and Biological Engineering 9: 79-85.

Hochmair, E. S. (1984). "System optimization for improved accuracy in transcutaneous signal and power transmission." IEEE transactions on biomedical engineering 31: 177-186.

John C. Schuder, J. H. G., Hugh E. Stephenson Jr (1971). "An inductively coupled RF system for the transmission of 1kW of power through the skin." IEEE transactions on biomedical engineering 18: 265-273.

Mani Soma, D. C. G., Robert L. White (1985). "Radio-frequency coils in implantable devices: Misalignment analysis and design procedure." IEEE transactions on biomedical engineering 34: 276-282.

N. de N. Donaldson, T. A. P. (1983). "Analysis of resonant coupled coils in the design of radio frequency transcutaneous links." Medical and Biological Engineering and computing 21: 612-627.

Ping Si, P. A. H., J. W. Hsu, M. Chiang, Y. Wang, Simon Malpas, David Budgett (2007). "Wireless power supply for implantable biomedical device based on primary input voltage reglation." 2nd IEEE conference on Industrial Electronics and Applications.

MECHANOMYOGRAPHIC SENSOR
A Triaxial Accelerometry Approach

Guilherme Nunes Nogueira-Neto
Departamento de Engenharia Biomédica, UNICAMP, Cidade Universitária Zeferino Vaz, P.O. 6040, Campinas, Brazil
nogueira@ceb.unicamp.br

Ronie Wesley Müller, Fábio Andrey Salles, Percy Nohama, Vera Lúcia da Silveira Nantes Button
CPGEI, Universidade Tecnológica Federal do Paraná, Av Sete de Setembro, 3165, Curitiba, Brazil
Departamento de Engenharia Biomédica, UNICAMP, Cidade Universitária Zeferino Vaz, P.O. 6040, Campinas, Brazil
roniemuller@gmail.com, fabiosallesctba@gmail.com, percy.nohama@gmail.com, vera@ceb.unicamp.br

Keywords: Mechanomyography, accelerometer, triaxial.

Abstract: Recently, accelerometers have been used to acquire mechanomyography signals. These signals are due to muscle lateral oscillations during contraction. In this study, a sensor acquired such vibrations in three directions. A triaxial accelerometer-based sensor was constructed and tested with a controlled mechanical vibrator and subwoofer speaker (both from 10Hz up to 40Hz) during isokinetic muscle contraction (3 volunteers, 50 extensions at 300 degrees/s). With triaxial accelerometry it was possible to compute the MMG modulus signal. For normalised and average values, MMG amplitude presented strong correlation coefficients (R=0,89) with RMS and peak torque. Below 80% of normalised data, MMG amplitude and torque values (RMS and peak) seem to converge.

1 INTRODUCTION

In the last decades, the acquisition of oscillatory waves of contracting muscles has been performed with diverse sensors like piezoelectric and condenser microphones (Brozovich & Pollack, 1983; Stokes & Cooper, 1992) and hydrophones (Orizio, 1993) under different acronyms: acousticmyography (AMG); sound-myography (SMG); vibromyography (VMG); and phonomyography (PMG). Such oscillations originate from lateral movement of muscle fibres (Orizio, Perini, & Veicsteinas, 1989b). Recently, these waves have been acquired by means of accelerometers (Watakabe, Mita, Akataki, & Ito, 2003) and the technique named mechanomyography (MMG). Laser displacement sensors have also been used (Orizio, Gobbo, Diemont, Esposito, & Veicsteinas, 2003).

The MMG literature presents studies performed with isolated muscles and voluntary contraction tests. Almost all of them have given emphasis in monitoring the vibratory axis orthogonal to the muscle belly. This could be assigned to the materials used in the manufacture of those sensors. As microelectromechanical systems (MEMS) advance, new, smaller, more precise and sensible sensors are developed. Today it is possible to find commercial monoaxial accelerometers of 1,2V/g and triaxial ones of 800mV/g.

The MMG signal can be useful for providing muscle function information different from that obtained by the electromyography (EMG) and torque analysis (Orizio, Perini, & Veicsteinas, 1989a). MMG signal time and frequency domain analyses can help in determining muscle fatigue (Shinohara, Kouzaki, Yoshihisa, & Fukunaga, 1998).

With efforts aimed at detecting localized muscle fatigue, defined as the failure to maintain muscle power output (Fitts, 1994), a triaxial accelerometer sensor and acquisition system were developed and described in this paper.

2 METHODS

In this section we will present the hardware and the methods employed for the sensor assessment.

2.1 Hardware

Taking into account that muscle displacements during isometric contraction are minimal, the sensor circuitry was greatly reduced (2,2x2,9cm^2, 4g). The hardware was divided into two boards. The first one (Figure 1) is a double-faced board. On one face is the triaxial accelerometer circuit (Freescale MMA7260Q, capacitive, high sensitivity 800mV/g@1,5g) and on the other face is the SMD passive filter circuit: one high-pass (fc=3Hz) and one low-pass (fc=1,5kHz) filter per axis. The static acceleration was eliminated with high-pass filtering. Therefore, as the inclination of body segments does not vary so abruptly, its influence is ignored.

The second board lays at 10 cm from the first one and consists of supply circuit (+/–10V) for the inverter operational amplifier (G=37,5dB) and 3,3V regulation circuit.

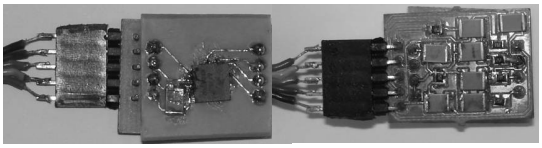

Figure 1: MMG sensor (both faces).

Sensor and cabling were completed shielded by aluminium foil and bandage.

For acquisition and assessment purposes, the signals were concentrated in a DT300 series Data Translation™ acquisition board, 12-bits, 8 differential input channels and 1kHz sampling frequency.

2.2 Hardware Assessment Tests

In order to assess the correct operation, the signals generated were analysed in an FFT-based LabVIEW™ program. The program used a 40Hz low-pass Butterworth filter since the MMG signal energy is primarily comprised below 50Hz (Zagar & Krizaj, 2005). Figure 2 presents the assessment test equipment, a PASCO™ digital function PI-9587C connected to a mechanical wave driver SF-9324. The MMG sensor was tightly fixed on a plastic support screwed to the driver.

For the subwoofer test, the sensor was fixed with double-faced adhesive tape on the woofer.

In the function generator, a sine wave of 0,5Vpp was set with the following frequencies: 10, 11, 12, 13, 14, 15, 16, 17, 18, 19, 20, 25, 30, 35, and 40Hz. These frequencies were selected because of the 8-50Hz MMG pass-band frequency range.

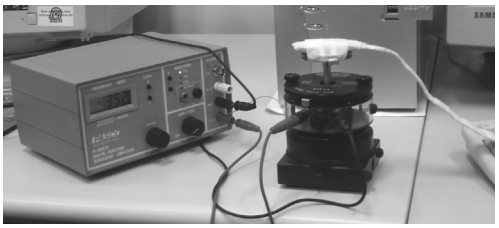

Figure 2: Assessment test equipment.

2.3 MMG Analysis Software

The MMG signal acquisition and analysis software was created in LabVIEW™ and described elsewhere (Salles, Müller, Nogueira-Neto, Button, & Nohama, 2006). Briefly, it processes MMG signals extracting amplitude (integrated MMG, root mean square or RMS) and frequency (mean power frequency) variables of interest. Signals were filtered at 40Hz.

For this test, torque signal acquired from an isokinetic dynamometer was added to the MMG analysis software.

2.4 Isokinetic Test Protocol

Three volunteers (between 24 and 30 years) performed an isokinetic muscle contraction test.

Firstly, they warmed up on a cycle ergometer. Then, they were asked to perform 50 consecutive leg extensions at the maximum voluntary contraction (MVC) they could get while a physician provided sound feedback. The angular velocity was fixed at 300º/s and the leg movement amplitude limited from 10º of flexion to complete extension (total 100º).

The sensor was placed over the muscle belly of the rectus femoris muscle, as indicated in Figure 3, fixed with double-face adhesive tape.

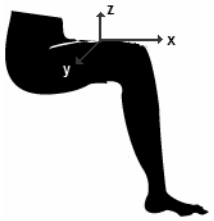

Figure 3: Sensor placement and triaxial orientation.

During the extensions, only the intermediate 270ms of both MMG and torque signals were taken into account for statistical analysis due to the dynamometer initial/final acceleration/deceleration.

The modulus (MMG_{MOD}) of the MMG signals from all three axes was calculated and correlated

with RMS and peak torque values ($Torque_{RMS}$ and $Torque_{PEAK}$, respectively).

3 RESULTS

Figure 4 shows the results from one of the controlled frequencies on both vibrators. As one can see, the subwoofer results presented less harmonic components, and these occurred for all frequencies from 10Hz to 20Hz. Moreover, the fundamental frequency matched the desired one near two-decimal digits of accuracy for all frequencies.

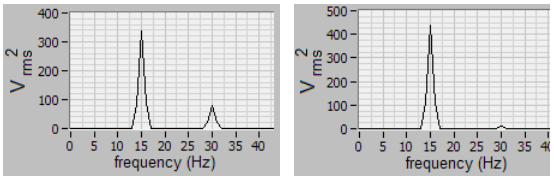

Figure 4: (a) Mechanical vibrator and (b) subwoofer results during test at 15Hz.

Table 1 shows the correlation coefficients between MMG_{MOD} and torque data. Only V3 did not presented strong coefficients. Figure 5 shows the curves with the average normalized MMG_{RMS}, $TORQUE_{RMS}$ and $TORQUE_{PEAK}$ as a function of the extensions.

Table 1: Correlation between MMG_{MOD} and torque.

Volunteers	V1	V2	V3
$TORQUE_{RMS}$	0,79	0,78	0,48
$TORQUE_{PEAK}$	0,75	0,76	0,46

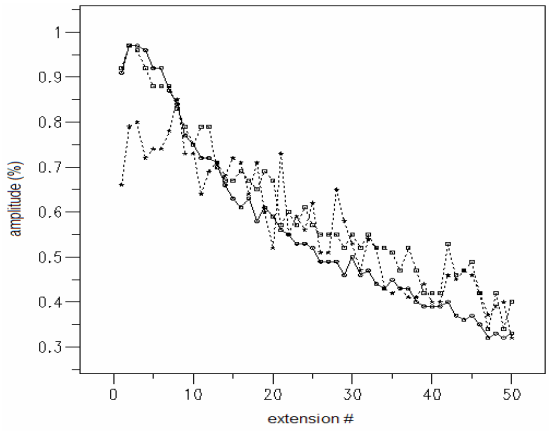

Figure 5: MMG_{MOD} (star), $TORQUE_{RMS}$ (circle), and $TORQUE_{PEAK}$ (square) vs. extension.

The MMG_{MOD} average signal presented strong correlation coefficient with both $TORQUE_{RMS}$ and $TORQUE_{PEAK}$ average signals (R=0,89 and R=0,89, respectively).

4 DISCUSSION

The results of the hardware assessment test showed that the mechanical vibrator introduced more harmonic components than the subwoofer. This can be partly due to the difference between the amplitudes of vibration, and partly assigned to the fixation method. The sensor was tightly fixed on the plastic support of the driver. However, it was loosely fixed on the subwoofer membrane. The damping effect can be responsible for the harmonic suppression. Also, the amplitude of vibration was maximal for the driver, but partial for the subwoofer because the sensor was not placed over the axis of movement. When analysing spectral indicators, it is important to have this in mind.

The triaxial sensor-based MMG analysis becomes acceptable when someone considers a physiological approach. Inside the thigh, the rectus femoris muscle is surrounded by subcutaneous fat layer under the skin (Hudash, Albright, McAuley, Martin, & Fulton, 1985). It is difficult to determine the exact direction of muscle vibrations. Fibres are constantly changing length. Moreover, in the quadriceps group there are other muscle oscillatory sources (e.g. vastus medialis) that can indirectly reduce and distort the MMG signal acquired by the sensor placed over the rectus femoris muscle belly.

MMG presents greater correlation with torque when it is measured at the muscle belly (Cescon, Farina, Gobbo, Merletti, & Orizio, 2004). A theoretical advantage of triaxial accelerometry is that MMG_{MOD} is less sensitive to variations in sensor positioning and orientation than individual axes.

On the other hand, triaxial accelerometers tend to have larger dimensions and can negatively affect MMG signal analysis due to distortions (Watakabe et al., 2003). However, it does not seem to be the case of the sensor described in this paper.

Regarding the correlation coefficients, the high values (R=0,89) obtained for the average MMG and torque data are similar to those previously obtained for peak torque during isokinetic contraction at 300º/s (Evetovich et al., 1997).

It was assumed that volunteers used the maximum voluntary contraction (MVC) at the beginning of the tests and, along with the exercise, torque loss occurred which would lead to localized

muscle fatigue. The average normalized MMG_{RMS}, $TORQUE_{RMS}$, and $TORQUE_{PEAK}$ curves seem to converge for values below approximately 80% of maximum normalized amplitude and diverge above it. Similar results were found by researchers studying isometric contractions (Orizio et al., 1989b). However, it is not possible to affirm that volunteers used MVC, because data have been normalized.

5 CONCLUSIONS

When computing spectral values based on MMG monitoring of muscle contraction, it is important to consider the effect of the sensor adhesion technique because it can influence the calculus of e.g. mean power frequency. The moduli of the signals acquired by the triaxial accelerometer sensor present good correlation with RMS and peak torque. MMG_{MOD} can be a good indicator of torque loss during isokinetic contractions. The MMG and torque amplitudes (RMS and peak) seem to converge for values below 80% of normalised data (presumably 80%MVC). The results obtained in the preliminary tests, with three volunteers, showed that the sensor is viable. These tests consist in the initial efforts for assessing the sensor and it will be complemented with a wider volunteer population.

ACKNOWLEDGEMENTS

Guilherme Nogueira would like to thank CNPq – Conselho Nacional de Desenvolvimento Científico – Fundação Araucária and FINEP for the financial support.

REFERENCES

Brozovich, F. V., & Pollack, G. H. (1983). Muscle contraction generates discrete sound bursts. *Biophysical Journal, 41*(1), 35-40.

Cescon, C., Farina, D., Gobbo, M., Merletti, R., & Orizio, C. (2004). Effect of accelerometer location on mechanomyogram variables during voluntary, constant-force contractions in three human muscles. *Medical and Biological Engineering and Computing, 42*(1), 121-127.

Evetovich, T. K., Housh, T. J., Stout, J. R., Johnson, G. O., Smith, D. B., & Ebersole, K. T. (1997). Mechanomyographic responses to concentric isokinetic muscle contractions. *European Journal of Applied Physiology and Occupational Physiology, 75*(2), 166-169.

Fitts, R. H. (1994). Cellular mechanisms of muscle fatigue. *Physiol Rev, 74*(1), 49-94.

Hudash, G., Albright, J., McAuley, E., Martin, R., & Fulton, M. (1985). Cross-sectional thigh components: computerized tomographic assessment. *Med Sci Sports Exerc, 17*(4), 417-421.

Orizio, C. (1993). Muscle sound: bases for the introduction of a mechanomyographic signal in muscle studies. *Crit Rev Biomed Eng, 21*(3), 201-243.

Orizio, C., Gobbo, M., Diemont, B., Esposito, F., & Veicsteinas, A. (2003). The surface mechanomyogram as a tool to describe the influence of fatigue on biceps brachii motor unit activation strategy. Historical basis and novel evidence. *European Journal of Applied Physiology, 90*(3 - 4), 326-336.

Orizio, C., Perini, R., & Veicsteinas, A. (1989a). Changes of muscular sound during sustained isometric contraction up to exhaustion. *Journal of Applied Physiology, 66*(4), 1593-1598.

Orizio, C., Perini, R., & Veicsteinas, A. (1989b). Muscular sound and force relationship during isometric contraction in man. *European Journal of Applied Physiology and Occupational Physiology, 58*(5), 528-533.

Salles, F. A., Müller, R. W., Nogueira-Neto, G. N., Button, V. L., & Nohama, P. (2006). *Sistema de análisis de señales mecanomiográficas (MMG)*. Paper presented at the XXIV Congreso Anual de la Sociedad Española de Ingeniería Biomédica, Pamplona, Spain.

Shinohara, M., Kouzaki, M., Yoshihisa, T., & Fukunaga, T. (1998). Mechanomyogram from the different heads of the quadriceps muscle during incremental knee extension. *European Journal of Applied Physiology, 78*(4), 289-295.

Stokes, M. J., & Cooper, R. G. (1992). Muscle sounds during voluntary and stimulated contractions of the human adductor pollicis muscle. *Journal of Applied Physiology, 72*(5), 1908-1913.

Watakabe, M., Mita, K., Akataki, K., & Ito, K. (2003). Reliability of the mechanomyogram detected with an accelerometer during voluntary contractions. *Medical and Biological Engineering and Computing, 41*(2), 198-202.

Zagar, T., & Krizaj, D. (2005). Validation of an accelerometer for determination of muscle belly radial displacement. *Medical and Biological Engineering and Computing, 43*(1), 78-84.

CONSIDERATIONS ON IMPROVING THE DESIGN OF CUFF ELECTRODE FOR ENG RECORDING

Geometrical Approach, Dedicated IC, Sensitivity and Noise Rejection

Fabien Soulier, Lionel Gouyet, Guy Cathébras, Serge Bernard
David Guiraud and Yves Bertrand
LIRMM, Université Montpellier II - CNRS - INRIA, 161 rue Ada, 34392 Montpellier, France
Firstname.Lastname@lirmm.fr

Keywords: Multipolar cuff electrode, regular tessellation, electroneurogram, action potential, Laplacian, selectivity, ASIC, multi-input differential amplifier.

Abstract: Cuff electrodes have several advantages for *in situ* recording of ENG signal. They are easy to implant and not very invasive for the patient. Nevertheless, they are subject to parasitic background noise, especially the EMG generated by the muscles. We show that the use of large numbers of poles can increase the sensitivity of cuff electrodes as well as their selectivity with respect to a efficient noise rejection. We investigate several configurations and compare the performances of a tripolar cuff electrode versus a multipolar one in numerical simulation.

One the other hand the use of cuff electrodes leads to the recording of the sum of the signals generated by all the axons within the nerve. This puts in evidence the need of signal separation techniques that require a large amount of information. Again, we show that multipolar electrodes can solve this problem since poles can be switched one to another, provided that they are distributed along a regular tessellation.

Finally, we present the structure of an ASIC preamplifier aimed to obtain the Laplacian of the potential by spatial filtering and rejecting low-frequency noise..

1 INTRODUCTION

Functional Electrical Stimulation (FES) techniques are used to restore motion or sensitive functions in people with neural system pathologies like spinal cord injury. These techniques consist in generating artificial contraction by electrical stimulation. In FES system a direct opened loop control doesn't allow efficient stimulation. In order to provide a loopback control we need sensory information (force, contact...) (Djilas et al., 2006). An attractive solution consists in using the natural sensors. The sensory information is propagated by associated afferent fibers and can be recorded as an electric potential variation, the electroneurogram (ENG).

Unfortunately, in peripheral nerves the complete nerve activity due to the large number of axons makes the extraction of the studied signal particularly hard. Moreover the sensory signal seen through the nerve is a very low amplitude signal compared with the amplitude of parasitic signals. For instance, on a monopolar recording, EMG created by muscle activity have amplitude about three orders of magnitude higher than the ENG. In this context, the two main objectives to be able to exploit natural sensors are:

- to find a solution to separate the useful information from the complete ENG signal;
- to reject the parasitic external signals.

The classical solution consists in using multipolar electrodes, but from tripole (Ramachandran et al., 2005) to nine pole electrode (Winter et al., 2000; Taylor et al., 2004), the selectivity of the neural information is not efficient enough to be suitable in closed loop FES system. To achieve both a better sensitivity and efficient background noise rejection we propose a new configuration of the cuff electrode with a large number of poles regularly distributed onto the cuff. In this configuration, a group of poles can behave, with suitable low level analog signal processing, like a kind of a directive antenna. Moreover, the large number of poles will allow enough channels in order to apply source separation signal processing on the ENG. Of course, the directivity of the sensor relies on the quality of the subsequent low-level analog signal processing.

In this paper, we first show how to generalize the preprocessing operations on the recorded signal from

tripolar to multipolar configuration using the Laplacian formalism. Then we discuss on the optimal pole placement around the nerve regarding tessellation methods. Both the electrode configuration and the associated preprocessing circuit result from this pole distribution and must be taken into account. We particularly focus on the hexagonal seven-pole electrode, presenting the associated seven input preamplifier and preliminary simulation results.

2 EMG NOISE REJECTION

Cuff electrodes have been the most used for ENG recording in the last ten years (Haugland et al., 1994; Jensen et al., 2002; Andreasen and Struijk, 2002). They are relatively easy to implant, they are not invasive for the nerve and implantation is very stable and thus allows chronic experiments. ENG can be

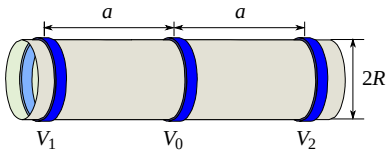

Figure 1: Tripolar electrode cuff model.

recorded as the potential difference created on the electrodes by the charges associated to the action potentials (AP) propagating along the nerve fibers. Fig. 1 shows a typical tripolar cuff electrode. When recording with this kind of electrode, a classic method to reject parasitic signals consists in calculating the average of the potential differences between the central pole and each of the outer poles (Struijk and Thomsen, 1995; Pflaum et al., 1996):

$$V_{\text{rec}} = \frac{(V_0 - V_1) + (V_0 - V_2)}{2} = V_0 - \frac{V_1 + V_2}{2} \qquad (1)$$

The last expression shows that this operation consists in:

1. averaging the signal on the outer poles, *i.e.* applying a low-pass spatial filter.
2. subtracting the result to the signal of the central pole, keeping only the high spatial frequencies.

Therefore, the recorded V_{rec} signal can be considered as spatial high-pass filtered.

More precisely, this filter is a second-order one considering that the expressions

$$\frac{1}{a}(V_2 - V_0) \quad \text{and} \quad \frac{1}{a}(V_0 - V_1) \qquad (2)$$

evaluate the first derivative $\frac{dV}{dx}$. Thus the difference

$$\frac{1}{a}\left(\frac{(V_2 - V_0)}{a} - \frac{(V_0 - V_1)}{a}\right) = \frac{2}{a^2}\left(\frac{(V_1 + V_2)}{2} - V_0\right) \qquad (3)$$

denotes the second derivative $\frac{d^2V}{dx^2}$ that is the one-dimensional *Laplacian* of the potential. We can identify in the last expression the equation (1) without the known constant factor $-2a^{-2}$.

Laplacian filters can reject both homogeneous potentials and linearly varying ones like those created by far EMG sources. The purpose of this new design is to build two-dimensional Laplacian using more poles to obtain isotropic rejection.

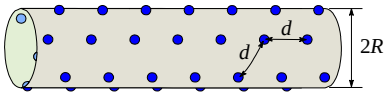

Figure 2: Multipolar electrode cuff model.

3 POSITIONING THE POLES

A tripolar cuff electrode (Demosthenous and Triantis, 2005) provides only one recording which is the superposition of all action potentials "seen" by the electrode at a given moment. The use of several poles on a cuff electrode (see Fig. 2) could allow us to record more signals, thus increase the quantity of neural data and facilitate the signal post-processing on the recording system.

In order to achieve optimal placement of poles, we must pay attention to three constraints:

1. The electrodes have to be placed all around the nerve, thus the poles have to be distributed onto the whole surface of the cuff.
2. The poles have to be equally spaced to simplify electronics in charge of analog signal preprocessing (weight coefficients in Laplacian preamplifier).
3. They have to be able to be substituted one to each other, so we take benefits of the maximum measurement locations, allowing powerful signal processing.

Since the cylindric shape of the cuff results from the wrapping of an initially plane device, these conditions imply to look for a regular tessellation of the plane as the positions of the poles or, more precisely, tessellations composed of regular polygons symmetrically tiling the plane. It is well known that there are exactly three type of regular tessellations (Weisstein, 2002). They can be specified using the Schläfli symbols: $\{3,6\}$, $\{4,4\}$ and $\{6,3\}$.

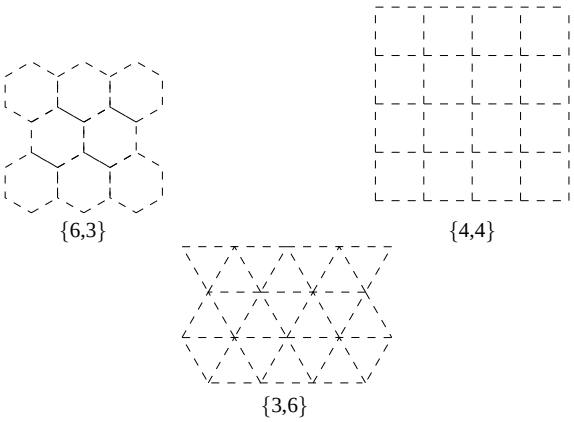

Figure 3: There are exactly three regular tessellations composed of regular polygons symmetrically tiling the plane.

The first symbol in the Schläfli notation denotes the shape of the patch (triangle, square or hexagon). On the figure 3, each vertex corresponds to a pole. Each of them being surrounded by a number of equidistant poles given by the second Schläfli symbol, respectively 6, 4 and 3.

From the previous tessellations, one can build three kinds of electrodes by selecting one central pole and its closest neighbors. Namely, we can define a mesh of:

- triangular 4-pole electrodes,
- squared 5-pole electrodes,
- hexagonal 7-pole electrodes.

These candidates can be seen on the figure 4 and the resulting expressions for the Laplacian are:

$$V_{\text{rec}} = V_0 - \frac{1}{3}\sum_{i=1}^{3} V_i \qquad \text{for } \{6,3\} \qquad (4)$$

$$V_{\text{rec}} = V_0 - \frac{1}{4}\sum_{i=1}^{4} V_i \qquad \text{for } \{4,4\} \qquad (5)$$

$$V_{\text{rec}} = V_0 - \frac{1}{6}\sum_{i=1}^{6} V_i \qquad \text{for } \{3,6\} \qquad (6)$$

One can notice that the $\{4,4\}$ configuration correspond to the 2D Laplacian filter used in image processing (Gonzales and Woods, 1992).

4 ENG AMPLIFIER

Because of the very low level of processed signals we propose to perform the maximum of signal processing as close as possible to the nerve. The more complex operations to be considered are those with the hexagonal electrode.

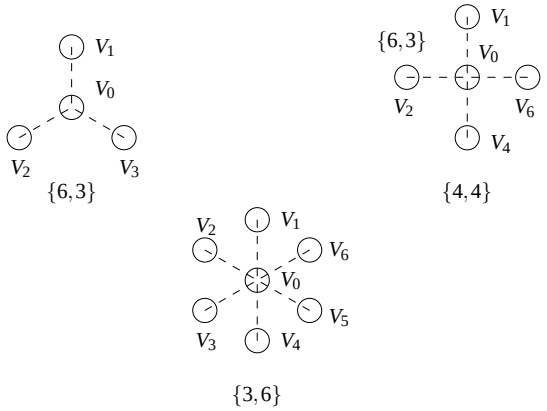

Figure 4: Three possible configurations of electrodes.

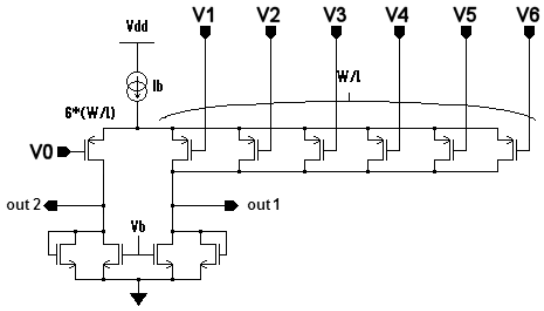

Figure 5: Seven input preamplifier.

For this purpose, we have designed a seven channels ASIC. Each channel compute a weighted difference between the measurement point and the six closest surrounding points. This is done in the analog domain using the preamplifier shown on figure 5. This preamplifier is build around a differential pair whose negative input transistor was split into six transistors (six times smaller, of course). It has a voltage gain that is about 100 and it is followed by an instrumentation amplifier whose gain is configurable between 6 dB and 80 dB. Each channel is composed of one preamplifier followed by an instrumentation amplifier.

This circuit was designed to give an input-referred noise below 1 μV_{rms}, a CMMR above 60 dB and a sufficient gain, i.e greater than 60 dB ; all these parameters in the bandwidth of interest (1 Hz $\leq f \leq$ 3 kHz). The performances expected for this amplifier are given in Table 1 (the noise is measured in the band 1 Hz-3 kHz).

A microphotography of the fabricated circuit is presented Fig. 6. This circuit was designed in CMOS AMS 0.35-μm technology.

Table 1: Amplifier characteristics (simulation).

Active area (7 channels)	1.16 mm^2
Supply voltage	3.3 V
DC Current (Preamp)	20 μA
Voltage gain (Preamp)	100 (40 dB)
CMRR (Preamp)	80 dB (10 kHz)
Voltage gain (Inst amp)	$2 \leq G \leq 10\,000$
CMRR (Full amp)	80 dB (10 kHz)
Input-ref. noise (Preamp)	0.672 μV RMS
Input-ref. noise (Full amp)	0.677 μV RMS
Bandwidth (Full amp)	76 kHz

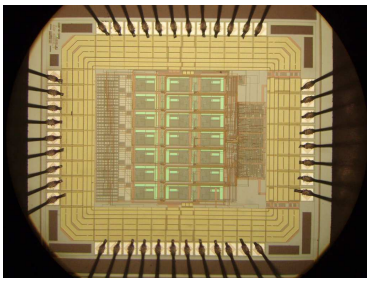

Figure 6: Microphotograph of the seven-channel prototype.

5 NUMERICAL RESULTS

5.1 Action Potential Modeling

In order to evaluate the performances of multipolar electrodes, we need a model for the extracellular electric field created by an action potential. Let us consider a 10 μm diameter myelinated axon. Its Ranvier nodes are 1 μm long, while their diameter is 6 μm and their spacing is 1 mm. Let us call Ω the center of the Ranvier node. When the AP is present at this node, we can model it as a 6 μm diameter circle, perpendicular to the axon axis, with a positive charge $+q$ at its center (Ω) and a negative charge $-q$ spread on the circle. The potential created at a point M of the space by this AP can be approximated by:

$$V(M) = \frac{qa^2}{8\pi\varepsilon_0\varepsilon_r r^3}\left(1 - \frac{3}{2}\sin^2\psi\right) \qquad (7)$$

In this expression, a is the radius of the Ranvier node (3 μm), r is the distance between Ω and M, while ψ is the angle between the axe of the axon and $\overrightarrow{\Omega M}$. This approximation, valid for $r \gg a$, is in good accordance with measurements. In particular, we can see that $V(M)$ is negative for $\psi = \pi/2$ (Stein, 1980, p. 81). Last, q can be easily estimated from the characteristics of the Ranvier node. For this study, we took $q \simeq 20$ fC and $\varepsilon_r \simeq 80$.

The model given by the equation 7 was used to evaluate the sensitivity of the electrodes to action potentials occurring inside the nerve. For the evaluation of the rejection of parasitic signals, we must first recall that EMG are also action potentials, creating the same kind of electric field. But, in this case, we cannot make any assumption on the value of ψ. So, to evaluate the external sensitivity of electrodes, we only used a $1/r^3$ model, unable to give voltages, but sufficient to compare the sensitivities of the electrodes.

We have limited the numerical study to the comparison of the classical tripolar cuff with the heptapolar (hexagonal shape $\{3,6\}$) electrode. We have also studied the effect of the wrapping to the performance of the heptapolar electrode: we consider a plane electrode and then a cylinder-wrapped one.

Given the position of a single AP we can easily calculate the induced potential on each pole of the cuff, since they are very small. For the tripolar cuff, we need to average the potential on each ring. This lead to an elliptic integral we have solved using numerical methods.

5.2 Tripolar and Heptapolar Electrodes Models

In the following, we compare a tripolar cuff electrode, whose diameter is $2R = 3$ mm and ring spacing is $a = 4R$, with one patch of the hexagonal cuff. To get comparable results, this hexagonal cuff has the same diameter ($2R$) and the spacing between poles is $d = R$. Since this patch is partially wrapped around the nerve, we considered also another patch perfectly flat.

For all the calculations, the coordinates were fixed as follow: the origin O is at the center of the cuff electrode. The Ox axis is the axis of the nerve (and, obviously, of the cuff). The Oy axis passes by the center of the considered patch (which is perpendicular to this axe). Last the Oz axe is placed to form a direct trihedron with Ox and Oy.

5.3 Internal Sensitivity

Figure 7 shows the radial sensitivities of the three electrodes (tripolar cuff, planar hexagonal patch and wrapped hexagonal patch) that we compare. The vertical axis is the value of V_{rec} (in dB μV) calculated for an AP placed on the Oy axis, at abscissa yR. The graph shows clearly that while the sensitivity of the tripolar cuff is quasi constant on the section of the nerve, the sensitivity of the hexagonal patch is far higher (up to 30 dB) when considering an AP located between the center of the patch and the center of the cuff.

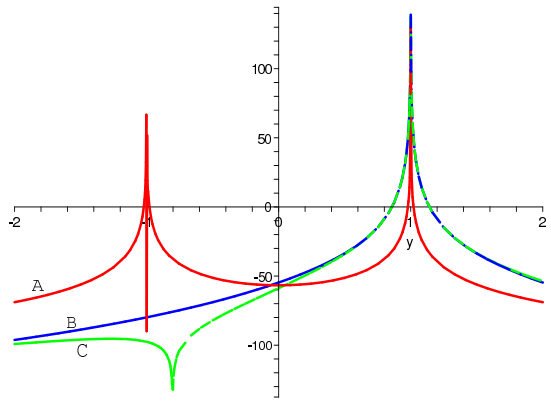

Figure 7: Radial sensitivities of (A) a tripolar cuff electrode, (B) a planar hexagonal patch and (C) a bent hexagonal patch. The vertical axis is in dB μV and the unit for the horizontal axis is the radius R of the electrode.

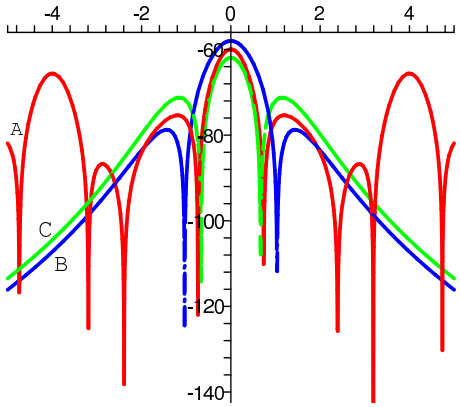

Figure 8: Longitudinal sensitivities on the axe of (A) a tripolar cuff electrode, (B) a planar hexagonal patch and (C) a bent hexagonal patch. The vertical axis is in dB μV and the unit for the horizontal axis is the radius R of the electrode.

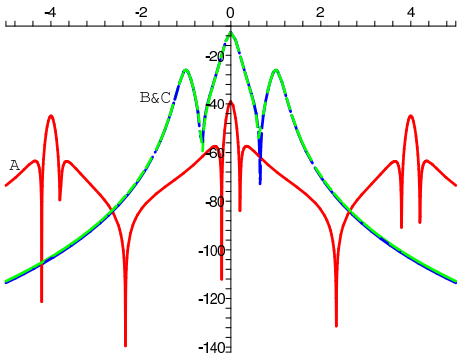

Figure 9: Longitudinal sensitivities on an off-center (80 % of R) axis of (A) a tripolar cuff electrode, (B) a planar hexagonal patch and (C) a bent hexagonal patch. The vertical axis is in dB μV and the unit for the horizontal axis is the radius R of the electrode.

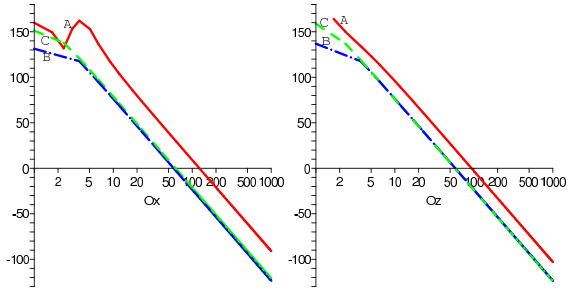

Figure 10: External relative sensitivity along Ox and Oz axes for (A) a tripolar cuff electrode, (B) a planar hexagonal patch and (C) a bent hexagonal patch. The vertical axis is in dB and the unit for the horizontal axis is the radius R of the electrode.

Figures 8 and 9 show the longitudinal sensitivities of the three considered electrodes. On figure 8, the sensitivity is computed for an AP placed on the Ox axe, while, on figure 9, the AP is placed on a line, parallel to Ox, cutting Oy at abscissa $0.8R$. On this later figure, we can see an increase of sensitivity of the tripolar cuff in the vicinity of the rings, but this remains far lower than the sensitivity of any of the hexagonal patches.

5.4 External sensitivity

The figure 10 show the external sensitivities of our three electrodes for an AP placed on the Ox or on the Oz axis of the electrode. As stated above, the quantity plotted is not a voltage, but is homogeneous to the reciprocal of the cube of a distance. Nevertheless, we can see on these two graphs that the hexagonal patches exhibit a better rejection of parasitic signals than the tripolar cuff. This improvement is of 32 dB for Ox and 20 dB for Oz.

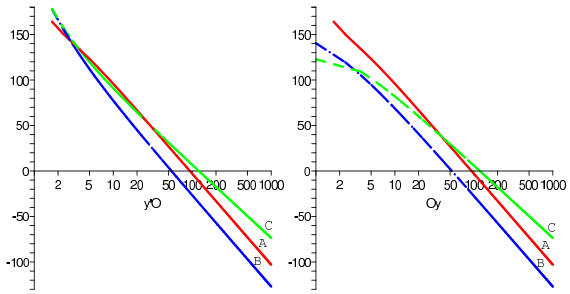

Figure 11: External relative sensitivity along the two halves of the Oy axis for (A) a tripolar cuff electrode, (B) a planar hexagonal patch and (C) a bent hexagonal patch. The vertical axis is in dB and the unit for the horizontal axis is the radius R of the electrode.

The same study conducted along the Oy axis (figure 11) shows that, while the planar patch continues

to have the better rejection of parasitic signals, the wrapped hexagonal patch has a sensitivity decreasing slowly along this *Oy* axis. In fact, the bent hexagonal patch only begins to have larger sensitivity than the tripolar cuff for action potentials placed at more than fifty times the radius of the cuff, corresponding to approximately 7 cm. At this distance, the parasitic signal could be neglected in comparison to ENG signal.

6 CONCLUSIONS AND PERSPECTIVES

We have presented here a method to build multipolar cuff electrodes and how to extract useful informations from the multiple channels. Although numerical investigations are still necessary to an exhaustive comparison of multipolar structures, the comparison between the classical tripolar cuff electrode for ENG recording and a multipolar electrode has shown that this new type of the design is very promising. In every simulation, multipolar electrodes prove to be more sensitive to sources located inside the nerve, and in almost every case they show better far source rejection.

We hope the improvement of the recorded signal given by this new design will allow the use of signal processing techniques such as source separation. Then, multipolar configurations could make it possible to estimate more precise parameters like the speed and the direction of propagation of the AP (Taylor et al., 2004; Rieger et al., 2006).

Future works include the complete test of the seven-channel amplifier. It requires special attention to electromagnetic interferences due to the high gain it can reach. Then, we will be able to process the *in vivo* qualification of the whole system.

REFERENCES

Andreasen, L. N. S. and Struijk, J. J. (2002). Signal strength versus cuff length in nerve cuff electrode recordings. 49(9):1045–1050.

Demosthenous, A. and Triantis, I. F. (2005). An adaptive ENG amplifier for tripolar cuff electrodes. 40(2):412–421.

Djilas, M., Azevedo Coste, C., Yoshida, K., and Cathébras, G. (2006). Interpretation of ENG signal for FES closed-loop control. In *IFESS'06: 11th Annual Conference of the International Functional Electrical Stimulation Society*, pages 85–87, Miyagi-Zao, Japan.

Gonzales, R. C. and Woods, R. E. (1992). *Digital Image Processing*. Addison-Wesley.

Haugland, M. K., Hoffer, J. A., and Sinkjaer, T. (1994). Skin contact force information in sensory nerve signals recorded by implanted cuff electrodes. *IEEE Transactions on Rehabilitation Engineering*, 2(1):18–28.

Jensen, W., Sinkjaer, T., and Sepulveda, F. (2002). Improving signal reliability for on-line joint angle estimation from nerve cuff recordings of muscle afferents. *IEEE Transactions on Neural Systems and Rehabilitation Engineering*, 10(3):133–139.

Pflaum, C., Riso, R. R., and Wiesspeiner, G. (1996). Performance of alternative amplifier configurations for tripolar nerve cuff recorded ENG. In *Engineering in Medicine and Biology Society, 1996. Bridging Disciplines for Biomedicine. Proceedings of the 18th Annual International Conference of the IEEE*, volume 1, pages 375–376, Amsterdam.

Ramachandran, A., Sacristan, J., Lago, N., Dörge, T., Osès, M., Koch, K., and Hoffmann, K. (2005). Multipolar cuff electrodes with integrated pre-amplifier & filter to interface peripheral nerves for FES application. In *10th Annual Conference of the International FES Society*, Montreal, Canada.

Rieger, R., Schuettler, M., Pal, D., Clarke, C., Langlois, P., Taylor, J., and Donaldson, N. (2006). Very low-noise ENG amplifier system using CMOS technology. *IEEE Transactions on Neural Systems and Rehabilitation Engineering*, 14(4):427–437.

Stein, R. B. (1980). *Nerve and Muscle*. Plenum Press.

Struijk, J. J. and Thomsen, M. (1995). Tripolar nerve cuff recording: stimulus artifact, EMG and the recorded nerve signal. In *Engineering in Medicine and Biology Society, 1995. IEEE 17th Annual Conference*, volume 2, pages 1105–1106, Montreal, Que.

Taylor, J., Donaldson, N., and Winter, J. (2004). Multiple-electrode nerve cuffs for low-velocity and velocity-selective neural recording. *Medical and Biological Engineering and Computing*, 42(5):634–643.

Weisstein, E. W. (2002). Tessellation. From MathWorld–A Wolfram Web Resource. http://mathworld.wolfram.com/Tessellation.html.

Winter, J., Rahal, M., Taylor, N., Donaldson, N., and Struijk, J. (2000). Improved spatial filtering of ENG signals using a multielectrode nerve cuff. In *5th Annual Conference of the International Functional Electrical Stimulation Society*, Aalborg, Denmark.

AUTOMATIC FALL DETECTION AND ALERT SYSTEM
A Compact GPS/GSM Enabled Unit based on Accelerometry

Hugo Silva, Filipe Silva, Hugo Gamboa
PLUX – Biosensor Engineering, Av. 5 de Outubro nº 70 – 8º, Lisbon, Portugal
{hsilva, fsilva}@plux.info

Vítor Viegas
EST – IPS, Setúbal, Portugal
vviegas@est.ips.pt

Keywords: Healthcare, Quality of Life, Accelerometry, Biomechanics, Kinematics.

Abstract: Accidental falls are among one of the main causes of death and disability on elderly people. This stands both as a healthcare problem, in the sense that, upon falling, if individuals are not assisted in an early stage severe long term consequences may arise; and as a limitation for the individual's daily life, in the sense that they generally deprive themselves of regular routines as a preventive measure to avoid falling. In this paper we describe a hardware unit conceived to automatically detect fall events, and trigger a set of alert actions which allow the remote detection of the occurrence and facilitate rapid assistance.

1 INTRODUCTION

Population aging is nowadays growing to a worldwide concern. In the U.S., projections for 2000 pointed a 14,3% population share for senior citizens of 65+; projections indicate that this number will grow by 2050 to an impressive 22,6% (U.S. Census Bureau, 2004), disturbing the balance in the population structure.

The leading cause of death by injuries, and one of the main causes of disability in elderly citizens, are accidental falls (CDC, 2006). Statistics show that, in the U.S., more than one third of the senior population with 65+ fall every year with dramatic outcomes (Hausdorff *et al*, 2001; Hornbrook *et al*, 1994). Besides the increase in the number of deaths resulting from involuntary falls (Stevens, 2006), fall-related injuries usually have severe mid- and long-term consequences (Jager *et al*, 2000; Bell *et al*, 2000).

Necessary financial and logistics resources to provide for appropriate nursing services are highly demanding on healthcare systems; in 2000 direct medical costs resulting from fatal falls ascended to $0.2 billion, and $19 billion for the non-fatal case (Stevens *et al.*, 2006). It is estimated that by 2020 the overall direct and indirect fall-related costs will surpass $43 billion (Englander *et al*, 1996).

Furthermore, fall consequences diminish the individual's quality of life, standing in many cases as a long-term limitation to a regular daily life. Fear of falling leads, among others, to mobility reduction and fitness degradation, further potentiating the risk of involuntary falls (British Columbia Ministry of Health Planning Office of the Provincial Health Officer, 2004).

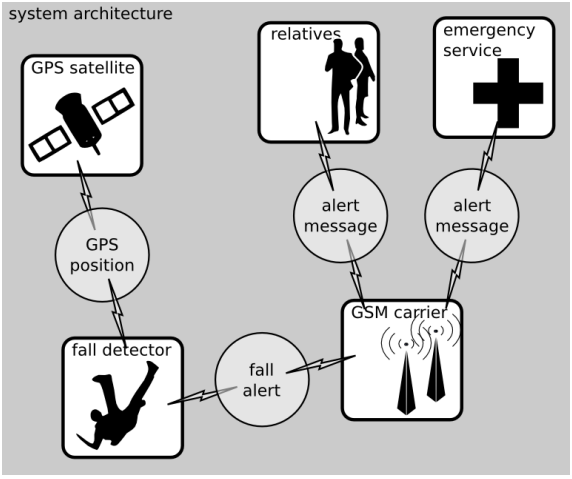

Figure 1: Fall detector system architecture.

This is a trend in most developing countries, and critical issues like the quality of life and healthcare for senior citizens are rapidly arising, thus making way for the development of novel, efficient and cost-effective methods and technologies.

In this paper we present a GPS/GSM enabled portable hardware unit, designed with the purpose of automatically detecting involuntary fall events to alert emergency or nursing teams upon fall detection (Figure 1). The system facilitates rapid assistance allowing remote detection of the occurrence, as well as the GPS coordinates to track the user location.

2 HARDWARE

Recent advances in hardware design and integration provide appropriate conditions for the development of compact, miniaturized systems with a wide application range in real-time signal acquisition and processing (Silva et al, 2005).

For the fall detector hardware unit, three main vectors guided the development process: *(a) automation*; *(b) autonomy*; and *(c) miniaturization*. With a small form factor, the unit was desgined to be worn at waist level, measuring 5.2x5.2x1.6cm, and weighting aproximately 55g.

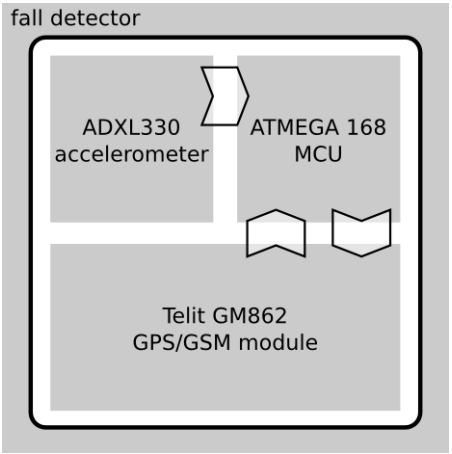

Figure 2: Fall detector block diagram.

Figure 2 depicts the block diagram for the fall detector hardware unit, in which there are three main components which will be detailed next: *(a) accelerometry sensor*; *(b) MCU*; and *(c) GPS/GSM module*.

2.1 Accelerometry Sensor

Fall events can be detected using a number of heuristics; we recur to accelerometry in order to detect sudden changes in magnitude, and angular position.

The fall detector hardware unit integrates one ADXL330 ±3G MEMS® tri-axial accelerometer which measures the acceleration in the cartesian tri-dimensional coordinate space.

To maximize the unit's autonomy, the system is maintained in an idle mode, only being activated if the accelerometer readings exceed a pre-defined magnitude level.

A set of comparators establishes the threshold, and a hardware interrupt is triggered in the MCU whenever the threshold is superseded by one of the axis, switching it to active mode. This works as a pre-filter for the fall detection algorithm discarding standard daily life actions as walking, trunk rotations, among others.

2.2 Microcontroller Unit

An ATMEGA168-20PU MCU is used to command the hardware unit, maintain runtime data, and implement the alert and working logic. It has 16KB program memory, one 16 bit and two 8 bit timers, serial interface, a built-in 6 channel Analog-to-Digital Converter (ADC), and two externally triggered interrupts.

The MCU is kept in idle mode, switching to active mode from time to time as established by the watchdog mode previously described in Section 2.1. Once activated by the accelerometer, the MCU is switched to active mode starting the real-time accelerometer output signal acquisition and processing routine.

If the fall detection software algorithm identifies a fall event, the MCU enters in alert mode, waking up the GPS/GSM module to conduct the procedure described in Section 3.2.

2.3 GPS/GSM Module

GPS/GSM services are assured by a low power, small form factor, Telit GM862 module. It is controlled via AT commands from the MCU through the serial interface, and it has a built-in GPS receiver and a fully functional GSM device.

Two antennas are necessary in order to guarantee the Radio Frequency (RF) signal reception for each function. For this hardware unit we used two low power consumption, small footprint, PCB antennas,

of 13.4x13.4x5.5mm and 42x16x1.6mm, for the GPS and GSM components respectively.

2.4 Power

The unit is powered by a Li-Ion rechargeable battery with 3.7V nominal tension, and 2000mAh nominal current. Table 1 presents the mean power consumption analysis for the hardware unit. From Table 1, and taking into account the operating modes of the unit, an estimated battery lifetime of 72h is achievable.

The GPS/GSM module described in Section 2.3 has a built-in battery charger, and charge level indicator. Since we are using a rechargeable battery, the battery status and charger functions from the GM862 are also used. Without introducing additional circuitry we are able to charge the battery on-board, and assess the battery level during the watchdog mode previously described in Section 3.1.

Table 1: Fall detector mean power consumption.

Item	Mode	Consumption (mA)
Accelerometry Sensor	Active	0.32
MCU	Idle	5.20
	Active	9.70
GPS/GSM	Idle	4.00
	GPS Search	60
Antenna	-	13

3 OPERATING MODES

When first connected from a complete power down state, the hardware unit has a cold start time of <60s. The Microcontroller Unit (MCU) starts in active mode and performs the following initialization tasks (Figure 3): *(a)* connect the GPS unit; *(b)* register the GSM in the carrier network; *(c)* search the SIM card memory for the predefined emergency phone number that should be used while in alert mode; *(d)* and store this number in the runtime memory.

During this sequence, a red led is used to indicate that the unit is in start up mode. When the initialization tasks are completed, the MCU puts the GPS/GSM module into sleep mode.

While connected, the hardware unit has two possible operating states: *(a) watchdog mode*; and *(b) alert mode*. The watchdog mode is the state in which the unit is normally working, while the alert mode is the state in which the unit will enter upon detection of a fall event.

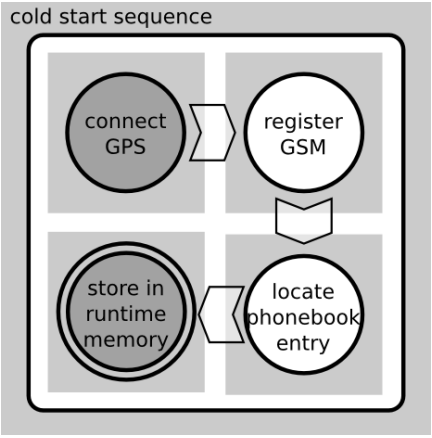

Figure 3: Cold start state diagram.

3.1 Watchdog

This is the mode in which the unit operates until a fall event is detected.

While in watchdog mode, every 4s the MCU wakes up to signal the battery status; the activity indicator led blinks with the colour varying according to the battery charge level: *(a) green*, >50%; *(b) yellow*, =50%; and *(c) red*, <50%.

Every 10m the MCU communicates with the GPS/GSM module in order to update the battery status and to determine the current GPS location of the hardware unit. The last known GPS location is stored in the runtime memory of the MCU.

3.2 Alert

If a potential fall detected by the pre-filter (described ahead in Section 2.1), the MCU is activated entering the alert mode.

In this stage the fall detection software algorithm traces the input signal in order to check if it is a real fall or a false alarm. If a false alarm is detected, the unit goes back into watchdog mode. If it is validated as a real fall, the MCU wakes up the GPS/GSM unit, a text string is formed containing the date, time, alarm notice, and last known GPS position, and sent as a Short Message Service (SMS) text message to the predefined emergency number loaded to the runtime memory during the initialization tasks.

Upon failure in sending the alert SMS, the hardware unit maintains the alert mode. If at first the message is not sent, the process is retried for three times. If the message fails sending in all consecutive tries, the GPS/GSM module is restarted, and the MCU initiates the alert message procedure once more. This process is repeated until the hardware

unit is disconnected or until the message is successfully sent.

4 CONCLUSIONS

This paper describes the implementation of an automatic fall detection hardware unit (Brown, 2005). Due to its compact size, it is easily worn, and it does not limit the actions of its bearer.

With the integrated GPS/GSM feature, it allows the remote detection of fall events and indicates the last known GPS location of the unit's bearer, therefore facilitating the rapid intervention of family members, emergency or nursing teams in case of fall (Figure 1).

Most accidental falls occur in contexts in which subjects are often alone and without means of calling for aid upon falling; also, involuntary falls have severe consequences, both in terms of healthcare and quality of life. Portable fall detection units are therefore a useful tool which play a major role, in minimizing the adverse health consequences of falls and in improving the confidence of fall victims so that they do not deprive themselves of their regular activities.

REFERENCES

Bell A., Talbot-Stern J., Hennessy A., 2000. Characteristics and outcomes of older patients presenting to the emergency department after a fall: a retrospective analysis. *Medical Journal of Australia*; 173(4):176–7.

British Columbia Ministry of Health Planning Office of the Provincial Health Officer, 2004. Prevention of falls and injuries among the elderly: A special report from the office of the provincial health officer. (online; accessed 2007 Sep 10). *Available from URL:* http://www.healthservices.gov.bc.ca/pho/special.html

Brown G., 2005. An accelerometer based fall detector: Development, experimentation, and analysis. *University of California, Berkeley, SUPERB Technical Report*.

Centers for Disease Control and Prevention, National Center for Injury Prevention and Control, 2006. Web-based injury statistics query and reporting system (WISQARS) (online; accessed 2007 Sep 10). *Available from URL:* www.cdc.gov/ncipc/wisqars

Englander F, Hodson T., Terregrossa R., 1996. Economic dimensions of slip and fall injuries. *Journal of Forensic Science*; 41(5):733–46.

Hausdorff J., Rios D., Edelber H., 2001. Gait variability and fall risk in community-living older adults: a 1-year prospective study. *Archives of Physical Medicine and Rehabilitation* 82(8):1050–6.

Hornbrook M., Stevens V., Wingfield D., Hollis J., Greenlick M., Ory M., 1994. Preventing falls among community-dwelling older persons: results from a randomized trial. *The Gerontologist* 34(1):16–23.

Jager T., Weiss H., Coben J., Pepe P., 2000. Traumatic brain injuries evaluated in U.S. emergency departments, 1992–1994. *Academic Emergency Medicine*; 7(2): 134–40.

Silva H., Gamboa H., Viegas V., and Fred A., 2005. Wireless physiologic data acquisition platform. In *Proceedings of the 2005 Conference on Telecommunications*.

Stevens J., 2006. Fatalities and injuries from falls among older adults — United States, 1993–2003 and 2001–2005. MMWR; 55(45).

Stevens J., Corso P., Finkelstein E., Miller T., 2006. The costs of fatal and nonfatal falls among older adults. *Injury Prevention*; 12:290–5.

U.S. Census Bureau, 2004. U.S. Web-based interim projections by age, sex, race, and hispanic origin. (online; accessed 2007 Sep 10). *Available from URL:* http://www.census.gov/ipc/www/usinterimproj

SENSORIZED MICROCATHETER
Smart Microinstrumentation Adressing Fetal Surgery – First Results

A. Sieber [1, 2], K. Houston [2], A. Menciassi [2], G. Nauer [3] and P. Dario [2]
[1] *Profactor Research and Solutions GmbH, Seibersdorf, Austria*
arne.sieber@profactor.at
[2] *Scuola Superiore Sant'Anna,Pisa, Italy*
[3] *ECHEM, Wiener Neustadt, Austria*

Keywords: Fetal surgery, Endoscopy, Fetoscopy, Pulmonary Atresia, Bio-impedance, Catheter.

Abstract: Pulmonary Atresia is a malfunction that is diagnosed in about 1 out of 20.000 fetus. The authors propose a novel surgical intervention where the fetal heart is accessed with an endoscopic intervention through the umbilical cord. The key for this innovative procedure is a novel micro-catheter that is equipped with sensor and actuators that allow active navigation inside the heart and also tissue characterisation. The present paper presents the first prototype.

1 INTRODUCTION

1.1 Fetal Surgery

Birth defects occur in 1/28 of births and are the leading cause of infant deaths. Costs for treatment after birth are sometimes higher than surgery costs. Surgical interventions on the fetus during pregnancy allow a higher intra-uterine survival rate and an improved postnatal outcome. Till now for a fetus with diagnosed congenital malformation abortion, continuation of the pregnancy until termination with a Cesarean delivery, change in timing mode or place of delivery were the only possibilities. Fetal surgery may now provide a solution in these cases.

Starting from the two main American centres (Harrison, M. R., 2003) that have been performing fetal surgery for more than twenty years - University of California, San Francisco Fetal Treatment Center and Children's Hospital of Philadelphia, Center for Fetal Diagnosis and Treatment - nowadays about a dozen worldwide centres provide prenatal surgical intervention and many others carry on research and experiments for specific fetal surgical applications. (Raul A. Cortes and Diana L. Farmer, 2004)

Fetal surgery is still intended for a restricted number of malformations that can not be successfully or efficaciously treated after birth. However, since 1981 many life-threatening fetal pathologies have been treated through in-utero surgical corrections, approaching prenatal interventions as a valid alternative to neonatal therapy or induced abortion.

At the moment open fetal surgery is the standard procedure. It is similar to standard surgical interventions, but causes a high level of stress for both the fetus and the mother. An alternative can be performing a key-hole surgical intervention on the fetus with the help of endoscopic microtools. This procedure is commonly known as fetoscopy and allows an intervention on the fetus in its natural environment causing less uterine trauma, less fetal manipulation but preterm labor, damage to uterine membranes and manipulation difficulties. (Sydorak, R. M. , Albanese, C.T., 2003; Danzer, E., Sydorak, R.M., Harrison M.R., Albanese C.T, 2003; Flake, A.W., 2003 ; Berris M., Shoham M., 2006; Papadopulos, N.A., Papadopoulos, M.A., Kovacs, L., Zeihofer, H.F., Henke, J., Boettcher, P., Biemer, E., 2005).

These procedures are performed through the use of small trocars and a combination of videofetoscopic and sonographic visualization. Paediatric surgeons are trying to apply standard minimal invasive instruments, designed by medical engineers for different kind of surgery, to fetal surgery applications. These instruments may be suitable for some interventions, but are far too big for interventions in an early development stage of the fetus. Thus one of the main problems fetoscopy is facing is the lack of suitable micro instrumentation.

1.2 Pulmonary Atresia

During pregnancy the necessary oxygen is not supplied through the fetal lungs but by the placenta. The Foramen Ovale is an opening between the right and the left atrium that allows blood to pass by the pulmonary tract. After birth this opening is usually closed. Pulmonary Atresia (Daubeney, P.E.F., Wang, D., Delany, D.J., Keeton, B.R., Anderson, R.H., Slavik, Z., Flather, M., Webber, S.A., K., 2005; Litovsky, S., Choy, M., Park, J., Parrish, M., Waters, B., Nagashima, M., Praagh, R.V. & Praag, S.V., 2000) is a malfunction that may appear during pregnancy: it is an incorrectly developed pulmonary valve.that is, instead of a valve there is just a membrane (compare Figure 1A and Figure 1B).

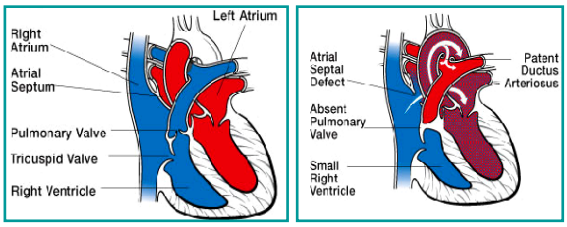

Figure 1A: Healthy heart 1B: Heart with absent pulmonary valve (http://www.americanheart.org/).

No blood supply to the lungs is possible in this case which usually causes the death of newborns when oxygen supply by the placenta is not given anymore. Furthermore anatomic obstruction to the right or left ventricular outflow tract may cause ventricular dysfunction, can divert fetal blood flow in the uterus and result in cardiac chamber hyperplasia. Thus severe aortic or pulmonary stenosis can result in a hypoplastic left or right ventricle with an inability for the ventricular chambers to support the systemic or pulmonary circulation. Theoretically early relief of the fetal aortic or pulmonary stenosis may prevent such occurrence and might preserve the right or left ventricular function. In the case of pulmonary atresia this can be achieved by a punctuation of the pulmonary membrane to enable a pulmonary blood flow and a further correct development of the valve. (Tworetzky, W., Wilkins-Haug, L., RW. Jennings, 2004; Kohl, T., Witteler, R., Strämper, D., Gogarten, W., Asfour, B., Reckers, J., Merschhoff, G., Marcus, A.E., Weyand, M., Van Aken, H., Vogt, J., Scheld, H.H., 2003)

Pulmonary atresia can be diagnosed in the 12-14th week of gestation. The surgical intervention should be performed as soon as possible. In the 14th week the fetus size is about 9-14cm and has a weight in the range of 60 - 200g. In this development stage the pulmonary membrane has a diameter of approximately 1mm.

Pulmonary atresia occurs in about one out of every 20,000 live births. An early surgical intervention is the only alternative to abortion and could allow normal development of the pulmonary valve and the right ventricle.

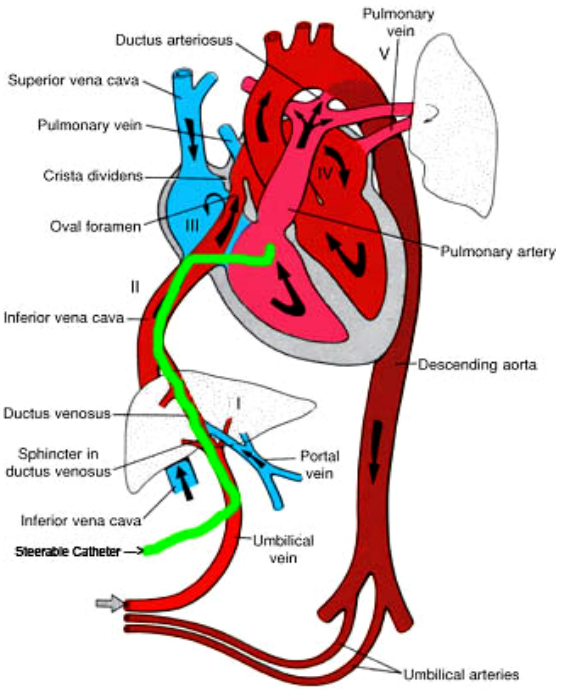

Figure 2: Fetoscopic approach to access the fetal right ventricular through the umbilical cord

2 METHODS

2.1 Fetoscopic Approach

We propose a minimally invasive surgical procedure in the case of pulmonary atresia which includes the following steps:

(1) Externalisation of the uterus where the fetus remains in its own environment

(2) Accessing the right ventricle with a flexible and steerable microcatheter through the umbilical cord (need for a microcatheter (outer diameter <1mm), steering mechanism (3 degrees of freedom), the catheter needs to be highly flexible, position feedback systems need to be available to track the catheters tip) (Figure 2)

(3) guiding the catheters tip in front of the pulmonary membrane (need for a steerable catheter)
(4) recognition of the tissue in front of the catheter: Due to the small dimensions of the pulmonary tissue and the surrounding tissue it is very difficult to distinguish between those just by vision on an ultrasound picture. Tissue characterisation and recognition sensors may then be the solution for a reliable tissue distinction.
(5) once the pulmonary membrane is detected the perforation takes place (need for a cutting tool)

It is clearly visible that the development of suitable microinstrumentation is the key to this novel surgical technique. To proof the feasibility of the approach, we designed a first prototype for such a smart catheter that is equipped with tissue characterisation sensors and a steering mechanism.

2.2 Steering Mechanism

To be able to reach the right ventricle through the umbilical cord (figure 2), the catheter needs to be equipped with steering capabilities (Ascari, L., Stefanini, C., Menciassi, A., Sahoo, S., Rabischong, P., Dario, P., 2003). The multi-lumen catheter consists of a very flexible ending and a less flexible part. In the walls of the catheter 4 thin diameter lumen are integrated, each one for one steering wire. Pulling on these 4 wires and releasing at the same time the wire which is on the opposite side in the catheter will primarily result in a movement of the flexible end part of the catheter. Two microcontroller driven servo drives are used to pull and release the wires. This microcontroller is then connected to a personal computer, which, equipped with a haptic force feedback joystick, allows a precise control of the catheter. A third degree of freedom is realized by either manually or servo supported driving the catheter forward and backwards.

2.3 Electrical Impedance Sensor

Bio-impedance spectroscopy allows tissue classification and identification by recording and analyzing the electrical impedance at different frequencies (Rigaud, B., Hamzaoui, L., Chauveau, N., Martinez, E., Morucci, J., 1994; Cao, H., Tungjitkusolmun, S., Choy, Y. B., Tsai, J. Z., Vorperian, V. R., Webster, J. G., 2002). From the electrical point of view cell membranes appear as capacitors. In comparison to low frequency electrical current where the current path is leading mainly through extra cellular fluid, high frequency electrical current is able to penetrate the cells. Different tissues can be distinguished by comparison of their characteristic impedance over frequency and phase over frequency plots. Principle Component Analysis can then be used to classify a tissue by a recorded data set.

For impedance spectroscopy two or four electrodes configuration are state of the art. Four electrodes impedance measurement allows higher accuracy, as two electrodes are used to drive in the electrical current and the other two, which are normally arranged in between the first two ones, are used the small sensing electrode.

It must be kept in mind that for tissue classification it is not necessary to record accurate impedance data from the electrical point of view. It is just important that the training data sets are recorded with the same electrode configuration to give comparable recordings.

2.4 Spectrophotometric Sensor

To enable a reliable tissue distinction a second sensor system based on a different principle is required. Tissues can be distinguished by their colour, so pulmonary valve tissue appears rather white in comparison to the surrounding more red endocardium. Integration of two optical fibres is the basis for the recording of optical reflectance spectrum in front of the catheters tip. One fibre is used for guiding the necessary light from a white LED to the point of interest. Reflected light is then received with a second fibre leading to an optical spectrophotometer working in the visible range. Unfortunately in normal condition the heart is filled with blood. Haemoglobin is a strong light absorber, where furthermore the wavelength dependent light absorption also is dependent on the oxygenation status of haemoglobin. Measuring tissue characteristics with a spectrophotometric method is therefore not possible in the presence of whole blood.

2.5 Washing System

To solve the above described problem we integrated another lumen in the catheter to provide washing solution with a small amount of physiological saline solution blood in front of the catheters tip can be washed away. Thus blood in the measuring zone is substituted with the washing solution, which enables

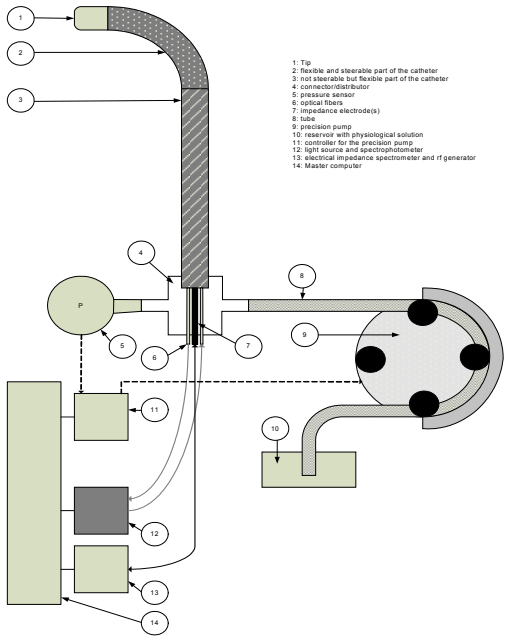

Figure 3: System setup.

spectrophotometric reflectance measurement (Sieber, A., 2007). In figure 3 the principle setup including the peristaltic pump for the physiological saline solution is shown.

2.6 Tissue Fixation

Impedance and photometric spectrum recording requires mechanically stable conditions – the tissue in front of the catheter should not move relatively to the catheter, which is difficult to realize in a moving environment like a beating heart. To solve this problem the washing system described above has a second functionality: After the blood in front of the catheter is substituted with a small amount of physiological saline solution (Figure 4, 1-3), the washing solution pump can be driven backwards, thus sucking in washing solution and creating suction in front of the catheter. Tissue in front of the catheter is sucked to the tip and a reliable electrical and mechanical connection is established (Sieber, A., 2007), and electrical impedance and optical spectroscopy are performed (Figure 4, 4-5). The maximum suction pressure used in this setup is -50 mbar.

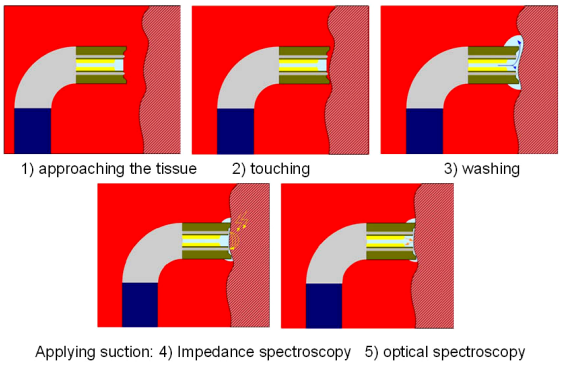

Figure 4: tissue characterisation scheme.

3 RESULTS

3.1 Catheter Prototype

To prove the feasibility of the concept a catheter was fabricated with the following specifications (Figure 5 and 6):

- diameter: 3,5 mm
- steerable tip, 2 DOF, servo actuated
- four electrodes for electrical impedance spectroscopy and radio frequency cutting
- two 500 µm optical fibers for optical reflectance spectroscopy
- housing micromachined from PEEK with 5 axis Kern CNC milling centre
- integrated washing / suction channel

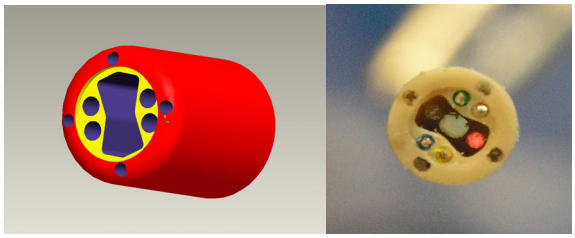

Figure 5: Catheter tip design (A) and first prototype (B).

Figure 6: Catheter prototype (A) and control with a joystick (B).

A joystick is deployed for the control of the bending of the catheter tip (Figure 6B).

3.2 System Setup

Figure 3 shows the principle setup. The catheter consists of the PEEK tip (1) with the integrated electrodes, the washing channel and the optical fibers, the steerable part (2) and the passive flexible part (3). It is connected to a distributor (4) where a pressure sensor (5) is mounted. Another port is connected to the pump providing the washing solution from a reservoir (10). The pump is connected to a microcontroller ATMEL Atmega 32 (11). This microcontroller also serves as a controller for two servos driving the Bowden cables of the catheter needed for active bending of the catheter tips (not displayed). The optical part (12) consists of a light source (white LED) and a microspectrometer [Microparts]. The electrodes are connected to a programmable precision LCR meter [TEGAM]. All the components 11, 12 and 13 are then connected to a PC. The software is written under National Instruments LabView.

3.3 Tissue Distinction

Several electrical impedance spectra of in total 10 dissected bovine pulmonary valves and surrounding endocardium were recorded (in the presence of saline solution).

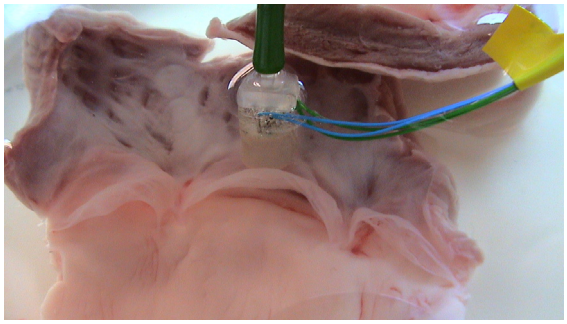

Figure 7: test setup: recording impedance spectra of pulmonary valve tissue.

Therefore a second slightly larger (5mm diameter) catheter tip was fabricated from peek again using the Kern CNC milling centre. During the recording the negative suction pressure was kept constant at -25 mbar.

The impedance spectra were recorded from 10kHz to 5 Mhz with a induced signal of 1V peak to peak. Pulmonary valve and endocardium tissue can be clearly distinguished by electrical impedance spectroscopy (see plots shown in Figure 8 and 9).

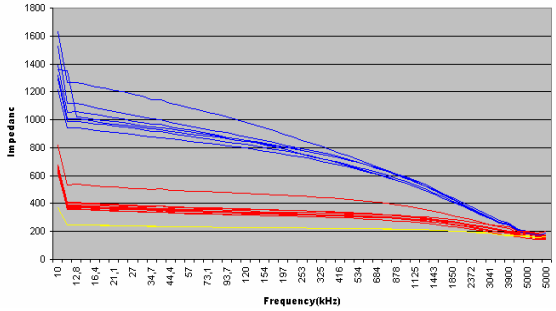

Figure 8: Impedance vs frequency endocardium: blue; pulmonary valve: red; saline solution: yellow.

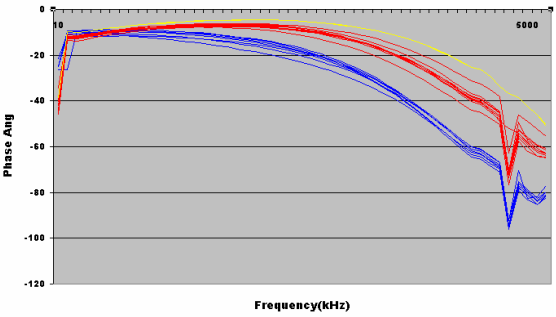

Figure 9: Phase vs frequency: endocardium: blue; pulmonary valve: red; saline solution: yellow. The negative peak at approximately 4 Mhz seems to be a result of resonance.

4 CONCLUSIONS

Pulmonary atresia is a malfunction that occurs in approximately 1 out of 20000 fetus. It can be diagnosed in the 15th week of pregnancy. A feasible approach to correct the malfunction is described, but it requires sophisticated instrumentation.
The fabrication of the first prototype is a major step towards the final catheter, which will be the key for a successful early treatment of pulmonary atresia thus offering an affected fetus a prospect to a future without handicaps.

5 FUTURE WORK

Next steps will be catheter insertion tests of the prototype on the animal model, enlargement of the impedance spectra database and in parallel the design of the miniaturized version. We envisage the substitution of the bowden wires (the actuation wires for bending of the catheters tip) by smart actuators such as Ion Polymer Metal Composites – which will enable a reduction of the overall

diameter of the catheter to 0,8 mm, or SMA actuators (Mineta, T., Mitsui, T., Watanabe, Y., Kobayashi, S., Haga, Y., Esashi, M., 2002) .
Additionally coils will be integrated, in order to give a position feedback (Salomon, O., Kosa, G., Shoham, M., Stefanini, C., Ascari, L., Dario, P., Zaaroor, M., 2006; Aurora NDI).

ACKNOWLEDGEMENTS

The work described in this paper was supported by the Austrian Research Centers GmbH, by the Fondazione Cassa di Risparmio di Pisa in the framework of the "microSURF" project for the development of innovative tools and techniques in fetal surgery, and by the ASSEMIC project, a Marie Curie Research & Training Network (MRTN-CT-2003-504826).

REFERENCES

Harrison, M. R., 2003, *Fetal Surgery: Trials, Tribulations, and Turf*, Journal of Pediatrics Surgery, 2003, Vol. 38, pp. 275-282.

Cortes, R.A., Farmer, D. L., 2004, *Recent advances in fetal surgery.* Seminars in Perinatology, 28(3):199–211

Sydorak, R. M., Albanese, C.T., 2003, *Minimal access techniques for fetal surgery*, World J Surg, Vol. 27, pp. 95–102.

Danzer, E., Sydorak, R.M.; Harrison M.R.; Albanese C.T, 2003, *Minimal assecc fetal surgery,* European Journal of Obstetrics & Gynecology and Reproductive Biology *1008 (2003) 3-13*

Flake, A.W., 2003*, Surgery in the human fetus: the future.* J Physiol (Lond), 547(1):45–51

Berris M., Shoham M., 2006, *Febotics – a marriage of fetal surgery and robotics, Computer Aided Surgery*; 11(4): 175–180

Daubeney, P.E.F.; Wang, D.; Delany, D.J.; Keeton, B.R.; Anderson, R.H.; Slavik, Z.; Flather, M.; Webber, S.A.; K., 2005, *Pulmonary atresia with intact ventricular septum: predictors of early and medium-term outcome in a population-based study*, J Thorac Cardiovasc Surg 130(4), 1071.

Litovsky, S.; Choy, M.; Park, J.; Parrish, M.; Waters, B.; Nagashima, M.; Praagh, R.V. & Praag, S.V., 2000, *Absent pulmonary valve with tricuspid atresia or severe tricuspid stenosis: report of three cases and review of the literature*, Pediatr Dev Pathol 3(4), 353--366.

Tworetzky, W., Wilkins-Haug, L., RW. Jennings, 2004, *Balloon Dilation of Severe Aortic Stenosis in the Fetus: Potential for Prevention of Hypoplastic Left Heart Syndrome: Candidate Selection, Technique, and Results of Successful Intervention*. CIRCULATION 2004,110: 2125-2131

Kohl, T., Witteler, R., Strämper, D., Gogarten, W., Asfour, B., Reckers, J., Merschhoff, G., Marcus, A.E., Weyand, M., Van Aken, H., Vogt, J., Scheld, H.H., 2003, *Operative techniques and strategies for minimally invasive fetoscopic fetal cardiac interventions in sheep*, JOURNAL OF DIGITAL IMMAGING , DECEMBER; 16, 3:

Ascari, L., Stefanini, C., Menciassi, A., Sahoo, S., Rabischong, P., Dario, P., 2003, *A new active microendoscope for exploring the sub-arachnoid space in the spinal cord,* in Proceedings of the 2003 International Conference on Robotics and Automation (ICRA), 2003.

Rigaud, B., Hamzaoui, L., Chauveau, N., Martinez, E., Morucci, J., 1994, *Tissue characterization and modeling by electrical bioimpedance spectrometry*, Proceedings of the 16th Annual International Conference of the IEEE Engineering in Medicine and Biology Society, 1994, Vol. 2, pp. 866 - 867.

Cao, H., Tungjitkusolmun, S., Choy, Y. B., Tsai, J. Z., Vorperian, V. R., Webster, J. G., 2002, *Using Electrical Impedance to Predict Catheter-Endocardial Contact During RF Cardiac Ablation*, IEEE Trans. Biomed. Eng., 2002, Vol. 49, pp. 247-253

Sieber, A., 2007, Patent: *Catheter Tip*, BI783F/BI/fpd, filed on May 30th, 2007

Mineta, T., Mitsui, T., Watanabe, Y., Kobayashi, S., Haga, Y., Esashi, M., 2002, *An active guide wire with shape memory alloy bending actuator fabricated by room temperature process*, Sensors and Actuators, A: Physical, 2002, Vol. 97-98, pp. 632–637.

Salomon, O., Kosa, G., Shoham, M., Stefanini, C., Ascari, L., Dario, P., Zaaroor, M., 2006, *Enanching endoscopic image perception using a magnetic localization system*, Computer Assisted Surgery

AURORA, NDI, http://www.ndigital.com/aurora.php

WIDE-BANDWIDTH, HIGH FRAME RATE ELECTRICAL IMPEDANCE TOMOGRAPHY / SPECTROSCOPY

A Code Division Multiplexing (CDM) Approach

A. L. McEwan, D. S. Holder
Department of Medical Physics and Bioengineering, University College London, Gower St London, UK
amcewan@ieee.org

J. Tapson
Department of Electrical Engineering, University of Cape Town, Cape Town, South Africa

A. van Schaik
School of Electrical and Information Engineering, University of Sydney, Sydney, Australia

Keywords: Electrical impedance tomography, electrical impedance spectroscopy, bioimpedance measurement, code division multiplexing.

Abstract: We present a proposal and proof-of-concept, experimental results for a new type of electrical impedance tomography / spectroscopy system that makes use of code division multiplexing to achieve two important technological advances. Assigning each channel an orthogonal code allow all the impedance measurements to be made simultaneously in time, thereby increasing the frame rate; and the use of pseudorandom input signals allows a very wide range of frequencies to be sampled simultaneously in each channel.

1 INTRODUCTION

Electrical impedance tomography (EIT), in which a volume is probed non-invasively by injecting currents (or magnetic fields) and measuring the electrical potential or magnetic fields at the periphery, has been used for physiological imaging for three decades (Holder, 2005). Its applicability in industrial situations, in which it is called process tomography, was recognized in the early 1980's (Beck and Williams, 1996), leading to a considerable investment in research into hardware, software, and reconstruction algorithms (West, 2002). More recently, there has been a growing interest in obtaining material contrast in the images by discriminating on the basis of the frequency response of impedance; this is electrical impedance spectroscopy (EIS) (Brown, 2001). The combination of the two methods is generally called EITS.

In the standard implementation of EIT, the complex impedance is measured in terms of resistance and capacitance. A ring of (usually 8 or 16) electrodes is placed around the volume to be imaged (generally, a single plane or slice is imaged, and volumes reconstructed from a number of planes; hence the use of the word tomography). A current is injected through a pair of the electrodes, and the resulting electrical potentials measured at all of the other electrodes. The signals are separated into a resistive and a capacitive signal, either by measuring the complex impedance directly, or by using separate ohmic and capacitive electrodes.

If the frequency of the injected current is swept through a range, or stepped through a set of fixed frequencies, the spectral response may also be obtained. The current excitation is then switched to a new pair of electrodes, and a new data set acquired. When all the desired combinations have been measured, a reconstruction algorithm is used to produce an approximation of the distribution of material within the image plane, based on its impedance (in EIT) or impedance spectrum (in EITS). The reconstruction of EITS images is an area of active research, and many different methods are available (Polydorides and Lionheart, 2002).

There are a number of standard patterns of excitation and measurement in EITS. The most commonplace is that adjacent pairs of electrodes are

used to inject current, and potentials are measured at all other adjacent pairs. This method has the advantage that once a pair of electrodes has been used for current injection, and its response at all other electrodes measured, it is thereafter redundant to measure potentials at that pair and therefore the number of measurements required is reduced. Regardless of the pattern used, a single frame of EIT data requires a great many measurements (the adjacent-pair method requires $k = n \times (n-1)$ measurements for n electrodes); and this number must be multiplied by the number of frequency points required.

Taking a frame of EIT data using sequential measurements – so-called time-division multiplexed or TDM measurements) is slow, so that frame rates in excess of 100 frames/second are extremely difficult to achieve. Wilkinson and co-workers (2003) have optimized the TDM process to a very high degree, achieving frames rates of up to 1000 frames/s; but most laboratory and commercial systems operate at orders of magnitude slower than this. EITS systems are slower still, with frame rates of 13 seconds/frame achievable with a frequency range of 20 Hz – 128 kHz in current systems (McEwan et al., 2006). A basic constraint in EITS frame rate is imposed by the lower limit of spectral bandwidth; for example, if the impedance at 20Hz is required, the frame rate per second will be limited to $20/k$, where k is the number of sequential measurements required per frame; even this limit implies sampling only a single cycle of the lowest frequency per measurement, which is somewhat difficult to achieve in practice.

A method which presents itself for increasing the frame rate is simultaneously to inject currents which are modulated to be mathematically orthogonal, so that their contributions to the potential at any electrode can be separated by demodulation. For example, if a current of frequency f_1 is injected at one pair of electrodes, and a current of frequency f_2 at a second pair, then the potential across a third pair of electrodes can be separated into a component due to f_1 and a component due to f_2 by synchronously demodulating with those frequencies. The complex components of impedance can be extracted by in-phase and quadrature synchronous demodulation. This is called frequency-division multiplexed (FDM) EIT.

FDM EIT appears to have been developed simultaneously by Tapson and colleagues (Tapson & Teague, 2002), and Zimmermann and colleagues (Zimmermann et al., 2002); although as both developments were patented and not published in the scientific literature, public domain details are few (Teague, 2002).

A number of problems are encountered in FDM EIT as a consequence of accommodating simultaneous current injection and voltage measurement on the same electrode. If the current and voltage form part of the same impedance calculation, this comprises a two-terminal impedance measurement; whereas it is generally considered that a four-terminal measurement is required to avoid the problem of inadvertently including the contact or terminal resistance in the specimen resistance. If the current and voltage form part of a separate calculation, then this problem is avoided.

A second issue is that the current through any terminal must be a sum of orthogonal component currents, and equal and opposite components must flow through some other terminal. Ensuring that the net current due to each component is zero is electronically complicated, and has not been attempted in any of the known FDM EIT systems. These systems have generally avoided these problems by using separate sets of current injection and voltage measurement electrodes, although this has the disadvantage that twice the number of electrodes are required to obtain the same resolution. Data comparing the resolution of FDM and TDM systems is scarce (Goldswain & Tapson, 2006), but those results as well as unpublished work (Elliot, 2006) suggest that FDM systems are at least as accurate as TDM systems.

In this paper we present a new approach to EITS instrumentation. We make use of Code-Division Multiplexing (CDM) to inject orthogonal currents simultaneously, and to demodulate the resulting potentials. This has an enormous advantage over FDM and TDM techniques, in that it is possible to sample at multiple frequencies simultaneously while sampling multiple physical channels. The result is a system in which wide-bandwidth multi-electrode spectroscopy can be performed in times equivalent to that taken for single measurements in current EITS systems. The CDM process can be seen as a natural extension of FDM EIT, and many of the same issues apply. In order to deal with the problem of sharing electrodes between multiple measurement channels, we have developed a simple current injection arrangement at the electrode, based on high-frequency transformers, which guarantees a net zero current flow for each orthogonal component. The new system is described in detail in the following sections.

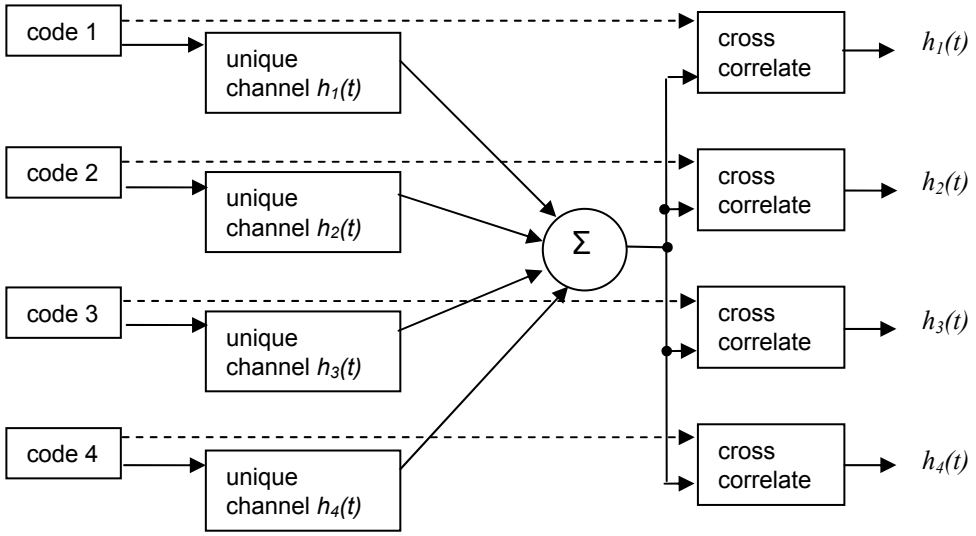

Figure 1: The code-division multiplexing principle. Each unique channel in the measurement system is stimulated using a driving signal modulated with a unique binary pseudorandom (PRN) code. The channels are then either deliberately or inadvertently mixed together. At the receivers, the contribution due to each channel is recovered by cross-correlating the signal at the receiver, and a copy of the driving signal containing the channel's characteristic code. If the codes are orthogonal or near-orthogonal, there should be complete separation of components. Serendipitously, the cross-correlation produces the impulse response of the channel (see Equations 1-6).

2 CODE-DIVISION MULTIPLEXING OF EIT CHANNELS

The principle of CDM is that the signal through a particular channel is modulated using a unique binary digital code (see Figure 1). A receiver which is receiving several channels can separate the data for each channel by demodulating using a copy of the same code. There are a number of different codes which may be used. The basic requirements are that there should be at least one code per channel; that the codes should be orthogonal, or nearly so; and that the autocorrelation functions of the codes should be flat with a single sharp peak (in the ideal case, approximating a delta function) (Sarwate & Pursley, 1980). The codes which we have used in this work are called Gold codes, and are used in the Global Positioning System (GPS) to encode the signals from the GPS satellite constellation; these signals can then be unambiguously demodulated by a terrestrial GPS receiver equipped with copies of the codes (Parkinson & Spilker, 1996). The codes are bit sequences which appear to be random, but in fact are deterministically generated, usually by means of a modulo-addition of bits in a shift register. Codes of this type are generally referred to as pseudorandom noise (PRN) sequences, as they appear to be random and have the characteristics of noise.

In this system, we achieve two important goals using CDM. Firstly, the use of CDM allows us to take measurements over all the channels simultaneously. Secondly, the spectral characteristics of the CDM input signal effectively interrogate the sample over a wide range of frequencies, and the output signals can be transformed to produce a spectrum, giving us simultaneous wide-band spectroscopy on all channels. The following two sections explain these features.

2.1 The Use of Code Division Multiplexing to Provide Simultaneous Measurement

The use of CDM in an EIT system is shown conceptually in Figure 1. We use the PRN codes as the input stimulus to a system. The system has a unique channel for each input, but unfortunately all the channel outputs are combined linearly, so that the unique response for each channel is not explicitly available.

When we perform a cross-correlation R_{IO} between the unique input signals I_n and the combined output signal O_n, we are calculating:

$$R_{I_1O}(m) = \frac{1}{N}\sum_{n=0}^{N-1} I_{1n} O_{n-m} \qquad (1)$$

where N is the epoch length of the PRN (nominally, 1023 bits, or the equivalent number of samples).

The output at any time k can be stated as the sum of the convolution of the impulse responses for the channels and the respective inputs:

$$O_k = \sum_{i=0}^{k} I_{1i} h_{1(k-i)} + \sum_{i=0}^{k} I_{2i} h_{2(k-i)} + \sum_{i=0}^{k} I_{3i} h_{3(k-i)} + \ldots \qquad (2)$$

If we substitute this into the cross-correlation, say for I_1 and the output:

$$\begin{aligned} R_{I_1O}(m) &= \frac{1}{N}\sum_{n=0}^{N-1} I_{1n}\left[\sum_{i=0}^{n-m} I_{1i} h_{1(n-m-i)} + \right. \\ &\qquad \left. \sum_{i=0}^{n-m} I_{2i} h_{2(n-m-i)} + \sum_{i=0}^{n-m} I_{3i} h_{3(n-m-i)} + \ldots \right. \\ &= \frac{1}{N}\sum_{n=0}^{N-1} I_{1n} \sum_{i=0}^{n-m} I_{1i} h_{1(n-m-i)} + \\ &\qquad \frac{1}{N}\sum_{n=0}^{N-1} I_{1n} \sum_{i=0}^{n-m} I_{2i} h_{2(n-m-i)} + \ldots \\ &= \frac{1}{N}\sum_{n=0}^{N-1}\sum_{i=0}^{n-m} I_{1n} I_{1i} h_{1(n-m-i)} + \\ &\qquad \frac{1}{N}\sum_{n=0}^{N-1}\sum_{i=0}^{n-m} I_{1n} I_{2i} h_{2(n-m-i)} + \ldots \end{aligned} \qquad (3)$$

Given that:

$$\sum_{i=0}^{k} I_{1i} h_{1(k-i)} = \sum_{i=0}^{k} I_{1(k-i)} h_{1k} \qquad (4)$$

We can rearrange as follows:

$$\begin{aligned} R_{I_1O}(m) &= \frac{1}{N}\sum_{n=0}^{N-1}\sum_{i=0}^{n-m} I_{1n} I_{1(n-m-i)} h_{1i} + \\ &\qquad \frac{1}{N}\sum_{n=0}^{N-1}\sum_{i=0}^{n-m} I_{1n} I_{2(n-m-i)} h_{2i} + \ldots \\ &= \sum_{i=0}^{n-m} R_{I_1I_1}(m-i) h_{1i} + \\ &\qquad \sum_{i=0}^{n-m} R_{I_1I_2}(m-i) h_{1i} + \ldots \\ &= R_{I_1I_i} * h_1 \\ &= h_1(m) \end{aligned} \qquad (5)$$

The cross-correlation terms (those R_{II} terms with non-identical indices for I) will sum to zero, because different Gold codes are effectively uncorrelated; so only the first correlation is non-zero. In continuous terms:

$$\begin{aligned} R_{I_1O}(t) &= R_{I_1I_1}(t) * h_1(t) \\ &= \delta(t) * h_1(t) \\ &= h_1(t) \end{aligned} \qquad (6)$$

The output of the cross-correlation is the impulse response of the channel, which represents the time-domain transform of the information we want.

2.2 Hardware Implementation

Part of the proposed hardware implementation is shown on the following page, with a number of elements not shown to improve clarity. We use transformer coupling of the drive currents to the EIT electrodes in order to ensure matched source and sink currents. There is a resistor in each transformer secondary, to allow direct measurement of the current in the secondary. The way in which the system works is as follows. The microprocessor system outputs currents which are modulated in polarity by the Gold codes (using push-pull drive from two port pins, with a series resistor for current limiting). Each of the eight transformer secondaries is connected to a pair of electrodes, so that each electrode is connected to the high side of one secondary and the low side of another.

In principle, the current between terminals T1 and T2 should have a fixed amplitude, modulated in polarity by Code 1. In practice, we measure this current by sampling the voltage at the points V_1 and VT_1, and dividing the difference by the resistor value.

We can then calculate the impulse response for the voltage between T_4 and T_5, with respect to the current between T_1 and T_2, by cross-correlating the voltages (V_1 - VT_1) and (V_5 – V_4); and so on.

2.3 Spectral Response of the CDM System

As discussed earlier, PRN sequences have the appearance of noise, and like uniformly distributed white noise, their spectrum is flat within the limits of bandwidth. They are also delta-correlated; that is to say, their autocorrelation function consists of a Dirac delta function at the origin. This is the basis of their usefulness in demodulation, as shown above. From (6) above we see that the input-output cross-correlation function of a channel in the system pro-

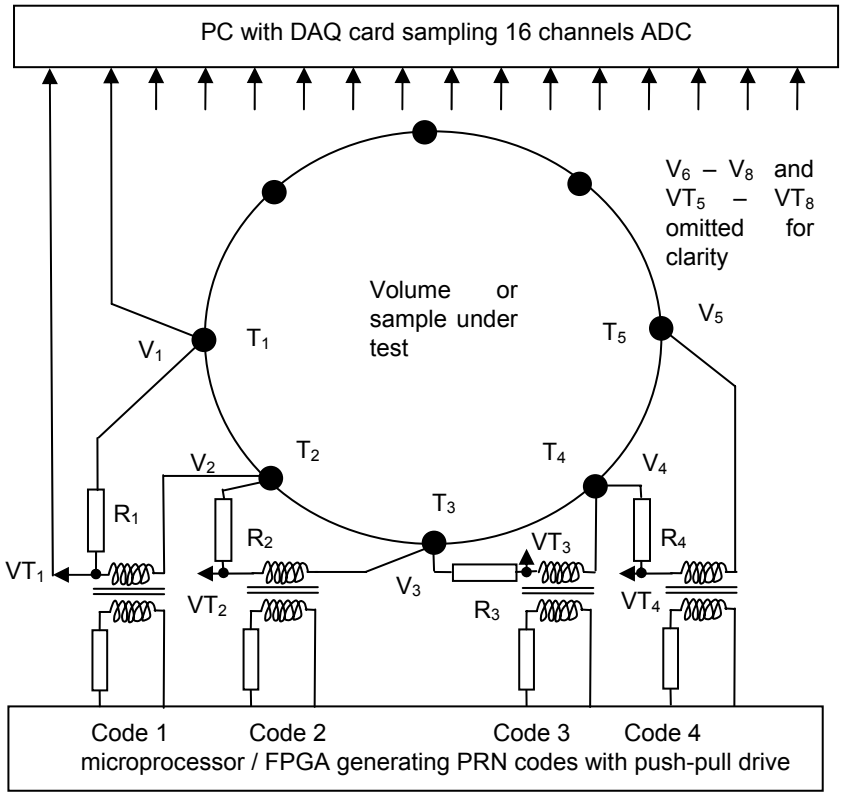

Figure 2: Block diagram of the proposed system, showing multiple electrodes at which drive and reception of signals is combined. Transformer coupling allows inflowing and outflowing currents due to each code to be exactly balanced, as well as providing isolation for safety. The voltage across each ballast resistor gives the current due to that code (e.g. the current due to Code 3 is $I_3 = (VT_3 - V_3)/R_3$).

duces the transfer function *h(t)* of the channel. If we take the Fourier transform of the cross-correlation function:

$$\begin{aligned} G(\omega) &= \int_{-\infty}^{\infty} R_{I,O}(t) e^{-j\omega t} dt \\ &= \int_{-\infty}^{\infty} h(t) e^{-j\omega t} dt \\ &= h(\omega) \end{aligned} \quad (7)$$

so, the Fourier transform of the cross-correlation function produces the frequency response of the channel; which is to say, the complex spectrum of the channel impedance.

3 PROOF OF CONCEPT – EXPERIMENTAL RESULTS

3.1 Method

In order to establish the workability of this concept, we require to demonstrate two methods:

- The feasibility of extracting wide-range, high resolution impedance measurements when driving the channels with PRN codes.
- The feasibility of simultaneously stimulating several channels and recovering the individual signals from the multiplexed signal by demodulation.

We have done this as a proof-of-concept by conducting an imaging experiment with an existing EITS system, using both the standard sinusoidal waveforms, and a new waveform based on the Gold code intended for CDM-EIT.

A serial, EITS system, the UCL Mk2.5, was reprogrammed with the 1st 1023-length code of a set of eight Gold codes. Only one code was used as the Mk2.5 is based on a single channel of the Sheffield Mk3.5 system multiplexed to 32 electrodes. In normal operation the Mk2.5 system measures the spectrum using a 2048-length composite waveform of 10 frequencies of equal amplitude, logarithmically spaced between 2kHz and 1MHz (McEwan et al., 2006; Wilson et al., 2001). The Gold code was sampled at 2samples/bit to meet the

Nyquist criteria with an additional zero bit added to ensure its length was 2^{12}. This is required by the matched filter which is performed by the system DSP processor. As the length of both test waveforms are the same, and the timing of the system clock (2MHz) was unchanged, they span the same frequency range of 2kHz-1MHz. For simplicity, and to ensure that the instrumentation did not saturate, the amplitude of the gold code waveform was set to the maximum of the composite waveform.

An often used test of an EITS system is its ability to produce images of an object in a tank filled with saline solution. Boundary voltage measurements are collected from the tank with and without the object (so-called *perturbation* and *reference* frames). These two sets of data are subtracted then used with a reconstruction algorithm to produce a *time-difference* image. In keeping with previous EITS measurements we chose to use a piece of banana as our object, as it changes impedance by over 100% between 2kHz and 1MHz (Yerworth et al., 2003). The saline solution's impedance will remain relatively unchanged over the same frequency range and hence it is possible to determine the spectrum of the object inside the tank from a sequence of images at the measured frequencies.

The tank was cylindrical, 10cm diameter, filled with 0.1% saline solution with 16 stainless steel electrodes in a ring. The test object was a cylinder of banana, 2 cm long and 1 cm in diameter. Image reconstruction was done using a linear solver (EIDORS) (Polydorides and Lionheart, 2002) and a 15,000 element FEM mesh of the tank.

3.1.1 Results

The spectra for the banana object were constructed by plotting the value of a pixel in the known position of the object, at 10 different frequencies.

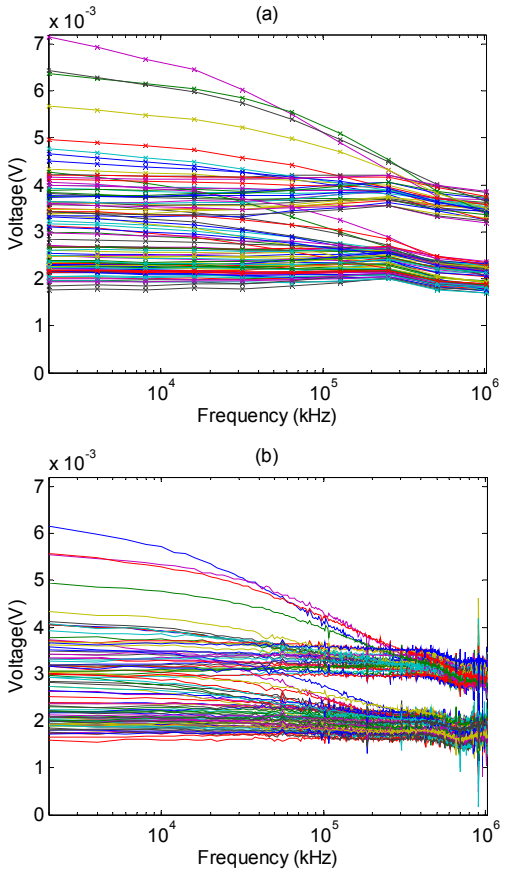

Figure 3: Comparison of boundary voltage measurements in a single frame. Each line is a different electrode combination measurement. Larger voltages occur when the voltage electrodes are near current-carrying electrodes. Combinations more sensitive to the perturbation show a greater change over frequency. Figure 3(a) shows a composite representation of the output of the standard 10 frequency system. Figure 3 (b) shows the output of the new system, using PRN codes for excitation and demodulation. It can be seen that the PRN codes provide the same response as the standard method, but with a much higher resolution in frequency.

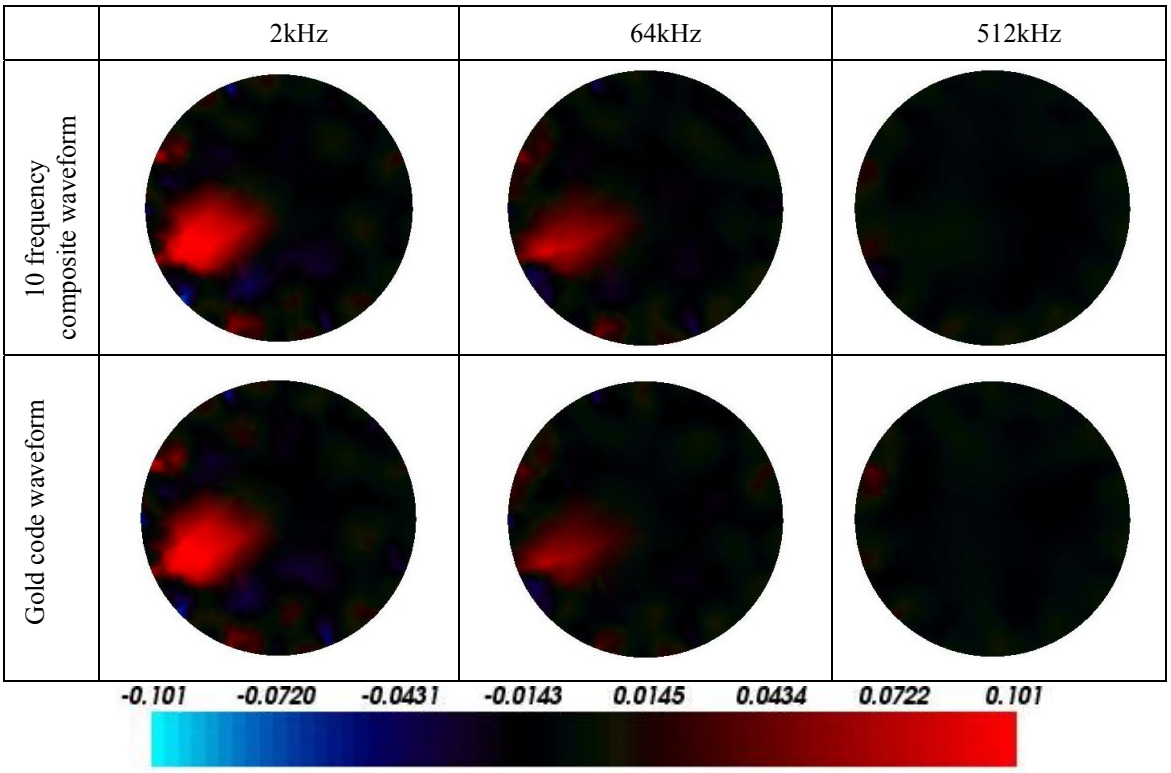

Figure 4: Time difference images collected at three frequencies using the two waveforms. As the frequency increases, the contrast (impedance difference) between perturbation and background decreases. It can be seen that the new PRN (Gold code) method offers the same resolution as the standard 10-frequency method, with the potential for significantly faster operation.

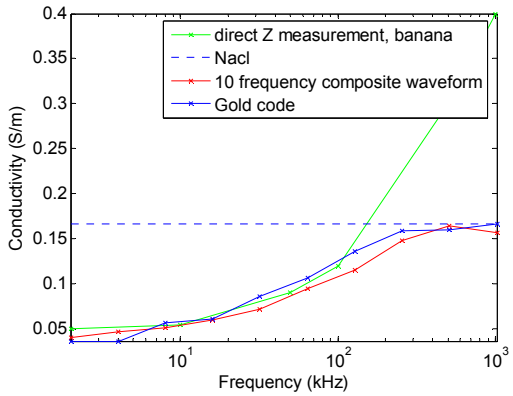

Figure 5: Spectra obtained from the data used in Figure 4. These spectra are similar to those that have been previously obtained from the Mk2.5 system. The new method produces a spectrum which is very similar to the standard method. Both EITS spectra deviate from a direct measurement at frequencies above 128kHz, for reasons explained below.

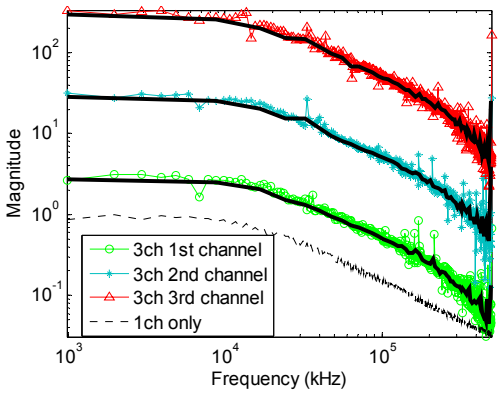

Figure 6: Spectral magnitude for three multiplexed channels, independently stimulated with PRN codes, mixed together on a single circuit impedance, and then demodulated. For clarity each channel has been multiplied by 10^x where x is the channel number. It can be seen that the multiplexed signals can be independently recovered after mixing, and are a good match (although noisier) to the single channel case. The thick black lines show a average spectra, possible due to the large number of frequencies available in this method.

4 DISCUSSION

The boundary voltages measurements using the two waveforms are similar, as shown in Figure 3. The PRN code voltage measurements are 1mV lower, due to the lower current per frequency component. As this is constant between the perturbation and reference frames, it is cancelled out in the subtraction process and is not apparent in the images. The PRN code boundary voltages appear to be noisier, particularly at higher frequencies. In practice these frequencies would be averaged together reducing the noise. The Mk2.5 EIT system has limited performance at frequencies above 128kHz due to the effect of 0.5m long unscreened cables. These are likely to be the cause of the increased noise seen in the PRN code spectra, a real effect which is not seen in the lower frequency resolution of the 10 frequency composite waveform. The 128kHz limit is also apparent in the spectra, which deviate from a direct impedance measurement above this frequency.

We have shown the feasibility of using PRN codes for EITS, both in extracting the system impulse response, and in terms of simultaneous excitation and demodulation. The images and extracted spectra are very similar to those obtained using the standard method, demonstrating the proof of the concept of using CDM waveforms for EIT acquisition. The primary advantage of greatly increased frequency resolution for the same acquisition time has been demonstrated. We are currently implementing a multiple source system which should lead to a system with two orders of magnitude increase in frame rate over the standard method, along with the improved frequency resolution demonstrated here.

ACKNOWLEDGEMENTS

Action Medical Research RTF 3110 and The University of Sydney International Visiting Research Fellowship 2007.

REFERENCES

Beck, M.S. & Williams, R.A. (1996). Process tomography: a European innovation and its applications, *Meas. Sci. Technol.* , 7, 215–24.

Brown, B.H. (2001). Medical impedance tomography and process impedance tomography: a brief review, *Meas. Sci. Technol.,* 12, 991-996.

Elliot, J. (2006). *Electrical impedance tomography imaging of a hydrocyclone*, M.Sc thesis (University of Cape Town).

Goldswain, G., & Tapson, J. (2006). Kernel ridge regression for volume fraction prediction in electrical impedance tomography, *Meas. Sci. Technol.,* 17, 2711-2720.

Holder, D.S. (ed.) (2005). *Electrical Impedance Tomography: Methods, History and Applications*, Bristol and Philadelphia: IOP.

McEwan, A., Romsauerova, A., Yerworth, R., Horesh, L., Bayford, R., & Holder, D. (2006). Design and calibration of a compact multi-frequency EIT system for acute stroke imaging, *Physiol. Meas*., 27, S199-S210.

Parkinson, B.W., & Spilker Jr., J.J. (1996). *Global Positioning System: Theory and Applications, vol. 1*, Am. Inst. Aeronautics and Astronautics Inc., Washington.

Polydorides, N. & Lionheart W.R.B. (2002). A Matlab toolkit for three-dimensional electrical impedance tomography: a contribution to the Electrical Impedance and Diffuse Optical Reconstruction Software project, *Meas. Sci. Technol.,* 13, 1871-1883.

Tapson, J., & Teague, G. (2002). *Method and Apparatus for Electrical Impedance Tomography*, SA Patent 2002/3689.

Teague, G. (2002). *Mass Flow Measurement of Multi-Phase Mixtures by Means of Tomographic Techniques,* PhD thesis, (University of Cape Town). retrieved June 24, 2007 from http://mysite.mweb.co.za/ residents/ jontapson/

Sarwate, D.V., & Pursley, M.B. (1980). Crosscorrelation properties of pseudorandom and related sequences, *Proc. IEEE*, 68, 593-619.

West, R. (ed,) (2002). Special Feature: Process Tomography, *Meas. Sci. Technol,*. 13, 1799-1902.

Wilkinson, A.J., Randall, E.W., Durrett, D., Naidoo, T. & Cilliers, J.J. (2003). The design of a 1000 frames per second ERT data capture system and calibration techniques employed. *Proc. 3rd World Congress on Industrial Process Tomography,* Banff, 504-509.

Wilson, A.J., Milnes, P., Waterworth, A.R., Smallwood, R.H., & Brown, B.H. (2001). Mk3.5: a modular, multi-frequency successor to the Mk3a EIS/EIT system, *Physiol. Meas.,* 22, 49-54.

Yerworth, R.J., Bayford, R.H., Brown, B., Milnes, P., Conway, M. & Holder, D.S. (2003). Electrical impedance tomography spectroscopy (EITS) for human head imaging, *Physiol. Meas.*, 24, 477-489.

Zimmermann, E., Glaas, W., Verweerd, A., Tillmann, A., & Kemna, A. (2002). *Method and apparatus for rapid tomographic measurements of the electrical conductivity distribution of a sample*, German patent DE 102 38 824.

SIMULTANEOUS WIRELESS MEASUREMENT OF BLOOD PRESSURE AND SYMPATHETIC NERVE ACTIVITY

A System for Investigating Neural Control Mechanisms in Long Term Blood Pressure Regulation

Daniel McCormick[1], Robert Kirton[1], Alan Easteal[2], Simon Malpas[1,3], Carolyn J. Barret[3]
Sarah Jane Guild[3], Poul Nielson[1], Augio Patrick Hu[4], David Budgett[1]
[1]*Auckland Bioengineering Institute,* [2]*Department of Chemistry* [3]*Department of Physiology*
[4]*Department of Electrical and Computer Engineering, University of Auckland, Symonds Street, Auckland, New Zealand*
d.mccormick@auckland.ac.nz, r.kirton@auckland.ac.nz, a.easteal@auckland.ac.nz, s.malpas@auckland.ac.nz
c.barrett@auckland.ac.nz, s.guild@auckland.ac.nz, p.nielsen@auckland.ac.nz, a.hu@auckland.ac.nz
d.budgett@auckland.ac.nz

Matthew Lim
Telemetry Research Ltd, PO Box 5504, Auckland, New Zealand
m.lim@auckland.ac.nz,

Bruce van Vliet
Division of BioMedical Sciences, Faculty of Medicine, Memorial University of Newfoundland, Saint John's, Newfoundland
vanvliet@mun.ca

Keywords: Telemetry, Inductively Coupled Power Transfer, Sympathetic Nerve Activity, Blood Pressure, Bio-potential.

Abstract: We report on the development of a combined sympathetic nerve activity and blood pressure telemeter for long term implantation in freely moving small animals. The devices simultaneously records and transmits blood pressure, temperature and sympathetic nerve data on the 2.4 GHz ISM band with a range of 5 m. Blood pressure is measured with a 400 Hz bandwidth, fluid filled catheter at a resolution of 0.1 mmHg. Sympathetic nerve activity is measured differentially using stainless steel electrodes attached to the renal nerve. The telemeter measures 29x37x12mm (a volume of approximately 9.5 cm^3) and weighs 17g, making it suitable for use in rats with a weight greater than 170 g. Battery life is 12 h when used continuously, however the device's lifespan is effectively indefinite due to the use of in vivo inductively coupled battery charging. Example data recorded in a conscious unconstrained rat is provided which verifies the telemeters operation.

1 INTRODUCTION

Elevated blood pressure is a well established factor in determining an individual's risk of developing a number of serious diseases, including heart failure, renal failure and stroke (Whelton and Klag 1989; MacMahon 2000). Although the short-term regulation of blood pressure is well understood, not much is known about the regulation of blood pressure over the longer-term.

Recently, with the development of long life implantable telemetry, researchers have been able to investigate the role of the sympathetic nervous system in regulating blood pressure over longer time periods and under more natural unconstrained conditions. It is clear that the sympathetic nervous system is key to the short term regulation of blood pressure. However, much less is known about its role in regulating blood pressure over long time periods (Mark 1996). One method of investigating this relationship is to measure the sympathetic nervous system's output directly by exposing nerve fibre bundles and recording action potentials directly. The level of sympathetic nerve activity

(SNA) can then be compared with simultaineoulsy aquired blood pressure measurements; allowing researchers to experimentally investigate their interaction.

Previously, researchers have had to implant two seperate devices in order to record blood pressure (Data Sciences International,St Paul, Minnisota) and SNA (Telemetry Research, Auckland, New Zealand) simutaineously over long periods of time (Barrett, Ramchandra et al. 2003). This has meant that research has typically been constrained to larger animals such as rabbits. In this paper we present a combined SNA and blood presssure telemeter that can be implanted in animals as small as rats.

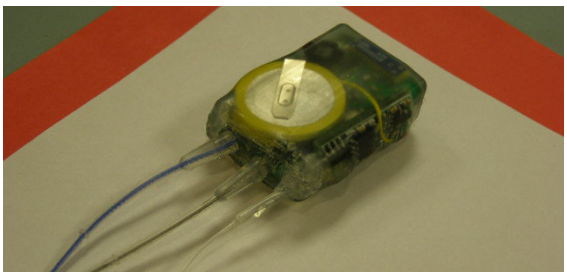

Figure 1: The SNA and BP telemeter.

Figure 2: Wireless charger (right rear) and charging pad (foreground), implantable telemeter (on charger pad), and analogue reconstruction units for pressure and SNA (left rear).

Figure 1 shows the new experimental telemeter. The leftmost leads are the nerve electrodes. At the right is the fluid filled catheter for BP measurements. Visible on top is the rechargable lithium ion coin cell which provides power to the telemeter between chargings. Inductive power transfer is used to recharge the battery anytime while still implanted. The electronics and electrodes are incapsulated in medical grade silicon elastomer. The telemeter measures 25x37x12mm (W x L x H, excluding electrodes and catheter), occupies a volume of approximately 9.5 cm^3 and weighs 17g, making it suitable for use in rats with a weight greater than 170 g (Moran, Roy et al. 1998).

Table 1: A Comparison between two existing commercial telemeters which are capable of measuring both blood pressure and bio-potential signals (Data Sciences International C50-PXT and Konigsberg T31F) and the new type.

	C50-PXT	T31F	New
LxWxH	30x15[1]	33x15x10	29x37x10
Volume	6	5	9.5
Weight	11	13	17
#Bio Channels	1	2	1
Bio Bandwidth	1-100Hz[2]	0.1-250 Hz[2]	1-4 kHz
Pk-Pk Range	Unknown	1 mV[3]	120 µV
BP Bandwidth	<100Hz[4]	>1KHz	120Hz
Stability	5 mmHg	3 mmHg[2]	T.B.D.
Batt Life	2 month	6 month	12 hour[5]
#Trans Ch.	1	20	12
Trans. Type	AM	FM	2.4GHz

1. Cylinder (Length x Diameter).
2. Best estimate based on other devices made by the manufacturer.
3. Smallest available input range.
4. Measured using frequency response rig.
5. Between charging.

Table 1 presents a summary of the specifications of the new telemeter and its nearest comercially available equivalents. These comparison devices were chosen based on their size (small enough to be used in a rat) and ability to measure both biopoential signals and blood pressure. The major areas where the new device differs from its equivelents are the higher bandwith and sensitivity of the biopotential ampifier, the abiltiy to recharge the new divice in vivo and the use of a digital transmision system.

2 METHODS

2.1 System Architecture

The heart of the system is an 8051 microcontroller which acts as an interface between the various systems. An 8 channel (multiplexed) 12 bit A/D converter is used to digitise recorded data. A bi-directional transceiver operating on the 2.4 GHz ISM band is used for communication, including data transmission. This has a number of advantages including the ability to wirelessly schedule

measurements in vitro. Additionally, 12 channels are available for communication, allowing multiple instrumented animals to be housed in close proximity.

Power is provided wirelessly to the implant using inductively coupled power transfer (Budgett, Hu et al. 2007). This has allowed high power devices (relatively speaking) such as A/D converters, microcontrollers and digital transmission systems to be used. During use, the implant can be charged by placing a coil under the animal's home cage through which high frequency AC current is passed. Power is received at the implant by a ferrite pickup which is magnetically coupled to the charging coil. Information about the charge state of the battery and power received are embedded in the BP/SNA data packets and transmitted to the wireless power supply. The magnetic field can then be controlled such that only the required amount of power is delivered to the implant. This reduces the temperature rise during charging to approximately 5°C.

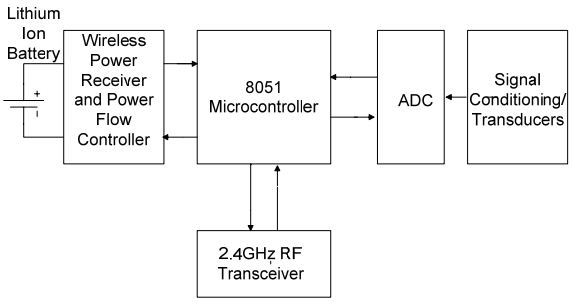

Figure 3: Block diagram of the telemeter.

Between charging, a 70 mAH lithium ion coin cell provides power. Consumption is 6 mA during continuous operation which results in a battery life of 12 h. In vivo charging takes between 2 and 4 hours and is dependent on how active the animal is and how close the implant's orientation is to the optimum for charging. During charging SNA recording is not possible as the nerve signal is swamped by noise generated by the 200 kHz charging field.

2.2 Blood Pressure Measurements

Blood pressure measurements are performed using a 10cm fluid filled polyurethane catheter, which acts as an interface between the measurement site (for instance the aorta) and the piezo resistive pressure transducer in the telemeter. Pressure waveforms are transmitted along the catheter using low viscosity biocompatible fluid. No obvious reference pressure is available internally to make measurements against. Therefore, an absolute pressure sensor (one with an internal vacuum reference) is used. Physiologically, the pressure of interest is the difference between the blood pressure and the ambient or atmospheric pressure. This pressure is derived by measuring the atmospheric pressure using a second absolute transducer and subtracting it from the internal pressure.

2.2.1 Frequency Response

Accurate measurements of systolic and diastolic pressure require the use of a wide bandwidth measurement system. One historical rule of thumb is that the bandwidth should be greater than 10 times the heart rate (Gabe 1972). For a rat, the maximum heart rate that can be reasonably expected is 500 beats per minute. This requires a bandwidth of greater than 80 Hz.

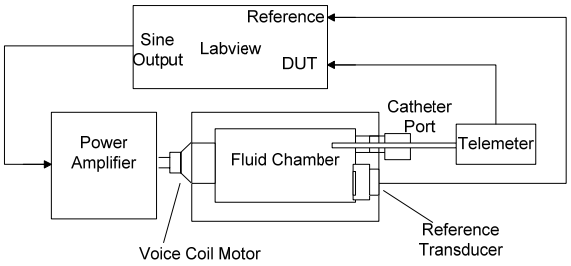

Figure 4: Frequency Response Measurement System.

In order to characterise the telemeters pressure measurement bandwidth, the rig represented by Figure 4 was constructed. A fluid filled chamber acts as a pressure source for frequency response measurements. Pressure waveforms are generated by a voice coil actuator which exerts force on the fluid through a thin brass diaphragm. The catheter of the device under test (DUT) is inserted into the chamber using a luer lock adaptor. A second high bandwidth transducer provides a reference pressure for calculations. Provided compliance of the chamber is minimized, the system's measurement bandwidth can be high. Bandwidths of 5 kHz (-3 dB) have been attained with usable signals present until approx 15 kHz.

Tests are preformed using the swept sine technique where sinusoidal perturbations are applied to the DUT. The LabVIEW Sound and Vibration Analysis Toolbox (www.labview.com) automatically calculates the magnitude transfer function from reference pressure (P_{ref}) to telemeter output (P_T) as defined by equation 1.

A typical transfer function is presented in Figure 5. The bandwidth (-3 dB point) of the catheter/amplifier combination (blue) is 400 Hz. This is more that four times greater than the required bandwidth of 80 Hz as described above. Gain peaking is evident at around 100 Hz, but its magnitude is exaggerated by the small vertical scale and only amounts to a 15% increase in gain. The small dip in magnitude at 50 Hz is due to power line interference (in the test rig).After sampling at 500 Hz, transmission, reconstruction and filtering the -3 dB frequency is reduced to 120Hz.

$$\left\|M(j\omega)\right\|_{dB} = 20Log\left\|\frac{P_T(j\omega)}{P_{ref}(j\omega)}\right\| \qquad (1)$$

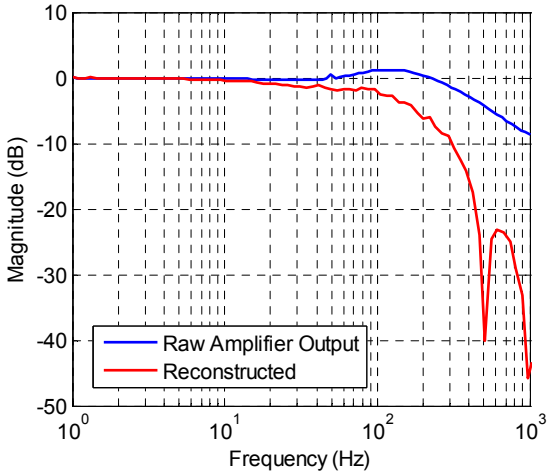

Figure 5: Frequency Response of the blood pressure measurement system. Amplified pressure sensor output (blue) and reconstructed response after transmission (red).

2.3 SNA

2.3.1 The Nature of SNA

Postganglionic sympathetic nerves are composed of multitudes of unmyelinated fibres. The action potentials generated by individual fibres are small and difficult to measure. Because of this, the entire nerve bundle is usually used when recording SNA. Typically two electrodes placed on the nerve and a differential measurement is made. Measurable voltages result as large numbers of fibres fire almost simultaneously whose contributions are additive in nature. Even so, the potentials generated by a whole bundle are still only in the µV range. This, combined with the relatively high frequency content of the signals (into the kHz range (Malpas 1998)) make instrumentation troublesome, and especially so in a micro power telemetry system.

2.3.2 Signal Acquisition

Figure 6 shows the approach taken, which is similar in nature to many previously described AC coupled bio-potential amplifiers (Prutchi and Norris 2005).

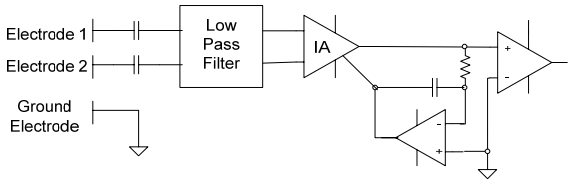

Figure 6: Nerve Electrode Amplifier.

With a system gain of 10000 and a 3V power supply, the amplifier is susceptible to saturation due to electrode polarization offsets. Capacitively coupling the active electrodes reduces the likely hood of this happening but requires the use of a third reference electrode. A low noise Instrumentation amplifier (IA) amplifies and level shifts the signal for analogue to digital conversion. A servo amplifier monitors the DC level of the nerve signal and centres it in the A/D converter's range. This is effectively a second form of AC coupling but also improves headroom by reducing the effects of input offset voltage. With a gain of 10000, the typical input offset voltage of an instrumentation amplifier (50 - 500 µV) could easily cause saturation. Digitization is performed using a 12 bit A/D running at 8 kHz. Full scale input range is ±60 µV. Intrinsic noise is 650 nV_{RMS} over the devices Bandwidth of 1 Hz-4 kHz. This results in a signal to noise ratio of 37 dB for a full scale sinusoidal input.

3 EXPERIMENTAL RESULTS

3.1 Experimental Procedure

Experiments were conducted in Wistar rats with initial minimum weight of 250g and were approved by the University of Auckland Animal Ethics Committee (approval R543). The rats were housed individually in standard rat cages, with food and water available ad libitum. The room was kept at a constant temperature (18 °C) and dark-light cycle (lights on from 0600 to 1800).

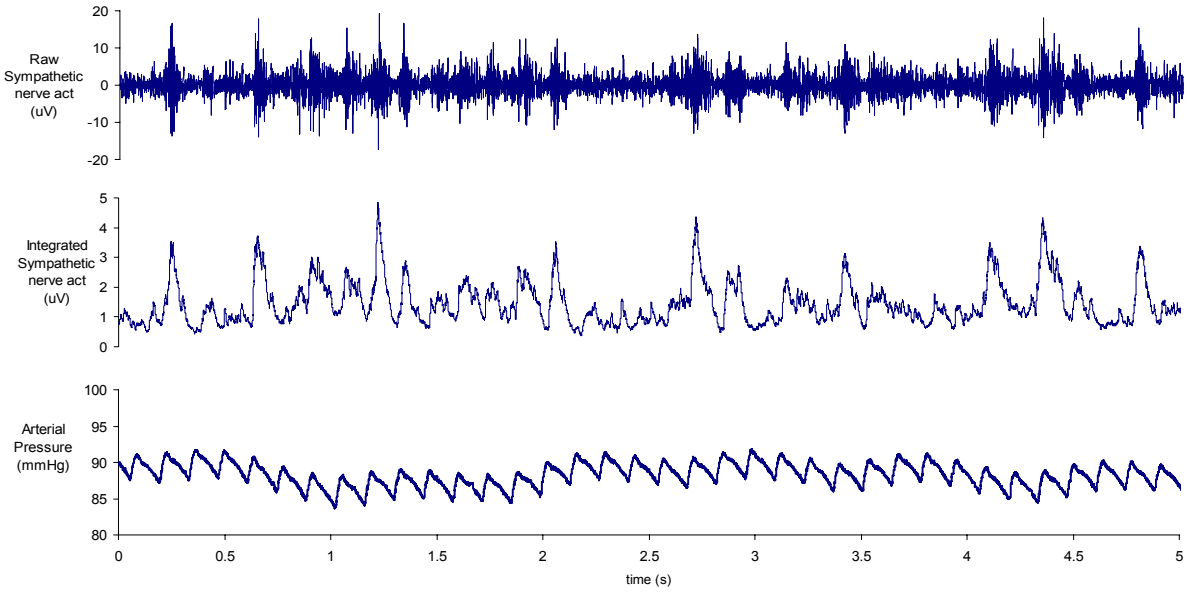

Figure 7: Example from one rat showing raw renal sympathetic nerve activity (top panel), rectified and integrated nerve activity (middle panel) and arterial blood pressure (bottom panel) recorded whilst conscious over a period of 5 s.

Prior to implantation the implant was sterilized in an 8% gluteraldehyde solution overnight and then rinsed in sterile saline. The surgery was performed using sterile procedures on a heated surgical table. Anesthesia was induced by placing the rat in a chamber filled with isoflorane, then a nose cone arrangement was used to maintain the isoflorane anaesthesia at a surgical level. An abdominal incision was made and the abdominal aorta cleared just above the iliac bifurcation. Using silk sutures the aorta was temporarily occluded and a 23 gauge needle used to pierce the aorta. The cannula of the transmitter was inserted into the aorta and advanced approximately 4cm. The cannula was secured in place using cyanoacryalate adhesive and blood flow restored. The body of the transmitter was placed in the abdominal cavity, with the nerve electrodes and ground electrode exteriorized, and the muscle incision closed. A left flank incision was then made and the electrodes tunneled under the skin to this incision. A retroperitoneal incision was made through the muscle and gentle retraction used to expose the kidney. The renal nerve was found near the renal artery and dissected free of the surrounding tissue using fine forceps and visualisation under a surgical microscope. The Teflon coating was removed from the last 3mm of the electrode leads and the stainless steel fashioned into small hooks.The electrode leads were will be sutured to the wall of the artery and the intact nerve placed over the hooks. The nerve/electrode assembly is insulated from the surrounding tissue using silicone elastomer (Kwik-sil, World Precision Instruments).

The muscle layer was then closed, with the earth electrode placed subcutaneously. Then both skin incisions were closed with staples. As soon as a rat regained consciousness it was returned to its home cage. A heating pad was placed under the cage for 24 h after the surgery. Rats received buprenorphine (Temgesic 1 µg/100 g) as an analgesic.

3.2 Results

Figure 7 is an example of data recorded from a conscious unconstrained rat. The recording shows the hallmark traits of SNA, with bursts of activity occurring synchronously with the cardiac cycle (Malpas and Ninomiya 1992). Evident in this trace are small expiration related decreases in blood pressure with a corresponding increase in the bursts of renal sympathetic nerve activity illustrating the arterial baroreflex response and its dependence on renal sympathetic nerve activity (Dorward, Riedel et al. 1985). BP recordings show good fidelity with a crisp reproduction of the diastolic inflection without ringing or undershoot. However, pulse pressure is considerably lower than expected with a peak to peak value of approximately 5 mmHg. The cause of this is unknown, but may be due to the positioning of the catheter or surgery trauma. Further verification of the coordination between blood pressure and SNA are shown in Figure 8 where 500

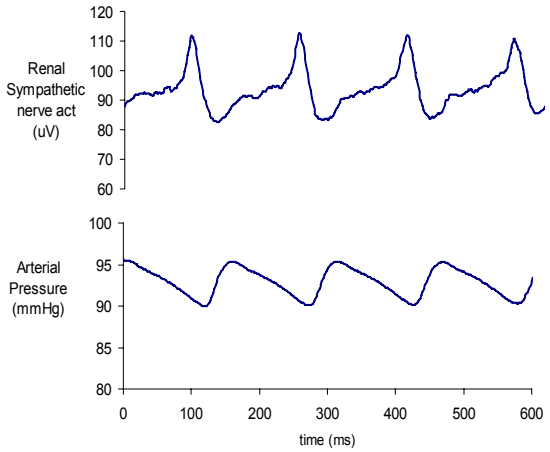

Figure 8: Example from one rat showing renal sympathetic nerve activity (top panel) and arterial blood pressure (bottom panel) averaged over 500 ms synchronized using peak systolic blood pressure.

ms intervals of blood pressure and SNA are averaged using peak systolic pressure as a trigger (similar to the triggering mechanism of an oscilloscope). This figure illustrates that the renal sympathetic nerve exhibited a clear cardiac related rhythm.

4 CONCLUSIONS

An implantable telemeter which simultaneously acquires blood pressure and microvolt level nerve signals has been presented. The telemeter is of a similar size to existing devices but posses many advantages such as inductive charging, digital transmission, and a high bandwidth microvolt input range bio-potential amplifier. Future work will concentrate on miniaturization and ascertaining the long stability of the blood pressure measurement system.

ACKNOWLEDGEMENTS

The authors wish to acknowledge the support of the Circulatory Control Group, University of Auckland and Telemetry Research Limited. Daniel McCormick was supported by a New Zealand Tertiary Education Commission Top Achiever Doctoral scholarship.

REFERENCES

Barrett, C. J., R. Ramchandra, et al. (2003). "What Sets the Long-Term Level of Renal Sympathetic Nerve Activity: A Role for Angiotensin II and Baroreflexes?" Circ Res 92(12): 1330-1336.

Budgett, D. M., A. P. Hu, et al. (2007). "Novel technology for the provision of power to implantable physiological devices." J Appl Physiol 102(4): 1658-1663.

Dorward, P. K., W. Riedel, et al. (1985). "The renal sympathetic baroreflex in the rabbit. Arterial and cardiac baroreceptor influences, resetting, and effect of anesthesia." Circ Res 57(4): 618-633.

Gabe, I. (1972). Pressure measurement in experimental physiology Cardiovascular Fluid Dynamics. D. Bergel. London, Academic Press: 11–50.

MacMahon, S. (2000). "Blood Pressure and the Risk of Cardiovascular Disease." N Engl J Med 342(1): 49-52.

Malpas, S. C. (1998). "The rhythmicity of sympathetic nerve activity." Progress in Neurobiology 56(1): 65-96.

Malpas, S. C. and I. Ninomiya (1992). "A new approach to analysis of synchronized sympathetic nerve activity." Am J Physiol Heart Circ Physiol 263(4): H1311-1317.

Mark, A. L. (1996). "The sympathetic nervous system in hypertension: a potential long-term regulator of arterial pressure." J Hypertens Suppl 14(5): S159-65.

Moran, M. M., R. R. Roy, et al. (1998). "Size constraints of telemeters in rats." J Appl Physiol 85(4): 1564-1571.

Prutchi, D. and M. Norris (2005). Design and Development of Medical Electronic Instrumentation. New Jersey, John Wiley & Sons, Inc.

Whelton, P. K. and M. J. Klag (1989). "Hypertension as a risk factor for renal disease. Review of clinical and epidemiological evidence." Hypertension 13(5 Suppl): I19-27.

MICRO-SHAFT-POKING
A Novel Instrument for Mechanically Characterizing Soft Biomimetic Membrance

Kuo-Kang Liu, Mark Ahearne, Eleftherios Siamantouras and Ying Yang
Institute of Science Technology in Medicine, Keele University, Stoke-on-Trent, UK
i.k.liu@keele.ac.uk

Keywords: Instrumentation, hydrogel, mechanical characterization, microengineering.

Abstract: Characterizing viscoelastic properties of soft biomimetic membranes has become increasingly important due to their biomedical applications such as tissue engineering/regenerative medicine and biosensors. This paper presents a new micro-shaft-poking (MSP) technique which is free from the complication of substrate backing, normally occurred as an intractable problem in the conventional indentation testing for soft membranes. A tailored indention apparatus with a spherical indenter was constructed to achieve the force resolution and displacement of 1μN and 1μm. The biomimetic membranes which were used for mechanical testing were made of two types of hydrogel, alginate and agarose. The results showed that the elastic modulus increased with gel concentration. A creep test has also been conducted to examine the time-dependent behaviors of various hydrogel and a viscoelastic model has been correspondingly developed and applied to describe the experimental results. Other potential applications of this new instrument to other membranes, both artificial and biological, have been addressed in the paper.

1 INTRODUCTION

Recent advancements in biomimetic materials have opened a new avenue for tissue regeneration/implant and the construction of next generation biomedical devices, such as developing engineered tissue and designing cell-based biosensor. In many cases, their viscoelastic/mechanical properties play an important role in the performance and durability of these membranes, and ultimately dictate whether the applications are successful or not. A great need therefore is required for the development of new techniques for mechanically characterizing these emerging biomimetic materials such as hydrogels (Ratner et al., 1996). However, mechanical characterization of these materials in a quantitative manner is highly challenging due to their unique mechanical characteristics, such as fragility and viscoelasticity

Despite the intractability in experimentally measuring the mechanical properties of soft biological materials, recent progress in the advanced instrument developments have made such microscale characterization more feasible (Lu et al., 2004). The common fundamental principle among these advanced methods is to measure the material deformation under an applied load. Among these, bulge or blister testing, nanoindentation, and microtensile testing are prevailingly used for mechanical characterization of soft biomimetic materials (Espinosa, et al., 2003; Liu et al., 2004). Testing via bulging or nanoindentation alleviate many of the problems such as mounting specimen and providing sufficient resolution of measurements (Scott et al., 2004). Moreover, the data measured by using different testing techniques are often scattered. Such variations have been recognized to be attributed to the technological means employed by each technique and the calibration. Also the different requirements for conducting the experiments and interpretation of results will also contribute to the diecrepancy (Liu et al, 2004; Menciassi et al., 2001). Therefore the mechanical properties of the soft materials are difficult to be unequivocally determined when the various techniques are compared (Espinosa et al., 2003).

In this work, a new ultra-precise measuring instrument, the MSP, for characterizing mechanical properties of biomimetic materials are described. Based on simultaneous force-displacement measurements, the elastic modulus of soft membranes can be determined. This instrument provides a broad range of measurements to facilitate large deformation analysis as well as time dependant

force measurements, with microscale resolution. Firstly, the testing technique has been used to characterize circular biomimetic hydrogel membranes whose properties are of great interest for biomedical applications and have not been investigated well before.

2 EXPERIMENTAL SETUP

2.1 Instrumental Setup

The system, schematically shown as Figure 1, was newly developed for measuring force as a function of displacement. The instrument is based around an inverted optical microscope (Eclipse TE 2000S, Nikon, USA), incorporated with a XYZ motorized motion control interfaced with as external PC. The microscope's Z-axis motorized stage, which is capable of 1μm step and a travelling distance up to 8.5mm, is used as a displacement actuator (ESP300, Newport, Irvine, CA). Attached to Z-axis stage was a specially designed solid arm, on which edge a force transducer (404A, Aurora Scientific Inc., Canada), with 1μN force resolution and 100mN maximum force capability, was mounted firmly. The stability of the arm prevents from the "dead" weight effect of the transducer's head in the output signal and avoids bending of the interior housing of the transducer, which might offset the output. In addition, it ensures precise loading in a vertical position. In the final form the instrument had a force and displacement resolution of 1μN and 1μm respectively.

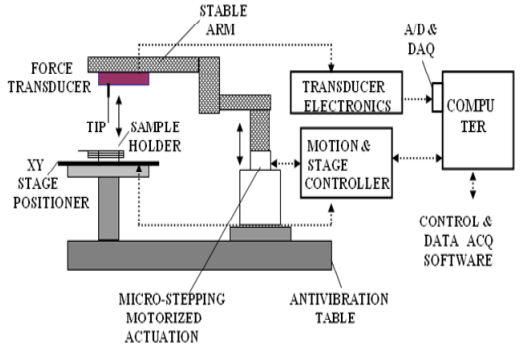

Figure 1: Schematic view of the instrumental set-up (not to scale).

A fine, spherical tip is attached at the end of the force transducer's output tube for deforming the sample. A handy sample holder facilitates mounting of a thin, circular membrane between a set of parallel plastic rings, without affecting the natural properties of the material. The position of the membrane for central alignment can be adjusted precisely by tuning a two dimensional (X-Y) translation stage (ASSY STAGE 25, Cell Robotics Inc., USA), with a resolution higher than 2μm. The force transducer signal is filtered and amplified by using differential amplification (S 400A, Aurora Scientific Inc., Canada). The amplified analogue signal is transmitted through a connector block (DAQ SCB-68, National Instruments, USA) into a data acquisition (DAQ) board (PCI DAQ-6036E, National Instruments, USA) for digitization and further processing. The acquired data were displayed and recorded by a tailored software design based on the Labview platform (National Instruments, USA). Figure 2 shows the interconnections among instrumentation, data acquisition and control.

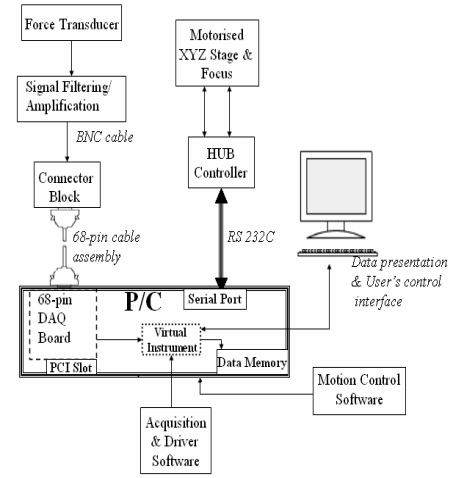

Figure 2: A block diagram of the system showing the interconnections between instrumentation, data acquisition and control interface.

2.2 Material Preparation

Two types of hydrogel, alginate and agarose, were prepared. Alginate is a co-polymer consisting of β-D-mannuronic (M block) and α-L-guluronic (G block) acid. The ratios and lengths of these blocks play an important role in the mechanical behaviours of the alginate. A 2% (w/v) solution of sodium alginate was formed by dissolving 2 g of Protanal LF200 S (FMC BioPolymer, Norway) in 100 ml of deionised water. The ratio of M block to G block in this type of alginate has been found to be 0.23 (Drury et al., 2004). Different concentrations of the

alginate solution were formed by adjusting the ratio of alginate powder to deionised water. When fully dissolved, the solution was autoclaved for sterilization. Autoclaving had the effect of decreasing the viscosity of the solution. To fabricate alginate hydrogels, rings made from filter paper (Millipore, USA) were placed on the bottom of small petri dish. These rings reduced the amount of shrinkage of the hydrogel after crosslinking and allowed the hydrogels to be lifted from the petri dishes. 200 µl alginate solution was poured inside a ring of inner diameter 11 mm. 5 ml of 0.5 M filtered calcium chloride solution ($CaCl_2$) was added over the alginate. The application of $CaCl_2$ caused the sodium in the alginate to be replaced by calcium, which resulted in crosslinking and formation of a hydrogel. Once applied, the $CaCl_2$ solution had to cover the alginate quickly to prevent the hydrogel from forming unevenly. After 10 minutes the $CaCl_2$ solution was removed and the hydrogel was washed twice in phosphate buffered saline (PBS) (Sigma, UK).

Agarose hydrogels were made using agarose type 1 (Sigma, UK). A 2% (w/v) agarose solution was produced by dissolving 0.2 g of agarose powder in 10 ml PBS. For lower concentrations, less agarose powder was required. The powder was dissolved by heating the solution to over 60°C. When fully dissolved, the solution was filtered to remove any impurities. 200 µl of the solution was applied to a petri dishes with circular filter paper rings of inner diameters 11 mm. The hydrogels were formed by cooling at room temperature. Once the hydrogel had formed, water or PBS was added to the petri dish to prevent the agarose from dehydrating.

3 THEORETICAL ANALYSES

The Young's modulus was calculated from the indentation data using a previously described theoretical model (Scott et al., 2004). For a hydrogel material suspended around its outer edge (Figure 3), the total displacement that the indenter is lowered (δ) is equal to the sum of the depth of penetration into the hydrogel (δ_1) and the vertical deformation displacement of the hydrogel (δ_2). δ_1 can be calculated using the Hertz model (Johnson, 1985);

$$E^* = \frac{3F}{4R^{\frac{1}{2}}\delta_1^{\frac{3}{2}}} \quad (1)$$

where F is the force applied to the hydrogel by the indenter, R is the radius of the indenter tip and E^* is the elastic modulus and can be derived from the equation;

$$\frac{1}{E^*} = \frac{1-\nu_I^2}{E_I} + \frac{1-\nu_H^2}{E_H} \quad (2)$$

where E_I and E_H are the moduli of the indenter and hydrogel respectively and ν_I and ν_H are their Poisson's ratios. Since the modulus of the indenter is much larger than the hydrogel, the term $(1 - \nu_I)/E_I$ was neglected and equation (1) can be rewritten as;

$$\delta_1 = \left(\frac{9F^2(1-\nu^2)^2}{16RE^2} \right)^{\frac{1}{3}} \quad (3)$$

where E and ν are the Young's modulus and Poisson's ratio of the hydrogel materials. The vertical deformation displacement of the hydrogel was calculated using plate-bending theory (Timoshenko & Woinowsky-Krieger, 1959) from the equation;

$$\delta_2 = \frac{3Fa^2(1-\nu^2)}{4\pi Eh^3} \quad (4)$$

where h is the thickness and a is the radius of the hydrogel inside the sample holder. By adding equations (3) and (4), the total displacement of the indenter on the bending-governing deformation was determined from the equation;

$$\delta = \left(\frac{9F^2(1-\nu^2)^2}{16RE^2} \right)^{\frac{1}{3}} + \frac{3Fa^2(1-\nu^2)}{4\pi Eh^3} \quad (5)$$

The Young's modulus was calculated from equation (5) using Matlab software (MathWorks, USA).

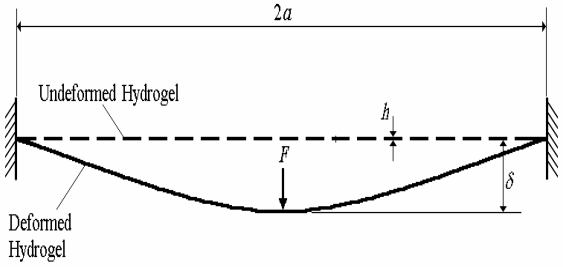

Figure 3: Schematic representations of a membrane deformed by micro-shaft poking (MSP) indentation.

Two theoretical models were used to examine the relaxation behaviour of the hydrogels during indentation. The 3-parameter standard linear model and 5-parameter Maxwell-Weichert model were both used to describe the viscoelastic relaxation response under a constant strain (Figure 4).

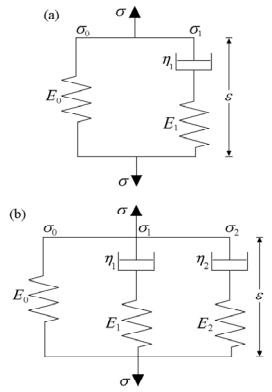

Figure 4: Schematic representation of the (a) 3-parameter standard linear model and (b) 5-parameter Maxwell-Weichert model.

For a 5-parameter Maxwell-Weichert model, which consists of a single spring and two Maxwell elements in parallel, the total stress, $\sigma(t)$, equals to the sum of the stresses applied to the spring and the Maxwell elements;

$$\sigma(t) = \sigma_0 + \sigma_1 + \sigma_2 \quad (6)$$

where σ_0 is the stress applied to the spring and σ_1 and σ_2 are the stresses applied to each Maxwell element and whose values can be described as;

$$\sigma_0 = \varepsilon E_0 \quad (7)$$

$$\sigma_1 = \varepsilon E_1 e^{\frac{-E_1 t}{\eta_1}} \quad (8)$$

$$\sigma_2 = \varepsilon E_2 e^{\frac{-E_2 t}{\eta_2}} \quad (9)$$

where η refers to the dashpot viscosity. By substituting equations (7), (8) and (9) into equation (6), the stress relaxation function $g(t)$, which equates to $\sigma(t)/\sigma(0)$, can be described as;

$$g(t) = A_0 + A_1 e^{\frac{-t}{\tau_1}} + A_2 e^{\frac{-t}{\tau_2}} \quad (10)$$

where A_0, A_1 and A_2 represents the strain dependent amplitudes, and τ_1 ($=\eta_1/E_1$) & τ_2 ($=\eta_2/E_2$) represent strain dependent time constants.
For the standard linear model, the stress relaxation function is written as;

$$g(t) = A_0 + A_1 e^{\frac{-t}{\tau_1}} \quad (11)$$

The values for A and τ were determined using non-linear regression analysis for both relaxation models.

4 RESULTS AND DISCUSSIONS

4.1 Young's Moduli of Hydrogels

A typical force-displacement curve for a 2% w/v alginate and 2% w/v agarose hydrogel indented to 1000μm are shown (Figure 5 (a) & (b)). It can be seen that the loading and unloading curves did not match. This type of behaviour, referred as hysteresis, is common in viscoelastic materials and is the result of energy dissipation during loading.

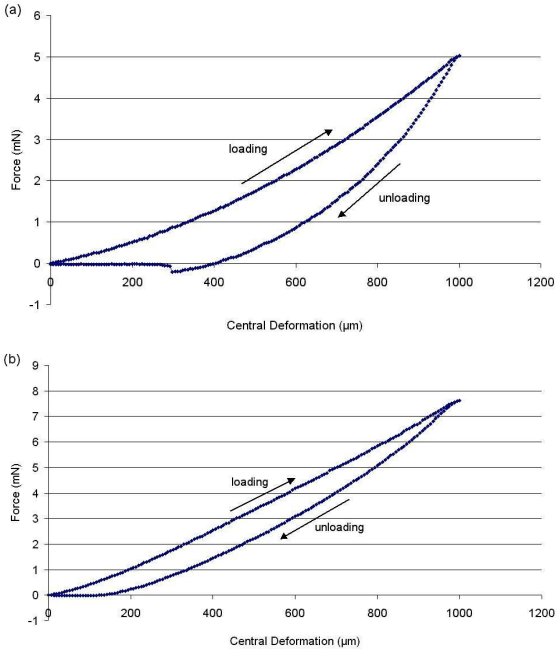

Figure 5: The MSP-measured loading-unloading curves of a hydrogel membrane with (a) 2% alginate & (b) 2% agarose.

The loading-unloading curves appear less linear for alginate hydrogel than agarose hydrogels and there was a more significant difference between the loading and unloading curves for alginate. This suggests that alginate has non-linear viscoelastic characteristics while agarose has more linear elastic characteristics. This type of mechanical behaviour agrees with the findings from previous publications (Bonn et al., 1998; Zhang et al., 2005). It was also found for some of the alginate hydrogels that the indentation force became negative for a short period during unloading. This can be explained by adhesion forces between the indenter and the hydrogel causing the indenter to adhere onto the hydrogel while unloading (Gupta et al., 2007).

Several loading and unloading cycles were recorded for individual hydrogels. It was noticeable

that different indentation cycles on the same hydrogel did not match although later indentation cycles appeared to match much more closely than earlier cycles. It can be seen (Figure 6) that for a 2% alginate hydrogel, after the first indentation cycle an increase in force was only detected after the indenter has been lowered by over 200 µm. This would suggest that plastic deformation of the alginate hydrogels had occurred in addition to elastic and viscoelastic deformation. The plastic deformation, in addition to the viscous properties of the hydrogel, prevented the hydrogel from fully returning to its original pre-indentation shape. There was also a small decrease in the amount of force required to indent the hydrogel with each cycle. This decrease in force was reduced with each cycle until reaching there was no functional force decrease was detectable. This phenomenon is common in biological materials (Fung, 1993) and is the combination of fibre reorganization and fluid movement within the tissue. The loading-unloading cycles for agarose appeared to match more closely than for alginate.

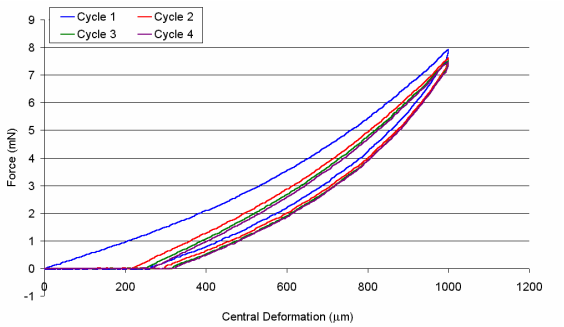

Figure 6: The MSP-measured loading-unloading cycles for a 2% alginate hydrogel.

The Young's moduli of agarose hydrogels of different concentrations indented up to 1000 µm are displayed (Figure 7). Agarose was preferred to alginate for calculating the Young's modulus since it had a more linear elastic response to indentation. The Young's modulus of alginate hydrogels varies in literature with a range between 1 kPa and 100 kPa (Awad et al., 2004; Drury et al., 2004). A non-linear loading curve would result in the values for Young's modulus becoming dependent on the indentation depth. It can be seen that there was an almost linear increase in Young's modulus with agarose concentration. Simple regression analysis was used to confirm the linearity of Young's modulus with agarose concentration between 0.4–1.2% with a coefficient of determination (R^2) equal to 0.9935.

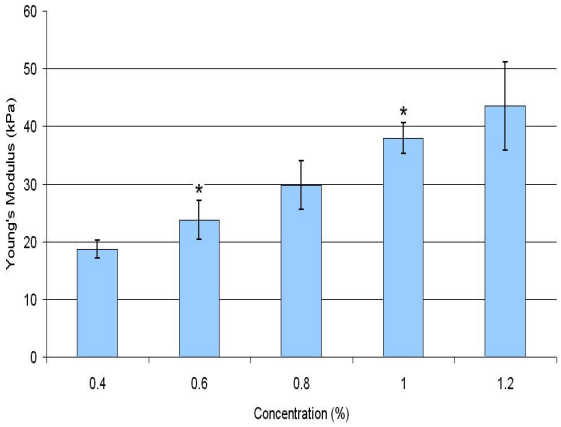

Figure 7: Young's modulus of agarose hydrogels measured by the MSP indentation (± standard deviation, n=4). *represents a significant difference with a 95% confidence over the previous concentration determined using ANOVA-tukey test.

The standard deviation bars show a high degree of repeatability in measuring different agarose hydrogel with the same concentration. Interestingly when the same hydrogel was measured several times, the standard deviation was further reduced i.e. for 0.5 % agarose hydrogel indented to 1000 µm four times, E = 20.9 ± 0.7 kPa. The values obtained for 1% agarose by the MSP method appear resemble those found by Bonn et al. (1998) using 3-point bending and Nyland & Maughan (2000) using atomic force microscopy.

4.2 Stress Relaxation of Hydrogels

Normalized force relaxation data was collected for both agarose and alginate hydrogels. The hydrogels were indented to a central displacement depth of 1000µm, which was maintained for 45 minutes. For times longer than 45 minutes, dehydration of the hydrogel would affect the measurement readings. Both agarose and alginate appeared to exhibit relaxation behaviour consistent with viscoelastic materials (Figure 8 (a) & (b)). The amount of force required to maintain the indentation displacement was reduced over time. The normalized force initially decreased quickly but then slowed until reaching a plateau. Alginate appeared to demonstrate a greater relaxation response than agarose, which suggests it is more viscoelastic than agarose, which has more elastic characteristics.

Nonlinear regression analysis, performed using XLStat (Addinsoft, USA), was used to determine the ability of the 3-parameter standard

linear model and 5-parameter Maxwell-Weichert model to describe the hydrogels' relaxation responses to the deformation applied by MSP. Both models appear to show a high degree of correlation between the actual data and the theoretical model data (Figure 8). The values for coefficients of determination (R^2) for agarose and alginate hydrogels were found to be greater than 0.9 using the standard linear model and greater than 0.95 for the Maxwell-Weichert model. This suggests that the 5-parameter Maxwell-Weichert model is capable of providing a more accurate representation of the relaxation response than the standard linear model.

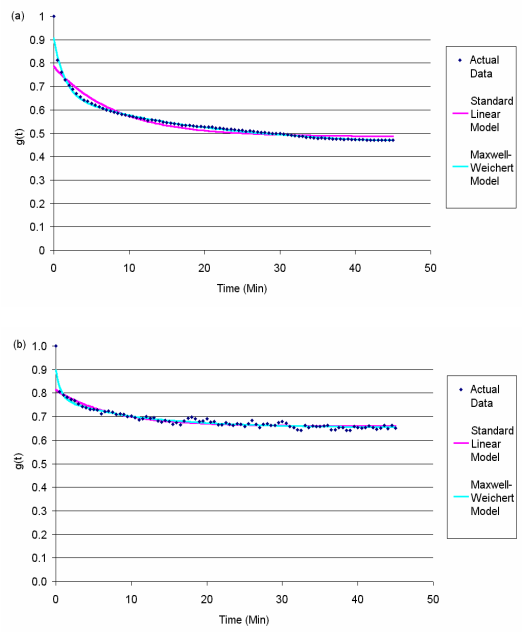

Figure 8: Actual and theoretical model normalised force data for (a) a 2% alginate and (b) a 1% agarose hydrogel at a constant indentation of 1000µm.

5 CONCLUSIONS

The MSP method has been applied to examine the mechanical and viscoelastic characteristics of various biomimetic materials, i.e., agarose and alginate hydrogel membranes and their results have been demonstrated to be satisfactory. Incorporated with simple analyses, the new instrument has been shown to be capable of determining quantitatively viscoelastic and mechanical properties based on experimental data of loading/unloading and stress relaxation curves. The instrument has potentials for testing other soft biological materials, such as human and animal skins.

REFERENCES

Awad H. A., Quinn Wickham M., Leddy H. A., Gimble, J. M., Guilak F. 2004, 'Chondrogenic differentiation of adipose-derived adult stem cells in agarose, alginate and gelatin scaffolds', *Biomaterials*, Vol. 25, no. 16, pp. 3211-3222

Bonn D., Kellay H., Prochnow, M. Ben-Djemiaa K., Meunier J. 1998, 'Delayed fracture of an inhomogeneous soft solid', *Science*, Vol. 280, no. 5361, pp. 265-267

Drury, J. L., Dennis, R. G. & Mooney, D. J. 2004, 'The tensile properties of alginate hydrogels', *Biomaterials*, Vol. 25, no. 16, pp. 3187-3199

Espinosa H. D., Prorok B. C., Fischer M. 2003, 'A methodology for determining mechanical properties of freestanding thin films and MEMS materials', *J. of the Mechanics and Physics of Solids,* Vol. 51, no. 1, pp. 47-67

Fung, Y.C. 1993, *Biomechanics: mechanical properties of living tissues*, Springer-Verlag, 2nd edition, New York.

Gupta, S., Carrillo, F., Li, C., Pruitt, L., Puttlitz, C. 2007, 'Adhesive forces significantly affect elastic modulus determination of soft polymeric materials in nanoindentation', *Materials Letters*, Vol. 61, no. 2, pp 448-451

Johnson, K.L. 1985, *Contact Mechanics*, Cambridge University Press, Cambridge

Liu K. K., Khoo, H. S., Tseng, F. G. 2004, 'In situ mechanical characterization of square microfabricated elastomeric membranes using an improved microindentation', *Review of Scientific Instruments*, Vol. 75, no. 2, pp. 524-531

Lu, S., Dikin, D. A., Zhang, S., Fisher, F. T. 2004, 'Realization of nanoscale resolution with a micromachined thermally actuated stage', *Review of Scientific Instruments,* Vol. 75, no. 6, pp. 2154-2162

Menciassi, A., Scalari, G., Eisinberg, A., Anticoli, C., Francabandiera, P., Carrozza, M. C., Dario, P. 2001, 'An instrumented probe for mechanical characterization of soft tissues', *Biomedical Microdevices*, Vol. 3, no. 2, pp. 149-156

Nyland, L. R., Maughan, D. W. 2000, 'Morphology and transverse stiffness of drosophila myofibrils measured by atomic force microscopy', *Biophysical Journal*, Vol. 78, no. 3, pp 1490-1497

Ratner, B. D., Hoffman, A. S., Schoen, F. J., Lemons J. E. 1996, 'An Introduction to Materials in Medicine', Academic Press, New York

Scott, O. N., Begley, M. R., Komaragiri, U., Mackin T. J. 2004, 'Indentation of freestanding circular elastomer films using spherical indenters', *Acta Materialia*, Vol. 52, no. 16, pp. 4877-4885

Timoshenko S. P.,Woinowshy-Kreiger S. 1959, *Theory of plates and shells*, McGraw-Hill, Singapore, 2nd Edition

Zhang, J., Daubert, C. R., Foegeding, E. A. 2005, 'Fracture analysis of alginate gels', *Journal of Food Science E: Food Engineering and Physical Properties*, Vol. 70, no. 5, pp. 425-431

INSTRUMENTED SPLINT FOR THE DIAGNOSIS OF BRUXISM

Pilar Lafont Morgado, Andrés Díaz Lantada, Alexander Martínez Álvarez, Antonio Barrientos Cruz
Héctor Lorenzo-Yustos, Pedro Luis Castedo Cepeda, Roberto González Herranz
Julio Muñoz García and Javier Echavarri Otero
Universidad Politécnica de Madrid
C/ José Gutiérrez Abascal, nº 2. 28006 – Madrid, Spain (+34) 913364217
adiaz@etsii.upm.es

Keywords: Telemedicine, Electroactive Polymers (EAPs), Biomaterials, Bruxism, Temporomandibular Joint.

Abstract: Bruxism is a health problem consisting in grinding or tightly clenching the upper and lower teeth. Both the grinding and sliding lead to wear of the teeth and produce a noise during the night that is sufficiently loud to disturb the sleep of anyone sharing the bedroom. The tension produced causes problems in the muscles, tissues and other structures surrounding the jaw, ear pain, headaches, lesions to the teeth and disorders in the jaw joints.

For an early, rapid, effective and economical diagnosis of bruxism, we propose the use of instrumented splints to detect and record the intensity and duration of interdental pressure episodes. This paper sets out the design, manufacture and testing of an instrumented splint for diagnosing the signs of bruxism.

The system stands out for its use of piezoelectric polymeric sensors which, because of their reduced thickness, do not cause any alteration to the patient's bite. It lets a quantitative assessment of intraoral pressure be made and bruxism behaviour be diagnosed at an early stage, so as to being able to programme corrective actions before irreversible dental wear appears. The first "in vitro" simulations and "in vivo" trials performed served to demonstrate the feasibility of the system in accordance with the initial objectives.

1 BRUXISM: CHARACTERISTICS AND PREVALENCE

Bruxism is a health problem consisting in grinding or tightly clenching the upper and lower teeth. Both the grinding and sliding lead to wear of the teeth and produce a noise during the night that is sufficiently loud to disturb the sleep of anyone sharing the bedroom. The tension produced causes problems in the muscles, tissues and other structures surrounding the jaw, ear pain, headaches, lesions to the teeth and disorders in the jaw joints. All these symptoms as a whole are usually described as temporomandibular joint problems (TMJ) or also as Craniomandibular Disfuntion Pain Syndrome.

The phenomenon was introduced to dental literature as bruxomania by Marie and Pietkiewkz in 1907. They described the habit of grinding the teeth. The term bruxism was introduced by Frohman in 1931. In 1936 Miller proposed using the term bruxomania for daytime grinding and bruxism for night time grinding. The terms traumatic neuralgia, the Karolyi effect and occlusive habit neurosis have all been used to refer to some form of teeth grinding or clenching.

According to a study by the Canadian Sleep Society nocturnal bruxism affects 8% of the adult population and 14% of the child population. A decrease in the population affected can be appreciated with age, attaining 3% for people over 60. However, for researchers like Melis and Granada prevalence is around 25%.

As to differences by sex there is no general agreement since there are publications that describe a greater bruxism activity in men (Quirch, Ozaki), others in women (Barreto, De los Santos) while others deem it to be an insignificant factor (Hayden, Kononean).

To summarise Nishigawa's study on the bite force produced during bruxism episodes, this can frequently reach 1100 N exceeding the maximal voluntary bite force. Pressures reached on the teeth surface can reach 40 MPa, high enough to cause high levels of wear and even breakages.

As to the duration of bruxism episodes, an average time of around 7 seconds has been found and when developing sensors it is necessary to

distinguish bruxism episodes from mioclonus or rapid contractions (< 0.5 s) of the jaw muscles.

However, it is important to point out that everybody subconsciously clenches their teeth at some time of the day and this could be considered as bruxism activity. The term bruxism is only used though when the duration and intensity of this activity has a bearing on dental wear and the appearance of TMJ problems.

One of the main problems associated with the traditional diagnosis of bruxism is that it is frequently made when the teeth are already highly worn and the prognosis of the illness is more severe. Bruxism activity can also be recorded by an EEG (electroencephalogram) as well as by EMG (electromiography) and S-EMG (surface electromiography). In many cases video-cameras are used in the study to distinguish the bruxism episodes of the mioclonus or rapid contractions (< 0.5 s) of the jaw muscles.

However, in order to be able to make an earlier, more rapid, more effective and economical diagnosis of bruxism, the research team that have written this paper propose using instrumented splints for detecting and recording the intensity and duration of interdental pressure episodes. Explained below are the design, manufacture and trials of an instrumented splint for the diagnosis of bruxism activity. It has been developed by researchers at Universidad Politécnica de Madrid in collaboration with Ibex Estética Dental S.L..

2 DESIGN OF THE DEVICE FOR DIAGNOSING BRUXISM USING ELECTROACTIVE POLYMERS AS SENSORS

Traditionally discharge splints or protection devices are used to treat bruxism and prevent the associated dental wear. As a diagnostic device we propose introducing pressure sensors into a splint so that patients' bite episodes can be recorded and the extent of their pathology be assessed. Piezoelectric polymers are used as pressure sensors for the reasons set out below.

Piezoelectric Electroactive Polymers as Pressure Transducers: PVDF (Polyvinylidene Fluoride)

Piezoelectricity was discovered in 1880 by Pierre and Paul-Jaques Curie, who observed that when certain crystals were compressed, like quartz or tourmaline, depending on certain directions they produced a voltage between zones on their surface. When force was applied the relative positions of the crystal molecules changed producing an internal displacement of charges which was the cause of this voltage.

These crystals also underwent the inverse effect since they became deformed when a voltage difference was applied. This property is found in materials lacking a centre of symmetry and the phenomenon is called ferroelectricity when a non-conductor crystal or dielectric material exhibits spontaneous electric polarisation.

Polyvinylidene fluoride or PVDF $-(CH_2-CF_2)-_n$ and its co-polymers such as poly(vinilydenefluoride-trifluoroethylene) or P(VDF-TrFE), are the polymers of this kind with the largest number of industrial applications. They posses partial crystalinity with an inactive amorphous phase and an elastic modulus close to between 1 and 10 GPa. Their use as actuators is limited by the need to apply high electric fields (around 20 V/μm for a 3% deformation), but their use as pressure sensors is taking the place of traditionally used piezoelectric ceramic materials.

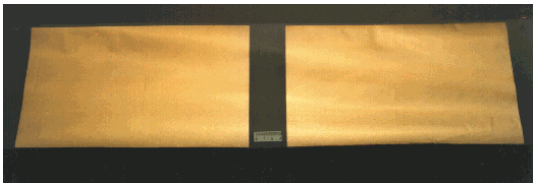

Figure 1: Metallized PVDF sheets. Piezotech S.A..

The use of this type of sensor was considered because of its reduced thickness, which does not cause any alteration to the patient's bite and because of its greater resistance and sensitivity compared to ceramic piezoelectrics. To make the sensors, we took PVDF 40 μm thick sheets from Piezotech S.A. with Au-Pt coated electrodes. These sheets were cut, joined to the connecting wires and suitably encapsulated to protect them and be inserted into the splint (see manufacturing process). The sensors obtained are shown below, together with the behaviour model allowing them to be simulated and the first results obtained in the trials carried out.

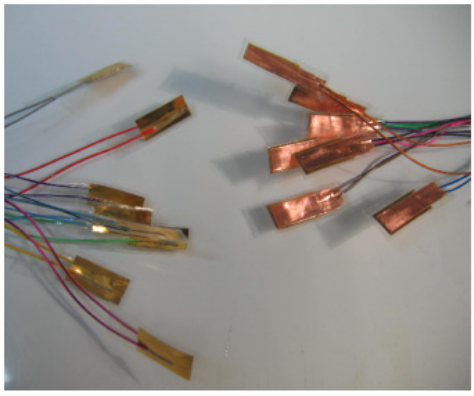

Figure 2: Piezoelectric sensors manufactured. Product Development Laboratory. Universidad Politécnica de Madrid.

Figure 3: a) shows the piezoelectric sensor layout. The charge displacement produced when a force is applied to the piezoelectric sensor can be represented using the equivalent electric circuit depicted in Figure 3 b).

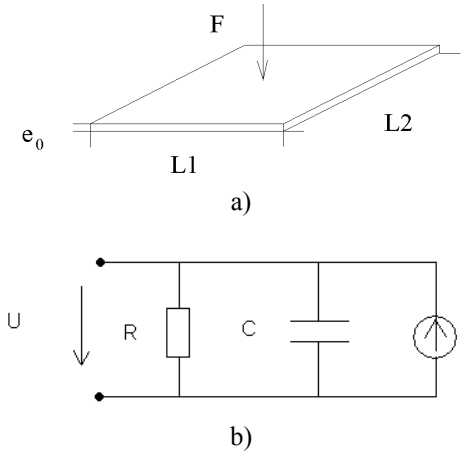

Figure 3: a) Piezoelectric Sensor. b) Electrical behaviour circuit diagram of the piezoelectric sensor.

Force F on the sensor acts as a generator of intensity powering a C capacity condenser. Ec (1).

$$C = C(F) = \varepsilon \cdot (L1 \cdot L2) / e \qquad (1)$$

Where:

ε.- The dielectric constant of the sensor.

L1·L2.- The effective area of the sensor.

e.- The thickness of the sensor.

The thickness of the sensor, e, depends on the initial thickness, e_0, on the pressure applied, $\sigma = F / (L1 \cdot L2)$, and the Young modulus of the material, E, using the following expression Eq. (2):

$$e = e_0 \cdot (1 - \sigma / E) \qquad (2)$$

Current intensity, I, generated by applying force F, depends on the transversal piezoelectric coefficient of sensor d33 according to Eq. (3).

$$Q = d33 \cdot F \rightarrow I = dQ / dt = d33 \cdot dF / dt \qquad (3)$$

When the sensor is connected to an external circuit, as is shown in Figure 3 b), it discharges in accordance with the equivalent R resistance of this external circuit (the oscilloscope input resistance in the first trials carried out). The intensity is given by Eq. (4).

$$I = d33 \cdot dF / dt = U / R + C \cdot dU / dt \qquad (4)$$

With the above equations and previous data a model was made in Simulink which permits a rapid assessment of the effect of modifying the parameters. The model and the results of the simulation are shown below, together with the first real trials carried out with the piezoelectric sensor connected directly to the oscilloscope when it was subjected to levels of pressure.

For the first simulations and trials with the sensors manufactured (Figures 5, 6 and 7) we have:

Piezoelectric coefficient (when applying forces perpendicular to the sensor plane).- d33 = 24 pC/N

Dielectric constant.- $\varepsilon = 1{,}1 \cdot 10^{-10}$ F/m;

Elasticity modulus of the PVDF.- E = 2000 MPa

Effective sensor area.- $L \cdot L2 = 4 \cdot 10^{-4}$ m^2

Sensor thickness.- 40 μm

Oscilloscope input resistance.- R = 10 MΩ

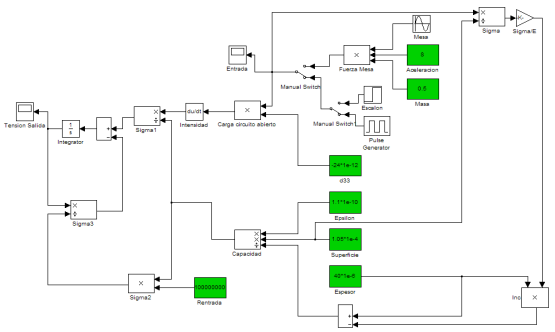

Figure 4: Simulink model for simulating piezoelectric polymer behaviour.

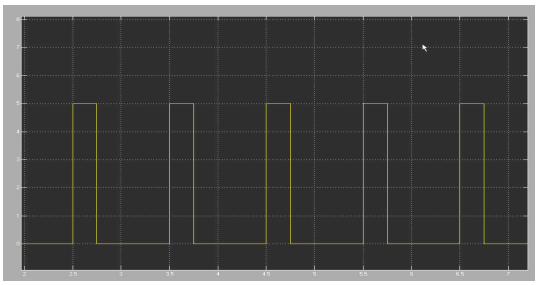

Figure 5: Simulation of levels of pressure as simulator input.

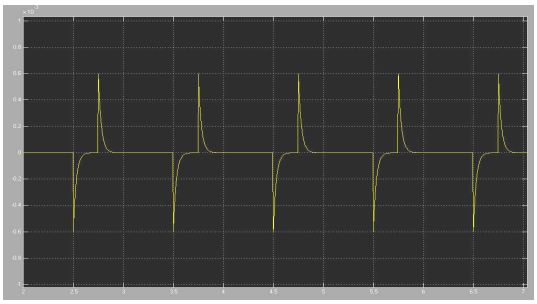

Figure 6: Output obtained (voltage) according to the simulation.

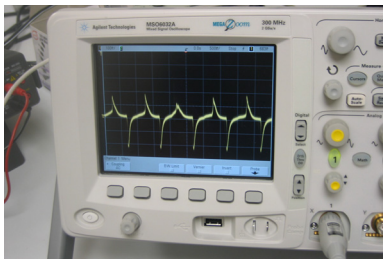

Figure 7: First trials: The oscilloscope shows sensor output voltage on applying levels of pressure as input.

3 MANUFACTURING THE DEVICE FOR DIAGNOSING BRUXISM

To obtain the instrumented splint some of the steps followed in the manufacture of thermoformed splints are followed. A model of the patient's teeth needs to be made, usually by shape copying. This model is put into a vacuum thermoforming machine in which a polymer wafer heated to a temperature higher than its softening temperature covers the model and reproduces the teeth geometry when a vacuum is applied on cooling.

The piezoelectric sensors are then placed on this first thermoformed layer and the operation is repeated with a second polymer wafer, whereupon the sensors become embedded within the two layers. It is important to control the thermoforming temperature since piezoelectric polymers used as sensors begin to lose their electromechanical coupling at temperatures above 80 ºC.

Finally the excess parts are trimmed off and the splint is subjected to an adjustment and polishing process to adapt it to the patient. In this way a splint is obtained like the one shown below in Figure 8, which enables interdental pressures to be detected for the purpose of diagnosing bruxism.

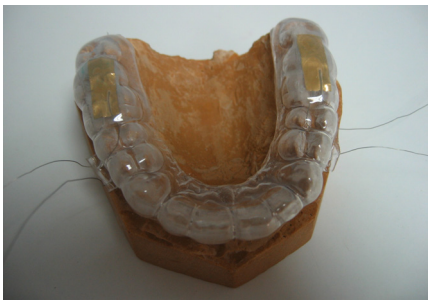

Figure 8: Splint with piezoelectric sensors for diagnosing bruxism.

4 FIRST "IN VITRO" AND "IN VIVO" TRIALS

4.1 "In Vitro" Trials

To simulate biting in "in vitro" trials, a pneumatically operated system was constructed in which moulds could be placed that reproduce patients' teeth, and on which the instrumented splints could be placed. The pneumatic system's actuators allow both perpendicular and transversal bruxism to be simulated with operating pressures of up to 6 bar in the pneumatic actuators providing bite forces of 750 N. This is shown in Figure 9.

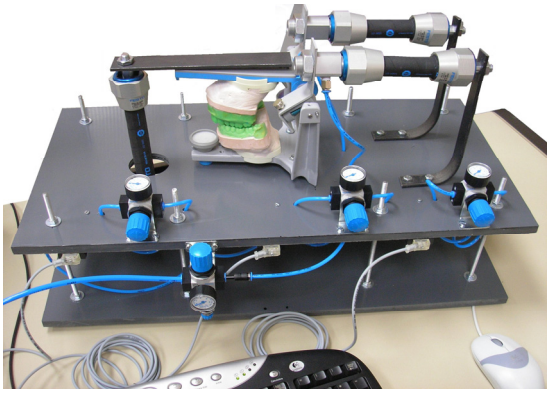

Figure 9: Bruxism simulator with pneumatic operation for the "in vitro" trials.

To carry out the "in vitro" trials moulds of the teeth of 3 patients taking part in the research were done. Resin reproductions of these teeth were made as a support for manufacturing the splints, which could also be placed in the bite simulator to artificially operate these instrumented splints.

Figures 10 and 11 show the response of the instrumented splints on being placed in the bite simulator and subjected to pneumatic operation. The connectors coming from the splint attached to the sensors were connected to a charge amplifier and an analogical-digital converter. This system's output was recorded using a data acquisition card commercially available known as "Measurement Computing USB 1208-FS".

The response to prolonged 10-second bites was studied for with 10-second relaxation between bites. The sensor response capacity and that of the A/D amplifier-converter system were also assessed, with successive bite episodes of different frecuencies.

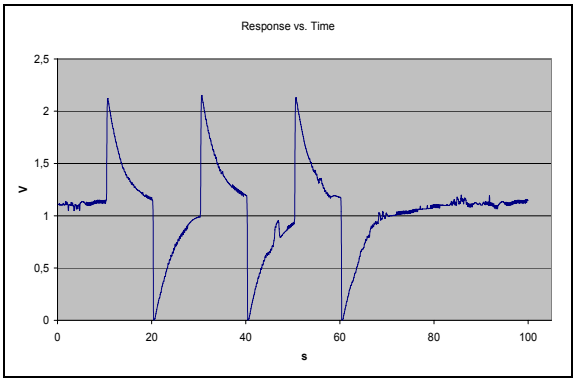

Figure 10: Simulation of 3 successive bites: Operation at 1 bar ≈ 150 N of bite during 10 s and relaxation during another 10 s.

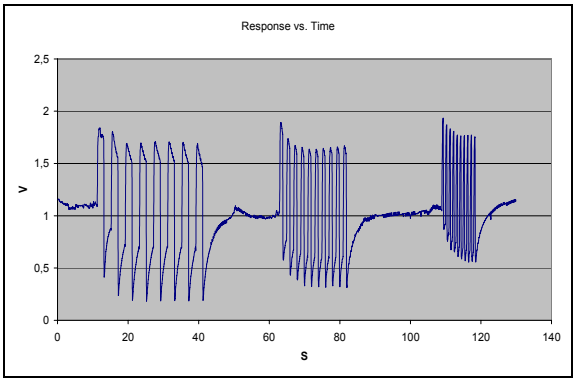

Figure 11: Simulation of successive bite episodes (operation at 1 bar ≈ 150 N of bite): First episode.- 8 bites with 2 s clenching and relaxation time. Second episode.- 10 bites with 1 s clenching and relaxation time. Third episode.- 10 bites with 0.2 s clenching and relaxation time.

After a positive assessment of the properties of the intrabucal pressure detection system and signal adjustment, processing and recording, "in vivo" trials were carried out, the results of which are presented below.

4.2 "In Vivo" Trials

The splints used for the previous trials were used again with the 3 patients taking part in the research for the first "in vivo" trials. They enabled the response of splints in actual mouths to be assessed and their resistance and duration to be tested, as well as their water-tightness to avoid any deterioration of the sensors. The responses recorded both of sudden and prolonged bites are shown in Figures 12 and 13.

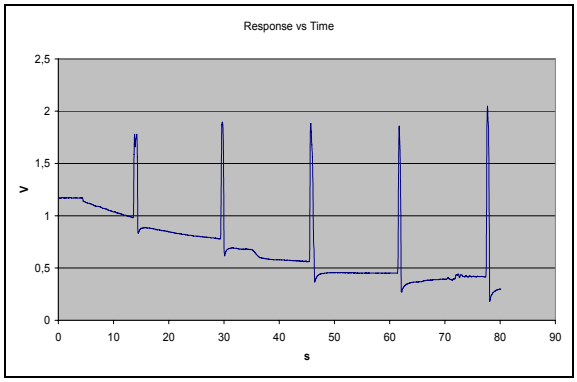

Figure 12: Output voltage in response to bite impacts every 15 seconds.

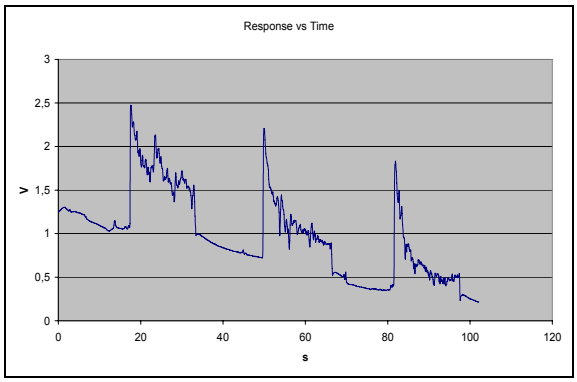

Figure 13: Output voltage with prolonged bites every 15 seconds and 15 seconds of relaxation.

The results of the trials carried out with the patients' splints show that it is possible to detect bruxism episodes of different intensities and duration which, combined with the ability to record and store the data, converts the system into a "Holter" for diagnosing bruxism and evaluating intrabucal pressures.

5 RESULTS ASSESSMENT AND FUTURE ACTIONS

The complete development of a splint to assess intrabucal pressure and diagnose bruxism and other occlusive pathologies has been presented. The system stands out for its use of polymeric piezoelectric sensors which, on account of their reduced size, do not produce any alterations to the patient's bite. The design process, modelling, simulation, manufacture and first trials have been described in detail, both in the pneumatic simulator and in 3 patients taking part in the research.

Currently, additional trials are being carried out with a total of 15 patients, with similar results to those shown in Figure 7. The electronics used (analogical-digital converter module and charge amplifier) need to be improved in order to optimise system response. The results of the "in vivo" trials are being compared with the behaviour models set out in order to improve control over the factors influencing the diagnosis of bruxism using instrumented splints.

However, what should be highlighted is the possibility to obtain a device that will enable intrabucal pressure to be quantitatively assessed and bruxism behaviour to be diagnosed at an early stage, so that corrective actions can be programmed before the appearance of irreversible dental wear. The first "in vitro" simulations and "in vivo" trials carried out serve to demonstrate the feasibility of the system in accordance with the initial objectives.

This work was partial result of "FEMAB Project: Micro-instrumented Anti-bruxism Splint" subsidised by the Spanish Ministry of Education and Science with Reference PROFIT (Promotion of Technical Research) CIT-020400-2005-17. It has been carried out in collaboration between Universidad Politécnica de Madrid and Ibex Estética Dental S.L..

REFERENCES

S. Ashley, *Artificial Muscles*. Scientific American 2003.

Y. Bar-Cohen, *Electroactive Polymer (EAP) Actuators as Artificial Muscles*. SPIE Press, Second Edition. Washington 2004.

Y. Bar-Cohen, et al. *Characterization of the Electromechanical Properties of EAP Materials*. Jet Propulsion Laboratory (JPL)/Caltech. SPIE. Newport, CA, 2001.

P. Dubois, et al., *Microactuators based on ion-implanted dielectric electroactive polymer membranes (EAP).* Microsystems for Space Technologies Laboratory, Lausanne. IEEE Transducers 2005.

M. Hafez, *Course on Polymer Based Actuators as Artificial Muscles*. FSRM (Swiss Foundation for Research in Microtechnology). Zurich 2006.

G. Lavigne et al., *Bruxism: Epidemiology, diagnosis, patho-physiology and pharmacology*. Advances in pain research and treatment 1995.

G. Lavigne et al., *Neurobiological mechanisms involved in sleep bruxism.* Faculté de Médecine, Université de Montréal 2003.

G. Lavigne et al., *Sleep bruxism: validity of clinical research diagnostic criteria in a controlled polysomnographic study.* Journal of Dental Research 1996.

Measurement Specialties, Inc., *Piezo Film Sensors Technical Manual.* Sensor Products Division 1999.

K. Nishigawa, et al., *Quantitative study of bite force during sleep associated bruxism*. Journal of Oral Rehabilitation 2001.

D. Cosme, et al., *Bruxism and voluntary maximal bite force in young dentate adults.* The International Journal of Prosthodontics 2005.

K. Baba, *Bruxism force detection by a piezoelectric film-based recording device in sleeping humans.* Journal of Orofacial Pain 2003.

METHOD FOR MEASURING PARYLENE THICKNESS USING QUARTZ CRYSTAL MICROBALANCE

Henna Heinilä, Maunu Mäntylä and Pekka Heino
Institute of Electronics, Tampere University of Technology, P.O. Box 692, FI-33101 Tampere, Finland
henna.heinila@tut.fi, maunu.mantyla@tut.fi, pekka.heino@tut.fi

Keywords: Parylene, Quartz Crystal Microbalance, Biomedical Coating.

Abstract: At present, the exact final thickness of parylene coating is difficult to specify in the beginning of the coating process since the parylene thickness is a function of many components. The elements that control the thickness are substrate surface area in a vacuum chamber, program parameters, and amount of dimer charge. This paper describes a method for measuring parylene coating thickness using quartz crystal microbalance. The thickness is measured by an oscillation frequency change of quartz crystal as parylene deposites on the quartz crystal plate. These results can be used for specifying the parylene thickness real-time during the coating process.

1 INTRODUCTION

Biomedical implants have many strict requirements as they are being implanted for a long time under the skin. Implantable medical devices need to be coated hermetically before implantation. The coating material has many strict requirements. One very important, biological aspect is that the implant must be biocompatible. To reduce inflammation, all of the components of an implant should be nontoxic to cells (Wolgemuth 2002). Since most of the materials used in the device's electronics are not biocompatible, the encapsulation of the device with nontoxic materials is needed to prevent elusion into the body. The human body is a very hostile environment for any foreign materials. Therefore, the implant must be biostable. This electrical characteristic means that the device operation must be protected from the living tissue (Wolgemuth 2002). Otherwise the body tries to destroy or isolate the device. These two fundamental aspects, the protection of the device against the biological environment and the protection of living tissue against device's materials must be ensured before the device is implanted in a human being (Wolgemuth 2002). In addition, the long-term stability of the device and the coating needs to be high and meet the specifications.

Materials, which are used as coating materials for medical applications and qualify above-mentioned requirements, include many metals, metal alloys, ceramics, polymers, and polymer composites (Ratner et al. 1996). Small and rigid implantable devices, like pacemakers and drug pumps, could be coated with a metal case unlike the devices that must be extremely small scale, like in MEMS applications, or devices that must conform to the tissue movements. These latter mentioned devices like neural prosthesis should be made from flexible substrate with flexible coating.

Many types of polymers are widely used for medical purposes. Polymers like epoxies, silicones, polyurethanes, and parylenes, have many desirable properties, such as ease of tailoring and processing, low cost, and an excellent corrosion resistance (Ratner et al. 1996). Parylene conformal coating is ideal for the medical applications because of its many unique properties. Vacuum deposited parylene is applied in a chamber by means of gas phase polymerization (Noordegraaf & Hull 1997). Compared to liquid coating processes, vacuum deposited parylene coatings exhibit uniform coverage of medical implants and electronics components without the presence of pinholes or pooling. During the coating process, all of the exposed substrates in evacuated vacuum chamber are coated and the coating grows as a conformal film simultaneously on all surfaces and parylene penetrates into the pinholes (Noordegraaf & Hull 1997). During the parylene coating process, no impurities are generated and hence parylene coatings

are, like silicone, one of the highest purity coatings on the market (Licari 2003). Parylene is flexible coating material just like silicone, but compared to silicone, parylene has better moisture and chemical resistance and also extremely thin coatings are tight enough for insulation and implants (Stieglitz et al. 2002). In addition, parylene has excellent adhesion to most surfaces (Licari 2003, p. 157).

2 BACKGROUND

2.1 Parylene

Parylene (poly-para-xylylenes) is a universal term for members of a unique polymer class (Licari 2003). By using dimer of di-para-xylylene, parylene has the ability to be deposited by vacuum deposition onto exposed surfaces at room temperature (Licari 2003). Varying the process parameters of deposition can control the thickness of parylene and the thickness may vary from 0,025 µm to several tens of micrometers. According to Licari (2003), the final thickness of coating can be controlled to ±10 % of desired thickness. Nevertheless, our laboratory results have proven that the thickness variance can be even greater. The parylene coating is inert and conformal and hence provides dielectric and environmental isolation. Parylene coating is used in many applications like aerospace, automotive and military industry, and also in medical applications. Nowadays, the four most frequently used commercially available parylene variations are parylene N, C, D, and HT. The two first have the longest history of use and are most commonly used in medical coating applications. This paper concentrates on coating with the polymer parylene C. (Specialty Coating System 2007)

Parylene C can provide extremely thin, uniform, and pinhole-free coating. It has low electrical dissipation factor, high dielectric and mechanical strength, and good chemical, electrical, and biological stability. It also has significantly lower moisture, chemical, and caustic gas permeability than parylene N. Above-mentioned reasons make parylene C very compatible for medical implants. In addition, parylene C is not cytotoxic and it is proven to be compatible with body tissue and blood. (Yang 1998)

2.2 Parylene Coating Process

The parylene coating process can be divided into three stages. The first stage is vaporization, the second is pyrolysis, and the third stage is deposit. In the beginning of the coating process, the raw material, dimer that is white powder, is vaporized under vacuum (1.0 mbar) and heated to a dimeric gas at approximately 150 ˚C. During the second stage, pyrolysis, the gas is pyrolized to cleave the dimer to its monomeric form under vacuum (0.5 mbar) to approximately 680 ˚C. In deposition stage the monomer reaches the room temperature deposition chamber. The monomer gas simultaneously absorbs and polymerizes on the substrate as a transparent parylene film. The substrate temperature never rises more than couple of degrees above the room temperature. (Specialty Coating System 2007; Pang et al. 2005, p. 4)

The surface area of substrates in deposition chamber can vary a lot. The substrates to be coated are positioned in a stand that spins in a vacuum chamber. When a small amount of dimer is used, it does not matter where the substrates are located in a stand. Also the stand area might vary a lot. The stand might for example have several levels and the grid on each level might be tight. The coating thickness is mainly a function of substrate surface area in chamber and amount of dimer charge. Program parameters have also minor importance. Even 1 µm thick coating is discovered to be tight enough for implants (Stieglitz et al. 2002). Thus it is very important to be able to measure the thickness of the coating accurately. The process is controlled by the deposition process parameters. The process parameters for our measurements are found from known coating process recipes that are used also in Para Tech Coating, Inc. in Sweden (Para Tech Coating, Inc. 2006). Recipes determine the amount of dimer, process temperatures and times, and approximate final parylene thickness. It has been proven that when different recipes are used for same amount of dimer, the final thickness might be different. Therefore, in addition to the amount of the dimer, also the process parameters affect the final thickness of parylene.

After the coating process, the achieved thickness could be measured by releasing a sample parylene film from the top of a preparat glass that has been in vacuum chamber, and then measuring the thickness of film. This does not give very accurate results, since the thin film is charged electrically and it might be creased. Also, after releasign the film from the top of a preparat glass, the film surface might already contain some impurities from the air that affect the result. Moreover, as the parylene thickness can depend on the location in the camber, the thickness of the film on the preparate glass can be

different from the thickness of the sample coating. Since the final thickness is hard to predict before the coating process or to measure accurately after the process, a real-time thickness monitoring system would be useful in many cases.

2.3 Quartz Crystal

A crystal oscillator is an electronic circuit that creates an electric signal with a certain frequency by using the mechanical resonance of a vibrating quartz crystal. The crystal is made of piezoelectric material and it is placed between a pair of electrodes. When these two electrodes are connected to an alternating electric field, the quartz crystal starts to oscillate at its resonance frequency due to the piezoelectric effect.

A quartz crystal microbalance (QCM) measurement technique is based on the oscillation at a precise frequency. When any type of mass is added on the surface of the crystal, the resonance frequency of the quartz crystal decreases. According to the Sauerbrey equation,

$$f_o - f = -\Delta f = \frac{2f_o^2}{A\rho_q v_q}\Delta m = \frac{2f_o^2\rho_p}{\rho_q v_q}\Delta x \qquad (1)$$

the change in mass, Δm, is proportional to the change in frequency, Δf. Here f_o is the initial resonant frequency of the crystal, f the resonant frequency of the coated crystal, A is the effective area of the crystal (between electrodes), ρ_q is the density of quartz, and v_q is the shear velocity in quartz. The change of mass is written in terms of parylene thickness, Δx and density, ρ_p. When very accurate measurements of very small mass changes need to be performed, the QCM technology is very appealing and it has already been studied as a system for measuring film thickness during deposition of different materials. (Eggins 2002; Gulati, Auras, & Rubino 2006) In addition to rigid deposits, the QCM has been widely used for its respond to changes in a liquid's viscoelastic properties. Some targets of using QCM have been for example humidity sensor (Ito et al. 2003), bacterial spores detector (Lee et al. 2005), and proteins detector.

3 MEASUREMENTS

3.1 Preliminary Study

The starting point for the real-time thickness measurements method was the conclusion that if parylene penetrates inside the crystal oscillator and covers the quartz crystal (Fig. 1), the mass of the quartz crystal must increase. Based on the QCM technology, the mass change of the crystal should be directly proportional to its frequency change. Moreover, since the mass change is proportional to crystal area and parylene thickness, the frequency change is proportional to parylene thickness, as given in eq. (1). By increasing the parylene thickness, the frequency of crystal oscillators placed in vacuum chamber should linearly decrease.

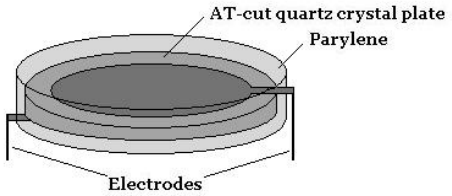

Figure 1: A quartz crystal covered with parylene.

In order to enable parylene penetration to the surface of the quartz crystal, small holes must be drilled to the metal case of the crystal oscillator. As a preliminary study for the measurements, the number of holes on the sides of the oscillator required to achieve the largest frequency change, was determined. It seemed that three 1 mm holes generated larger resonance frequency change than one or two holes, even if all of the crystal oscillators were in the same run of parylene equipment in vacuum chamber. At the same time making four holes on both sides gave the same result as three holes so there was not need to increase the hole number to more than three. Thus it seems that full covering of the quartz resonator was not obtained with only one or two holes in the resonator case. These results bear evidence that parylene can not penetrate through all pinholes easily.

3.2 Measurement Set-up

For the measurements, 21 crystal oscillators were used. The resonance frequency of these crystal oscillators was 3.579 MHz. Three 1 mm holes were drilled on both sides of the crystals' metal case. Each crystal was numbered with consecutive numbers. After drilling the holes, the resonance frequency of

each oscillator was measured with a network analyzer.

The measurement arrangement was carried out in the following order. After measuring the initial frequency, all of the crystals in metal case were coated with parylene. Model 3000 Labtop, Parylene Deposition System, Para Tech Coating (Aliso Viejo, USA) equipment was used for coating. The resonators were coated using 1.7 g of dimer and process parameters for 2 µm coating. Therefore the estimated thickness of the parylene film was 1.7–2.0 µm. The same procedure was repeated 11 times for all crystals. Each time there was an estimated 1.7–2.0 µm growth on the preceeding coating. The frequency of each crystal was measured with network analyzer after each coating run, and results were documented. The frequency decreased due to the mass increment on the quartz crystals.

To be able to analyse the results, an accurate film thickness after each parylene coating must be known. These measurements were done visually, by using microscope Olympus BX60M. For reference data, silicon samples were coated in the same processes with the crystal resonators. Eleven silicon chips (approximately 1.0 cm x 1.0 cm), in addition to crystals, were placed into the vacuum chamber in the beginning of the first coating. One silicon chip was taken away from the chamber after every coating and marked with consecutive numbering. Meaning chip having number i should have approximately $i \times 1.7$–2.0 µm parylene film on the silicon. To be able to define the accurate thicknesses of parylene coats, each chip was placed in a mould and covered with epoxy. The cross-sectional samples were then mechanically prepared for microscopic thickness examination by grinding and polishing.

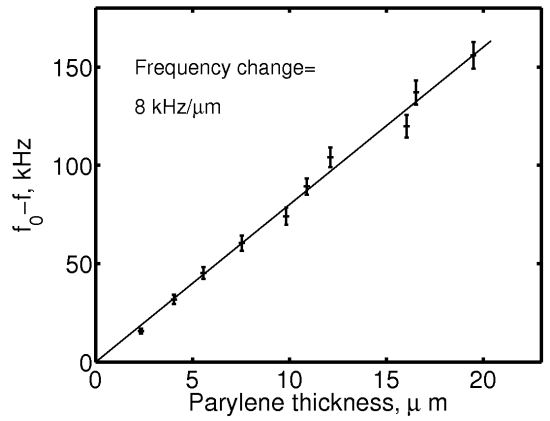

Figure 2: The frequency change of crystals as a function of parylene thickness. The vertical lines indicate the average value ± standard deviation of 21 crystal samples.

4 RESULTS

After 11 coating runs, measurement results proved that there is a certain interrelation between the resonance frequency and the thickness of parylene. The measurement results are illustrated in Fig. 2. The frequency change of crystals increases linearly as parylene thickness increases. The slope of this line is 8.0 kHz/µm.

The coefficient appearing in the Sauerbrey equation, (1), is 3.64 kHz/µm. As compared to this value, the frequency change in Fig. 2 is quite a lot larger. There are several possibilities that can explain this discrepancy.

On each coating run, parylene was added on the last coat of parylene. It is possible that these layers or the interfaces had collected some impurity that affected the results; though impurities were not seen in visual microscope examination. Another source of discrepancy might be in the coating process parameters. When different recipes for same amount of dimer are used, the final thicknesses are unequal. Therefore, it seems that the process parameters affect the final density of parylene, and/or the parylene coats different locations in the chamber with different thicknesses. Furthermore, the parylene density after each coating is not measured, and hence it is unreliable to use the literature value for parylene density in Sauerbrey equation. Finally, when the crystal is coated, parylene covers the entire quartz crystal area including the sides of the crystal and the electrodes connected to the quartz crystal. Hence it might prevent the vibration of the quartz crystal and measurement results in frequency change are not equal to frequencies measured with Sauerbrey equation.

In the future, these measurement results are usable basis for developing the parylene thickness measurement set-up, though additional experimental results will be needed for accurate reference data. Idea is to control the deposition thickness of parylene during the deposition process by monitoring the resonance frequency change of crystal oscillator in vacuum chamber. The real-time measurement set-up would be composed of the crystal oscillator placed in vacuum chamber, the network analyser, and the measuring cables for generating the connection between the crystal oscillator's electrodes and the network analyser. The possibility to produce sealed hole, for example to the observation window of vacuum chamber to allow measuring cables to pass through, should be studied. In real-time measurement, the network analyser measures the resonance frequency change and as the

earlier defined frequency change for target parylene thickness is reached, the coating run could be cut off.

5 SUMMARY

We have presented a method to measure the thickness of parylene coating, especially for medical electronic devices. The method is based on frequency change of coated quartz crystals. We proved that the frequency change is proportional to the parylene thickness, and determined the factor relating the thickness and frequency change. The applicability of this factor to different parylene coating processes was discussed. The method is applicable also for real-time measurements enabling the measurement of parylene thickness during the growth process. In real-time measurements, the growth process could be stopped after the target thickness has been reached.

REFERENCES

Eggins, B. R. 2002, '*Chemical Sensors and Biosensors',* John Wiley & Sons. 291 p.

Gulati, N., Auras, R., Rubino, M. 2006, '*Determination of barrier properties of poly(lactide) polymers using a quartz crystal microbalanc*e', ANTEC 2006 Platics, North Carolina, 2006, p. 1530–1534.

Ito, H., Kakuma, S., Ohba, R., and Noda, K., 2003, 'Development of a Humidity Sensor using Quartz Crystal Microbalance', *SICE Annual Conference*, Fukui, Japan, August 4.-6., 2003, pp. 1175–1178.

Licari J., 2003, *Coating Materials for Electronic Applications: polymers, process, reability, testing,* Noyes/William Andrew, New York, pp. 154–168

Noordegraaf J. and Hull, H. 1997, 'C-shield parylene allows major weight saving for EM shielding of microelectronics′, *1st IEEE International Symposium on Polymeric Electronics Packaging*, Norrkoping, Sweden, October 26.-30., 1997, pp. 189–196.

Pang, C., Cham, J. G., Nenadic, Z., Musallam, S., Tai, Y-C., Burdick, J. W., and Andersen, R. A. 2005, 'A New Multi-Site Probe Array with Monolithically Intergrated Parylene Flexible Caple for Neural Prostheses', *27th IEEE Annual Conference on Engineering in Medicine and Biology*, Shanghai, 2005, 4p.

Para Tech Coating, Inc. 2006. Retrieved September 7, 2007, from http://www.parylene.com/index.html.

Ratner, B. D., Hoffman, A. S., Schoen, F. J., and Lemons, J. E., 1996, '*Biomaterials science: an introduction to materials in medicine',* Academic press, San Diego, 484 p.

Lee, S.-H., Stubbs, D. D., Cairney, J., and Hunt, W., D, 2005, 'Rapid Detectioon of Bacterial Spores Using a Quartz Crystal Microbalance (QCM) Immunoassay', *IEEE Sensors Journal,* vol. 5, no. 4, pp. 737–743.

Specialty Coating System 2007, Retrieved March 27, 2007, from http://www.scscoatings.com/.

Stieglitz, T., Kammer S., Koch K. P., Wien S., Robitzki A. 2002, 'Encapsulation of Flexible Biomedical Microimplants with Parylene C', *International Functional Electrical Stimulation Society* (IFESS):231-3.

Wolgemuth, L. 2002, 'The Surface Modification Properties of Parylene for Medical Applications', *Medical Device Manufacturing & Technology*, pp. 1–4.

Yang, G. R., Ganguli, S., Karcz, J., Gill, W. N., and Lu T. M. 1998, 'High deposition rate parylene films'. *Journal of crystal growth*, vol. 183, pp. 385–390.

APPLICATION OF MODAL ANALYSIS FOR EXTRACTION OF GEOMETRICAL FEATURES OF BIOLOGICAL OBJECTS SET

Mchal Rychlik, Witold Stankiewicz
Division of Methods of Machine Design, Poznan University of Technology, ul. Piotrowo 3, Poznan, Poland
Michal.Rychlik@put.poznan.pl, Witold.Stankiewicz@ put.poznan.pl

Marek Morzyński
Division of Methods of Machine Design, Poznan University of Technology, ul. Piotrowo 3, Poznan, Poland
Morzynski.Marek@ put.poznan.pl

Keywords: 3D geometry reconstruction, anthropometric measurements, PCA (Principal Component Analysis), registration, reverse engineering.

Abstract: This article presents application of modal analysis for the computation of data base of biological objects set and extraction of three dimensional geometrical features. Authors apply two types of modal analysis: physical (vibration modes) and empirical (PCA – Principal Component Analysis) for human bones. In this work as the biological objects the fifteen human femur bones were used. The geometry of each bone was obtained by using of 3D structural light scanner. In this paper the results of vibration modal analysis (modes and frequencies) and PCA (mean shape and features – modes) were presented and discussed. Further the possibilities of application of empirical modes for creation three dimensional anthropometric data base were presented.

1 INTRODUCTION

Nowadays, many engineering CAD technologies have an application not only in mechanics but also in different disciplines like biomechanics, bioengineering, etc. This interdisciplinary research takes advantage of reverse engineering, 3D modelling and simulation, PCA analysis and other techniques. The 3D virtual models have a numerous applications such as visualisation, medical diagnostics (e.g. virtual endoscopies), pre-surgical planning, FEM analysis, CNC machining, Rapid Prototyping, etc. Several engineering technologies can be used for analysis of biological objects.

Usually the populations of the biological objects like bones, are used to be described only in two dimensional space, by the set of the dimensions (e.g. distance). Thereby traditional anthropometric data base contains information only about some characteristic points, while other parameters are not collected. Generally data acquisition process is made with usage of the conventional measurements equipment (e.g. calliper). For any new research work (when not existing parameter is needed) completely new study and measurements process must be done.

The new methods of statystical analysis and storage of complete parametric data for each of all elements from population are researched. The methods which can be used to describe a geometrical parameters of 3D objects are modal analysis.

2 MODAL ANALYSIS METHODS

In this chapter authors present modal analysis methods which are used for geometry description of three dimensional objects and data base creation. These methods are used to simplify and minimize the number of parameters which describe 3D objects.

One of the methods that is based on modal decomposition is PCA (Principal Component Analysis, known also as POD – Proper Orthogonal Decomposition). While empirical modes (PCA) are optimal in the sense of information included inside each of the modes (Holmes, Lumley and Berkooz, 1998), often other decompositions, based on mathematical (e.g. spherical harmonics) or physical modes (vibration modes) are used. The kind of

modal method (mathematical, physical or empirical) which is applied to analysis has a fundamental importance for results.

The goal of using mathematical modes is conversion of physical features onto mathematical features (synthetic form). In the case of the mathematical modes the features which describe geometry of 3D object are usually saved as the vectors. Each vector is obtained through splitting of the 3D model onto several classes (different diameter spheres) and calculation of common areas between 3D object and surfaces of individual spheres. All areas are described by a set of vectors (spherical functions). For spherical functions Fourier transformation is used, resulting in easier multidimensional description of feature vectors. For representation of feature vectors spherical harmonics are used (figure 1.).

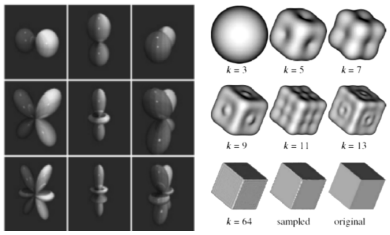

Figure 1: Example of spherical harmonics of 3D model of aeroplane and application of spherical harmonic in reconstructtion of geometry of the cube (Vranic and Saupe, 2002).

Application of spherical modes is not optimal solution and sometimes causes increased computation costs, because all objects are approximated by deformed sphere. Reconstruction of geometry of the cube requires very large number of spherical harmonics. This problem is analogous to Fourier decomposition of rectangular signal.

The second group of modal decompositions of 3D objects is represented by physical (mechanical) modes. These modes – also known as the vibration modes – are obtained by solution of eigenproblem for elastic model of analyzing object. Vibration modal decomposition provides alternative parameterisation of degrees of freedom of the structure (translations of the nodes in x, y, z directions only) based on eigenmodes of the objects and correlated frequencies (eigenvalues). Usually eigenmodes related with low frequencies, describing deformation vectors for individual nodes of FEM grid, are used. This way the deformation of geometry of base object and its fitting into searched object is possible. Vibration modes computed for rigid body represent translations and rotations of 3D model and vibration modes of elastic body describe different variations of the base model's shape (figure 2.).

Figure 2: Graphical representation of seven low frequency vibration modes for surface model of ellipsoid (Syn and Prager, 1994).

PCA transformation gives orthogonal directions of principal variation of input data. Principal component which is related with the largest eigenvalue, represent direction in data space of the largest variation. This variation is described by eigenvalue of largest magnitude. The second principal component describes the next in order, orthogonal direction in the space with the next largest variation of data. Usually only a few first principal components are responsible for a majority of the data variations. The data projected onto other principal components often have small amplitude and can be treated as measurement noise. Therefore, without the loss of accuracy, components related to smallest eigenvalues can be ignored.

3 PHYSICAL MODES – VIBRATION MODES

Decomposition basis on vibration modes uses similar procedure like in analysis of dynamical problems. For describing of complicated moving they used set of simple functions (1):

$$u(x,y,z,t)=\sum_{n=1}^{N} q_n(t)\phi_n(x,y,z) \qquad (1)$$

where N is the number of used functions, ϕ_n is the vector (mode) of the object's vibration, and q_n is coefficient for n-th mode in time t.

Linear elastic structures can be described by surface or volume finite elements. After discretization in FEM software the eigenanalysis is done, using the mathematical oscillation model (2):

$$M\ddot{u}+C\dot{u}+Ku=f(t) \qquad (2)$$

where M, C and K are adequately: mass, damping and stiffness matrix, and u is vector of grid node displacements.

3.1 FEM Model

Computations have been done using NASTRAN software. Model geometry is based on surfaces resulting from 3D-scanning of real human femoral bone. Finite element mesh consists of approximately 4800 nodes and 5500 elements of two types. External layer of 1940 triangular plate elements represents compact (cortical) bone and 2560 tetrahedral elements represent internal, trabecular bone. Model was fixed in condyles part.

In both cases, orthotropic material, based on measurement data (Ogurkowska et al, 2002), was used.

3.2 Eigenmodes

The result of eigenproblem solution is a set of eigenvalues (representing the vibration frequencies) and eigenmodes. The eigenmodes related with lowest frequencies, added to mean shape of femur, are presented at figure 3.

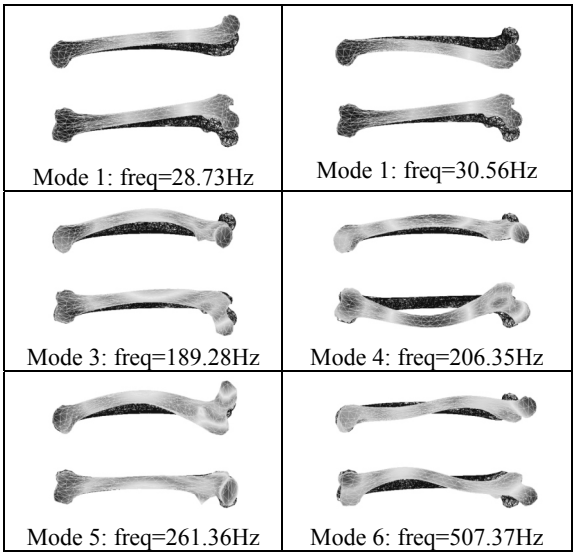

Figure 3: Eigenmodes related with lowest frequencies.

Gray scale levels represent total translation and dark bone is a mean, undeformed shape. Each bone is presented in two views: posteriori and anterior view.

Practical application of vibrational modes is strongly limited due to high number of modes required to reconstruct different geometries. Additionally eigenmodes don't represent any biophysical features of human femoral bones.

4 EMPIRICAL MODES – PCA

Despite the fact that the method is called differently in various application areas, the used algorithm is generally the same and is based on statistical representation of the random variables.

The shape of the every object is represented in the data base as the 3D FEM grid and described by the vector (3)

$$S_i = [s_{i1}, s_{i2}, \ldots, s_{iN}]^T,\ i = 1,2,\ldots,M, \qquad (3)$$

where $s_{ij} = (x, y, z)$ describes coordinates of each of the nodes of FEM grid in Cartesian coordinates system. M is the number of the objects which are in database, N is the number of the FEM nodes of every single object. The decomposition is based on computation of the mean shape $\overline{S}$ and covariance matrix C (4):

$$\overline{S} = \frac{1}{M}\sum_{i=1}^{M} S_i,\ C = \frac{1}{M}\sum_{i=1}^{M} \widetilde{S}_i \widetilde{S}_i^{\,T} \qquad (4)$$

The difference between mean shape and current object from data base is described by the deformation vector $\widetilde{S}_i = S_i - \overline{S}$. The statistical analysis of the deformation vectors gives us the information about the empirical modes. Modes represent the features: geometrical (shape), physical (density) and others like displacement and rotation of the object. Only few first modes carry most of the information, therefore each original object S_i can be reconstructed by using some K principal components (5):

$$S_i = \overline{S} + \sum_{k=1}^{K} a_{ki}\Psi_k,\ i = 1,2,\ldots,M, \qquad (5)$$

where Ψ_k is an eigenvector representing the orthogonal mode (the feature computed from data base), a_{ki} is coefficient of that eigenvector and i-th data base model. The example of low dimensional reconstruction for three different values of the coefficient of the first mode is presented on the figure 4. For $a_{ki} = 0$ we obtain mean value, for different values we get new variants of object's shape.

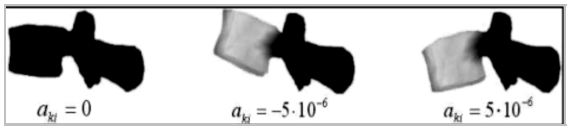

Figure 4: The visualisation of the reconstruction for different coefficient values.

4.1 Data Acquisition – 3D Scanning

As the input data (data base) 15 femur bones were measured (6 female, 9 male). For 3D scanning (Rychlik Morzyński and Mostowski, 2001) the structural light 3D scanner – accuracy 0,05mm – was used (figure 5). Each bone was described by individual point cloud (1.5mln points) and triangle surface grid (14000nodes, 30000 elements).

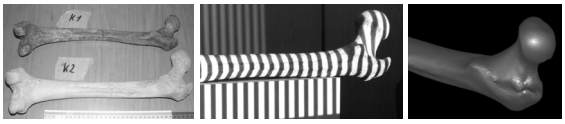

Figure 5: Data acquisition: a) input femur bones, b) measurement process, c) final triangle surface grid.

4.2 Data Registration

The Principal Component Analysis requires the same topology of the FEM mesh for all objects (the same number of nodes, connectivity matrix, etc.). To achieve this, every new object added to data base, must be registered. The goal of registration is to apply the base grid onto geometry of the new objects. The registration is made in two steps. First step (preliminary registration) is the rigid registration - a simple geometrical transformation of solid object in three-dimensional space (rotation and translation). The second step is the viscous fluid registration. For this registration the modified Navier-Stokes equation in penalty function formulation (existing numerical code: Morzynski, Afanasiev and Thiele, 1999; source segment: F Bro-Nielsen and Gramkow, 1996) is used (6):

$$\underbrace{\dot{V}_i + V_{i,j}V_j - \frac{1}{\mathrm{Re}}V_{i,jj} + \frac{\varepsilon - \lambda}{\rho}V_{j,ji}}_{\text{existing numerical code}} + \underbrace{(f-g)f_{,i}}_{\text{source segment}} = 0 \qquad (6)$$

where ρ is fluid density, V_i velocity component, Re Reynolds number, λ bulk viscosity. In this application parameters ε and λ are used to control the fluid compressibility, f is the base object, g is the target object (input model). The object is described by the FEM grid. The displacements of the nodes are computed from integration of the velocity field. Computed flow field provides information about translations of the nodes (FEM grid) in both sections. After computation we obtain dislocation of nodes of the base grid onto new geometry (figure 6.).

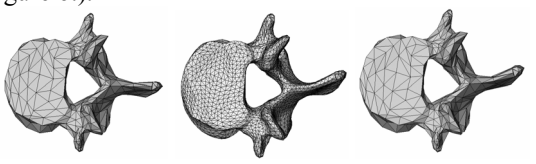

Figure 6: FEM grid deformation (from the left): base object, new object, base FEM grid on geometry of the new objects.

4.3 Empirical Modes – PCA

For that prepared database of 15 femur bones the Principal Component Analysis was done. The result of this operation is the mean object, fifteen modes and coefficients (figure 7).

Table 1: Participation of the modes in reconstruction.

Number of the mode	Participation of the mode [%]	Total participation of the modes [%]
1	74.9212416	74.9212416
2	10.5438352	85.4650767
3	4.2699519	89.7350286
4	3.3128685	93.0478971
5	1.6659793	94.7138765
6	1.4234329	96.1373093
7	1.0359034	97.1732127
8	0.6781645	97.8513772
9	0.5866122	98.4379894
10	0.4796167	98.9176061
11	0.3301463	99.2477523
12	0.3080968	99.5558492
13	0.2516839	99.8075330
14	0.1924670	100.0000000
15	0.0000000	100.0000000

The first fourteen modes include one hundred percent of information about decomposed geometry (table 1.). Fifteenth mode contains only a numerical noise and it is not used for further reconstruction.

Modes describe the features of the femur bones. First mode describes the change of the length of the femur bone, second mode – the change of the position of the head of the bone, third - change of the arc of the shaft (body). Further modes describe more complex deformations. For example fourth mode describes the change of position of the greater trochanter and lesser trochanter and also the thick-

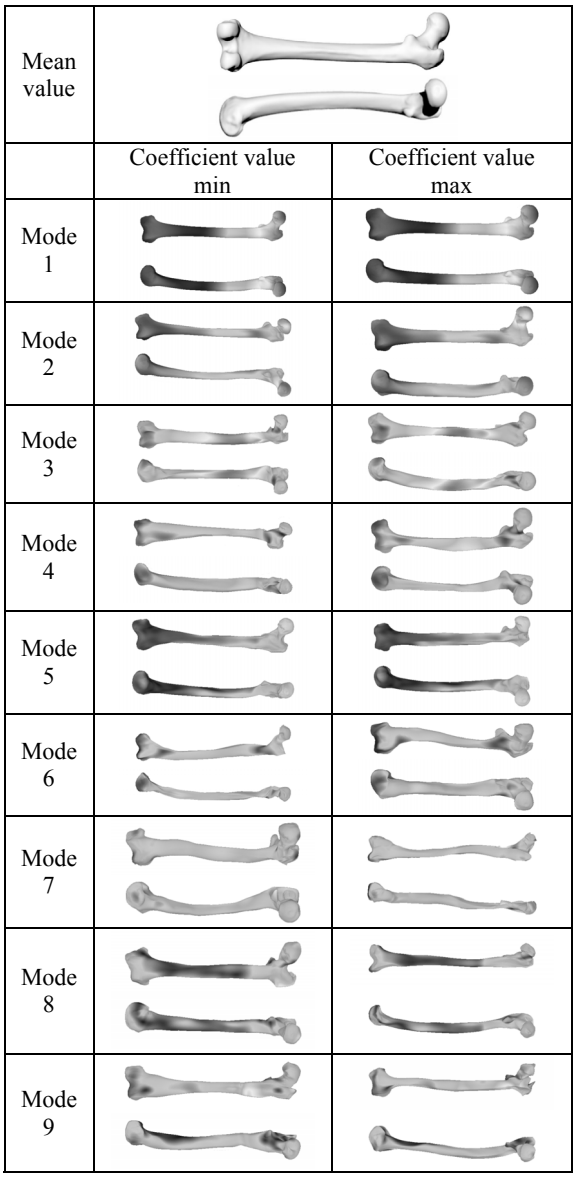

Figure 7: Visualisation of the mean value and first nine empirical modes of femur bones (anterior and posterior view).

ness of the shaft (body). Fifth mode describes deformation of the greater trochanter in other directions. Sixth describes deformation of the greater trochanter and lesser trochanter, and position of the shaft (body) in other directions.

Results of the statistical analysis (empirical modes) can be used for reconstruction of the geometry (in CAD systems) of individual features of the object. Empirical modes give as information about 3D mean shape of population of objects and a set of the geometrical features that describes principal deformations in analyzed population of the objects.

This method can be used for creation of complete 3D anthropometric database and gives us possibility to measure any dimension on the surface of the bone.

Real 3D anthropometric database is also necessary in practical application of the method of reconstruction of 3D biological objects basing on the few RTG images (Rychlik, Morzynski and Stankiewicz, 2005).

5 CONCLUSIONS

Although we can use several modal methods to describe the geometry of 3D objects, only empirical modes give us an optimal statistical data base.

Graphical representation of spherical harmonics is very specific and it is impossible to find similarity with input model, with exception of algebraic relations.

There are several differences between methods producing physical (vibration) modes and empirical modes (PCA, POD, Karhunen-Loeve), that are used in modeling of 3D objects.

A large limitation of usage of physical modes (vibration modes) is the impossibility to obtain the modes that describe resizing (scaling) of whole object or it's parts. These features are skipped out and they cannot be used in decomposition. The problem is also the large number of the modes that must be used in description of the shape of the object. Sometimes for reconstruction of a very simply geometry (e.g. cube) we must use a lot of modes (even up to 200 modes).

In case of physical modes, the only available determinant of mode's suitability is the vibration frequency (eigenvalue). One can assume that modes with high frequencies will represent numerical noise only, but the number of modes related with low eigenvalues that have to be used in reconstruction of another 3D object of the population is unknown. While the total number or eigenmodes is equal to the number of degrees of freedom of the model (in our case: 3x4800 DOF), the modal description of the population using physical modes might require larger data storage than input data (separate grids for each of the objects), and might still be incomplete (the scaling mentioned before).

Empirical modes describe features of the object that are dependent on frequent occurrences in population. The largest eigenvalues are related with

modes describing the most important features, what makes the reduction of data storage quite simple.

For Karhunen-Loeve analysis of data base which consists of several similar, but not the same objects, differing from each other only in the scale, this feature (size of the object) will be the most dominant empirical mode. Additionally, the number of modes required to reconstruct the whole population of objects without quality losses is assured to be smaller or equal to the number of objects in that population. In practice, a number of empirical modes can be used to describe the population with accuracy higher than in case of any other modes (optimality of PCA mentioned before).

For empirical modes (in data base) it is possible to keep the additional information's, e.g. data from diagnostic systems, density, Young's modulus, and other material properties.

PCA can be used for creation of complete three dimensional anthropometric data base.

REFERENCES

Bro-Nielsen, M., Gramkow, C., 1996, *Fast fluid registration of medical images*, In: *Proc. Visualization in Biomedical Computing (VBC'96)*, Springer Lecture Notes in Computer Science, vol. 1131, Hamburg.

Holmes, P., Lumley, J., L., Berkooz, G., 1998, *Turbulence, Coherent Structures, Dynamical Systems and Symmetry*, Cambridge University Press, Cambridge, New Ed edition.

Morzynski M., Afanasiev K., Thiele F., 1999, *Solution of the eigenvalue problems resulting from global non-parallel flow stability analysis,* Comput. Methods Appl. Mech. Eng., 169 (1999).

Ogurkowska, M.B., Kabsch, A., Glema, A., Kakol, W., Lodygowski, T., Wierszycki, M., Morzynski, M., Nowak, M., Roszak, R., Rychlik, M., Stankiewicz, W., 2002, *The interaction of L4-L5 spinal segments by FEM, Part 1 Methods of geometrical data acquisition and validation*, 13th Conference of the Society of Biomechanics, Wroclaw.

Rychlik M., Morzyński M., Mostowski R., 2001, *Metody przetwarzania obiektów skanowanych przestrzennie do modeli CAD,* CAD in Machinery Design Implementation and Educational Problems, ISBN 83-9164442-4-3, Warszawa.

Rychlik, M., Morzynski, M., Stankiewicz, W., 2005, *Applications of CDF and PCA methods for geometry reconstruction of 3D objects*, Proceedings of the 10th International Conference mathematical Modeling and Analysis, Vilnius.

Syn, M., H-M., Prager, R., W., 1994, *Mesh models for three-dimensional ultrasound imagining*, CUED/F-INFENG/TR 210, Cambridge University Engineering Department, Cambridge.

Vranic, D., Saupe, D., 2002, *Description of 3D-shape using a complex function of the sphere*, Department of Computer and Information Science, University of Konstanz.

A WIRELESS ACQUISITION SYSTEM FOR MONITORING THE INFLUENCE OF LOADS ON VERTEBRAL COLUMN BEHAVIOUR

João Eduardo Castro Ribeiro[ξ] and João Paulo Pereira do Carmo[χ]
[ξχ]*Instituto Politécnico de Bragança, Bragança, Portugal*
[ξ]*Departamento de Tecnologia Mecânica*
[χ]*Departamento de Electrotecnia*
[ξ]*jribeiro@ipb.pt*

Keywords: Biotelemetry, biomechanical and Wireless electromyography (EMG).

Abstract: This paper presents a wireless acquisition module (WAM). This allows the monitoring of heavy loads influence on vertebral column's behaviour. Each module makes the electromyography (EMG), to measure the electric potentials on the iliocostalis and longissimus thoracis muscles, and use a dual-axis accelerometer to get the movements of the body, in order to obtain the complete behaviour of the vertebral column. The solution chosen to transmit the body's measured signals for further processing, is a wireless link working in the 433 MHz ISM band. The acquired information is transmitted with a maximum rate of 40 kbps, a resolution of 9.8 μV, and accommodates two analog channels. An analog channel with differential input connected to the electrodes, is used to measure the EMG signal, while the remained channel is used in the patient's movements measurements. The dimensions of the proposed acquisition system are about 7×5×2 cm, and will help to understand the influence of heavy loads as a risk factors in the vertebral column, such as the scoliosis and lordosis.

1 INTRODUCTION

The human posture has been an object of studies in biomechanics, once some deviations of structural and functional positions induce an unbalanced body.
These deviations usually, affects the vertebral column and are caused by physical efforts, bad postures in work, deficiency in sustentation muscles, infections and congenital causes. The main pathologies of vertebral column caused by the referred deviations, are the scoliosis and lordosis. Sometimes these pathologies appears in children when they carry the heavy backpacks on the backs, in this case, it's very important monitoring the influence of loads (backpack weight) in vertebral column behaviour.
The vertebral column has very important functional requirements, which the most significant are: it carries and supports the thoracic cage, maintaining the balance between it and abdominal cavity; it gives attachment to many muscles of the pectoral and pelvic girdles; it provides anchorage for many powerful muscles, which move the vertebral column, these same muscles maintaining the balance and erectness of the human trunk; it acts as shock absorber, by virtue of its curvatures and the intervertebral discs, receiving and distributing the impacts associated with the dynamic functioning of the body; it is able, by virtue of its flexibility, to produce and accumulated moments of force as well as to concentrate and transmit forces receiving from other parts of the body (Palastanga *et al*, 2002).
When someone carries a heavy object like a backpack on the back, the center of gravity of body changes and it will be necessary some adaptations to maintain the balance, these adaptations are possible because the action of powerful muscles like iliocostalis or longissimus thoracis, and the relative movement among the intervertebral discs. In the children who carries heavy backpacks repeatedly and for long time they could suffer injuries in the vertebral column that can develop pathologies like scoliosis. Figure 1 show vertebral column with a scoliosis.
The study of influence of backpack weighs on the vertebral column of children is an important issue, that has been worked by many researchers for years (Nissinen *at al*, 1994; Widhe, 2001; Skaggs *et al*, 2006).
In this work it is used a different approach, applying indirect information, using the electrical potential

generated by the muscles, when they contract and when they are rest. The technique which could measure this electrical potential is the electromyography (EMG). Based on the results of EMG, combined with the movements of the body, measured by the accelerometers, it is possible to know by numerical simulation, the displacement occurred on the insertions points between the muscles and the vertebral column (Conceição, F. *et al*, 2007; Pato, M. *et al*, 2007). Using these values of displacements in a finite element code, like ANSYS®, we can compute the value of stress field in the vertebral column, especially it is possible to observe where are the points more affected and the respective stress value.

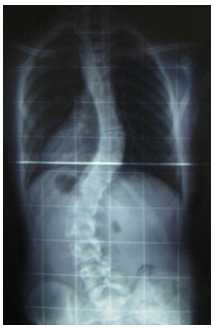

Figure 1: Radiograph showing a vertebral column with a scoliosis.

2 KINEMATICS

The skeletal system of the trunk comprises the pelvis, vertebral column and rib cage. The vertebral column is divided into four regions: cervical; thoracic; lumbar and sacrum.

The vertebral column is a flexible rod with seven mobile segments in the cervical region, twelve segments in the thoracic region and five segments in the lumbar region. The fourth region of the vertebral column, the sacral-coccyx region, includes nine fused vertebrae that together with the right and left ilia form the pelvis.

Two adjacent vertebrae and their interposed intervertebral disk form a motion segment of the vertebral column. Each segment has six degrees of freedom (DOF). In the vertebral column, there are two types of joints: the intervertebral joints between the vertebrae and adjacent disks and the facet joints between the facets (articular processes) of the neighbouring vertebrae. Movement at the intervertebral and facet joints of the same motion segment is coupled.

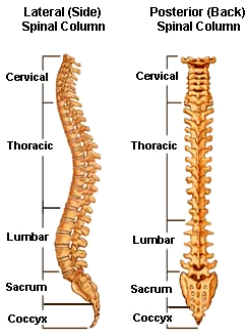

Figure 2: The regions of the vertebral column (Bridwell, 2007).

The intervertebral disks are flexible spacers between adjacent vertebrae. The disk consists of a central nucleus pulposus, which is a ball of hydrophilic jelly, and the outer annulus fibrosus, a series of laminae formed by collagen fibers. The disc height (thickness) increases from the cervical lumbar region from about 3 mm to 9 mm.

Any change in vertebral column posture involves the joined movement of several motion segments. People cannot move the individual motion segments independently.

Kinematics of the vertebral column deals either with the specific motion segments or with the entire region of the vertebral column or both (Zatsiorsky, 1998).

Each of the motion segments has six DOF: because the intervertebral disks can deform, the vertebrae, in addition to being able to rotate, and translate. The vertebral column as whole can produce only three movements: flexion-extension, lateral flexion and axial rotation. The vertebral column movement results from concurrent rotation and translation of the vertebrae. The amount of motion available at various motion segments depends mainly on the size of the disks, while the orientation of the facet joint surfaces, which changes from region to region, defines the direction of the allowable movement.

The relative movement of the motion segments of the vertebral column is allowed by an elastic connection provide by the intervertebral disks. Vertebral flexion and extension causes compression in one part of the disk and traction in another part. When a relative motion between two consecutive vertebrae is analyzed, the lower vertebra is usually considered a fixed body and the upper vertebra is treated as moving body. The coordinate axes are taken along the inferior and posterior margins of the stationary, lower vertebra.

Because the disks can deform, the same resultant force and torque being applied to various vertebrae produces different movements depending on the disk stiffness and its dimensions, height and diameter.
The rotation and translation of the vertebrae results in a torsion and bending of intervertebral disks. In case of torsion, the disk is subjected to equal and opposite twisting couples at the two adjacent vertebrae. The axial rotation, α_a, is the angle by which the top vertebra turns with respect to the bottom vertebra. For a disk of a height H, radius r, and cross-sectional area A, on which a torque M_a is acting, the angle of twist is:

$$\alpha_a = \frac{M_a H}{G I_p} \tag{1}$$

where G is the shear modulus and I_p is the polar moment of inertia. The bending occurs when the line of force does not coincide with the symmetry axis of de column, and appears a bending stress (Adams and Dolan, 1991). The equation relating angular displacement of the disk, α_b, with the applied bending moment, M_b, is

$$\alpha_b = \frac{M_b H}{E I_d} \tag{2}$$

where E is the modulus of elasticity and I_d is a diametral moment of inertia, $I_d = 0.5 I_p$.
Considering that the column is loaded with two forces, F and –F, acting in opposite directions along the same line of action.
The line of action does not pass through the center of gravity (G). The center of gravity is the location of the resultant force acting in compression and proportional to the elements of area. The column is under joint action of compression and bending and is stressed correspondingly (Adams and Dolan, 1988).
The compressive stress is F/A, where A is the area of the horizontal section. The bending stress is M.y/I, where M is the bending moment; y is the distance from the neutral line of the column (this is the line that experiences neither compression nor tension during bending); and I is the area moment of inertia. The bending moment equals the product F×e, where e is the eccentricity (distance from the line of force to the center of the column). This distance is crucial in provoking bending stress.
The relative movement of a vertebra with regard to the vertebra immediately below it can be viewed as a combination of rotation and translation. An infinite number of combinations of rotation and translation can describe the same movement. To simplify the kinematics analysis is assuming that a vertebra rotates around a pole whish (1) is located on the inferior end plate of the moving vertebra and (2)

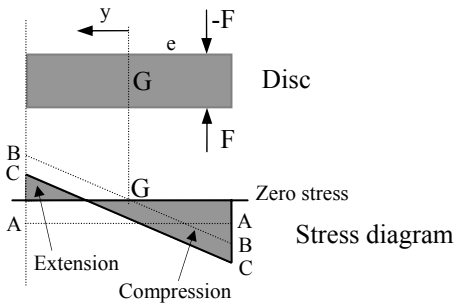

Figure 3: A model of intervertebral disk bending: the stress distribution is in vertical cross section of a column loaded by off-center forces, F and –F.

moves parallel to the inferior margin of the reference vertebra, axis X of the coordinate system.
In framework of this model, the vertebral motion is viewed as a translation along the axis X and the rotation around the pole, the center of rotation (Cossette, J. *et al*, 1971). Because a rotation about the instantaneous center of rotation (ICR) is equal to the rotation about any parallel axis, the angle subtended at the ICR by the arc of motion of C is equal to the angle of rotation (θ) undergone by the whole vertebra. Because the triangle CC'R is an isosceles triangle, HR = CC'/2tan(θ/2), where HR and CC' are the height and base of the triangle. If the location of the ICR is experimentally determined, location of C can be found as

$$X_{CR} = X_{IRC} - \frac{CC'}{2} \tag{3}$$

$$Y_{CR} = Y_{IRC} - \frac{CC'}{2\tan\left(\theta/2\right)} \tag{4}$$

The position of the ICR is determined by the location of the center of the rotation, the translation of the vertebra in parallel with the axis X and the rotation of the vertebra. In some patients, as compared with healthy people, the ICR is displaced. The displacement can be explained in terms of the three mentioned factors. For example, elevation of the ICR can occur only when the translation is decreased, the rotation is increased, or both. The three mentioned mechanisms can be explained by a combination of biomechanical changes, such as increased muscle pull.

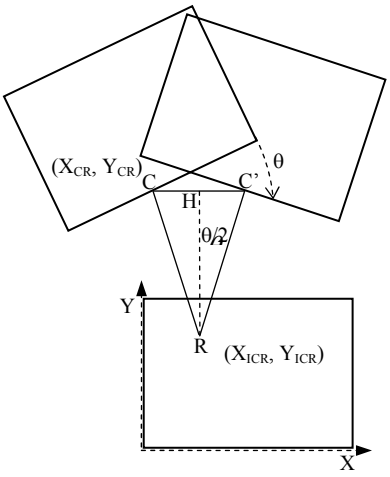

Figure 4: An illustration of a vertebra that has rotate and translated from an initial position to a final position about an ICR located at *R*. The center of rotation C translates to C'. H is the midpoint of interval CC'. θ is the angle of rotation.

3 WIRELESS ACQUISITION MODULE

The application described in this paper, needs wireless acquisition modules (WAMs), to simultaneously acquire the information from the muscles and the movements of the patient. In the first case, the use of standard electrodes makes possible to measure the electrical potential, above the patient's tissue. In the second case, a dual-axis accelerometer will measure the motion and the positioning of the patient.

Normally, the barrier layer forms the typical 50 kΩ impedance for 1 cm^2 of skin. There is also a skin potential between the inside and outside of the barrier layer of typically 30 mV. When the skin stretches, the skin potential decreases to about 25 mV and this 5 mV change is what we observe as motion artifact (Webster *et al*, 1984). These are the signals that are being acquired by the electrodes, and further amplified by the instrumentation and further converted to the digital domain.

The Figure 5 shows the architecture of a WAM, which is composed by an amplifier, followed by an analog-to-digital converter (ADC) to convert the amplified EMG signals to the digital domain, and a dual-axis accelerometer.

The amplifier is a chain composed by the MAX4460 instrumentation amplifier, and by the MAX4249 single-ended low-noise amplifier. The MAX4460 was chosed due to its characteristics, e.g., the low-power consumption, the ultra low-power input current and the increased common-mode rejection performance. This chip amplify the differential signals obtained from the two potentials collected with the EMG electrodes, placed in the patient's skin. The high input impedance of this amplifier matches with the small-signal differential voltages collected in the electrodes. The microcontroller automatically selects the most appropriated gain of this amplifier, which can be: one, ten and one hundred. The MAX4249 makes the differential to single ended conversion of the acquired EMG signal, while makes a further amplification. This amplifier was choosed due its low-noise characteristics, to not contaminate the EMG signal.

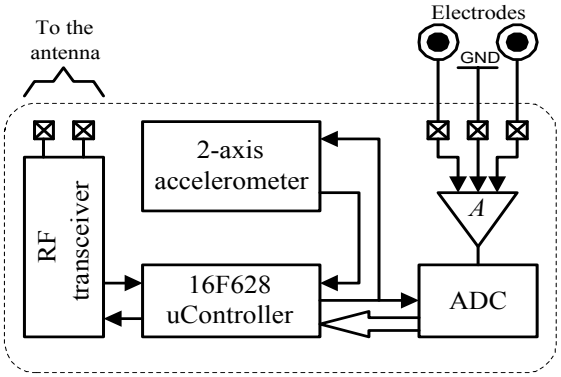

Figure 5: The block diagram of the wireless acquisition module.

The analysis of the EMG signal is made in the amplitude domain, thus, before proceeding to the ADC conversion, it is required a peak detection of the amplified EMG signal, followed by an integration (Robertson *et al*, 2004). This is mandatory process eliminates the fluctuations that characterise the EMG signal. As shown in Figure 6, the discharge of the capacitor, is made with a bipolar junction transistor (BJT). The pulse transformer is made in the WAM's PCB, in order to not compromise the compactness of the WAM. The circuit size WAM achieved, using surface mount (SMDs) devices, for all the components, including the micropower, rail-to-rail output, dual op-amp MAX4471, used in the circuit of the integrator.

The measurements of the motion and the positioning of the patient's body is made with the use of the ADIS16003, dual-axis accelerometer of MEMS type. This chip connects to the microcontroller, by way of an integrated Serial Port Interface (SPI). This accelerometer was choosed, due its build-in temperature sensor. This sensor is very useful to make the compensation of the temperature gradients, specially when the devices are placed in contact with the human body.

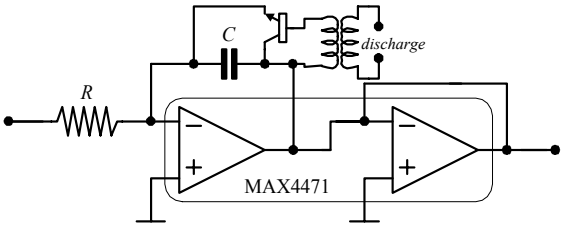

Figure 6: Integration circuit.

The microcontroller PIC16F628 from the Microchip manufacturer, controls all the electronics, as well as the communication between WAMs, and from the WAM and the external base-station, where all the processing of the acquired data is made by a health professional, or a medical doctor. It was selected the BiM433 radio-frequency (RF) transceiver, from the Radiometrix manufacturer to wirelessly send the data. A set of routines and services were developed to make the RF communication the most reliable as possible. The most important of these routines are the Manchester line coding, used to solve de DC balancing problem in the communication, when long sequences of zeros or ones must be transmitted. It was included a mechanism of error control in all data frames (information, control and acknowledge frames), e.g., the CRC field. This field makes the detection of transmission errors in the received bitstream (Schmidt, 2000). To make the multi-element communication possible and reliable, the WAMs use the Carrier Sense Multiple Access with Collision Avoidance protocol (CSMA-CA) to start the transmissions (Chandra *et al*, 2000). This simplifies the management procedures of the communication among modules, and between the base-station. This makes easy to place (or remove) new WAMs in the clothes of patients, in a plug-and-play fashion.

4 CONCLUSIONS

It was described in this paper, a wireless acquisition module, which will be used on the diagnosis of vertebral column risk factors, such as the scoliosis and lordosis. These factors normally associated to appears in children when they carry the heavy backpacks on the backs. Thus, it's of extremely importance to characterise the influence of heavy loads (backpack weight) in the vertebral column behaviour. This solution fits the medical doctors requirements for an easy placement and removal of the WAMs. This is true for the target application, because it is needed only with a low number of WAMs (no more than five), making possible to mount a wireless network with these plug-and-play modules. The main advantage of this solution, is the maintenance of the mobility and lifestyle of patients during the diagnosis.

A set of two alkaline 1.5-V class AA bateries supplies the wireless acquisition module. When the RF subsystem is on, these modules have a power consumption of 46 mW. With the RF subsystem off, these modules have a consumption of only 10 mW.

REFERENCES

Adams, M., Dolan, P., 1991, A technique for quantifying bending moment acting on lumbar spine in-vivo, Journal of Biomechanics, Vol. 24, pp. 117-126.

Adams, M., Dolan, P., Hutton, W., 1988, The lumbar spine in backward bending, Spine, Vol. 13, pp. 1019-1026.

Choi, P., *et al*, 2003, An experimental coin-sized radio for extremely low-power WPAN (IEEE 802.15.4) application at 2.4 GHz, IEEE Journal of Solid State Circuits, Vol. 38, No. 12, pp. 2258-2268.

Conceição, F. *et al*, 2007, Modelação do actuador músculo-tendão: os elementos elásticos em série como slemento central de potenciação de força, Proceedings of CMNE/CILAMCE, *In Portuguese*.

Cossette, J. *et al*, 1971, The instantaneous center of rotation of the third lumbar intervertebral joint, Journal of Biomechanics, Vol. 4, pp. 149-153.

Bridwell, K., 2007, http://www.spineuniverse.com/ displayarticle.php/article1286.html.

Kaggs D., *et al*, 2006, Back pain and backpacks in school children, Journal of Pediatric Orthopedy, Vol. 26, Nr. 3, pp. 358-363.

Nissinen M, *et al*, 194, Anthropometric measurements and the incidence of low back pain in a cohort of pubertal children, Spine, Vol. 19, Nr. 12, pp. 1367-1370.

Pato, M., Martins, J., Pires, E., 2007, Um modelo de elementos finitos para músculos esqueléticos, proceedings of CMNE/CILAMCE, *In Portuguese*.

Robertson, D., *et al*, 2004, Research methods in biomechanics, Human Kinetics.

Schmidt, T., 2000, Microchip Technology Inc., CRC generation and checking, Application note AN730.

Webster, J. *et al*, 1984, Reducing motion artifacts and interference in biopotential recording, IEEE Transactions on Biomedical Engineering, Vol. 31, No. 12, pp. 823-826..

Widhe T., 2001, Spine: posture, mobility and pain - A longitudinal study from childhood to adolescence, European Journal of Spine, Vol. 10, Nr. 2, pp. 118-123.

Palastanga, N., *et al*, 2002, Anatomy and human movement, Fourth Edition, Edited by Butterworth Heinemann, pp. 445-537.

Zatsiorsky, V., 1998, Kinematics of human motion, Edited by Human Kinetics, pp. 311-326.

A NEW METABOLISM MODEL FOR HUMAN SKELETAL MUSCLE

Dayu Lv and Bill Goodwine
Department of Aerospace and Mechanical Engineering, University of Notre Dame, Notre Dame, IN 46556, USA
dlv@nd.edu, jgoodwin@nd.edu

Keywords: Glucose, Insulin, Skeletal Muscle, Metabolism.

Abstract: The human body metabolic regulatory system is very complex, containing thousands of metabolites involved in biochemical reactions. Glucose metabolism is one of the key procedures maintaining daily energy balance. Mobility of glucose is implemented by glucose transporters with different transporting characteristics locally, which are distributed in cells of brain, liver, pancreas, kidney and skeletal muscle, *etc.* This paper presents a component of a new model that is focused on skeletal muscle which consume energy consistently due to either slight movement or high-energy demanded activities, such as running or swimming. This paper presents a mathematical model where glucose, insulin, glucose-6-phosphate (G6P), *etc.* are introduced and connected by ordinary differential equations.

1 INTRODUCTION

This paper presents a new model for the metabolic regulation of glucose in skeletal muscle in humans. It is part of a larger effort to develop a detailed whole-body human metabolic regulation model. Modeling of such systems is useful for several reasons. First, the mathematical structure of an accurate model will provide concise insight into the relevant physiology and also the pathophysiology of disease. Second, it will allow for inexpensive "experimentation" or biosimulation, which if predictive, can serve as a supplement to, and perhaps provide guidance to, *in vivo* and *in vitro* experimentation.

Of course this work is motivated by the epidemic of diabetes, which is a disease characterized by a failure to regulate blood glucose level. Many models have been constructed to describe glucose mobility in humans. What distinguishes this work from others is the scope, or dimension, of the model.

For many years, people have been investigating pathways of carbohydrates metabolism in order to establish mathematical models to reflect biology and control mechanisms. In (Srinivasan et al., 1970), a model composed of glucose, insulin and fatty acids was proposed to explain a two-hour metabolism responding to IV infusions of glucose, insulin, *etc.* Later, another hormone, glucagon, was added to a glucose-insulin system, (Cobelli et al., 1982). A few years ago, the mass of β-cells was connected to the system of glucose and insulin (Topp et al., 2000). Others were interested at kinetic properties of hormones, particularly insulin. A three-compartment insulin model was introduced in (Sherwin et al., 1974). It was composed of a plasma compartment, a quick compartment equilibrating with plasma and a slower one. Also the pulsative characteristic of insulin was well simulated (Tolić et al., 2000).

Although many models have been proposed, they are mainly restricted to metabolites without reflecting transporters' activities. In contrast, the model presented in this paper includes details regarding effects of, for example, various glucose transporters (GLUTs) in different organs, as well as *G6P*, which plays a key role in metabolism participating glycogenesis, glycogenolysis and glycolysis.

2 MODEL CONSTRUCTION

Skeletal muscle is actively involved in daily life. So the initial focus of our investigation into modeling whole-body glucose metabolism will be skeletal muscle. This model is constituted of two main parts: the interstitial fluid space (*IFS*) and the intracellular space (*ICS*). In the *IFS*, cells are surrounded by a liquid environment for nutrition exchange. *Via* diffusion, glu-

cose passes through capillaries to the *IFS*, then enter the *ICS* mediated by GLUT4. In the *ICS*, glucose is converted to G6P for storage and utilization. Glycogen can also break down to form G6P.

2.1 Intercellular Transport

The mechanism for glucose transport in the *IFS* is illustrated in Figure 1. It is assumed to diffuse through capillaries into the *IFS* and the direction is determined by the difference of glucose concentration between them, given by

$$f_{gs} = K_{01} \times ([G] - [G]_{si}), \tag{1}$$

where f_{gs} is positive for glucose out of plasma.

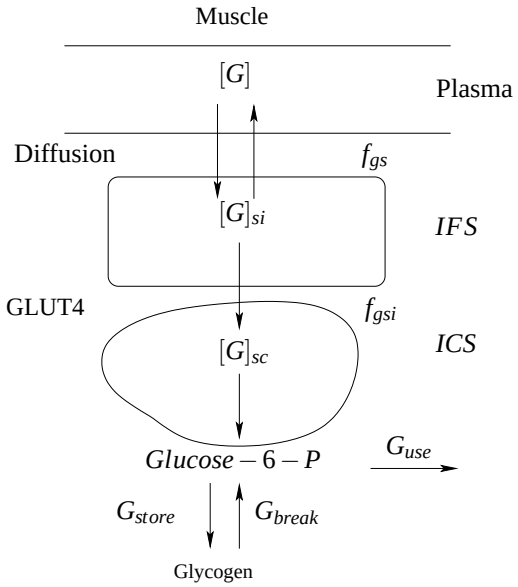

Figure 1: Three compartments of skeletal muscle.

Mediated by GLUT4, glucose is carried into the *ICS* described by Michaelis-Menton kinetics with $V_{\max} = 1.0$ mmol/kg-muscle/min and $K_m = 5.7$ mM in the basal state (Perriott et al., 2001). Insulin and exercise may stimulate more GLUT4 activity. The rates of insulin stimulation can be determined from (Sarabia et al., 1992), and exercise from (Fujimoto et al., 2003) and are given by

$$In_V = \frac{1.4331}{1 + e^{-0.2473 \times \lg([In]/(16.7 \times 10^{-10})) - 3.271}} \tag{2}$$

$$Ex_V = \frac{4.4531}{1 + e^{-198.5 \times (\dot{V}_{O_2}/\dot{V}_{O_2 \max}) + 60.95}} + 1, \tag{3}$$

$$V_{\max} = 1.0 \times Mass \times In_V \times Ex_V, \tag{4}$$

where $[In]$ represents insulin concentration in plasma, In_V represents the insulin effect on $V_{\max}$ and Ex_V represents the exercise effect on $V_{\max}$. Consequently, the glucose exchange rate between the *IFS* and the *ICS* is

$$f_{gsi} = -V_{\max} \frac{[G]_{si}}{K_m + [G]_{si}}, \tag{5}$$

where $[G]_{sc}$ and $[G]_{si}$ represents the glucose concentration in the *ICS* and the *IFS* respectively, f_{gsi} represents the rate which is positive for glucose transported out of the *ICS*.

In the model, insulin concentration is only considered in plasma, which is stimulated by increasing glucose concentration determined by dose-response on the secretion of insulin from isolated human islets of Langerhans (Frayn, 2003) and the data are fitted as

$$In_g = \left(\frac{79.21}{1 + e^{-1.934 \times [G] + 10.52}} + 29.84 \right) \times \frac{n \times 0.7}{V_p \times 60}, \tag{6}$$

where In_g represents the glucose stimulation on insulin secretion (mU/l/min), n represents the number of Langerhans, approximately one million (Frayn, 2003) assuming 70% of which are β-cells and V_p represents the plasma volume.

The degradation of insulin (In_d, mU/l/min), is modeled by a half-life given by

$$In_d = [In] \times e^{-K_{02} \times t}, \tag{7}$$

where $[In]$ represents insulin concentration in plasma and K_{02} represents the half-life coefficient (assuming $K_{02} = 20$). Therefore the dynamics of insulin concentration is

$$\frac{d[In]}{dt} = In_d + In_g. \tag{8}$$

2.2 Intracellular Space

After glucose uptake, it enters the intracellular metabolic process illustrated in Figure 2. The construction is based on an energy balance where the concentration of ATP remains almost constant (Frayn, 2003). G6P is generated from glucose and glycogen, and utilized through aerobic and anaerobic processes.

2.2.1 ATP Conservation

To meet the energy need of *Work* (mol/min), ATP is generated from aerobic and anaerobic glycolysis, the difference between which is the amount of ATP produced. Assuming oxygen is fully utilized by muscle, about 30 mol ATP is generated from 1 mol G6P and

6 mol oxygen (*Aerobic* - mol/min, G6P consumed) while in anaerobic glycolysis (*Anaerobic*, mol/min, G6P consumed), only 2 mol ATP is produced from 1 mol G6P. Also, converting glucose to G6P ($Rate_1$, mol/min, G6P produced) and synthesis of G6P to glycogen (*Syn* - mol/min, glycogen produced) are consuming energy. The energy of *Work* can be expressed as metabolic rate (Frayn, 2003). While this paper focuses on glucose metabolism, it is important to note that in the Randle-cycle, with competition between glucose and fatty acids, under different intensities of exercises, the proportion of fuels utilization between glucose and FFA will change. For example, under rest or light housework, the proportion of glucose as a fuel is providing about 10% of required energy while during swimming it will increase to about 70%. This is expressed by

$$ATP_{O_2} = \frac{1.429 \times 5}{32} \times \dot{V}_{O_2}, \quad (9)$$

$$Aerobic = \frac{1.429}{32 \times 6} \times \dot{V}_{O_2}, \quad (10)$$

where the oxygen has the density of 1.429 g/l and mole mass of 32 g/mol, ATP_{O_2} represents the ATP generated by aerobic respiration and *Aerobic* represents the *G6P* consumed during aerobic respiration. Then *Anaerobic*, the needed rate of G6P for anaerobic glycolysis can be calculated from

$$ATP_{O_2} - Rate_1 + Anaerobic \times 3 - Syn \times 20 = Work, \quad (11)$$

where $Rate_1$ represents the rate from glucose to G6P and *Syn* represents the synthesis rate of glycogen.

2.2.2 Glycogen Conservation

Glycogen conservation is simply determined by the synthesis and breakdown rates, given by

$$Syn - Dwn = \Delta(GLY). \quad (12)$$

2.2.3 G6P Conservation

Glycogen is a highly branched polymer that can be looked on as a set of multi-G6Ps. In this model, the proportion of glycogen to G6P is assumed to be 1:10 and the change of G6P is given by

$$\Delta G6P = Rate_1 + 10Dwn - 10Syn - Aerobic - Anaerobic. \quad (13)$$

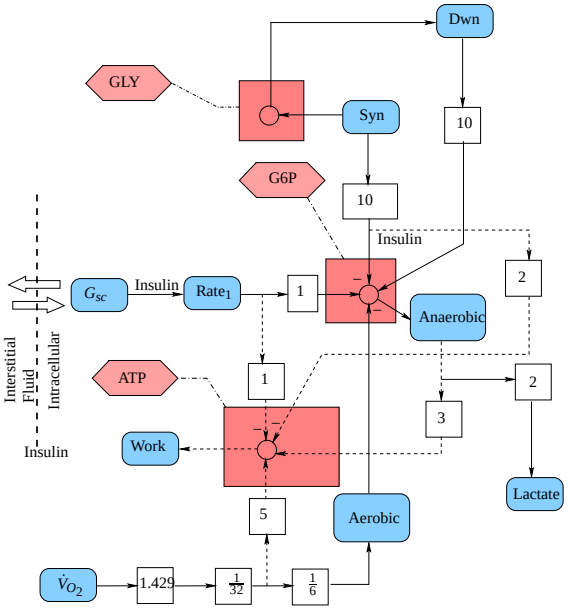

Figure 2: ATP Metabolism in Muscle.

2.2.4 Variables

- $Rate_1$ is the hexokinase (*HK*) rate on converting glucose to G6P. Under 456 pM of insulin, $Rate_1$ was determined as 0.0048 mmol/kg-muscle/min (Rothman et al., 1992). Assuming
  1. $Rate_1$ is a sigmoidal function of insulin concentration;
  2. $Rate_1$ is a sigmoidal function of [G6P]; and
  3. $Rate_1$ is a sigmoidal function of $[G]_{sc}$,

$$R_0 = 1.5 \times Mass, \quad (14)$$

$$In_R = \frac{2}{1 + e^{(-[In]+40.0)/20}}, \quad (15)$$

$$G6P_R = \frac{2}{1 + e^{([G6P]-0.12\times Mass/V_{sc})/10}}, \quad (16)$$

$$Gsc_R = \frac{2}{1 + e^{-[G]_{sc}+3.0}}, \quad (17)$$

$$Rate_1 = R_0 \times In_R \times G6P_R \times Gsc_R, \quad (18)$$

where R_0 is the basal value, *Mass* represents muscle weight, In_R, $G6P_R$ and Gsc_R represents their effects on $Rate_1$ respectively, $[In]$, $[G6P]$ and $[G]_{sc}$ represents concentrations respectively, V_{sc} represents the volume of the *ICS*.

- The synthesis rate of glycogen, *Syn*, is determined by the concentration of glycogen and G6P, insulin fitted from the data (Kelley and Mandarino, 1990), presented in Table 1 giving

$$GLY_{syn} = \frac{1}{1+e^{[GLY]-0.95\times[GLY]_{\max}}}, \quad (19)$$

$$In_{syn} = \frac{2}{1+e^{-2.2765\times\lg\frac{[In]}{[In]_0}}}\times \quad (20)$$

$$\frac{2}{1+e^{0.3517\times\lg\frac{[G6P]}{[G6P]_0}}}, \quad (21)$$

$$G6P_{syn} = 0.15\times e^{\lg\frac{[G6P]}{[G6P]_0}}, \quad (22)$$

where $[GLY]$ and $[GLY]_{\max}$ represents current and maximum glycogen concentration, In_{syn} and $G6P_{syn}$ represents their effects on Syn respectively. Referring to the data, $[In] = 28.2 \pm 4.2$ pM, $[G6P] = 0.133 \pm 0.014$ mM, glycogen synthesis rate (mM/hr) was

$$Syn_1 = \begin{cases} 15.8 \pm 1.7, & [\text{GLY}] < 35 \text{ mM} \\ 2.9 \pm 0.2, & [\text{GLY}] > 35 \text{ mM} \end{cases} \quad (23)$$

(Price et al., 1996). In the model, we assume $Syn_0 = Syn_1 \times 8$ for reasonable simulation results, and thus

$$Syn = Syn_0 \times In_{syn} \times G6P_{syn} \times GLY_{syn}. \quad (24)$$

Table 1: Insulin(Basal: 9.6 mU/l; Clamp 77 ± 3mU/l) and G6P (0.1mM; 10mM) effects on *Syn*.

Activity	Basal	Clamp
0.1 mM	1.59 ± 0.29	2.82 ± 0.43
10 mM	6.14 ± 0.62	7.21 ± 0.67

- The breakdown rate of glycogen, *Dwn*, is determined by G6P, glycogen and insulin concentrations as follows

$$In_{dwn} = \frac{2}{1+e^{[In]-20.0}}, \quad (25)$$

$$G6P_{dwn} = \frac{2}{1+e^{[G6P]-1.8}}, \quad (26)$$

$$GLY_{dwn} = \frac{1}{1+e^{-[GLY]+0.1\times[GLY]_{\max}}}, \quad (27)$$

where $[In], [G6P]$, $[GLY]$ and $[GLY]_{\max}$ represents the concentrations of insulin, G6P, glycogen and maximum glycogen. Assuming variables of needed G6P ($G6P_1$) and of test ($test_1$):

$$G6P_1 = Anaerobic + Aerobic + 10Syn \quad (28)$$

$$test_1 = G6P_1 - 0.5 \times \text{current G6P}. \quad (29)$$

If $test_1$ is near or less than zero, which means current *G6P* is enough for consumption, we set the rate (mol/min) as Equation 30 and otherwise as Equation 31,

$$Dwn_0 = 0.02, \quad (30)$$

$$Dwn_0 = test_1 \times 30 \times 10^{-3}/dt, \quad (31)$$

$$Dwn = Dwn_0 \times In_{dwn} \times G6P_{dwn} \times GLY_{dwn}. \quad (32)$$

3 SIMULATION RESULTS

Assuming glucose clamp $[G] = 5$ mM, the simulations assume the following activity plans

- 4 hours rest;
- 1hr rest + 40min light housework + 2hr20min rest;
- 1hr rest + 40min swimming + 2hr20min rest.

and shown in Figures 3 through 7.

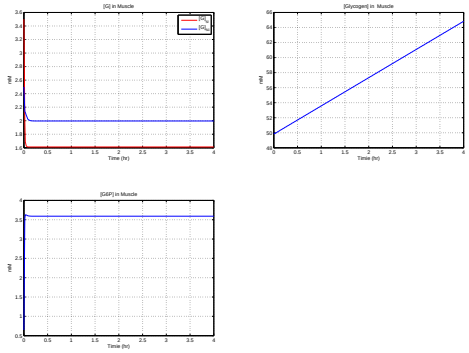

Figure 3: 4hr rest.

For the plan of swimming, we also simulate it with higher glucose levels $[G] = 7$ mM and $[G] = 14$ mM, and the results are illustrated in Figures 6 and 7. Note that in Figure 7, intracellular glucose concentration increase rapidly in the last part of simulation, which is due to the saturation of muscle glycogen and *G6P*, and it may bring about critical health problems.

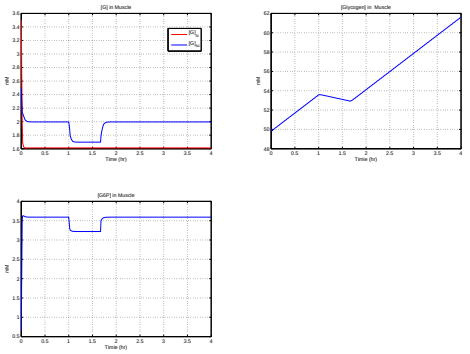

Figure 4: 1hr rest + 40min light housework + 2hr20min rest.

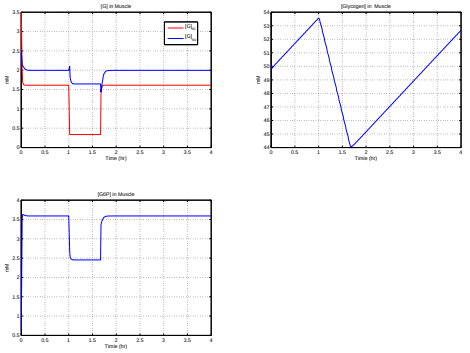

Figure 5: 1hr rest + 40min swimming + 2hr20min rest.

4 CONCLUSIONS AND PERSPECTIVES

In this paper, we have presented a mathematical metabolism model in human muscle. It is based on the kinetics of glucose transporters, GLUT4 and also considers the key role of *G6P*, whose regulation will determine the flow between storage and utilization. It works well in simulations. Under different activities, it reflects the interrelationships among glucose, insulin, G6P and glycogen.

The model has some limitations which we are currently addressing. First, the role of the glucose transporter GLUT1, with different kinetics is not yet considered. This transporter clearly plays a role in the basal state. Second, insulin concentration is considered only in plasma for simplification. And third, experiment data are still needed for a few of the equations. We indicated throughout the paper where a numerical value had to be assumed. Subsequent work will include a series of numerical experiments to better define the value, or range of values, that are feasible for such parameters.

In future work, the dynamics of insulin will be investigated and improved. Its resistance due to lasting high glucose level may be considered. Also, during exercises, increased level of lactate may be connected to other organs, such as liver. The overall goal, as mentioned previously, is a whole-body model expressed at a level of detail and fidelity similar to that for the muscle presented in this paper.

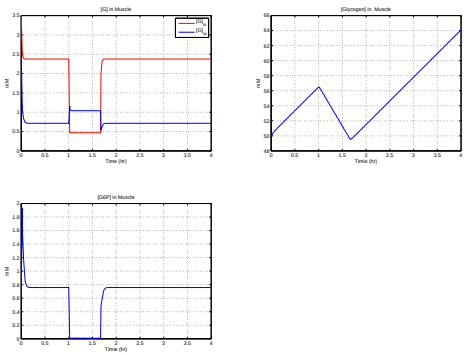

Figure 6: $[G] = 7$ mM, swimming.

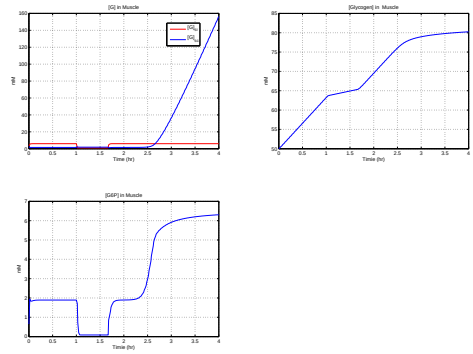

Figure 7: $[G] = 14$ mM, swimming.

ACKNOWLEDGEMENTS

Partial support from the Center for Applied Mathematics of University of Notre Dame and the Notre Dame Faculty Research Program are gratefully acknowledged.

REFERENCES

Cobelli, C. et al. (1982). An integrated mathematical model of the dynamics of blood glucose and its hormonal control. *Mathematical Biosciences*, 58:27–60.

Frayn, K. N. (2003). *Metabolic Regulation: A Human Perspective*. Blackwell Science Ltd, Oxford, 2nd edition.

Fujimoto, T. et al. (2003). Skeletal muscle glucose uptake response to exercise in trained and untrained men. *Med. Sci. Sports Exerc.*, 35:777–783.

Kelley, D. E. and Mandarino, L. J. (1990). Hyperglycemia normalizes insulin-stimulated skeletal muscle glucose oxidation and storage in noninsulin-dependent diabetes mellitus. *J. Clin. Invest.*, 86:1999–2007.

Perriott, L. M. et al. (2001). Glucose uptake and metabolism by cultured human skeletal muscle cells: rate-limiting steps. *Am. J. Physiol. Endocrinol Metab.*, 281:72–80.

Price, T. B. et al. (1996). Nmr studies of muscle glycogen synthesis in insulin-resistant offsprings of parents with non-insulin-dependent diabetes mellitus immediately after glycogen-depleting exercise. *Proc. Natl. Acad. Sci. USA*, 93:5329–5334.

Rothman, D. L. et al. (1992). ^{31}p nuclear magnetic resonance measurements of muscle glucose-6-phosphate. *J. Clin. Invest.*, 89:1069–1075.

Sarabia, V. et al. (1992). Glucose transport in human skeletal muscle cells in culture. *J. Clin. Invest.*, 90:1386–1395.

Sherwin, R. S. et al. (1974). A model of the kinetics of insulin in man. *J. Clin. Invest.*, 53:1481–1492.

Srinivasan, R. et al. (1970). A mathematical model for the control mechanism of free fatty acid-glucose metabolism in normal humans. *Computers and Biomedical Research*, 3:146–166.

Tolić, I. M. et al. (2000). Modeling the insulin-glucose feedback system: the significance of pulsatile insulin secretion. *J. Theor. Biol.*, 207:361–375.

Topp, B. et al. (2000). A model of β-cell mass, insulin, and glucose kinetics: pathways to diabetes. *J. Theor. Biol.*, 206:605–619.

APPENDIX

The variables, parameters and initial values are shown in this appendix.

$G/[G]$	mmol/mM	Glucose amount/concentration in plasma.
$G_{si}/[G]_{si}$	mmol/mM	Glucose amount/concentration in interstitial space.
$G_{sc}/[G]_{sc}$	mmol/mM	Glucose amount/concentration in intracellular space.
$G6P/[G6P]$	mmol/mM	G6P amount/concentration
$[In]$	mU/l	Insulin concentration.
$\dot{V}_{O_2}/\dot{V}_{O_2\max}$	l/min	Oxygen consumption rate/Maximum.
$Mass$	kg	Skeletal muscle weight,
n	N/A	Number of Langerhans
V_{si}/V_{sc}	l	Volume of interstitial space /intracellular space.
V_b/V_p	l	Blood/Plasma Volume.
$GLY/GLY_{\max}$	mM	Glycogen concentration /Maximum concentration.
$V_{\max}$	mmol/min	Maximum reaction rate.
K_m	mM	Michaelis constant.
K_{01}	l/min	Diffusion coefficient.
K_{02}	N/A	Insulin half-life coefficient.
$Aerobic$	mol/min	aerobic glycolysis rate.
$Anaerobic$	mol/min	anaerobic glycolysis rate.
Syn	mol/min	Glycogen synthesis rate.
Dwn	mol/min	Glycogen breakdown rate.

$[G]$	5
$[G]_{si}$	3.5
$[G]_{sc}$	2.5
$G6P$	$0.12\times Mass$
Body weight	70
$Mass$	45% of *Body weight*
n	10^6
$[In]$	10
$\dot{V}_{O_2}$	Percentage of $\dot{V}_{O_2\max}$: rest - 10% light housework - 25% swimming - 75%
V_{si}	10% of $Mass$
V_{sc}	$0.1852 \times Mass$
V_b	5
V_p	55% of V_b
$GLY_{\max}$	1% of $Mass$
K_m	5.7
K_{01}	2
K_{02}	20

A NOVEL DESIGN AND DEVELOPMENT OF A SINGLE CHANNEL INTEGRATED DIGITAL BODY SOUND DATA ACQUISITION DEVICE

Ali Alouani, Omar Elkeelany and Mohammed A. S. Abdallah
Department of Electrical and Computer Engineering,Tennessee Technological University,Cookeville, TN 38505,USA
{AAlouani, OElkeelany, MASadik21}@tntech.edu

Keywords: Integrated Data Acquisition, Network-ready Medical Device, Systems-On-a-Chip, FPGA, Flash memory.

Abstract: This paper discusses the design, development, and testing of an integrated compact digital stethoscope capable of performing body sound measurement and processing without the need of a personnel computer and hardware interface. The cost of the proposed device is a fraction of that of the data acquisition system used with current digital stethoscopes to collect body sound, such as lung sound, in a digital format. Preliminary testing of the device shows faithful reproduction of the body sound signals used. Not only the new design strategy saves hardware, space, and power consumption but also it allows for the signal processing and data interpretation in the same device. This is due to the proposed integrated design of the subsystems involved in the data acquisition process. It also has the capability of sending collected data to remote location through the Internet.

1 INTRODUCTION

Auscultation is the most popular method for the diagnosis of pulmonary dysfunction. The breath sound that originates in the lungs was first subjectively acquired by a stethoscope and it is at present the most effective mechanism for the analysis of lung sounds by human audition. Lung sounds are used to detect diseases such as the obstruction during bronchial provocation testing. They have drawn much attention because it does not require maximal breathing effort and can therefore be used with young and elderly patients (Oavriely, N., 1996). In recent years, the diagnostic power using auscultation has significantly improved because of the advances in data acquisition, digital signal processing and signal analysis. (Cohen, A. and Landsberg, D., 1984)(Cohen, A., 1986)(Druger, O., 1973)(Hartman, X., 2001)(Kiyokawah, H., Yonemarum, M., Horie, S. et al, 1995)(Kraman, S.S. and Austrheim, D., 1983)(Lehrer, S., 1989)(Urquhart, R.B., McGee, J., Macleod, J.E., Banham, S.W. and Moran, F., 1981)

Current digital measurement of body sound requires a personnel computer and a data acquisition system beside the stethoscope, see Figure 1. The current technology is cumbersome and expensive. The cost of the data acquisition card used by one of the authors, (Alouani, A.T. and A. Kamal, 2006), to collect digital lung sound was over $1,400 (National Instruments, 2007). Nowadays, handheld devices like Personal Digital Assistants, cell phones, and other handheld gadgets use sophisticated chip technology, which allows for lightweight, compact and very limited power consumption. Field Programmable Gate Array (FPGA) technology is currently used in these devices. Not only this technology consumes power in milli watts but also it allows the integration of processing power, on-chip memory and various control interfaces.

The objective of this paper is to design, implement, and test an integrated digital stethoscope capable of acquiring body sound in a digital format without the need of a data acquisition system or a personnel computer. Using the great computational power of modern FPGAs, the proposed device is capable of performing the desired signal processing and analysis of the lung sound. The total cost of the proposed body sound measurement and processing device is expected to be a fraction of that of the existing data acquisition system (National Instruments, 2007).

This paper is organized as follows: section 2 reviews the basics of the FPGA highlighting its capability for integration and compactness. Section 3 contains the conceptual design of the proposed body

sound measurement device. Sections 4 and 5 discuss the hardware implementation and testing of the device. Then, section 6 contains the conclusions and discussions.

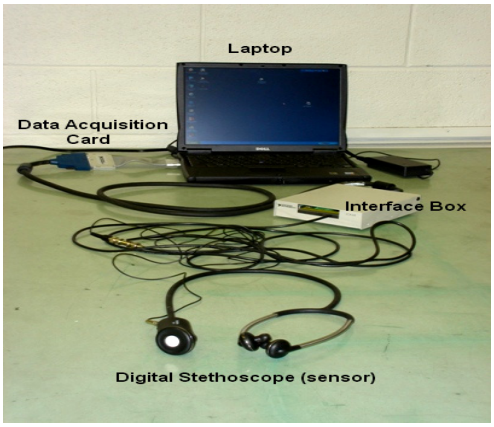

Figure 1: Digital Body Sound Measurement Using Current Technology.

2 FPGA OVERVIEW

FPGA is a programmable integrated circuit that is manufactured with high density of internal blocks. Typically, an FPGA is made up of digital signal processors (DSPs), configurable logic blocks (CLB), memory cells, input output blocks, and microprocessors (Xilinx Inc. 2007), see Figure 2. By configuring these blocks, the FPGA is capable of communicating with external peripherals, processing and storing data.

The FPGA is a stand-alone reconfigurable system-on-chip with the above capabilities. Using this FPGA technology, the development of new applications becomes very affordable. Examples of advanced commercial FPGA-based low cost battery operated handheld devices are Personal Digital Assistants (PDAs), cell phones, and MP3 players.

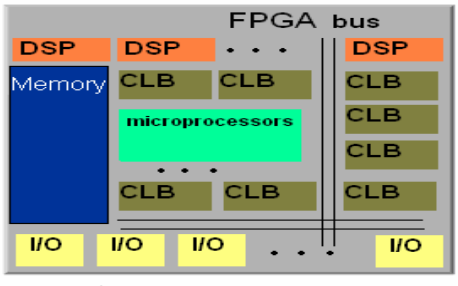

Figure 2: Advanced FPGA technology can have embedded memory, Central Processor, Digital Signal Processors (DSP), input/output (I/O) blocks, interconnects, and configurable logic blocks (CLB) in one chip.

3 CONCEPTUAL DESIGN

Existing computer based data acquisition systems, such as the portable digital stethoscope system shown in figures 1 or the portable EEG system (Comet®, 2007) shown in Figure 3, are complexes of many components. A general structure of such systems is shown in figure 4. The sensor(s) output is connected to a dedicated Analog/Digital (A/D) converter. The A/D converter sends data to a computer. The computer analyzes the acquired signals using its signal processing and decision making capabilities. The computer system contains programming memory, storage memory (i.e., hard disk) and is connected to the internet through its internal network interface card. Even though these systems are portable, they are quite cumbersome and expensive. In addition, their power consumption is much higher than that of handheld devices.

The cumbersomeness of existing portable medical data acquisition devices is due to the lack of integration and the reliance on a personal computer, Figure 3. The connections between the different subsystems require special cables and at times connection boxes, such as the one in Figure 1. On the other hand, the FPGA allows for the integration of various components on one chip. In addition, it has all the processing, storage and display capabilities needed by a medical data acquisition system. Finally the proposed device is Internet ready. This research provides a new design philosophy that takes advantage of the capabilities of the FPGA to eliminate the need of a computer and cable based connection between subsystems. This new design strategy is summarized in Figure 5.

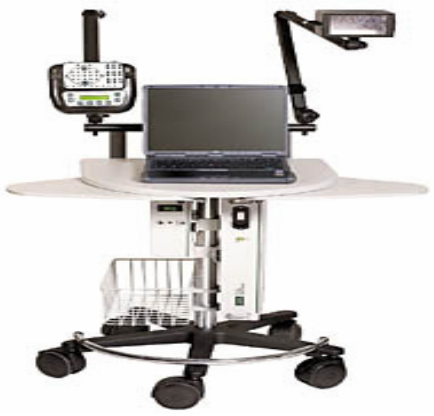

Figure 3: Comet® portable EEG with, stimulator, and isolated power supply (Comet®, 2007).

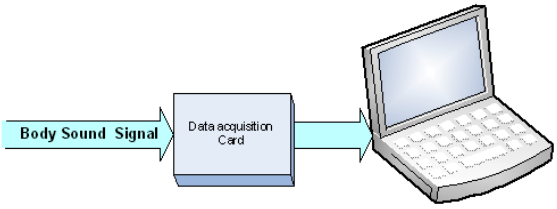

Figure 4: Existing Body Sound Data Acquisition System.

4 HARDWARE DESIGN AND IMPLEMENTATION

A centre piece of the proposed compact body sound data acquisition system is the FPGA. The FPGA communicates directly to the A/D converter. The proposed FPGA design includes an A/D configuration module, which issues configuration words containing desired A/D sampling rate, resolution, gain, etc. Also, the FPGA collects data from the A/D converter, via the Data Recording unit. Preliminary digital signal processing, such as power spectrum density computation and display can be done by the FPGA data processing unit. Writing the processed data into the Flash memory device takes more time than that of all operations preceding it. So, care is given to the design of the Data Recording unit, to avoid timing problems. It is advantageous to use the FPGA's internal memory cells for buffering because their access time is much smaller than that of external memories. However, FPGA's internal memories are limited. External off-chip memory is used to store the sound samples in a buffer of large blocks of data. As this buffer is filled, the write operation is performed for the entire buffer. This ensures the continuity of recorded data. The size of the whole buffer is set to sufficiently hold a contiguous useful data set from a body sound site. Of course, the maximum size of the buffer is limited by the size of the external memory. The Data Recording unit writes the collected data into the detachable external Flash memory device for further analysis. The Data Recording unit follows an error detection algorithm in the data writing process to ensure the integrity of the stored data.

Particularly, the FPGA writes acquired data after filling data buffer. In order to optimize the acquire-and-write processes, the Data Recording unit can use single or multiple block writing mechanisms. Data block writing uses an integrity check value (Cyclic redundancy check) at the end of each block. In multiple block writing, the total write time is reduced significantly by use of a more sophisticated write mechanism. The time reduction is important as it allows for fast A/D sampling rate. This will in turn improve the faithful reproduction of the acquired data.

4.1 Design Requirements

Mixed FPGA hardware/software architecture is employed using Hardware description language (HDL). As a rule of thumb, all time-critical tasks are implemented in hardware, while other functions are developed in software using embedded C programming language. For example, the software is used to process the captured data, while the hardware is used to configure the A/D converter, and provide proper timing signals. The FPGA bus signals and the parallel input output lines form a common interface between the hardware and the software components.

In traditional systems, Flash memories are written by a host personal computer, through a permanent interface (i.e. soldered chips on circuit boards). Such use of Flash memory devices is common in embedded systems to store configuration information.

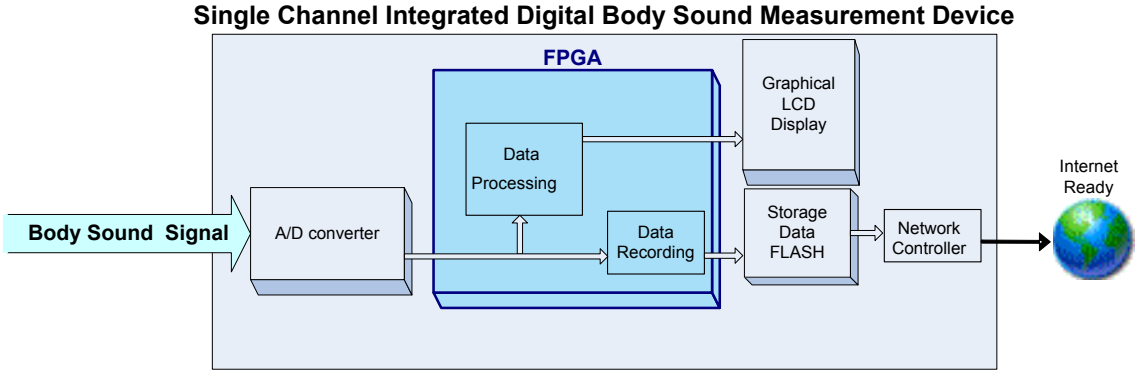

Figure 5: Proposed Integrated Body Sound Data Acquisition System.

One design choice made here is to use detachable Flash memory devices. Sampled data must be written to the Flash memory device to allow further remote analysis and interpretation. This introduces various technical design challenges. Particularly, Flash memory must be written by a customized hardware not by a personal computer. Hence, the proposed Compact Body sound Data Acquisition System must address the following design requirements.

4.1.1 High Data rate

A Detachable Flash memory should have a small and robust physical interface. This limits the maximum number of data and control pins in the interface. Consequently, this affects the writing speed, as serial data communication must be employed. We have used high clock frequency in serial mode to overcome this challenge. Timing and clock signals between the FPGA and the A/D converter are properly matched. We have used Phase Locked Loop (PLL), and clock dividers to achieve this matching.

4.1.2 Data Integrity

Flash memory must be initialized before the storing process. As Flash memory cards are detachable, card detection and initialization are required. The storing process can not be done unless the Flash memory is initialized. Continuous monitoring of the Flash memory during both the reading process and the writing process is done to ensure that the data is passed to the Flash memory. We have used Error check code to check the valid arrival and storage of the data into the Flash device.

4.1.3 Data Quality

The writing process is limited by the access time of the Flash memory device (typically 10 to 200 µs (Western Digital, 2007)). High quality data should be received fully (without dropped blocks), in proper order and in time. There is no need to store data which is incomplete or out of order. One solution we have used is to use internal buffer. We assume no data compression, and fixed data arrival rate. We have made sure that the processing rate is faster than the arrival rate. In future work, we will consider variable data arrival rate (e.g. compressed data), and will evaluate the optimal buffer depth, such that no blocks are dropped.

4.2 Design Implementation

Firstly, the Altera SoPC ™ builder is used to layout the contents of the FPGA; the NIOS-II processor, peripheral components and memory cells, as well as the custom hardware logic we have designed. The FPGA layout is compiled and mapped to the target device in the Altera Quartus environment. Finally, the NIOS-II integrated development environment (IDE) is used to design the software components of the FPGA.

The NIOS-II processor core is connected to rest of the FPGA components through the Altera Avalon bus interface. The Avalon interface contains the arbitration logic to manage various module connections (Altera Quartus II, 2006) (Sadik C. Esener, 2006). The NIOS-II processor is a 32-bit Reduced Instruction Set processor. Since the NIOS-II processor follows Harvard Memory architecture, the data and the program are stored on separate memories. It has a 4-KB instruction cache and a 2-KB data cache. The processor runs on 50 MHz clock frequency.

The A/D converter used in the proposed system is a WOLFSON WM8731. It can support a range of sampling frequencies from 8 KHz to 96 KHz. It has internal digital filters to improve the sound quality. Sound data is fed to the NIOS-II processor in FPGA serially (Altera DE2, 2006).

The proposed system stores body sound input signals in pulse code modulation using the Wave (.wav) file format (Bashir A., 2007)(Wolfson Microelectronics, 2006). The sound is stored as a 16-bit mono with a sampling frequency of 48 KHz.

5 EXPERIMENTAL TESTING

Figure 6 shows the proposed system prototype implemented using FPGA. The produced prototype uses only 15% of the total chip capacity that is 5114 out of the 33,216 Logic Elements of the Altera Cyclone-II EP2C35F672C6 FPGA chip. The worst-case prorogation delay observed for the system is 12.04 ns, which is less than the 50 MHz clock period of 20ns. The Cyclone-II FPGA consumes as low as 12 mW of power, which rivals semi-custom ASIC counterparts of similar cost.

Several tests have been performed using this prototype. We have used the existing computer based system to acquire a lung sound. The same signal was provided to the newly designed device, figure 6. Only the results of one experiment are reported in this paper.

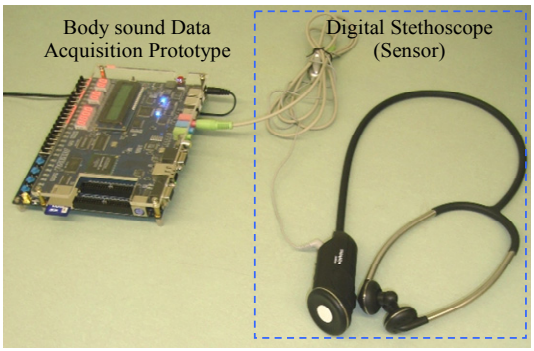

Figure 6: FPGA prototype of the Integrated Data Acquisition System.

The computer based system acquired the lung sound shown in figure 7. The experiment run length is 2.6 seconds (horizontal axis). Plotted on the vertical axis is the normalized signal amplitude. The data recorded using the proposed integrated data acquisition system is shown in figure 8. Figure 9 provides a zoomed in view to show the faithful reproduction of the body sound signal.

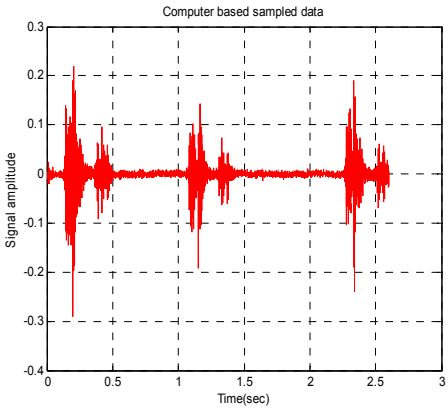

Figure 7: Data recorded using the existing Data Acquisition System.

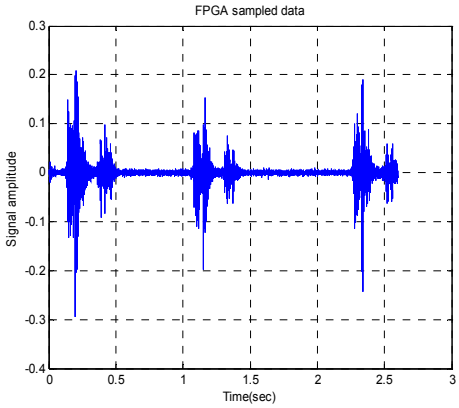

Figure 8: Data recorded using the proposed Compact Integrated Data Acquisition System.

6 CONCLUSIONS

This paper provided a new design philosophy of future integrated and compact medical data acquisition systems. The design takes advantage of latest development in the system-on-chip technology.

In this paper, the design, development, and testing of the body sound measurement device took place using the Altera development board. The design of an optimized custom board for this application is underway. The new board will eliminate components, such as off-chip-memory devices, extension header network ports, that are not needed by this device. In addition, the sound sensor (microphone) will be integrated in the new board. This will eliminate the need for the stethoscope, which in turns reduces the cost of collecting digital body sound.

This new design direction in medical data acquisition systems saves hardware, power consumption, and more importantly money. Future work will focus on developing universal medical data acquisition systems using the design philosophy reported in this paper. It is believed that the long term benefit of this research will provide affordable handheld medical data acquisition systems with remote data transfer capability. This will in turn make health screening affordable and feasible from the patient location.

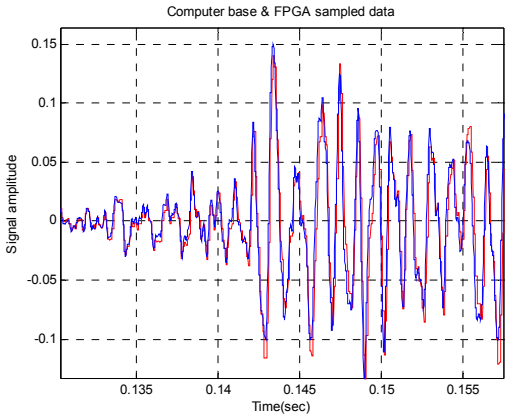

Figure 9: (Time zoom) Superimposed Data recorded using both Data Acquisition Systems.

ACKNOWLEDGEMENTS

We would like to acknowledge the Department of Electrical and Computer Engineering (ECE), and the Centre for Manufacturing Research (CMR) at

Tennessee Technological University for their support to this work. The authors also would like to acknowledge the anonymous reviewers of this paper for their suggestions and advices.

REFERENCES

Alouani, A.T. and A. Kamal, 2006. " Pulmonary Tumor Detection Using Respiratory Lung Sound," Proc. Cairo International Bioengineering Conference, Cairo, Egypt.

Altera DE2, 2006."Using the SDRAM Memory on Altera's DE2 board with Verilog Design".

Altera Quartus II, 2006. version 6.0 Handbook, Volume 4: SOPC Builder.

Bashir A., 2007. "Wave File Format." Internet: http:// technology.niagarac.on.ca/courses/ctec1631/WavFileFormat.html

Cohen, A. and Landsberg, D., 1984. "Analysis and Automatic Classification of Breath Sounds", IEEE Trans. Biomed. Eng., BME-31, pp. 585-590.

Cohen, A., 1986. Biomedical Signal Processing, CRC press, Boca Raton, FL.

Comet®,2007. portable EEG and PSG system.

Druger, O., 1973. The Chest: It's Sign and Sounds, Humetrics, Los Angles, CA.

Hartman, X., 2001.Cross Correlation in Signal, Sound and Sensation, New York. AIP, 346.

Kiyokawah, H., Yonemarum, M., Horie, S. et al, 1995. "Frequency Analysis of Crackles Recorded with a Stethoscope-Equipped Recorder", Nippon Kyobu Shikkan Gakkai Zasshi, 12, pp. 1341-1347.

Kraman, S.S. and Austrheim, D., 1983. "Comparison of Lung Sounds and Transmitted Sound Amplitude in Normal Men", Am. Res. Respir. Dis., 128, pp. 451-454.

Lehrer, S., 1989. Understanding Lung Sound, W.B. Saunders, Philadelphia, PA.

National Instruments, 2007. Data Acquisition Card for Laptops and PDAs, Internet: http://sine.ni.com/nips/ cds/view/p/lang/en/nid/13122.

Oavriely, N., 1996. "Analysis of Breath Sounds in Bronchial Provocation Tests" (editorial), Am. J., Respir. Crit. Care Med., 153, pp. 1469-1471.

Sadik C. Esener, 2006. "Flash memory cards. "Internet: http://ww.wtec.org/loyola/hdmem/01_01.htm#f01_01

Urquhart, R.B., McGee, J., Macleod, J.E., Banham, S.W. and Moran, F., 1981. "The Diagnostic Value of Pulmonary Sounds", A preliminary Study by Computer Analysis, Comput. Biol. Med., 11, pp.129-139.

Western Digital, 2007. "*Western Digital Caviar RE2 WD4000YR."* Internet: http://www.storagereview.com /articles/200510/WD4000YR_2.html.

Wolfson Microelectronics, 2006. WM8731/WM8731L, Production data, Rev 3.4.

Xilinx Inc. 2007. "The 65nm Virtex-5 SXT FPGA" Internet:http://www.Xilinx.com.

DIFFERENTIAL ELECTRIC FIELD SENSITIVE FIELD EFFECT TRANSISTOR

Characteristics, Modeling and Applications

Yehya H. Ghallab[1, 2] and Wael Badawy[2]
[1] *Department of Biomedical Engineering, Helwan University, Cairo, Egypt*
[2] *Department of Electrical and Computer Engineering,University of Calgary, Calgary, Alberta, Canada*
yghallab@ucalgary.ca, badawy@ucalgary.ca

Keywords: Electric Field Sensor, CMOS technology, Electric Field, Field Effect Transistor, lab-on-a-chip, Integrated sensors.

Abstract: This paper presents the Differential Electric Field Sensitive Field Effect Transistor (DeFET) as a CMOS electric field sensor. The DeFET is based on a standard 0.18-µm Taiwan Semiconductor Manufacturing Company (TSMC) CMOS technology. This paper also presents the DeFET's DC and AC models. The experimental and simulation results which validate the different models of the DeFET are presented. Moreover, some applications of the DeFET on the biomedical and lab-on-a-chip are presented.

1 INTRODUCTION

The Differential Electric Field Sensitive Field Effect Transistor (DeFET) device is a new electric field sensor which can sense the electric field and convert the electric field into a corresponding electrical signal such as voltage or current (Ghallab et al., 2005) (Ghallab et al., 2006) Its physical structure has two adjacent gate terminals (Ghallab et al., 2005). With the split-gate structure, DeFET can sense the electric field which is perpendicular to the gate channels of the device. Using the DeFET, we can get direct real-time information about the electric field, and consequently, we can extract useful information such as identify and characterize the biological cells (Ghallab et al., 2006). Also, the DeFET can be simply integrated with the CMOS-based lab on a chip and read-out circuits. As a new device, the DeFET is not a standard device in the (**S**imulation **P**rogram with **I**ntegrated **C**ircuit **E**mphasis) SPICE simulator libraries, so we need a macro model to evaluate the performance of circuits composed of DeFET and MOSFET devices.

In this paper, SPICE macro models (dc and ac models) of DeFET will be offered to evaluate the performance of the circuits. Also, some applications of the DeFET are presented.

This paper is constructed as follows. The operational principle of the DeFET is reviewed in part2. The SPICE macro models (dc and ac) are formed and described in Section 3. Experimental and simulation results which confirm the proposed models are shown and discussed in part 4. Some applications of the DeFET are presented in part 5. Section 6 concludes this paper and discusses the merits of the proposed DeFET based on the experimental findings.

2 THE DeFET

The DeFET consists of two complementary eFETs, one of them is a P eFET type and the second is an N eFET type (Ghallab et al., 2006). The eFET structure is shown in Fig. 1. The eFET contains two split drains, two split gates and a single source, see Fig. 1.

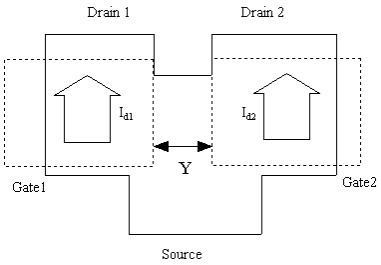

Figure 1: Schematic structure of an DeFET.

The equivalent circuit of the DeFET is shown in Fig. 2.

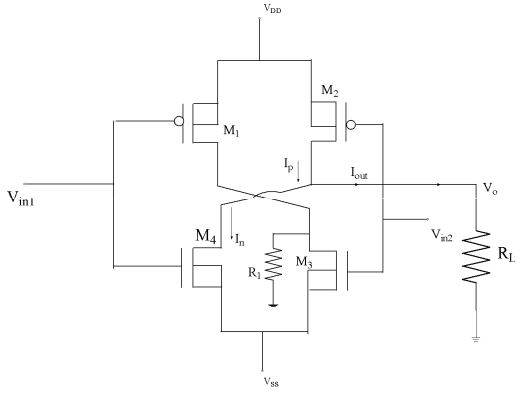

Figure 2: An equivalent circuit of a DeFET and schematic of the DeFET used in SPECTRE simulation.

From Fig. 2, the two gates of P eFET and N eFET are connected with each other, and there is a cross coupling between the two drains of the P eFET and the N eFET. The output current I_{Out} is equal to the difference between the two drain currents Ip-In (i.e. I_{Out} = Ip-In, see Fig.2). On the other hand, Ip and In are functions of the two applied gate voltages V_{in1} and V_{in2}, respectively. The DeFET is designed to achieve an output voltage V_{Out}, directly related to the difference between the two applied gate voltages (V_{in1}-V_{in2}), and as V_{in1}-V_{in2} is equal to the applied electric field above the two gates (E) multiplied by the distance between them (V_{in1}-V_{in2}/Y = E), where Y is the distance between the two split gates, which is constant. So, V_{Out} is related directly to the intensity of the applied electric field. Thus by measuring V_{Out} we can detect the intensity of the electric field to be as follows (Ghallab et al., 2006):

$$V_{Out} = g_m Y R_L E + V_{Uni} \quad (1)$$

Eq. 1 shows a liner relationship between the DeFET's output voltage and the intensity of the applied electric field.
Also, from Eq. 1, we can observe that there is two cases, they are:

1) **Null electric-field case (Uniform case)**: This special case will be obtained when the intensity of the electric filed is zero, and consequently getting the same potential on the two gates (i.e., $V_{in1} = V_{in2}$), and from Eq.1V_{out}=V_{uni}

2) **Nonzero electric-field case (Nonuniform case)**: This implies any electric-field condition that leads to a potential difference between the two gates (i.e., $V_{in1} \neq V_{in2}$). So, we can rewrite Eq. 1 as:

$$V_{out} = V_{Non} + V_{Uni} \quad (2)$$

where: V_{non} = SE= $g_m Y R_L E$ is the output voltage when we have a nonuniform electric field case, and V_{uni} is the output voltage when we have a uniform electric field case and S (sensitivity) = $g_m Y R_L$.

3 MODELING THE DeFET

As a new device, the DeFET is not a standard device in the simulator libraries, so a macro model to evaluate the performance of circuits composed of DeFET and MOSFET devices is needed. A Dc model has been proposed and tested using SPECTRE version 5. Also, an equivalent dc circuit of the DeFET using PSPICE version 9.1 have proposed. So, it can be used in the SPICE environment.

3.1 A Simple DC Model

Fig. 2 shows the proposed DeFET circuit used for SPECTRE simulation. The channel length and the width of the Pmos and Nmos used are 0.4µm / 10µm and 0.4µm / 1µm, respectively. Fig. 3 shows the simulation results of the output voltage V_{Out} against the input voltage difference V_{in1}- V_{in2} (ΔV), where V_{in1} varies from –2.5V to 2.5V and V_{in2} is 0V.

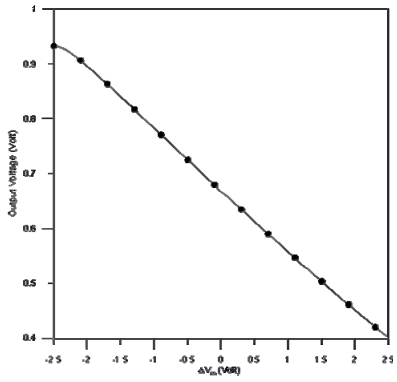

Figure 3: DC response of the DeFET.

From Fig. 3, a linear relationship between V_{Out} and ΔV can be observed. As the external electric field E= -ΔV/Y, and Y=0.5µm, Fig.4 shows the output voltage V_{Out} against the intensity of the applied electric field. We can observe that V_{Out} is linearly related to E, as we expected from the theory of the DeFET (see Eq. 1). The sensitivity can be determined from this figure as S= $\Delta V_{out}/\Delta E$ = 51.7(mV/V/µm). If we vary V_{in1} from –2.5 to 2.5 Volt and V_{in2} from –3 to 3Volt, we can get the same

linear relationship between V_{Out} and V_{in1} for different V_{in2}, as shown in Fig. 5.

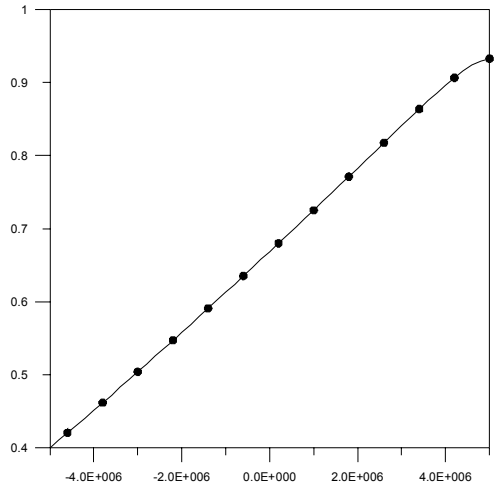

Figure 4: Output voltage versus electric field intensity.

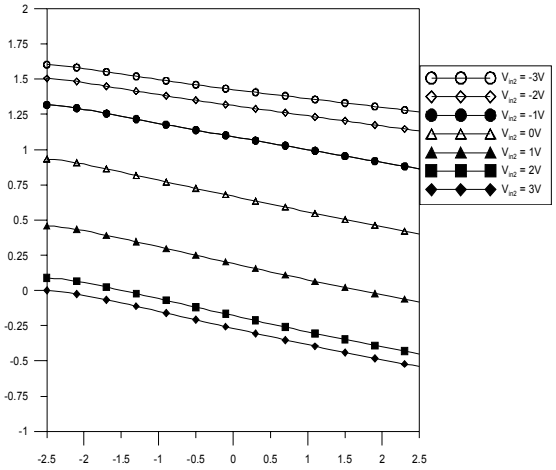

Figure 5: Spectre's simulation results.

3.2 SPICE's DC Equivalent Circuit

Fig. 6 shows the SPICE equivalent circuit of the DeFET. As it is outlined before in The DeFET's theory of operation (section 2), there are two cases of electric field. The first one is a uniform electric field case, and the second is a nonuniform electric field, both of these field cases can control the output voltage (V_{out}). The output voltage caused by the uniform case (V_{uni}) is represented by the four MOSFETs (M_1-M_4) with the two gates are connected, see Fig. 6. In other words, V_{Uni} represents the output voltage when the two gates are connected. The output crrent caused by a nonuniform electric field (I_{Non}), is represented by an electric field controlled current source (ECCS). I_{Non} is related to the electric field E, and the sensitivity S by the equation (I_{Non}= SE).

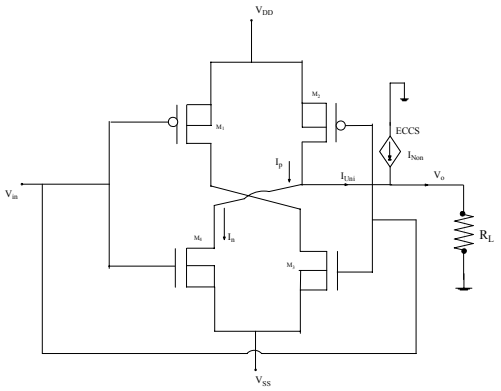

Figure 6: DeFET's SPICE equivalent circuit.

Fig. 7 shows the SPICE equivalent circuit of ECCS. In this SPICE circuit, the external electric field applied is represented as a voltage source V_{Ele}. The value of R_{sen} is proportional to the inverse value of the sensitivity "S". I_{Non} is a current source controlled by I_1, which caused by the nonuniform external electric field.

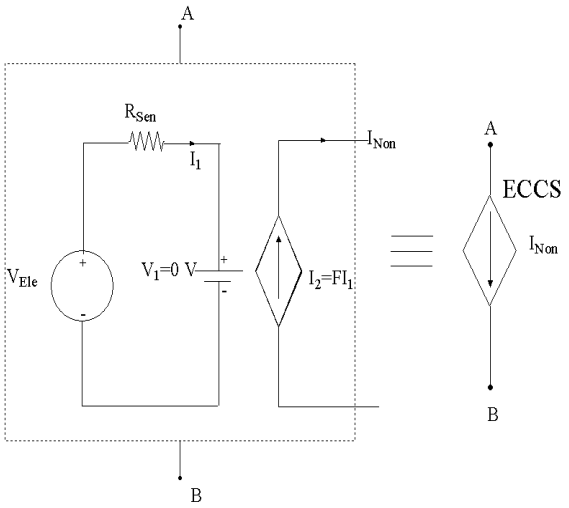

Figure 7: Electric field controlled current source (ECCS) model.

As a simple model, Fig. 8 shows this simple DC model, where the output current (I_{out}) is the summation of two dependent sources of current. The first is an electric field controlled current source (I_{Non}), which represents the nonumiform electric field, and the second is a voltage controlled current source (I_{Uni}), which represents the output current obtained when having a uniform electric field.

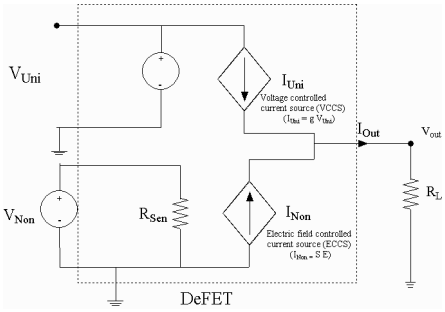

Figure 8: A simple DC model.

3.3 AC Model

Fig. 9 Shows the AC model of the DeFET, where the media is represented by a capacitor in parallel with a resistor (C_{ext}//R_{ext}). The media here can be the dielectric fluid above the DeFET sensor, or any neutral body, such as: biocells, DNA molecules, or virus, or it can be both.

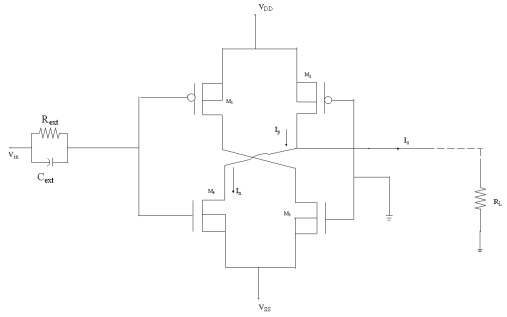

Figure 9: The AC model of the DeFET.

The AC response for different C_{ext} values is shown in Fig. 10. From this figure we can observe that the DeFET is working as a bandpass filter. The magnitude, bandwidth and the frequency range of operation of this filter depend on the external media; see Fig. 9, these factors are very important to extract useful information about the media itself. A summary of these results is shown in Table 1.

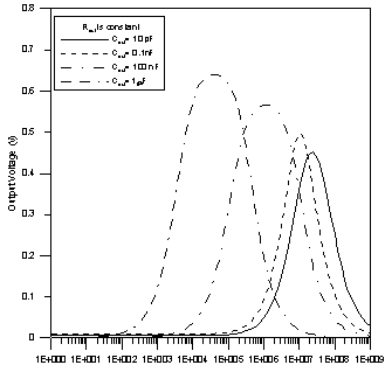

Figure 10: AC response with Rext =500K Ohm and Cext varies (Ghallab et al., 2006).

Table 1: Summary of the AC response when R_{ext} =500 KΩ and C_{ext} varies.

C_{ext}	Central frequency	Bandwidth
10 pF	26.7 MHz	116 MHz
0.1 nF	10 MHz	26.59 MHz
100 nF	2.6 MHz	9.84 MHz
1µF	50.1 KH	311 KHz

4 SIMULATION AND EXPERIMENTAL RESULTS

Fig. 11 shows the schematic input file for the PSPICE, we have used level 7 models for the used Pmos and Nmos transistors. Fig. 12 shows the simulation results of the output voltage V_{Out} against the input voltage V_3, where V_3 varies from –2.5V to 2.5V and V_4 varies from –3 to 3Volt. From Fig. 12, V_3 represents the uniform electric field source, while V_4 represents the nonuniform electric field source. Also we can observe the linear relationship between V_{Out} and V_{in1} for different V_{in2}. In Fig. 12, both the simulation results obtained from the two different models that were proposed, i.e. using PSPICE and SPECTRE simulators, and we can observe the good agreements between these two models. Thus, both of these models can properly represent the DC response of the DeFET.

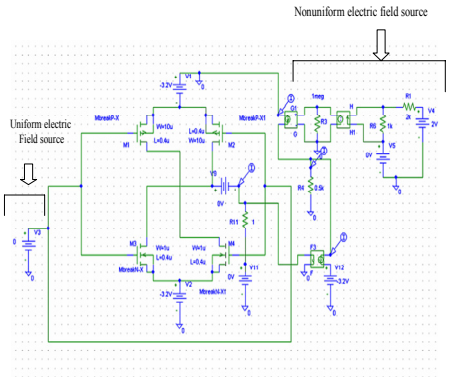

Figure 11: DeFET's PSPICE equivalent circuit.

As the external electric field E = -ΔV/Y, and Y=0.5µm, Fig. 13 shows the output voltage V_{Out} against the electric field applied. We can observe that V_{Out} is linearly related to E, as we expected from the theory of the DeFET (see equation 1).

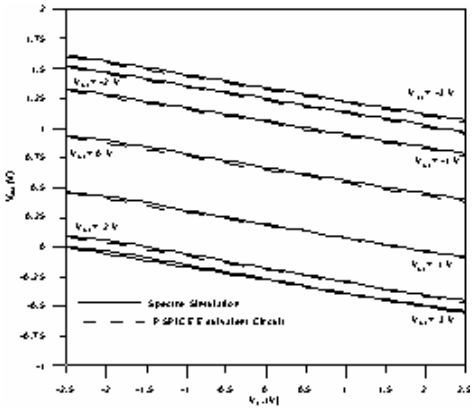

Figure 12: SPECTRE and PSPICE simulation.

As the external electric field E = -ΔV/Y, and Y=0.5μm, Fig. 13 shows the output voltage V_{Out} against the electric field applied. We can observe that V_{Out} is linearly related to E, as we expected from the theory of the DeFET (see equation 1).

The proposed DeFET is implemented in the standard CMOS 0.18-μm technology. Fig. 14 shows a microscopic picture of two DeFETs and the electrodes used to apply the required electric-field pattern. To test experimentally the DC response of the DeFET, a DC voltage with different values, signs and different configuration have been applied to the four electrodes surrounding the DeFET sensors, hence, varying the magnitude and sign of the applied electric field (E) (Ghallab et al., 2006). At the output, the output voltage associated with each value of the measured electric field above the gates will be measured and compared with the simulation results, i.e., Specter's circuit Simulator.

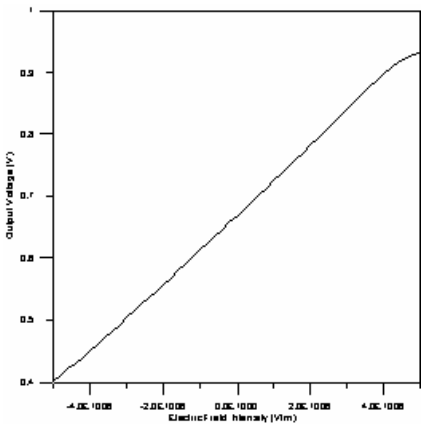

Figure 13: PSPICE Output voltage versus electric field intensity.

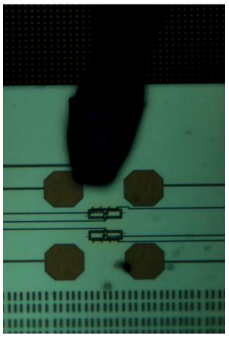

Figure 14: The die picture shows the DeFET sensor (Ghallab et al., 2006).

The result is shown in Fig.15, from which a good agreement between the experimental and the simulation results can be observed. Also, we can observe that the sensitivity of the DeFET, which is the slope of the line shown in Fig. 15, is about 51.7mV/ (V/μm).

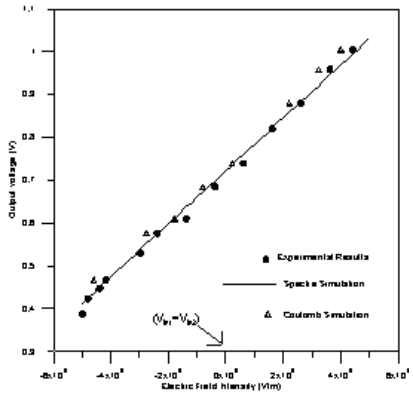

Figure 15: The DC response of the DeFET (Ghallab, 2005).

5 DeFET'S APPLICATIONS

Differential Electric Field Effect Transistor (DeFET) sensor can be used in many applications: for example, it can be used in microfluidic applications, to extract some useful properties of the fluid that is used. Also; it can be used in nonuniform electric field (Dielectrophoresis) applications to get information about the biocells that are used. To achieve this (Burt et al, 1989), DeFET can measure the disturbance that occurs from the existence of the biocells in the applied electric field; it is well known that each kind of biocell will provide a different disturbance based on its electrical properties, i.e. its conductivity and permittivity. Moreover, if we use the DeFETs in array form, i.e., array of sensors, then

we can sense the electric field at different locations. In its array form, the proposed DeFET sensor can be applied to the DNA analysis, because we can use it to detect the radius of the DNA molecule (Washizu M. et al, 1990).

6 CONCLUSIONS

This paper presents the characteristics and the alternative models of the DeFET, as a new electric field sensor. Although DeFET is not a standard device in the SPICE library, the macro models for the DeFET device is presented to evaluate the performance of circuits composed of the MOSFET and DeFET devices. The experimental results have been compared with the simulation results of the proposed models. The correctness and flexibility of the proposed SPICE models have been verified. The proposed methods are expected to make the prediction of the circuits using the DeFET and MOSFET devices possible. The proposed DeFET sensor can be used in many applications in the biomedical field.

REFERENCES

Ghallab, Y. H. and Badaw, W. 2006, 'DeFET, A Novel Electric field Sensor for Lab-on-a-Chip and Biomedical Applications', IEEE Journal of Sensor, vol.6, no.4, pp. 1027-1037.

Ghallab, Y. H. and Badawy, W. 2006, 'A Single CMOS Chip for Biocell Tracking, Levitation, Detection, and Characterization', International symposium on Circuit and system (ISCAS 06), pp. 3349-3352.

Ghallab, Y. H. and Badawy, W. 2005, 'A CMOS Lab-on-a-Chip for Biomedical Applications', International symposium on Circuit and systems (ISCAS 05), pp. 1346-1349.

Ghallab, Y. H. 2005, 'A Novel CMOS Electric Field Imager for Lab-on-a-chip and Biomedical Applications', PhD Thesis, University of Calgary, Canada.

Burt J. P. H., Al-Ameen T. A. K., Pethig R., and Wang X., 1989, "An optical dielectrophoresis spectrometer for low frequency measurements on colloidal suspensions," *J. Phys. E, Sci. Instrum.*, vol. 22, no. 11, pp. 952–957.

Washizu M. and Kurosawa O. 1990, "Electrostatic manipulation of DNA in microfabricated structures," *IEEE Trans. Ind. Appl.*, vol. 26, no. 6, pp. 1165–1172.

PROGRAMMABLE CYTOGENETIC SUBMICROLITRE LAB-ON-A-CHIP FOR MOLECULAR DIAGNOSTIC APPLICATIONS

Daniela Woide, Veronika Schlentner, Teresa Neumaier, Thorsten Wachtmeister
Herwig G. Paretzke, Zeno von Guttenberg[1], Achim Wixforth[2]and Stefan Thalhammer[*]
GSF, National Research Center for Environment and Health, Institute of Radiation Protection
Ingolstädter Landstrasse 1, 85764 Neuherberg, Germany
[1]Advalytix AG, Sauerbruchstrasse 50, 81377 Munich, Germany
[2]University Augsburg, Chair for Experimental Physics I, Universitätsstrasse 1, 86135 Augsburg, Germany
[*] stefan.thalhammer@gsf.de[£]

Keywords: Nanobiotechnology, lab-on-a-chip, cytogenetics, microfluidic PCR, surface acoustic waves, laser-based microdissection.

Abstract: This project focuses on the development of an acoustic driven, freely programmable multifunctional biochemical lab-on-a-chip. By combining different platform elements, like microdissection-, nanofluidic- and detection-modules, the lab-on-a-chip can be adapted to question- and patient-specific cytogenetic and forensic applications. In contrast to many common lab-on-a-chip approaches presently available, the fluidic handling is done on a planar surface of the lab-on-a-chip. Minute amounts of biochemical fluids are confined in 'virtual' reaction chambers and 'virtual' test tubes in the form of free droplets. The droplets, fluidic tracks and reaction sites are defined at the chip surface by a monolayer chemical modification of the chip surface. Surface acoustic waves are employed to agitate and actuate these little 'virtual' test tubes along predetermined trajectories. Well-defined investigations, controlled in the submicrolitre regime, can be conducted quickly and gently on the lab-on-a-chip.

1 INTRODUCTION

Over the past decade, advances in molecular biology have helped to enhance understanding of the complex interplay between genetic, transcriptional and translational alterations in, e.g., human cancers. These molecular changes are the basis for an evolving field of high-throughput cancer discovery techniques using microscopic amounts of patient-based material to detect genetic changes such as mutations, insertions, deletions or imbalances.

To be able to reproducibly and reliably handle, process and analyse such small samples, many laboratories all over the world are intensively investigating the applicability of biochips for this purpose. Biochips are small sample carriers, where biological material is attached for analysis. In dependence of the kinds of molecules attached to the surface analytical biochips are divided into DNA-chips, protein-chips, cell-chips and lab-on-a-chip systems. Most progress in this field occurs especially in the area of DNA-chips (Schneegass et al., 2001; Lagally et al., 2001; Ng and Ilag, 2003). Existing gene chips developed by the Affymetrix Company are a new approach in microarray technology. Oligonucleotide arrays (e.g. genome-wide human SNP array as well as human gene array) are based on hybridisation to small, high-density arrays containing tens of thousands of synthetic oligonucleotides. The arrays are designed based on sequence information alone and are synthesized *in situ* using a combination of photolithography and oligonucleotide chemistry. Chromatin immuno-precipitation (ChiP) coupled with whole-genome DNA-microarrays allows determination of the entire spectrum of *in vivo* DNA binding sites for any given protein (Buck and Lieb, 2004).

In parallel, another kind of test systems was developed, i.e. bead-technologies (Edelmann et al., 2004) and microfluidic systems (Harrison et al.,

[£]The authors wish to be known that, in their opinion the first two authors should be regarded as joint First Author.

1993; Thorsen et al., 2002; Kwakye and Baeumner, 2003). There is growing interest in performing chemical reactions in microfluidic devices as they offer a variety of significant advantages over macroscopic reactors, such as high surface-area-to-volume ratios and improved control over mass and heat transfer.

Several companies and universities are working on programs employing new electronic DNA analysis technologies. These automated techniques are often developed in non-forensic fields, such as medical research, genetics or biochemistry. In genetic forensics, nucleic acid is usually extracted from saliva, blood, semen, bone, hair and dried skin; these are the sources for most crime scene DNA isolations. Chemical kits for DNA isolation, amplification and detection are available today. The future of forensic testing will follow the path of greater automation e.g. of the DNA fingerprinting process. If a particular kind of polymorphism can be detected through automation, reducing the analysis time and expense, it may be of interest to the forensic community. Developments, however, for forensic applications are rare. Only Nanogen Inc. has developed this technology with applications to STR analysis termed APEX® - automated programmable electronic matrix, by using an electric chip as heart of the analysis (Ibrahim et al., 1998; Rau, 1997).

While DNA-chips become commercially important, scientific and technical development in the last years generated different approaches of multiparameter tests particular for medical applications, so-called 'lab-on-a-chip' systems (LOCs). Miniaturisation of analysis systems will yield in an enormous cost-saving in regard to materials like test tubes or microtitre plates as well as biochemical reagents. Furthermore, a smaller sample volume implies in the end a higher sensitivity and homogeneity of detection. Additionally, in comparison to serial single analyses, parallelisation of analyses enables an enormous time saving due to automation. These micro- and nanolaboratories on the scale of a computer chip are equipped with all components necessary for cytogenetic analysis, they are portable, easy to use, flexible, inexpensive, biocompatible and, like computer chips, full programmable.

Here, we present an acoustic driven lab-on-a-chip for cytogenetic and forensic applications (Thalhammer et al., 2007). In contrast to many other lab-on-a-chip approaches, the fluidic handling is done on the planar surface of this chip, the fluids being confined in 'virtual' reaction chambers and 'virtual' test tubes in form of free droplets. The droplets, fluidic tracks and reaction sites are defined at the chip surface by a monolayer chemical modification of the chip surface. In comparison to conventional closed microfluidic systems with external pumping, afflicted with the difficulty to further miniaturize, surface acoustic waves are employed to agitate and actuate these little 'virtual' test tubes along predetermined trajectories. These surface acoustic waves propagate on a substrate surface, to move and mix smallest fluidic volumina. Liquid amounts in the range from 1 micro- down to 100 picolitre are precisely moved on monolayers of thin, chemical processed fluidic 'tracks' without any tubing system. The surface acoustic waves are generated by high frequency electrical impulses on microstructured interdigital transducers embedded into the lab-on-a-chip.

Minute amount of sample material is extracted by laser-based microdissection out of e.g. histological sections (Thalhammer et al., 2003; Thalhammer et al., 2004). A few picogram of genetic material are isolated and transferred via a low-pressure transfer system onto the lab-on-a-chip. Subsequently the genetic material inside single droplets, which behave like 'virtual' beakers, is transported to the reaction and analysis centres on the chip surface via surface acoustic waves, probably best known from their use as high frequency filters in mobile phones. At these 'biological reactors' the genetic material is processed, e.g. amplified via polymerase chain reaction methods, and genetically characterized (Guttenberg et al., 2005).

Well-defined analyses, controlled in the submicrolitre regime, can be quickly and gently conducted on the lab-on-a-chip. Apart from its nearly unlimited applicability for many different biological assays, its programmability and extremely low manufacturing costs are another definite advantage of this 'cytochip'. In fact, those LOCs can be made so cheap that their use as disposables in many areas of diagnostics can be envisioned.

2 MATERIAL & METHODS

In most microfluidic systems liquids are confined and moved in tubes or capillaries. Usually, the application of such systems is restricted to continuous flow processes. However, when carefully looking at a microscale fluid, one realizes that the effects of e.g. surface tension by far exceed those of gravity. The shape of a droplet on a surface is given

by the properties of the substrate. It either remains a droplet or it wets the surface, depending on whether the substrate is hydrophobic or hydrophilic. The technology to create such fluidic tracks (fig. 1) is very much similar to define conducting paths on an electronic semiconductor device.

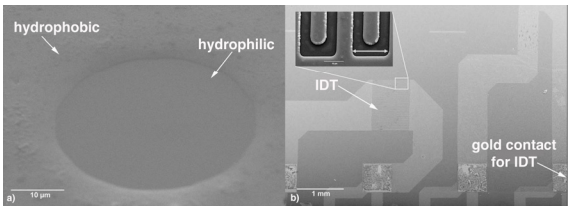

Figure 1: Chemical functionalization of the chip surface creating a hydro-philic/hydrophobic structure. Electron microscopy of a) the hydrophilic reaction centre on the hydrophobic LOC surface, scale bar 10 µm, and b) the arrangement of interdigital transducers (IDT) and electric conduction to control the SAW, scale bar 1 mm. Enlargement in b), electron microscopy of the interdigital transducer in detail with comb periodicity of the double-headed arrow, scale bar 10 µm.

Small amounts of liquids do not really need to be confined in tubes and trenches. They form their own test tubes, held together by surface tension effects. These micro volumina, due to the fact that in small droplets the effect of surface tension dominates gravity, do not need any reservoir as surface tension keeps the droplets in shape. Visualizing dewdrops hanging on a spider's web, one can observe that average droplet size obviously depends on the thickness of the strand: smaller droplets are attached to finer fibres and bigger ones to thicker threads. Apparently droplet shape conforms to the geometry as well as the wettability of the subsurface.

A 'lab-on-a-chip', however, requires more than just test tubes. More important, their cargo has to be moved around, mixed, stirred or processed in general.

2.1 Lab-on-a-Chip Design

The layout of the lab-on-a-chip is shown layer by layer in a schematic drawing (fig. 2). The basic material of the lab-on-a-chip is a lithium niobate ($LiNbO_3$) single crystal wafer polished on both sides. The first metal layer is platinum (Pt) or nickel (Ni) for the heater and sensor structure, followed by a gold layer for the SAW transducer and the contact wires. The complete chip is protected with sputter oxide, which is removed above the contact pads. All structures are patterned by photolithography.

A chemical functionalization of the surface or parts thereof can be employed to laterally define a modulation of the wetting properties, thus creating fluidic pathways or tracks forming virtual potential wells for a fluid on the flat surface of a chip (fig. 3). To form a high contact angle of the oil on the chips, the surface has to be lipophilic. However, the hybridization array has to be wetted easily and needs active coupling groups for the oligo DNA spots. Therefore a chemically heterogeneous surface modification is needed achieved by photo-lithography. The tracking system for biochemical reactants and oil droplet movement and heaters on the chip is patterned with photoresist. An organic layer of a hydrophobic silane is bound to the whole surface. After removing the photoresist, epoxysilane is grafted from an organic solution.

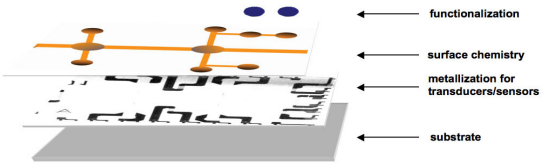

Figure 2: Design of LOC functionality. The ground substrate ($LiNbO_3$) is covered by a layer of Pt, Ni and Au for transducers and sensor metallization. Subsequent silanisation of the surface accounts for a hydrophilic/hydrophobic surface chemistry, facilitating a planar tracking system, which could be further functionalised.

2.2 Actuation

Actuation of single droplets or closed loops of liquid on a fluidic track is achieved by so-called surface acoustic waves, which have been widely used in the completely different field of radio frequency signal processing over the last twenty years or so. Each cell phone, for instance, contains two or more devices operating on SAW.

Actuation of small droplets on the surface of a SAW chip is caused by the effect of acoustic streaming. This phenomenon appears when intensive sound fields are travelling through a liquid. Two major actuation forms can be described: internal flow inside the droplet versus transport of the droplet.

2.2.1 Interdigital Transducer

Electronic devices employing the SAW normally utilize one or more interdigital transducers (IDTs) to convert acoustic waves to electrical signal and vice versa utilizing the piezo-electric effect of certain materials (i.e. $LiNbO_3$) (fig. 1). These devices are

fabricated utilizing common processes used in the manufacture of silicon integrated circuits. Piezo-electricity is the ability of crystals to generate a voltage in response to applied mechanical stress. Depending on their design, the interdigital transducers produce a special type of acoustic surface wave, which can efficiently transfer energy into liquids. Typical SAW frequencies for the fluidic application presented here range from 100 to 200 MHz, the wavelengths are then around 20 micrometers. Transducers are copied from a transducer mask (Advalytix); a distance of 26.5 µm between two combs results in a resonance frequency on the $LiNbO_3$ of 150.6 MHz (fig. 1).

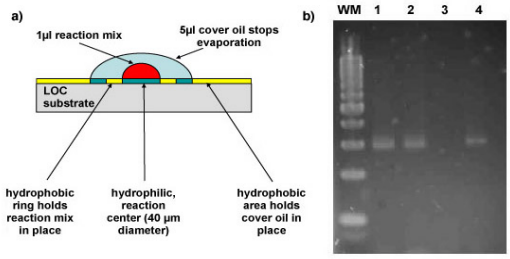

Figure 3: a) Side-view of the lab-on-a-chip amplification unit displaying single droplet PCR. The PCR reaction mix (1 µl) on the hydrophilic reaction centre (40 µm in diameter) is covered with mineral oil to avoid evaporation. The hydrophobic area around the reaction centre holds reaction mix and cover oil in place. b) Gel electrophoresis of 1 µl β-Actin PCR. WM: weight marker, PeqGold 100 bp DNA ladder; lane 1+2: positive control; lane 3: negative probe; lane 4: LOC-PCR, 500 pg target DNA.

2.2.2 Surface Acoustic Wave

Surface waves, so-called Rayleigh-waves, are applied on the piezo-electric system without any mechanical contact to realize actuation of the reactants on the LOC with interdigital transducers.

A surface acoustic wave is an acoustic wave travelling along the surface of a material having some elasticity, with amplitude that typically decays exponentially with the depth of the substrate. It is the nanometre analogue of an earthquake. This kind of wave is commonly used in piezo-electric devices called SAW devices in electronic circuits. Its amplitude and wavelength, however, can be controlled by an electrical signal applied to an appropriate transducer.

At low amplitudes, e.g. below one nanometre, a striking SAW pulse creates internal streaming within the fluid. Its energy is strongly absorbed and radiated into the fluid under the Rayleigh angle. At larger amplitudes, the internal streaming becomes a movement of the whole droplet into the desired direction on the chip with a desired speed (Wixforth et al., 2004). Velocities close to one m/sec can be achieved in this way. In this sense, the transducer generating the surface acoustic waves can be regarded as pump without moving parts that may be remotely operated to control the position of one or more single droplets on the planar fluidic network on a LOC system.

3 PROTOTYPE

Here, we present a multifunctional lab-on-a-chip combining different platform elements like microdissection-, nanofluidic- and detection-modules (fig. 4) with the aim of providing a new platform for fast, cheap and easy investigation of genetic material in patient or forensic samples.

Without any mechanical structuring the lab-on-a-chip exhibits 'virtual' tracks, whereon samples and reagents are acoustically driven, actuated by electrical nanopumps (fig. 5). For the LOC, specific reaction-predefined 'spots' can be generated for total genome amplification via PCR, labelling of the amplified material and detection.

The recent developed lab-on-a-chip system combines serial processing with parallel downstream applications by using a minimum amount of genetic material as source for further investigation. Amplification, labelling and detection of the isolated genetic material are subsequently carried out on the chip surface driven by surface acoustic waves.

Each lab-on-a-chip (fig. 5) has two areas operating as biochemical reaction points, controlled by the temperature sensor. The sensors of the chip are calibrated by a thermoplate and resistance measurements controlled by a *LabView* program. The chip has 10 separately addressable SAW transducers, two on each side for aligning the reactant droplet on the heaters and for mixing during the biochemical reactions. Opposing transducers have different spatial periods to avoid crosstalk.

Extraction of sample material is performed via laser-based microdissection providing the possibility to isolate samples in the range from several cells down to a single chromosomal band with minimum risk of contamination. These small amounts of genetic material, which lay in the range of several picogram, are then transferred via a low-pressure transfer system onto the lab-on-a-chip. This newly developed transfer system (publication in preparation) extracts microdissected material using

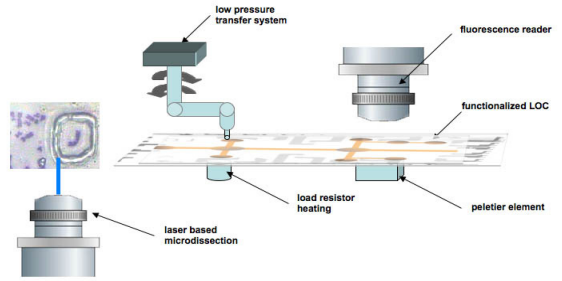

Figure 4: The modular lab-on-a-chip system consists of several units for isolating, processing and analysing minute amounts of sample material: laser-based microdissection is followed by processing of the extracted material and detection of hybridized probes or amplified material by a fluorescence reader. All operations on the LOC are controlled by SAW actuated microfluidics.

low-pressure and transfers it to the reaction centre on the LOC. The patented transfer device allows the precise positioning of the isolated material on top of the LOC.

Subsequently, the sample material inside single droplets is transported very efficiently and contact-less to the reaction and analysis centres on the chip surface via surface acoustic waves. Processing of isolated genetic material like specific or unspecific amplification is conducted on the nanofluidic device via polymerase chain reaction methods followed by labelling with fluorochromes.

Qualitative as well as quantitative analyses such as real-time PCR or microarray will be carried out using a novel 'fluorescence reader', especially designed for the LOC system and forming the principal component of the detection unit. Thus different applications for point-of-care diagnostics are practicable on one single lab-on-a-chip.

4 POSSIBLE APPLICATIONS

This freely programmable lab-on-a-chip system will open new potentials in research and development in different fields of applications ranging from cytogenetics to pathology and forensics.

Apart from its nearly unlimited applicability for many different biological assays, possible applications of this system in cytogenetics are e.g. detection of chromosomal imbalances and detection of genomic imbalances in solid tumour tissue. After isolation of the genetic material by laser-based microdissection the sample is transferred to the lab-on-a-chip using a low- pressure transfer system. Furthermore, in a first biochemical reaction the extracted material is enzymatically digested and prepared for subsequent amplification e.g. *Alu* PCR for SNP analyses. Whole genome amplification of e.g. individually isolated single cells and chromosomes followed by labelling the material with fluorochromes can be used for e.g. fluorescence *in situ* hybridization (FISH) experiments. After mixing with different-labelled reference-DNA the mixture can be transferred to the specific CGH array via wetting modulated surface chemistry, hybridized and finally detected. To make sure that fluorochromes are incorporated uniformly into the sample DNA as well as the reference DNA, the labelling process can be monitored using online PCR detection. In the same way the amount of DNA product after amplification can be determined exactly. This provides the possibility to mix equal amounts of sample and reference DNA for the hybridization mixture. The detection array, microarray on the lab-on-a-chip, will be question- and patient-specific spotted by dot blot technology. Again acoustic actuation will be adopted to solve e.g. lyophilized reagents in a specific buffer.

With regard to the emerging field of forensics, this LOC system can also be applied to genomic sample material as blood cells, buccal swaps or other human cell material performing DNA fingerprint, paternity tests or SNP analysis. As forensic analysis should be cost and time saving, the development of a new miniature analytical lab-on-a-chip system could serve the market in a novel and promising way. Real-time PCR and STR analysis could not only be applied to the novel LOC system separately but also be combined on one single lab-on-a-chip in a modular way.

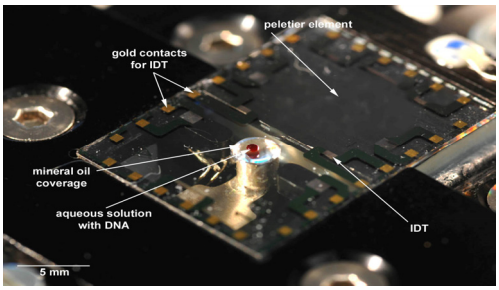

Figure 5: SAW driven lab-on-a-chip system with 10 interdigital transducers, two heaters and biochemical reactant containers. Transport of minute amounts of sample material in 'virtual' beakers is actuated by surface acoustic waves generated via interdigital transducers. The liquid phase comprising the genetic material (red) is covered by a thin layer of mineral oil avoiding evaporation. A load resistor heating and a peltier element provide for precise temperature profiles required for molecular biological methods.

A further application in the field of systems radiation biology is to investigate the influence of low-dose irradiation on cell-cell interactions and possible bystander effects. The medical use of ionizing radiation contributes the largest fraction to the population's anthropogenic radiation exposure. Thus, biopsies of suspicious diagnostic findings, which were irradiated with standard low-dose, will be extracted for histological examination and isolated cell clusters will be analysed on the LOC. By spotting a specific protein array on one part of the LOC and moving cells and media via SAW onto this particular array, it should be possible to detect cancer cascades and involved proteins. This method can be further used to determine the relation and interaction between cancer associated proteins i.e. p53, TGF-β and caspase.

5 OUTLOOK

This system, the acoustically driven, freely programmable multifunctional biochemical lab-on-a-chip system, will be applied on different diagnostic approaches at the single cell or single chromosome level e.g. cytogenetics, tumour genetics and genetic forensics.

Competitive LOCs, combining these techniques, are worldwide not on the market. An essential advantage of the LOC system is the modular set-up, which allows reacting to different diagnostic questions in a preventive medical check-up. This implements the rapid adaptation to patient-specific point-of-care diagnostics as well as the operator-specific development of new molecular markers for imaging techniques. Fields of applications for the newly developed LOC system range from the analysis of cell compartments and single cells in tumour diagnosis to chromosomal imbalances in the human genome.

ACKNOWLEDGEMENTS

The authors would like to thank Klaus Macknapp, Deutsches Museum Munich, for providing the electron microscopy images.

Financial support of the Bavarian Research Foundation, Deutsche Forschungsgemeinschaft (DFG) SFB 486 grant and German Excellence Initiative via the 'Nanosystems Initiative Munich (NIM)' is gratefully acknowledged.

REFERENCES

Buck M.J. and Lieb J.D., 2004. ChiP-chip: considerations for the design, analysis, and application of genome-wide chromatin immunoprecipitation experiments. *Genomics* 83: 349-360

Edelmann, L., Hashmi, G., Song, Y., Han, Y., Kornreich, R., Desnick, R.J., 2004. Cystic fibrosis screening: validation of a novel method using Bead Chip technology. *Genet Med.* 6(5): 431-438

Guttenberg, Z., Müller, H., Habermüller, H., Geisbauer, A., Pipper, J., Felbel, J., Kielpinski, M., Scriba, J., Wixforth, A., 2005. Planar chip device for PCR and hybridization with surface acoustic wave pump. *Lab on a chip* 5: 308-317

Harrison, D.J., Fluri, K., Seiler, K., Fan, Z., Effenhauser, C.S., Manz, A., 1993. Micromaching a miniaturized capillary electrophoresis-based chemical analysis system on a chip. *Science* 261: 895-897

Ibrahim, M.S., et al., 1998. Real-time microchip PCR for detecting single-base differences in viral and human DNA. *Anal Chem*. 70: 2013

Kwakye, S., Baeumner, A., 2003. A microfluidic biosensor based on nucleic acid sequence recognition. *Anal. Bioanal. Chem.* 376(7): 1062-1068

Lagally, E.T., Emrich, C.A., Mathies, R.A., 2001. Fully integrated PCR-capillary electrophoresis microsystem for DNA analysis. *Lab on a chip* 1: 102-107

Ng, J.H., Ilag, L.L., 2003. Biochips beyond DNA: technologies and applications. *Biotechnol. Annu. Rev.* 9: 1-149

Rau, R., 1997. The National Institute of Justice Forensic DNA Laboratory Improvement Program. *Profiles DNA* 1: 5

Schneegass, I., Brautigam, R., Kohler, J.M., 2001. Miniaturized flow-through PCR with different template types in a silicon chip thermocycler. *Lab Chip* 1(1): 42-49

Thalhammer, S., Lahr, G., Clement-Sengewald, A., Heckl, W.M., Burgemeister, R., Schütze, K., 2003. Laser microtools in cell biology and molecular medicine. *Laser Physics* 13(5): 681-692

Thalhammer, S., Langer, S., Speicher, M.R., Heckl, W.M., Geigl, J.B., 2004. Generation of chromosome painting probes from single chromosomes by laser microdissection and linker-adaptor PCR. *Chromosome Research* 12: 337-343

Thalhammer, S., von Guttenberg, Z., Koehler, U., Zink, A., Heckl, W.M., Franke, T., Paretzke, H.G., Wixforth, A., 2007. Programmierbares, zytogenetisches Submikroliter-Chiplabor für molekular-diagnostische Anwendungen. *GenomXPress* ISBN: 1617-562X, 1.07: 29-31

Thorsen, T., Maerkl, S.J., Quake, S.R., 2002. Microfluidic large-scale integration. Science 298: 580-584

Wixforth, A., Strobl., C., Gauer, C., Toegl, A., Scriba, J., Guttenberg, Z., 2004. Acoustic manipulation of small droplets. *Anal. Bioanal. Chem.* 379: 982-991

LAB-ON-A-CHIP WITH FLUID ACOUSTIC MICROAGITATION
Piezoelectric Polymer β-PVDF used as Ultrassonic Transducer

V. F. Cardoso, J. G. Rocha, F. O. Soares, G. Minas
Dept. Industrial Electronics,University of Minho, Campus de Azurem, 4800-058 Guimaraes, Portugal
vanessa@dei.uminho.pt, gerardo@dei.uminho.pt, filomena.soares@dei.uminho.pt, gminas@dei.uminho.pt

S. Lanceros-Mendez
Dept. Physics,University of Minho, Campus de Gualtar, 4710-057 Braga, Portugal
lanceros@fisica.uminho.pt

Keywords: Lab-on-a-chip, PVDF, acoustic microagitation, SU-8.

Abstract: The main objective of this article is to describe the development of a fully-integrated disposable lab-on-a-chip for point of care testing and monitoring of biochemical parameters in biological fluids. The lab-on-a-chip is composed mainly by two dies: the fluid and the detection. The fluid die, fabricated in SU-8, comprises three microfluidic cuvettes, containing the fluids into analysis, and a β-PVDF microagitation system. The detection die is fabricated in a CMOS standard process and contains the photodetectors and the electronics for signal actuation and detection. The main innovation of this lab-on-a-chip is the application of an acoustic microagitation technique by the deposition of the β-PVDF piezoelectric polymer underneath the microfluidic structures, with automatic electronic control. This piezoelectric polymer produces mechanical vibrations, which allow the enhancement of the mixing and the reaction.

1 INTRODUCTION

Microfluidic technology has become an important tool for analytical biochemistry applications. It enables the fabrication of precise and small structures in glass, quartz, silicon or polymeric materials: the lab-on-a-chip concept. The great interest in that technology stems from the inherent performance gains: reduced sample size, higher degree of integration and thus enhanced potential for automation and control fluids of submicroliter volumes, shortened response time, potential for improved analytical performance, reduced storage of chemicals and hence laboratory safety, and reduced costs (Kopp et. al, 1997).

There is a large demand in the healthcare system to develop lab-on-a-chips for rapid and reliable point of care (POC) testing and monitoring. Such lab-on-a-chips would significantly enhance the quality of a diagnostic by offering immediate measurement of several clinically relevant parameters that can be used to assess the health of the patient. The biochemical analysis of the patient's biological fluids is a good start. Most diseases leave a molecular fingerprint in those fluids and by measuring that fingerprint in the right way, the precision of the diagnostic can be improved (Connolly, 1995). However, the physician or the patient has no routine in performing the advanced biochemical analysis on-chip. Therefore, to develop point of care disposable lab-on-a-chips, avoiding cross-contamination of samples and measurements errors, it is necessary to have a reliable and highly automated microfluidic control system. This system should be fully integrated with the control and the detection electronics implemented on a low-cost substrate and performed by a low-cost fabrication process. The use of MEMS (Micro Electro Mechanical Systems) based devices, such as microvalves and micropumps, increases the cost of the system, needs complex control systems and are difficult to integrate (Reyes et. al, 2002). Mixing only by diffusion avoids these drawbacks. However, long transit times and consequently long microchannels are necessary, if large molecules with small diffusivities must react. This illustrates how dramatic the diffusion limitation is.

To overcome the long transit times due to diffusion and to enable high-efficient reactions it is

necessary to induce the microfluidic die by a mechanism that accelerates the mixing and the reaction, preferably with no moving parts. In this paper, such mechanism is presented.

2 BACKGROUND

The need for rapid and in-situ measurements with low sample volumes has led to the development of miniaturized analyses devices with the fluidic, detection and readout systems integrated in a single chip. The vision of those devices was presented in 1990 (Manz et. al., 1990) and has been since then the inspiration for an intense research effort pursuing miniaturization of macroscopic biochemical analyses methods. Within the field of clinical diagnostics, several lab-on-a-chip approaches have been published (Auroux et. al, 2002, Reyes et. al., 2002).

Our group has developed a lab-on-a-chip for measuring the concentration of some biomolecules in urine samples by optical absorption technique (Minas, et. al., 2005). It comprises three parts in a multi-chip-module: (1) a microfluidic system die containing the microchannels fabricated using SU-8 techniques (Ribeiro et. al., 2005); (2) an optical filtering system based on highly selective Fabry-Perot optical resonators using a stack of CMOS process compatible thin-film layers (Minas et. al., 2006); (3) a detection and readout system fabricated in a CMOS microelectronic process (Minas et. al., 2004). The optical filtering system enables the measurement using white light illumination, thus avoiding the use of a wavelength dependent light source. This characteristic makes the lab-on-a-chip portable and ensures that the analysis can be performed at any location with instantaneous results. However, in that lab-on-a-chip, mixing the samples with the reagents was performed by diffusion, which leads to long transit times, especially when large molecules with small diffusion coefficients must be analysed. Therefore, to be valuable for point of care testing and monitoring, the microfluidic die of the lab-on-a-chip requires a microagitation mechanism. It is desirable that this mechanism does not require any external apparatus, internal moving parts or valves.

The flows used in microfluidic systems are very small, of the order of 100 µm, with velocities of the order of 1 mm/s, which leads to Reynolds number less than 1. For this small Reynolds numbers the flow is dominated by the viscous effects and turbulent mixing is impossible. Therefore, mixing in a straight channel rely on diffusion, but since diffusion coefficients of some biological species (e.g. enzymes and other proteins) are very small, mixing may take several minutes or even hours. This may be undesirable for some applications and alternative mixing methods must be developed.

Acoustic waves are an interesting solution for this problem. They have been used both to promote mixing (Bengtsson et. al., 2004) and to pump fluids (Rife et. al., 2000). Sound waves that propagate in the fluid generate pressure differences that induce the so called acoustic streaming. Secondary flows can be created in the plane perpendicular to the main flow in the channel. These secondary flows promote mixing by convection between otherwise parallel currents. Therefore, acoustic microagitation could be a simple actuation source for mixing and promoting fluids reaction.

In order to produce the ultrasounds, the channels and the reaction chambers of the microfluidic die must have an ultrasound transducer, which can be fabricated from a piezoelectric polymer, such as the PVDF - Poly(Vinylidene Fluoride) in its beta-phase. PVDF is a polymer with interesting piezoelectric properties, which allows important electro-optical, electromechanical and biomedical applications. This polymer shows at least four crystalline phases. The one with the best piezo- and pyroelectric properties, after poling, is the beta-phase (Sessler, 1987). Until recently, this phase was exclusively obtained by mechanical stretching of films originally in the non-polar alfa-phase, which is the most stable one from a thermodynamic point of view and directly obtained from the melt. This process results in films mostly in the beta-phase, but with a small percentage of alfa-phase material (Sencadas et. al., 2004). Unoriented films exclusively in the beta-phase were obtained from the crystallization of PVDF from solution with N,N-Dimethyl Formamide or Dimethyl Acetamide at temperatures below 70ºC. The electromechanical properties of this film were improved by a patented process by our group (Lanceros-Mendez et. al., 2006).

3 DEVICE DESCRIPTION

This paper describes the concept, operation and implementation of a portable, low-cost, plastic based, disposable and highly automated lab-on-a-chip for biochemical analyses of biological fluids. It uses optical absorption spectrophotometry as measurement analytical technique and acoustic microagitation for mixing the fluids. Its application is for point-of-care systems.

3.1 Measurement Analytical Technique

The spectrophotometric analysis, the study of the interaction of electromagnetic radiation with (bio)chemical compounds, is a very convenient and often used analytical technique in clinical laboratories for routine tests analyses, especially the ones based on colorimetric detection (Sigma, 2006). However, many of the analytes of interest for clinical analysis do not have chromophores that absorb light in a useful part of the visible range. Specific chemical reagents are available to transform these analytes into colored products that do have adequate absorbance. Therefore, in that detection method, the sample (ex: urine) is mixed with a proper reagent for the biochemical parameter in analysis (ex: uric acid reagent) and from that mixture, a visible colour is produced. The intensity of that colour is proportional to the biochemical parameter concentration and can be quantified by measuring the optical absorption of the mixture, once the mixture has an absorption maximum at a specific wavelength. As an example, for determining the uric acid concentration in a urine sample, the mixture has an absorption maximum at 495 nm (Figure 1). For an accurate measurement a complete and homogeneous mixing must be achieved.

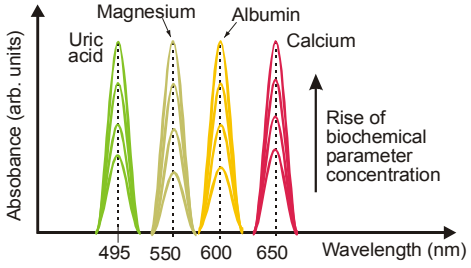

Figure 1: Absorption spectra for some biochemical parameters with different concentrations in urine.

3.2 Lab-on-a-chip Operation

The lab-on-a-chip is composed by two dies: the fluidic die and the detection die (Figure 2). For the measurement of the concentration of the biochemical parameters, a light beam is directed to the three fluidic cuvettes. The intensity of the light beam transmitted through the mixture is measured using the three photodetectors, placed underneath the microfluidic cuvettes, forming three optical channels. The photodetectors signal is converted, by the readout electronics, into a digital signal that allows simpler computer interfacing. The accurate sample and reagent mixing is performed by the control electronics that actuates an electroactive polymer (β-PVDF), deposited underneath the microfluidic cuvettes. This polymer vibrates and produces the proper acoustic microagitation of the mixture, e. g., the produced waves are coupled to the slide and propagate into the microfluidic cuvette.

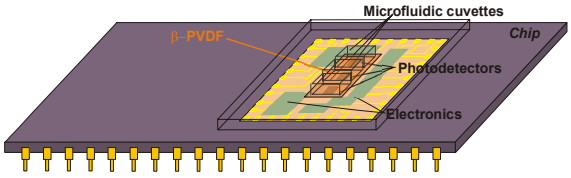

Figure 2: Schematic drawing of the lab-on-a-chip structure.

3.3 Microfluidic Die

The microfluidic die includes the microfluidic cuvettes containing the fluids to be analysed (Figure 2). Three cuvettes are needed for each analysis: one for the chemical reagent, in order to obtain the baseline reference; other for the mixture of the sample plus the reagent, to perform the analysis of the coloured mixed solution; and a third one with a standard sample with a well-known concentration of the biochemical parameter that is being analyzed, for the calibration of the biochemical parameter concentration.

Under the microfluidic cuvettes a piezoelectric polymer, β-PVDF, is deposited (Figure 2). This material will be responsible for the acoustic microagitation of the fluid. β-PVDF is a transparent piezoelectric polymer that will produce the necessary vibration, when an electrical alternating voltage is applied to its contacts. These vibrations result in the acoustic microagitation necessary to mix the sample with the reagent inside the cuvettes. Moreover, it accelerates the required time for the complete and homogeneous mixing, improving the efficiency of the reaction.

The microfluidic cuvettes are fabricated using a photoplastic material: the photoresist SU-8. This photoresist is an epoxy-based material that offers relevant properties, such as high mechanical strength, good adhesion on many different substrate materials and biocompatibility. The SU-8 based fabrication is a low-cost process, UV (from 350 nm to 400 nm) lithography semiconductor compatible and does not require expensive masks. It can be processed by using a spincoating and an UV maskaligner. In addition, the microfluidic system can be a disposable die, which minimize the costs associated with cleaning of the microfluidic cuvettes and avoids the contamination between analyses.

Moreover, SU-8 based processing enables the fabrication of deep structures with very low sidewall roughness which is suitable for optical absorption measurements (IBM, 1989).

The negative mask to be used for patterning the structure of the microfluidic cuvettes is fabricated from a regular transparency foil, such as the ones used in printed circuit boards. The chosen SU-8 photoresist is the SU-8-2150, which has a high viscosity and is the most appropriate for the required depth (≥ 500 μm). The following paragraphs describe the microfluidic cuvettes processing steps, including the SU-8 and the β-PVDF depositions.

After cleaning and drying the glass substrate, a thin-film of Itrium-Tin-Oxide (ITO) of approximately 40 nm is deposited by PVD, in order to form the bottom contact of the piezoelectric β-PVDF. Then, a 600 nm β-PVDF layer is spun of on top of the ITO. The coated β-PVDF is activated by applying an electrical field of tens of megavolts by meter, which is known as the electrical poling of the polymeric material. After that, the top electrical contact of the β-PVDF is deposited using the same procedure used for the bottom contact. These steps complete the fabrication of the microagitation mechanism.

Next, the fabrication of the microfluidic cuvettes starts with the spin of 1.25 ml/cm^2 of SU-8 on top of the β-PVDF top ITO contact. This process requires two steps: first, ramping up the spin rotation to 500 rpm during 5 s and keeping that velocity for 10 s; second, ramping up again the spin rotation up to 1000 rpm during 3 s and keeping it for 30 s. Then, a soft bake process is needed for evaporation of the solvent and for the hardening of the SU-8. The soft bake is performed at 65 ºC during 420 s and at 95 ºC during 3600 s. The initial temperature allows a slower evaporation, which results in a better coating and, mainly and very important, without grooves. Then, the cuvettes are exposed to UV light, using a negative mask, for patterning the structure. Figure 3a shows a cross-section of the device after the aforementioned steps.

An excessive dose of light with wavelength lower than 350 nm results in an excessive absorption at the surface of the film. The effect can be a pyramidal shape of the microfluidic cuvettes. To avoid this effect, a commercially available glass optical filter was used to cut of the wavelengths lower than 350 nm. The used exposition energy was 700 mJ/cm^2. The post-exposure bake is performed at 65 ºC during 60 s, followed by 900 s treatment at 95 ºC. The fabrication ends with the development, during 2400 s, with the SU-8 developer: an agitation bath of 1 methoxy-2-propanol acetate. In this way, the unexposed resist is dissolved and the microfluidic cuvettes are formed. The structure is then cleaned with isopropanol and deionised water and dried with nitrogen. Figure 3b shows a cross section of the patterned structure. The structure of the microfluidic cuvettes is shown in Figure 4. Each cuvette is 1 mm wide, long and height, having a 1 μl sample volume.

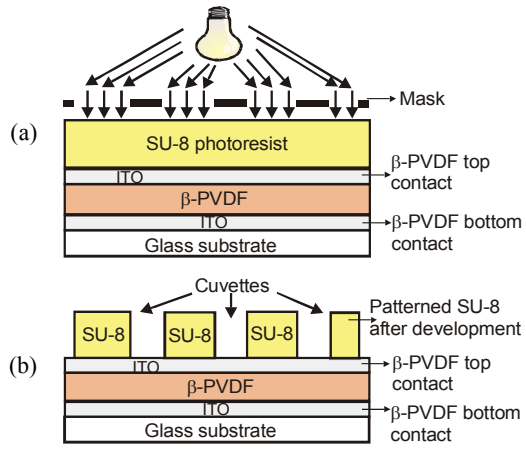

Figure 3: Fabrication sequence of the microfluidic cuvettes of the prototype: (a) deposition, spin coating, soft bake, UV exposure; (b) development of the SU-8.

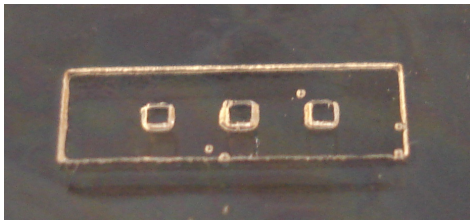

Figure 4: Picture of the microfluidic cuvettes.

3.4 Detection Die

The detection die includes the detectors and the electronics for signal actuation and detection, all fabricated in CMOS technology. Specifically, it comprises the photodetectors, its readout electronics and the electronics that control the voltages and frequencies applied to the β-PVDF. Figure 5 shows a block diagram of the photodiode and its readout electronics.

The readout electronics consists basically in a current amplifier and in a sigma-delta analog to digital converter. The circuit is repeated for each microfluidic cuvette. An additional circuit for the photodiode dark current compensation is also implemented.

After the light reaches the photodiodes, the four analog to digital converters start the conversion and their output signal is placed in four separated lines. Further computer processing perform additional calculations of these four output signals to achieve the concentrations of the biochemical parameters into analysis. The oversample frequency of the sigma-delta converters is determined by the desired number of output bits (signal to noise ratio). For this particular application, an oversampling ratio of 64 and a first order one-bit sigma-delta analog to digital converter is adequate since the input signal has no time variations, allowing a high oversample ratio without the need for a high clock frequency.

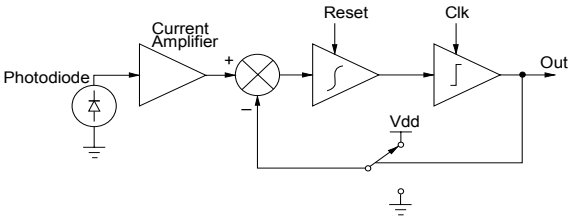

Figure 5: Block diagram of the readout electronics for each microfluidic cuvette.

For these sigma-delta converters, the gain of the integrator is very high, so, it is finite and larger than the oversampling ratio. At these conditions, the noise in the signal band increases only 0.15 dB (Candy et. al., 1992). Finally, the integrator must be initialized with a known voltage level at the beginning of each conversion. This initialization allows an improvement in the sigma-delta modulator of 3 dB in the signal to noise ratio (Netravali, 1977).

It was used a digital filter with constant weights (simple average) and the Pearson coefficient obtained for the response curve is larger than 0.99, which demonstrates a good linearity of the device. This result can even be improved by increasing the oversampling ratio and by using an optimized digital filter. Figure 6 shows a picture of the detection die.

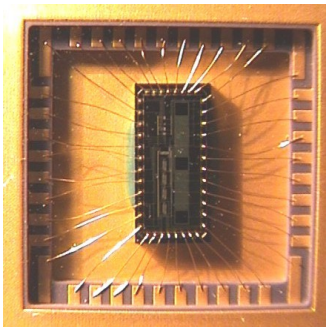

Figure 6: Picture of the detection die.

4 EXPERIMENTAL RESULTS

The evaluation of the mixing process was carried out using the Sigma Diagnostic kit (Infinity™ Uric Acid Reagent) and standards of urine with 30 mg/dl of uric acid concentration (Sigma, 2006). The reagent reacts with a sample of urine containing uric acid in a 50:1 ratio, and produces a pink colour with an absorption maximum at 495 nm. Its manual procedure states that a gentle inversion of the cuvette that contains the mixture is enough for the complete and homogeneous mixing. Performing this manual agitation, and after approximately 5 minutes at room temperature, the mixing is complete. Without any agitation and due to the high diffusion coefficients of uric acid in the Infinity™ reagent, the complete mixing is achieved but it takes approximately 15 minutes at room temperature. In clinical laboratories, the macroscopic equipments have mechanical agitation of the cuvettes for improving mixing and reducing the reaction time.

The experimental results for evaluating the mixing process are presented in Figure 7. The microagitation was performed by powering the β-PVDF though the electrical contacts, with a sinusoidal signal of 5 V amplitude at the frequencies shown in the Figure 7. The system was calibrated for an absorbance of 0 a. u. filling the cuvette with deionised water, and for an absorbance of 1 a. u. filling the cuvette with the perfectly mixed solution (perfectly mixing was guaranteed by external agitation of the mixture using a slow-rotation vortex).

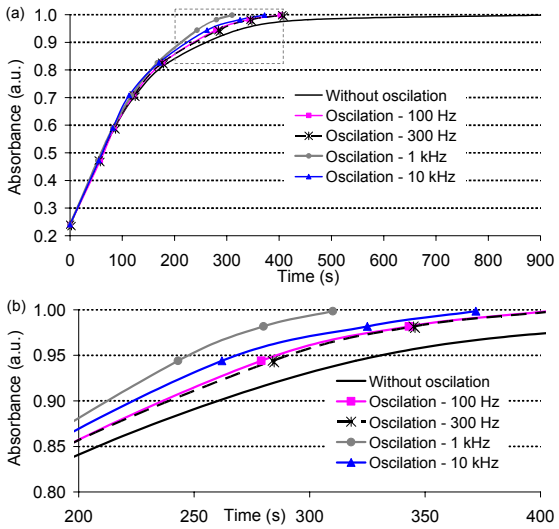

Figure 7: (a) Measured absorbance at 495 nm for 30 mg/dl of uric acid concentration in urine as a function of time for different driving frequencies. (b) Zoom of dashed-square.

The analysis cuvette is filled with the reagent. Its measured absorbance is 0.24 a. u.. Afterwards, the urine standard with 30 mg/dl of uric acid is dispensed on the reagent. The absorbance increases as the sample is being mixed with the reagent. From Figure 7 it can be seen that with the application of oscillations, the mixing occurs in a faster way, being the time necessary to obtain the complete mixing (absorbance of 1 a. u.) at 1 kHz only one third (300 s) of the complete mixing time without oscillation (900 s).

From those results it can be concluded that the application of acoustic microagitation by the β-PVDF piezoelectric polymer improves the mixing time. Moreover, uric acid has high diffusion coefficients, which is a good characteristic for mixing by diffusion only: after 15 minutes the mixture will be completed, even without agitation. However, when other biochemical parameters present in biological fluids have to be analysed, such as enzymes and some macromolecules, the mixing by diffusion can take hours or can even not occur. An example is a DNA analysis when PCR (Polymerase Chain Reaction) must be performed.

5 CONCLUSIONS

A lab-on-a-chip device with fluidic acoustic microagitation that reduces the mixing time of the analytes with the reagents was reported. The device consists of two dies: a microfluidic die, composed by three cuvettes and a β-PVDF acoustic microagitator, fabricated on a glass substrate; and an electronic detection die, composed by the readout circuits and the microagitation control electronics. The main innovative concept is the application of a β-PVDF film that produces acoustic microagitation, increasing the mixing velocity. Experimental results show that at 1 kHz microagitation, the mixing time is reduced to one third of the time needed without microagitation. As a conclusion, it can be stated that, for decreasing device sizes, acoustic microagitation becomes a preferred technology for effective mixing.

ACKNOWLEDGEMENTS

Work supported by the Portuguese Science Foundation (grants PTDC/BIO/70017/2006 and POCI/CTM/59425/2004).

REFERENCES

Kopp, M. U., Crabtree, H. J. Manz, A., 1997, Developments in technology and applications of microsystems, *Current Opinion in Chemical Biology*, 1, p. 410-419.

Connolly, P., 1995, Clinical diagnostics opportunities for biosensors and bioelectronics, *Biosensors & Bioelectronics*, 10, p. 1-6.

Reyes, D. R., Iossifidis, D., Auroux, P., Manz, A., 2002, Micro Total Analysis Systems. 1.Introduction, Theory, and Technology, *Anal. Chem*., 74, p. 2623-2636.

Manz, A., Graber, N., Widmer, H. M., 1990, Miniaturized total chemical systems: a novel concept for chemical sensing. *Sensors and Actuators B*, 1, p. 244-248.

Auroux, P., Iossifidis, D., Reyes, D. R., Manz, A., 2002, Micro Total Analysis Systems. 2.Analytical Standard Operations and Applications, *Anal. Chem.*, 74, p. 2637-2652.

Minas, G., Wolffenbuttel, R. F., Correia, J. H., 2005, A Lab-on-a-Chip for Spectrophotometric Analysis of Biological Fluids, *Lab-on-a-Chip*, 5, p. 1303-1309.

Ribeiro, J. C., Minas, G., Turmezei, P., Wolffenbuttel, R. F., Correia, J. H., 2005, A SU-8 Fluidic Microsystem for Biological Fluids Analysis. *Sensors and Actuators A*, 123-124 p. 77-81.

Minas, G., Wolffenbuttel, R. F., Correia, J. H., 2006, An array of highly selective Fabry-Perot optical-channels for biological fluids analysis by optical absorption using white light source for illumination. *Journal of Optics A: pure and applied optics*, 8, p. 272-278.

Minas, G., Martins, J. S., Ribeiro, J. C., Wolffenbuttel, R. F., Correia, J. H., 2004, Biological microsystem for measuring uric acid in biological fluids, *Sensors and Actuators A*, 110, p. 33-38.

Bengtsson, M., Laurell, T., 2004, Ultrasonic agitation in microchannels, *Anal Bioanal Chem*, 378-7, p. 1716-1721.

Rife, J.C. et. al., 2000, Miniature valveless ultrasonic pumps and mixers, *Sensors and Actuators B,* 86, p. 135–140.

Sessler, G.M, 1987, Topics *in Applied Physics: Electrets*, 2nd Ed., Springer, Berlin Heidelberg New York.

Sencadas, V., Lanceros-Mendez, S., Mano, J.F., 2004, *Thermochimica Acta*, 424, p. 201.

Lanceros-Mendez, S., Sencadas, V., Gregorio Filho, R., 2006, Portuguese patent n.º 103318.

Biochemistry and Organic Reagents: for bioscience investigation. Sigma-Aldrich Diagnostics®, 2006.

IBM, Photoresist composition and printed circuit boards and packages made therewith. J. D. Gelorme, R. J. Cox, S. A. R. Gutierrez, US Patent 4882245, 1989.

Candy, J. C., Temes G. C:, 1992, editors, *Oversampled Delta-Sigma Data Converters*, IEEE Press, New York.

Netravali, A. N., 1997, Optimum digital filters for interpolative A/D converters, *Bell Syst. Tech. J.,* 56, p. 1629.

YEAST ON A CHIP
Single-cell Analyses of MAPK Signaling Pathways in Saccharomyces Cerevisiae using Cell Chips

Min Cheol Park, Moon Kyu Kwak, Hye Sung Cho, Kahp Y. Suh
School of Mechanical and Aerospace Engineering, Seoul National University, Seoul 151-742, Korea
parkmc2@snu.ac.kr, kwak8099@snu.ac.kr, lelle01@snu.ac.kr, sky4u@snu.ac.kr

Jae Young Hur, Sang-Hyun Park
Department of Biological Sciences, Seoul National University, Seoul 151-742, Korea
hurjy77@snu.ac.kr, biopark@snu.ac.kr

Keywords: Cell chip, single-cell, MAPK signaling pathway, stochastic kinetics, receding meniscus, florescent protein.

Abstract: The mitogen-activated protein kinase (MAPK) signaling pathways are essential for cell growth, cell differentiation and survival in eukaryotes. The MAPK signaling pathways transmit signals from the cell surface to nucleus. The mating and high osmolarity responses in the budding yeast, *Saccharomyces cerevisiae*, depend on the MAPK signaling pathways. Here we analyzed the mating and high osmolarity responses in the budding yeast, *S. cerevisiae* at single-cell level using cell chips. The cell chip analyses of the mating and high osmolarity responses were performed using fluorescent proteins fused to genes whose transcription is specifically upregulated by each signaling. Using the technique, we have determined the real-time gene expression patterns of the mating and high osmolarity responses at single-cell level. In this study, we observed that the mating and high osmolarity MAPK signaling showed a non-uniform, fluctuating flux in the population of yeast cells analyzed.

1 INTRODUCTION

Cellular behavior has been typically investigated by utilizing bulk-scale methods that measure average values for a population of cells. For example, commonly used methods for high-throughput, cell-based assays are adapted to 96- and 384-well plate (recently 1536-well plates) formats (Hertzberg & Pope, 2000). Despite the success of these assays, such population-wide studies mask the behavior of individual cells and are often insufficient for characterizing biological processes in which cellular heterogeneity plays a key role (i.e., ensemble averaging problem).

Single-cell measurements are necessary for investigating the stochasticity of gene expression because cell-to-cell variation cannot be quantified using population measurements. Flow cytometry and automated microscopy are some of the most widely used techniques for single-cell measurements. Owing to the stochastic nature of gene expression, the optimal experimental setup for analyzing gene expression dynamics will be capable of both monitoring the behavior of a large population of cells and of tracking individual cells. Flow cytometry can be used to obtain gene expression data for thousands of cells, but only provides a snapshot of gene expression at single time points. Traditional microscopy experiments can track gene expression dynamics in individual cells, but can only monitor a ralatively small population of cells. Microfluidics or "lab-on-a-chip" technologies can be used to track gene expression changes in individual cells, enable large populations of cells to be monitored, and allow the precise control of the cellular microenvironment.

These microfluidic "lab-on-a-chip" technologies offer the ability to work with smaller reagent volumes, shorter reaction times, and the possibility of high-throughput analysis (Figeys & Pinto, 2000; Reyes, Iossifidis, Auroux, & Manz, 2002). Utilizing these technologies, one possible approach to analyze individual cells is based on cell-trapping including hydrodynamic confinement (Wheeler et al., 2003), negative dielectrophoresis (Voldman, Gray, Toner,

& Schmidt, 2002), optical tweezers (Ashkin, 1997), and microwells etched at the tip of a fiber-optic bundle (Biran & Walt, 2002). These methods, however, would have some limitations for easy, cheap, high-throughput microscopic studies of single cells.

Recently, we reported highly improved version of the soft lithographic approach using surface tension driven cell seeding and subsequent cell docking induced by receding meniscus (Park, Hur, Kwon, Park, & Suh, 2006). Using this method, single to multiple yeast cells can be accurately deposited onto microwells depending on the size of the microwell with a cheap, easy and high throughput manner. Here, we incorporated the receding meniscus induced docking method into high-throughput automated fluorescent microscopy for analyzing stochastic nature of the MAPK signaling pathways in the budding yeast, *S. cerevisiae*. Using the technique, we have determined the real-time gene expression patterns of the mating and high osmolarity responses at single-cell level. In this study, we observed that the mating and high osmolarity MAPK signaling showed a non-uniform, fluctuating flux in the population of yeast cells analyzed.

2 RESULTS AND DISCUSSION

2.1 Receding Meniscus Induced Docking

Inside a microfluidic channel, receding meniscus can be a powerful tool for arraying yeast cells at single-cell level in a high-throughput manner. To utilize the receding meniscus induced docking method, we fabricated PUA microwells onto glass substrate using capillary molding (Suh, Kim, & Lee, 2001), and the patterned glass substrate was bonded to a PDMS microfluidic mold (Khademhosseini et al., 2004) (Fig. 1).

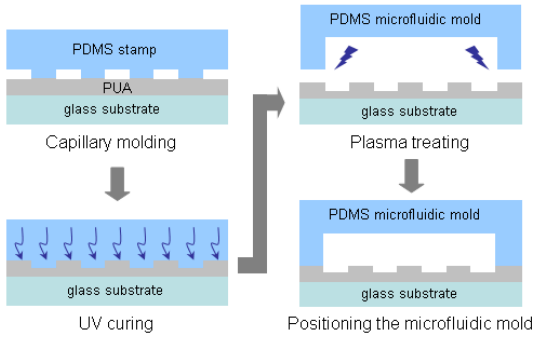

Figure 1: Fabrication of a patterned microfluidic channel.

Some representative SEM images of the fabricated PUA microwells are shown in Fig. 2. The pattern dimension of circular wells was 8 μm in diameter, allowing for a feature density of 3906 wells/mm^2 which is similar to Affymetrix GeneChip^{TM}. A higher-magnification (×3500) right column SEM images shows the well-defined PUA structures with good edge definition. The depth of each PUA microstructure was measured to be 8 μm corresponding to the original height of the silicon master (not shown).

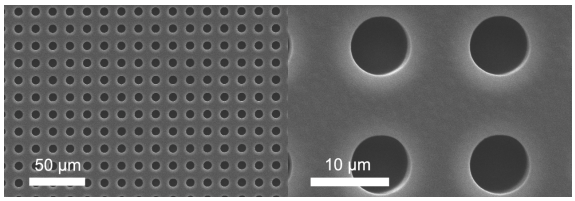

Figure 2: SEM images of PUA microwells.

As previously described (Park et al., 2006), yeast cells were docked into the microwells at single-cell level. As shown in Fig. 3, the docking efficiency is more than 90 % that allows high-throughput and high-content single-cell analysis.

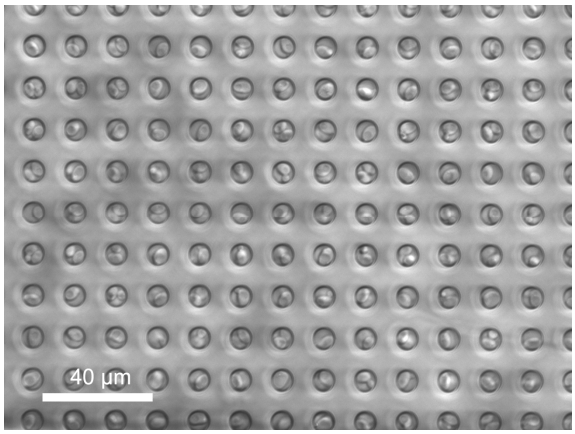

Figure 3: Single-cell docking of yeast cells in large-area.

2.2 Monitoring Gene Expression

Using this cell chip platform, we monitored the mating (α-factor) and high osmolarity (KCl) responses in the budding yeast, *S. cerevisiae* at single-cell level over time. The cell chip analyses of the mating and high osmolarity responses were performed using fluorescent proteins fused to genes whose transcription is specifically upregulated by each signaling. To do this, we constructed three kinds of yeast strain such as SH129 (*MATa, leu2, trp1, met15,* P_{Fus1}*-EGFP,* P_{Gpd1}*-Tdimer2*), SH133 (*MATa, leu2, trp1, met15,* P_{Fus1}*-EGFP-Cln2(PEST),*

P_{Gpd1}-Tdimer2) and SH135 (*MATa, leu2, trp1, met15, Kar4_EGFP, P_{Gpd1}-Tdimer2*) using homologous recombination.

For microscopic monitoring, we used DeltaVision™ system (Applied Precision, LLC.) which provide real-time live cell imaging. In order to image multiple fields of cells automatically and repeatedly over time, we controlled the microscope and camera with commercially available software, softWorx™ suite (Applied Precision, LLC.). We monitored 20 image fields which contain 42 ~ 49 well so that the total number of monitored cells were about one thousand. Some representative merged fluorescent images of each yeast strain are shown in Fig. 4 (scale bars are not shown).

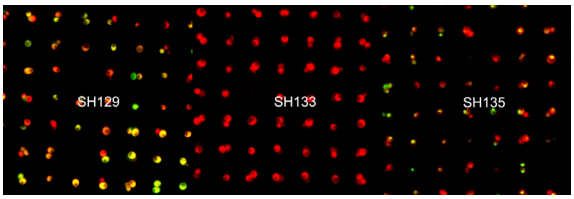

Figure 4: Merged fluorescent images of yeast strains.

2.3 Analyses of Stochastic Gene Expression

The acquired time-course merged fluorescent images were pre-processed for more accurate extraction of single-cell expression level. The pre-processing includes background subtraction, HiGauss filtering, Sharpen filtering and Flatten filtering. After image pre-processing, we extracted quantitative gene expression information with ImagePro™ software (Media Cybernetics, Inc.) (Fig. 5).

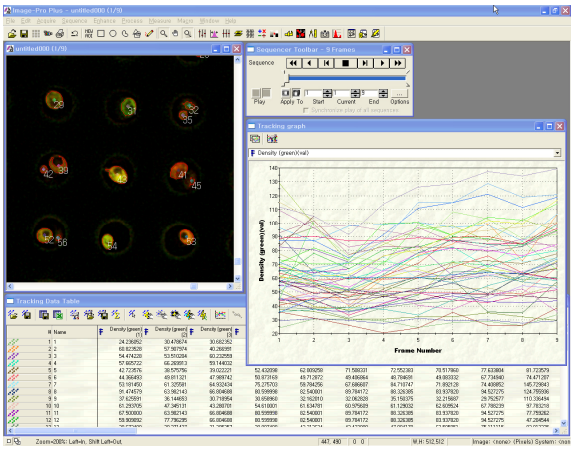

Figure 5: Extraction of quantitative information.

Genetically identical cells exhibit remarkable diversity even when they have identical histories of environmental exposure (Elowitz, Levine, Siggia, & Swain, 2002; Raser & O'Shea, 2004).

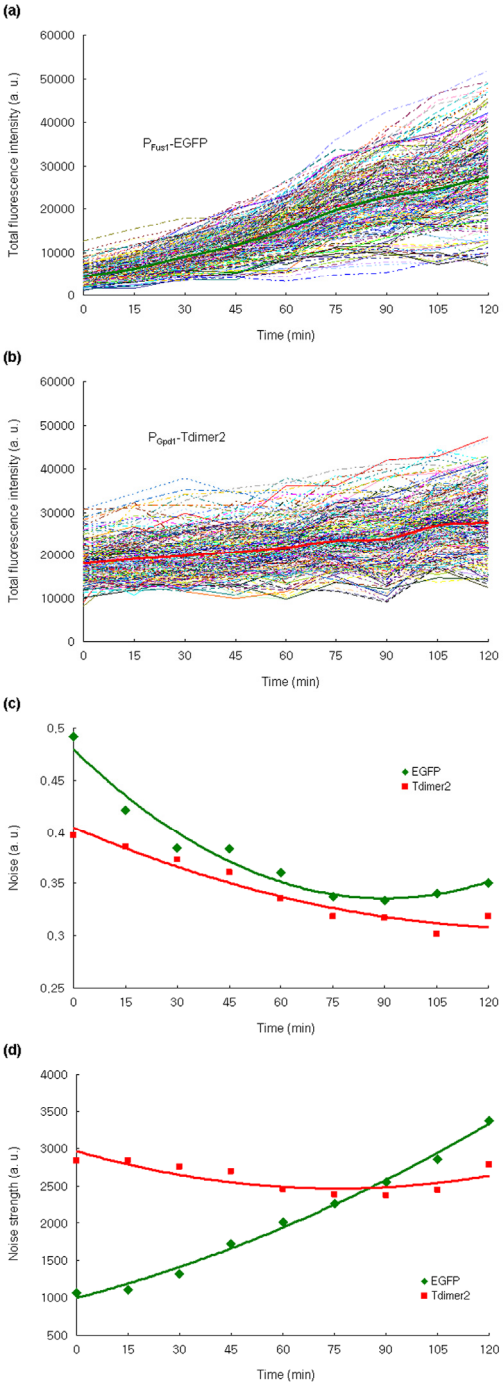

Figure 6: Analysis of stochastic gene expression in SH129.

As expected, we observed that the mating and high osmolarity MAPK signaling showed a non-uniform, fluctuating flux in the population of yeast cells analyzed. For example, when we used strain

with EGFP and Tdimer2 reporters driven by the α-factor-responsive P_{Fus1} promoter or by the α-factor-independent P_{Gpd1} promoter (i.e., SH129), the total fluorescence intensity, noise and noise strength upon stimulation of 10 μM α-factor are characterized as shown in Figure 6.

Figure 7 shows the stochastic gene expression in SH133 strain which contain C-terminal residues Cln2 (yeast G1 cyclin) PEST motifs. The Cln2 (PEST) destabilized EGFP so that it allows dynamic monitoring of transcription over time. Figure 7a shows dose-dependent gene expression of P_{Fus1}-EGFP upon stimulation of α-factor. Interestingly, the mating MAPK signaling has different kinetic gene expressions as increasing cellular area (Fig. 7b).

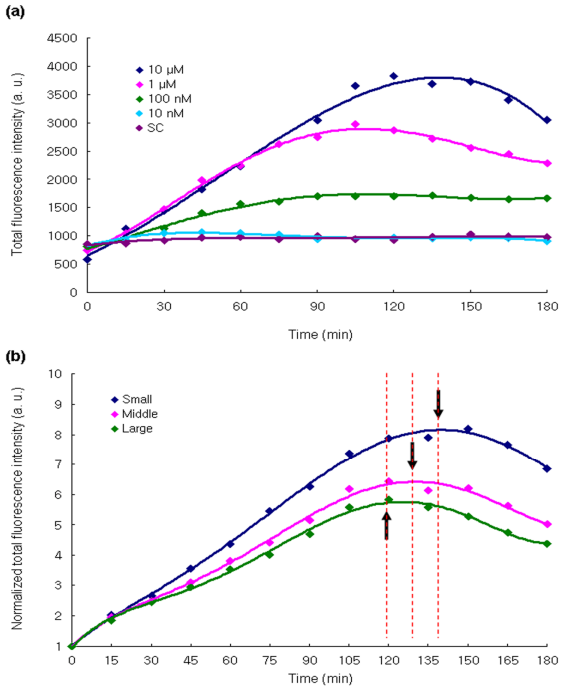

Figure 7: Analysis of stochastic gene expression in SH133.

Similarly, the SH135 strain whose character is protein localization exhibits the stochastic gene expression (not shown).

3 CONCLUSIONS

We have presented an optimal experimental setup for analyzing gene expression dynamics which would be capable of both monitoring the behavior of a large population of cells and of tracking individual cells. It was composed of yeast strain construction, single-cell docking, automated image acquisition, extraction of quantitative information, analyzing and modelling of the stochastic gene expression. Using this cell chip platform, we could successfully have an insight into the stochastic nature of gene expression, so we hope that many other investigators also will have such insight more easily aided this high-throughput and high-content single-cell analysis method.

REFERENCES

Ashkin, A. (1997). Optical trapping and manipulation of neutral particles using lasers. *Proceedings of the National Academy of Sciences of the United States of America, 94*(10), 4853-4860.

Biran, I., & Walt, D. R. (2002). Optical Imaging fiber-based single live cell arrays: A high-density cell assay platform. *Analytical Chemistry, 74*(13), 3046-3054.

Elowitz, M. B., Levine, A. J., Siggia, E. D., & Swain, P. S. (2002). Stochastic gene expression in a single cell. *Science, 297*(5584), 1183-1186.

Figeys, D., & Pinto, D. (2000). Lab-on-a-chip: A revolution in biological and medical sciences. *Analytical Chemistry, 72*(9), 330a-335a.

Hertzberg, R. P., & Pope, A. J. (2000). High-throughput screening: new technology for the 21st century. *Current Opinion in Chemical Biology, 4*(4), 445-451.

Khademhosseini, A., Suh, K. Y., Jon, S., Eng, G., Yeh, J., Chen, G. J., et al. (2004). A soft lithographic approach to fabricate patterned microfluidic channels. *Analytical Chemistry, 76*(13), 3675-3681.

Park, M. C., Hur, J. Y., Kwon, K. W., Park, S. H., & Suh, K. Y. (2006). Pumpless, selective docking of yeast cells inside a microfluidic channel induced by receding meniscus. *Lab on a Chip, 6*(8), 988-994.

Raser, J. M., & O'Shea, E. K. (2004). Control of stochasticity in eukaryotic gene expression. *Science, 304*(5678), 1811-1814.

Reyes, D. R., Iossifidis, D., Auroux, P. A., & Manz, A. (2002). Micro total analysis systems. 1. Introduction, theory, and technology. *Analytical Chemistry, 74*(12), 2623-2636.

Suh, K. Y., Kim, Y. S., & Lee, H. H. (2001). Capillary force lithography. *Advanced Materials, 13*(18), 1386-1389.

Voldman, J., Gray, M. L., Toner, M., & Schmidt, M. A. (2002). A microfabrication-based dynamic array cytometer. *Analytical Chemistry, 74*(16), 3984-3990.

Wheeler, A. R., Throndset, W. R., Whelan, R. J., Leach, A. M., Zare, R. N., Liao, Y. H., et al. (2003). Microfluidic device for single-cell analysis. *Analytical Chemistry, 75*(14), 3581-3586.

A NEW INSTRUMENTED BIOLOGICAL DEVICE DESIGNED TO APPLY MECHANICAL SHOCKS TO BONE CELLS

Laurent Navarro[1], Jean-Charles Pinoli[1], Henri Besset[2], René Guyonnet[2]
Ecole Nationale Supérieure des Mines de Saint-Etienne
[1] *Centre Ingénierie et Santé (CIS) and LPMG-UMR CNRS 5148*
[2] *Sciences des Processus Industriels et Naturels (SPIN)*
158 cours Fauriel, 42023 Saint- Etienne cedex 2, France
navarro@emse.fr, pinoli@emse.fr

Laurence Vico, Alain Guignandon
Université Jean Monnet de Saint Etienne, Laboratoire de Biologie du Tissu Osseux (LBTO) and INSERM U890
15 rue Ambroise Paré, 42023 Saint-Etienne Cedex 2, France

Keywords: Mechanical shocks, biomechanical device, energy, acceleration forces, Fourier analysis.

Abstract: A new device called biomechanical stimulation device (BSD) has been recently developped and is under patenting process. This BSD allows to apply shocks to a biomaterial disc, on which bone cells have been seeded. To observe the real behaviour of the biomaterial under shock loading, the BSD is instrumented with an impact hammer and an accelerometer. Force and acceleration signals are recorded, and signal analysis can be performed, in particular Fourier analysis. The results obtained lead to a better understanding of the stimulus that the cells can perceive at the top surface of the biomaterial disc. It appears that mechanical shocks applied at 1 Hps (Hit per second) or 10 Hps generate a frequency content up to 35 kHz. The main further objective will be to characterize the influence of mechanical shocks on bone cells proliferation.

1 INTRODUCTION

Bone cells activity deals with several medical stakes like osteoporosis and osteogenesis imperfectae, but also with biocompatibility in the case of bone prosthesis implantation. Bone cells activity is related to mechanical stimulation. Actually, the right term for "bone cells activity" is osteogenesis. Osteogenesis consists in a balance between bone synthesis (ensured by osteoblastic cells) and bone resorption (ensured by osteoclastic cells) (Bilezikian JP, 2002). Osteoblasts and osteoclasts do not act at the same time : it is a continuous looped process. First, the osteoclasts destroy the bone and make holes. Then, the osteoclasts withdraw and the osteoblasts take their place to form the bone. After bone creation, osteoblasts leave and osteoclasts come again to destroy the bone.

H. M. Frost showed with his Mechanostat (Frost, 1987) that the osteogenic process is strongly influenced by mechanical stimuli. Previous studies have reported different kinds of mechanical stimuli that are efficient for osteogenesis: ultrasounds, hydrostatic pressure, fluid shear stress, biaxial and uniaxial stretch, bending, nanostimulation with atomic force microscopy and acceleration forces (Tjandrawinata et al., 1997; Kacena et al., 2003; Hatton et al., 2003). The effect of acceleration forces on osteogenesis has already been analysed, but the exact stimulation that the cells could perceive remains not entirely known.

Recently, a new biomechanical stimulation device (BSD) has been developed and patented. It has been built in the Ecole Nationale Superieure des Mines de Saint Etienne (ENSMSE). This device aims at applying shocks to cells without direct contact (acceleration forces) between the cells and a mechanical impactor. Shocks are applied to a biomaterial disc on which cells are seeded. This allows to use different biomaterials in order to test their biocompatibility. Adhesion of the cells on the biomaterial depends on the physicochemical properties of this biomaterial. This adhesion is a very important factor for the cellular activity (Anselme et al., 2000; Ignatius et al., 2005; Jayaraman et al., 2004).

In order to better understand the mechanical strain and vibrational content involved, a signal acquisition and signal processing study have been performed on the BSD. More precisely, the purpose of this study was to analyse the vibrational content resulting from a

shock on a biomaterial. Biomaterial biocompatibility can be tested with the BSD, and the size of the biomaterial enables imaging and force investigations by using Atomic Force Microscopy (AFM) (with 10 mm diameter and 2 mm thickness disc). The BSD will be presented in this paper in section 2. Then, the experimental setup allowing the signals to be recorded is detailed in section 3. Next, in section 4, results of the signal acquisition will be analyzed. Furthermore, a synthesis on this study and a conclusion will be given.

2 EXPERIMENTAL DEVICE (BSD)

A schematic diagram of the BSD is shown in Fig. 1. Four different biomaterial discs (Titanium (Ti6Al4V), Hydroxy-apatite (HAP), cortical bone and trabecular bone) have been used. The discs are normally sealed into a culture chamber filled with culture medium, and cells are seeded on the top of the disc. However, all signal acquisitions have been performed without medium and cells in order to only characterise the mechanical behaviour of the disc. This is a fundamental step that is necessary to better understand what kind of vibratory stimuli the cells can perceive at the top of the biomaterial disc. During the mechanical stimulations, a vertical actuator is activated with a small and short stroke, high force solenoid, and a titanium hammer head is adapted to the solenoid stalk.

The mechanical impacts are directly driven through a current amplifier. Square type stimulation signals are used according to the current supply mode of the solenoid (DC current). Since the input signal waveform is not sinusoïdal, the signal frequency is defined in terms of hits per second (Hps) rather than in Hz. This notation is used to avoid misunderstanding between shocks application and resulting frequency content. Some authors have shown that in vitro cultured osteoblasts respond to mechanical strain at frequency values between 1 Hz and 10 Hz (Lanyon, 1984; Neidlinger-Wilke et al., 1994; Kaspar et al., 2000). The 1 Hz stimulation frequency corresponds to the human locomotor behaviour. In this study, mechanical shocks are applied at these two stimulation rates : 1 Hps and 10 Hps.

3 SIGNAL ACQUISITION

Signal acquisition is performed using two sensors coupled on the BSD, as shown in Fig. 2.

An Integrated Circuit Piezoelectric (*ICP*®) accelerometer (model 352C23, PCB Piezotronics, Inc., NY, USA) is fixed on the discs top surfaces by direct adhesive mounting and an Impulse Force Test Hammer (model 086D80, PCB Piezotronics, Inc., NY, USA) is adapted to the solenoid stalk and used as mechanical impactor. These sensors are connected to a signal conditioner (model 442B104, PCB Piezotronics) and acquired signals are recorded in a PC by means of an acquisition card (NI DAQ Pad-6015, National Instruments) with a sampling rate of 100 kHz using a program written with *LabVIEW*® software. A functional diagram of sensors monitoring, and main sensors characteristics are given in Fig. 3, 4 respectively. Accelerometer and Impulse force Test Hammer signals are recorded simultaneously during the impact. Acceleration and Force signals samples are interlaced to ensure synchronized acquisition for future joint analysis.

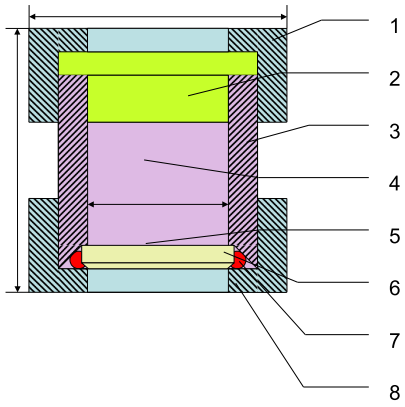

Figure 1: Schematic diagram of the BSD culture chamber used for in vitro experiments. Impact hammer is activated by a solenoid, the head of the impact hammer strikes the external surface of the biomaterial disc. Bone cells are cultured on the surface of biomaterial and the culture chamber is filled with medium. The impact hammer strikes the biomaterial with predefined frequency and duration. The different components of culture chamber and hammer head represented in the figure : (1) *Macrolon*® top lid, (2) teflon cork,(3) *Macrolon*® main part of culture chamber, (4) culture medium, (5) cell culture, (6) biomaterial disc, (7) *Macrolon*® bottom lid, (8) seal.

4 RESULTS

4.1 Signal Analysis

The experimental BSD produces two different types of signal : force signals from the instrumented impact hammer and acceleration signal from the accelerometer. Ten discs of each biomaterial have been pro-

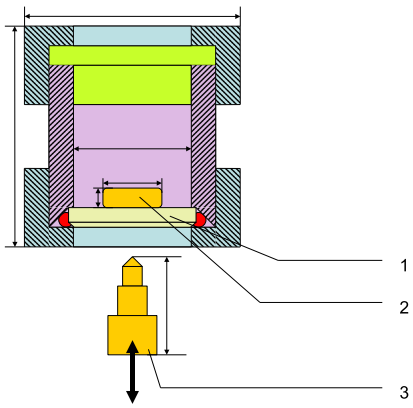

Figure 2: Schematic diagram of the culture chamber used for signal acquisition in air : (1) Biomaterial disc, (2) *ICP*®. accelerometer, (3) *ICP*® Impulse Force Test Hammer.

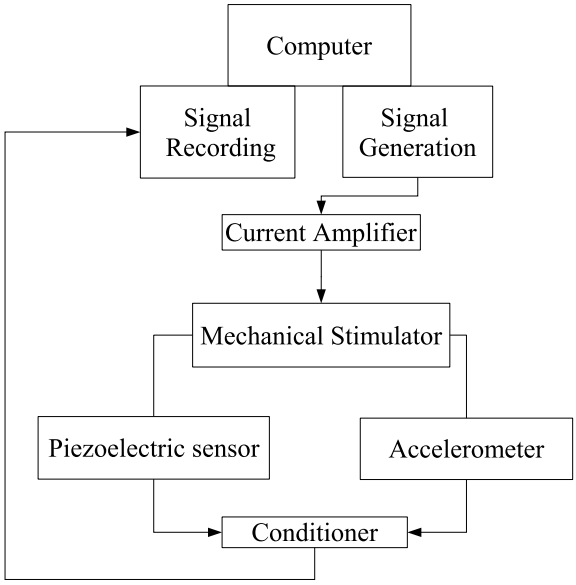

Figure 3: BSD is driven by amplified voltage current signals from the computer. During mechanical shocks, signals of *ICP*®. accelerometer and *ICP*® impulse hammer connected to BSD are simulteanously transmitted to the computer.

Accelerometer : 5 mV/g (15%) sensitivity
50 kHz frequency range

Impact hammer : 22.5 mV/N sensitivity
12 kHz Frequency Range (5%)

Figure 4: Sensitivity and frequency range given by the manufacturer for the two sensors.

cessed. Standard mean deviation have been calculated for each acceleration signals: Ti6Al4V, 783±31 g; HAP, 1197±87 g; Cortical bone, 1215±21 g; Trabecular bone, 225±24 g; and for each force signals: Ti6Al4V, 34±0.6 N; HAP, 28±0.2 N; Cortical bone, 23±0.2 N; Trabecular bone, 8±0.6 N. These values exhibit that Trabecular bone is softer than the other biomaterials.

The first step of the signal analysis consists in a zoom on the force and acceleration signals (Fig. 5) of the four materials : Ti6Al4V, Hydroxy-apatite (HAP), cortical bone and trabecular bone. This analysis enables to show important characteristics that can not be seen easily. For example, several rebounds between the impactor and the disc can be seen for only one hit. The delay between two rebounds is shortening as their amplitude decreases. A flat part can also be seen at the end of all the signals : it corresponds to the sustain time of the solenoid due to the square driving signal.

The second step of the signal analysis is the calculation of the Fourier Transform (FT) and the representation of the magnitude (Flandrin, 1993). The Fourier Transform (FT) $X(f)$ of a signal $x(t)$ is expressed as :

$$FT_x(f) = \int_{-\infty}^{+\infty} x(t)e^{-i2\pi ft}dt$$

where t denotes the time and f the frequency.

The FT has the property of expressing a signal in a frequency space.

The magnitude of the Fourier transform gives the global frequency content of a signal (Fig. 5). Usually, only the positive frequencies of the Fourier Transform magnitude are shown in Fig. 6, since they possess a physical meaning. In addition, the Shannon principle is taken into account to avoid aliasing effect. This principle is respected by the BSD signal acquisition process.

The frequency spectrums of the signals are multimodal and different for the four discs. The Ti6Al4V force signal frequency spectrum (Fig. 6a) shows that a slightly higher amplitude occurs for the Ti6Al4V than for the other materials. It is interesting to notice that HAP and cortical bone force frequency spectrums are regular (Fig. 6b,c), it might be due to the fact that they have almost the same chemical composition. Nevertheless, the cortical bone force frequency spectrum's pattern is smooth, whereas the HAP force frequency spectrum pattern is sharper. The frequency spectrum of the trabecular bone is very low, up to 1500 Hz, because the trabecular bone is softer than the cortical bone. The acceleration frequency spectrums are not regular and present several peaks, but relevant peaks can not be observed on these spectrums. However, it

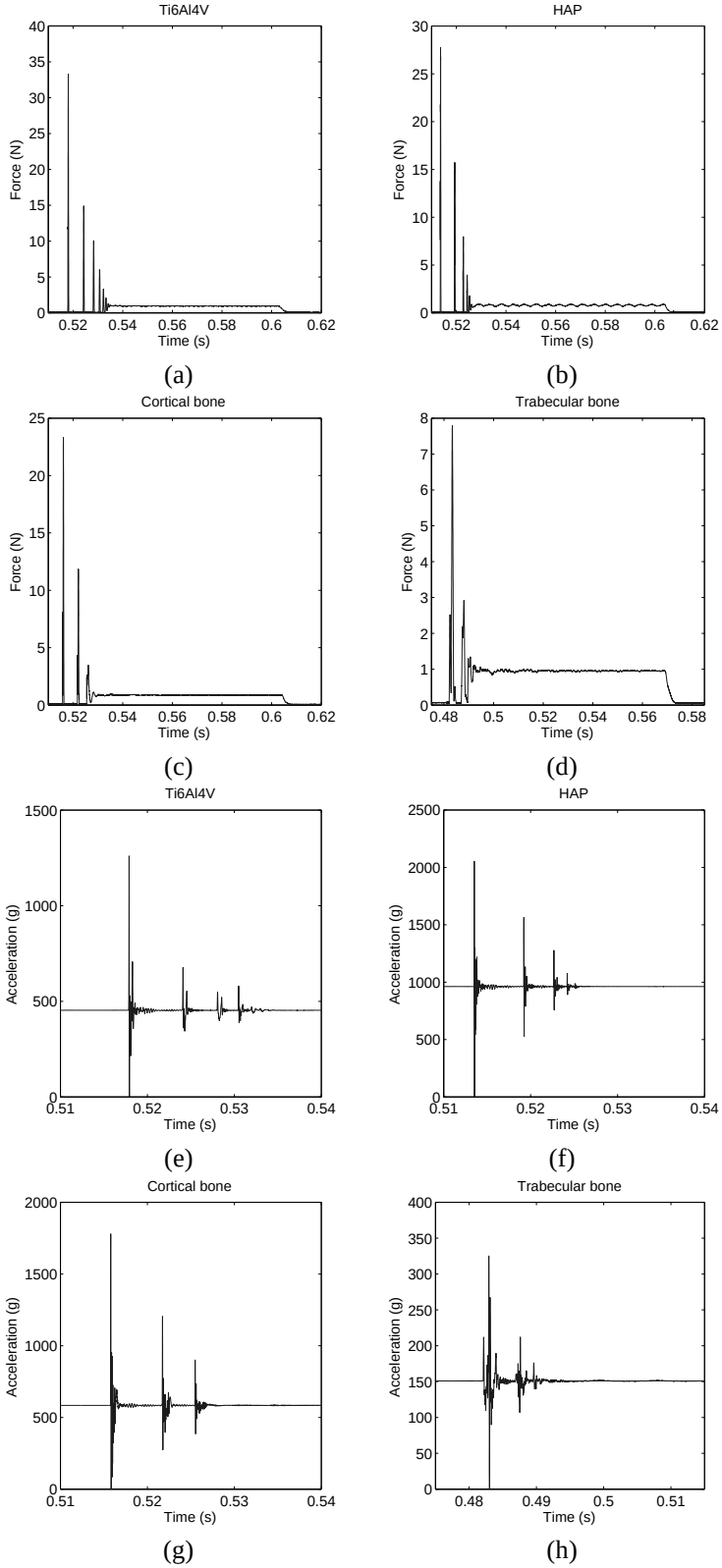

Figure 5: Force and Acceleration signals, recorded at 100 kHz sampling frequency with 12 bit amplitude resolution. (a) : Ti6Al4V acceleration signal. (b) : HAP acceleration signal. (c) : Cortical Bone acceleration signal. (d) : Trabecular bone acceleration signal. (e) : Ti6Al4V force signal. (f) : HAP force signal. (g) : Cortical Bone force signal. (h) : Trabecular bone force signal.

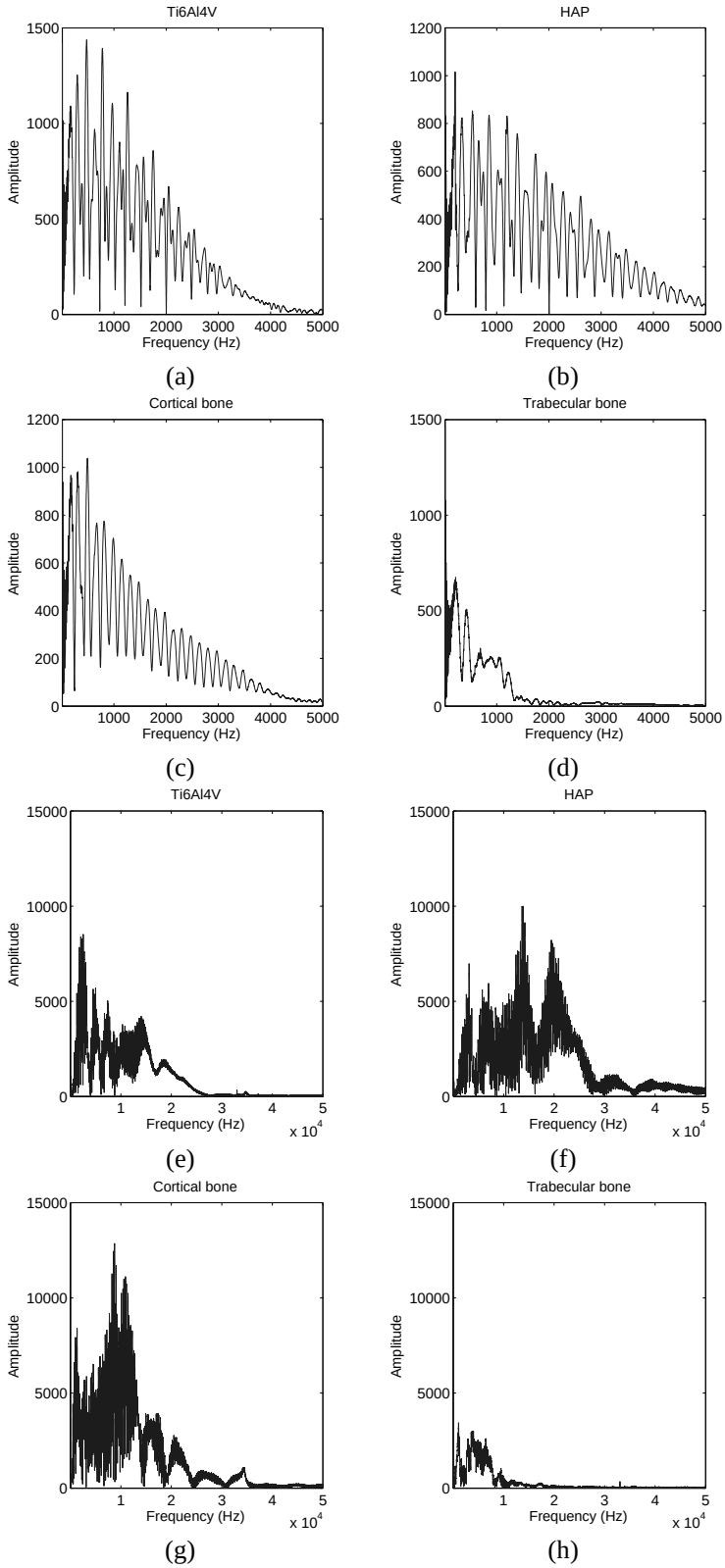

Figure 6: Fourier transform (FT) spectrums of the acquired force and acceleration signals. (a) : magnitude of Ti6Al4V force FT. (b) : magnitude of HAP force FT. (c) : magnitude of cortical bone force FT. (d) : magnitude of trabecular bone force FT. (e) : magnitude of Ti6Al4V acceleration FT. (f) : magnitude of HAP acceleration FT. (g) : magnitude of cortical bone acceleration FT. (h) : magnitude of trabecular bone acceleration FT.

is noticeable that the cortical acceleration frequency spectrum is higher than the others.

4.2 Energy

From the acceleration signal recorded, the kinetic energy of the Ti6Al4V disc/accelerometer unit during the mechanical shock is computed with the classical formula

$$E_k = \frac{1}{2} m \int v(t)^2 dt.$$

(with E_k: kinetic energy, m: mass , v: speed, given for each disc-accelerometer unit.)

The speeds of the different disc-accelerometer units are computed by integration of the acceleration signals, which occurs in the data processing sequence after application of 30 Hz Butterworth high-pass filter to remove continuous component. The frequency response curve of the Butterworth filter is practically flat in the passband. However, the use of this kind of filter introduces a non linear frequency dephasing. In this study, only the frequency content is expected and not the signal phase, thus the application of Butterworth filter is well adapted. The kinetic energy is calculated per surface unit: Ti6Al4V, 4.8$\pm$0.1 pJ/μm^2 for 1 Hps and 50.2$\pm$1.1 pJ/μm^2 for 10 Hps; HAP, 2.0$\pm$0.04 pJ/μm^2 for 1 Hps and 20.6$\pm$0.6 pJ/μm^2 for 10 Hps; Cortical bone, 8.5$\pm$0.2 pJ/μm^2 for 1 Hps and 65.1$\pm$3.6 pJ/μm^2 for 10 Hps; Trabecular bone, 0.9$\pm$0.2 pJ/μm^2 for 1 Hps and 8.8$\pm$3.2 pJ/μm^2 for 10 Hps. Notice that values of kinetic energy at 10 Hps are 10 times higher than those at 1 Hps.

5 SYNTHESIS

This new BSD was initially developed to simulate the effects of mechanical impacts on bone cells cultured on biomaterials to compare them with the effects of impacts during walking or running activities. A previous study on Ground Reaction Forces (GRF) (Giakas G, 2001) has shown that frequency content during impact phase of running is limited to 100 Hz, acceleration magnitude is $\sim$10 g. During shocks applied with the BSD, a frequency range comprised between 100 Hz and 4 kHz, an acceleration magnitude of 783,1$\pm$ 32,5 g at 1 Hps and an acceleration time of $\sim$1 ms have been found on Ti6Al4V for example. So it is quite difficult to directly put in relation the results obtained during this kind of mechanical impact with those obtained by GRF studies.

In this study, recording conditions for acceleration and force signals were slightly different from conditions used in case of in vitro experiments, particularly concerning the sealing of the culture chamber.

The disc should be excited by a frequency higher than his resonnant frequency to enter in resonnance. To verify this assumption, a numerical simulation was perfomed and the first resonant frequency mode of the Ti6Al4V disc was found to be at 144 kHz, which is much higher than the frequencies observed on the force signal Fourier transform. Consequently, the disc can not enter in resonance and induces some self-frequencies. The results found during signal recording can be extrapolated to in vitro conditions.

When mechanical shocks were applied to the discs, whatever the signal stimulation frequency was (1 Hps and 10 Hps), one could observe that the shape and the mean maximal value of the force and acceleration signals were identical. Analysis of acceleration signals leads to an estimation of the kinetic energy of the tested disc during one impact. It has been found that the amount of kinetic energy at 10 Hps is 10 times greater than that calculated at 1 Hps. Considering these results, in the case of mechanical shock, it appears that it is more interesting to analyse more accurately the frequency content of force signals, to compare kinetic energy derived from accelerations signals, and to focus on the force perceived by cells when they are subjected to acceleration phase. By applying the fundamental law of dynamic, the acceleration force during impact has been calculated by estimating cellular mass (1 picogramm): a force of $\sim$1 nN per cell has been found. This acceleration force is comparable to forces for which biological events have been previously observed. Consequently, it can be expected that this new kind of mechanical stimulation would have biological effects on bone cells.

A critical analysis can be done concerning the reproducibility of the acceleration and force peaks' measurements. The values and their errors are for each material: Ti6Al4V, 783$\pm$31 g; HAP, 1197$\pm$87 g; Cortical bone, 1215$\pm$21 g; Trabecular bone, 225$\pm$24 g; and for each force signals: Ti6Al4V, 34$\pm$0.6 N; HAP, 28$\pm$0.2 N; Cortical bone, 23$\pm$0.2 N; Trabecular bone, 8$\pm$0.6 N. The error is less important in the case of hard materials (cortical bone acceleration error is $< 2\%$ for example). However, a 10% error occurs on the measurements of acceleration and force peaks on the trabecular bone. This can be due to the non-heterogeneity of the material and probably to the non-flatness of the surface. In fact, the guidance of the hammer is not perfect so the head of the hammer does not hit in the same place every time. This is an improvement to ensure to the BSD for future work. An other improvement has been already done, it consists in a screw that allows to ajust the stroke of the

hammer. This leads to the possibility of controlling the peak value and it reduces drastically the errors between different discs (The error for one disc is about 10 times smaller than that between discs).

6 CONCLUSIONS

A new device designed to apply mechanical shocks to bone cells cultured on biomaterials has been developed. It allows to measure and compute shock parameters during impact : value and frequency content of force impact, acceleration and kinetic energy for each disc. When signals' characteristics during impact at different stimulation frequencies (1 Hps and 10 Hps) are compared, similar characteristics are found for force signals but acceleration signals and kinetic energy are different. Moreover, the computed value of the acceleration force should lead to the observation of cellular responses. In conclusion, this new mechanical stimulator could be used for in vitro studies to better understand bone cells mechanotransduction during impacts.

Further studies, particularly concerning the biological effects of mechanical shocks on bone cells, will be presented in future papers. Studies concerning other signal analysis tools like time-frequency or time-scale representations will also be held, since it seems interesting to know if the BSD is a new way to characterize biomaterials. Other biomaterial will be tested, and Atomic Force Microscopy (AFM) will be used in order to observe the bone cells behaviour before and after mechanical shocks loading.

REFERENCES

Anselme, K., Linez, P., Bigerelle, M., Le Maguer, D., Le Maguer, A., Hardouin, P., Hildebrand, H., Iost, A., and Leroy, J. (2000). The relative influence of the topography and chemistry of tial6v4 surfaceson osteoblastic cell behaviour. *Biomaterials*, 21(15):1567–77.

Bilezikian JP, Raisz LG, R. G. (2002). *Principles of Bone Biology-Second Edition*. ACADEMIC PRESS.

Flandrin, P. (1993). *Temps-fréquence*. Hermès.

Frost, H. (1987). Bone "mass" and the "mechanostat": a proposal. *The Anatomical record*, 219(1):1–9.

Giakas G, Baltzopoulos V, D. P. D. J. D. S. (2001). Comparison of gait patterns between healthy and scoliotic patients using time and frequency domain analysis of ground reaction forces. *Spine*, 21(19):2235–42.

Hatton, J., Pooran, M., Li, C., Luzzio, C., and Hughes-Fulford, M. (2003). A short pulse of mechanical force induces gene expression and growth inmc3t3-e1 osteoblasts via an erk 1/2 pathway. *J Bone Miner Res.*, 18(1):58–66.

Ignatius, A., Blessing, H., Liedert, A., Schmidt, C., Neidlinger-Wilke, C., Kaspar, D., Friemert, B., and Claes, L. (2005). Tissue engineering of bone: effects of mechanical strain on osteoblasticcells in type i collagen matrices. *Biomaterials*, 26(3):311–8.

Jayaraman, M., Meyer, U., Buhner, M., Joos, U., and Wiesmann, H. (2004). Influence of titanium surfaces on attachment of osteoblast-like cells invitro. *Biomaterials*, 25(4):625–31.

Kacena, M., Todd, P., and Landis, W. (2003). Osteoblasts subjected to spaceflight and simulated space shuttle launchconditions. *In Vitro Cell Dev Biol Anim.*, 39(10):454–9.

Kaspar, D., Seidl, W., Neidlinger-Wilke, C., Ignatius, A., and Claes, L. (2000). Dynamic cell stretching increases human osteoblast proliferation and cicpsynthesis but decreases osteocalcin synthesis and alkaline phosphataseactivity. *J Biomech.*, 33(1):45–51.

Lanyon, L. (1984). Functional strain as a determinant for bone remodeling. *Calcif Tissue Int.*, 36(Suppl 1):S56–61.

Neidlinger-Wilke, C., Wilke, H., and Claes, L. (1994). Cyclic stretching of human osteoblasts affects proliferation and metabolism:a new experimental method and its application. *J Orthop Res.*, 12(1):70–8.

Tjandrawinata, R., Vincent, V., and Hughes-Fulford, M. (1997). Vibrational force alters mrna expression in osteoblasts. *FASEB J.*, 11(6):493–7.

MPSOC ARCHITECTURAL DESIGN AND SYNTHESIS FOR REAL-TIME BIOMEDICAL SIGNAL PROCESSING IN GAMMA CAMERAS

Kai Sun, Hongxing Wei, Tianmiao Wang
Robot Research Institute, Beihang University, Beijing 100083, China
{*wtm, mounthorse, whx*}*@me.buaa.edu.cn*

Meng Wang, Zili Shao*
Department of Computing, Hong Kong Polytechnic University, Hung Hom, Kowloon, Hong Kong
{*csmewang, cszlshao*}*@comp.polyu.edu.hk*

Hui Liu
Software Engineering Institute, Xidan University, Xi'an, China
liuhui@xidian.edu.cn

Keywords: MPSoC, Gamma Camera.

Abstract: In this paper, we propose an MPSoC architecture for implementing real-time signal processing in gamma camera. Based on a fully analysis of the characteristics of the application, we design several algorithms to optimize the systems in terms of processing speed, power consumption, and area costs etc. Two types of DSP core have been designed for the integral algorithm and the coordinate algorithm, the key parts of signal processing in a gamma camera. We implement our MPSoC architecture on FPGA, and synthesize DSP cores and Network-on-Chip using Synopsys Design Compiler with a UMC 0.18um standard cell library. The results show that our technique can effectively accelerate the processing and satisfy the requirements of real-time signal processing for 256 $\times$ 256 image construction.

1 INTRODUCTION

The growing demand for increasing sophisticated biodevices requires high-performance processing techniques. MPSoC (Multi-Processor System-on-Chip) is an ideal architecture for biomedical applications with its high throughput. With MPSoC, we can integrate multiple heterogeneous processors, hierarchy memory systems, custom logic, and on-chip interconnection to implement complex functions. Therefore, in the previous work, application-specific MPSoC architecture has been studied for biomedical applications. In (Khatib et al., 2006), a novel MPSoC architecture is proposed for real-time ECG (Electrocardiogram) analysis. By employing multi-issue VLIW DSPs with system interconnect from STMicroelectronics and commercial off-the-shelf biomedical sensors, the proposed MPSoC architecture can perform real-time ECG analysis with high sampling frequencies. In this paper, we propose an MPSoC architecture to solve real-time digital signal processing for gamma cameras, most commonly used medical imaging devices in nuclear medicine.

Gamma cameras generate images based on gamma radiation detection. PMT (PhotoMultiplier Tube) is one of the key components in a gamma camera which can detect fluorescent flashes generated by a crystal and produce current. Then the current and voltage are converted to digital signals by ADC (Analog to Digital Converter) behind a PMT, and finally images are obtained by processing the digital signals. To generate images, multiple PMTs are placed in hexagon configurations behind the absorbing crystal. In a typical scheme, a PMT array may consist of more than 30 PMTs. Using a serial 2D images obtained by gamma cameras from the different angles, 3D information can be acquired by SPECT (Single Photon Emission Computed Tomography).

To accelerate data processing, in current gamma cameras, DSP (Digital Signal Processing) boards based on PC platforms are widely used. With such platforms, typically, it takes about 15 - 30 seconds to generate one 64 $\times$ 64 image and 15 - 20 minutes to

*The corresponding author.

finish a complete scan in SPEC. The platforms can not efficiently produce higher-quality images such as 256×256. Their slow processing speed and big size limit the effective use of gamma cameras. The problem become particularly severe for portable gamma cameras (Sanchez et al., 2004; Sanchez et al., 2006) which work with nuclear radiation detectors with room-temperature. To improve image construction speed, a technique called PMT-PSPMT (Position Sensitive PhotoMultiplier Tube) (Jeong et al., 2004) is proposed. PMT-PSPMT is very effective in optimizing image construction times. But it reduces the image quality and cannot construct 256 × 256 image dynamically.

To solve these problems, we propose an MPSoC architecture for PMT data processing in a gamma camera. Our MPSoC architecture consists of the following four parts: one general-purpose embedded processor, a high speed data interface (HSDI), application-specific DSP cores and a Network-on-Chip with an interconnection bus. In the paper, we design two types of DSP core to implement two key algorithms, integral and coordinate, for real-time biomedical applications. We implement a prototype of our MPSoC architecture with FPGA, and synthesize DSP cores and Network-on-Chip using Synopsys Design Compiler with a UMC 0.18um standard cell library. The results show that our technique can effectively accelerate the processing and implement communication with small area cost. It can satisfy the requirements of real-time signal processing for 256 × 256 image construction.

The rest of this paper is organized as follows: in Section 2, we introduce necessary backgrounds related to gamma camera technique. In Section 3, we present the MPSoC system design. Section 4 presents the implementation of the prototype system. Section 5 provides the experimental results and discussions. In Section 6, we conclude the paper.

2 BACKGROUND

In this section, we provide an overview of basic knowledge related to gamma cameras. We first introduce the basic operating mechanism of gamma cameras and then present the algorithms used for image processing.

2.1 The Mechanism of Gamma Cameras

A gamma camera is a commonly used medical imaging device in nuclear medicine. In a gamma camera, images are generated by detecting gamma radiation. Basically, the counts of gamma photons that are absorbed by a crystal are accumulated, and the crystal produces a faint flash of light at the same time. The PMT array behind the crystal detects the fluorescent flashes and generates current. The current signal generated by the PMT is captured by the ADC, and two corresponding voltage signals are converted into digital signals. Digital signals are used to calculate the coordinate and energy of the gamma photons. With these coordinate and energy data, the final image can be produced.

2.2 Image-Construction Algorithms in Gamma Camera

During the whole medical imaging procedure, three algorithms, the integral, coordinate and amendment algorithms, are applied to the collected data.

The integral algorithm, as shown in Figure 1, is to calculate the energy of the voltage signal. In this algorithm, the serial data of each PMT is accumulated based on system status conditions.

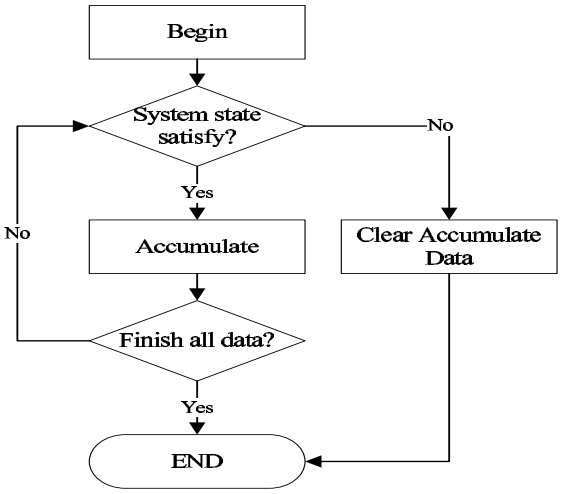

Figure 1: The integral algorithm.

The coordinate algorithm, as shown in Algorithm 2.1, includes the calculation for two parts, position and energy. In this algorithm, $P_1, P_2 \cdots P_m$ and $N_1, N_2 \cdots N_m$ are the internal data obtained from the two voltage signals, m is the count of the PMTs, and $T_1, T_2 \cdots T_m$ and $R_1, R_2 \cdots R_m$ are constant numbers. With these position and energy data, the gamma photon pulse can be determined. Then, an image can be constructed with a serial of the gamma photon pulse.
The amendment algorithm is used to amend energy

Algorithm 2.1 The Coordinate Algorithm.

Require: $P_1, P_2 \cdots P_m$,{ the internal data from the two voltage signal, m is the count of the PMTs}
$N_1, N_2 \cdots N_m$, { the internal data from the two voltage signals, m is the count of the PMTs}
$T_1, T_2 \cdots T_m$,{ constant numbers}
$R_1, R_2 \cdots R_m$,{ constant numbers}

1: $X_p \Leftarrow \frac{\sum_{i=1}^{m}(P_i \times T_i)}{\sum_{i=1}^{m} P_i}$, $Y_p \Leftarrow \frac{\sum_{i=1}^{m}(P_i \times R_i)}{\sum_{i=1}^{m} P_i}$, $X_n \Leftarrow \frac{\sum_{i=1}^{m}(N_i \times T_i)}{\sum_{i=1}^{m} N_i}$, $Y_n \Leftarrow \frac{\sum_{i=1}^{m}(N_i \times R_i)}{\sum_{i=1}^{m} N_i}$

2: calculate the position: $x \Leftarrow \frac{(X_p - X_n)}{(X_p + X_n)}$, $y \Leftarrow \frac{(Y_p - Y_n)}{(Y_p + Y_n)}$

3: calculate the energy: $E \Leftarrow \sum_{i=1}^{m} P_i + \sum_{i=1}^{m} N_i$

and position data with three table-lookup operations. This algorithm consists of two parts, energy and linearity emendation. After the data of every pulse is corrected by the correction table, a two-dimensional image of the relative spatial count density is constructed. With more pulse data, we can obtain more accurate image. To achieve that, multiple PMTs are placed in a hexagon array. In practical, a typical scheme usually uses 37 PMTs. The frequency of the pulse is limited to 1KHz in a typical gamma camera in order not to keep pulse data. Thus, with such a gamma camera, it takes about 15-30 seconds to build up one 64×64 image.

To reduce the image construction time, we can increase the pulse frequency of gamma photons. But with the limitation of the device, the maximum pulse frequency currently we can achieve is 500KHz-1 MHz. Correspondingly, we have to improve the speed of digital signal processing in order to generate image with such high pulse frequency. In this paper, our goal is to design an MPSoC architecture that can generate one 256×256 image in less than one second for gamma cameras with 1 MHz pulse frequency.

3 MPSOC SYSTEM DESIGN

In this section, we first introduce the MPSoC architecture in Section 3.1. Then we present issues related to general processors and HSDI in Section 3.2 and Section 3.3, respectively. Finally, the design of DSP cores and interconnection synthesis are discussed in Section 3.4 and Section 3.5, respectively.

3.1 Architecture Overview

Our MPSoC architecture is a typical heterogeneous multi-core architecture targeting on the application of gamma camera. It is specially designed for processing PMT data in parallel with multi-processors. In practice, fast image processing speed and high-quality image are the two of the most important performance metrics for gamma cameras. In order to achieve these goals, an MPSoC architecture, as shown in Figure 2 is proposed to speed up the image generation and improve image quality.

As shown in Figure 2, our MPSoC architecture consists of four parts: general processor, HSDI (High Speed Data Interface), DSP, and interconnection synthesis. Besides the four key parts, the MPSoC architecture also consists other components, e.g., the general embedded micro-controllers. In this architecture, the processor speed and the 32-bit on-chip interconnection are 200MHz, which are compatible with the 0.18um ASIC technology and the 32-bit bus interface IP cores. Next, we present the design issues for each key part of MPSoC architecture.

3.2 The General Processor

The general processor has one general purpose processor and some necessary IP cores, such as timer, UART, and SPI etc. Among these IP cores, the most important components are the on-chip RAM, SRAM/Flash controller, SDRAM controller and Ethernet MAC controller. The amendment algorithm and other general purpose computing are implemented in the general processor. The SRAM/Flash controller provides an interface to SRAM, ROM, NOR Flash and NAND Flash. The instruction code is stored in NOR Flash which is boot memory of the general processor. A reliable file system that stores the configurations using in the amendment algorithm is implemented in the NAND Flash. With an external Ethernet PHY chip, the Ethernet MAC controller is used to establish the communications with remote computers. In this way, the images and videos can be transferred to the remote computers through network, thus to help the doctors do some diagnosis. The on-chip RAM capacity is $512KB$ with 5 partitions. The first 2 partitions contain two amendment tables which are $256 \times 256 \times 16$ bit. The third partition contains one $256 \times 256 \times 8$ bit amendment table. The fourth partition contains the image constructed, which is 256 pixel $\times$ 256 pixel $\times$ 16 bit. The last partition is used as a high speed memory.

3.3 The High Speed Data Interface (HSDI)

The HSDI has a PMT data buffer and several LVDS (Low Voltage Differential Signaling) interfaces which

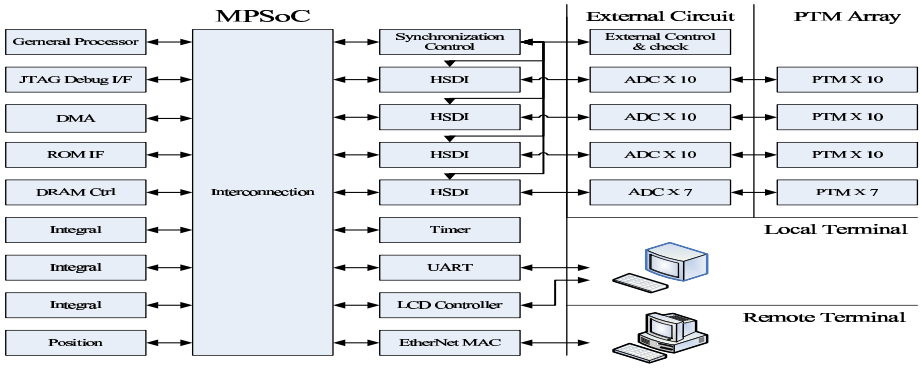

Figure 2: The MPSoC Architecture.

build a connection with external high speed ADCs. Since the sample speed of the ADC for PMTs is far lower than the processing time, buffers are used to store the PMT data of the external ADC. To exert the processing capability and diminish the interconnection area, the mount of the HSDI is determined by two factors: 1) the ADC sample speed; and 2) the on-chip interconnection speed. Usually, the common sample speed of the ADC for PMTs is 30MHz with the data width less than 16 bit, and the typical processor speed and on-chip interconnection with 0.18um technology and 32 bit width are 200MHz. Considering the bus arbitration cost, the maximum capacity of one HSDI is to take charge on 11 ADC data channels. For all of the 37 ADC data channels as discussed above, we use 4 HSDI as shown in Figure **??**(a) in which 3 of them take charge of 10 ADC data channels, and the last one takes charge of 7 ADC data channels.

3.4 The DSP Core Design

The customized DSPs used in our MPSoC architecture are designed for implementing the integral algorithm and the coordinate algorithm. We design two types of DSP, integral and coordinate, to implement the integral and coordinate algorithm, respectively. The corresponding block diagrams of the integral DSP and coordinate DSP are shown in Figure 3 and Figure 4, respectively.

The integral DSP has two bus interfaces, *Master* and *Slave*. The *Master* interface implements the data load/store, and the *Slave* interface implements the control and status logic accessing from other devices. The parameters for the integral algorithm are obtained through the *Slave* interface. Since there are 60 16-bit data for every gamma photons with two groups, upper and lower, which are implemented in the same integral algorithm, the data from HSDI is placed into the

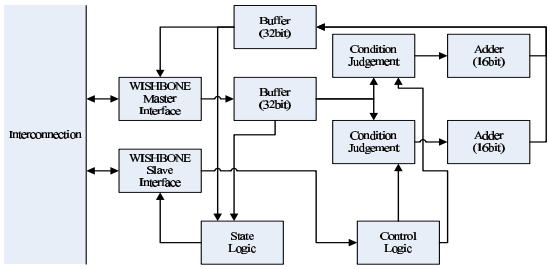

Figure 3: The Integral DSP.

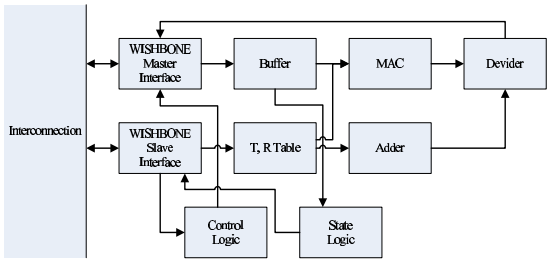

Figure 4: The Coordinate DSP.

buffer with 32-bit format, 16-bit for the upper group and 16-bit for the lower group. In other words, the integral algorithm is processed in parallel in the integral DSP. Thus, the integral DSP is designed with same units to accelerate the processing speed. For 30 PMTs data, the integral DSP uses 36 cycles to process them in which each integral DSP processes 10 gamma photons pulses within 2us. Thus, 4 integral processors are needed to process all of the 37 channel PMTs data.

The block diagram of the coordinate DSP is shown in Figure 4. The main components of the coordinate DSP are *MAC* (Multiply Accumulate) and *Divider*. The coordinate DSP has two bus interfaces, *Master* and *Slave*, which are as same as those of the

integral DSP. The *T* and *R* parameter tables are accessed through the *Slave* interface, and the data to be processed is placed in the buffer through the *Master* interface. As the *MAC* and *Adder* can work in parallel, we can process the numerator and denominator in algorithm 2.1 simultaneously. Since the throughput of the coordinate algorithm is much lower than the integral algorithm, only one coordinate DSP is required in the DSP design.

3.5 Interconnection Synthesis

As shown in Figure 2, interconnection serves the communication among DSP cores and other components. In most on-chip bus standards, such as AMBA(SPE, 2001), CoreConnect(SPE,), STBus(SPE, 2003) and WISHBONE(SPE, 2002), a share structure is used in the embedded processor. In the structure, the total bandwidth of the interconnection is limited to the bandwidth of each node since all buses are connected to one node and only one master can access the interconnection at one time. In order to fully utilize bandwidth, we need to perform careful analysis. In (Wang et al., 2007), we propose an interconnection synthesis algorithm to solve the problem.

4 PROTOTYPE IMPLEMENTATION

We have implemented the MPSoC prototype in an Altera Cyclone II FPGA EP2C35F672. In the implementation, we use the OpenRisc 1200 processor core as the general processor that runs at 20MHz which is 10% of the speed of the final ASIC implementation. We add one 512KB ZBT SRAM to our prototype since the on-chip RAM in Cyclone II FPGA can not meet our requirements. Besides the external SRAM, the prototype has 64MB SDRAM, 32MB NOR Flash ROM, 128MB NAND Flash ROM, 10M/100M Ethernet PHY, 640 $\times$ 480 16bit TFT LCD and other chips.

Table 1: The information for the prototype.

LEs	RAM(KB)	Multiplier(9-bit)
23468 (71%)	54 (92%)	16 (23%)
IO	PLL	Max Speed(MHz)
465 (98%)	1 (25%)	42

We test the prototype with input signals based on a real gamma camera, and check the output signals. The results show that it functions correctly. The numbers of resources we use are shown in Table 1. In this table, LEs denotes logical elements, RAM represents the on-chip-memory, and PLL denotes phase loop lock. The number inside the brackets for each resource represents the percentage between the number of resource we really use and the total number of resource provided by the system.

5 EXPERIMENTAL RESULTS AND DISCUSSIONS

To compare our MPSoC architecture with the general architecture, we have implemented the integral and coordinate algorithm both with an ARM9 processor and with our custom designed DSPs. In the experiment, we obtain the results of processing time, the area, RAM, power cost of our custom DSPs. For the interconnection, we have implemented our interconnection with WISHBONE protocol and our bus interconnection synthesis algorithm. We compare our technique with the crossbar and the reduce crossbar structure in terms of the area cost. In this section, we first present the results of processor comparison in Section 5.1, and then we present and analyze the results of interconnection optimization in Section **??**.

5.1 Processor Comparison

The typical sustaining time of the PMT reactivity electric current signal for gamma photons pulse is 2us. In this time interval, the ADC produces 60 data in which every 30 data is applied with the integral algorithm. The cycles and time for the integral and coordinate algorithm to process data that is produced within 2us are shown in table 2. We have tested the ARM9 program in SimpleScalar (Burger and Austin, 1997) and a hardware platform based on ARM 920T (ARM 920T, 2001) running with 203 MHz. The results are shown in Table 2.

Table 2: The testing results of ARM9 program in SimpleScalar and S3C2410.

	Condition	**Cycle**	**Time (us)**
The Integral Algorithm	SimpleScalar	2104	10.5
	S3C2410		21.6
The Coordinate Algorithm	SimpleScalar	1692	8.5
	S3C2410		24.2

In the table, we can see that it takes 2104 and 1692 clock cycles to finish the integral and coordinate algorithms, respectively, on the SimpleScalar simulator.

Based on the hardware platform, the times we need are 21.6 and 24.2 μs, respectively.

We design two types of DSP to implement the algorithms separately. In order to accelerate the processing speed, we use several integral DSPs with same design. The integral and coordinate DSPs are coded in Verilog HDL, and are synthesized to gate-level circuits using Synopsys Design Compiler and a UMC 0.18um standard cell library. The results generated by our technique is shown in Table 3. The comparison of the results generated using ARM9 and our customized DSP is shown in Table 4. From the table, we can see that our customized DSPs can preform with very high performance. With 5 integral DSP cores, we can achieve the requirements. The results show great performance improvement and cost reduction with our MPSoC architecture.

Table 3: The results with our DSP cores.

	Integral DSP	**Coordinate DSP**
Cycle	37	340
Time(us)	0.185	1.700
Area(um^2)	0.14	2.03
RAM(KB)	1	4
Power(mW)	18	264

Table 4: The comparison of the results from ARM9 and our DSP cores.

	DSP	**ARM920 Processor**
Quantity	5	197
Area(um^2)	2.59	1026.8
RAM(KB)	8	3152
Power(mW)	336	120

6 CONCLUSIONS

In this paper, we have proposed an MPSoC architecture for implementing real-time signal processing in gamma camera. Based on a fully analysis of the characteristics of the application, we designed several algorithms to optimize the systems in terms of processing speed, power consumption, and area costs etc. Two types of DSP core have been designed for the integral algorithm and the coordinate algorithm, the key parts of signal processing in a gamma camera. A prototype of our MPSoC architecture has been implemented with FPGA, and the test results show that it can function correctly. Various experiments have been conducted and discussed. We synthesized DSP cores and Network-on-Chip using Synopsys Design Compiler with a UMC 0.18um standard cell library. The results show that our technique can effectively accelerate the processing and satisfy the requirements of real-time signal processing for 256 $\times$ 256 image construction.

ACKNOWLEDGEMENTS

The work described in this paper was partially supported by the grants from the Research Grants Council of the Hong Kong Special Administrative Region, China (PolyU A-PH13, PolyU A-PA5X, PolyU A-PH41, and PolyU B-Q06B), the National Nature Science Foundation of China (60525314), the 973 Program of China (2002CB312204-04) and the 863 Program of China (2006AA04Z206).

REFERENCES

Ibm on-chip coreconnect bus architecture. *www.chips.ibm.com*.

(2001). Arm amba specification (rev2.0). *www.arm.com*.

(2002). Wishbone system-on-chip (soc) interconnection architecture for portable ip cores revision: B.3. *www.opencores.org*.

(2003). Stbus communication system: Concepts and definitions, reference guide. *STMicroelectronics*.

ARM 920T, R. . (2001). *Technical Reference Manual*.

Burger, D. and Austin, T. M. (1997). The simplescalar tool set, version 2.0. *SIGARCH Comput. Archit. News*, 25(3):13–25.

Jeong, M. H., Choi, Y., Chung, Y. H., Song, T. Y., Jung, J. H., Hong, K. J., Min, B. J., Choe, Y. S., Lee, K.-H., and Kim, B.-T. (2004). Performance improvement of small gamma camera using nai(tl) plate and position sensitive photo-multiplier tubes. *Physics in Medicine and Biology*, 49(21):4961–4970.

Khatib, I. A., Poletti, F., Bertozzi, D., Benini, L., Bechara, M., Khalifeh, H., Jantsch, A., and Nabiev, R. (2006). A multiprocessor system-on-chip for real-time biomedical monitoring and analysis: architectural design space exploration. In *DAC*, pages 125–130.

Sanchez, F., Benlloch, J. M., Escat, B., Pavon, N., Porras, E., Kadi-Hanifi, D., Ruiz, J. A., Mora, F. J., and Sebastia, A. (2004). Design and tests of a portable mini gamma camera. *Medical Physics*, pages 1384–1397.

Sanchez, F., Fernandez, M. M., Gimenez, M., J.M., J. M. B., Rodriguez-Alvarez, M. J., Quiros, F. G. D., Lerche, C. W., Pavon, N., Palazon, J. A., Martinez, J., and Sebastia, A. (2006). Performance tests of two portable mini gamma cameras for medical applications. *Medical Physics*, pages 4210–4220.

Wang, T., Sun, K., Wei, H., Wang, M., Shao, Z., and Liu, H. (2007). Interconnection synthesis of mpsoc architecture for gamma cameras. In *EUC*.

SMART DIELECTRIC ELASTOMERS AND THEIR POTENTIAL FOR BIODEVICES

Todd A. Gisby, Iain A. Anderson
Biomimetics Laboratory, Auckland Bioengineering Institute, The University of Auckland, Level 6, 70 Symonds Street Auckland, New Zealand
t.gisby@auckland.ac.nz, i.anderson@auckland.ac.nz

Emilio P. Calius
Industrial Research Limited, P.O. Box 2225, Auckland, New Zealand
e.calius@irl.cri.nz

Shane Xie
Mechatronics Engineering, Department of Mechanical Engineering, The University of Auckland, New Zealand
s.xie@auckland.ac.nz

Keywords: Dielectric Elastomers, Artificial Muscles.

Abstract: Dielectric Elastomer (DE) actuators are compliant, ultra light-weight electromechanical devices that can be used as actuators, sensors, and power generators. While a relatively new technology, DE actuators can be produced using biocompatible materials and have already exhibited excellent performance in terms of strain, speed, pressure, specific energy density, and efficiency when compared to conventional actuation technologies and natural muscle. Further research is required in order for promising laboratory results to be translated into real-world applications, particularly in the areas of modelling and control, but the potential for multiple functions to be integrated into a single element is an exciting prospect for flexible smart structures and biodevices.

1 INTRODUCTION

Dielectric Elastomer (DE) actuators are compliant, ultra-light weight electromechanical devices that are emerging as an attractive emerging technology for a range of biomedical applications. They are fabricated from inexpensive biocompatible polymers that have highly tuneable material properties. They are also scale invariant, operate silently and efficiently over a range of speeds, and are capable of being used not only as actuators, but also as sensors and power generators (Kornbluh, 2004).

DE actuators have demonstrated remarkable performance characteristics in terms of active stress, strain, strain rate, energy density and electromechanical efficiency. Their unique properties offer a number of advantages with respect to weight, scalability, and simplicity of design over conventional transducer technologies such as electrostatics, piezoelectrics, electromagnetics, and shape memory alloys (Bar-Cohen, 2004; Kornbluh et al., 2004; Madden et al., 2004). They also compare very favourably with human skeletal muscle (Hunter and Lafontaine, 1992).

Table 1 compares the key performance figures of DE actuators with those of other tranducer technologies. While it is apparent that DEs do not excel in every category, it is clear that their key strength lies in their excellent overall performance.

2 DIELECTRIC ELASTOMER OPERATING PRINCIPLE

2.1 Basic DE Structure

A DE actuator is a compliant capacitor consisting of an incompressible soft polymer membrane dielectric with compliant electrodes applied on both sides.

When used as an actuator, the charge accumulated on the electrodes when a voltage is

Table 1: Actuator Technology Comparison.

Characteristic	DEA* (Madden et al., 2004)	Skeletal Muscle (Hunter and Lafontaine, 1992)	Piezoelectric (Kornbluh et al., 2004)	Electro-magnetic (Kornbluh et al., 2004)	Electrostatic (Kornbluh et al., 2004)	Shape Memory Alloy (Hunter and Lafontaine, 1992)
Stress (MPa)	7.7	0.35	131	0.1	0.03	200
Strain (%)	380	>40	1.7	50	50	5
Relative Strain Rate	Medium	Medium	Fast	Fast	Fast	Slow
Energy Density (kJ/m^3)	34,000	40	0.13	0.003	0.003	10,000
Efficiency (%)	60-80	35	>90	>90	>90	2-3

**figures taken for a VHB dielectric membrane (see section 2.4). Stress, strain, strain rate and energy density figures vary depending on membrane material.*

applied gives rise to electrostatic forces that generate deformation in the DE. The opposite charges act to draw the positive and negative electrodes together while the like charges on each electrode act to expand the area of the electrode. When the charge is removed, the elastic energy stored in the dielectric returns it to its original shape (Fig. 1). The linear motion produced by this electromechanical response can be used for actuation purposes.

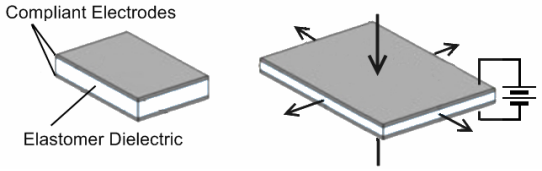

Figure 1: Deactivated (left) and activated (right) states of a simple DE actuator.

2.2 Pressure Capabilities

DEs are driven by electric fields. The pressure that can be generated in a DE is widely accepted to be defined by the following equation (Kofod, 2001):

$$P = \varepsilon_r \varepsilon_0 (V/d)^2 \quad (1)$$

Where P is the electrostatic Maxwell pressure, ε_r is the relative permittivity of the dielectric material, ε_0 is the permittivity of free space ($\varepsilon_0 = 8.854 \times 10^{-12}$ F/m), V is the voltage and d is the thickness of the dielectric membrane. This is twice the pressure generated by a rigid plate electrostatic device due to the addition of the area expansion to thickness compression upon activation. The level of deformation achieved at any given electric field is dependent on the combined stiffness of the polymer dielectric and electrode materials. The peak field that can be applied is limited by the dielectric breakdown strength of the DE membrane.

2.3 Power Generation

The phase difference between the electrical and mechanical stimulus applied to a DE determines whether it acts as an actuator or a generator. When the mechanical deformation leads the electrical excitation the DE will generate electrical power.

The electrical charge stored on a DE device (Q), the capacitance of the device (C), and the voltage difference between the electrodes (V) are related by the following equation:

$$Q = CV \quad (2)$$

And the electrical energy, $e_{electrical}$, stored in the DE is defined by:

$$e_{electrical} = \tfrac{1}{2}CV^2 \quad (3)$$

Assuming, for simplicity, charge is kept constant (i.e. the DE is electrically isolated) work done by an external force acting to increase the separation between the electrodes against the electrostatic forces is converted to electrical energy and stored in the DE. This is because the capacitance of the device will decrease as the electrode separation increases and the electrode area decreases, thereby causing the voltage to increase. As the electrical energy stored in the DE is related to the voltage squared a net increase in the electrical energy is achieved; energy that can then be used to power other electrical devices.

2.4 Materials

Silicone and polyacrylate polymers have garnered much attention in the field of DE research due to their highly elastomeric nature and high breakdown strengths. Silicones typically exhibit low viscous

losses and some can operate in temperatures ranging from -100ºC to 260ºC, making them well suited to dynamic, high speed applications in harsh environments. Their availability in monomer form (e.g. NuSil CF19-2186, Dow Corning Sylgard 184) enables the tuning of material properties (e.g. stiffness, elongation at break, and geometry) and facilitates the creation of silicone based composites through the incorporation of additional material prior to polymerization.

3M's commercially available VHB4905 double-sided polyacrylate tape has a high degree of viscoelasticity, but at low speeds is capable of the highest reported active displacement (380%) and energy density (3.4MJ/m^3) of any DE polymer. Fig. 2 illustrates a simple, easily fabricated DE made from a prestrained, partially electroded VHB membrane at rest (Fig. 2 left), and activated with an electric field of 252V/µm (Fig. 2 right). The electroded area expands by 125% at this field.

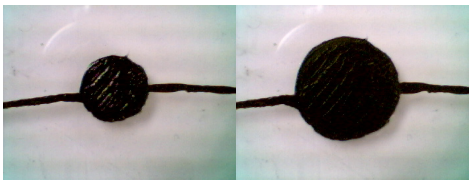

Figure 2: A VHB DE actuator at rest (left), and actuated with an electric field of 252V/µm (right).

While silicone and VHB4905 are popular choices for DE materials, a wide variety of other materials can be used and which is appropriate is highly dependent on the application. It is convenient therefore to define a relationship between the key properties of a material that results in an index value that can then be used to compare materials. The DE "Figure of Merit" relates a material's dielectric constant (ε_r), the breakdown strength (E_b), and the Young's modulus (Y), using the following formula (Sommer-Larsen and Larsen, 2004):

$$Figure\ of\ Merit. = 3\varepsilon_r E_b^2/Y \quad (4)$$

It is important to note that typical polymers with suitably low stiffness and high dielectric breakdown strengths have low dielectric constants (typically <5). Substituting this value into Equation (1) it is clear that high electric fields (~50-150V/µm) are required to generate enough pressure to deform a DE more than a few percent.

3 DIELECTRIC ELASTOMERS IN BIODEVICES

DEs acting either in an actuator, sensor, or power generator mode show great promise for a number of biomedical applications. The key strength of DE technology however is the ability for a single lightweight device to operate in multiple modes., thereby reducing device volume, complexity, and component count. This ability, coupled with their biocompatibility, opens up a number of possibilities not only for implantable or prosthetic devices, but also for tools to assist both surgeons and patients during operative and post-operative procedures.

3.1 Artificial Muscles

With performance metrics that exceed that of natural muscle, DEs show great promise as artificial muscles. Like natural muscle, DEs can be controlled in terms of position, speed and stiffness. Controlling the charge stored on a DE results in stable position control. By controlling the rate of charging the speed of actuation can be controlled. Similarly, utilising the geometry of the device and the level of charge stored on the DE, it is possible to determine the electroactive forces, which in conjunction with knowledge of the mechanical behaviour of the DE itself, can be used to control stiffness.

To achieve accurate control in terms of any these parameters it is necessary to obtain feedback data from which a physical aspect of the device can be inferred. Conventionally an external sensor is required to obtain this data but applying such an approach to DEs adds to the complexity, volume, mass, cost and power requirements of the device. Instead, self-sensing using inherent characteristics of the DE eliminates the constraints an external sensor implies and enables the creation of entirely compliant smart devices. Such devices, with an overall texture and consistency comparable to natural muscle, will have a natural look and feel; a factor that has been found to have a significant impact on patient acceptance of such devices (Popovic et al., 2002).

DE device properties such as electrode resistance (O'Brien et al., 2007), capacitance (Toth and Goldenberg, 2002), and electrical current (Bauer and Paajanen, 2006) have all been used to infer the physical state of a DE actuator subject to specific operating conditions. As self-sensing develops further and the richness of the feedback information increases, so too will the accuracy with which DE devices can be made to respond to a control signal.

In the case of artificial muscles this control signal should be derived from human nerve signals, and already basic proportional control of a DE device has been achieved with the magnitude of a variety of electrophysiological signals as the input signal (Carpi et al., 2006). Further development of not only artificial muscles but also of the human-device interface, including enabling bi-directional information flow between artificial muscle and human, could eventually lead to a true artificial muscle capable of being fully integrated into the human body.

3.2 Bio-sensors

Self-sensing and the ability of a DE device to convert mechanical energy into electrical energy enable DEs to be used in the monitoring of various biological functions. As discussed previously, various electrical characteristics of a DE will change when the DE is deformed from its rest state. These characteristic features have been used to demonstrate simple, highly compliant, low voltage strain and pressure sensors (Kornbluh, 2004).

The highly tuneable nature of the mechanical impedance and elongation of DE sensors can be exploited to enable strains of several hundred percent to be monitored without adding significant mechanical resistance to the movement itself. This would make them suitable for devices that monitor activities such as respiration, muscle movement, or limb articulation. For monitoring muscle movement in particular, feedback data from lightweight conformable sensors synchronised with relevant electrophysiological signals could be used to analyse the dynamic stress-strain-time behaviour of muscles. Biocompatible DE sensors could also potentially be used to monitor stresses/strains in vivo, whether this is in conjunction with another implanted device or simply to generate data that a sensor external to the body would be incapable of providing.

3.3 Surgical Tools

Compliant smart devices offer an ideal solution for procedures where “soft” manipulation is appropriate. In invasive surgeries such as endoscopic procedures, DE devices could fulfil multiple roles: they could operate as a multiple-degree-of-freedom actuator for directing/propelling sensory devices or fibre-optic cables whilst also providing a compliant interface between the patient and the device that serves to protect both.

Lightweight accurate sensors and actuators could be incorporated into portable glove-type devices with built in force feedback for surgical training or performing remote surgery. Already a prototype device has been devised that has been used to provide force feedback for a virtual reality simulation of grasping an object (Fig. 3)(Zhang et al., 2006). Low device mass and volume would ensure the device is portable and able to be used for extended periods without user fatigue.

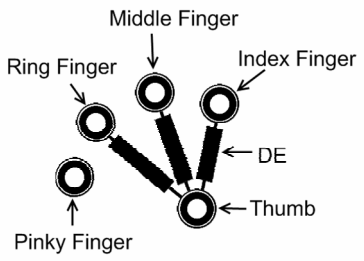

Figure 3: Lightweight compliant actuators for virtual reality feedback of grasping related hand gestures.

Furthermore, a smart device with the dexterity and flexibility of a human hand could be used as the manipulator in remote surgical operations. With feedback from pressure sensors embedded in the manipulator used as a control input for a DE force feedback device a complete DE solution could be created. An inherently muscle like actuator combined with realistic haptic feedback would result in an apparatus with an intuitive feel that could offer advantages in terms of flexibility and patient safety in comparison to heavy and rigid surgical robots driven by electromagnetics or hydraulics.

Other features of DE actuators such as their low current requirements and non-magnetic nature also provide advantages with regard to surgical tools. A prototype serpentine, DE based manipulator for needle positioning in close proximity to an MRI machine has been developed (Fig. 4)(Plante, 2006). Similar devices incorporating ferromagnetic materials or that use high currents would degrade the quality of the MRI scan.

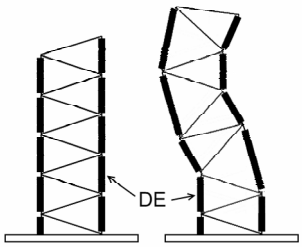

Figure 4: A conceptual design for a serpentine needle positioning device.

In the longer term there is the possibility of using nanoscale DE actuators in biology to stimulate the growth, migration and differentiation of stem cells. Mechanically deforming these cells can expose or activate different functional sites on their proteins, thereby affecting the biochemical reactions and intracellular pathways that ultimately regulate cell development (Vogel, 2006). Such a process may even create new opportunities for the treatment of diseases associated with mechanical cell dysfunction such as cancer, cardiac hypertrophy, genetic malformation, and immune disorders.

3.4 Power Generators

DEs are capable of operating as highly efficient generators. With appropriate driving circuitry DEs can be used to harvest energy from vibrations and motions inherently present in the environment. Already a heel-strike generator embedded in the heel of a boot (Fig. 5), is capable of generating up to 1W by using the downwards pressure of each footfall to stretch a DE membrane (Kornbluh, 2004).

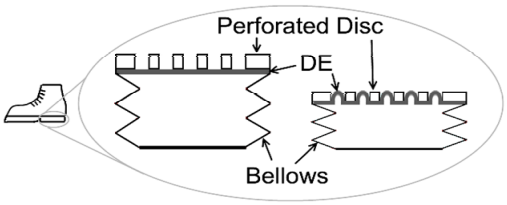

Figure 5: Heel strike generator capable of generating up to 1W.

The implication for biodevices is that lightweight power generators could be used to trickle charge or perhaps even directly power other low power devices on or within the body. A DE based prosthetic device subjected to intermittent usage patterns could make use of a DE generator combined with an energy storage device such that it would need recharging less frequently, if at all. Alternatively the energy storage device (e.g. battery pack) could be downsized.

The conformable and compact nature of DE generators means initially they could be strategically integrated into fabrics so as to take advantage of naturally occurring stretching as a result of human ambulation. In the future these generators may eventually be able to be implanted within the body itself, enabling a completely encapsulated, low maintenance power supply. Such a generator could be used to power wireless implantable sensors.

4 FUTURE DIRECTIONS FOR DIELECTRIC ELASTOMERS

As a smart material, a single DE element offers a multi-functional platform from which devices suited to a variety of applications can be developed. There are a number of hurdles yet to be overcome however and at the Biomimetics Laboratory we are actively investigating key issues that are currently limiting the practical implementation of DEs in biodevices.

DEs exhibit complex non-linear and hysteretic behaviours in both the mechanical and electrical domains that make modelling and precision control of these devices difficult. Current models can accurately predict behaviours based on specific parameters (e.g. the instantaneous uniaxial stress-strain response of a material subjected to a constant strain rate deformation), but have such a narrow scope that their accuracy degrades significantly if one or more of the parameters change (e.g. strain rate, mode of deformation, external loads, temperature). The ability to accurately describe the transient response of a DE device is especially limited. Improved modelling, particularly with respect to the electrical subsystem will greatly facilitate the development of more robust devices.

Improved modelling and self-sensing techniques will result in an increased understanding of the behaviour of a DE system that will greatly facilitate optimisation in terms of control, feedback, and device efficiency. In artificial muscles especially, owing to the desirability of ultra-thin dielectrics, devices will consist of large arrays of micro/nanoscale DE actuators in order to amplify force and displacement. It will be of critical importance therefore to develop a balance between the volume of feedback information and the control methodology such that the computational requirements are not prohibitively high.

The use of high electric fields (~50-150V/μm) in DEs also presents an issue given that current prototype membrane thicknesses typically range from 10μm to 50μm. While this is primarily a limitation of current fabrication techniques it nevertheless necessitates operating voltages in the kilovolt range. The impact of these high electric fields in proximity to the human body, including the efficacy of a soft polymer insulative layer encapsulating the device is being investigated.

ACKNOWLEDGEMENTS

Work at the Biomimetics Laboratory is partly funded by the University of Auckland's VCUDF.

REFERENCES

Bar-Cohen, Y., Ed. (2004). *Electroactive Polymer (EAP) Actuators as Artificial Muscles: Reality, Potential, and Challenges*. Bellingham, WA, SPIE Press.

Bauer, S. and M. Paajanen (2006). Electromechanical characterization and measurement protocol for dielectric elastomer actuators. *Proceedings of SPIE - The International Society for Optical Engineering*, 6168.

Carpi, F., S. Raspopovic, et al. (2006). Activation of dielectric elastomer actuators by means of human electrophysiological signals. *Proceedings of SPIE - The International Society for Optical Engineering*, 6168.

Hunter, I. W. and S. Lafontaine (1992). Comparison of muscle with artificial actuators. *Technical Digest-IEEE Solid-State Sensor and Actuator Workshop*.

Kofod, G. (2001). *Dielectric Elastomer Actuators*. Department of Chemistry, Riso - The Technical University of Denmark. PhD.

Kornbluh, R. (2004). "Dielectric elastomer artificial muscle for actuation, sensing, generation, and intelligent structures." *Materials Technology* 19(4): 216-224.

Kornbluh, R. D., R. Pelrine, et al. (2004). Electroactive polymers: an emerging technology for MEMS. *MEMS/MOEMS Components and Their Applications*, 5344, San Jose, CA, USA, SPIE.

Madden, J. D. W., N. A. Vandesteeg, et al. (2004). "Artificial muscle technology: Physical principles and naval prospects." *IEEE Journal of Oceanic Engineering* 29(3): 706-728.

O'Brien, B., J. Thode, et al. (2007). Integrated extension sensor based on resistance and voltage measurement for a dielectric elastomer. *Electroactive Polymer Actuators and Devices (EAPAD) 2007*, 6524, San Diego, California, USA, SPIE.

Plante, J. S. (2006). *Dielectric Elastomers for Binary Robotics and Mechatronics*. Department of Mechanical Engineering. Cambridge, Massachussetts Institute of Technology. PhD: 80.

Popovic, M. R., D. B. Popovic, et al. (2002). "Neuroprostheses for grasping." *Neurological Research* 24(5): 443-452.

Sommer-Larsen, P. and A. L. Larsen (2004). Materials for dielectric elastomer actuators. *Smart Structures and Materials 2004: Electroactive Polymer Actuators and Devices (EAPAD)*, 5385, San Diego, CA, USA, SPIE.

Toth, L. A. and A. A. Goldenberg (2002). Control system design for a dielectric elastomer actuator: The sensory subsystem. *Proceedings of SPIE - The International Society for Optical Engineering*, 4695.

Vogel, V. (2006). "Mechanotransduction involving multimodular proteins: Converting force into biochemical signals." *Annual Review of Biophysics and Biomolecular Structure* 35: 459-488.

Zhang, R., P. Lochmatter, et al. (2006). Spring roll dielectric elastomer actuators for a portable force feedback glove. *Smart Structures and Materials 2006: Electroactive Polymer Actuators and Devices (EAPAD)*, 6168, San Diego, CA, USA, SPIE.

PUNCTURE DEPTH AND THE MECHANICAL STABILITY OF MICRONEEDLES

D. C. C. Lam, Y. H. Lee, K. T. Shek
Department of Mechanical Engineering, The Hong Kong University of Science and Technology
Clear Water Bay, Kowloon, Hong Kong SAR China
David.lam@ust.hk

G. Pang
Department of Electrical and Electronic Engineering, The University of Hong Kong
Pokfulam, Hong Kong SAR China

Keywords: Drug delivery, microneedles, mechanical behaviour, punctures, silicone rubber.

Abstract: Microneedles penetrating less than 1mm beneath the skin can deliver the drugs directly without piercing blood vessels or damaging nerves. The mechanical stability and the puncture behaviour were investigated experimentally by inserting steel needles into silicone rubber and pig skin. Puncture tests revealed that the length of needle buried in the flesh is less than 50% of the nominal insertion depth when the insertion depth is less 1mm. The mechanical stability of the buried needle-flesh assembly, characterized by the force needed to retract the needle, decreased with buried depth and needle diameter. Analysis of the load data suggested that a 100-micron diameter microneedle buried 100 microns deep in pig skin would have a retraction force of 0.1mN, which is only 1% of the retraction force of a conventional needle inserted 5mm into the skin. This suggests that the usage of microneedles in arrays is necessary to increase stability and to enable stable drug delivery.

1 DRUG INJECTION

Drug delivery in hospitals involves modalities as diverse as hypodermal injection, intravenous delivery and oral intake. Drugs taken orally must pass through the digestive system and deal with the first-pass effect of the liver. Numerous drugs, particularly those developed in genetics laboratories, are chemically incompatible with the oral intake route (Orive et al., 2004) They must be directly injected into the body. Hypodermal injection involves training, some pain and potential blood loss, making self-injection at home unwelcome for patients.

Other than direct injection, drugs can be delivered via absorption through the skin. The skin is a natural barrier to foreign chemicals and biological agents. A few drugs such as nicotine and its substitutes have been customized for absorption by the skin. Chemical customization of individual drugs for such absorption is technically challenging, and in many cases, economically unfeasible. Instead of traversing the skin via absorption, solid or hollow microneedles can be used to physically puncture the skin. Drugs can pass through a capillary-scale channel in the hollow needle, or can be delivered as a soluble coating on the needle surface. For such.

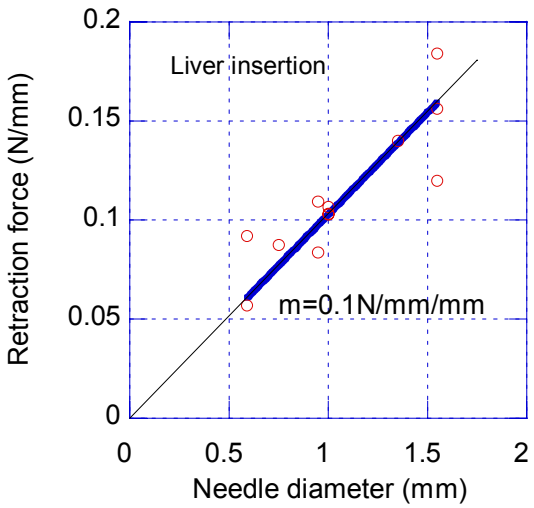

Figure 1: Retraction load for needles with conical and beveled tips. Data from (Okamura).

applications, the microneedles must be long enough to bridge the surface skin layer, but short enough to avoid piercing the blood vessels and nerves that are typically 0.5 – 1mm under the skin surface

There is now a large body of knowledge, processes and tools that have been developed for the design and fabrication of micro- and nanoelectromechanical systems (MEMS and NEMS). A number of researchers have developed silicon microneedles using MEMS processes. (Stoeber & Liepmann, 2005; Staples et al., 2006; Ji, et al., 2006). Silicon microneedle arrays have been fabricated successfully and tested in trials with rats (Nordquist et al., 2007). These tests were concept demonstrations showing that drugs can be delivered using microneedles. However, a variety of issues, including safety concerns about the use of brittle silicon microneedles, remains to be solved. Titanium and polymers are potentially better material choices, and the fabrications of titanium and polymeric microneedles (Parker et al., 2007; Park, Allen & Prausnitz, 2006) has been investigated using MEMS-based processes.

As another alternative to MEMS-based technologies, lasers have been used to create arrays of holes in substrates (Davis et al., 2005). Microneedle pads have been created by plating a metal shell onto the holed surface. The microneedles in arrays fabricated in this fashion are hundreds of microns long, with walls limited to several microns thick because of plating limits. Silicon or metal microneedles fabricated in this way are inherently small because the processes are inherently micron and submicron processes. Recognizing the inherent process limits, microinjection molding suited for fabricating millimeter-scale parts has been used to make polymer microneedles (Sammoura et al., 2007).

Conventional hypodermic needles are typically more than a few millimetres long with diameters typically ranging from 220 microns on up. Such needles are designed to puncture skin and deliver drugs deep underneath the skin. They are not designed for drug delivery at insertion depths of 1mm or less. Limited studies had been conducted to examine systematically the puncture behaviour of such large needles at deep and shallow depths. Long needle puncture studies were conducted by Nguyen & Vu-Khanh on rubber sheets (Nguyen & Vu-Khanh,, 2004) and by Sherwood's group (Sherwood & Fleck, 2004) on solid rubber. They observed significant indentation deformation occurred before puncture in these tests.

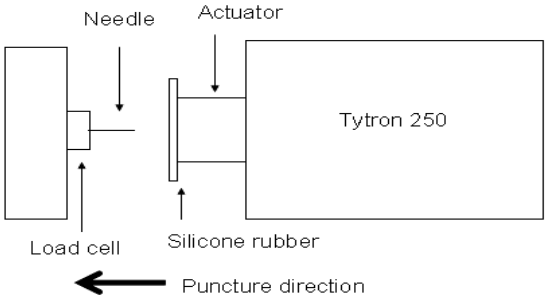

Figure 2: Mechanical testing setup.

For microneedles, where penetration is less than 1mm into the skin, indentation is expected to be significant and to affect drug delivery. The effect of needle diameter had been examined in a study of needle insertion into the liver (Okamura, 2004). The study revealed that the force required to retract the needle was strongly dependent on the needle diameter and the insertion depth (Figure 1). Small microneedles inserted into the surface of the skin should have retraction forces in the mN range and each individual puncture may have low mechanical stability. The effect of depth and needle diameter on the insertion and retraction behaviour were examined this study.

2 INVESTIGATIVE APPROACH

The puncture behaviour of single steel needles pressed to depths of 0.2 to 8mm was examined in this study. Following the methods pioneered by (Sherwood & Fleck, 2004), microstructurally uniform and homogeneous silicone rubber was used

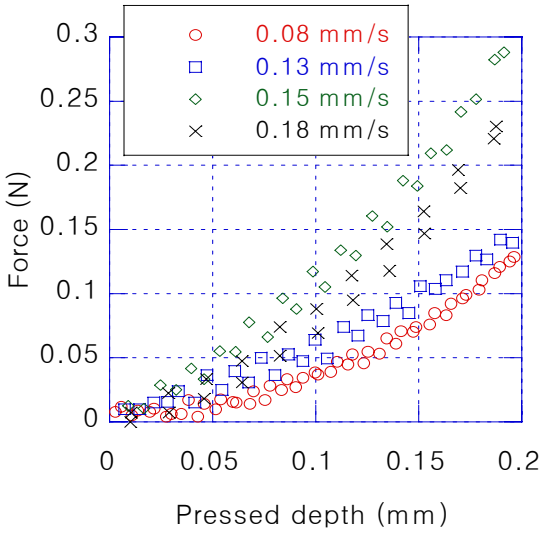

Figure 3: 130-micron needle insertion behaviour in silicone rubber at 0.2mm pressed depth.

as a reference puncture material to examine the puncture behaviour. The puncture behaviour of pig skin was also examined to determine the load and depth range of puncture behaviour in biological materials.

The puncture experiments were conducted on a Tytron 250 press from MTS Systems Corporation equipped with a linear drive actuator. Silicone rubber blocks were cast from a Shin-Etsu silicone premix and cured according to the manufacturer's specifications. Medical grade stainless steel needles 130, 220 or 300 microns in diameter were mounted on a custom designed jig for puncture testing (Figure 2). Once mounted, the loads and positions were calibrated. The needle was held fixed while the silicone rubber casting was moved toward the needle

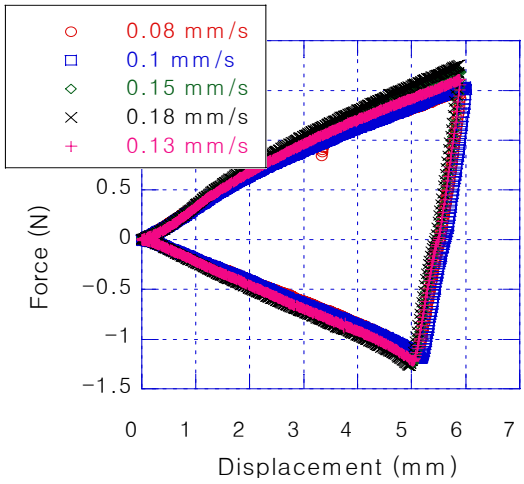

Figure 4: 130-micron needle insertion behaviour in silicone rubber at 6mm maximum pressed depth.

at displacement rates of 0.1 mm/s, 0.13 mm/s, 0.15 mm/s or 0.18 mm/s to a target maximum pressed depth (MPD), and then reversed at the same rate. The experiment ended when the displacement reached zero. The experiment was repeated for a range of MPDs from 0.2 mm to 8 mm.

3 RESULTS AND ANALYSES

3.1 Shallow Insertion Depths

The load-displacement results at 0.2mm MPD are shown in Figure 3. The curves indicate that the peak load was displacement rate dependent. At each displacement rate, the unload curve collapsed onto the load curve. This indicates that the deformation recovered elastically without puncture. The absence of a hysteresis between the load and unload curves indicates that no energy was dissipated at 0.2mm MPD. In addition, the higher peak loads at higher

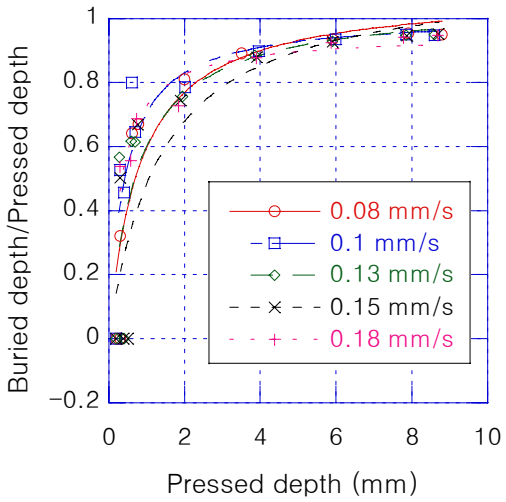

Figure 5: Ratio of buried to pressed depth for needle insertion into silicone rubber using 130-micron needles.

displacement rates did not result in puncture. This suggests that needles less than 0.2mm long have difficulty in puncturing soft silicone rubber.

3.2 Puncture Depth

The results at 6mm MPD are plotted in Figure 4. As with the tests in Figure 3, the displacement was reversed from loading to unloading in each trial upon reaching the 6mm maximum set displacement. The unloading curves did not retrace the loading

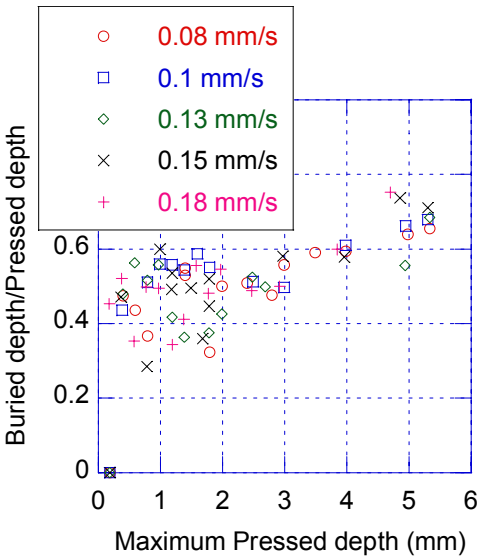

Figure 6: Ratio of buried to pressed depth for needle insertion in pig skin using 130-micron needles.

curves, but rather intersected the zero load line to the right of the triangle, crossing into the tension region. Unlike the penetration behaviour at 0.2mm MPD, where the needle was fully withdrawn at zero load, the needle retracting from 6mm MPD remained buried in the rubber. This zero load depth on retraction was taken to represent the buried depth on insertion. A plot of the buried needle depth normalized by the MPD is plotted in Figure 5. At large MPDs, the ratio approached unity, but at MPDs less than 1mm, the ratio was significantly less than one. The low ratios at settings below 1mm indicate that an increasingly significant proportion of the needle was left outside the solid during the loading phase.

The MPD for needle insertion into pig skin is plotted in Figure 6. Biological materials are less uniform and the ratio is more scattered. Despite this, the trend is similar to that observed with the silicone rubber in that the ratio approaches unity at large pressed depth, but is 0.5 or less when the pressed depth was 2mm or less.

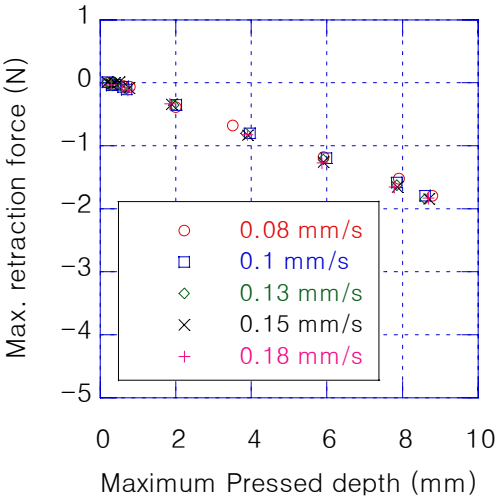

Figure 7: Maximum retraction force for 130-micron needle insertion into silicone rubber.

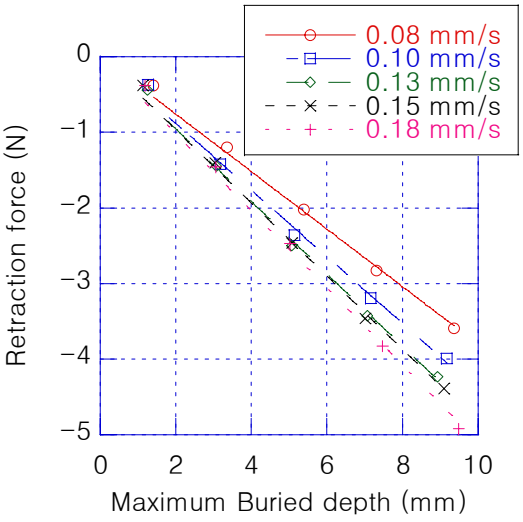

Figure 8: Maximum retraction force for a 300-micron needle inserted into silicone rubber.

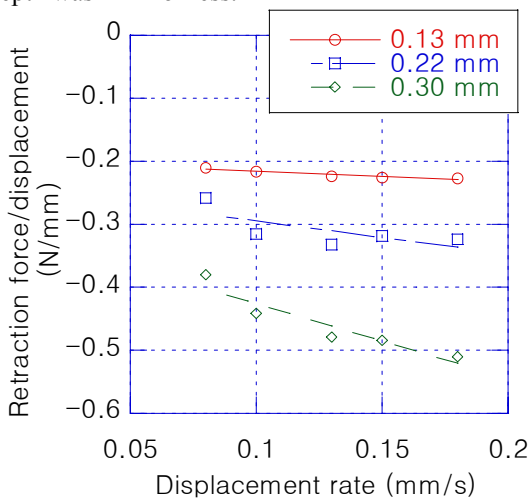

Figure 9: Rate dependence of retraction force per unit of buried needle length for needle insertion into silicone rubber.

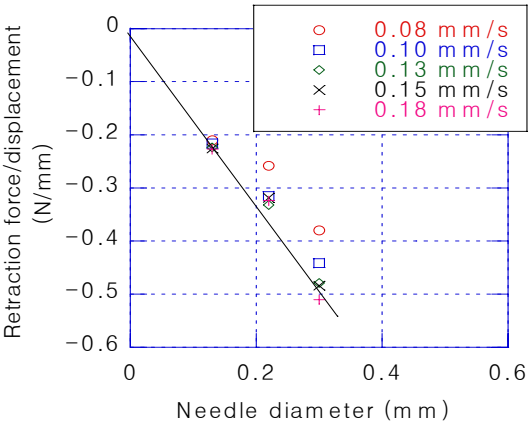

Figure 10: Diameter dependence of retraction force per unit of buried depth in silicone rubber.

3.3 Retraction Force

The maximum retraction load (MRL; bottom right apex in Figure 3) required to pull a 130-micron needle out after pressing is shown in Figure 7. The data show that the retraction forces at different displacement rates collapsed onto a single line for the 130 micron-needle. The MRL for the 300-micron needle is plotted in Figure 8. The MRL for this larger needle was clearly displacement

dependent. The MRL was markedly higher at higher retraction rates. Thus, while the 130-micron needle's rate dependence appeared negligible, this was not the case with larger diameter needles. The rate of change of the MRL with buried depth as a function of the displacement rate is plotted in Figure 9. The plot shows that the rate dependence was linear for all the needles tested, and that the MRL decreased with decreasing needle diameter. The influence of needle diameter is plotted in Figure 10. The MRL was greatest at high displacement rates. Fitting a straight line through the data with the highest displacement gives a slope of -1.6N/mm/mm, which is the MRL per unit of buried depth and needle diameter. Using this as a basis for estimate, in Figure 11 a line is plotted and compared with the retraction loads observed with a 130-micron needle at depths less than 1000 microns. The comparison showed reasonable agreement between the data and the prediction.

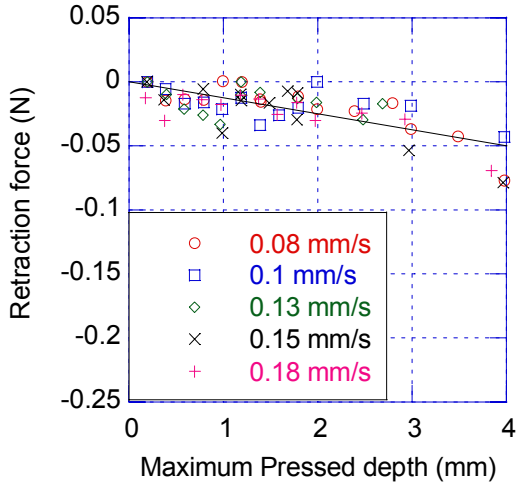

Figure 11: Comparison of maximum retraction force with model (line) at shallow pressed depth.

The MRL for insertion into pig skin is plotted in Figure 12. As expected, the magnitude of the MRL increased with the actual buried depth, but the displacement rate dependence cannot be delineated given the greater scatter. The rate of change of the MRL per unit of buried depth and needle diameter was approximately 0.1N/mm/mm.

4 DISCUSSION

The length of the needle buried in the flesh during hypodermal insertion is generally assumed to equal to the pressed depth. This assumption is reasonable for deep insertions, but breaks down when the needle is less than 2000 microns long. At pressed depths under 1000 microns, less than half of the needle maybe buried; and no penetration was observed at pressed depths less than 200 microns. Since the lengths of microneedles fabricated using MEMS processes are limited by the thickness of the wafer, which is typically less than 300 microns thick. Silicon microneedles less than 300 microns long may have difficulty in puncturing the skin. If punctured, the maximum buried depth will likely be less than 100 microns.

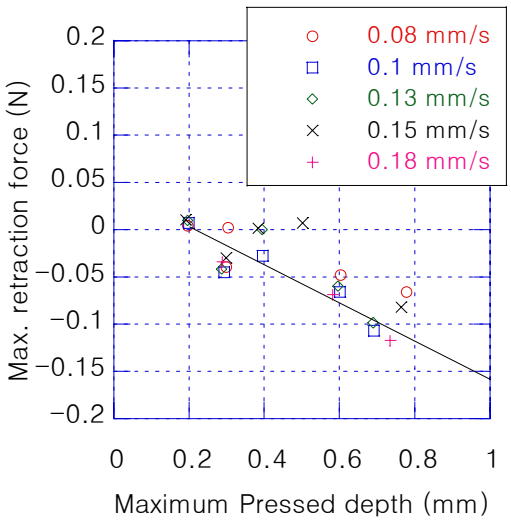

Figure 12: Retraction force for 130-micron insertion in pig skin.

Another issue is the mechanical stability of the microneedles. When punctured, the surrounding material in the puncture will exert traction onto the buried needle and prevents it from slipping out of the puncture hole. The retraction force was found to decrease at a rate of -1.6N/mm of buried depth/mm of needle diameter for silicone rubber, and -0.1N/mm/mm for pig skin (Figure 12). In comparison, the corresponding value for the case of needle puncture into liver is -0.1N/mm/mm. Using this as an estimate for biological materials, a 0.1mm microneedle buried 0.1mm into the skin would have a retraction force of 1mN. A conventional 0.22mm needle inserted into flesh 5mm would have a retraction force of 110mN, which is 100 times greater. If an array of 110 microneedles were used, the retraction force can be increased to 100mN such that the microneedles can remain stably buried to allow stable drug delivery. The puncture behavior and the design guidelines for stably drug delivery are reported in another paper.

5 CONCLUSIONS

Examination of the puncture behaviour needles with a silicone rubber model indicated that indentation effects are significant at shallow insertion depths for both silicone rubber and pig skin. Less than 50% of the needle may be buried because of indentation when short microneedles are used. The investigation also revealed that the retraction force providing mechanical stability to the needle in the skin was linearly proportional to the buried depth and the needle diameter. Short microneedles with small diameters will have low retraction forces and poor mechanical resistance against being dislodged.

ACKNOWLEDGEMENTS

This work was supported by grants from Hong Kong's Research Grants Council. The authors also acknowledge the use of equipment provided by the Advanced Engineering Materials facility at the HKUST.

REFERENCES

Orive, G., Gascon, A.R., Hernandez, R.M., Dominguez-Gil, A., Pedraz, J.L., 2004. *Techniques: New approaches to the delivery of biopharmaceuticals,* Pharma. Sci., Vol 25 No. 7 pp. 382-7.

Stoeber, B., Liepmann, D., 2005. *Arrays of hollow out-of plane microneedles for drug delivery*, J. MEMS Vol 14 No. 3 pp. 474-9.

Staples, M., Daniel, K., Cima, M.J., Langer, R., 2006. *Application of micro- and nano-electromechanical devices to drug delivery,* Pharma Res. Vol 23 No. 5 pp. 847-63.

Ji, J., Tay, F.E.H., Miao, J., Iliescu, C., 2006. *Microfabricated microneedle with porous tip for drug delivery,* J. Micromech. Microeng. Vol 16 pp. 958-964.

Nordquist, L., Roxhed, N., Griss, P., Stemme, G., 2007. *Novel microneedle patches for active insulin delivery are efficient in maintaining glycaemic control: An initial comparison with subcutaneous administration,* Phama. Res. (in print).

Parker, E.R., Rao, M.P., Turner, K.L., Meinhart, C. D., MacDonald, N.C., 2007. *Bulk micromachined titanium microneedles,* J. MEMS Vol 16 No. 2 pp. 289-95.

Park, J., Allen, M.G., Prausnitz, M.R., 2006. *Polymer microneedles for controlled-released drug delivery,* Pharma. Res. Vol 23 No. 5 pp. 1008-19.

Davis, S. P., Wijaya, M., Allen, M. G., Prausnitz, M. R., 2005. *Hollow metal microneedles for insulin delivery to diabetic rats,* IEEE Trans. Biomed. Eng. Vol 52 No.5 pp. 909-15.

Sammoura, F., Kang, J.J., Heo, Y., Jung, T.S., Lin, L., 2007. *Polymeric microneedle fabrication using a microinjection molding technique,* Microsys. Tech.. vol 13 Issue 5 pp. 517-22.

Nguyen, C.T., Vu-Khanh, T., 2004. *Mechanics and mechanisms of puncture of elastomer membranes,* J. Mater. Sci. Vol 39 No.4 pp. 7361-4.

Sherwood O.A., Fleck, N.A., 2004. *Mechanisms of deep penetration of soft solids with application to the injection and wounding of skin,* Proc. R. Soc. Lon. A vol. 460 pp. 3037-68.

Okamura, A. M., Simone, C., O'Leary, M. D., 2004. *Force Modeling for Needle Insertion Into Soft Tissue,*IEEE Trans. Biomed. Eng. Vol 51 No.10 pp. 1707-1716.

JUST PUSH PRINT

Biodevice Printing Using Bioinks, Electroinks and Quantum Dot Inks

Jan Lawrence Sumerel and Kai Sudau
FUJIFILM Dimatix, Inc.,2230 Martin Avenue, Santa Clara, California 95050-2704, U.S.A.
jsumerel@dimatix.com, ksudau@dimatix.com

Keywords: Ink jet, piezoelectric, biomaterials, microarray, bioink, electroink, quantum dot.

Abstract: Many advanced medical and environmental test devices require microscale patterning of cells, proteins, or other biological materials, and the need for these devices to contain active functional material components has increased dramatically. In addition, the biological material oftentimes requires an interface with an electrical or optical output signal. Efficient production methods are paramount to meeting market demands, and ink jet printing offers an easy, low cost alternative to materials deposition used in current biodevice manufacturing. However, fluid development and proper printing parameters at the research level are required for manufacturing processing and will be critical to process adoption. In this paper, operating parameters and fluid characterization have been developed through processing biomaterials, organic and inorganic conductive fluids and semiconductor nanoparticles. Because of the inherent versatility, uniformity and scalability of this system, established operating parameters coupled with proper fluid characterization will ultimately be translatable to production line systems of biodevice components.

1 INTRODUCTION

Biological monitoring devices and medical devices generally have two material components used in a stepwise fashion, a biological material that works as both a reaction beacon and the biochemical reactive site followed by an optical, piezoelectric or electronic material that amplifies the signal to allow a measurable readout of the reaction. Typically, manufacturing protocols are distinct for each component, but ink jet printing can be used for the deposition of both materials. Interfacing processing of these two components may be critical to biodevice success, and electronic file pattern formation allows component alignment. Ink jet printing is inherently compatible to high throughput (Antoniadis, 2007). Already, interesting technological phenomena have spawned from the patterning of structurally and functionally different materials including high performance ceramics Lewis, et al, 2006). For this reason, drop-on-demand ink jet printing, a simple fabrication process, has become a prominent player in materials processing for biodevice components (Padinger, 2007). However, it is a big step for biodevice developers to jump into robust in-line manufacturing production systems. This type of equipment requires a sizable financial investment plus sufficient experience so that manufacturing specifications and in-house knowledge can be established. Thus, a low cost, easy-to-use laboratory scale system is required for preliminary experimentation. This strategy then allows substrate evaluation, on-site development, and fluid manufacturing to all occur simultaneously. This need has been addressed with an R&D tool that offers printhead maintenance, substrate alignment, nozzle inspection and drop analysis, and ease-of-use (Sumerel et al, 2006).

Just push print, the most common command for the desktop printer, can now be used in the laboratory or in manufacturing lines. Ink jet printing is a simple and cost effective technique with applications in the fields of electronics and biomedicine and has been shown to have specific applications in these industries (Sirringhaus et al., 2000, Calvert, 2001, Haber et al., 2005). In contrast to other multi-step production methods, ink jet printing is an additive process that precisely deposits metered quantities of fluid onto a variety of substrates including glass, silicon, plastics, organic thinfilms, and metals based on a user generated pattern. The resolution of the printed pattern is determined by a number of factors, including

substrate/fluid contact angle, nozzle size, and lateral resolution of the printhead (Song and Nur, 2004). Ink jet printers can dispense fluid drops with volumes in the picoliter (ρL) to microliter (μL) range, and an integral step in bringing this processing technique from the laboratory to manufacturing systems is the development of jettable fluids. The chemical properties of the fluid, including density, surface tension and viscosity, determine its jettability (Sumerel, et al., 2006). During drop formation, energy is distributed between the fluid's viscous flow, surface tension, and kinetic energy (Xu et al., 2005). The deposited fluid volume is directly proportional to nozzle size. This flexibility enables microscopic patterned thinfilms of functional materials at a variety of resolutions. The physical properties of the patterned thinfilms (film thickness and pixel values) are dependent on the fluids coupled with the drive electronics of the printing device. In general, 2D drawings, pictures or structures, formatted as a bitmap image, can be translated into X and Y print coordinates for materials deposition (drop-on-demand). Each individual nozzle ejects a drop with a ligament. The ligament and the drop coalesce during flight to make a volumetric sphere and upon contact with the substrate, the sphere alters its three dimensional structure to become columnar. The resulting printed image is a compilation of drops where the third dimension is equal to film thickness, a physical property that is dependent on particle loading, drop spacing and drop spread. Once this critical but iterative R&D phase of process and material evaluation is complete to allow sustainable ink jet printing, the fluids are scalable for production use.

1.1 Ink Jet Printing Employing MEMS Devices

The required heating process for thermal ink jet printing (300°C) will damage thermally-sensitive materials, thereby limiting their use in devising functional devices (Calvert, 2001, Xu et al., 2005). In contrast, using piezoelectric ink jet printing, thermally sensitive materials are deposited under ambient conditions. Piezoelectric printheads contain a lead zirconate titanate (PZT) piezoelectric ceramic, nozzles, and a fluid chamber. When a voltage is applied to the PZT, mechanical vibrations create acoustic waves that in turn force fluid out of the chamber through the nozzles (Brünahl and Grish, 2002). Piezoelectric printheads are categorized based on the deformation mode of the PZT (e.g., squeeze mode, bend mode, push mode, or shear mode) (Myatt et al., 2006). MEMS fabrication has increased the precision and resolution of the deposited materials (Menzel, C., 2005). These silicon devices increase jet-to-jet uniformity and drop placement accuracy. The inertness of the silicon expands the operating ranges to allow higher chemical diversity and fluid throughput expanding piezoelectric ink jet printing from the ability to print graphic inks to the realm of printing functional fluids required for biodevice manufacturing.

The ink jet printhead is powered by a piezoelectric unimorph, which is constructed in the plane of the wafer and consists of patterned PZT bonded to a silicon diaphragm (Brünahl and Grish, 2002). The effective diameter of the nozzle is 21.5 mm; this nozzle size is approximated to generate 10 ρL drops. An important operating parameter of this particular device is the negligible void volume due to the direct fluid/printhead interface.

Fluid flow properties like low viscosities, low boiling points, high surface tensions and non-Newtonian behaviors are hallmarks of functional materials and are also generally unfavorable chemical characteristics for ink jet printing. Manipulating the parameters that generate the electronic signal to drive the movement of the PZT, including its frequency, wave shape, wave duration and voltage has provided a significant advancement in printing an array of functional materials and has been one of the areas of our research. The ability to adjust the jetting parameters has been critical to the success of printing bioinks and electroinks.

1.2 Functional Fluid Deposition

Thermal ink jet printing has been employed for the deposition of biomaterials (Xu et al, 2005, Setti et al., 2005). A glucose biosensor was fabricated by thermal ink jet printing, and the enzyme, glucose oxidase was made into a biological ink using phosphate buffer and 10% glycerol (Setti et al., 2005). In contrast to piezoelectric ink jet printing where there are requirements for viscosity (8-14 centipoise (cps)) and surface tension (28-32 $dynescm^{-1}$), most biological materials exhibit very low viscosities (1 cps) and very high surface tension values (60 $dynescm^{-1}$). In addition, biological fluids generate steam at high temperatures just like inks in thermal ink jet printers. This heating process causes bubble formation and fluid output at the nozzle plate (Bae, et a., 2005). Major fabrication advances have been made using thermal ink jet printing (Lemmo et al., 1998) due to the low cost and wide availability,

and at first glance this method should simplify biomaterials deposition due to the looser requirements for fluid formulation. However, the thermal ink jet process may cause damage to thermally-sensitive materials used in biology and medicine. In contrast, piezoelectric ink jet printing is a thermally constant process and does not require heat thereby increasing the chances of biomaterial stability.

Rapid detection employing microarray methods are necessary to biomedical and chemical sciences (Diehl, F., 2002). Miniaturization and automation of arrays may lead to decreased costs and faster analysis times (Peck, 2007). As drop sizes decrease, feature sizes decrease and array densities increase. Many forensic samples obtained in the field have restricted amounts of recoverable material, and in some cases, two polymerase chain reactions are required to reach the levels of sensitivity and verification required in the amplified deoxyribonucleic acid (DNA) product (Vuorio et al., 1990). Since piezoelectric ink jet printing only requires 10 ρL per sample, the amount of DNA needed for a precise polymerase chain reaction assay is greatly reduced. For example, this technique may provide an important advance in studying the variation in a segment of mitochondrial DNA (a non-coding region between two transfer ribonucleic acid genes) (Salas et al., 2001). Variations in this section of the gene is one obvious choice for forensic identification because of sample number (Wilson et al., 1995), and the predominant isolated sample, human hair, shows low keratin protein variation between individuals (Rodriguez-Calvo et al., 1992). Unlike contact printing techniques (e.g., pin spotters) or expensive industrial ink jet printheads, the single-use ink jet printhead technology requires minimal deposition of fluids and minimal cross-contamination (Manning, H., 2007).

The need for continual reiterations of circuit design gestures for new approaches away from the reductive process of masking and etching to create metal patterns (Hwang, 2002) towards additive processing. There are also market drivers for organic electronic materials due to their adherence to substrates, flexibility, performance and the ability to process these materials at low temperatures (Shaw and Seidler, 2001). Ink jet printing provides the necessary technological platform to increase throughput and lower processing costs. Indeed, low capital costs, process simplicity, and flexibility have been the important attributes that make this technique practical for conductive trace patterning. Many conductive precursor fluids are being jetted using both thermal and piezoelectric ink jet printers (Sirringhaus et al., 2000, Sawhney et al., 2006, Teng and Vest, 1988; Volkman, et al., 2004). In fact, ink jet printing is considered one of the key technologies in defined polymer deposition (Sawhney, 2006). Polymer structural confirmation varies with temperature thus ambient processing conditions are required. At low temperatures, typically below the glass transition temperature (T_g), polymers maintain their natural, globular structure. At higher temperatures, above the T_g, they swell into open conformations, essentially breaking their entropically favorable π-π interactions (Baiesi et al., 2001). With the conformational collapse, the material becomes less conductive. In order to move towards feasible ink jet manufacturing processes for either conductive polymers or metallo-organic fluids, initiating formulation, printing and post-processing techniques are required. The fluids must maintain solvent monodispersity; once printed, they must properly adhere to the surface (Mei et al., 2005). These criteria are integral for successful printing, for even the smallest amount of discontinuity will make the material non-conductive and lower its mechanical strength.

Early attempts at ink jet printing silver metallo-organic fluids capitalized on its advantageous annealing temperature post-printing (200°C). The resultant silver conductive traces on a variety of materials including flexible substrates and substrates are left with a low thermal budget (Volkman et al., 2004). The direct writing of silver ink onto a grid pattern of solar cells has been previously done using a self-built printer and a Siemens ink jet printhead (Teng and Vest, 1988). They modified their printhead by machining restrictive nozzle plates that varied drop size. The printer was run between 100 and 200 Hz which resulted in a printing speed of a few cmsec-1. This single laboratory technique was a slow throughput process and required multiple printing cycles for effective deposition, so although it is not agreeable to manufacturing protocols, it was an important proof of concept step.

The choice of additional organic material in the starting fluid greatly influences the obtained conductivity (Mei et al., 2005). Once printed, the silver in the fluid must be annealed to convert the nanoparticles to a bulk silver thinfilm so that the resistance values can closely mimic bulk silver. The resulting amount of silver per volume of fluid is controlled by the annealing temperature cycle controls, and the effect of the organic decomposition into the gas phase during annealing determines the porosity of the printed material, which affects its

continuity (Mei et al., 2005). Additionally, the proper jetting parameters required for high performance printing is fundamental for reproducible deposition. The final feature size of the material on the substrate is determined by these parameters, and the overall conductivity is established according to the applied thermal processing (Mei et al., 2005).

2 MATERIALS AND METHODS

Proteins were dissolved in phosphate buffer saline solution (Fisher Scientific, Fair Lawn, NJ, USA) and 1.6 μM solution. 1 % of polysorbate 20 surfactant (Fisher Scientific, Fair Lawn, NJ, USA). 10 mg/mL of human genomic DNA was dissolved in 50% ethanediol.

Two percent (2%) glycerol (Sigma Aldrich, St. Louis, MO) was added to a poly (3,4-ethylenedioxythiophene) poly(styrenesulfonate) (PEDOT/PSS) aqueous dispersion (H.C. Stark, Goslar, Germany). ANP Silverjet nanopaste (Advanced Nanoproducts, Chungcheonguk-do, Korea) and Cabot Inkjet Silver Conductor (Ag-Ij-G-100-S1, Albuquerque, NM) were used as packaged. Fluids were sonicated in a water bath in a Branson 1510 sonicator at room temperature using highest sonic level for 30 minutes. Fluids were degassed for 2 hours at 5 mbar pressure in a degassing chamber.

Quantum dots were obtained from UT Dots (Savoy, IL, USA) and were serially diluted in 53% polypropylene glycol 400, 45% propylene carbonate solution containing 0.01% tetramethyl-5-decyne-4,6-diol, 2,4,7,9-propanol (Surfynol 104PA; Air Products, Allentown, PA).

Clean glass wafers were purchased from VWR (VWR Scientific, West Chester, PA). Both Kapton® (Dupont, Wilmington, DE) and Teslin® synthetic thinfilms (PPG Industries, Pittsburgh, PA) were kept clean after purchasing and cut into 8 x 11 inch sheets using laboratory scissors that had been cleaned with 70% ethanol (Sigma-Aldrich, St. Louis, MO). Single-side polished 150 mm silicon 100 wafers were obtained from Silicon Quest International (Santa Clara, CA) and sputtered with 300 nm gold layer using an Au target and a converted TES sputterer.

The DMP-2831 (FUJIFILM Dimatix, Santa Clara, CA) was used according to packaging instructions. Contact angle measurements were carried out using a VCA Optima XE (AST, Billerica, MA). 2 μL samples were manually pipetted for the measurements.

Scanning electron micrographs were obtained using a Philips XL30 ESEM. Resolution was obtained based on operating voltage of 5 kV.

Tapping mode AFM was conducted on a Digital Instruments Dimension 3100 using an etched silicon tip with a nominal radius of curvature of 10 - 20 nm. Scan sizes were varied, depending on the feature size. The scan rate was 0.1 - 0.3 Hz. The set point was set to 60 - 70% of the free-standing root mean square of the voltage of the oscillating tip.

Resistance measurements were obtained using a Fluke 110 True RM multimeter. Anode was put at one end of silver contact on glass wafer and cathode was placed on top of other end of silver contact. Electrodes were manually held during measurements.

3 DISCUSSION

Both DNA and proteins were ink jet printed after fluid formulation trials. Human genomic deoxyribonucleic acid was printed in 10 ρL of 50% ethanediol in the bottom of a 384 well assay plate or onto a silicon wafer in a 254 μm grid with high fidelity drop formation and uniform drop speed (Figure 1). The high surface tension of the DNA in water was mediated by the lower surface tension of the 1,2 ethanediol (47 dynescm-1) but the short ligaments in Figure 1 demonstrated how the surface tension of the fluid is still the predominant force in drop formation.

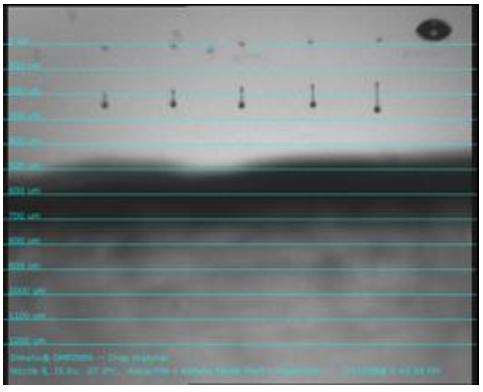

Figure 1: Deoxyribonucleic acid leaving the nozzle plate.

The only way to successfully print this fluid was by lowering the jetting frequency and extending the wave pulse from 11.52 μs to 14.1 μs. After successful printing, the samples were air-dried and tested for polymerase chain reaction amplification. A 750 base pair fragment was resolved on a 1.2%

agarose gel and visualized using ethidium bromide (data not shown). These successful results suggest that a significant cost savings may be obtained by using piezoelectric ink jet printing for the detection of clinically or environmentally relevant DNA species.

In general, globular proteins are stable in phosphate buffered saline with a small amount of non-denaturing detergent. We employed 1 % of polysorbate 20 surfactant, a detergent that is often used in protein purification due to its biochemical compatibility and protein stabilization (Sumerel et al., 2001). It has a second chemical attribute that it lowers the surface tension of the fluid. Bovine serum albumin was printed in 10 ρL drops, and then an α-BSA polyclonal antibody (Sigma Aldrich, St. Louis, MO) labelled with Cy3 was printed in random array over the protein drops. The protein array is shown where the antibody/antigen reaction is shown in green and protein alone is shown in blue (Figure 2).

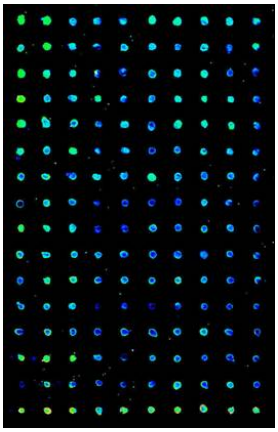

Figure 2: BSA protein incubated with a-BSA polyclonal antibody labelled with Cy3.

Due to appropriate fluid formulations required for ink jet printing, glycerol was added to the stock PEDOT/PSS solution to increase fluid viscosity. A waveform was employed for successful PEDOT/PSS printing (maximum jetting frequency of 1.0 kHz for a pulse width of 17.0 µs). This waveform is a critical parameter for jetting this particular fluid.

The applied voltage was tuned specifically for each nozzle to provide uniform jetting speed to ensure reproducible drop volumes. Images of the jetting fluid were captured by light micrographs using this camera and software system (Figure 3).
In panel A, the fluid is leaving the nozzle with the ligament still evident. In panel B, at 500 µm, the ligament has drawn into the drop, and the fluid is flying towards the substrate at 9.25 msec-1, ten times faster than the homebuilt printer discussed above (Teng and Vest, 1988). The resulting PEDOT/PSS on a silicon wafer pattern is shown (Figure 4). The PEDOT/PSS spreads on an untreated glass wafer with a contact angle of 18° (data not shown).

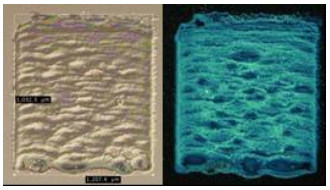

Figure 3: Light micrographs of fluid jetting from printhead nozzle and time of flights. A. Fluid leaving nozzle. B. Drop formation at 500 µm.

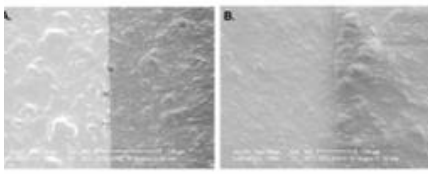

Figure 4: PEDOT/PSS printed on silicon wafer. A. Bright field. B. Dark field + UV.

Reliable printing procedures for two commercially available conductive silver precursors have been examined. Both fluids have ideal fluid flow properties for ink jet printing and have higher than 50% silver nanoparticle load. The viscosity and surface tension values of the ANP Silverjet nanopaste are 9 cps and 26.5 dynescm-1 respectively. This fluid jetted at a maximum frequency of 5.0 kHz with a pulse width of 13.2 µs.

Because of its high particle load (54%) and uniform particle size as demonstrated by transmission electron microscopy, low-temperature annealing produces a traceable conductivity in the printed material. Scanning electron micrographs were obtained of the annealed printed nanoparticles to compare the films produced (Figure 5).

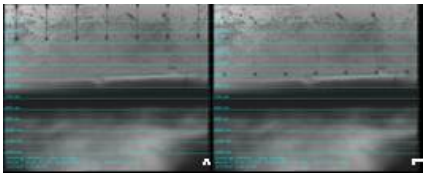

Figure 5: Electron micrographs of ANP silverjet nanopaste on Teslin®. Before annealing. B. After annealing.

Panel A shows the ANP Silverjet nanopaste on Teslin® before annealing (silver on left, Teslin® on right). With single-pass printing, the fluid makes a

uniform film on the Teslin® substrate in spite of the material's surface roughness (Panel A). Figure 5, panel B shows the same film on the same substrate after annealing for 1 hour at 200°C (annealed silver on left, Teslin® on right). Not only do the edges look slightly more uniform, but full coverage of the film on the substrate with single pass printing created a very thin silver full coverage film on the Teslin®. Because accurate feature measurements are difficult on flexible substrates, feature thickness was measured on gold-coated polished silicon nitride wafers (contact angle 41.8º, data not shown). We measured feature sizes using atomic force microscopy (AFM) with features printed at 20 mm drop spacing. Figure 6 shows the overall scan area of a single row of drops (Panel A).

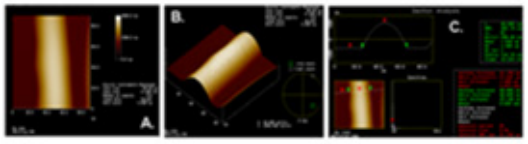

Figure 6: Atomic force microscope images of single row of ANP silver nanopaste drops. A. Overall scan area of a single row. B. 3D rendering C. Feature measurements.

The three-dimensional rendered view in Panel B shows the overall jetting uniformity. Panel C shows the calculated feature measurements. The width of the feature was 40.6 µm, and the film thickness of 1.59 µm demonstrates the utility of producing patterned thinfilms using ink jet printing technology. Because electrical performance is often described in terms of the bulk resistivity, resistance values were measured after annealing the silver nanoparticles. The resistance of the ANP Silverjet nanopaste is 1.1Ω, and the resistance of the Cabot Inkjet Silver Conductor is 0.3Ω (data not shown). The low resistance measurements in both cases were taken on equally-sized patterns on identical glass wafers. These values are in the same range as resistance values obtained by Sawhney and colleagues.

In order to achieve even finer features in manufacturing electronic applications, drop volumes below 10 ρL are required. Employing 1 ρL printheads, the reduced drop volume will produce 20 µm silver fluid features on Kapton® employing the ANP Silverjet nanopaste fluid. The miniaturization of drop volumes is demonstrated by ink jet printing with the 10 ρL cartridge followed by ink jet printing with a 1 ρL cartridge on the same wafer substrate and performing scanning electron microscopy (data not shown) where the radius of the 1 ρL feature is more than twice as small as the radius of the 10 ρL feature. Smaller drop volumes will lead to fine conductive traces required for appropriate feature sizes in photovoltaic and electronic applications and directly address market demands.

Quantum dots were diluted in 53% polypropylene glycol 400, 45% propylene carbonate solution containing 0.01% tetramethyl-5-decyne-4,6-diol, 2,4,7,9-propanol and printed onto a clean silicon wafer (Figure 7) using an optimized waveform.

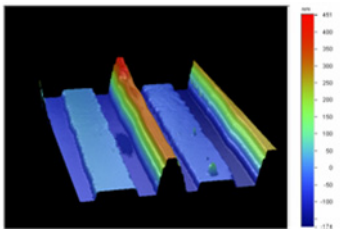

Figure 7: Scanning atomic force image of quantum dots printed on silicon wafer.

Although these particles are identical in synthesis methods and solvent composition, their concentration had a radical effect on their deposition on a silicon wafer substrate. The 2.6 nm quantum dots spread on the substrate whereas the 4.0 nm quantum dots did not spread to the same extent. The thinfilm produced by the 2.6 nm quantum dots was only 50 nm thick whereas the thinfilm produced by the 4.0 nm quantum dots was about 450 nm strongly suggesting that contributions to the final 3D structure of the thinfilm are particle-concentration dependent.

4 CONCLUSIONS

The software interface and waveform tuning allowed fluid process development for a scalable ink jet printing process. Ink jet printing of biologically active, electronic and semiconducting materials is a cost-effective manufacturing process. The printing parameters for these materials have been demonstrated, and the resulting interaction with the substrate demonstrates that ink jet printing is an iterative process where the interplay between the chemical properties of the fluid, the cartridge assembly, the machine operating procedure, the substrate and post-ink jet processing all determine whether this process is viable. Printing of two silver nanoparticle fluids has demonstrated the flexibility of the Dimatix Materials Printer, and these silver nanoparticles were successfully processed into conductive traces. Fluid formulation and ink jet

printing operating parameters are both key to the success of ink jet printing functional materials. Established operating parameters can now be translatable to production line systems with built in versatility, uniformity and scalability for biodevice production. Future directions will be to incorporate ink jet printing with circuit printing and biological fluid deposition for single deposition biodevice processing methods.

REFERENCES

Antoniadis, H. Low-cost solar cells exploiting solar ink. in IEEE San Francisco Bay Area Nanotechnology Council Monthly meeting, 2007. Santa Clara, CA, USA.

Bae, K.D., et al., Development of the new thermal head on SOI wafer. Microelect. Eng, 2005. 78-79: p. 158-163.

Baiesi, M., et al., Zipping and collapse of diblock copolymers. Physical Review E, 2001. 63: p. 41801-41811.

Brünahl, J. and A.M. Grishij, Piezoelectric shear mode drop-on-demand ink jet actuator. Sens. Act. A, 2002, 101:371-382.

Calvert, P., Ink jet printing for materials and devices. Chem. Mater. , 2001. 13: p. 3299-3305.

Diehl, F., et al., Manufacturing DNA microarrays from unpurified PCR products. Nucleic Acids Res., 2002. 30: p. 79-84.

Grishij, Piezoelectric shear mode drop-on-demand ink jet actuator. Sens. Act. A, 2002. 101: p. 371-382.

Haber, C., M. Boillat, and B. van der Schoot, Precise nanoliter fluid handling system with integrated high-speed flow sensor. Assay Drug Dev Technol, 2005. 3(2): p. 203-12.

Hwang, J.S., Solder materials and process for electronic assembly fabrication, in Electronic Assembly Fabrication, chips, circuit boards, packages and components, C.A. Harper, Editor. 2002, McGraw-Hill: New York, NY. p. 305-362.

Lemmo, A.V., D.J. Rose, and T.C. Tisone, Ink jet dispensing technology: applications in drug discovery. Curr. Opin. Biotechnol., 1998. 9: p. 615-617.

Lewis, J.A., et al., Direct ink writing of three-dimensional ceramic structures. J. Am. Ceram. So, 2006. 89: p. 3599–3609.

Manning, H., Application of ink jet technology for miroarrays and other bio printing, in Bioprinting. 2007: London, England.

Mei, J., M.R. Lovell, and M.H. Mickle, Formulation and processing of novel conductive solution inks in continuous ink jet printing of 3-D electric circuits. IEEE Trans. Electron. Packag. Manuf., 2005. 28: p. 265-273.

Menzel, C. MEMS solutions for precision micro-fluidic dispensing application. in NIP20: International Conference on Digital Printing Technologies. 2005. Salt Lake City Utah.

Myatt, C., N. Traggis, and K.L. Dessau, Optical fabrication: optical contacting grows more robust. Laser Focus World, 2006. 42: p. 95-98.

Padinger, F., Biosensors and printed electronics for life sciences, in Bioprinting 2007: London, England.

Peck, W., in-situe microarray manufacturing using ink jet technology at Agilent Technologies, in Bioprinting. 2007: London, England.

Rodriguez-Calvo, M.S., et al., Isolectric focusing of human hair keratins: correlation with sodium dodecyl sulfate-polyacrylamide gel electrophoresis (SDS-PAGE): patterns and effect of cosmetic treatments. J. Forensic Sci., 1992. 37: p. 425-431.

Salas, A., et al., Fluorescent SSCP of overlapping fragments (FSSCP-OF): a highly sensitive method for the screening of mitochondrial DNA variation. Forensic Sci. Inter., 2001. 124: p. 97-103.

Setti, L., et al., An amperometric glucose biosensor prototype fabricated by thermal ink jet printing. Biosensors and Bioelectronics, 2005. 20: p. 2019-2026.

Sawhney, A., et al., Piezoresistive sensors on textiles by ink jet printing and electroless plating. Mater. Res. Symp. Proc., 2006. 920: p. 4-13.

Shaw, J.M. and P.F. Seidler, Organic electronics: Introduction. IBM Journal of Research and Development, 2001. 45(1): p. 3-10.

Sirringhaus, H., et al., High-resolution ink jet printing of all-polymer transistor circuits. Science, 2000. 290(5499): p. 2123-6.

Song, J.H. and H.M. Nur, Defects and prevention in ceramic components fabricated by ink jet printing. Mater. Proc. Technol. , 2004. 155: p. 1286-1292.

Sumerel, J., et al., Cyclin E and its associated cdk activity do not cycle during early embryogenesis of the sea urchin. Dev Biol., 2001. 234(2): p. 425-40.

Sumerel, J., et al., Piezoelectric ink jet processing of materials for medical and biological applications. Biotechnol J, 2006. 1(9): p. 976-87.

Teng, K.F. and R.W. Vest, Metallization of solar cells with ink jet printing and silver metallo-organic inks. IEEE Trans. Compon. Hyb. Manuf. Tech., 1988. 11: p. 291-297.

Volkman, S.K., et al., Ink-jetted silver/copper conductors for printed RFID applications. Mat. Res. Soc. Symps. Proc., 2004. 814: p. 1-6.

Vuorio, A.F., et al., Amplification of the hypervariable region close to the apolipoprotein B gene: application to forensic problems. Biochem. Biophys. Res. Comm. , 1990. 170: p. 616-620.

Wilson, M.R., et al., Validation of mitochondrial DNA sequencing for forensic casework analysis. Int. J. Legal. Med. , 1995. 108: p. 68-74.

Xu, T., et al., Ink jet printing of viable mammalian cells. Biomaterials, 2005. 26(1): p. 93-9.

ELECTRONIC DEVICES FOR RECONSTRUCTION OF HEARING

Albrecht Eiber
Institute of Engineering and Computational Mechanics, University of Stuttgart, Pfaffenwaldring 9, Stuttgart, Germany
eiber@itm.uni-stuttgart.de

Keywords: Hearing devices, mechanical models, sound transfer, feedback, distortion.

Abstract: The effect of specific hearing impairments can be alleviated or compensated using electrically driven hearing aids. There is a broad variety of devices for stimulating the hearing either acoustically, mechanically or electrically. Their applications depend on the type, the severity and the location of a particular impairment. In order to get an optimal reconstruction, additionally to the medical aspects the dynamical behavior of the implant has to be regarded together with the individual situation of the patient simultaneously. Because of the broad variation of individuals and situations, the belonging parameters are time dependent and vary in a wide range, too. Thus, the design of a hearing device must be robust or insensitive against parameter variation and a sensitivity analysis with respect to parameters of the device, variation of anatomy and variation of insertion is needed. By means of mechanical simulation models enhanced by the behavior of the actuator and its control, the dynamical behavior of implants can be calculated and optimized. Such simulations helps to shorten series of experiments in the lab and in clinical practice and guidelines for the designer and for the surgeon can be derived.

1 INTRODUCTION

Hearing is a highly dynamical process, a sound event expressed as fluctuation of pressure in the air acts at the ear drum and excites the three tiny ossicles malleus, incus and stapes to vibrate. Due to the coupling of the stapes footplate, these motions are transmitted to the fluid of the inner ear bringing the basilar membrane in motion. The stereocilia of the inner hair cells are bended and electrical spikes are transferred to the brain by the nerves. For low excitation, the outer hair cells of the organ of Corti are activated serving as an amplifier.

Impairments may have various reasons: mechanical defects in the middle ear like missing ossicles, stiffened ligaments or damaged hair cells in the inner ear. In order to get an appropriate reconstruction, the surgeon must know the mechanical behavior of the available implants, their function and use as well as their dynamical behavior when they are inserted in the body.

2 RECONSTRUCTION

Depending on the specific impairment, several possibilities of reconstruction exist. Conventional devices act at the outer ear canal driving the natural ear acoustically. A mechanical reconstruction may be a simple replacement of a natural structure or a directly driven element of the hearing like an ossicle of the middle ear or the skull. Moreover, a direct electrical stimulation in the inner ear is possible.

Implants replacing missing ossicles are passive mechanical elements. Actively driven devices consist of a microphone, a sound processor, an amplifier, a power source and an actuator. Conventional devices produce an amplified sound pressure applied to the outer ear canal, they can be used in case of intact hearing with moderate hearing loss.

Other implants are imposing mechanical vibrations directly to the middle ear ossicles (middle ear implants, MEI) or to the skull for transferring the sound by structural vibrations to the inner ear (bone anchored hearing aids, BAHA). These implants can be used in case of a sensorineural defect in the inner ear.

Another possibility is to stimulate the nerves of the inner ear electrically via an electrode inserted into the cochlea (cochlear implant, CI) or acting at the brainstem. Such implants work even when the hair cells are inactive or destroyed.

3 ACTIVE MIDDLE EAR IMPLANTS

Depending on the degree of integration into the body, totally and partially implantable hearing aids are distinguished. Further categories are due to the driving principle, the transfer of actuation to the hearing organ, the point of actuation, the manner of coupling to the driven ossicle, the type of suspension to the base and of the location the elements between the force is acting.

3.1 Driving Concept

Two different principles of driving are common: magnetic coils like in classical loudspeakers and piezoelectric elements. Such elements may work in diverse modes of operation like bending effect of beams or discs as well as elongation of staples.

3.2 Force/Displacement Transmission

Due to the transfer of force or displacement from the actuator to the ossicles, the devices can be categorized in groups working with an acoustical coupling via air cushion, hydraulical coupling via fluid in a tube and mechanical coupling.

Principally, an actuator can be attached at an ossicle transferring its forces due to inertial effects of a moved internal mass. This type is called floating mass transducer (FMT) (Hong et al, 2007). It needs a proper coupling to an ossicle.

If such type of actuator is attached to the skull, the sound information is transferred to the inner ear via structural vibrations of the skull and the device is called bone anchored hearing aid (BAHA). It needs a fixed coupling which is maintained by an osseo-integrated screw (Tjellstroem, 1990).

Other actuators are placed between ossicle and temporal bone, they may act even as force transducer or as displacement transducer and need an appropriate coupling at both ends.

3.3 Mechanical Coupling

One of the most important issue in reconstruction is the mechanical coupling of the actuator to the ossicle or/and skull because it governs significantly the dynamical behavior of the reconstructed ear. It is important to which ossicle and at which location the actuator is coupled, in which spatial direction the actuation takes place and how the coupling is maintained.

Coupling of implants to the skull is commonly achieved by means of screws in a mechanical ideal way. More problematic is the connection to an ossicle, it is achieved by gluing, crimping or clamping. In the latter cases, mucosa, fascia or cartilage is present as an intermediate layer between the implant and the ossicle.

The mechanical description of such coupling elements leads to nonlinear force/displacement laws similar to the description of the ligaments or joints. Generally, the relative displacements in the coupling area are smaller than in the joints, but depending on the specific design of coupling, pronounced asymmetry in push-pull direction up to unilateral coupling is possible. Moreover, kinks and discontinuities may occur, leading to distorted sound transfer.

4 MODELS AND MECHANICAL BEHAVIOR

Classical models of the hearing organ have been developed by acoustical or electrical engineers based n electrical analogies. These circuit models are mostly one directional described by scalar differential equations (e.g. Zwislocki, 1963) and it is difficult to describe the three dimensional nature of ossicles motion (Hudde and Weistenhoefer, 1997). Moreover, the parameters of such models are not directly related to the geometrical dimensions or physical quantities like mass and stiffness.

Due to the anatomy of the hearing organ and the function based on the relation between forces and displacements, three-dimensional mechanical models are adequate for description and simulation, well developed modelling techniques like Multibody Systems approach (MBS) or Finite-Element-Method (FEM) are available (Wada et al, 1992; Beer et al, 1999; Gan et al, 2004; Prendergast el al, 1999; Eiber et al, 1999).

The mechanical considerations presented here take into account the spatial arrangement of the

ossicles and their three dimensional motions in a vectorial description. They allow to regard the spatially oriented direction of excitation, the mechanical properties of the coupling of implants and the nonlinear behavior of the coupling region, of the joints and of the ligaments.

In Figure 1, a typical Multibody System model is shown with its rigid bodies malleus, incus and stapes. The ear drum, the air in the outer ear canal and the fluid of the inner ear are modelled as lumped mass points or bodies. The ligaments and the two muscles tensor tympani and musculus stapedius are described as visco-elastic elements with an active part. The model has 83 degrees of freedom and the vector $\boldsymbol{z}$ contains the generalized coordinates. The crucial ones are indicated in the Figure.

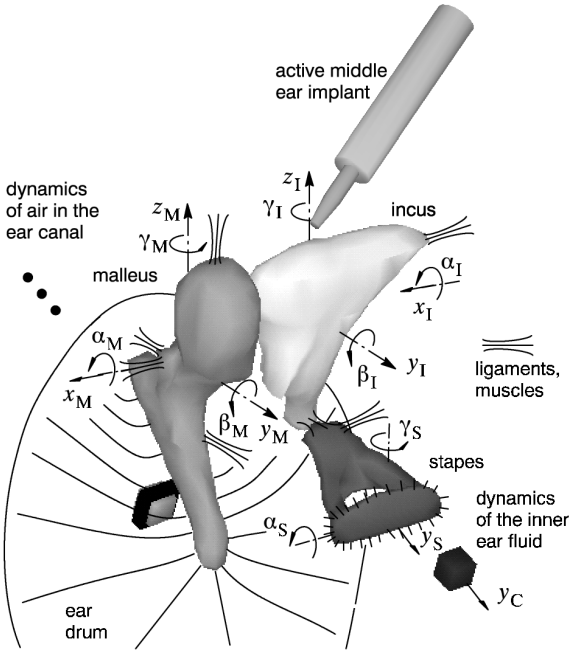

Figure 1: Multibody System model of the middle ear with its adjacent structures and an active middle ear implant acting at the incus.

The dynamical behaviour of the system is described by the equation of motion

$$\boldsymbol{M}(\boldsymbol{z})\cdot\ddot{\boldsymbol{z}}+\boldsymbol{k}(\boldsymbol{z},\dot{\boldsymbol{z}})=\boldsymbol{q}(\boldsymbol{z},\dot{\boldsymbol{z}},t)\,, \qquad (1)$$

where $\boldsymbol{M}$ denotes the mass matrix, $\boldsymbol{k}$ the vector of generalized forces, $\boldsymbol{q}$ the vector of applied generalized forces. Generally, such models are highly nonlinear due to nonlinear coupling elements, i.e. ligaments and joints of ossicles or due to large amplitudes of ossicles´ motion (Eiber and Breuninger, 2004 a). The latter is not the case in the physiological range of hearing (Eiber and Breuninger, 2004 b). Figure 2 shows some typical force/displacement relations of ligaments and joints of the middle ear. Typically, coupling of implants are similar to that of the incudo-stapedial joint with asymmetry and kinks causing a distorted sound transmission.

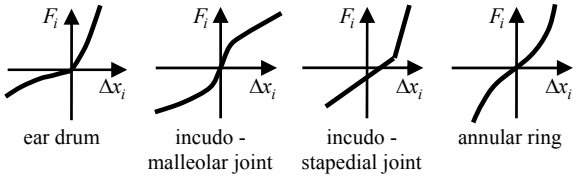

Figure 2: Nonlinear characteristics of middle ear elements.

Static preloads acting at the ossicular chain deflect it to a specific working position $\boldsymbol{y}_{wp}$, where the small physiological sound pressure variations are superposed.

For the investigation of these small variations, the equation of motion (1) can be linearized with respect to $\boldsymbol{y}_{wp}$

$$\boldsymbol{M}(\boldsymbol{y}_{\mathrm{WP}})\cdot\ddot{\boldsymbol{y}}+\boldsymbol{D}(\boldsymbol{y}_{\mathrm{WP}})\cdot\dot{\boldsymbol{y}}+\boldsymbol{K}(\boldsymbol{y}_{\mathrm{WP}})\cdot\boldsymbol{y}=\boldsymbol{h}\,, \qquad (2)$$

where $\boldsymbol{M}$ denotes the mass matrix, $\boldsymbol{D}$ the damping matrix, $\boldsymbol{K}$ the stiffness matrix and $\boldsymbol{h}$ the vector of applied forces. Thus, the dynamical behavior of the chain depends on the working position and shows changed natural frequencies. Such static prestress may occur due to static pressure differences in the outer ear canal, in the middle ear cavity or in the inner ear, due to scar tissues of healing structures or preloads from inserted implants. Particularly active implants with a driving rod acting at the incus need such a preload.

After linearization, the linear equation of motion (2) is valid and frequency domain procedures can be applied to investigate the dynamical behavior represented by the linearized vector $\boldsymbol{y}$. For specific nonlinearities like unilateral constraints or kinks in the force/displacement relation as illustrated in Figure 2, linearization is not possible and there is a distorted sound transfer even for small sound pressure variations.

By means of time-integration the time history of specific stimulations of hearing, in particular of transient sound events, can be investigated based on the equations of motion of the entire system consisting of ossicular chain and the actuator with its control elements.

5 CASE STUDIES

Two different types of hearing aids driven by magnetic coils and piezo elements are considered for the case of totally implantable device. They are very compact but the surgical effort for insertion is very high. In case of partially implantable device the core respectively the magnet are arranged in different positions leading to a simpler surgery process.

5.1 Totally Implantable Hearing Aid

A magnetically driven device on the market is the Otologics Middle Ear Transducer MET (OTOlogics, LLC). All components even the microphone are placed in a cavity of skull behind the ear. The battery is inductively charged once per day. In particular, the actuator is mounted in the mastoid behind the ear canal, it pushes against the ossicular chain by means of a driving rod (Waldmann et al, 2004).

Because of the unphysiological orientation of the actuator, the motion imposed to the stapes contains much higher components of rocking of stapes around its short and the long axis of footplate when compared to the natural hearing. Recent studies revealed the influence of such motions on hearing (Sequeira, 2007).

Coupling of the driving rod with the incus is accomplished by pressing the rod against the ossicle. In order to have a fixed attachment point, a notch has to be burred using a drill or burned using a laser. Mechanically, such a contact is nearly an unilateral constraint, which needs a reasonable preload leading to a pre-stressed ossicular chain. Due to the shifted working point, the middle ear shows higher natural frequencies but in particular, higher amplitudes of the actuator are necessary to achieve the vibrations of stapes which are demanded for compensation of a hearing loss.

As a negative consequence, the malleus and the ear drum are driven with larger amplitudes, too, radiating sound into the outer ear canal. Picked up by the microphone, this sound may lead to ringing effects because of a loop. Such effects have been observed particularly on implants driven by piezoelectric actuators.

Thus, depending on nonlinear behavior of the chain and the coupling, even powerful actuators are not able to compensate a severe hearing loss.

For optimizing a reconstruction, the entire system of ossicular chain, the particular impairment, the characteristics of implant and its coupling to the chain has to be regarded. A very sensitive entity in the function is the adjustment of the actuator with respect to the skull during surgery, which defines the applied preload (Rodriguez Jorge et al, 2006), (Eiber et al, 2007).

In Figure 3, the mechanical model of the considered actuator is sketched showing the adjustment of the device relative to the skull and the inner stiffness between the mass of housing frame and the driven mass. For a magnetically driven actuator, this stiffness is relatively low in comparison to the piezo actuator.

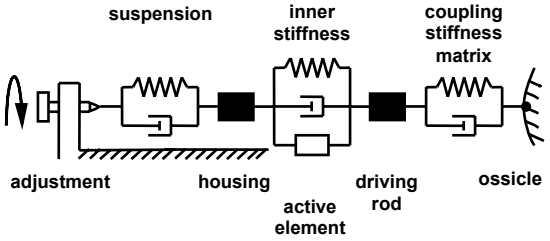

Figure 3: Model of actuator attached at the ossicle and the skull.

Concerning the two driving principles there are significant differences. The piezo elements can produce high forces imposing prescribed displacements to the chain. But due to its high inner stiffness, such devices show a high sensitivity against the adjustment of preload given by the surgeon during insertion and also against static pressure variations during daily use.

Therefore, a relatively high preload is commonly applied by the surgeon, which leads to extremely shifted working points with the effects of feedback and distortion as described above. On the other hand, ligaments exhibit a time dependent mechanical behavior. In a long time range they elongate under static load in a creeping effect releasing the imposed preload.

Due to the lower internal stiffness, the implants driven by magnetic coils are less sensitive against variations in static pressure or preload. But even in this case, the sensitivity against adjustment travel as shown in Figure 3 remains and is crucial for the surgeon. A high preload stiffens the chain and requires higher force amplitudes with a significant sound radiation by the ear drum as a consequence. Modelling this feed back loop allows a stability analysis and the calculation of a gain margin. It defined as the maximal allowed amplification so that the system is still stable. This amplification can be used to compensate a hearing impairment of the inner ear. In Figure 4 this gain margin is shown qualitatively for various adjustment travel a_0 and it

becomes clear, that there is a trade-off between a good coupling and the risk of feedback particularly in the lower frequency range. For that calculation, the microphone was placed in the mastoid at the posterior wall of the outer ear canal.

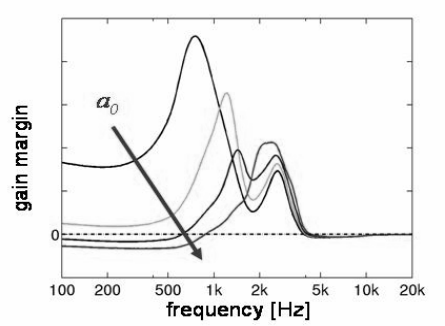

Figure 4: Gain margin for different travels of adjustment screw. Increasing adjustment cause higher static preload. A negative gain margin signifies risk of ringing.

Totally implantable hearing aids are a very elegant reconstruction because there is no obvious stigmatization of the patient. They are technically sophisticated devices, their insertion is challenging for the surgeon and needs some experience.

5.2 Partially Implantable Hearing Aid

In order to reduce the surgical effort, parts of the active hearing aid are placed outside the skull like in conventional devices. Another concept is to separate the coil of actuator from the core.

In a current project, the placement of a permanent magnet at the manubrium driven by a magnetic coil placed behind the ear is investigated as illustrated in Figure 5.

That concept ensures the kinematical unconstrained motion of the ossicular chain free of static preload. The chain is able to find its natural working position and the actuator can work at this particular position.

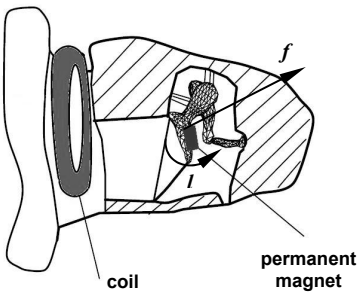

Figure 5: Partially implantable hearing aid with separated coil and magnet. Force $\boldsymbol{f}$ and torque $\boldsymbol{l}$ imposed to the magnet.

Depending on the orientation of the magnetic field and the direction of magnetization of the permanent magnet, there is a moment superposed to the force acting at the magnet to drive the ossicular chain in a quite physiological way. The position and the mass of the magnet influence both the dynamical behavior of the chain and the applied force effects. Based on mechanical models of the chain together with Finite Element models of the electrical part, an optimization of the components could be accomplished. First tests in the lab show an easy and safe procedure to couple the magnet at the malleus handle using an elastic clip. This is a mechanically stable coupling, which guaranties a perfect transfer of forces from the magnet to the ossicle.

6 CONCLUSIONS

Mechanical models serve as a base for simulating the hearing process and for the design of active hearing implants. Three-dimensional models are able to describe the complex spatial motion of the ossicular chain and their relation to the forces and moments applied by an implanted hearing aid. A crucial point is the coupling of implants to the natural structures of the ear, which is governed by nonlinear force/displacement relations. As a consequence, the transmitted forces are limited leading to an incomplete compensation of hearing loss, the transfer of sound may be distorted leading to a bad sound discrimination due to higher overtones or the gain of amplification must be restricted to avoid ringing due to feedback.

Due to their close relation to the anatomy, mechanical models give a better insight into the dynamic behavior of the middle ear than electrical circuit models. Multibody system models with a low number of degrees of freedom are well suited to describe the global behavior of systems regarding their nonlinear properties and to design the mechanical part of hearing implants. Finite Elemente models with a high number of degrees of freedom are capable to describe distributed properties like magnetic fields and mechanical stress. Simulations with mechanical models facilitate an optimization during design of hearing aids and may shorten the clinical trial and error process.

ACKNOWLEDGEMENTS

On this work participated Dipl.-Ing. C. Breuninger and several students financed by the German Research Council (DFG).

REFERENCES

Beer, H.J., Bornitz, M., Hardtke, H.J., Schmidt, R., Hofmann, G., Vogel, U., Zahnert, T., Huettenbrink, K.B., 1999. Modelling of Components of the Human Middle Ear and Simulation of Their Dynamic Behaviour. *Audiology and Neuro-Otology*. 4: 156 -162.

Eiber, A., Freitag, H.-G., Burkhardt, C., Hemmert, W., Maassen, M., Rodriguez Jorge, J., Zenner, H.-P., 1999. Dynamics of Middle Ear Prostheses - Simulations and Measurements. In *Audiology and Neuro-Otology*. 4: 178 - 184.

Eiber, A., Breuninger, C., 2004 a. *Mechanical Problems in Human Hearing*. Proceedings in Applied Mathematics and Mechanics, Vol. 4, No. 1, p. 51 - 54. http://www.wiley-vch.de

Eiber, A., Breuninger, C., 2004 b. *Nonlinear Properties of the Middle Ear: Some Influences on Hearing and Diagnosis.* In: *Gyo, K., Wada, H. (eds), Middle ear Mechanics in Research and Otology, p. 19 - 28* . World Scientific. Singapore.

Eiber, A., Breuninger, C., Rodriguez Jorge, J., Zenner, H.-P., Maassen, M., 2007. *On the Optimal Coupling of an Implantable Hearing Aid – Measurements and Simulations.* In: *Huber, A., Eiber, A. (eds), Middle ear Mechanics in Research and Otology, p. 246 - 252.* World Scientific. Singapore.

Gan, R.Z., Feng, B., Sun, Q., 2004. Three-Dimensional Finite Element Modelling of Human Ear for Sound Transmission. *Annals of Biomedical Engineering.* 32, (6): 847 – 859.

Hudde, H., Weistenhoefer, C., 1997. A Three-Dimensional Circuit Model of the Middle Ear. *Acustica united with Acta Acustica.* 83, (3): 535 – 549.

Hong, E.-P., Kim, M.-K., Park, I.-Y., Lee, S.-H., Choi, J.-H., 2007. Vibration Modeling and Design of Piezoelectric Floating Mass Transducer for Implantable Middle Ear Hearing Devices. *IEICE Transactions on Fundamentals of Electronics, Communications and Computer Sciences.* 90, (8):1620 - 1627.

OTOlogics LLC, Boulder.
http://www.otologics.com/

Prendergast, P.J., Ferris, P., Rice, R.J., Blayney, A.W., 1999. Vibro-acoustic modelling of the outer and middle ear using a finite-elemente method. *Audiol Neurootol,* 4, 185 – 191.

Rodriguez Jorge, J., Pfister, M., Zenner, H.-P., Zalaman, I., Maassen, M., 2006. In Vitro Model for Intraoperative Adjustments in an Implantable Hearing Aid (MET). In *Laryngoscope,* 116, 246 - 252.

Sequeira, D., Breuninger, C., Eiber, A., Huber, A., 2007. *The Effect of Complex Stapes Motion on the Cochlea in Guinea Pigs.* In: *Huber, A., Eiber, A. (eds), Middle ear Mechanics in Research and Otology, p. 130 - 135.* World Scientific. Singapore.

Suzuki, J. I. (ed), 1988. *Middle Ear Implant: Implantable Hearing Aids*, Karger. Basel.

Tjellstroem, A., 1990. Osseointegrated implants for replacement of absent or defective ears. *Clinics in Plastic Surgery,* 17: 355 – 365.

Wada, H., Metoki, T., Kobayashi, T., 1992. Analysis of dynamic behavior of human middle ear using finite-elemente-analysis. *J Acoust Soc Am*. 96: 3157 - 3168.

Waldmann, B., Maier, H.,Leuwer, R., 2004. *Nonlinear Properties of the Middle Ear: Some Influences on Hearing and Diagnosis.* In: *Gyo, K., Wada, H. (eds), Middle ear Mechanics in Research and Otology, p. 377-383.* World Scientific. Singapore.

Zwislocki, J., 1963. Analysis of the Middle-Ear Function. Part II: Guinea Pig Ear. *J Acoust Soc Am.* 35, (7), 1034 - 1040.

METHODOLOGY AND SYSTEM OF EVALUATING THE DRIVER'S VIGILANCE LEVEL IN AN AUTOMOBILE TRANSPORTATION EXAMINING BOTH PHYSIOLOGICAL AND MECHANICAL DATA

A. Giusti, C. Zocchi and A.Rovetta
Politecnico di Milano, Piazza Leonardo da Vinci 32, Milan, Italy
alessandro.giusti1@polimi.it ,chiara.zocchi@polimi.ti, alberto.rovetta@polimi.it

Keywords: Sleep-attack, vigilance level, physiological and mechanical data, automobiles.

Abstract: This paper deals with the methodology followed in order to design a new intelligent system to improve the driver's safety in an automobile transportation and the actual realization of a first prototype. The results of the study are reported. A simulator system has been developed at the Robotics Laboratory of the "Politecnico di Milano". A description of the necessary hardware and architecture is made in detail. Driver's physiological data, acquired from sensors on the wheel, is correlated, using statistical multivariate analysis, with his/her vigilance level evaluated using polysomnography. This statistical model is applied on the data off-line in order to define a controller, to be applied on real time acquired data. The platform's mechanical data is also acquired and studied. All the elaboration of the data results in one vigilance level index for the current driver and situation. Future steps and possibilities are also discussed.

1 INTRODUCTION

Many projects in European Union (EU) programs are devoted to the increase of safety in automobiles, in order to reduce deaths and accidents down to 50% in the next few years (Istat, 2001) Project PSYCAR (Psycho physiological Car) funded by EU in a Regional plan, starting from Lombardy Italian Region and Austrian Region, is one of these projects. The "Politecnico di Milano" university, along with the Linz Kepler University cooperated in the development of the project.

Apart from these EU programs, almost all automobile industries are studying new methods to improve active safety. Most of these methods are based on examining the engine's mechanical and the car's dynamical parameters or on camera vision systems continuously monitoring the driver (Citroen, 2007, Seat, 2006). Nevertheless, the greatest disadvantage of such systems lies on the fact that a possible driver's head turning or lowering can be a huge problem for the camera's view and so can put the whole system out of order. In addition to that, the high complexity of vision software can add financial and technical obstacles in the system. Such systems have been proposed by BMW and SEAT. Mercedes-Benz is also working on the same direction according to a recent article (Omniauto, 2006).

The methodology presented by this paper is innovative for the field of automotive safety. Its innovation lies on the fact that all the driver's physiological parameters are acquired using sensors on the wheel, which are continuously in contact with the driver's body. The driver does not have to do anything in particular or, in any mode, different from what he is used to do when entering and driving his/her vehicle, as in other safety systems (Saab, 2006, Gizmag, 2005). Intelligent sensor placement is fundamental for the system's applicability. A possible loss of contact with the driver's body, is by itself a safety decrease information, because can only mean that the driver has taken his hands off the wheel. Several car's dynamical and mechanical parameters are also acquired and evaluated. This combination of the car's behaviour with the driver's physiological state is another innovation presented by this paper and the future of automotive safety may lie on this combination. The system also stores all the data acquired in order to self- improve with time, using

neural network techniques which will be implemented in the next phase of the project.

The output of the system proposed by this paper is a vigilance level index, easily interpreted by the driver. Indices can be collected and can be sent to a centre of suggestions, in a tele-assistance shape (Rovetta, 1995).

2 SELECTION OF THE PHYSICAL PARAMETERS TO BE MEASURED

Since the number of parameters to measure in such a system is enormous, a very important part of the procedure is the selection of the right parameters to measure (Zocchi, 2005, Rovetta, 2005). The physiological parameters that can be measured and that can determine the driver's condition and ability to drive are not so categorically determined.

A large scale research has been done through years by numerous universities and research teams, to define the physiological and neurological parameters that can determine a possible drop in the person's vigilance level. Using the results from these researches, a selection of the necessary sensors is made. Based on that, blood pressure, cardiac and respiratory frequencies, hand trembling, galvanic skin resistance, heart rate variability, body temperature, blood alcohol and oxygen concentration and cerebral waves are physiological parameters that can possibly detect a person's neurophysiologic state (Rovetta, 2001).

Two different sets of parameters are chosen to be measured. The discrimination is made because of the fact that some parameters are measured only to determine the driver's attention level and are used only in the research phase as an index to which the second set of the parameters is correlated. The second set consists of the parameters that will continue to be used on the real cars, and that obviously are only the signals from the sensors on the wheel.

The first set consists of the polysomnography parameters along with the driver's reaction time. A medical team is assisting the Robotics Laboratory of the Politecnico di Milano team in acquiring all these parameters and also in their interpretation. The polysomnography parameters acquired are presented in the table (Table 1) and they are used as an index of the driver's attention, to which all the other acquired parameters are correlated.

The second set of measured parameters consists of the driver's Galvanic Skin Resistance (GSR), Heart Rate Variability (HRV) and body temperature (THE), which are measured using sensors on the wheel.

Table 1: The physical parameters acquired with the medical equipment.

Polysomnographical parameters acquired
Electro- Cardio- Graph (EKG)
Electro- Encephalo- Graph (EEG), 4 channels
Electro- Oculo- Graph (EOG), 2 channels
Chin Electro- Myo- Graph (EMG)
Peripheral Body Temperature (THE)
Nasal Pressure
Blood Oxygen Concentration
Respiratory Frequencies, 2 channels

3 SIGNAL ACQUISITION, CONDITIONING AND DATA STORING

In order to collect the GSR (Galvanic Skin Resistance), THE (Peripheral Body Temperature) and HRV (Heart Rate Variability) signals from the steering wheel, a portable system has been developed by the ELEMAYA Company, on demand. For the GSR, two silver plates are used and the skin's galvanic resistance is measured across them. For the HRV signal a photoplethysmographic sensor is used, while for the THE a simple thermocouple is used. All these signals are filtered and amplified by the same ELEMAYA system. The A/D converter is a National Instruments DAQ-card 6062E. All electronic board aspects were studied (Klaassen, 1996, O'Dell, 1991, Sangwine, 1994, Doebelin, 2004). The digitization of the signals is made at a sampling frequency of 200Hz, following the Nyquist criteria.

The data from the mechanical platform is acquired using a PC and a C program. The program is the same that simulates the road and the car movement. The sampling rate was set to 65 Hz. The data analysis was concentrated on the straight parts of the road, since the turning highly depends on each driver's ability to drive and in addition to that it highly unlikely that someone falls asleep when turning. In addition to that, the data acquired during the driver's attempt to avoid the appearing obstacles was also neglected.

Especially for the calculation of the error in the car's position, the ideal position that the driver had to follow was the right lane of the circuit that corresponded to constant y position in the Cartesian coordinates space. Based on this, the error that the driver made was calculated as the difference from the ideal position. The error data was normalized for each driver separately to eliminate as much as possible the interference of each person's driving capacity and style. In this way, the final available data for analysis were vectors containing for each driver the normalized error in the car's position.

The polysomnographical hardware used consists of a portable medical apparatus capable of acquiring all the necessary signals. The analysis of these signals determines the driver's status. In total, these signals are 37 and are presented in Table 1. The software for this polysomnographical acquisition is the Madcare's Somnological Studio. The software is capable of saving all the acquisition session data in one and only European Data Format file (.edf), which then is converted into a simple ASCII text file, using the NeuroTraces edfAsc program. These text files are loaded and examined in MATLAB. The sampling rate frequency is set to 200 Hz.

The polysomnographical and mechanical platform signals are automatically filtered, while the signals from the steering wheel are first filtered by the acquisition system, using hardware, and then by software because of their specific needs. In particular, for the HRV signal the cut off frequency has been set to 10 Hz, for the GSR to 0.1 Hz and for the THE to 0.8 Hz. For determining the correct cut-off frequencies for every signal, medical advises has been followed and Fourier analysis has been made.

Steering wheel signals data storing is made using MATLAB data acquisition files (.daq). These files are easily handled by MATLAB and also allow storing the exact acquisition start time and date. All the data is stored in one matrix, where every column array corresponds to one sensor and every row array corresponds to one sampling session (1/200 sec.). The data from the mechanical platform is stored in simple text files.

4 PROTOCOL FOR THE SIMULATION SYSTEM

The simulations are made on two different driver conditions. In the first part, the driver has slept during the last night, while in the second he/ she has been awake for twenty-four hours. In the first state the nominal conditions of the person are evaluated, while in the second the altered ones. During the tests made with the driver not having slept, when sleep is detected while he/she is undertaking the simulation, the driver is waken up. In this way, the transition phases are better examined. The simulations are always made in dark and noiseless conditions in order for the person to have much more possibilities to fall asleep or to lose attention.

Before starting the data acquisition, a questionnaire is completed by the person responsible for the simulation, on which the date, the time and environmental conditions are written. The car at the start of every simulation session is always positioned at the same point of the virtual circuit. Each subject, before driving on the simulation for the first time is also trained to use the simulator and to always follow the same pre-defined route.

After these initial procedures, the driver starts the simulation and the data acquisition is also initialized. During the procedure and in pre-defined times that the subject does not know, an obstacle appears on the screen and the driver has to push the brake. In this way, his/her reaction time is measured and stored among all the other parameters acquired. This response time along with the data from the polysomnography signals (Rovetta, 1997, Pinelli 1998) determine his/her attention level.

5 OFF-LINE ANALYSIS. STATISTICS ON THE ACQUIRED DATA

At the end of every simulation data from both the sleepy subjects and the control group is divided in three categories, as shown in table 2.

The purpose of the statistical analysis is to find a relation between all the measured parameters and the driver's vigilance level decrease. The index of the driver's vigilance is measured by studying the EEG signals and the driver's reaction time to the appearing obstacles. These analyses focus on two different directions. First, the general behaviour of the signals as the driver moves towards sleepiness is studied. Then, the behaviour of the same signals the exact minute before a sleep-attack is studied. The exact time of a sleep-attack is determined, using EEG Power Spectral Density (PSD) analysis and medical experience.

For the EEG PSD analysis, after studying all the possible solutions, the $\alpha+\beta$ (Eoh, 2005) cerebral waves method is chosen as the most appropriate

method. After determining the exact time of the sleep-attack, all the data from the minute before this sleep-attack is divided in ten-second intervals and analyzed statistically. This procedure is necessary for also studying the exact time interval before the sleep-attack in which some interesting phenomena occur.

Table 2: The signals acquired during the driving simulations for evaluation and statistical analyses.

Physiological data from the steering wheel	**Mechanical data from the simulator**	**Reference data**
HRV	Steering wheel position	Polysomnographical signals
GSR	Accelerator pedal position	Reaction time
THE	Brake pedal position	
	Car's position on the road	
	Car's speed	

The stored data is statistically analyzed using MATLAB (ver. 7, rev. 14). The observed phenomenon is not linear and so a standard linear analysis is not adequate. Multivariate analysis is used in order to identify categories of input that are related to a certain output index.

Different analysis types are used to determine all the necessary statistical parameters. First an analysis is made based on simple mean value and variation observation for every signal acquired and every different driver condition status. In addition, correlation and cross-correlation matrices are calculated to determine a possible correlation of one acquired parameter to another, but also to correlate all the acquired parameters with the driver's safety index, derived from the polysomnographical data.

Furthermore, a cluster analysis is made on the data, in order to investigate grouping in the data, simultaneously over a variety of scales, by creating a cluster tree that is not a single set of clusters, but rather a multi-level hierarchy, where clusters at one level are joined as clusters at the next higher level. This allows deciding what level or scale of clustering is most appropriate in the application. Discriminant analysis, also used and applied on the data, determines one ore more parameters that better discriminate two populations.

The data from the mechanical platform is also analyzed in the same way. The results of these analyses are presented on the appropriate section of this article.

6 REAL-TIME PROCEDURE

The off-line statistical procedure is useful for setting up the real-time system prototype. In this prototype, the only parameters acquired are the non-invasive ones (GSR, THE, HRV) with the sensors on the steering wheel and also the data from the mechanical platform (Table 2). Together with the data, the driver's ID is also stored. In this way, the system becomes personalized and will be in a later phase trained based on the driver's personal characteristics. The driver's ID is obtained by his key, in a real car, or by a password, on the simulator. The saved data is in this phase also used for calculating the mean values of the heart beats number and the steering wheel's standard deviation values, needed for normalizing the data.

All the parameters enter a Fuzzy logic classifier that, based on the statistical results made off-line, determines if the driver has a high possibility of being sleepy. Practically, the classifier continuously monitors the acquired data in order to determine a possible movement of the driver versus sleep. If the driver is found to be probably sleepy, then the system is put into alertness in order to focus on detecting a possible sleep attack and alert the driver.

The simulator system program uses a MATLAB function to call the fuzzy system and calculate the safety index as well as for retrieving the important parameters for every signal. This is because the signals do not enter directly the Fuzzy classifier, but first need a small elaboration. For example, in order to retrieve the heart beats per minute number from the HRV signal.

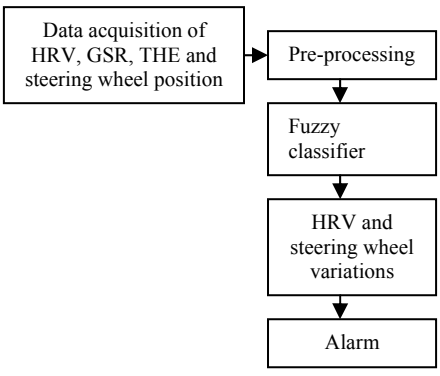

Figure 1: Real-time procedure flow diagram.

As shown in figure 1 (Fig.1), if the classifier detects a high possibility of sleepiness, then the system stays alert for monitoring the heart beats number variations as well as the steering wheel position variations. If high standard deviation values are detected in the heart beats signal or very low standard variations in the steering wheel position signal, the system alerts the driver with a sound. The thresholds were chosen to be 10 beats for the heart beats number and 0.5 in the normalized steering wheel position standard deviation. This procedure was chosen according to the results reported in section 7.

7 RESULTS

By observing the data acquired during simulations made with persons that did sleep during the night before, some interesting facts on their mean GSR value can be noticed. The more difficult the driving conditions, the lower the GSR values. The skin's galvanic resistance is inversely proportional to its perspiration and so this result means that the driver skin's perspiration is higher when the driving conditions are difficult (curved circuit, fast car speed). This also means that the driver is more vigilant when the simulation conditions are difficult, because of the fact that the skin's perspiration is inversely proportional to the person's relaxation (Hancock, 1996). Examined from another point of view, the lower the GSR value, the more vigilant the driver. The raise of the GSR can be quite important, even ten times higher than the normal value for every person.

In addition to that, the number of heart beats per minute decreases in sleepy subjects. Generally, as a driver moves towards sleepiness his/her number of heart beats decreases, something that was expected as this phenomenon is common knowledge in medicine. Finally, the THE value tends to drop slowly as the subject get sleepy, but only of a few decimals.

Using this information the fuzzy logic classifier was designed and trained. Afterwards, some driving simulations were made and the output of the classifier was compared with the actual vigilance level of the driver, defined by the medical analyses. The results show a success of 60,68% to 79,61% and are shown in figure 2 (Fig.2).

Apart from these observations concerning the general behaviour of the chosen parameters towards sleepiness, the most important results concern the analysis of the data the minute before a sleep attack. In these analyses the heart beats number and the steering wheel position signals presented some very interesting behaviour.

So, the heart rate generally tends to drop but the most important thing noticed is that it presents some significant variations twenty to thirty seconds before the microsleep (Fig.3). At least in 76% of the cases these variations were present. The percentage can improve using a lower threshold value.

Finally, very small standard deviation values were observed in the error in the car's position (Table 3) as well as in the steering wheel position. The error the driver is making was calculated as the difference from the ideal position of the car on the road. Each driver has his/her own driving style and so his/her own mean error values. The data were normalized using these values. The important thing noticed is that during the minute before the microsleep the standard deviation value of the error made is much lower that usual and so is the standard deviation value of the steering wheel's position. This implies that, even if the driver is driving far from the ideal position he/she is not moving the wheel as usually does. This phenomenon was observed in 87,5% of the cases and can be augmented by lowering the threshold value by only a little.

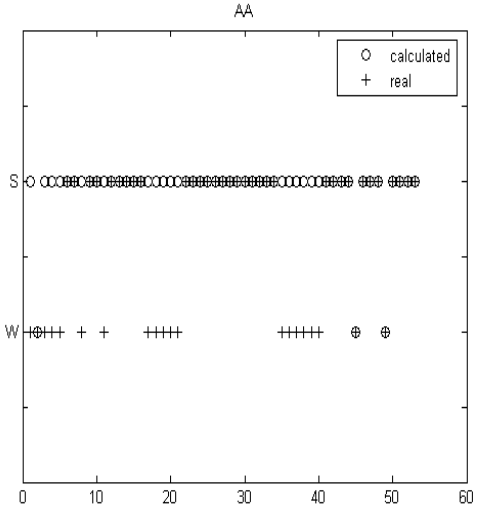

Figure 2: Confrontation between calculated and real sleepiness level for 52 epochs with two sleepiness levels. The '+' symbols present the real sleepiness level while the 'o' ones present the calculated value for every epoch. For every epoch, when the '+' and the 'o' symbols coincide the result is considered successful.

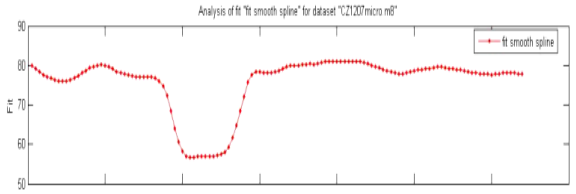

Figure 3: High variations in the heart beats number 40 seconds before a sleep-attack. The plot shows a B-spline polynomial fit for a subject's heart beat data. The number of beats per minute vary from 55 to 80.

Table 3: A subject presenting very low standard deviation values in the steering wheel's movement, in respect to his usual value. The six cells correspond to the six 10-second intervals before the sleep-attack. The 6th interval are the final 10 seconds before the sleep attack.

	1	2	3	4	5	6
Mean	2.9958	1.1638	1.1764	0.9943	1.0264	1.1572
Std_var	2.8497	*0.2137*	*0.0908*	*0.0822*	*0.2035*	*0.1555*

8 FUTURE STEPS

A study on the applicability of neural networks to the system described is in progress at the Politecnico di Milano's Laboratory of Robotics. The idea is to use all the data acquired during a driving session along with the current driver's identity in order to adapt the system to each particular driver. This will be made at the end of every driving session, when the engine stops, in order to ensure that the system's real time speed is not affected by this procedure. The neural network shall be used to re-train the fuzzy logic controller and make the system better with time.

9 CONCLUSIONS

The results of the research here discussed are promising. A control strategy based on the fuzzy classifier and a controller that monitors the heart beats number and the steering wheel position could be applied for determining a high risk of sleep attack and alert the driver.

The decrease in the heart beats number and the peripheral body temperature, as well as the increase in the GSR value are indicators of sleepiness that could set the system into a general alert status. These phenomena have a quite slow progress and so they can only be used as pre-cursors of sleepiness and not of an actual sleep-attack, which is a very fast phenomenon (3-15 seconds). On the other hand, the standard deviation values of the steering wheel position and the heart beats number occur very fast and permit an early notification of the driver, since the phenomenon occurs usually 20- 30 seconds before the sleep-attack. The standard deviation value of the error in the car's position cannot be used in an actual car, as the ideal position is unknown but is a useful parameter in simulated driving sessions (For example if using this system in driving licence exams).

The methodology discussed and proposed by this paper among with the constructed simulation prototype is innovative for the field of safety in automobiles and is used in a daily basis to acquire more data for the statistical analysis and the fuzzy controller set-up. The final tests on a real car will prove the applicability of the safety system discussed and its capability to cover with the maximum safety the drivers all over the world.

ACKNOWLEDGEMENTS

Thanks to Dr. Fanfulla and his medical team for their help on valuating the polysomnographical data as well as for their clinical advices. Thanks to all the partners making suggestions such as Centro Stile Alfa, Elasis, Brembo, Alcatel, Cefriel, Magneti Marelli, STM, and particularly Fondazione Politecnico for planning further research, together with Regione Lombardia.

REFERENCES

Istat, 2001. Statistica degli incidenti stradali. Retrieved Oc14, 2007 from, http://www.istat.it/salastampa/comunicati/non_calendario/20051013_00/novita_editoriale_incidenti _stradali_2004.pdf.

Citroen, 2007. Lane Departure Warning System – LDWS. Retrieved October 14, 2007 from http://www.citroen.com/cww/enus/technologies/security/afil/

Seat, 2006. Nuevos euipamientos. Retrieved on June 16, 2007 from http://media.seat.com/view_manager.html?root=35,40

Omniauto, 2006. Mercedes contro il Colpo di Sonno. Retrived on October 14, 2007 from http://www.omniauto.it/magazine/2219/mercedes-contro-il-colpo-di-sonno.

Saab, 2006. Saab AlcoKey Helps Drivers Steer Clear of Drinking and Driving. Retrieved on October 14, 2007 frohttp://www.saabvideos.com/2006/10/11/saab-

alcokey-helps-drivers-steer-clear-of-drinking-and-driving/
Gizmag, 2005. Volvo experimenting with new safety features. Retrieved on October 14, 2007 from http://www.gizmag.com/go/4448/
Rovetta, A., Cosmi, F., 1995. Teleoperator Response in a touch task with different display conditions. IEEE Transaction on System, Man and Cybernetics, vol 25.
Zocchi, 2005. Report and Tables with sensors and characters. Retrieved on October 14, 2007 from ftp://robo55.mecc.polimi.it
Rovetta, 2005. Report on Parameters to be identified in automotive Environment. Retrieved on October 14, 2007 from ftp://robo55.mecc.polimi.it
Rovetta A., 2001. Biorobotics: an Instrument for an Improved Quality of Life. An Application for the Analysis of Neuromotor Diseases. Int. Conf. Proceedings On Automation and Robotics.
Klaassen, K., 1996. Electronic measurement and instrumentation. Cambridge University Press.
O'Dell, T., 1991. Circuits for electronic instrumentation. Cambridge University Press.
Sangwine, 1994. Electronic Components and technology. CRC press.
Doebelin, E., 2004. Measurement Systems : Applications and Design. Mc Graw Hill.
Rovetta, A., 1997. Detection and Multimodal Analysis of Brain Weak Signals to Study Brain Funtion and Disease. European Union Workshop.
Pinelli P., Baroni L., Zara D., Battaglia S., 1998. Impairment of Delay Verbal Reactions in Dementia. Advances in Occupational Medicine and Rehabilitation, vol. 4, no. 3, pp. 87-93.
Eoh, J., Chung M., Kim, S., 2005. *Electroencephalographic study of drowsiness in simulated driving with sleep deprivation.* International Journal of Industrial Ergonomics vol. 35, pp. 307–320
Hancock, P., Parasuraman, R., 1996. Driver-Centred Issues in Advanced Automation for Motor Vehicles, pp 337-364.

AUTHOR INDEX

AUTHOR INDEX (CONT.)

AUTHOR INDEX (CONT.)

Proceedings of BIODEVICES 2008
International Conference on Biomedical Electronics and Devices
ISBN: 978-989-8111-17-3